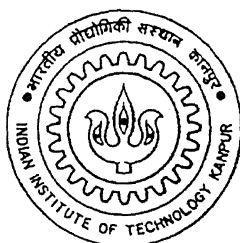


EXPERIMENTAL STUDY OF CONVECTION IN DIFFERENTIALLY HEATED FLUID LAYERS USING LASER INTERFEROMETRY

A Thesis Submitted
In Partial Fulfilment of the Requirements
for the Degree of
Doctor of Philosophy

by

Sunil Punjabi



to the
DEPARTMENT OF MECHANICAL ENGINEERING
INDIAN INSTITUTE OF TECHNOLOGY KANPUR
INDIA

September, 2002

23 SEP 2003 / ME

पुरुषोत्तम
भारतीय प्रौद्योगिकी संस्थान दिल्ली
नया दिल्ली 110029

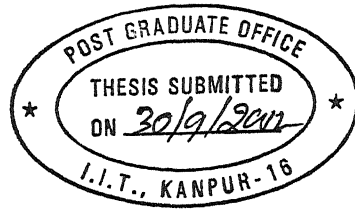
145044



A145044

To

My Loving Parents



Certificate

It is certified that the work contained in the thesis entitled **Experimental study of convection in differentially heated fluid layers using laser interferometry** by Sunil Punjabi, has been carried out under our supervision and that this work has not been submitted elsewhere for a degree.

K Muralidhar

K. Muralidhar

Department of Mechanical Engineering
IIT Kanpur

P. K. Panigrahi

P. K. Panigrahi

Department of Mechanical Engineering
IIT Kanpur

September, 2002

Acknowledgements

It is indeed a great moment for me to express my sincere gratitude, regards and thanks to my supervisors Dr. K. Muralidhar and Dr. P. K. Panigrahi for their excellent guidance and immeasurable help. I am indebted to them for the support they have provided during the difficult phase of my thesis work. Their encouragement and faith in me has been the constant source of inspiration ever since I entered the exciting field of experimental research.

I am specially thankful to Mr. S. N. Sharma and Mr. Rajesh Singh for working day and night for the fabrication of the experimental test cells and other accessories employed for experimentation.

I thank Ms. Anamika Sethia and Mr. Atul Srivastava for the useful technical discussions during the course of my thesis work.

I am thankful to Mr. Andallib Tariq, Mr. Debashis Karmakar, Mr. Jyotirmay Banerjee, Mr. Sushanta Dutta and Mr. Atul Sharma for helping me to overcome all technical difficulties during my thesis work.

I am grateful to Dr. Debasish Mishra, Dr. Arun Saha, Dr. Tanuja Sheorey and Mr. N. G. Ghata for their initial support.

The new entrants to the Fluid mechanics laboratory namely Mr. Atanu Phukan, Mr. Arvind Rao, Mr. Malay Das and Mr. Arnab Dey helped me during the course of thesis work. I express my thanks to them.

The services rendered by Mr. Amit Agarwal, Mr. Rajneesh Bhardwaj and Mr. Kapil Varshney are also acknowledged.

I am thankful to Dr. B. K. Singh and other faculty members of my parent institute, Engineering College Ujjain, for their help and cooperation.

My wife Shilpi and my son Shubham has been a great source of inspiration. They motivated me time to time and created an excellent environment in the home front. I express my indebtedness towards them.

I have been supported by the QIP scheme run by Ministry of HRD, Govt. of India for pursuing higher studies. I take this opportunity to thank them for providing the financial assistance.

Last, but not the least the blessings of my parents and all other well wishers has helped me to accomplish the task.

Sunil Punjabi

Abstract

An experimental study of buoyancy-driven convection in superposed fluid layers is reported. Combinations of air and water, air and silicone oil, and silicone oil floating over water have been considered. The grade of silicone oil employed in the experiments is 50 cSt. Fluid layers are confined between two horizontal isothermal plates and the enclosure is heated from below and cooled from above. The thermal configuration leads to a modified form of the Rayleigh-Benard problem, that has been widely studied in the literature for theoretical as well as practical reasons. The thermal fields in the individual fluid layers have been mapped using a Mach-Zehnder interferometer.

Two cavities of different overall geometry have been designed and fabricated for performing the experiments. These are: (i) a cavity rectangular in plan and square in cross-section and (ii) a cavity octagonal in plan. The latter approximates a circular cavity and permits viewing the flow field from various directions. The two cavities are expected to bring out the dependence of post-critical Rayleigh-Benard convection on the geometry of the confining surfaces. Three layer heights in the rectangular and equal layer heights in the circular cavity have been examined during the experiments. The flow field in the circular cavity has been scanned through four different view angles namely 0, 45, 90, and 135° for generating the projection data. The cavity dimensions are such that they constitute intermediate aspect ratio enclosures ($A = 5 - 10$).

The overall temperature difference across the two walls has been decided on the basis of the expected flow regimes in the cavity. Both steady and unsteady three-dimensional flows have been permitted to occur in the two fluid layers. A large range of Rayleigh numbers from as low as 25 to as high as $10E+06$ in the respective fluid layers has been explored. A majority of Rayleigh numbers considered are well beyond the first critical point of instability. The nature of the convective fields, their coupling and the deformation of the interface have been addressed in the present work. The loss of symmetry in the thermal field of the circular cavity has been examined using a tomographic reconstruction technique. For the range of parameters studied, surface tension and its

gradient at the fluid-fluid interface are of secondary importance.

In the air-water experiments reported for the rectangular cavity, the fluid layers are found to be thermally coupled at the interface. However, unsteadiness noticed in air at higher Rayleigh numbers is linked to the destabilizing influence of water via the mechanical coupling mode. In air-silicone oil experiments, the field-of-view in air is seen to be completely bright, while straight fringes occurred in oil at very low Rayleigh number. Convection in oil leads to incipient convection in air at a subcritical Rayleigh number of 1100. A time-dependent flow in air is realized at a Rayleigh number higher than 12,900. The fluid layers are found to be thermally coupled for small layer heights of silicone oil. In silicone oil-water experiments, the conductivity ratio determines the Rayleigh number ratio in the cavity and hence the flow regimes. In general, the convective flow in water is retarded owing to the stabilizing influence of silicone oil floating over water. This is indicative of the flow to be mechanically coupled at the interface. The interface temperature and the width-averaged Nusselt number match well with the single fluid correlations at lower Rayleigh numbers and wherever the coupling is thermal in origin. Larger discrepancies are seen when the layers are mechanically coupled and beyond the onset of unsteadiness. The interface deformation is uniformly small in all the experiments. The movement of interfaces and oscillation of light streaks in the shadowgraph indicate the presence of three dimensional effects in the experiments involving water.

In the circular cavity, the fluid layers of air and water show a degree of axisymmetry in the thermal field at a lower Rayleigh numbers. With an increase in the Rayleigh number, three dimensionality is seen to be dominant in water while axisymmetry still persists in air. With a further increase in the Rayleigh number, a dynamic steady-state is observed. In the air-oil experiments, Ω -shaped fringe patterns indicating steady two dimensional thermal field is obtained in the oil layer. Axisymmetry in the thermal field in oil is seen to increase with that in the Rayleigh number, with the Ω -roll shifting towards the center. In the oil-water experiments, \cup -shaped isotherms in oil and a distorted thermal field in water has been noticed. At very high Rayleigh numbers, steady three dimensional flow in oil and time-dependent flow in water are realized. The experimental interface temperature match the estimated temperature from single fluid correlations fairly well for all fluid combinations. Discrepancy in the Nusselt number is seen at higher Rayleigh numbers in fluid layers that involve water. For all fluid combinations, the layers have been found to be thermally coupled. Tomographic reconstruction show the loss of symmetry in the thermal field, in particular in water at higher Rayleigh numbers. The reconstruction also shows a plume structure near the axis of the cavity. The interface deformation is uniformly small in all the experiments.

Contents

Certificate	iii
Acknowledgements	vii
Abstract	ix
List of Figures	xvii
List of Tables	xxxv
Nomenclature	xxxix
 1 Introduction	 1
1.1 Buoyancy-driven flow	1
1.2 Two-layer convection	3
1.3 Engineering applications	7
1.4 Optical methods	11
1.5 Objectives of the present work	14
1.6 Thesis organization	14
 2 Literature Survey	 17
2.1 One-layer convection	18
2.2 Two-layer convection	30

2.2.1	Theoretical aspects of two-layer convection	32
2.2.2	Combined experimental and theoretical studies in two-layer convection	48
2.3	Closure	62
3	Apparatus and Instrumentation	65
3.1	Description of the experimental apparatus	66
3.1.1	Rectangular cavity	66
3.1.2	Axisymmetric cavity	68
3.2	Design of the test cells	70
3.3	Range of parameters	73
3.4	Experimental procedure	76
3.5	Instrumentation	78
3.5.1	Mach-Zehnder interferometer	79
3.5.2	Shadowgraph	80
3.5.3	Laser source	81
3.5.4	CCD camera	81
3.5.5	Pneumatic isolation mount	82
3.5.6	Constant temperature bath	82
3.5.7	Temperature recorder	83
3.6	Alignment of the interferometer	83
3.7	Recording interferometric projections	87
4	Data Reduction	89
4.1	Interferometry	89
4.1.1	Refraction effects	93
4.2	Evaluation of interferograms	98

4.3	Temperature data over a grid	101
4.4	Image processing	101
4.4.1	Filtering of images	103
4.4.2	Image enhancement	106
4.4.3	Fringe thinning	108
4.5	Local and global heat transfer rates	114
4.6	Interface temperature from correlations	116
4.7	Calculation of interface shape	117
4.8	Benchmarking	120
4.8.1	Convection in a cavity filled with air	120
4.8.2	Convection in a cavity filled with water	124
4.9	Tomography	127
4.9.1	Convolution backprojection	129
4.10	Uncertainty and measurement errors	132
5	Two-layer Convection in a Rectangular Cavity	137
5.1	Air-water experiments	138
5.1.1	Cavity filled 2/3rd with water	138
5.1.2	Cavity filled with equal layer heights of air and water	144
5.1.3	Cavity filled 1/3rd with water	149
5.1.4	Temporal evolution	153
5.2	Air-silicone oil experiments	158
5.2.1	Cavity 2/3rd filled with silicone oil	158
5.2.2	Cavity filled with equal layers of air and silicone oil	164
5.2.3	Cavity 1/3rd filled with silicone oil	169
5.3	Silicone oil-water experiments	173

5.3.1	Cavity 2/3rd filled with silicone oil	173
5.3.2	Cavity filled with equal layers of silicone oil and water	178
5.3.3	Cavity 2/3rd filled with water and 1/3rd oil	183
5.3.4	Temporal evolution	187
5.4	Nature of coupling	189
5.5	Flow characteristics at comparable Rayleigh numbers	192
5.6	Interface deformation	195
5.7	Closure	201
6	Two-layer Convection in a Circular Cavity	203
6.1	Air-water experiments	205
6.1.1	Steady state thermal field	206
6.1.2	Transient evolution of thermal field	211
6.1.3	Three dimensional structures	214
6.1.4	Interface deformation	220
6.2	Air-silicone oil experiments	220
6.2.1	Steady state thermal field	223
6.2.2	Three dimensional structures	229
6.3	Silicone oil-water experiments	239
6.3.1	Long-time thermal field	239
6.3.2	Three dimensional structures	244
6.3.3	Unsteady thermal field	251
6.3.4	Interface deformation	256
6.4	Nature of coupling	257
6.5	Closure	257

7	Conclusions and Scope for Future Work	261
7.1	Conclusions	261
7.1.1	Rectangular cavity	262
7.1.2	Circular cavity	263
7.2	Scope for future work	264
	References	265
A	Fast Fourier Transform Algorithm	273
B	Numerical study of buoyancy-driven convection in air-water layers	279
B.1	Numerical solution	280
B.1.1	Effect of surface-tension on the shape of the free surface	281
B.2	Comparison of results	282
B.2.1	Convection in an air-filled cavity	282
B.2.2	Convection in a water-filled cavity	285
B.2.3	Convection in superposed air-water layers	287
B.2.4	Deformation of the air-water interface	294
B.3	Conclusions	295

List of Figures

1.1	Schematic drawing of Rayleigh-Benard convection in a differentially heated fluid layer.	2
1.2	Aspect ratios of a differentially heated fluid layer.	2
1.3	Schematic drawing of the flow-coupling mechanism in two-layer convection.	6
1.4	Schematic drawing of two-layer mantle convection (Schubert <i>et al.</i> (2001)).	8
1.5	Schematic drawing of Czochralski technique, after Prasad <i>et al.</i> (1997).	8
1.6	Schematic drawing of crystal growth from its aqueous solution.	9
1.7	Mixing of hot and cold water streams in a steam generator in the presence of a free surface.	10
1.8	Schematic drawing of Cumulus clouds (Scorer, 1972).	10
2.1	Experimentally recorded regimes in Rayleigh-Benard convection, after Krishnamurti (1970a, 1970b).	19
2.2	Shadowgraph observations of spoke pattern convection in a layer of methyl alcohol ($Pr = 7$) with increasing Rayleigh numbers from (a) to (d), after Busse (1980).	22
2.3	Summary of Flow Transitions in Rayleigh-Benard Convection, after Mishra (1998).	28
2.4	Streamline (top) and temperature (bottom) contours at various temperature gradients, after Koster and Nguyen, 1996.	39
2.5	Comparison of critical Marangoni numbers versus aspect ratio for various modes for the case of $Ra = 100$ and $Bi = 1$ in (a) Zaman and Narayanan (1996) with the experiments of (b) Koschmieder and Prahl (1990).	42

2.6	Interferograms (left) and isotherms from numerical simulation (right) in superposed layers of silicone oil 100 cSt over ethylene glycol. For experiments, $(Ra/Ra_c)_t=0.9$ and $(Ra/Ra_c)_b=5.9$, and for simulation $(Ra/Ra_c)_t=0.3$ and $(Ra/Ra_c)_b=9.9$, after Prakash and Koster (1996b).	54
2.7	Schematic drawing of the codimension-2 point, after Johnson and Narayanan (1996).	55
2.8	Interferograms (top) and roll patterns (bottom) that show mechanical coupling in silicone oil 4.6cSt floating over Fluorinert FC-70, after Prakash <i>et al.</i> (1997).	58
2.9	Plot of the bounded, linear calculations made with an insulating, no-slip radial wall, after Johnson <i>et al.</i> (1999).	61
3.1	Schematic drawing of a rectangular test cell to study convection in superposed fluid layers.	67
3.2	Schematic drawing of an axisymmetric test cell to study convection in superposed fluid layers (All dimensions are in mm).	69
3.3	Complete view of the experimental setup to study convection in superposed fluid layers.	70
3.4	Schematic drawing of the traversing mechanism.	73
3.5	Schematic drawing of thermal loading patterns in a two-layer system seen in numerical calculations and experiments.	78
3.6	Schematic drawing of the Mach-Zehnder interferometer.	80
3.7	Infinite fringe setting of the Mach-Zehnder interferometer.	85
3.8	Candle flame seen in the infinite fringe setting of the interferometer. . . .	86
3.9	Wedge fringe setting of the interferometer.	86
3.10	Candle flame seen in the wedge fringe setting of the interferometer. . . .	87
3.11	Infinite fringe setting in the axisymmetric cavity containing fluid layers of (a) air and water, (b) air and silicone oil, and (c) silicone oil floating over water.	87
3.12	Definition of a view angle.	88

3.13 Schematic drawing to show projection angles of 0 (left) and 45° (right) for the nominally axisymmetric test cell.	88
4.1 Calculation of the bending angle of a light ray due to refraction effects. .	94
4.2 Bending of a light ray in the fluid medium due to refraction effects. . . .	95
4.3 Calculation of the fringe temperature from an idealized fringe skeleton. .	99
4.4 An original interferogram recorded with a CCD camera in air.	104
4.5 Two dimensional Fourier transform of the intensity function.	105
4.6 Schematic drawing of a one dimensional band pass filter.	105
4.7 Original and Fourier-filtered intensity distributions.	106
4.8 Filtered Interferogram	106
4.9 Contrast-improved Interferogram	107
4.10 Interferogram with sharpened edges (edge enhancement).	108
4.11 Two major directions for tracing of fringes.	110
4.12 Four possible turning options for fringes.	111
4.13 Eight possible directions for movement.	111
4.14 (a) Filtered and contrast improved interferogram. (b) Thinned image obtained using the automatic fringe thinning algorithm.	113
4.15 (a) Thinned image obtained by the paint-brush method. (b) Superimposed thinned image with original image.	114
4.16 A thin liquid film rests upon a heated solid surface.	118
4.17 Thermal fluctuations occur within the film, resulting in temperature inhomogeneties along the interface.	118
4.18 The interfacial tension gradients drive flow in the bulk liquid phase, creating cellular convection patterns.	119
4.19 The buoyancy driven instabilities generates flow in the bulk liquid phase, creating cellular convection patterns.	119

4.20	Long-time isotherms (a) and the corresponding roll patterns (b) in a cavity filled with air; cavity temperature difference is 10 K.	121
4.21	Transient evolution patterns in air for a cavity temperature difference of 10 K; time interval between two successive interferograms is 30 minutes. .	123
4.22	(a) Temperature profiles at three columns along the width of the cavity and (b) local Nusselt number variation at the two walls for a cavity filled with air; Cavity temperature difference is 10 K.	124
4.23	Steady state interferograms in a cavity filled with air; cavity based temperature differences are (a) 2 K, (b) 4 K, and (c) 7 K.	125
4.24	Long-time interferogram obtained for a cavity filled with water; cavity temperature difference is 10 K.	126
4.25	Transient evolution of fringe patterns in water for a cavity temperature difference of 10 K; time interval between two successive interferograms is 5 seconds.	126
4.26	Long-time interferograms in a cavity filled with water; cavity based temperature differences are (a) 1.4 K and (b) 5.3 K.	127
4.27	Nomenclature for the convolution backprojection algorithm.	131
5.1	Long-time interferograms (a,b,c) and the corresponding roll patterns in the side view (a1,b1,c1) for air-water system. Cavity 2/3rd filled with water. Temperature differences are (a) 10 K, (b) 15 K and (c) 18 K. Layer Rayleigh numbers are marked on the right column.	140
5.2	Depth-averaged temperature profiles in a cavity 2/3rd filled with water in air-water experiments; Cavity temperature differences are (a) 10 K, (b) 15 K and (c) 18 K.	142
5.3	Local Nusselt number variation at the hot and the cold walls of the cavity 2/3rd filled with water in air-water experiments; Cavity temperature differences are (a) 10 K, (b) 15 K and (c) 18 K.	143
5.4	Long-time interferograms (a,b,c) and the corresponding roll patterns in the side view (a1,b1,c1) for a cavity half-filled with water, the rest being air; Cavity temperature differences are (a) 10 K, (b) 15 K and (c) 18 K. Layer Rayleigh numbers are marked on the right column.	145

5.5	Depth-averaged temperature profiles in a cavity half filled with water in air-water experiments; Cavity temperature differences are (a) 10 K, (b) 15 K and (c) 18 K.	147
5.6	Local Nusselt number variation at hot and cold walls in a cavity half filled with water in air-water experiments; Cavity temperature differences are (a) 10 K, (b) 15 K and (c) 18 K.	148
5.7	Long-time interferograms (a,b,c) and the corresponding roll patterns in the side view (a1,b1,c1) for air-water system in a cavity 1/3rd filled with water; Cavity temperature differences employed are (a) 10 K, (b) 15 K and (c) 18 K. Layer Rayleigh numbers are marked on the right column. .	150
5.8	Depth-averaged temperature profiles in a cavity 1/3rd filled with water in air-water experiments; Cavity temperature differences employed are (a) 10 K, (b) 15 K and (c) 18 K.	151
5.9	Local Nusselt number variation at the hot and cold walls of the cavity 1/3rd filled with water; Cavity temperature differences employed are (a) 10 K, (b) 15 K and (c) 18 K.	152
5.10	Time sequence of interferograms in a cavity 2/3rd filled with water for a cavity temperature difference of 15 K; air-water experiments. Time interval = 20 seconds between successive images.	154
5.11	Time sequence of interferograms in a cavity 2/3rd filled with water for a cavity temperature difference of 18 K; air-water experiments. Time interval = 10 seconds between successive images.	155
5.12	Time sequence of interferograms in a cavity half filled with water for a cavity temperature difference of 15 K; air-water experiments. Time interval = 1 minute between successive images.	156
5.13	Time sequence of interferograms in a cavity half filled with water for a cavity temperature difference of 18 K; air-water experiments. Time interval = 30 seconds between successive images.	157
5.14	Steady state interferograms (a) and the corresponding roll patterns in the side view (a1) in a cavity 2/3rd filled with silicone oil. Cavity temperature difference is 0.3 K. Layer Rayleigh numbers are marked on the right column.	159

- 5.15 (a) Depth-averaged temperature profile and (b) local Nusselt number variation in a cavity 2/3rd filled with oil in air-oil experiments; Cavity temperature difference is 0.3 K. 160
- 5.16 Steady state interferograms (a,b,c) and the corresponding roll patterns in the side view (a1,b1,c1) in air for a cavity 2/3rd filled with silicone oil. Cavity temperature differences are (a) 10 K, (b) 15 K and (c) 18 K. Layer Rayleigh numbers are marked on the right column. 161
- 5.17 Depth-averaged temperature profile in the air layer of a cavity 2/3rd filled with oil; Cavity temperature differences are (a) 10 K, (b) 15 K and (c) 18 K. 163
- 5.18 Local Nusselt number variation at the cold wall in air. Cavity 2/3rd filled with oil; Cavity temperature differences are (a) 10 K, (b) 15 K and (c) 18 K. 164
- 5.19 Steady state interferograms in a cavity filled with equal layer heights of air and silicone oil. Cavity temperature difference is 0.3 K. Layer Rayleigh numbers are marked on the right side. 165
- 5.20 (a) Depth-averaged temperature profile and (b) local Nusselt number variation at the hot wall in a cavity filled with equal fluid heights in air-oil experiments; Cavity temperature difference is 0.3 K. 165
- 5.21 Steady state interferograms (a,b,c) and the corresponding roll patterns in the side view (a1,b1,c1) in air for a cavity filled with equal layer heights of silicone oil and air. Cavity temperature differences are (a) 10 K, (b) 15 K and (c) 18 K. Layer Rayleigh numbers are marked on the right column. 166
- 5.22 Depth-averaged temperature profile in air for a cavity filled with equal layer heights of air and oil; Cavity temperature differences are (a) 10 K, (b) 15 K and (c) 18 K. 168
- 5.23 Local Nusselt number variation at the cold wall in air for a cavity filled with equal layer heights of air and oil; Cavity temperature differences are (a) 10 K, (b) 15 K and (c) 18 K. 168
- 5.24 Steady state interferograms in a cavity 1/3rd filled with silicone oil. Cavity temperature difference is 0.3 K. Layer Rayleigh numbers are marked on the right side. 169

- 5.25 (a) Depth-averaged temperature profile in oil and (b) local Nusselt number variation at the hot wall in a cavity 1/3rd filled with oil; Cavity temperature difference is 0.3 K. 170
- 5.26 Steady state interferograms (a,b,c) and the corresponding roll patterns in the side view (a1,b1,c1) in air for a cavity 1/3rd filled with oil, the rest being air. Cavity temperature differences are (a) 10 K, (b) 15 K, and (c) 18 K. Layer Rayleigh numbers are marked on the right column. 171
- 5.27 Air-silicone oil experiments with $Ra(\text{air}) = 15,193$. The sequence of fringe patterns (1,3,5) and the corresponding roll patterns (2,4,6) formed during the switching phenomenon: Unicellular pattern (1,2) tricellular pattern (3,4) and a return to unicellular rolls (5,6) are to be seen. 172
- 5.28 Steady state interferograms (a) and the corresponding roll patterns in the side view (a1) in a cavity 2/3rd filled with silicone oil in oil-water experiments; Cavity temperature difference is 0.3 K. Layer Rayleigh numbers are marked on the right column. 174
- 5.29 (a) Depth-averaged temperature profile and (b) local Nusselt number variation at the two walls in a cavity filled with 2/3rd oil and 1/3rd water; Cavity temperature difference is 0.3 K. 175
- 5.30 Steady state interferograms (a,b,c) and the corresponding roll patterns in the side view (a1,b1,c1) in water for a cavity filled with 2/3rd silicone oil and 1/3rd water. Cavity temperature differences are (a) 10 K, (b) 15 K and (c) 18 K. Layer Rayleigh numbers are marked on the right column. . 176
- 5.31 Depth-averaged temperature profile in water in a cavity filled with 2/3rd oil and 1/3rd water; Cavity temperature differences are (a) 10 K, (b) 15 K and (c) 18 K. 178
- 5.32 Local Nusselt number variation at the hot wall in a cavity filled with 2/3rd oil and 1/3rd water; Cavity temperature differences are (a) 10 K, (b) 15 K and (c) 18 K. 178
- 5.33 (a) Steady state interferograms and (a1) the corresponding roll patterns in a cavity filled with equal layer heights of silicone oil and water; Cavity temperature difference is 0.3 K. Layer Rayleigh numbers are marked on the right column. 179

- 5.34 (a) Depth-averaged temperature profile and (b) local Nusselt number variation at the two walls in a cavity filled with equal layer heights of oil and water; Cavity temperature difference is 0.3 K. 180
- 5.35 Steady state interferograms (a,b,c) and the corresponding roll patterns in the side view (a1,b1,c1) in water for a cavity filled with equal layer heights of silicone oil and water. Cavity temperature differences are (a) 10 K, (b) 15 K and (c) 18 K. Layer Rayleigh numbers are marked on the right column. 181
- 5.36 Depth-averaged temperature profile in the water portion in a cavity filled with equal layer heights of oil and water; Cavity temperature differences are (a) 10 K, (b) 15 K and (c) 18 K. 182
- 5.37 Local Nusselt number variation at the hot wall in a cavity filled with equal layer heights of oil and water; Cavity temperature differences are (a) 10 K, (b) 15 K and (c) 18 K. 182
- 5.38 (a) Steady state interferograms and (b) corresponding roll patterns in a cavity filled with 1/3rd silicone oil and 2/3rd water; Cavity temperature difference is 0.3 K. Layer Rayleigh numbers are marked on the right column. 184
- 5.39 (a) Depth-averaged temperature profile and (b) local Nusselt number variation at the two walls in a cavity filled with 1/3rd oil and 2/3rd water; Cavity temperature difference is 0.3 K. 184
- 5.40 Steady state interferograms (a,b,c) and the corresponding roll patterns (a1,b1,c1) in water for a cavity filled with layer heights of 1/3rd silicone oil and 2/3rd water. Cavity temperature differences are (a) 10 K, (b) 15 K, and (c) 18 K. Light streaks are possibly inter-roll boundaries. 185
- 5.41 Depth-averaged temperature profile in water for a cavity filled with layer heights of 1/3rd oil and 2/3rd water; Cavity temperature differences are (a) 10 K, (b) 15 K and (c) 18 K. 186
- 5.42 Local Nusselt number variation at the hot wall in a cavity filled with 1/3rd oil and 2/3rd water; Cavity temperature differences are (a) 10 K, (b) 15 K and (c) 18 K. 187
- 5.43 Time sequence of interferograms in water for a cavity temperature difference of 18 K; silicone oil-water experiments with equal layer thicknesses. Time interval between two successive images is 15 seconds. 188

- 5.44 Time sequence of interferograms in water for a cavity temperature difference of 18 K; silicone oil-water experiments with 2/3rd water and 1/3rd oil in the cavity. Time interval between two successive images is 5 seconds. 189
- 5.45 Comparison between experiment (left column) and reference (right column) for the cavity temperature difference as a function of the temperature drop across the upper fluid layer for all fluid combinations and layer heights. 191
- 5.46 Interferograms obtained in air in a cavity containing layers of (a) 1/3 air and 2/3 water, $\Delta T = 15$ K and (b) 1/3 air and 2/3 oil, $\Delta T = 15$ K. . . . 193
- 5.47 Interferograms obtained in air in a cavity containing layers of (a) 1/2 air and 1/2 water, $\Delta T = 10$ K and (b) 1/2 air and 1/2 oil, $\Delta T = 10$ K. . . . 193
- 5.48 Interferograms obtained in water in a cavity containing layers of (a) 1/2 air and 1/2 water, $\Delta T = 15$ K and (b) 1/3 water and 2/3 oil, $\Delta T = 10$ K. 193
- 5.49 Interferograms obtained in water in a cavity containing layers of (a) 1/3 air and 2/3 water, $\Delta T = 18$ K and (b) 1/2 water and 1/2 oil, $\Delta T = 10$ K. 194
- 5.50 Interferograms obtained in oil in a cavity containing layers of (a) 1/2 air and 1/2 oil, $\Delta T = 0.3$ K and (b) 2/3 water and 1/3 oil, $\Delta T = 0.3$ K. . . 194
- 5.51 Interferograms obtained in oil in a cavity containing layers of (a) 1/3 air and 2/3 oil, $\Delta T = 0.3$ K and (b) 1/2 water and 1/2 oil, $\Delta T = 0.3$ K. . . 195
- 5.52 Interface deformation in a cavity for equal layer heights consisting of air-water (a-b), air-oil (c-d), and oil-water (e-f) respectively; Cavity temperature difference of 0 (a,c,e) and 18 K (b,d,f) imposed across the cold (top) and hot (bottom) walls. Deformed interfaces are emphasized in black. The vertical scale is for y/h 196
- 5.53 Interface deformation in a cavity 2/3rd filled with water in air-water experiments; Cavity temperature differences are (a) 5 K, (b) 10 K, (c) 15 K and (d) 22 K. Deformed interfaces are emphasized in black. 197
- 5.54 Interface deformation in a half-filled cavity in air-water experiments; Cavity temperature differences are (a) 5 K, (b) 10 K, (c) 15 K and (d) 22 K. Deformed interfaces are emphasized in black. 198

5.55	Moving interface in water for a cavity temperature difference of 18 K; silicone oil-water experiments with equal layer thicknesses. Time interval between two successive images is 15 seconds. Moving interfaces are emphasized in black.	199
5.56	Moving interface in water for a cavity temperature difference of 18 K; silicone oil-water experiments with layer thicknesses of 2/3rd water and 1/3rd oil. Time interval between two successive images is 5 seconds. Moving interfaces are emphasized in black.	200
6.1	Roll formation in (a) rectangular and (b) circular cavities, after Velarde and Normand (1980), at moderate Rayleigh numbers.	205
6.2	Idealized isotherms in orthogonal viewing of (a) rectangular and (b) circular cavities, corresponding to the rolls in Figure 6.1.	205
6.3	Interferograms obtained at steady state in the cavity containing air and water for a temperature difference of 6.5 K. View angles considered: (a) 0° and (b) 90°	207
6.4	Initial (a) wedge fringe setting and (b) wedge fringes during convection obtained in the water layer at a temperature difference of 6.5 K; View angle considered is 0°	208
6.5	(a) Depth-averaged temperature profiles and (b) local Nusselt number variation at the interface in a cavity half filled with water, the rest being air; Cavity temperature difference is 6.5 K.	208
6.6	Long-time interferograms obtained in the axisymmetric cavity containing air and water for a temperature difference of 8.5 K. View angles considered are (a) 0° and (b) 90°	210
6.7	(a) Depth-averaged temperature profiles and (b) local Nusselt number variation at the interface in a cavity half filled with water, the rest being air; Cavity temperature difference is 8.5 K.	211
6.8	Transient evolution of fringe patterns in the cavity containing air and water. View angle considered is 0° , and the cavity temperature difference is 13 K. Time in hr:min.	212

6.9	Transient evolution of fringe patterns in the cavity containing air and water. View angle considered is 90° , and the cavity temperature difference is 13 K. Time in hr:min.	213
6.10	Long-time interferograms obtained in a cavity filled with air and water for a temperature difference of 6.5 K. View angles are (a) 0° , (b) 45° , (c) 90° and (d) 135°	215
6.11	Long-time interferograms obtained in a cavity filled with air and water for a temperature difference of 8.5 K. View angles are (a) 0° , (b) 45° , (c) 90° and (d) 135°	216
6.12	Projection data in water at three horizontal planes along the width of the cavity. Cavity half-filled with water, the rest being air for a temperature difference of 6.5 K.	216
6.13	Projection data in water at three horizontal planes along the width of the cavity. Cavity half-filled with water, the rest being air for a temperature difference of 8.5 K.	217
6.14	Consistent projection data in water at three horizontal planes along the width of the cavity. Cavity half-filled with water, the rest being air for a applied temperature difference of 6.5 K.	217
6.15	Consistent projection data in water at three horizontal planes along the width of the cavity. Cavity half-filled with water, the rest being air for a applied temperature difference of 8.5 K.	217
6.16	Reconstructed temperature contours in the water layer. Cavity is half-filled with water, the rest being air. Temperature differences are 6.5 K (a,c,e) and 8.5 K (b,d,f) respectively at lower, mid and upper planes of the cavity.	218
6.17	Possible roll formation in a circular cavity.	219
6.18	Interferograms obtained in water in the cavity containing half filled water, the rest being air at $\Delta T = 18$ K; Time interval between two consecutive images is 1 minute.	221
6.19	Deformed interfaces in the cavity half-filled with water, the rest being air; $\Delta T = 18$ K; Time interval between two consecutive images is 1 minute. Interfaces are emphasized in black.	222

6.20 Interferograms obtained at steady state in the cavity containing air and silicone oil for a temperature difference of 0.4 K. View angles considered: (a) 0° and (b) 90°	223
6.21 (a) Depth-averaged temperature profiles and (b) local Nusselt number variation at the hot wall in a cavity half-filled with silicone oil, the rest being air; Cavity temperature difference is 0.4 K.	224
6.22 Interferograms obtained at steady state in the cavity containing air and silicone oil for a temperature difference of 1.8 K. View angles considered: (a) 0° and (b) 90°	225
6.23 (a) Depth-averaged temperature profiles and (b) local Nusselt number variation at the hot wall in a cavity half-filled with silicone oil, the rest being air; Cavity temperature difference is 1.8 K.	226
6.24 Interferograms obtained at steady state in the containing air and silicone oil for a applied temperature difference of 3.1 K. View angles considered: (a) 0° and (b) 90°	227
6.25 (a) Depth-averaged temperature profiles and (b) local Nusselt number variation at the hot wall in a cavity half-filled with silicone oil, the rest being air; Cavity temperature difference is 3.1 K.	227
6.26 Interferograms obtained at steady state in the cavity containing air and silicone oil for a temperature difference of 4.0 K. View angles considered: (a) 0° and (b) 90°	228
6.27 (a) Depth-averaged temperature profiles and (b) local Nusselt number variation at the hot wall in a cavity half-filled with silicone oil, the rest being air; Cavity temperature difference is 4.0 K.	228
6.28 Interferograms in a cavity filled with air and silicone oil; Cavity temperature difference is 0.4 K. View angles are (a) 0° , (b) 45° , (c) 90° and (d) 135°	230
6.29 Interferograms in a cavity filled with air and silicone oil; Cavity temperature difference is 1.8 K. View angles are (a) 0° , (b) 45° , (c) 90° and (d) 135°	230

6.30 Interferograms in a cavity filled with air and silicone oil; Cavity temperature difference is 3.1 K. View angles are (a) 0° , (b) 45° , (c) 90° and (d) 135°	231
6.31 Interferograms in a cavity filled with air and silicone oil; Cavity temperature difference is 4.0 K. View angles are (a) 0° , (b) 45° , (c) 90° and (d) 135°	231
6.32 Interferograms in a cavity filled with air and silicone oil; Cavity temperature difference is 5.4 K. View angles are (a) 0° , (b) 45° , (c) 90° and (d) 135°	232
6.33 Interferograms in a cavity filled with air and silicone oil; Cavity temperature difference is 8.5 K. View angles are (a) 0° , (b) 45° , (c) 90° and (d) 135°	232
6.34 Projection data in oil at three horizontal planes along the width of the cavity. Cavity half-filled with silicone oil, the rest being air for a temperature difference of 0.4 K.	233
6.35 Projection data in oil at three horizontal planes along the width of the cavity. Cavity half-filled with silicone oil, the rest being air for a temperature difference of 1.8 K.	234
6.36 Projection data in oil at three horizontal planes along the width of the cavity. Cavity half-filled with silicone oil, the rest being air for a temperature difference of 3.1 K.	234
6.37 Projection data in oil at three horizontal planes along the width of the cavity. Cavity half-filled with silicone oil, the rest being air for a applied temperature difference of 4.0 K.	234
6.38 Consistent projection data in oil at three horizontal planes along the width of the cavity. Cavity half-filled with silicone oil, the rest being air for a temperature difference of 0.4 K.	235
6.39 Consistent projection data in oil at three horizontal planes along the width of the cavity. Cavity half-filled with silicone oil, the rest being air for a temperature difference of 1.8 K.	235

6.40	Consistent projection data in oil at three horizontal planes along the width of the cavity. Cavity half-filled with silicone oil, the rest being air for a temperature difference of 3.1 K.	235
6.41	Consistent projection data in oil at three horizontal planes along the width of the cavity. Cavity half-filled with silicone oil, the rest being air for a temperature difference of 4.0 K.	236
6.42	Reconstructed temperature contours in the oil layer in the cavity half-filled with silicone oil, the rest being air at temperature differences of 0.4 K (a,c,e) and 1.8 K (b,d,f) respectively at lower, mid- and upper planes of the cavity.	237
6.43	Reconstructed temperature contours in the oil layer in the cavity half-filled with silicone oil, the rest being air at temperature differences of 3.1 K (a,c,e) and 4.0 K (b,d,f) respectively at lower, mid- and upper planes of the cavity.	238
6.44	Long-time interferograms obtained in the cavity containing silicone oil floating over water for a applied cavity temperature difference of 0.4 K. View angles considered: (a) 0° and (b) 90°.	241
6.45	(a) Depth-averaged temperature profiles and (b) local Nusselt number variation at the interface in a cavity filled with equal layer thicknesses of silicone oil and water; Cavity temperature difference is 0.4 K.	241
6.46	Long-time interferograms obtained in the cavity containing silicone oil floating over water for a cavity temperature difference of 1.8 K. View angles considered: (a) 0° and (b) 90°.	242
6.47	(a) Depth-averaged temperature profiles and (b) local Nusselt number variation at the cold wall in a cavity filled with equal layer thicknesses of silicone oil and water; Cavity temperature difference is 1.8 K.	243
6.48	Local Nusselt number variations at the hot wall in a cavity filled with equal layer thicknesses of silicone oil and water; Cavity temperature differences are (a) 0.4 K and (b) 1.8 K.	244
6.49	Long-time interferograms in a cavity filled with silicone oil and water; Cavity temperature difference is 0.4 K. View angles are (a) 0°, (b) 45°, (c) 90° and (d) 135°.	246

- 6.50 Long-time interferograms in a cavity filled with silicone oil and water; Cavity temperature difference applied 1.8 K. View angles are (a) 0° , (b) 45° , (c) 90° and (d) 135° 247
- 6.51 Long-time interferograms in a cavity filled with silicone oil and water; Cavity temperature difference is 3.1 K. View angles are (a) 0° , (b) 45° , (c) 90° and (d) 135° 248
- 6.52 Long-time interferograms in a cavity filled with silicone oil and water; Cavity temperature difference is 4.0 K. View angles are (a) 0° , (b) 45° , (c) 90° and (d) 135° 248
- 6.53 Projection data in oil at three horizontal planes along the width of the cavity. Cavity filled with silicone oil and water at a temperature difference of 0.4 K. 249
- 6.54 Projection data in water at three horizontal planes along the width of the cavity. Cavity filled with silicone oil and water at a temperature difference of 0.4 K. 249
- 6.55 Projection data in oil at three horizontal planes along the width of the cavity. Cavity filled with silicone oil and water at a temperature difference of 1.8 K. 249
- 6.56 Projection data in water at three horizontal planes along the width of the cavity. Cavity filled with silicone oil and water at a temperature difference of 1.8 K. 250
- 6.57 Consistent projection data in oil at three horizontal planes along the width of the cavity. Cavity filled with silicone oil and water for a temperature difference of 0.4 K. 250
- 6.58 Consistent projection data in water at three horizontal planes along the width of the cavity. Cavity filled with silicone oil and water for a temperature difference of 0.4 K. 250
- 6.59 Consistent projection data in oil at three horizontal planes along the width of the cavity. Cavity filled with silicone oil and water for a temperature difference of 1.8 K. 251

6.60	Consistent projection data in water at three horizontal planes along the width of the cavity. Cavity filled with silicone oil and water for a temperature difference of 1.8 K.	251
6.61	Reconstructed temperature contours in the oil (a,c,e) and the water layer (b,d,f) respectively at the three planes; Cavity temperature difference is 0.4 K.	252
6.62	Reconstructed temperature contours in the oil (a,c,e) and the water layer (b,d,f) respectively at the three planes; Cavity temperature difference is 1.8 K.	253
6.63	Unsteady patterns in water in the oil-water experiments for a temperature difference of 8.5 K. View angle considered is 0° . Time interval between two successive interferograms is 5 seconds.	254
6.64	Unsteady patterns in water in the oil-water experiments for a temperature difference of 13 K. View angle considered is 0° . Time interval between two successive interferograms is 5 seconds.	255
6.65	Interferograms (a-g) and their corresponding interfaces (a1-g1) in water in the oil-water experiments for a temperature difference of 17.5 K. View angle considered is 90° . Time interval between two successive interferograms and shadowgraphs is 5 seconds. Interfaces are emphasized in black. . . .	259
A.1	Schematic of Butterfly Algorithm, for Implementation of FFT	276
B.1	Comparison of the numerical isotherms (a) with experimental fringe patterns (b) for a cavity filled with air; Cavity temperature difference $\Delta T = 10$ K.	283
B.2	Comparison of the numerically calculated temperature profiles with experiments at selected planes for a cavity filled with air; Cavity temperature difference $\Delta T = 10$ K.	283
B.3	Isotherms for depth-averaged temperature obtained in a three-dimensional simulation of convection in a cavity filled with air at (a) transverse and (b) longitudinal planes; Cavity temperature difference is 10 K.	284

B.4	Depth-averaged velocity field obtained in a three-dimensional simulation in a cavity full of air at (a) transverse and (b) longitudinal sections; Cavity temperature difference is 10 K.	285
B.5	Comparison of isotherms obtained in simulation (a and c) and (b) experimental projection data; Cavity filled with water for an imposed temperature difference of 10 K. Temperature values for isotherms are equally spaced.	286
B.6	Velocity vectors obtained in a three-dimensional simulation at (a) transverse and (b) longitudinal sections; Cavity filled with water for an imposed temperature difference of 10 K.	287
B.7	Silicone oil 100 cSt over ethylene glycol; equal layer height: interferograms (left column) and numerical simulation (right column), after Prakash and Koster, 1996.	289
B.8	Isotherms generated numerically (left column) and experimentally (right column) for cavity temperature differences of 10 K (a,b), 15 K (c,d), and 18 K (e,f). In numerical calculation, isotherms in air and water were generated step-by-step with a temperature increment of 1 K.	290
B.9	Comparison of the experimentally obtained temperature profiles with numerical calculations at selected columns for a cavity half filled with water in air-water experiments; Cavity temperature differences are (a) 10 K, (b) 15 K, and (c) 18 K.	291
B.10	Numerically generated velocity vectors (left column) and roll patterns (right column) for cavity temperature differences of 10 K (a,b), 15 K (c,d), and 18 K (e,f).	292
B.11	Experimentally recorded air-water interface shapes at cavity temperature differences of $\Delta T=10$ K (b), 15 K (c) and 18 K (d) and comparison with the analytic model (a).	294

List of Tables

3.1	Thermophysical properties of air, water and silicone oil (50 cSt) at 25°C.	71
3.2	Rayleigh number range for a rectangular cavity; Cavity filled with air (A) and water (W).	74
3.3	Rayleigh number range for a rectangular cavity; Cavity filled with air (A) and silicone oil (O).	75
3.4	Rayleigh number range for a rectangular cavity; Cavity filled with water (W) and silicone oil (O).	76
3.5	Rayleigh number range for an axisymmetric cavity; Cavity filled with air (A) and water (W).	76
3.6	Rayleigh number range for an axisymmetric cavity; Cavity filled with air (A) and silicone oil (O).	77
3.7	Rayleigh number range for an axisymmetric cavity; Cavity filled with water (W) and silicone oil (O).	77
3.8	Specifications of the Helium-Neon laser.	81
3.9	Specifications of the constant cold temperature bath (Huber model: variostat).	83
3.10	Specifications of the constant hot temperature bath (Raagaa model: cryostat) with proportional digital indicating controller.	83
3.11	Specifications of the multi-channel Temperature Recorder.	84
4.1	Comparison of refraction errors in air, water and silicone oil as a function of the temperature difference in the rectangular cavity.	98

4.2	Comparison of refraction errors in air, water and silicone oil as a function of the temperature difference in the axisymmetric cavity.	98
4.3	Values of constants for fluid properties of water and air.	117
5.1	Comparison of the experimentally determined width-averaged Nusselt number and interface temperatures with the correlations (marked 'Ref') in a cavity 2/3rd filled with water in air-water experiments.	144
5.2	Comparison of the experimentally determined averaged Nusselt number and interface temperature with correlations (marked 'Ref') in a cavity half-filled with water.	148
5.3	Comparison of the experimentally determined averaged Nusselt number and interface temperature with correlations (marked 'Ref') in a cavity 1/3rd filled with water.	153
5.4	Fourier number as a function of Rayleigh number in an air-water cavity. .	158
5.5	Comparison of the experimentally determined width-averaged Nusselt number and interface temperatures with the correlations (marked 'Ref') in a cavity 2/3rd filled with oil in air-silicone oil experiments.	163
5.6	Comparison of the experimentally determined width-averaged Nusselt number and interface temperature with the correlations (marked 'Ref') in a cavity filled with equal layer heights of air and oil.	167
5.7	Comparison of the experimentally determined width-averaged Nusselt number and interface temperature with the correlations (marked 'Ref') in a cavity 1/3rd filled with oil.	173
5.8	Comparison of the experimentally determined width-averaged Nusselt number and interface temperature with the correlations (marked 'Ref') in a cavity filled with 2/3rd oil and 1/3rd water.	177
5.9	Comparison of the experimentally determined width-averaged Nusselt number and interface temperature with correlations (marked 'Ref') in a cavity filled with equal layer heights of oil and water.	183
5.10	Comparison of the experimentally determined width-averaged Nusselt number and interface temperature with correlations (marked 'Ref') in a cavity filled with layer heights of 1/3rd oil and 2/3rd water.	187

5.11	Summary of Mechanical (M) and Thermal (T) coupling modes obtained in air-water, air-oil and oil-water experiments for all layer heights. A dominant thermal coupling in which mechanical coupling is present but secondary is indicated as T_M . When both modes are important, the notation T-M is employed.	190
6.1	Comparison of the interface temperature and Nusselt number with Gebhart <i>et al.</i> (1988) (marked 'Ref') in a cavity containing layers of air and water of equal thickness.	210
6.2	Comparison of the interface temperatures and Nusselt numbers with Gebhart <i>et al.</i> (1988) (marked 'Ref') in a cavity containing layers of air and silicone oil of equal thickness. View angle is marked as 'V'.	229
6.3	Comparison of the interface temperatures and Nusselt numbers with Gebhart <i>et al.</i> (1988) (marked 'Ref') in a cavity containing layers of silicone oil and water of equal thickness. View angle is marked as 'V'.	245
6.4	Summary of Mechanical (M) and Thermal (T) coupling modes obtained in air-water, air-oil, and oil-water experiments for equal layer heights. . .	257
B.1	Comparison of the numerical and the experimental interface temperatures with Gebhart <i>et al.</i> (1988) (marked 'Reference') in a cavity containing layers of air and water of equal thickness.	293
B.2	Comparison of the Numerical and the Experimental average Nusselt numbers on the air-side with Gebhart <i>et al.</i> (1988) (marked 'Reference'). . .	293
B.3	Comparison of the Numerical and the Experimental average Nusselt numbers on the water-side with Gebhart <i>et al.</i> (1988) (marked 'Reference'). .	293

Nomenclature

A	Aspect ratio, L/H
g	Acceleration due to gravity, m/s^2
h	Height of the fluid layer, m
H	Height of the cavity, m
L	Length of the cavity between a pair of parallel optical windows, m
n	Refractive index of the fluid
n_o	Reference value of refractive index
dn/dT	Refractive index change with temperature, K^{-1}
Nu	Nusselt number, $\frac{-H}{\Delta T} \frac{\partial T}{\partial y} \Big _{y=0,H}$
Pr	Prandtl number, ν/α
r	Radial coordinate
Ra	Rayleigh number, $g\beta(T_{\text{hot}} - T_{\text{cold}})h^3/\nu\alpha$
s	In-plane coordinate required for projections other than 0 and 90°
T	Temperature, °C
T_{hot}	Temperature of the bottom hot wall, °C
T_{cold}	Temperature of the top cold wall, °C
T_I	Interface temperature, °C
W	Width of the cavity, m
y/H	Non-dimensional vertical coordinate

Greek Symbols

α	Thermal diffusivity, m^2/s
β	Coefficient of volume expansion, K^{-1}
λ	Wavelength of the laser, nm
ν	Kinematic viscosity, m^2/s
ϕ	Contact angle (also, polar angle in CBP algorithm)
ρ	Fluid density, kg/m^3
σ	Surface tension, N/m
$d\sigma/dT$	Surface tension gradient with respect to temperature, N/m-K
τ	time, sec
θ	Nondimensional temperature, $(T - T_{\text{cold}})/(T_{\text{hot}} - T_{\text{cold}})$; also View angle for projection data
ΔT	Temperature difference across the cavity, $(T_{\text{hot}} - T_{\text{cold}})$, K
ΔT_{ϵ}	Temperature difference between successive fringes, K

Chapter 1

Introduction

Convective heat transfer refers to energy transport in a fluid medium, enhanced by the fluid velocity. In natural convection, the fluid motion is set up solely by the buoyancy forces arising from the presence of density gradients. Changes in density can be induced by thermal fields, concentration fields or a combination of the two. Buoyancy-driven flows abound in nature, for example, in the atmosphere and water bodies such as lakes and oceans. Mantle convection in earth is an extreme example where fluid motion is influenced by viscosity changes with temperature, in addition to density differences. A variety of applications can also be seen in engineering, for example, electronic devices and energy storage systems. Buoyancy-driven convection is intrinsically complex because of the intricate coupling between the temperature field that drives fluid flow and the flow field that in turn distorts the temperature distribution.

1.1 Buoyancy-driven flow

Much of the fluid motion and transport that affect our immediate surroundings, and the near and far environment are induced by buoyancy. The density difference that sustains buoyant convection can arise from temperature and concentration gradients, as well as material inhomogeneities. The resulting flow pattern will additionally depend on the orientation of the density gradient with respect to the gravity field, the geometry of the confining boundaries and boundary conditions.

The complexities in buoyancy-driven convection are brought out even in fairly simple configurations. Consider a thin horizontal layer of a fluid differentially heated in the vertical direction, namely the direction parallel to the gravity vector. The lower surface is heated, while the top is cooled. Let the horizontal extent of the fluid layer

be very large compared to its thickness. This configuration is often called the *Rayleigh-Benard* system. Due to the temperature gradient imposed across the plates, the fluid layer near the lower wall expands and is lighter than the overlying fluid. This is a gravitationally unstable configuration. In order to achieve stability, the warmer/lighter layer at the bottom tends to rise and the cooler/heavier layer at the top sinks downwards. This results in a convective flow, leading to a cellular pattern in the fluid motion. The Rayleigh-Benard configuration is schematically shown in Figure 1.1.

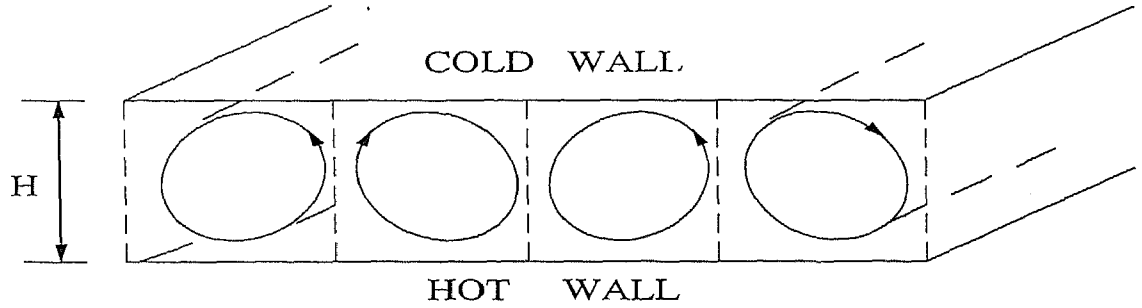


Figure 1.1: Schematic drawing of Rayleigh-Benard convection in a differentially heated fluid layer.

The convection pattern in the fluid layer depends strongly on the location of the side boundaries¹ in the two lateral directions. Thus, even for the simplest configuration (as in Figure 1.1), two additional parameters that characterize the flow field appear in the discussion. These are the aspect ratios A_x and A_z , defined respectively as the two horizontal dimensions of the fluid layer scaled by its height, Figure 1.2.

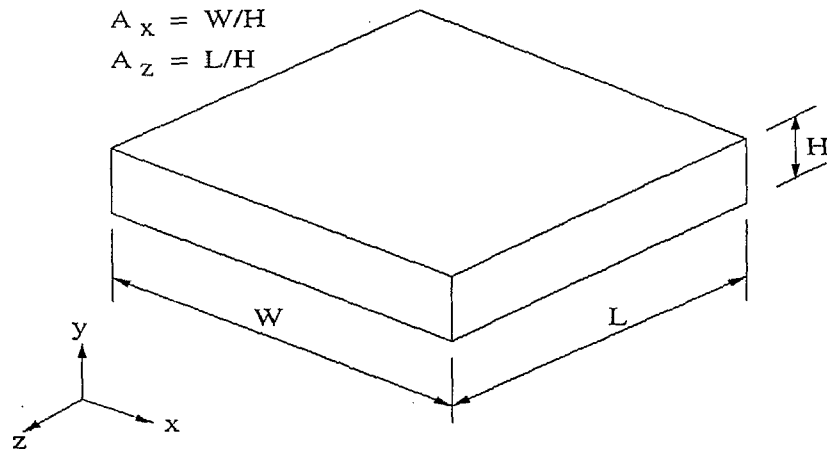


Figure 1.2: Aspect ratios of a differentially heated fluid layer.

¹It is implicitly assumed here in the discussion that the boundaries are rigid; they may be partly or fully conducting.

The driving force responsible for the convective motion in a homogeneous fluid is buoyancy. If buoyancy force is smaller than a certain threshold, the viscous forces between the fluid layers act as internal friction and inhibit fluid motion. Heat transfer across the fluid layer is then purely by conduction. Once the buoyancy forces exceed a threshold value, convective motion is initiated. The relative strength of the two forces i.e. buoyancy and viscous can be characterized using a dimensionless quantity, the Rayleigh number. It is defined as

$$\text{Ra} = \frac{g\beta(T_{\text{hot}} - T_{\text{cold}})H^3}{\nu \alpha} \quad (1.1)$$

Here g is acceleration due to gravity, and β , ν and α are respectively the coefficient of thermal expansion, kinematic viscosity and thermal diffusivity of the fluid medium. More appropriately, Ra can be understood as the ratio of the gravitational potential energy to be gained by reversing the unstable fluid stratification set up by the thermal gradient, to the energy cost associated with this reversal due to viscous dissipation and thermal diffusion (Chandrasekhar, 1961: Drazin and Reid, 1981: Bejan, 1984). Thus Rayleigh number is a quantitative measure of when the transition from conduction state to convection for a given configuration².

The second non-dimensional quantity that affects thermal convection is Prandtl number. It is defined as

$$\text{Pr} = \frac{\nu}{\alpha} \quad (1.2)$$

The Prandtl number is a measure of the ratio of the molecular diffusivity of momentum to that of thermal energy and is a fluid property. This in turn affects the nature of the instabilities to which convection rolls are subjected, after the onset of convection. The first instability that indicates incipient fluid motion beyond the conduction state is however independent of the Prandtl number. The transitional Rayleigh numbers are strong functions of the aspect ratio.

1.2 Two-layer convection

The problem of convection in superposed fluid layers has received much attention in the recent years. Originally most of the research was motivated by the suggested occurrence of two-layer convection in the earth's mantle. The 670 km seismic discontinuity has been interpreted by geophysicists as an interface separating two different types of mantle

²Higher order transitions, for example steady to unsteady can also be characterized by the Rayleigh number.

material. A novel feature of the two-layer system is the possibility of a Hopf bifurcation, namely an oscillatory instability at the onset of convection. First suggested by Gershuni and Zhukhovitskii (1982), this has provided the impetus for a number of theoretical investigations.

Two-layer convection is the result of differentially heating confined superposed fluid layers. The two layers can be a combination of liquid and gas or two immiscible liquids. The layers are confined between two rigid, horizontal surfaces, heated from below and cooled from the top. Two-layer convection can also be conceived as an extension of the frequently studied problem of natural convection in a differentially heated cavity with a single fluid that is either completely confined, or featuring a free surface. The resulting transport problem is affected by the ratios of thermophysical properties such as dynamic viscosity, density and thermal diffusivity of the two fluid layers and the confinement geometry. While single layer convection is governed by the Rayleigh number and the Prandtl number, a larger number of non-dimensional parameters are important for two-layer convection. Specifically, the fluid property ratios, Rayleigh numbers of the individual fluid layers, Marangoni number at the interface, layer thickness ratio and cavity aspect ratio are a few of them.

The main difference between one and two layer convection is in formation of an interface. With a liquid-gas combination, the interface is a free surface that may give rise to surface-tension-driven convection apart from being buoyancy-driven. Variations in surface tension along a liquid-gas interface induce a shear stress on the interface. In superimposed immiscible liquids, two-layer convection gives rise to deformable interfaces. Interfacial surface-tension-gradient-driven convection is caused by the variation of surface tension with temperature. Therefore any temperature gradient established across the surface of the liquid will be accompanied by a gradient in the surface tension. The surface tension gradients can induce flow in the bulk of the liquid, usually referred to as Marangoni convection. Like density, the surface tension decreases as temperature increases and flow is induced from the warmer regions towards the cooler portions of the interface.

A non-dimensional parameter that relates surface tension and viscous forces within a liquid is the Marangoni number, and is defined as

$$\text{Ma} = \frac{\frac{d\sigma}{dT}(T_{\text{hot}} - T_{\text{cold}})H}{\mu \alpha} \quad (1.3)$$

Here σ , μ and α are respectively the coefficient of surface tension, dynamic viscosity and thermal diffusivity of the liquid in which convection has been set up. In the definition, T_{hot} and T_{cold} refer to the maximum and the minimum temperatures over the interface

and H is their vertical separation. In thin liquid layers, the temperatures can be replaced by global maximum and minimum values, and H by the layer thickness. Convection sets in first when the Marangoni number Ma exceeds a critical value. Convective motion can be initiated by surface tension gradients alone, even in the absence of a gravity field.

An intriguing feature of convection driven by surface-tension gradients is that it alters the shape of the interface. Regions of enhanced surface tension tend to pucker, so that they reduce their total exposed area (Velarde and Normand (1980)). The consequences of this effect are contrary to intuition. At the boundary of a convection cell where the fluid rises, the surface is depressed; at the edges of the cell, where the fluid falls, the surface is raised. The reverse phenomena that match our expectations are realized for buoyancy-driven convection. In the absence of surface tension, the surface gets elevated when the fluid has positive vertical velocity; and the surface is depressed when this velocity changes sign.

The interactions of gravitational and surface tension are subtle and complex. A theory that incorporates both buoyant and surface-tension forces known as Benard-Marangoni convection was formulated in 1964 by D.A.Nield of the University of Auckland. This theory is applicable for a liquid-gas system. Buoyancy is initiated in the upper gas layer, and simultaneously sends a thermal signature to the surface. This generates either surface tension or buoyancy convection in the lower layer. For example, in small fluid heights, interfacial-tension-driven convection (Marangoni) dominates. However, for greater fluid layer heights, buoyancy-driven convection (Rayleigh-Benard) is the dominant transport mechanism.

The other important difference between one and two-layer convection is in terms of coupling of the flow fields in each layer across the well-defined interface. If one of the fluids is a gas, the interface could be a free surface, and the motion of the fluids could be practically uncoupled. When the fluids are placed in an enclosure and the motion is thermally driven, flow patterns in the fluid layers are coupled even when one of the phases is a gas. Two distinct modes of flow coupling between the fluid phases are possible. These are thermal and mechanical coupling respectively. The resulting cellular patterns in each of the fluid layers is shown in Figure 1.3.

Irrespective of the nature of coupling, the continuity of temperature at the interface is realized³. In thermal coupling, the recirculation patterns in the individual layers are driven by the temperature difference appropriate for each of them. It is thus possible for the rolls in each phase to have identical sense, clockwise or anti-clockwise. In mechanical

³The normal heat fluxes are also strictly continuous, irrespective of the nature of the coupling.

coupling, the circulation in one phase drives that in the other by the mechanism of viscosity. Thus the two rolls can be oppositely oriented and the flow along the interface is in the same direction in both layers. In mechanical coupling, the fluid particles in one layer mechanically drag those in the other. This implies that regions of ascending hot fluid in one layer coincide with regions of descending cold fluid in the other layer. Viscous drag at the interface is large enough to force the two fluids to flow in the same direction.

The present thesis is an investigation of buoyancy-driven convection in differentially heated superposed fluid layers. Experiments have been carried out in a rectangular and an axisymmetric cavity. For the choice of fluids considered, Marangoni convection is expected to be of secondary importance due to (i) a negligible temperature gradient established at the interface, (ii) greater influence of thermal buoyancy on the flow field and (iii) large fluid layer heights.

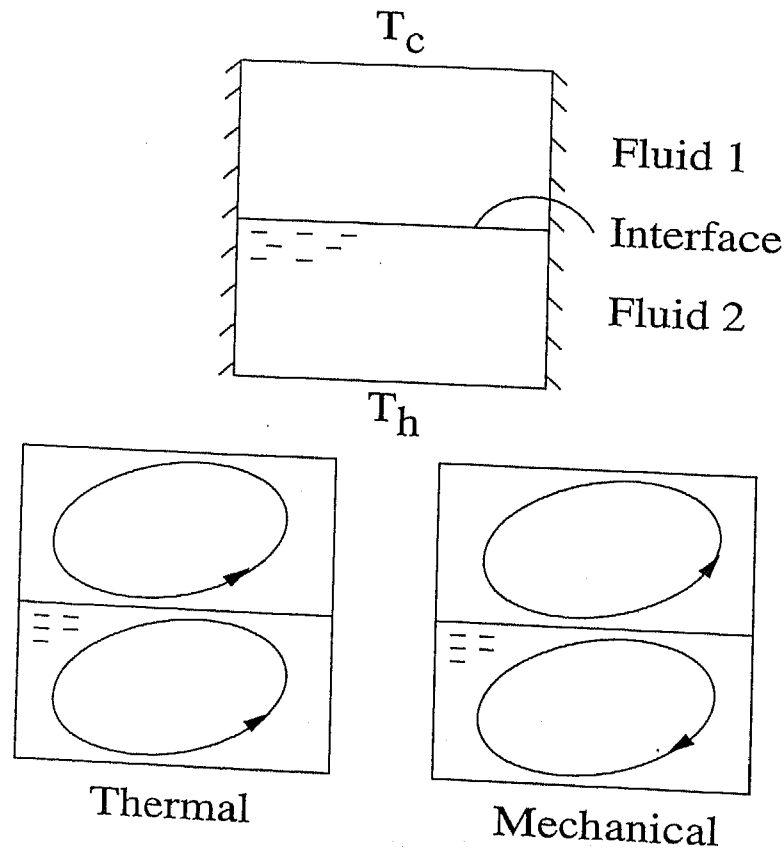


Figure 1.3: Schematic drawing of the flow-coupling mechanism in two-layer convection.

1.3 Engineering applications

Buoyancy driven convection in overlying fluid layers is of interest in a variety of engineering applications and has a great scientific importance. It has direct relevance to atmospheric convection. The importance can be seen from geophysical studies to astronomical research. The need to study fluid convection is very strongly felt for theoretical as well as fundamental reasons.

Important applications of buoyancy-driven flows in two-layer convection are:

- convection in the earth's mantle.
- liquid-encapsulated crystal growth.
- crystal growth from its aqueous solution.
- steam generators of nuclear power plants.
- evaporation mass fluxes at the surface of large water bodies.

The following discussion summarizes each of the applications in brief.

One of the most complex convective systems in nature is that which apparently operates in the earth's mantle (Figure 1.4). The heat that drives the circulation is liberated not at a boundary but rather throughout the volume of the material, mainly as a result of the decay of the radioactive elements. A temperature gradient is formed under these circumstances because heat is lost from the system only at its boundary. As a result the temperature increases with depth. There is little doubt that the gradient is large enough to induce convection, but the properties of the system are complicated and the mantle is inaccessible to measurement. Hence the form and dimensions of the convection patterns are highly uncertain. Viscosity increases sharply with depth, and at some level in the convective zone the material undergoes a transition from one crystalline phase to another. These factors significantly increase the complexity of the flow phenomena.

In liquid-encapsulated crystal growth, the crystal material in molten form is placed in a cylindrical crucible. Another layer of liquid of low volatility, called an encapsulant, is placed on top of the lower liquid, and the arrangement has a layer of inert gas above. The role of the encapsulant is to prevent the evaporation of certain species from the molten material below⁴. The crystal is grown from its melt by initially suspending a

⁴Such an arrangement for crystal growth is popularly known as the Czochralski technique.

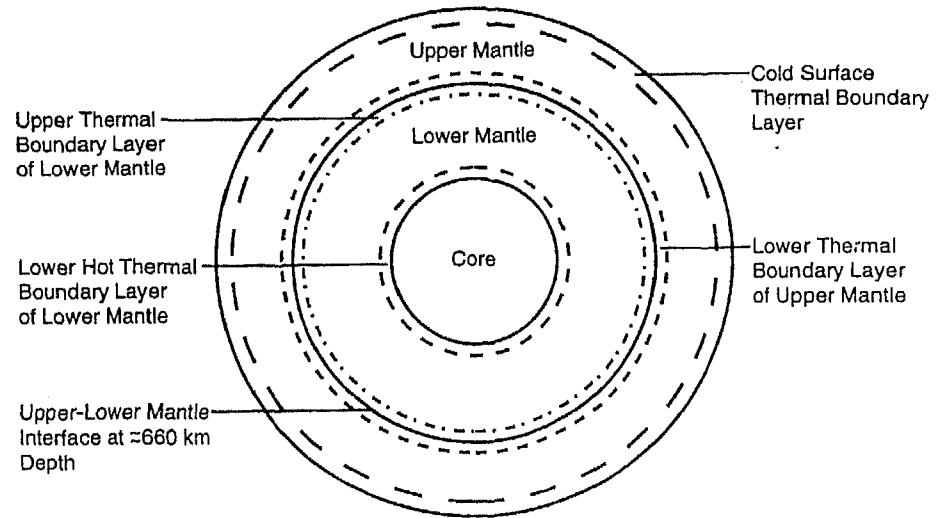


Figure 1.4: Schematic drawing of two-layer mantle convection (Schubert *et al.* (2001)).

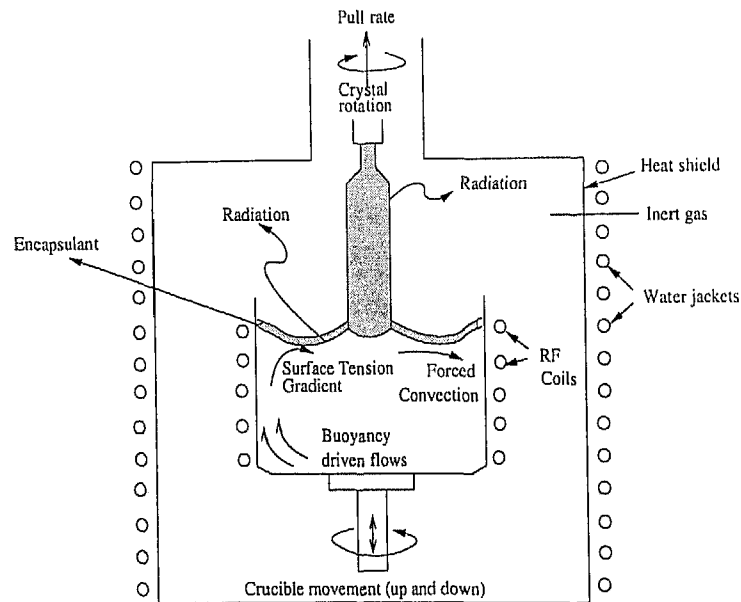


Figure 1.5: Schematic drawing of Czochralski technique, after Prasad *et al.* (1997).

seed at the melt surface. As the crystal grows in size, definite temperature differences across the encapsulant as well as the molten material appear in the apparatus. The temperature difference then causes convection in the fluid layers, partly by the interfacial tension gradient, but mainly by buoyancy forces (Figure 1.5). Convection is important in crystal growth as it will affect the quality of the crystal structure and the distribution of dopants in alloys.

High grade optical crystals can be grown from an aqueous solution that is initially

supersaturated with the salt (Figure 1.6). The process comprises of applying a negative ramp rate in temperature and allowing the excess salt to crystallize on the seed. While growing a crystal from the aqueous solution, the growth mechanism of the crystal as well as its morphology are intricately linked to the temperature and concentration gradients at the crystal surface. Since these gradients set up a density field as well, the crystal will experience buoyancy-driven motion around it. The convective field in practice will be modulated by the free surface of the aqueous solution. Hence, understanding and controlling the convection mechanism is necessary for the formation of good quality crystals. In Figure 1.6, the black dots represents water molecules, while the hollow dots denote the dissolved solute. Here the solute nearest to the crystal attaches to the surface, leaving water behind. The water particles being light, rise in the beaker and the denser solution moves next towards the crystal.

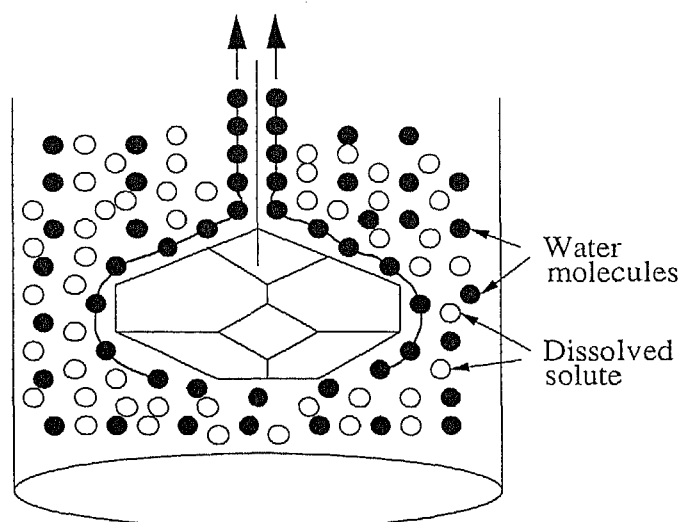


Figure 1.6: Schematic drawing of crystal growth from its aqueous solution.

Modelling convection patterns is also of importance for the successful operation of nuclear power plants. Specific applications include passive heat removal in advanced reactor systems, stratification phenomena in steam vessels in which hot and cold water streams mix (Figure 1.7) and thermal pollution in the reservoirs. The liquid metal pools in fast breeder reactors are also subjected to density stratification.

In the earth's atmosphere, convection phenomena can be observed at several length scales. Local heating of the atmosphere near the earth's surface gives rise to small-scale convective flows, including wind and storms. Cumulus clouds that form when warm humid air rises and cools and thereby becoming supersaturated with moisture, often mark the convective overturning of the atmosphere. Clouds formed as a result of convective

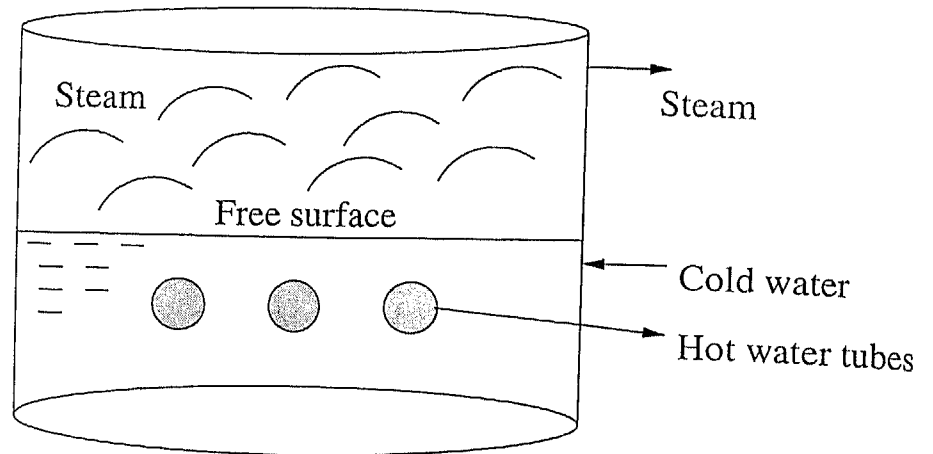


Figure 1.7: Mixing of hot and cold water streams in a steam generator in the presence of a free surface.

circulation are themselves unstable, leading to further convective motion. The cloud is cooled at the top by the loss of heat into space and warmed at the bottom by radiation absorbed from the ground. If the magnitude of these effects is large enough, a convection cell within the cloud can be established (Figure 1.8).

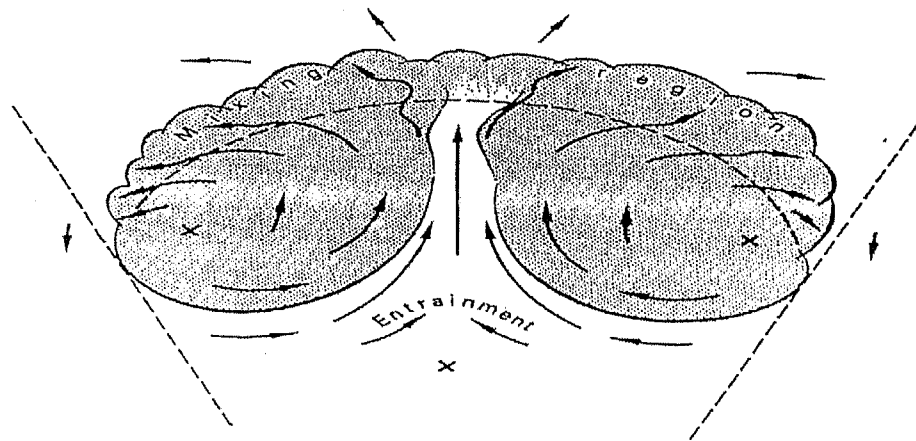


Figure 1.8: Schematic drawing of Cumulus clouds (Scorer, 1972).

Convection in the oceans also spans a wide range of scales, from a meter or two to the size of the ocean basins themselves. The simplest of these flows has a straightforward explanation. Because some wavelengths of solar radiation penetrate a few tens of meters into the ocean the water is heated to a considerable depth. Cooling, on the other hand, results almost entirely from evaporation and from the loss of heat through conduction and radiation to the atmosphere, processes that are essentially confined to the surface. Hence heat is introduced into the oceans at a level below that at which it is removed, and a layer of water several meters deep can become convectively unstable.

The compressibility of seawater is small, and it can influence convective motion only at the greatest depths. Another variable that has an important influence is salinity. The density of seawater varies not only with temperature but also with the concentration of dissolved salts; the density increases with the salinity. As a result two independent factors can work together to establish a density gradient. The interaction of these factors can give rise to new types of convective motion not seen when only a single gradient is present.

The problem of two-layer convection addressed in the present thesis is at the laboratory-scale. It can however form the basis of understanding of natural phenomena that occur over lakes and oceans on one hand and specific configurations in nuclear power plants, on the other.

1.4 Optical methods

Optical visualization of flow fields is a well-established method for the experimental study of many physical processes and engineering applications. Examples can be seen in compressible and plasma flows, combustion and flames, convective heat transfer and mixing flows.

The non-intrusive nature and the ability to record the instantaneous flow or thermal field makes optical techniques a very effective means of investigation in engineering measurements. These techniques generally employ radiation sources as probes. Radiation-based measurements share a common feature in that they generate data of a cross-sectional field-of-view. This is to be contrasted with mechanical probes that are concerned with measurements at a point in space and can accomplish this task only after the field to be studied has been physically perturbed. Hence the scanning of a cross-section of the physical region using radiation-based probes results in a large volume of information with practically no time delay.

The choice of the energy source in a radiation-based measurement is problem specific and cannot be generalized to all classes of problems. The technique to be chosen for a problem has to be decided from both experimental and theoretical points-of-view. The radiation employed in any measurement is generally required to be monochromatic. Its wavelength depends on the application concerned. A variety of sources such as gamma rays, ultrasonics and lasers have been used in engineering. Material testing employs ultrasonic waves or X-rays to permit the transmission of radiation in the solid region. Oil exploration, on the other hand uses phenomena such as disturbances in the earth's mag-

netic field and scattering of mechanical vibrations that are directed towards the earth interior. In optical systems specific to fluid mechanics applications, lasers in the visible range are employed. One can then collect the information on optical path length or frequency shifts of the scattered light from particles contained in the fluid. The selection of the detector system depends on the radiation employed and the measurement accuracy desired. The method of data reduction also shows considerable variability, depending among other factors on the quantity to be measured.

When the wavelength of radiation used is in the visible range, the measurement procedure classifies as an *optical technique*. The region being scanned appears then on a screen as an image that is visible to the naked eye. Optical techniques require the medium under study to be transparent. In thermal sciences as well as fluid mechanics, there has been a revival of optical techniques for temperature and velocity measurements in fluids, primarily for the following reasons:

- Commercially available lasers have a high degree of coherence (both spatial and temporal) and are cost-effective.
- Optical images can be recorded conveniently through computers and can be processed as a string of numbers through numerical algorithms.

The implications are that: (1) coherence generates stable image patterns which truly reflect fluid behaviour and (2) computer programs now simplify and replace very tiring manual data extraction procedures.

Broadly the optical techniques employed in fluid-flow measurements can be divided into three categories: (i) flow visualisation through the injection of tracer particles, (ii) measurement of frequency shift of scattered illumination from an injected tracer medium in the flow field and (iii) measurement of index of refraction of the fluid or its spatial derivatives. The present thesis utilizes the method belonging to the third category to study buoyancy-induced convection in superposed fluid layers in a Rayleigh-Benard configuration. Optical methods which utilize the dependence of refractive index of light on quantities such as density, concentration and temperature can be configured in many different ways. Three popular routes are:

1. Shadowgraph, where the reduction in light intensity on beam divergence is employed. This specifically measures the variation of the second order derivative of the index of refraction normal to the light beam.

2. Schlieren, where the deflection of light in a variable refractive-index field is captured. This technique handles the variation of the first order derivative of the index of refraction normal to the light beam.
3. Interferometry, where the image formation is related to changes in the refractive index with respect to a reference environment. This method responds directly to the refractive index field of the flow system.

For a wide class of applications where temperature differences are within certain bounds, interferometry appears to be a versatile tool for accurate measurement of three dimensional unsteady temperature fields, and with some modification, for velocity fields. In fact, if refraction errors are taken care of, interferometry is a promising tool for measurements including high temperature gradients. Many applications that involve free and forced convective heat transfer are included in this category. One large-scale application worth mentioning is the satellite-based imaging of the planetary atmosphere using coherent optics. Shadowgraphy and schlieren techniques are well suited for problem of high temperature/density gradients such as flames and shocks.

Information about temperature is present in interferometry in the optical path difference between the test and the reference beams and hence their phase difference. This necessarily requires a coherent and monochromatic light source. In contrast, the schlieren and shadowgraph techniques do not rely on coherence though a monochromatic source is needed. The requirement of a coherent light source and coherent optics makes interferometry expensive compared to the other refractive index-based methods. However interferometry can generate accurate and unambiguous data. For a purely two dimensional flow field with the light ray direction oriented at normal incidence, interferometry generates interference patterns representing either isotherms or the temperature profile depending on the optical adjustment. If the flow field is three dimensional interferometry still gives an overall idea of the flow mechanism in terms of an average effect along the direction of the light ray. Hence interferometry has the advantage of visualising the thermal phenomenon under study while the experiment is in progress in a more appealing way, compared to the schlieren and shadowgraph techniques. All the three methods belonging to the class of refractive index based-methods are capable of being used in real-time applications. Since each of them produces an integrated effect of a three dimensional field in the form of a two dimensional image, it is possible to employ the tomographic method to reconstruct the three dimensional field of refractive index or its derivative. As far as measurements are concerned interferometry is more complex compared to the other two methods.

Optical techniques can be used for validating numerical solutions of the flow and heat transfer equations. If the three dimensional field from a numerical solution is computed, schlieren, shadowgraph and interferometric images can be numerically constructed and can be compared with those in the respective experiments.

1.5 Objectives of the present work

In the present thesis, buoyancy-driven convection in differentially heated superposed horizontal fluid layers has been studied experimentally using laser-interferometry. The thermal field has been mapped using a Mach-Zehnder interferometer. The interferograms have been obtained as a collection of fringe patterns. The interferograms give line-averaged information along the direction of the light ray. Hence they represent a projection of the thermal field in that direction. The interferograms can also be used to identify qualitatively the flow pattern prevailing within the cavity.

Fluid layers comprising of air-water, air-oil and oil-water combinations have been selected for the present experiments. The oil referred here is 50 cSt grade silicone oil. Fluid layers were confined in between two horizontal, isothermal plates heated from below and cooled from the top. The configuration leads to a modified form of the Rayleigh-Benard problem, that has been widely studied in the literature. Two-different geometries of cavity have been designed and fabricated for performing the experiments. These are: (i) a cavity rectangular in plan and square in cross-section and (ii) an axisymmetric cavity octagonal in plan. The latter approximates a circular cavity. Three layer heights in rectangular and equal layer heights in the axisymmetric cavity for each combination of fluid-layers were examined during the experiments. The overall temperature differences across the two walls were decided on the basis of the expected flow regimes in the cavity. Both steady and unsteady three-dimensional flows were permitted to occur in the two fluid layers. The nature of the convective fields, their coupling and the deformation of the interface have been addressed.

1.6 Thesis organization

The present thesis has been organized in the following manner. Chapter 2 is a review of the published literature on one and two-layer convection. The classification is broadly based on the physical mechanisms studied, geometry of the cavity selected, fluids considered, visualization techniques, analysis of data and major conclusions. Chapter

3 presents the description of the test cells utilized in the present study for two-layer convection and the instrumentation employed for experimentation. Chapter 4 focusses on the data reduction and the uncertainty involved in the experimental data that was recorded in the form of interferograms. Chapter 5 presents the results of two-layer convection in a rectangular cavity for different layer heights and temperature differences imposed across the two walls. Chapter 6 presents the results of two-layer convection in an axisymmetric cavity for equal heights of the fluid layers. Chapter 7 summarizes the conclusions arrived at in the present work and the scope for future work.

Chapter 2

Literature Survey

To quote the remarks of Busse (1978), "Thermal convection is arguably the most commonly occurring fluid flow phenomena in the Universe."

The subject of Rayleigh-Benard convection has been extensively investigated in the past and continues to be an important topic of research. This is because of its applicability in areas as diverse as astrophysics, atmospheric sciences, and engineering. Rayleigh-Benard convection appears in a fluid layer bounded by two flat horizontal surfaces heated uniformly from below and cooled from above. An unstable vertical density gradient settles across the fluid layer when, the driving force, namely buoyancy overcomes the dissipative effect of viscosity, convective motion is triggered. The nature of fluid motion exhibits considerable variability in practice owing to a wide range of length and temperature scales encountered, as well as the fluid properties. The flow physics can be unified to a great extent when examined through dimensionless parameters such as the Rayleigh number and the aspect ratio (Chapter 1).

In a two-layer Rayleigh-Benard system, instabilities and convection patterns depend on several dimensionless groups. Specifically fluid property ratios, Rayleigh numbers of the individual fluid layers, layer thickness ratio, cavity aspect ratio and the overall geometry of the confining surfaces are important. In addition, surface tension and its gradient at the interface can play a significant role, particularly in fixing the critical points and at low Rayleigh numbers.

Two-layer convection has been studied in a cylindrical, rectangular as well as square geometries by many authors. The cylindrical geometry was adopted mainly because of its application to crystal growth. Here the melt is placed in a crucible, cylindrical in shape and the grown crystal is drawn from it by inserting a seed. Often, an encapsulant layer floats over the liquid alloy to prevent the volatile components leaving the crucible.

The rectangular and square geometries have been studied mainly to explore the nature of the interface deformation and the onset of steady and unsteady convection. In most studies reported, convection is driven by buoyancy (*Benard*) as well as surface tension gradients (*Marangoni*) at the interface.

The research reported in the present thesis is concerned with convection in superposed fluid layers. Quantities such as the roll patterns and heat transfer rates have been compared with those for a single layer, where appropriate. Hence, the present chapter reviews literature available for Rayleigh-Benard convection in both single and two fluid layers.

2.1 One-layer convection

The classical Rayleigh-Benard problem of a single layer heated from below occupies a central place in the study of non-linear hydrodynamics. The appearance of numerous spatial and temporal bifurcations in this system make the problem an ideal model for the study of flow transitions to turbulence. Accordingly, it has attracted a diverse group of theoreticians and experimentalists.

Rayleigh-Benard convection in small ($\approx 2-10$), to moderate ($\approx 10-30$) size containers is fundamentally different from that in large ($\approx 30-60$) aspect ratio containers, since the presence of vertical side walls strongly modulates pattern formation and mode selection. Side walls have a stabilizing effect on the onset of convection itself owing to an increased viscous drag. Within each range of aspect ratios, the flow transitions strongly depend on the Prandtl number of the fluid and the geometrical structure of the side walls. The published work on each of the three ranges of aspect ratio is scattered and a uniform trend is not discernible. A large amount of literature is available for low aspect ratio enclosures. This is because numerical calculations are easier to perform over a physically small domain. Experiments with small aspect ratio enclosures are also conveniently carried out. This improves the possibility of a direct comparison of theory with the experiments.

For small Rayleigh numbers the flow is generally stable with respect to all disturbances. As the Rayleigh number increases, the flow become unstable to specific forms of disturbances. Over certain ranges of Rayleigh numbers, the disturbances perturb the flow pattern but the system slowly returns to the stable state, in the sense that the disturbances do not grow with time. As the Rayleigh number is further increased, the flow becomes unstable to all disturbances and becomes chaotic. The flow field during

Rayleigh-Benard convection undergoes a number of discrete transitions and the flow structure in each of the transitions is well-defined over a range of Rayleigh numbers.

Krishnamurti (1970a, 1970b) has presented a regime diagram for the different transitions in a Rayleigh-Benard convection system as a function of Rayleigh number and Prandtl number (Figure 2.1).

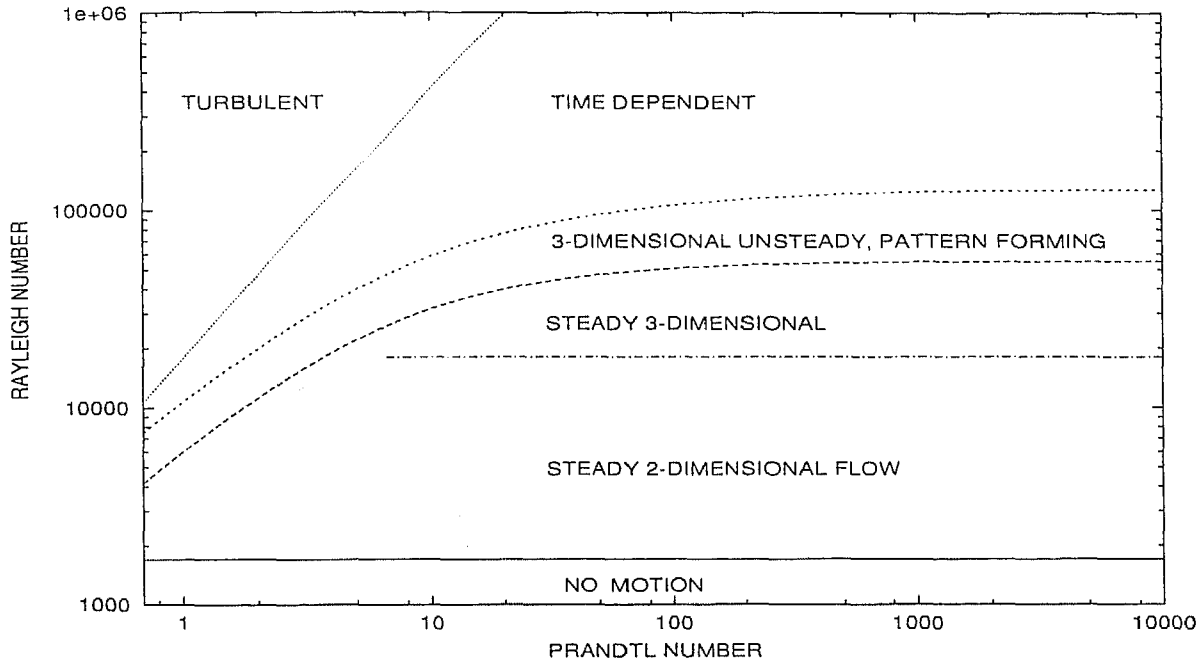


Figure 2.1: Experimentally recorded regimes in Rayleigh-Benard convection, after Krishnamurti (1970a, 1970b).

This is one of the earliest experimental studies where a number of different fluids and a variety of cavity sizes were considered. In these experiments, the bottom plate was made of a low conductivity methyl methacrylate layer sandwiched between two high conductivity aluminium plates. An electric heater was employed for heating and chilled water for cooling the plates. Flow was visualized by tracer particles and the heat transport was measured by means of thermocouples located in the confining horizontal plates. The associated flow field was observed through the records of tracer particles injected in the fluid. The data for heat flux from the walls corresponding to different Rayleigh number was also reported. Owing to the experimental method adopted, this work has a large uncertainty for low Prandtl number fluids such as gases. The main conclusion of the author is that flow undergoes a sequence of transitions. Flow patterns encountered are steady two dimensional flow, steady three dimensional flow, unsteady three dimensional flow with pattern formation, time dependent flow and finally the field becomes turbu-

lent. Each transition in the flow configuration is marked by a change in slope of the heat flux curve with respect to the cavity temperature difference. Specifically four distinct changes in the slope were seen, each marking a bifurcation of the flow pattern. Above the third change in heat flux curve the corresponding flow patterns were found to be time dependent, with movement of hot or cold spots along the cells. The effect of strong hysteresis¹ was also observed in the wall heat flux and flow patterns.

In a subsequent study, Krishnamurti (1973) extended the flow regime diagram with respect to the Prandtl number, covering the range $2.5 \times 10^{-2} < Pr < 0.85 \times 10^4$. For low Prandtl number fluids the change in the slope of the heat flux curve associated with bifurcations in the flow pattern was again observed. The general observation was that there was an increase in the slope of the heat flux curve in the presence of a bifurcation. However, for low Prandtl number fluids there was a decrease as well as an increase in the slope of the heat flux curve with an increase of Rayleigh number. For air, the increase in slope of the heat flux curve was found at Rayleigh numbers of 1700 and 6000. These two points correspond respectively to the onset of convection and time-dependent oscillations in the cavity. A decrease in slope was observed at a Rayleigh number of 10000 and again at a Rayleigh number of 17000. The response time for the low Prandtl number fluid, specifically for air was found to be very long when compared with higher Prandtl number fluids. When Rayleigh number was increased by a small amount it was found that the steady state for the new Rayleigh number was achieved after a longer time as compared to other fluids. This can be explained because the thermal diffusion time decreases in comparison to the viscous diffusion time as the Prandtl number decreases. By considering cavities of rectangular cross-section in plan, Krishnamurti (1973) has shown that rolls parallel to the shorter side of the cavity are stable. This orientation minimizes the ratio of the rate of viscous dissipation of kinetic energy to the rate of release of potential energy by the buoyancy force. Expressed in another way, the preferred orientation is one in which the rolls meet most of the side boundaries at right angles. Although the theory is for perfectly conducting side walls which would almost never be used in an experiment, certain features controlled by viscous dissipation can still be expected to be observed. A couple of experiments were also performed in circular cavity of different sizes. The interior rolls were not seen to be axisymmetric while those near the side walls had defects and met the side boundaries mostly at right angles.

Ahlers and Behringer (1978) used a cavity with a cylindrical geometry for experimentation on Rayleigh-Benard convection with different fluids. The largest aspect ratio was 57 and Prandtl numbers of 4.40 and 2.94 were employed. The authors reported that

¹namely, the heating rate of the bounding surfaces

beyond the onset of convection the flow field was unsteady but nonperiodic. For cavities with an aspect ratio in the range of 2 to 6 and for a Prandtl number of around 0.8, the flow field was seen to follow two different routes to the turbulent state. For the cavity size with an aspect ratio of 5, the flow was seen to become nonperiodic, after remaining in the periodic state over a range of Rayleigh numbers. For a small cavity with an aspect ratio of 2, the flow field passed through a quasiperiodic state between a time dependent and a nonperiodic state.

Kim and Viskanta (1984) reported the effect of wall conductance on buoyancy-driven convection in a two dimensional rectangular cavity. The study included both experimental as well as numerical investigations. The working fluid considered was air. The size of the cavity employed for experimentation had a cross-section of 3.6 cm \times 3.6 cm, and the length of test-cell along the viewing direction was 19 cm. The walls were made of Lexan. A Mach-Zehnder interferometer with 25 cm optics was used for data collection. Three different configurations for convection in enclosures were considered, the side walls being conductive in all the three cases. Of the three, one of the problems considered was Rayleigh-Benard convection. In the experiments, the flow revealed a circulation pattern inside the cavity. The walls were seen to conduct heat to and from the fluid. The direction of heat transfer from the conducting side walls showed a wave-like behaviour. Near the bottom wall there was an addition of heat to the system by the conducting side walls. The vertical conducting walls had a stabilizing effect on the flow. At steady state the interference fringes were distorted and formed cells. Here the flow was assumed to be turbulent (random laminar flow) that has resulted from thermal-plume activity since the Rayleigh number reached a value of the order of 10^6 . Despite the optical axis being aligned parallel to the long side, cellular motion was noticed in the central core of the cavity. Symmetry in energy balance was not seen between the two horizontal walls, the Nusselt number for the top wall being lower than the bottom wall.

A typical flow pattern which has received considerable attention in the past is cellular convection in a rectangular parallelepiped of a small aspect ratio. Both calculations (Davis 1967) and experiments (Stork and Muller 1972) show that convection near its onset usually has the form of rolls oriented parallel to the short side of the cell; these are referred to as the short rolls. Later, theoretical results of Bueller *et al.* (1979) showed in a definite manner that although rolls parallel to the short side are more likely, rolls parallel to the long side can also exist; these are commonly known as long rolls. Furthermore, Kolodner *et al.* (1986) did in fact observe long rolls experimentally for intermediate aspect-ratio rectangular container for large Prandtl number fluids. This is an important issue. Small aspect ratio Rayleigh-Benard convection with short rolls

have been assumed in the past to study the various routes to chaos and turbulence. If stable long roll patterns can indeed be generated, this could be a useful starting point for further investigation in the time-dependent domain.

The second related observation in a differentially heated fluid layer is the loss-of-roll phenomenon. It is realized over a continuous range of Rayleigh numbers². For a fixed Prandtl number and a range of Rayleigh numbers the roll pattern is the most stable form of convection. Thus, subsequent to an instability the roll pattern is most likely to be restored, though with a change in the structure. Different types of instability mechanisms that change the wavelength of the roll system have been discussed by Busse (1980). The zigzag instability bends the longitudinal rolls in a wave-like fashion. This is followed by a lengthening of the boundaries between the rolls, resulting in an increase in the wavenumber of the roll system. Experimentally, it has been observed that new rolls are formed in two directions enclosing angles of 40° and 140° with the direction of the original rolls (Busse, 1980). The cross-roll instability occurs in the form of rolls at a right angle to the given rolls such as to minimize the interaction between the original pattern and its disturbance. The cross-roll instability can also lead to knots appearing

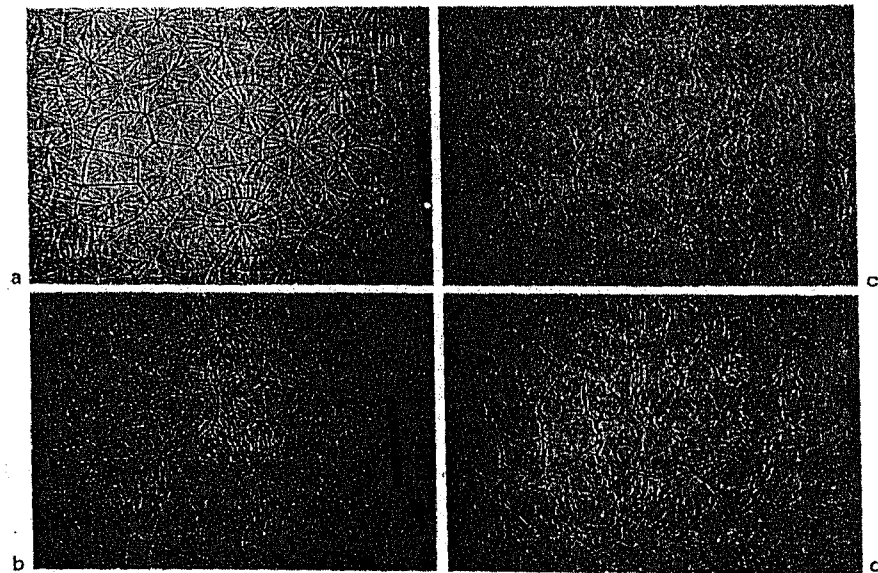


Figure 2.2: Shadowgraph observations of spoke pattern convection in a layer of methyl alcohol ($Pr = 7$) with increasing Rayleigh numbers from (a) to (d), after Busse (1980).

on the boundaries of the rolls. As indicated by its large wavelength, the knot instability tends to develop into spoke pattern cells. As the Rayleigh number increases, the spoke

²Loss of rolls refers to the formation of fewer rolls compared to the cavity aspect ratio, rounded off to the closest integer. In addition, the rolls could also be of unequal sizes.

pattern cells seem to evolve gradually into those shown in Figure 2.2. Another important instability mechanism that is responsible for the loss-of-roll phenomena is the skewed-varicose instability. The roll structure gets distorted along the axis of the roll. As a result, the roll size changes along the axis of the roll. A subharmonic wave develops, that causes later the pairing of two of the distorted rolls. The skewed-varicose instability has been found to be the main cause for the loss-of-roll phenomena in a low Prandtl number fluid such as air.

Roll orientation in Rayleigh-Benard convection has been reviewed in the following discussion. This aspect is of relevance to the present thesis on convection in superposed fluid layers.

Kolodner *et al.* (1986) studied Rayleigh-Benard convection experimentally in an intermediate-aspect-ratio rectangular container. The aspect ratios were 10.61 and 9.25 with respect to the height of the container. A constant heat flux boundary was used in the experiment instead of the isothermal boundary condition. However, according to the authors, isothermal boundary conditions would have produced the same experimental observations. The authors used a lower plate made of copper and a sapphire top plate with horizontal walls of acrylic plastic. The top plate was cooled with flowing water and the bottom plate was electrically heated. Optical access from the top of the apparatus allowed visualization. A shadowgraph technique was employed for this purpose. Visualization from the side walls gave images of the horizontal view. These images were projected to a screen and the entire flow process was recorded on video tapes. The authors observed that at the onset of convection, stable patterns in the form of rolls were parallel to the short side of the container for a Prandtl number range of $2 < \text{Pr} < 10$. The roll pattern was not stable when the Rayleigh number reached the critical value of approximately 11,100, obtained by continuous slow heating. At this value of the Rayleigh number, the loss-of-roll phenomena was seen to occur.

Kolodner *et al.* (1986) observed the reverse trend also, namely the rolls aligned parallel to the long side of the container for the Prandtl number range $10 < \text{Pr} < 20$. The shape of the rolls was distorted while time dependence was initiated when the Rayleigh number reached the critical value of approximately 45,600. The authors concluded that several transitions in the flow pattern was possible with increasing Rayleigh number before the onset of time dependence.

Kirchartz and Oertel (1988) have shown the transition from 4-rolls to 3 and finally to 2-rolls for a box of small aspect ratio. The cavity was developed using copper plates. The upper plate was thermostatically controlled using chilled water and the lower plate

was electrically heated. Perfectly conducting side walls were setup by employing surfaces made of quartz. Differential interferometry along with a scanning mirror and laser Doppler anemometer were employed to study the flow and thermal phenomena. The authors concluded that in horizontal boxes, the rolls parallel to the shorter side of the box seemed to be the preferred solution. Numerical analysis showed the smallest eigenvalue to be 1817 as against 1883 for the rolls parallel to the longer side of the box.

Michael and Yang (1992) reconstructed the three dimensional temperature field in a differentially heated fluid layer from its interferometric projections. The authors saw the presence of rolls in a water filled cavity of aspect ratios 8.7 and 9.0. The two horizontal confining walls of the cavity were made of aluminium. The top plate was cooled using water at a constant temperature flowing over the aluminium sheet. The bottom plate temperature was maintained using three electric foil heaters connected in series. Two sides of the vertical side walls were made from delrin and the other two sides were made from 25 mm thick optical flats. Three thermistors were used in each aluminium plate to measure the temperature of the plates. A Mach-Zehnder interferometer with 20 cm diameter optics and a Helium-Neon laser of 10 mW power were employed for collecting the projection data. The wedge fringe setting of the interferometer was used to record the convection pattern inside the cavity. For the tomographic reconstruction of the three dimensional temperature field the authors employed the corresponding numerical solution of the physical problem as an initial guess to the reconstruction algorithm. The results showed the formation of T-defects in the longitudinal rolls near the region of the short side of the box. The movement of hot and cold spots along the roll was observed.

Michael and Yang (1992) also concluded that often, the rolls were aligned with their axis parallel to the longer side of the cavity. The authors chose to study the field only when the rolls were aligned in this direction for two reasons. First, the number of rolls could be clearly obtained in the experiments, making it easier for a comparison with the numerical prediction. Secondly, the direction with the least amount of three-dimensional effects was along the main direction of the light, being consistent with the traditional two-dimensional use of the Mach-Zehnder interferometer.

Mukutmoni and Yang (1992) studied numerically the stability of long rolls in Rayleigh-Benard convection in a small aspect ratio rectangular box with insulated side walls. The aspect ratios were taken to be 3.5 and the Prandtl was set at 2.5. These parameters are identical to those in the experiments of Gollub and Benson (1980). Mukutmoni and Yang (1992) performed the numerical computation on a $30 \times 20 \times 30$ grid, selected on the basis of a grid refinement study. The numerical solution revealed a flow field that consisted of two counter-rotating rolls parallel to the long side. This is in contrast

with the investigations of Gollub and Benson (1980), in which the two counter-rotating rolls were aligned parallel to the short side. The two fields were otherwise similar except that the wavenumber of the long rolls in the simulation was somewhat larger. In the two-roll structure, the fluid rises along the side walls and descends along the plane of symmetry between the rolls. Mukutmoni and Yang (1992) concluded that the rolls parallel to the long side are stable below a Rayleigh number of 20,000 in water. The flow eventually was seen to undergo two separate bifurcations and become oscillatory.

In an earlier work, Mukutmoni and Yang (1991) reported the transition from long rolls to short rolls in their simulated results that was carried out between Rayleigh numbers of 24,000 and 26,000³. Finite perturbations were required for the transition to take place. For finite perturbations, the Rayleigh number of the fluid was increased abruptly to a very high value and then brought back to the original state. Physically, this means that the fluid was suddenly heated from the boundary and then cooled. This 'quenching' operation has been used by Giglio *et al.* (1981) in their experiments. Their interpretation was that if this approach was not used, the rectangular cell pattern consisting of long rolls was quite stable and no transition occurred. Mukutmoni and Yang (1992) thus concluded on the basis of above studies that long rolls are akin to a metastable state and could become unstable not to infinitesimal but to finite disturbances.

Koizumi and Hosokawa (1996) studied the effect of side-wall temperature on the flow pattern of Rayleigh-Benard cells in a rectangular enclosure. Both experiments and numerical computations were performed. The aspect ratio of the cavity was taken to be 6.0. Experiments were carried out with air as the working fluid at Rayleigh number (Ra) mainly at 8,000, but a few of them were carried out at $Ra=16,000$ to investigate the effect of a changing Rayleigh number. For the experiments, two enclosures, [A] and [B], of equal size, but different side-wall structure were designed and fabricated. In enclosure [A], the side walls were constructed with four 10 mm thick copper plates, each being independently heated. The bottom wall had an identical structure as the side walls. The top wall, which was composed of an acrylic sheet 2 mm thick, was cooled with water. In enclosure [B], the bottom and top walls were similar to the structure of [A]. The side walls were constructed using four water-tanks made of a transparent acrylic sheet 2 mm thick. For flow visualization in the enclosures, an incense smoke was used as a tracer. The authors found that at $Ra=8000$, there are four types of flow patterns: four roll-cells in region I, five rolls in region II, six roll-cells in region III with axes parallel to the short side-walls (short rolls), and two roll-cells in region IV with axes parallel

³long and short rolls refer to those whose axes are respectively parallel to the long and short sides of the cavity.

to the long side-walls (long rolls). At the higher Rayleigh number of 16,000, only two types of flow patterns were obtained: four short or transversal rolls in region I and long or longitudinal two-roll structure in region IV. These roll-cells at $Ra=8000$ and 16,000 were steady, reproducible, and stable against disturbances. The authors concluded that the flow pattern consists of a steady, even or odd number of roll-cells with axes parallel to the short or long side of the enclosure at all side-wall temperatures below a Rayleigh number 16,000.

With regard to the orientation of the rolls, the research described above shows that the rolls are generally parallel to the shorter side of the cavity in a small aspect ratio rectangular container. At the same time, the possibility of realizing stable long rolls aligned parallel to the longer side cannot be ruled out. This has been numerically and experimentally documented in the literature both at small as well as intermediate aspect ratio containers.

Muralidhar *et al.* (1996) studied transient convection in a two dimensional square cavity. The fluid considered was air. Rayleigh numbers in the range of 10^4 to 10^5 were employed. The cavity had a width of 74 cm and the aspect ratio of the cross-section was unity. The horizontal surfaces were developed using brass sheets. The vertical side walls employed were made of a low thermal conductivity material such as perspex. The isothermal conditions on the brass sheets were obtained by flowing water at constant temperature through them. A Mach-Zehnder interferometer was employed to map the thermal field. These experiments showed that the flow was mostly bicellular during the early transient period whereas it became unicellular at steady state. The Nusselt number in the cavity was found to be a maximum at the steady state. The associated thermal field was found to be symmetric with respect to the vertical axis at the lowest Rayleigh number studied, namely 8.79×10^4 . The symmetry was lost at higher Rayleigh numbers. The growth rate of Nusselt number when the flow approaches steady state from the transient was not uniform. The initial growth in Nusselt number with time was seen to be rapid followed by a slow transient till the Nusselt number stabilized at steady state at its maximum value. This was explained in terms of the boundary layer near the hot and cold walls of the cavity during the initial stages. The corners of the cavity were found to be region of high heat transfer for short times but regions of low heat transfer at steady state.

Application of computerised tomography for measurements in heat and mass transfer has been a topic of research over the past decade. Many authors have reported the three-dimensional reconstruction of thermal fields using the tomographic algorithms. Mayinger (1994) has reviewed different optical measurements techniques and application

of tomographic algorithms to evaluate three dimensional fields.

Mishra *et al.* (1999-2000) in a series of papers, reported an experimental study of Rayleigh-Benard convection in an intermediate aspect ratio box that was square in plan. An intermediate range of Rayleigh numbers was considered in the study. The fluid employed was air. A Mach-Zehnder interferometer was used to collect the line-of-sight projections of the temperature field in the form of interferometric fringes. Images were recorded after a sufficient time had elapsed for the initial transients to have been eliminated. Interferograms were collected from four to six view angles. These are used to obtain the three dimensional temperature field inside the cavity by using tomography. An algebraic reconstruction technique was used for the inversion of the projection data. The convergence of the iterative inversion procedure was unambiguous and asymptotic. The reconstructed temperature field with a subset of the total data was found to be consistent with the remaining unused projections.

Mishra *et al.* (1999-2000) presented results for three Rayleigh numbers, namely 13900, 34800 and 40200. These were found to correspond to two distinct flow regimes. At these Rayleigh numbers, a well-defined steady state was not observed. At the lower Rayleigh number, the fringes away from the wall showed mild unsteadiness. At the higher Rayleigh number, the fringes were found to switch between two patterns. Results for the dominant mode were presented for this experiment. At a Rayleigh number of 13900, three dimensional flow structures, whose influence is equivalent to longitudinal rolls were observed. At Rayleigh numbers of 34800 and 40200, the flow was seen to be organised in the form of cubic cells. The associated flow pattern was inferred to be a plume rising from the heated plate. The local Nusselt number variation was consistent with the observed flow patterns for all the Rayleigh number studied. Mishra (1998) has summarized the flow transitions in the fluid layer with increasing Rayleigh number based on the work of other researchers as well as his own. This summary is shown in Figure 2.3.

Most recent studies on one-layer convection in the Rayleigh-Benard configuration are based on the fluid working at a very high Rayleigh number wherein the flow regime is invariably turbulent. Krishnamurti (1998) has reported a locally time-periodic flow in Rayleigh-Benard convection in the range of Rayleigh number of 10^7 to 10^8 , Prandtl number of 7, and an aspect ratio of 12. The time periodicity is associated with organized clusters of tilted plumes travelling steadily across the fluid layer. A scavenging plume model was presented by the author in which a prior passage of a plume depletes the thermal boundary layer in a history-dependent way. The boundary layer is very thin where the plume has just passed, but has had time to thicken where the plume passed

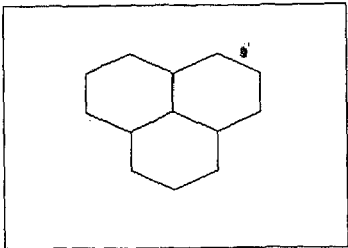
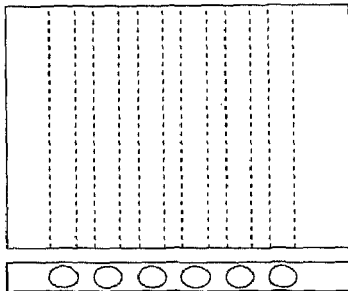
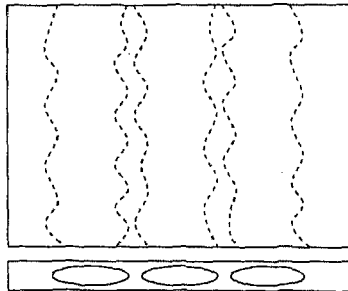
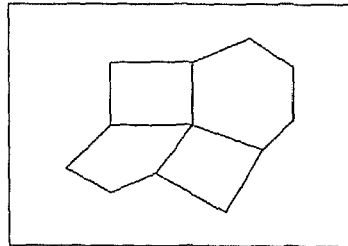
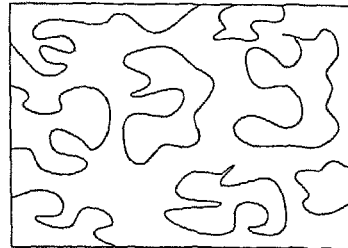
Transitions in Rayleigh-Benard Convection	Remarks	Source
	<p>Onset of convection Hexagonal Cells $Ra > 1707$</p>	Chandrasekhar, 1961
	<p>Longitudinal Rolls Roll Size $\sim h$ Two Dimensional $Ra < 6000$</p>	Krishnamurti, 1970
	<p>Longitudinal Rolls Three Dimensional Roll Size Variable Mild Unsteadiness Loss of Roll $Ra < 15000$</p>	<p>1. Kolodner et al., 1986 2. Mishra, 1998</p>
	<p>Polygonal Cells Unsteady $Ra \sim 30000$</p>	<p>1. Mukutmoni and Yang, 1995 2. Mishra, 1998</p>
	<p>$Ra > 50000$ Completely Unsteady Turbulent</p>	<p>1. Gollub and Benson, 1980 2. Mishra, 1998</p>

Figure 2.3: Summary of Flow Transitions in Rayleigh-Benard Convection, after Mishra (1998).

some time ago. Thus at any instant of time, there was a thermal boundary layer of varying thickness, and the pressure gradient in it drives flow towards the thicker regions. There was then a shear and a vertically downwards gradient of momentum flux at the wall. The boundary layer was anticipated to erupt when its thickness reached a critical value. Assuming that the interior momentum flux was entirely by Reynolds stresses, and matching the interior and the boundary layer fluxes of heat and momentum, the author determined the time scale of periodicity. The estimate was shown to be in reasonable agreement with the experimental observations.

Manga *et al.* (1999) have performed experiments, in which a layer of fluid was heated from below and cooled from above, in order to study convection at higher Rayleigh and Prandtl numbers. The working fluid, corn syrup, has a viscosity that depends strongly on temperature. Viscosity within the fluid layer varied by a factor of 6 to 1.8×10^3 in the experiments. A total of 28 experiments were performed for Rayleigh numbers in the range from 10^4 to 10^8 and Prandtl numbers in the range from 10^3 to 10^6 . As the Rayleigh number increased above 10^5 , flow changed from steady to a time-dependent behaviour. As the Rayleigh number increased further, large scale flow was gradually replaced by isolated rising and sinking plumes. At a Rayleigh number greater than 10^7 , there was no evidence of any large scale circulation, and flow consisted only of plumes. Plumes were seen to have mushroom-shaped “heads” and continuous “tails” attached to the respective thermal boundary layers. The characteristic frequency for the formation of these plumes was consistent with a $Ra^{2/3}$ scaling. The authors have also reported that the Nusselt number (Nu) at high Rayleigh number was lower than that expected, based on the extrapolation of low Rayleigh number experimental data; at the highest Rayleigh number, the equivalent Reynolds number approaches unity. The authors have suggested that the reduction in the Nusselt number was the result of inertia decreasing the speed of the ascending and descending thermals, and thus the rate of advective heat transport.

Theerthan *et al.* (2000) performed experiments in turbulent free convection in a horizontal fluid layer above a heated surface. Experiments were carried out above a heated surface to obtain the planform structure and the heat transfer characteristics. Water was the working fluid and the range of the flux Rayleigh number⁴ covered was $3 \times 10^7 - 2 \times 10^{10}$. The experimental conditions corresponded to Rayleigh-Benard convection, with either the top water surface open to atmosphere or covered with an insulating plate, and with an imposed external flow over the heated boundary. The visualization of the planform was carried out using an electro-chemical dye technique.

⁴The flux Rayleigh number is defined as $Ra = \frac{g\beta(\frac{qH}{k_f})H^3}{\nu\alpha}$ and is useful for prescribed heat flux boundaries.

Without the external flow, the planform was one of randomly-oriented line plumes. At a large Rayleigh number and a small aspect ratio, the line plumes seemed to align along the diagonal, presumably due to a large scale flow. The side view showed inclined dyelines, again indicating a large scale cross-flow. When the external flow was imposed, the line plumes clearly aligned in the direction of the external flow. The nondimensional average plume spacing, $Ra_\lambda^{1/3}$, varied between 40 and 90. The heat transfer rate, for all the experiments conducted, were represented as $Ra_\delta^{-1/3}$, where δ is the conduction layer thickness. It was seen to vary only between 0.1-0.2. The results showed that in turbulent convection the heat transfer rates were self-similar for different boundary conditions.

In continuation with the studies on turbulent Rayleigh-Benard convection Chavanne *et al.* (2001) have experimented with helium (He) at a low temperature. This allowed the Rayleigh number (Ra) to be raised to 2×10^{14} , while the Prandtl number (Pr) was slightly larger than 0.7. Density changes continued to be small enough for the Boussinesq approximations to remain valid. The authors have concluded through the calorimetric measurements that departure from the 2/7 regime occurs above $Ra = 10^{11}$ toward a new regime where heat transfer is enhanced. From measurements of two nearby thermometers, the change was traced to a laminar-turbulent transition of the velocity boundary layer induced by the large-scale flow near the walls of the cell. The experimental data showed that the thermal boundary layer lies within the viscous sublayer of the turbulent boundary layer.

The literature review on one-layer convection reveals considerable complexities of Rayleigh-Benard convection. Issues addressed include roll alignment, loss-of-roll phenomena, stability criteria for unsteadiness, three dimensionality of the temperature field and turbulence in the flow field. The essential characteristics of one-layer convection help in understanding the flow characteristics of two-layer convection in a confined cavity. The present thesis is an experimental study of convection in superposed horizontal fluid layers confined in rectangular and axisymmetric cavities. The following section reviews the literature on two-layer convection, from this perspective.

2.2 Two-layer convection

Two-layer convection is an interesting transport process to study, for reasons both theoretical and practical. Theoretically, the problem is one of nonlinear dynamics with a wide range of parameters. This includes ratios of the properties of the fluids, the total depth of the layer and the depth fraction of one fluid. Some of the important applications

of two-layer convection can be seen in the model for convection in earth's mantle and liquid-encapsulated crystal growth.

Two-layer convection differs from that in a single layer mainly in terms of the appearance of an interface. In the absence of an interface, single fluid convection is driven solely by the gravitational field through the mechanism of buoyancy, leading to Benard convection. Inclusion of an interface means that additional factors such as surface tension gradients also determine the onset conditions as well as the planform of the convective flow. Fluid motion driven solely by surface tension gradients is known as Marangoni convection. When a temperature difference is applied across a liquid layer with a free surface, convection can be initiated by two mechanisms: Marangoni (gradients in interfacial tension) and Benard (gradients in density)⁵. Interfacial tension gradient-driven convection is caused by the variation of interfacial tension with temperature. It can occur when the liquid is heated from above or from below. Buoyancy-driven convection occurs only when the fluid, with a negative thermal expansion coefficient, is heated from below. Dynamic viscosity acts in a manner that dissipates the kinetic energy of the convective flow. At the same time, thermal diffusivity leads to an equalization of density in the fluid medium and a reduction in the buoyancy potential. The configuration of differentially heated superposed fluid layers leads to a modified form of the original Rayleigh-Benard problem, in which a larger number of factors determine the flow pattern.

An important criterion that differentiates two-layer from one-layer convection is the flow coupling mechanism established at the interface. In a two-layer system, Rayleigh-Benard convection is characterized by two distinct modes of flow coupling between the fluid layers. These are respectively called thermal and mechanical coupling. Thermal coupling is identified as the situation where vorticity has the same sign on both sides of the interface. Mechanical coupling is characterized by opposite signs of vorticity on either side of the interface. This is possible if shear develops in a very thin region along the interface.

Despite the numerous interesting features of two-layer convection, there are difficulties that are in part responsible for the fact that it did not receive sufficient attention in earlier years. First, there is the high-dimensional parameter space of the problem. This has made it difficult to gain an overview over the manifold of solutions of the linear problem. Convection in a single layer of a Boussinesq fluid is governed by two dimensionless parameters, the Rayleigh and the Prandtl number, of which the latter drops out from the linear version of the problem. In contrast, of the order of ten non-dimensional

⁵Buoyancy driven convection in a differentially heated fluid layer is variously known as Benard, Rayleigh and Rayleigh-Benard convection.

parameters may be important in the two-layer problem. Some of those parameters, such as the Marangoni number for the interface can be eliminated from the problem by the consideration of special limits.

Only a very small region of the parameter space is accessible in laboratory experiments. The experimental difficulties are compounded by the fact that there are few combinations of liquids that are truly immiscible. In most cases some diffusion of material occurs across the interface and the experiments have to be carried out in such a way that the time scale of the dynamic processes is short in comparison with time scale of the change of properties by the effects of diffusion. Nevertheless, there are a number of interesting features that can be realized in the laboratory. Examples are the flow coupling mechanism at the interface and the interface deformation with a change in temperature difference across the cavity. Careful measurements are highly desirable, especially with respect to nonlinear effects which are not amenable to simplified theoretical analysis.

2.2.1 Theoretical aspects of two-layer convection

The phenomenon of cellular convection discovered by Benard (1901) has attracted the attention of many researchers. A fundamental theoretical paper is that of Rayleigh (1916), who associated instability with buoyancy resulting from the expansion of a heated fluid. Later, other workers have extended and refined Rayleigh's analysis to superposed fluid layers. In all these treatments the agency causing instability has been buoyancy.

Pearson (1958) neglected buoyancy but offered a new explanation for the onset of instability. The author showed that if the upper surface was free, then Benard-type cells could be produced by tractions arising from the variation with temperature of surface tension. It was argued that in many of Benard's experiments the cells observed must have been due to a surface-tension effect rather than buoyancy. The analysis involved a more complicated set of boundary conditions, but a simpler differential equation system, than the corresponding formulation based on the Rayleigh number. Surface tension was assumed to be a linearly decreasing function of temperature and the deficit of surface tension force between two points on the interface was balanced by shear forces. Gravity was ignored and therefore density-gradient effects, and the effect of the superposed fluid did not contribute to the final solution. In addition the interface was assumed to be flat (undeformed) and the heat-transfer coefficient on the upper surface was assumed to be independent of the convective motion.

Nield (1964) studied the surface tension and buoyancy effects numerically in cellu-

lar convection. The buoyancy and surface tension effects were jointly considered. Linear perturbation techniques were applied to derive a sixth-order differential equation subject to six boundary conditions. A Fourier series method was used to obtain the eigenvalue equation for the case where the lower boundary was a rigid conductor and the upper free surface was subject to a general thermal condition. In the discussion, the author predicted that since the critical Marangoni number decreases with an increase in the Rayleigh number, the two agencies causing instability reinforce each other. It was concluded that the two agencies namely buoyancy and surface tension reinforce each other and are tightly coupled when the free surface is insulating. When the free surface was conducting, the coupling was weak. It was observed that the cells formed by surface tension are approximately the same size as those formed by buoyancy. Since Marangoni number contains a factor of d^2 while Rayleigh number depends on d^4 , d being the layer height, it was expected that surface tension would become more important for thin layers of the liquid⁶.

The problem of convection in two superimposed layers of immiscible liquids has attracted considerable attention because of the possibility of Hopf bifurcation. This denotes the transition from a motionless state to either a pair of travelling or a single standing wave. A single layer of fluid heated from below becomes unstable only through a monotonically growing instability, but the possibility of overstable oscillations cannot be excluded in two superimposed layers.

Busse (1981) has examined the onset of linear nonoscillatory instability of the arrangement where the unperturbed fluids are static and lie in two layers of unequal thickness with a flat horizontal interface. In particular, the focus was on the range of parameters pertinent to a model of mantle convection in which the two layers represent the upper and lower mantles. The depth of the upper mantle is small compared with that of the lower mantle. It was concluded that the horizontal scale of convection in the lower mantle can determine a horizontal scale of flow in the upper mantle. Hence, it is possible that the horizontal scale of convection in the upper mantle may not necessarily indicate the depth of convection in this layer. In numerical analysis, the author did not consider distortion at the interface and excluded time-periodic motions.

Two-layer convection has been studied in a cylindrical geometry by quite a few authors, mainly due to its application to crystal growth. Here the melt is placed in a crucible, cylindrical in shape and the grown crystal is drawn from it. The top layer corresponds to the encapsulant floating over the liquid alloy.

⁶This dependence on the layer height assumes one of the boundaries to be of the constant flux type. For isothermal surfaces, Marangoni and Rayleigh numbers depend on d and d^3 respectively.

Vrentas *et al.* (1981) applied a linear theory with some aspects of a nonlinear analysis to study jointly the surface tension-driven and buoyancy-driven convection. These studies were carried out in a bounded cylindrical geometry with a free surface configuration for a range of aspect ratios and Nusselt numbers. The aspect ratios (with the horizontal dimension as the radius of the cylinder) were chosen in the range of 0.5 to 20, while the Nusselt number range was 0.01 to 100. The top free surface of the vertical cylinder was in contact with an inviscid gas phase. The other objective of the study was the development of a somewhat different method for analyzing free convection problems. This method involves the use of Green's function to reduce the problem to the solution of an integral equation. The following assumptions have been adopted in the analysis for studying thermal convection in the axisymmetric configuration: (a) the gas phase is inviscid and the liquid phase is a one-component Newtonian fluid; (b) the surface phase is an ideal surface liquid with mechanical properties determined solely by the surface tension; (c) all physical properties with the exception of density and surface tension are constant; (d) there is no mass transfer between the gas and liquid phases; (e) viscous dissipation is negligible; (f) the standard Boussinesq approximation is introduced so that the surface tension and the density in the body force term are linear functions of temperature; (g) the Prandtl number of the liquid is infinity; (h) the surface tension is sufficiently high so that deformation of the free surface is negligible, and it is possible to assume that the interface is effectively flat; (i) the velocity and temperature fields are axisymmetric.

Vrentas *et al.* (1981) have determined the values of the critical Marangoni and Rayleigh numbers $((Ma)_0$ and $(Ra)_0$) at the first bifurcation point, as functions of the Nusselt number and aspect ratios. The simplicity of the eigenvalues implies that they are bifurcation or branch points for the system. At a given value of Nusselt number, there is a general reduction of both $(Ma)_0$ and $(Ra)_0$ with increasing aspect ratio, and as much as nearly an eight-fold drop was observed for the considered cases. This effect was of course expected since the lateral wall can severely inhibit convective motion and thus have a stabilizing effect. The effect of the side wall diminishes along with an increase in the Nusselt number for both Marangoni and Rayleigh problems. Vrentas *et al.* (1981) claimed their results to be the first comprehensive computations for the free surface geometry. Their simulation for the Marangoni problem shows that only radial rolls appear in the container and there is no vertical stacking of the cells at the first bifurcation point. Thus the number of rolls gives a representative picture of the nature of the cellular motion. For buoyancy-driven convection, there was no vertical stacking of rolls for the higher order bifurcation points. The authors have concluded that it is preferable to study cellular convection in geometries with small aspect ratios (less than

about 4). This is to avoid the possibility that more than one solution may be observed owing to the inevitable thermal fluctuations present in the physical systems.

Renardy and Joseph (1985) performed a linear stability analysis in a two-dimensional Benard problem with two layers. The fluid layers lying between infinite parallel plates were heated from below. The study concentrated on the Benard problem without the Marangoni effect and showed that the equations were not self-adjoint. For the fluids, Boussinesq approximation⁷ was adopted. Renardy and Joseph (1985) have provided a theoretical proof that demonstrates that the onset of convection can occur through an oscillatory instability if the deformation of the interface is considered. Also, the two fluids can have time-periodic solutions near criticality. Thus the system can lose stability to time-periodic disturbances. It has been shown numerically that when the viscosities and coefficients of volume expansion of the fluids are different, a Hopf bifurcation can occur, resulting in a pair of travelling waves or a standing wave. This result may have an application in the modeling of convection in the earth's mantle.

The geometry other than axisymmetric, studied by many authors for the two-layer convection problem is a cavity rectangular or square in plan.

Dijkstra *et al.* (1992) numerically studied the structure of cellular solutions in Rayleigh-Benard-Marangoni flows in small-aspect ratio containers. The problem addressed was to identify pattern selection for flows driven by surface-tension gradients at the onset of instability. The geometry was such that interface deformations were small but Marangoni convection was significant, in addition to buoyancy effects. Techniques of numerical bifurcation theory were used to study the multiplicity and stability of two-dimensional steady flow patterns (rolls) in rectangular small-aspect-ratio containers. Owing to computational limitations, the problem was restricted to two-dimensional containers. Though the basic flow is three-dimensional, two-dimensional results give an insight into the processes that govern convection dynamics in confined flows and are a necessary starting point for any three-dimensional calculation. Dijkstra *et al.* (1992) have modeled a two-dimensional container which was partially filled with a Newtonian viscous liquid. An ambient gas surrounds the liquid at its top. The temperature of the gas far away from the gas-liquid interface was T_0^* . The lower wall was heated to a temperature of T_1^* . The sidewalls were assumed to be perfectly insulated. Due to a vertical temperature gradient established over the layer, heat is transferred from the liquid to the gas. Boussinesq approximation was applied to the liquid phase. It was assumed to be an incompressible fluid, while density varied with temperature alone. For

⁷This calls for all the fluid properties to remain constant with temperature, except density in the gravity term of the Navier-Stokes equations.

pure Marangoni flows at moderate Biot and Prandtl numbers, the transitions occurring when paths of codimension 1 singularities intersect determine to a large extent the multiplicity of the stable patterns. These transitions lead to Hopf bifurcations and stable periodic flows over a small range of aspect ratios. The authors have also considered the effect of sidewalls on the multiplicity of stable and unstable patterns. The influence of the no-slip sidewalls with that of slippery sidewalls have been compared. The following were the reported observations: (i) The critical Marangoni numbers at onset are larger for no-slip sidewalls and therefore the no-slip condition stabilizes the conduction solution. (ii) Transcritical primary bifurcation points occur in the no-slip case when an even number of cells branch off. All bifurcation points are of pitchfork type for slippery sidewalls because of the break in the additional translational symmetry. Hence, subcritical convection is absent for slippery sidewalls. (iii) The double points at onset, where two modes compete, occur at a larger aspect ratio in the no-slip case. (iv) The multiplicity of stable patterns is smaller in the no-slip case. This is due to the occurrence of additional limit points and closed branches. Finally, the no-slip lateral walls lead to hysteresis effects and typically restrict the number of stable flow patterns through the appearance of saddle node bifurcations. In this way no-slip sidewalls induce a selection of certain patterns, which through secondary bifurcation lead to the largest Nusselt number.

During solidification of electronic materials, thermal convection within the melt may cause undesirable crystallographic inhomogeneties in the solid phase. The technique of liquid encapsulated crystal growth has been used to reduce component evaporation and thus non-stoichiometric solidification within the melt, with the ultimate goal to produce defect-free mono-crystalline electronic material. In this connection, Prakash, Koster and co-workers have published a series of papers on multilayer and thermocapillary convection. These studies have been carried using numerical simulation, and are described below.

Doi *et al.* (1993) studied thermocapillary convection in two immiscible liquid layers with one free surface and a liquid/liquid interface. Differential heating was applied parallel to the interfaces. An analytical solution was introduced as an initial condition for infinite horizontal layers. The defining parameter for the flow pattern was λ , the ratio of the temperature coefficients of the interfacial tension and the surface tension. Four different flow patterns were seen to exist under zero gravity conditions. *Halt* conditions which stop the fluid motion in the lower liquid layer that is encapsulated were found. A numerical experiment was carried out to study the effect of vertical end walls on the double layer convection in a two-dimensional cavity. The halt condition obtained from the analytical study was found to be valid in the limit of small effective Reynolds number.

The flow in the encapsulated liquid layer could be substantially suppressed.

Prakash *et al.* (1993a) presented their studies of convective flow in a three layer liquid system with rigid upper and lower boundaries. The middle liquid layer was encapsulated on both sides by immiscible liquids, and featured two interfaces. The driving mechanism for convective flow were the two interface tension gradient forces and buoyancy. To study mechanical coupling across interfaces between immiscible liquids, the influence of varying encapsulant layer viscosity and height was investigated, both in terrestrial and low gravity environments. Regions of distinct flow patterns were identified.

Prakash *et al.* (1993b) studied convective flow with surface tension and buoyancy effects in a liquid layer with two horizontal interfaces. The flow resulted from the interaction of two forces of interface tension of different magnitude in the horizontal direction with additional buoyancy forces acting perpendicular to the interfaces. To study the contribution of buoyancy on the convective flow, the gravity level perpendicular to the interfaces was varied from microgravity level to earth gravity and beyond to high gravity. This created a fluid mechanical system where buoyancy forces of variable strength could augment or oppose interfacial tension driven convection. Regions of distinct flow patterns were again identified.

Prakash *et al.* (1994a) considered the problem of convective flow in three immiscible liquid layers. The layers were enclosed in a shallow rectangular cavity that is differentially heated with rigid and insulated upper and lower boundaries. As a model for multiple layers, a three-layer system featuring two non-deformable interfaces was investigated. The method of matched asymptotic expansions was used to determine the flow in the two distinct regions: the core region characterized by parallel flow; and the end-wall regions where flow turns around. The driving mechanism for convection was buoyancy. To study mechanical coupling across interfaces between immiscible liquids, the influence of varying encapsulant viscosity was investigated.

Prakash *et al.* (1994b) studied convection in multiple immiscible liquid layers with deformable interfaces. The fluid layers were confined in a shallow rectangular cavity with rigid and insulated upper and lower boundaries. The three-layer system was once again considered as a model for multiple liquid layers. The middle layer was encapsulated on both sides by immiscible liquids, and featured two deformable interfaces. The method of matched asymptotic expansions was used to determine the flow in the two distinct regions: the core region characterized by parallel flow; and the end-wall regions where flow turns around. Interfacial tension gradients induced by differential heating of the cavity led to fluid flow. Mechanical coupling across interfaces between immiscible liquids

was investigated by varying the encapsulated viscosity and the height of encapsulant layers.

Prakash *et al.* (1994c) presented the results from an analytical study of thermocapillary convection in an immiscible three-layer liquid system. The liquids were confined in a box. In the absence of gravity, two parallel interfacial tension gradients drive the flow. Thermocapillary flow in select combinations of immiscible liquids were analyzed in support of a space flight experiment aboard the Second International Microgravity Laboratory (IML-2).

Burkersroda *et al.* (1994d) investigated the variation of interface tension with temperature on thermocapillary flow in a microgravity environment. Measurements of surface and interface tension coefficients as a function of temperature for various silicone oil and fluorinert liquid combinations were reported. The measurements were compared with theoretical estimates obtained from Antonow's rule and from a method proposed by Girifalco and Good.

Prakash and Koster (1996a) further pursued studies on thermocapillary convection. The authors studied analytically a two-dimensional layer of GaAs which is symmetrically encapsulated by liquid B_2O_3 . The unknown interface tension gradient between B_2O_3 and GaAs was parameterized, and its influence, along with the influence of varying encapsulant thickness on flow in the GaAs melt was investigated. A thinner B_2O_3 layer was found to be more efficient for reducing flow in the GaAs melt.

Koster and Nguyen (1996) studied natural convection in two immiscible liquid layers with density inversion present in the lower layer. Their objective was to evaluate numerically the flow pattern and heat transfer when the density inversion temperature had a value between the hot and the cold side wall temperatures. The two immiscible fluids were silicone oil (2 cSt) on top of the density inversion fluid, namely water. The two fluids were enclosed in a rectangular box having a cavity aspect ratio of 2. The aspect ratio of individual layers was unity. The right wall was cold with a temperature T_c that was kept constant and fixed below the density inversion point. The left wall was heated to T_h , and kept at, or above, the density inversion temperature. The temperature difference between the side walls was increased by increasing the temperature T_h . The horizontal top and the bottom walls were thermally insulated. Simulation for the double layer problem was carried out on the commercial finite element computer code FIDAP. Interface deformation was considered to be so small that it was neglected in the discussion. The authors concluded from their results (Figure 2.4) that the two layers were viscously as well as thermally coupled. Two counter-rotating natural convection

rolls of opposite vorticity developed when side wall temperature in the density inversion fluid was above and the other below the density inversion temperature. In contrast,

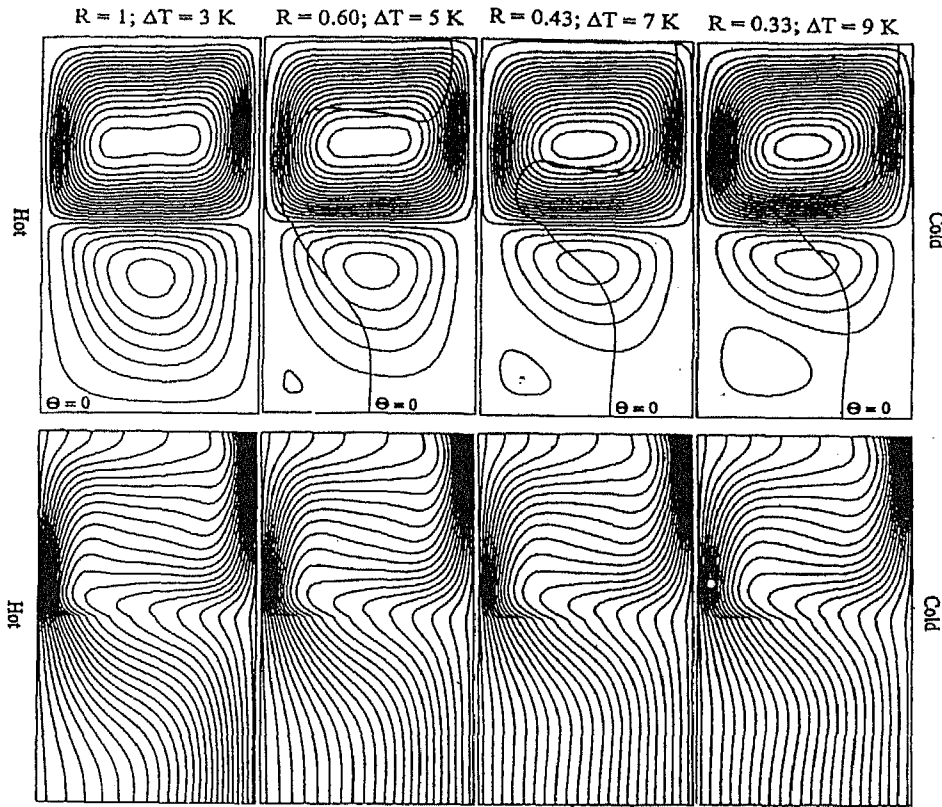


Figure 2.4: Streamline (top) and temperature (bottom) contours at various temperature gradients, after Koster and Nguyen, 1996.

only one roll cell develops in a liquid layer with Boussinesq properties. Viscous coupling between the two immiscible layers strengthened the roll with opposite vorticity in the density inversion layer. At large Rayleigh numbers the flow patterns in the water layer were seen to become very complex. The largest heat transport occurred in the upper layer. The two-roll pattern in the water layer was seen to impede the total horizontal heat transfer. A vertical heat transport mechanism existed across the interface from the density inversion layer into the encapsulating upper layer. The moving interface between the immiscible liquids improved the heat transfer in each layer when compared to the differentially heated cavity of Rayleigh-Benard convection.

Dauby and Lebon (1996) studied Benard-Marangoni convection in a three-dimensional rectangular container with rigid lateral walls. It was assumed that the upper surface of the layer was flat and non-deformable and that the lateral walls were thermally insulated. The authors considered both linear and nonlinear analyses. The dependence of the results of linear analysis on non-zero Rayleigh and Biot numbers was also examined.

In the nonlinear study, the Rayleigh and Biot numbers were fixed to zero and the Prandtl number was equal to 10^4 (silicone oil). The basic equations were derived assuming a thin viscous layer filling a rectangular container at its boundaries. The thickness of the layer was equal to d and the length and width of the container were a_1d and a_2d respectively (a_1 and a_2 being the aspect ratios). The surface tension at the upper surface was assumed to be temperature dependent. The fluid was heated from below. The bottom of the box was rigid and perfectly heat conducting. A spectral tau method was used to determine the critical Marangoni number (Ma_c) and the convective pattern at the threshold as functions of the aspect ratios of the container. For $Ra = Bi = 0$, the calculations were performed for aspect ratios varying by discrete steps of 0.2. The critical Marangoni number was seen to be a globally decreasing function of the lateral dimensions of the container. When both a_1 and a_2 became greater, Ma_c tended to 79.607, the value found for an infinite box. Dauby and Lebon (1996) have also provided a general overview on convection in 'actually' rectangular containers (a_1 and a_2 being different). The dimensions $(a_1, a_2) = (3.2, 1.5)$ of the rectangular box enabled the authors to study the nonlinear evolution of a unique roll parallel to the longer sides of the box. The other two boxes $[(a_1, a_2) = (5.4, 3.2)$ and $(a_1, a_2) = (6.6, 3.2)]$ were selected to study the competition between three or four rolls parallel to the shorter sides and the two rolls parallel to the longer ones that were nearly unstable at the threshold. The cavity $(a_1, a_2) = (6.6, 5.2)$ showed the evolution of four linearly unstable rolls parallel to the shorter sides when three rolls parallel to the longer sides were nearly critical at $Ma = Ma_c$.

The onset of flow from a quiescent state, when a layer of fluid is heated from below with an upper free surface, is one of the classical stability problems of fluid mechanics and the subject of many investigations. Zaman and Narayanan (1996) presented their findings on pattern formation at the bifurcation point starting from the quiescent state for free surface convection in a circular container. The problem of pattern formation as affected by side walls is strongly associated with crystal growth by the Bridgman technique. The aspect ratio keeps changing during crystal growth on account of a moving interface. The other reason of the research was to perform detailed numerical calculations that examine the splitting of solutions and generation of cascaded bifurcation as the aspect ratio of the containers increase. Zaman and Narayanan (1996) modelled the physical system as consisting of a right circular cylinder having liquid (oil) underlying a gas (helium or air). The lower solid boundary was at a constant temperature T_0 and the upper solid surface was at a temperature of T_1 . The temperature of the interface in the conductive state was T_i . The thermal conditions on the side walls were specified to be either perfectly insulating or perfect conducting. For the conduction case, the conductivity of the side walls was set equal to that of the liquid. Boussinesq form of

the continuity, Navier-Stokes, and energy equations were used for the simulation of the convection problem. The flow pattern at the onset of convection was obtained from the calculations. These were determined from the eigen functions while the eigenvalues were identified as the critical Marangoni numbers. The Rayleigh and Biot numbers as well as aspect ratios and the azimuthal mode m were fixed for a given calculation. Zaman and Narayanan (1996) calculated the first three critical Marangoni numbers or bifurcation points for the axisymmetric case ($m=0$) when Rayleigh number is equal to zero, for a variety of aspect ratios and Biot numbers of 1 and 100. These results were compared with the reported numerical work of Vrentas *et al.* (1981). For the case of the first bifurcation point for $Ma = 0$ and $Bi = 100$, there was a discrepancy for the pure Marangoni problem only at small aspect ratios while the comparison for the pure Rayleigh problem was very good. Comparing critical Marangoni numbers between the case of insulated and conducting side walls, it was seen in nearly all the cases that conducting side walls lead to a higher critical Marangoni number. This indicates a greater stability to disturbances. The authors have also compared their results with the experimental work of Koschmieder and Prahl (1990). The critical temperature differences were calculated and the corresponding critical Rayleigh and Marangoni numbers were compared with the experiments. It was observed that the calculated Marangoni numbers were above the experimental values by about 22% (Figure 2.5). The reasons given for this discrepancy was partly due to the transcritical nature of Rayleigh-Marangoni convection, possible imperfections of the side walls, and an uncertainty in the thermophysical properties of the fluids considered in the experiments. The other area of comparison was in terms of the predicted and the observed flow patterns. The results matched with the experiments for the aspect ratio of 2.16 while there was a difference for other aspect ratios of 2.655, 3.295 and 4.145. The principal observation was that narrow containers give rise to definite stable patterns at the onset of convection. However, the medium aspect ratio containers (aspect ratio >3) show spectral crowding and closed branches. Also, it was found that for a large range of aspect ratios the axisymmetric mode ($m = 0$) was the most unstable and that codimension-2 points occur for either large or somewhat small (<1.0) aspect ratios⁸.

Convection is important in crystal growth from its melt as it will affect the quality of the crystal structure and the distribution of the dopants. A cylindrical geometry is commonly employed for the liquid-encapsulation crystal growth. In this context, Johnson and Narayanan (1997) studied the effects of boundaries on bilayer convection in a cylinder with idealized boundary conditions. In their mathematical model, a system

⁸At codimension-2 points, two flow modes coexist at the smallest Marangoni number.

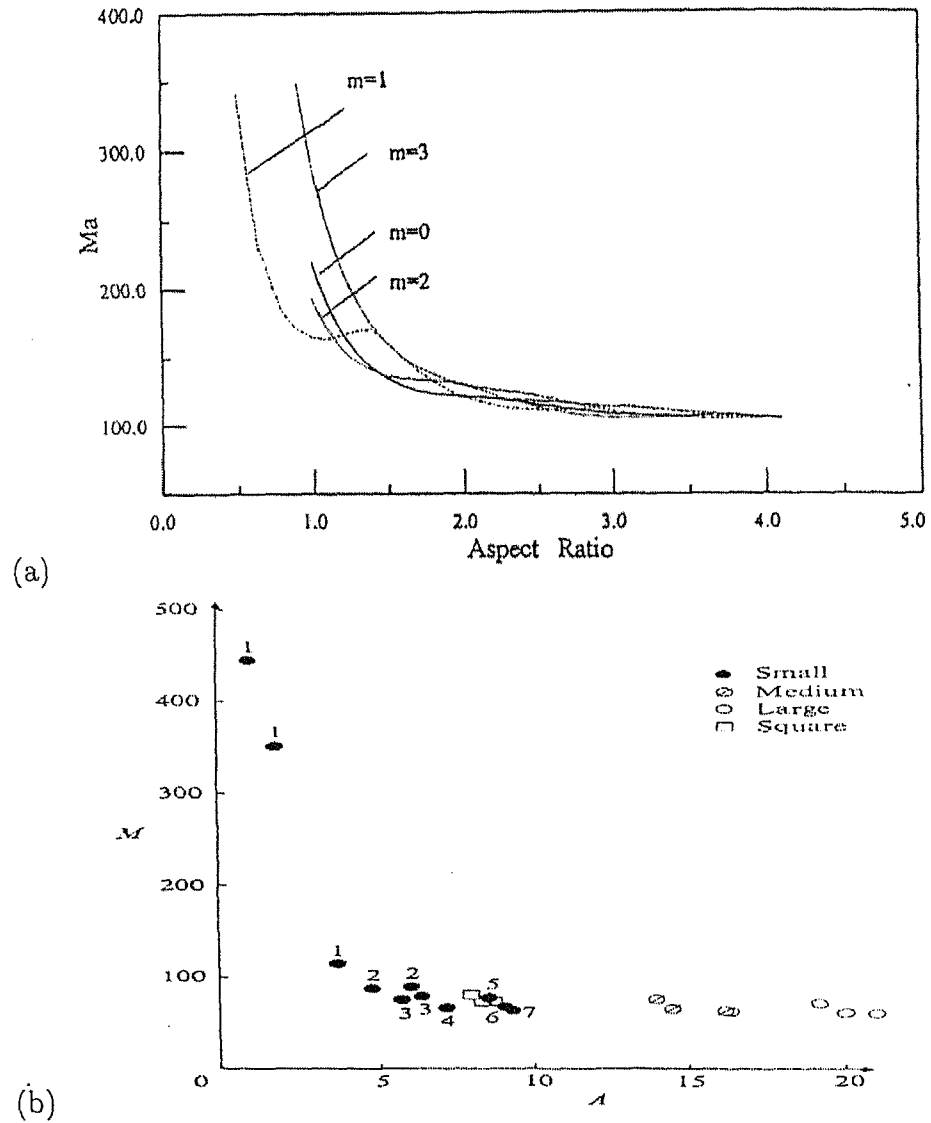


Figure 2.5: Comparison of critical Marangoni numbers versus aspect ratio for various modes for the case of $Ra = 100$ and $Bi = 1$ in (a) Zaman and Narayanan (1996) with the experiments of (b) Koschmieder and Prahl (1990).

of two fluid layers was bounded on the top of the upper fluid, and the bottom of the lower fluid by rigid conducting plates. The interface between the lower and the upper fluids was allowed to deform. The mathematical model of this geometry was bounded in the vertical direction by rigid plates, and was taken to be infinite in the horizontal direction. The density and interfacial tension for both fluids were assumed to be a linear function of the temperature. For solving the governing equations, the Chebyshev spectral tau method was used. This method easily incorporates the complicated boundary conditions and provides the accuracy needed using only a few terms. On applying this method, the ordinary differential equations in terms of the coefficients generates an

eigenvalue problem. The eigenvalue is the critical Rayleigh number for the transition being studied. Johnson and Narayanan (1997) presented their findings by giving the qualitative picture of the different ways in which convection can occur in a bounded cylinder. The different types of two-layer convection depend upon the layer in which the convection is most dominant. The types of convection also depends upon how the layer that did not initiate convection responds to the layer that did initiate convection. The hierarchy of convection mechanisms has been explained in the study by looking at interfacial structures and also by considering the perturbed temperature and velocity profiles through the fluid layers. Specific examples of silicone oil-air and glycerol-silicone oil have been used to exemplify the arguments. The sidewall conditions posed some difficulties in computations; therefore it was assumed that the vertical and tangential components of vorticity vanished at the vertical sidewalls. This assumption has allowed the results of the unbounded case and the qualitative features as a function of the aspect ratio to be determined. It was observed that the aspect ratio did indeed affect the nature of the onset of convection. As the depths of the fluid were assumed constant, it was apparent that the change in radius could affect the physics of the flow and the flow structures. This was shown in terms of the convection coupling, either thermal or viscous to change with the width of the container, even as the height was fixed. Thus, as the aspect ratio changed, the convection switched from viscous coupling, to oscillatory flow, and to thermal coupling. This unusual result was explained by the observation that a change in the radius changes the aspect ratios of both fluid layers. The energy required for each layer to sustain convection changes differently with aspect ratio because of differing thermo-physical properties. Moreover, the onset of oscillations and sudden pattern changes at the codimension-2 points were observed.

Marangoni convection is seen in the context of heat or mass transfer across the liquid layer(s). If heat or mass transfer occurs in the vertical direction, there exists two monotonic modes of Marangoni instability. One mode is caused purely by surface tension gradients leading to the formation of a cellular convective structure; deformations of the free liquid surface are subservient to this cellular convective motions, and are usually negligible. The other mode is connected with deformations of the free surface governed by gravity and capillary forces.

Golovin *et al.* (1997) presented a theory on nonlinear evolution and secondary instabilities in Marangoni convection in a two-layer liquid-gas system with a deformable interface, heated from below. In the analysis, the effect of buoyancy was neglected, and Marangoni convective instability was considered to be predominant. The objective was to take into account the convective motion and heat transfer both in the liquid and in

the gas phases. A system of nonlinear evolution equations was derived that describes a general case of slow longscale evolution of a short-scale hexagonal Marangoni convection pattern near the onset of convection, coupled with a long-scale deformational Marangoni instability. Two cases were considered: (i) when interfacial deformations are negligible; and (ii) when they lead to a specific secondary instability of the hexagonal convection. In the first case, the extent of the subcritical region of the hexagonal convection cells, selection of convection patterns - hexagons, rolls and squares - and transitions between them were studied. The effect of convection in the gas phase was also investigated. Theoretical predictions were compared with experimental observations. The authors observed that the liquid Prandtl number and heat transfer between the liquid and the gas layers play an important role in the selection between rolls and squares. There was a clear tendency for the hexagons-to-squares transition in liquids with larger Prandtl numbers, whereas in liquids with a smaller Prandtl number, the hexagons-to-rolls transition was seen to occur. Heat transfer in the gas phase also plays an important role in transition from hexagons to other patterns. In the second case, the interaction between the short-scale hexagonal convection and the long-scale deformational instability, when both modes of Marangoni convection were excited, was studied. The authors concluded that the short-scale convection suppresses the deformational instability. The latter could appear as a secondary long-scale instability of the short-scale hexagonal convection pattern. This secondary instability was shown to be either monotonic or oscillatory, the latter leading to the excitation of deformational waves, propagating along the short-scale hexagonal convection pattern and modulating its amplitude.

Results of a linear analysis of convection in confined geometries must tend to Nield's results (1964) corresponding to horizontally infinite domains when the aspect ratio becomes large. In Zaman and Narayanan's paper (1996), the critical numbers for an aspect ratio equal to 8 were within Nield's values by 1.2% but are smaller than these values. Dauby *et al.* (1997) commented that this was astonishing since side walls should play a stabilizing role. Accordingly these authors developed a linear analysis for the coupled gravity (Benard) and capillarity driven (Marangoni) instability. They carried out studies in a rigid circular container. The fluid assumed to be Newtonian was filled with a layer of thickness d in a circular container having radius ad , where a is the aspect ratio. The surface tension at the upper free surface was temperature dependent and the fluid was heated from the below. The aim was to develop a computer code which allows one to determine altogether the Rayleigh and Marangoni numbers defining criticality. Also, the experimental arrangement used by Koschmieder and Prahl (1990) was carefully modelled. In particular, it was shown that the Biot number in the calculations depends on the aspect ratio of the container. A numerical scheme based on the spectral tau method

with Chebishev decompositions in both the z and r directions was used in the study. The boundary conditions assumed was that the bottom of the box is rigid and perfectly heat conducting and the upper surface of the fluid was taken to be free, planar, and nondeformable. The lateral side wall was rigid with both conducting and adiabatically insulated thermal conditions being modelled. From the results, the authors concluded that the critical Marangoni numbers for finite boxes were larger than the values corresponding to an infinite domain. This indicates the rigid side walls are stabilizing as expected. Also it was noticed that the critical Marangoni numbers for insulating side walls are always smaller than for conducting ones. This is due to the fact that a temperature perturbations arriving at an insulating boundary is reflected towards the bulk of the fluid, while it is dissipated near the walls when these are conducting. Because of this reason, it was predicted that the conducting side walls give rise to more stable systems. Results were also presented for the critical Marangoni number as a function of aspect ratio for the case of insulating side walls when $Ra = Bi = 0$. The aspect ratio was varied from 0.5 to 5. It was observed that the critical Marangoni numbers are globally a decreasing function of the aspect ratio of the box for the azimuthal wave number range of 0 to 3. For a Biot number other than zero, the authors concluded that for insulating side walls, Ma_c was not globally decreasing. The reason was that in small aspect ratio boxes, the instability is mainly driven by gravity, while in larger boxes, the Marangoni effect is dominant and the critical Rayleigh number tends to zero. The authors also presented results based on the convective patterns obtained at the threshold. It was observed that for very small aspect ratio (0.7), the critical mode was $m=1, i=0$ (radial wave number). The convective structure showed an upflow in the right-hand half of the container and a symmetrical downflow in the left-hand part. For an aspect ratio of 1.8, the pattern was axisymmetric and consisted of a circular roll centered in the middle of the box. For $a = 2.5$, the structure was made of three transverse and somewhat deformed rolls. Near $a = 3.4$, the pattern was axisymmetric and consisted of two concentric rolls. For $a = 4.15$, the wave numbers were $(m,i)=(1,2)$ and five deformed transverse rolls were displayed. In summary, it can be said that an increase in the Rayleigh number lowered Ma_c but no significant variation in the flow pattern was observed. An increase of the Biot number made the critical Marangoni number larger since perturbations could be dissipated in the upper gas layer. In this case, the cells become smaller as Bi increases but the succession of the patterns for increasing aspect ratios remain unchanged. Thus, it was concluded that buoyancy and the Biot number were not important for the sequence of eigenmodes generated by Marangoni convection.

Boeck and Thess (1999) studied surface-tension driven Benard convection in low Prandtl number fluids by direct numerical simulation. The flow was computed in a

three-dimensional rectangular domain with periodic boundary conditions in both horizontal directions and either a free-slip or no-slip bottom wall. A pseudospectral Fourier-Chebyshev discretization was used. Deformations of the free surface were neglected. The smallest possible domain compatible with the hexagonal flow structure at the linear stability threshold was selected. As the Marangoni number was increased from the critical value for instability of the quiescent state to approximately twice this value, the initially stationary hexagonal convection pattern was seen to become time-dependent, eventually reaching a state of spatio-temporal chaos. For a free-slip bottom wall, the flow remained three-dimensional. For the no-slip wall, two-dimensional solutions were observed over a range of Marangoni numbers. Beyond the Marangoni number for the onset of inertial convection in a two-dimensional simulation, the convective flow became strongly intermittent because of the interplay of the flywheel effect⁹ and three-dimensional instabilities of the two-dimensional rolls. The velocity field in this intermittent regime was characterized by the occurrence of very small vortices at the free surface which form as a result of vortex stretching processes. Similar structures were found with the free-slip bottom at slightly smaller Marangoni number. These observations demonstrate that a high numerical resolution is necessary even at moderate Marangoni numbers in order to capture properly the small-scale dynamics of Marangoni convection at low Prandtl numbers.

Biswal and Ramachandra (1999) studied the onset of oscillatory Marangoni convection in a two-layer system of conducting fluids in the presence of a uniform vertical magnetic field. A combination of numerical and analytical techniques were used to analyze the effect of the magnetic field and encapsulated layer on the onset of instability in a two-layer system. Oscillatory Marangoni instability was possible for a deformed free surface only when the system was heated from above. It was observed that the existence of a second layer has a positive effect on Marangoni overstability with magnetic field whereas it has an opposite effect without the magnetic field.

Bau (1999) demonstrated numerically that the no-motion state in the Marangoni-Benard problem can be controlled. The author showed its possibility by using a simple control strategy, wherein one can postpone the transition from the no-motion, conductive state to time-dependent motion. The controller delays loss of stability both in the case of a non-deforming surface and in the case of a deforming surface when very long wavelengths are excluded. In the linear stability analysis, the author assumed that the sensors and actuators were continuously distributed. This may not be essential for the

⁹the amount of energy dissipated per rotation of the roll is much less than the total kinetic energy of the fluid motion.

success of the controller. The proposed control strategy could be implemented in the microgravity condition. Here, in the absence of buoyancy, Marangoni convection plays an important role in fluid layers of all depths. The author also concluded that the same control strategy that delays the onset of Marangoni-Benard convection could be effective in suppressing Rayleigh-Benard convection.

A majority of the authors have presented their work in a cavity containing two fluids heated from below, though a few authors including Biswal and Ramachandra (1999) presented their study on the fluid layers heated from above. In continuation, Rednikov *et al.* (2000) analysed the motion in a horizontal liquid layer with an undeformable open surface heated from the air side. The geometry matched the work described by Nield (1964) with the only exception that in their work, the Benard layer was heated from the air side or cooled at the lower side. Rednikov *et al.* (2000) have shown that a Benard layer, not too shallow may become oscillatory when it is heated from above or cooled from below, due to the joint action of buoyancy and thermocapillary effects. This result was obtained when the liquid layer was analyzed with the Boussinesq approximations and with a deformable open surface. The critical (negative) Marangoni and (negative) Rayleigh numbers start at rather high absolute values for moderate Prandtl number fluids, although achievable in standard experiments on low viscosity liquids such as water. The convective heat transport in the air gap overlying the liquid was negligible when the air layer was relatively thin. Moreover, surface deformability was relevant only for thin, say sub-millimeter, liquid layers, while the Rayleigh-Marangoni instability described here was observed for thicker layers in the centimeter range. Marginal stability curves have been presented by the authors for Marangoni number as a function of the wavenumber when either the negative Rayleigh number or the dynamic Bond number¹⁰ was fixed. The authors have shown that the marginal stability curves have the form of a 'bubble' enclosing the region of instability. As the Rayleigh number is increased, the bubble grows and rises at higher values of the Marangoni number. As the Bond number is increased, the critical wave number shifts from long to short waves. There exists an optimum Bond number for which the critical Marangoni number is the lowest. This corresponds to the optimal balance between buoyancy in the bulk and the Marangoni stresses at the open surface. The instability threshold increases with the increase in Prandtl and the Biot numbers.

Ruediger and Feudel (2000) studied the formation of various patterns in the classical Rayleigh-Benard convection in a cylindrical geometry. A low Prandtl number fluid was enclosed in a moderate aspect ratio container. The spatial structure of the convec-

¹⁰It is the ratio of the Rayleigh and Marangoni number.

tive dynamics was also examined for moderate Rayleigh numbers. The stability limits of targets and spirals¹¹ were determined. The upper stability boundary of targets was represented by the focus instability in which the center of the target moves toward the boundary and thereby breaks the axisymmetry of the roll pattern.

Biswal and Ramachandra (2001) studied Benard-Marangoni convection in a three-dimensional container with thermally insulated lateral walls and prescribed heat flux at the lower boundary. The upper surface of the incompressible, viscous fluid was assumed to be flat with temperature dependent surface tension. A Galerkin-tau method with odd and even trial functions satisfying all the essential boundary conditions except the natural boundary conditions at the free surface was used to solve the governing equations. The critical Marangoni and Rayleigh numbers were determined for the onset of steady convection as a function of the two aspect ratios for the cases of Benard-Marangoni, pure Marangoni and pure Benard convection. It was observed that critical parameters decreased with an increase in the aspect ratios. The flow structures corresponding to the values of the critical parameters were presented in all the cases. It was observed that the critical parameters were higher for prescribed heat flux than those corresponding to the prescribed temperature. The critical Marangoni number for pure Marangoni convection was higher than the critical Rayleigh number corresponding to pure Benard convection for a given aspect ratio whereas the reverse trend was observed for the two-dimensional infinite layer.

2.2.2 Combined experimental and theoretical studies in two-layer convection

Buoyancy induced convection in superposed fluid layers has been the subject of numerous theoretical and experimental investigations over the past two decades. Zeren and Reynolds (1972) presented an analytical and experimental study of thermally induced instability in horizontal two-fluid layers. A linear stability analysis was carried out for two initially motionless, viscous immiscible fluids confined between horizontal isothermal solid surfaces. The authors developed a model to include all the effects which would be present in an experiment, in which Marangoni instability is dominant. Their model includes the following effects: (i) possibility of instability in one or both fluid layers, (ii) combined Benard and the Marangoni effect (buoyancy should have a significant influence on stability limits), (iii) a deformable interface to account for the effect of mean surface

¹¹target, represents a class of convective pattern in the form of concentric roll with focus at the center, while spiral indicate the roll in the form of a spiral with specific sense of rotation.

tension and (iv) continuity in temperatures and heat fluxes across the interface. Calculations were reported for layers of benzene over water with a total depth of 2 mm and various water depth fractions. Two heating configurations, namely heating from above and below, were utilised for predicting instability in the fluid layers. The response of the fluid layers was seen to be strongly dependent on the ratios of the properties of the fluids, the total depth of the layer and the depth fraction of one fluid. Three different response modes occurred depending on the fluid depth fractions. These modes are related to interfacial tension gradient, buoyancy and surface-deflection. When the heating was from above, the buoyancy mechanism was stabilizing for most wave numbers, including the critical one. Heating from below lowered the critical Marangoni number and added a buoyancy-driven response mode.

Zeren and Reynolds (1972) also presented their experimental results for the critical Marangoni number. Both heating configuration i.e. heating from above and below were achieved in the experiments, as in the calculations. Fluid layers consisting of benzene over water with a total depth of 2 mm and water depth fractions of 0.40 were enclosed in a glass cylinder. The confining plates were made of copper, being electrically heated on one side and cooled on the other. Each plate assembly was constructed so that either the heated or the cooled plate could be the upper or the lower side of the test section. Heat transfer was deduced from the energy balance calculation for the heated plate. Both plates were carefully guard heated or cooled as necessary to minimize energy losses to the environment. The primary plate temperature difference was measured with a four-couple thermopile; additional thermocouples allowed monitoring of the plate temperature level and the plate-to-guard temperature difference. It was observed from the experiments that no instability was detected in any case for heating from above, even though the Marangoni number exceeded the predicted critical value by as much as a factor of five. The critical Rayleigh number for heating from below fell between the critical values predicted with and without the Marangoni effect. The presence of surface contamination was believed to be responsible for the apparent lack of convection when heating was from above. Also, surface contamination was responsible for the difference between the predicted and measured critical Rayleigh numbers when heating was from below.

Rasenat *et al.* (1989) investigated theoretically and experimentally the onset of convection in two layers of superimposed immiscible fluids heated from below. The primary objective of the theoretical analysis was to study completely the linear problem at the onset of convection. Owing to a high-dimensional parameter space of the two-layer problem, the authors chose parameters that would give interesting dynamical features.

A guiding principle of the analysis was the selection of fluid properties that would lead to instabilities by overturning motions. It was expected that the corresponding part of the parameter space was the most likely one to offer new features. In the mathematical formulation, two horizontal fluid layers with the lighter fluid of density ρ^* on the top of the heavier fluid with density ρ was considered. The fluids were assumed to follow the Boussinesq approximation. From the analytical results, the authors predicted that the onset of convection can occur in the form of both viscously and thermally coupled motion. In addition to the oscillatory interfacial instability, which depends on a non-vanishing distortion of the interface, there existed oscillatory instability¹² as well, that corresponded to a cyclic variation between viscous and thermal coupling. This is because it connected the two monotonic branches that describe the onset of convection, with high and low wavenumbers predominating in the upper and lower layers, respectively. When the distortion of the interface was included, a much richer problem was obtained¹³. The results of monotonic bifurcations obtained in oscillatory interfacial instability were identical to the oscillatory coupling instability except that they were shifted to slightly higher Rayleigh numbers.

Rasenat *et al.* (1989) presented the experimental results at the onset of convection in layers of immiscible fluids for validating the theoretical predictions. The combination of ethylene glycol-oil and ethylene glycol-decane were selected as the fluid layers. The reason for this selection was based on miscibility which was less than 0.1%, and of a relatively small difference in the adhesion to the glass wall. The experimental test-cell was made up of two horizontal rectangular copper blocks forming a channel in between. The channel carried the superposed fluid layers that was in turn heated from below (electrical heating) and cooled from the top (water cooling). Two different channels with the dimensions $90 \times 20 \times 12 \text{ mm}^3$ and $140 \times 8 \times 12 \text{ mm}^3$ were used, where $d = 12 \text{ mm}$ is the height of the channel. The sidewalls were made from 1 mm thick glass. The form of a horizontal channel was chosen in order to force alignment of the convection rolls parallel to the short side of the channel. The pattern of convection was visualized with the shadowgraph method. Parallel light intersecting the channel along the axis of the rolls was slightly deflected because of the varying index of refraction. The light intensity received on the other side of the channel thus measured the change in the index of refraction and thereby the distribution of the temperature over the horizontal plane. A photo-diode was moved parallel to the long side of the channel by a stepper motor and a curve measuring the light intensity at a certain height of the channel was obtained. The authors concluded from the experiments that convection predominates in the upper

¹²also called, Hopf bifurcation, noticed first by Gershuni and Zhukhovitskii (1982);

¹³An extra time derivative enters the analysis here, together with one or two additional parameters.

layer at Rayleigh numbers beyond the critical value for onset, until the variation of temperature becomes clearly noticeable in the lower layer as well. The relative phase of the temperature signals in the fluid layers indicated thermal coupling. The weak variation of the temperature in the lower layer after onset of convection was resolved, indicating viscous coupling before the transition to thermal coupling. The theoretical analysis agreed with these observations. The main goal of the experiments that was to visualize the onset of oscillatory convection, was not however achieved.

The tendency to form hexagonal convection cells in surface-tension-driven convection when the liquid layer is exposed to air is a unique consequence of the pattern selection mechanism. However, many of the observed patterns were more polygonal than hexagonal, presumably because of imperfections in the uniform temperature boundary conditions either beneath or above the fluid. Koschmieder and Prahl (1990) performed a series of experiments to gain insight into the formation of the patterns, and conditions that lead to a preference for the hexagonal cells. The experiments were aimed at an investigation of the planform of the motion as well as the value of the critical Marangoni number for the onset of surface-tension-driven convection in three different circular and one small square container. The apparatus consisted of 5 cm thick copper block of 17.8 cm diameter, the bottom of which was heated electrically with a resistance wire. The upper surface of the copper block was expected to have a practically uniform temperature. On top of the copper block was a lucite frame with a circular inner opening of 13.55 cm diameter. Into this opening and on the top of the copper blocks, a bakelite plate of 8 mm thickness was placed. Three circular holes of different diameter and one square hole were cut into it. These holes received the small containers with which the experiments were performed. Flow visualization of convection patterns in silicone oil was carried out by aluminium powder suspended in the fluid. Experiments were performed in a container having a small aspect ratio A , where A is the ratio of the width of the fluid layer to its depth. For circular containers, the width has been taken to be the diameter of the fluid layer. It was observed in the smallest circular container that with increasing aspect ratio, the pattern consisted of first a circular roll and then segments of a circle outlined by different numbers of azimuthal nodal lines, with up to six segments. When the aspect ratio increased from 4.32 to 8.96, the Marangoni number decreased from 330 to 67 along with the cross-over from one-cell to seven-cell solutions. The form of the pattern observed in the square container was a surprise. Unexpected solutions appeared when the number of the cells in the square container was itself not a square integer. When the aspect ratio of $A = 4.98$ permitted two cells, two triangular cells were observed. With space for three cells, one square and two wedge-shaped cells formed. The onset of convection in all fluid layers was characterized by a steep increase of the

critical Marangoni number from $Ma_c = 48$ to 61, with decreasing aspect ratio from $A = 188$ to 75.

Pattern formation is an area of active research in a wide variety of applications. One of the most studied systems that presents this phenomenon is the Benard-Marangoni convection. The role played by the boundary conditions was not completely understood in the past. Ondarcuhu *et al.* (1993) investigated pattern formation in their experiments on Benard-Marangoni convection in a small aspect ratio vessel. Experiments were performed in a container with square insulating lateral walls, filled with a silicone oil of a high Prandtl number ($Pr = 3200$). Flow visualization was carried out by a Schlieren technique. The images obtained contained bright lines that corresponded to the cold parts of the pattern, i.e., descending motion of the fluid. In their experiments an aspect ratio of 4.46 was used while the temperature of the bottom plate varied between 35 and 60°C, maintaining the ambient temperature near the free surface at 21°C. Thus the corresponding Rayleigh number obtained was between 10,308 and 33,504. The above parameters led the system to organize itself into four internal cells. In some cases, the four cells were quadrilateral, and in others two the cells were quadrilateral and the remaining pentagonal. An increase in the temperature of the bottom plate resulted in the first convection pattern to consist of four square cells. A further increase led to the axisymmetric pattern, and for an additional increase of the temperature, the stable pattern began to oscillate. The authors also reported that a few of the patterns could undergo secondary and tertiary bifurcations displaying oscillatory behavior. Moreover, one of these oscillations constituted a dynamical version of the elementary topological processes observed in two-dimensional cellular patterns, for example side-swapping, present in a variety of physical systems.

Busse and Sommermann (1996) discussed double-layer convection for geophysical applications from a theoretical and an experimental viewpoint. The first set of results were presented for an annular channel containing fluids in a 1:2 ratio of the layer heights¹⁴.

Andereck *et al.* (1996) presented experimental results for two immiscible fluid layers, driven by a vertical temperature difference slightly greater than the critical for Benard instabilities. Both rectangular and annular cavities were considered. The conditions under which the onset of convection is time-dependent was seen to be a function of the property ratio of the liquids constituting the fluid layers.

As described earlier, convection in the two-layer system is characterized by two distinct coupling modes between the layers. They are mechanical and thermal cou-

¹⁴The full version of this paper could not be made available.

pling. Prakash and Koster (1996b) presented experimental and numerical studies in a two-dimensional cavity of two immiscible liquids heated from below in the context of determining the coupling modes. To achieve two-dimensionality in the experimental test-cell, a narrow vertical slot was considered to form the rectangular cavity. The fluids were confined in this cavity whose dimensions were a width (L) of 68 mm, height (H) of 56 mm, and a depth (D) of 8 mm. The horizontal (top/bottom) and vertical side walls of the test-cell were made of copper. This provided isothermal conditions at the top and the bottom boundaries, and perfectly conducting boundary conditions along the vertical side walls. A vertical temperature gradient was generated by circulating constant hot and cold water in the brass water jackets soldered respectively to the bottom and top horizontal boundaries. Real-time holographic interferometry was used to obtain the temperature field. The view direction was aligned parallel to the short side walls of the cavity i.e. in the direction along the depth (D). Experiments were performed with two immiscible fluid layers composed of 100 cSt silicone oil floating on top of ethylene glycol. Prakash and Koster (1996b) also numerically simulated two-layer convection using the commercial finite-element computer code FIDAP. Simulation was restricted to a two-dimensional model. The governing Navier-Stokes equations and the energy equation were discretized using the finite element method. The test cavity was discretized with a graded mesh of 51×71 . This mesh was found to be optimal for convergence, constancy of maximum streamfunctions, and CPU time. No-slip conditions for velocity along the rigid walls were applied. At the interface, normal and shear stress balance conditions, along with the kinematic condition were prescribed. Interface deformation was assumed to be negligible. Continuity of velocity and temperature, and heat flux balance were imposed at the interface. For interpreting the experimental results, the authors introduced the parameter P , the ratio of individual layer Rayleigh numbers. Also, to include the influence of the cavity geometry, a modified parameter \bar{P} was introduced as $\bar{P} = P/(Ra_t/Ra_b)_c$, where P was normalized by the ratio of the individual critical Rayleigh numbers of the top (t) and bottom (b) layers. The authors concluded that both modes of coupling (thermal and mechanical) between the layers were possible. Another distinguishing feature of double-layer convection i.e. oscillatory motion at the onset of convection was not observed in their studies. When driving forces in both layers were similar ($\bar{P} \approx 1$), thermally coupled flow was observed. As the difference in buoyancy forces between the layers increased, the thermal coupling mode that develops at the onset of convection, underwent a transition to the mechanical coupling at higher Rayleigh numbers. When driving forces in the two layers were very different ($\bar{P} > 3$ or $\bar{P} < 1/3$), mechanically coupled flow was again observed. These results were applicable to a system with a dynamic viscosity ratio of 5.6. In the results (Figure 2.6), a

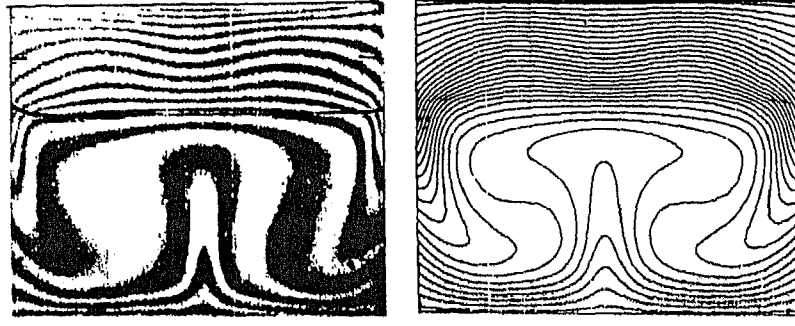


Figure 2.6: Interferograms (left) and isotherms from numerical simulation (right) in superposed layers of silicone oil 100 cSt over ethylene glycol. For experiments, $(Ra/Ra_c)_t=0.9$ and $(Ra/Ra_c)_b=5.9$, and for simulation $(Ra/Ra_c)_t=0.3$ and $(Ra/Ra_c)_b=9.9$, after Prakash and Koster (1996b).

few disparities between experiments and the two-dimensional simulation were observed. These were attributed, not to interfacial contamination, but to constraining effects of the gap geometry. It was pointed out that the gap geometry modifies the critical driving force and the thermal boundary conditions for each layer. Further, the modified critical driving force should be accounted for while comparing convection in the different layers.

During liquid encapsulated crystal growth, the layer aspect ratio changes with time due to depletion of the melt. The effect of lateral boundaries on the flow pattern that arises when interfacial and gravity driven convection are present is an interesting aspect of two-layer convection. Johnson and Narayanan (1996) studied numerically and experimentally the effect of the container geometry on the flow pattern that forms near the onset of interfacial-driven convection. The numerical studies were carried out in a cylindrical geometry with two aspect ratios (radius/height) of 1.5 and 2.5. The critical Marangoni numbers were calculated from the linearized Boussinesq equations. The liquid was bounded on the vertical sides by a rigid, no-slip side wall. The lower surface was rigid and assumed to be at a constant temperature. The upper surface of the floating layer was in contact with a passive gas. Interface deformations were assumed negligible. The numerical results revealed that each azimuthal mode 0, 1, 2, and 3 represented a different flow pattern, each associated with its own critical Marangoni number. For example, $m = 0$, represented the “toroidal” flow pattern. The toroidal flow was expected to occur at the smallest critical Marangoni number ($Ma_c = 90.45$) for the onset of convection at an aspect ratio of 1.5. In special cases, two modes coexisted at the smallest Marangoni number¹⁵. The critical Marangoni numbers obtained at an aspect ratio of 2.5 were 70.84 and 70.41 associated respectively with mode 1 and 2. These values are quite close to

¹⁵These are once again, the codimension-2 points.

each other and thus it was concluded that the aspect ratio of 2.5 is near a codimension-2 point (Figure 2.7). The linearized instability calculations near the codimension-2 point

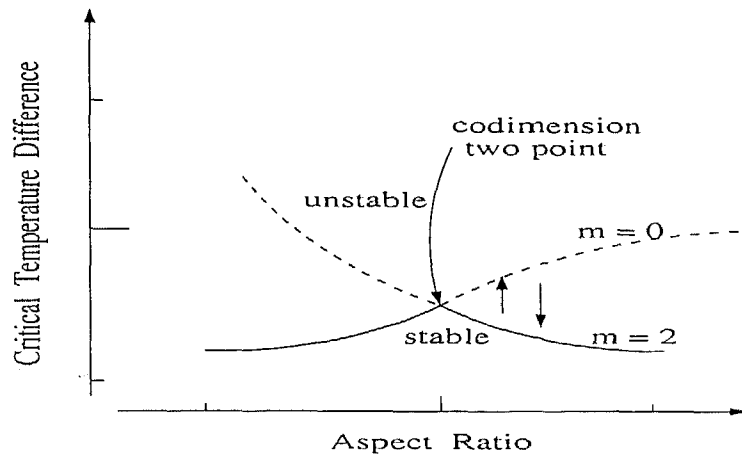


Figure 2.7: Schematic drawing of the codimension-2 point, after Johnson and Narayanan (1996).

for Marangoni and Rayleigh convection indicated that only a steady pattern should be seen.

Johnson and Narayanan (1996) also experimentally investigated the codimension-2 point in a liquid layer of 100 cSt silicone oil with an upper air gap above. The two fluids were enclosed between two conductive plates with an upper plate consisting of zinc selenide, which was transparent to infrared radiation in the 8 to 12 μm range. The depth of the silicone oil was 5.0 mm and the air gap was 11.2 mm for all the experiments reported in their work. This system gave a ratio of the Rayleigh (Ra) to Marangoni (Ma) number of around 4.6. The flow visualization tool used was an infrared (IR) camera to measure the temperature field of the upper liquid surface. The IR camera was placed above the apparatus to view the surface in the vertically downward direction. As IR radiation was readily absorbed by silicone oil, the radiation detected by the camera was only from the very upper layer of the silicone oil. In the experimental results at an aspect ratio of 1.5, the authors were able to visualise the toroidal flow that shows fluid rising up from the center, moving radially across the top of the surface, and then falling down the sides of the container. At an aspect ratio of 2.5, they observed a dynamic switching between two different flow patterns, or modes. This confirmed the codimension-2 point to appear for an aspect ratio of 2.5, as in the numerical predictions. Finally the authors concluded that the study has implications in liquid encapsulated crystal growth, where multiple mode interactions can be another mechanism for unsteady convection, which in turn can lead to dopant stratification.

Prakash and Koster (1997) studied analytically, numerically and experimentally the problem of thermal convection in two horizontal layers of immiscible liquids differentially heated from the sides. The experimental test cell consisted of a rectangular cavity with length $L = 38$ mm (length between the temperature-controlled side walls), height $H = 28.5$ mm and a side wall separation in the viewing direction $D = 28.5$ mm. The cavity was filled with 10 cSt silicone oil on top of Fluorinert FC-70 liquid with equal liquid layer heights of $d = 6$ mm. The vertical side walls of the test volume were made of copper for providing isothermal boundary conditions. The top of the cavity was of plexiglas. This material insulated the cavity from the outer environment while allowing for the transmission of a light sheet for flow visualization. The front and back walls were optical windows. The flow field was visualized with the aid of tracer particles (titanium dioxide or silver coated glass microspheres) suspended in the fluids. Movement of the particles with the flow was recorded as streaklines. Single component velocity measurements were carried out using laser Doppler velocimetry (LDV). Real time holographic interferometry was used for measuring the temperature field. Numerical simulation in the two-layer system was performed using the finite element computer code FIDAP. Interface and the free surface both were considered to be deformable. Simulation of the experimental system was restricted to a 2-D model. The steady Navier-Stokes equations, the energy equation, and the stress balance equation at the interface were discretized using the finite element method. The test cavity was discretized with a nonuniform mesh of 51×71 . A finer mesh gradation was utilized in regions where strong velocity and temperature gradients were anticipated. The analytical model assumed a shallow, rectangular, two-dimensional cavity of aspect ratio $H/L \ll 1$. The two layers heights were not necessarily equal, but the aspect ratio of each layer was assumed to be small. The total cavity height was, therefore, considered to be much smaller than the cavity length L . Utilizing the streamfunction-vorticity formulation of the Navier-Stokes equations, the non-dimensional governing equations of fluid flow in each liquid layer were derived. The governing equations were scaled using the thermo-physical properties of the bottom layer, the corresponding layer height d , the length of the cavity L and the applied temperature difference ΔT .

Prakash and Koster (1997) arrived at the following conclusions from their research. The experimentally observed flow and the temperature fields were in good qualitative agreement with the theoretical predictions of the analytical model and the finite element simulation. Across the interface, the two liquids were mechanically and thermally coupled. In addition to buoyancy, thermocapillary stresses provide a driving force for flow. From the interaction of the free surface and interface thermocapillary stresses, along with viscous and thermal coupling, a thin interfacial roll develops between the layers.

Thermocapillary stresses tended to increase the height of the interfacial roll. Flow in the interfacial region was significantly weaker than the bulk flow and did not extend very far into the bulk of the layer. For the fluid combinations considered in the study, coupling between the layers, particularly mechanical coupling, led to a significant reduction in the velocities of the lower layer as compared to the flow velocities in a single layer. For some fluid combinations, thermocapillary stresses were diminished, and the interface velocity was close to zero. Thus, in these circumstances the flow in the two-layers appeared to be mechanically decoupled. In the corresponding experiments, the interfacial roll could not be observed at all.

Prakash *et al.* (1997) reported experimentally recorded temperature fields in a two-layer Rayleigh-Benard convection. The fluid layers were confined in a shallow rectangular cavity. The objective of the study was to characterize the coupling mechanism as a function of the two parameters: viscosity ratio and ratio of the driving buoyancy forces. The experimental set up and procedure for the experiments was essentially similar to that outlined in the earlier work of Prakash and Koster (1996b). The only difference was in the geometry of the test cell and construction. The test volume formed a rectangular cavity of width $W = 60$ mm, height $H = 15$ mm, and depth $D = 8$ mm. Real time holographic interferometry was used to obtain the temperature field. An argon laser was used as the light source for the interferometer. The light beam was aligned parallel to the shorter side wall of the cavity i.e. along depth D . Experiments were performed in two-layer systems composed of different combinations of liquids. Under isothermal conditions, no diffusion in the form of schlieren streaks could be detected with monochromatic laser light. Thus the combinations of fluid layers were considered practically immiscible. The summary of their experimental findings are as follows:

Mechanical coupling (Figure 2.8) was the preferred mode in systems where viscosities of the two liquids were similar, and a significant contrast in the buoyancy driving forces was enforced. When the driving forces and the viscosities of the two layers were similar, either mechanical or thermal coupling was theoretically possible. Flow patterns in each layer of the two-layer system were found to be very similar to those reported in a single layer confined in a rectangular container. Onset of convection led to a steady flow that comprised of a finite number of rolls or convection cells, whose axes were aligned parallel to the shorter side. Beyond the onset of convection, the flow was seen to undergo spatial transitions that were “quasi-steady” in nature and led to distinctly different, yet stable, flow patterns. Temporal transitions leading to time dependent flow were not observed in the range of temperature differences covered in the experiments.

Georis *et al.* (1999) presented the first experimental results on Marangoni-Benard

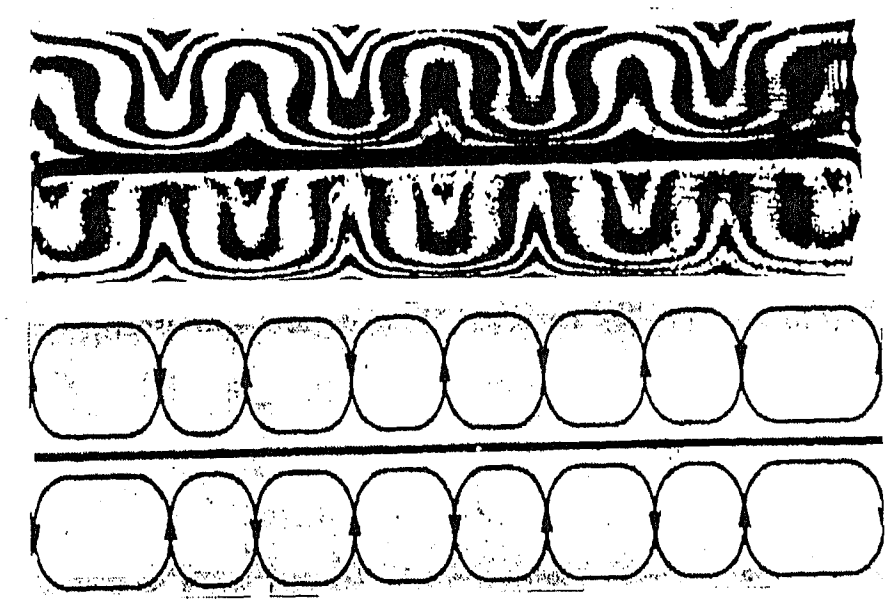


Figure 2.8: Interferograms (top) and roll patterns (bottom) that show mechanical coupling in silicone oil 4.6cSt floating over Flourinert FC-70, after Prakash *et al.* (1997).

instability in a symmetrical three-layer system. The experimental test-cell was made of a rectangular quartz frame closed on two sides by two sapphire windows. The thickness of each window was 10 mm. Fluids consisting of Flourinert FC70 (3M) for the first and the third layers and silicone oil 10 cSt (Dow Corning) for the central layer were selected for the experiments. Each liquid layer was 8 mm thick, 50 mm wide and 35 mm deep. Initially, the layers were separated by two 50 μm thick stainless steel curtains to prevent mixing before the beginning of the experiment. The curtains were then gently pulled out and wound on the rollers creating two free liquid-liquid interfaces subjected to a Marangoni effect. Heating and cooling were achieved with electrical resistance and Peltier elements located along the edges of the sapphire windows. The liquids were seeded with silver-coated ceramic spheres whose diameters were in the range between 80 and 100 μm . The flow was visualized using a Helium-Neon (He-Ne) laser light oriented parallel to the longest side of the container and located 10 mm from the wall. To avoid sedimentation due to the residual acceleration, the densities of the particles matched the densities of the liquids to within a few percent. The findings of this work can be summarized as follows: A pure thermocapillary phenomenon was observed by performing the experiment in a microgravity environment where buoyancy forces are negligible. This configuration enabled the study of hydrodynamic stability of two identical liquid-liquid interfaces subject to a normal gradient of temperature. The flow was driven by one interface only and obeyed the criterion based on the heat diffusivity ratio proposed by Scriven

and Sterling (1959) and Smith (1966)¹⁶. The measured critical temperature difference for the onset of convection was compared to the value obtained from a two-dimensional numerical simulation. The predictions of the simulation were in reasonable agreement with velocimetry and the experimental data for a moderate degree of supercriticality. Numerically and experimentally, the convective field for temperature exhibited a transition between different convective regimes for similar temperature gradients.

Hexagonal flow patterns have been associated with the onset of convection ever since Benard observed them in thin fluid layers heated from below. Recent experimental results with Prandtl number of around 100 demonstrated a transition from hexagons to square patterns with higher heating. Schatz *et al.* (1999) reported experimental observations of time-dependent square patterns related to secondary instability in surface-tension-driven Benard convection. The experimental test cell consisted of a cylindrical vessel containing a layer of silicone oil with air above it. The silicone oil layer was heated from below by a 1 cm thick gold-coated aluminium mirror, and air was cooled from above by a 0.3 cm thick sapphire window. For a small temperature difference, the oil-air interface was isothermal and the surface tension was uniform. With a sufficiently large temperature difference, instability induced surface tension variations at the interface led to fluid flow in the bulk of both fluids. The thermal patterns were visualized using the shadowgraph method. An infrared camera was used to measure the horizontally averaged temperature at the interface. An infrared detector was adopted for the measurement of thermal radiation emitted from the surface of the oil. For interpreting the experimental results, Schatz *et al.* (1999) used a reduced Marangoni numbers $\epsilon = (Ma - Ma_c)/Ma_c$, where Ma_c is the critical value of the Marangoni number determined from linear stability theory. The experimental runs started at low values of ϵ , where the stationary hexagons were stable. At the onset of convection, a hexagonal pattern with a few nonhexagonal defects appeared and persisted till ϵ reached a value of 1.61. Some hexagons transformed into pentagons and squares with an increase of ϵ to 3.90. Increasing ϵ to sufficiently large value of 7.22 resulted in square cells, with nonsquare cells limited to the periphery of the apparatus to accommodate the circular lateral boundary. The square pattern lost stability (for ϵ larger than 3.90) while the hexagonal cells reappeared, when ϵ decreased to 3.5. Pattern competition between hexagons and squares in Marangoni convection posed an interesting challenge, similar to pattern selection in a ferrofluid layer. In the latter, experiments show that a steady hexagonal planform may lose stability either to stripes or square patterns. An open experimental issue was the nature of instability

¹⁶If deformations of the interface are disregarded, the sign of the marginal Marangoni number, which corresponds to the sign of the temperature gradient, is governed only by the ratio of the heat diffusivities of the liquid phases.

of square patterns for sufficiently large Marangoni number. Preliminary observations indicated that the squares transformed into disordered polygonal patterns at the onset of time dependence, the cell size continually increasing with the Marangoni number.

Johnson *et al.* (1999) presented theoretical and experimental findings on the effect of the layer height on the pattern formation in liquid-air convection in a cylindrical geometry. Two different linear stability calculations were performed. In the first set of calculations, laterally unbounded layers of two fluid was assumed. The second set of calculations assumed a single, bounded liquid layer with a passive overlying gas in a rigid, circular cylinder with no-slip lower and radial walls¹⁷. The first set of calculations analyzed the different coupling mechanisms, as the heights of the silicone oil layer was changed. Calculations for laterally unbounded geometries could be extended to reveal qualitative features of convection in laterally bounded circular cylinders, despite unrealistic boundary of vanishing tangential and vertical components of vorticity along the radial walls. Calculations were performed to determine the critical temperature difference as well as the flow pattern at the onset of convection. These computations were based on a linear stability analysis for both the laterally unbounded and bounded geometries. Two features in particular were investigated. First, the effect of the height of the air phase on the convective threshold was studied. The second feature that was examined was the effect of the air height on the type of the convection coupling. The following conclusions for a bounded geometry (depth of 5 mm of silicone oil for a Biot number 0.3) were arrived at. The critical Marangoni number was not a monotonic function of the aspect ratio (Figure 2.9). At small aspect ratios, the minimum value of each mode was much greater than the asymptotic minimum reached at aspect ratios greater than 4.0. The flow patterns also changed with the aspect ratio. At specific aspect ratios, two patterns could coexist, resulting in a codimension-2 point.

Along with calculations, Johnson *et al.* (1999) also studied experimentally the effect of the air height on the flow patterns in the lower liquid layer. The experimental test-cell consisted of four pieces: the liquid insert, air insert, the clamp, and a zinc selenide window. The first three pieces were made of lucite. The lower cylindrical block was heated using a resistive element along with a heating plate. For ensuring the liquid-gas interface to be flat, a pinning edge was used in the liquid insert. The liquid insert could be made of different radii and heights to achieve the desired liquid aspect ratio. The zinc selenide optical window was placed at the top of the test-cell. For flow visualization, an infrared camera was used. The camera was placed directly above the

¹⁷A passive gas is completely quiescent and its temperature is not perturbed by the instability mechanism.

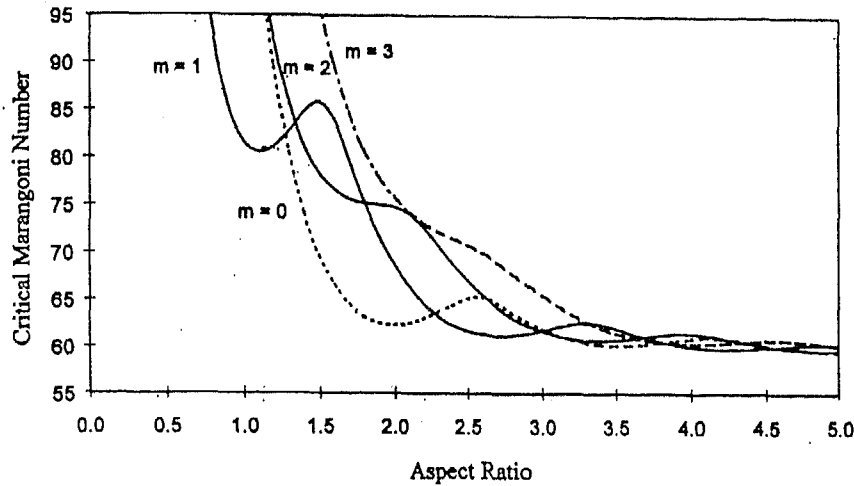


Figure 2.9: Plot of the bounded, linear calculations made with an insulating, no-slip radial wall, after Johnson *et al.* (1999).

test section and measured the infrared radiation emitted by the silicone oil. As silicone oil readily absorbs infrared radiation, only the radiation from the silicone oil interface could be detected. A large number of experiments were carried out to test whether convection in the upper layer could drive the lower layer. For each experiment, a liquid layer insert, 5.0 mm deep and 20 mm in diameter (liquid aspect ratio of 2) was used. Three different air heights of 3, 14, and 20 mm were adopted for two different grades of silicone oil. A double-toroid pattern ($m = 0$) was observed for the 3 mm air layer over the silicone oil. As the air depth increased from 14 to 20 mm, the double-toroid pattern changed respectively to skewed and unicellular ($m = 1$) pattern. The experiments revealed a new convection coupling mechanism, also confirmed by the calculations. This mechanism required the convection to be predominant first in the upper layer. The upper fluid layer would generate a transverse thermal gradient along the fluid-fluid interface, immediately causing surface-tension-gradient-driven and buoyancy-driven convection in the lower fluid. It was concluded that the viscosity of air layer was quite low compared to that of the silicone oil, and convection in the air had no influence on the oil¹⁸. Thus this property became advantageous in isolating the new convection mechanism in the layer of silicone oil.

Juel *et al.* (2000) have reported experiments with the upper plate hotter than the lower plate in a surface-tension-driven convection in two liquid layers. The two superposed liquid layers displayed a variety of convective phenomena that were not seen when the upper layer was a gas. The authors considered several pairs of immiscible liquids.

¹⁸other than initially setting up thermal gradients over the interface.

Perfluorinated hydrocarbon and silicone oil were used as the fluids in the experimental test cell. The independent controlling parameters in the experiments were the applied temperature difference and the depths of the layers. As the fluid in the top layer was less dense compared to the bottom layer, the system became stably stratified. Thus the convective patterns were linked only to the thermocapillary forces. Oscillatory motion was seen at the onset of convection in an acetonitrile and n-hexane system heated from below. The experimental observations were in a reasonable agreement with the linear stability analysis.

2.3 Closure

A survey of the literature shows that differentially heated two-layer convection is a topic of considerable practical importance. It shares certain features with convection in a single fluid, but differences are more often observed. Surface tension gradients can drastically alter buoyancy-driven flow, and in some cases can be the sole factor determining the flow field. However, in large containers or when the layer depth is high, the flow is entirely buoyancy-driven.

The literature quoted in the present Chapter shows that research has focussed on identifying the critical points of transition, possibility of multiple solutions at transitions, oscillatory instabilities and pattern formation. The literature on liquid-gas systems in which gas-phase convection is significant, is however sparse. Thermal fields away from the point of criticality (specifically, onset of convection) have not been characterized. Issues such as single versus two-layer convection and cavity-averaged heat transfer rates have not been addressed. Against this background, the present work is focussed on two-layer convection:

- (1) when Marangoni effects are negligible;
- (2) interface deformation is possible; and
- (3) over a higher range of Rayleigh and Prandtl numbers and layer-depth ratios.

Two test cells have been constructed for studying convection patterns in superposed fluid layers. Combinations of air and water, air and silicone oil, and silicone oil and water have been selected in the experiments. Individually the test cells form a rectangular and an axisymmetric cavity respectively. The grade of silicone oil employed in the experiments was 50 cSt.

The first cavity is rectangular in plan and square in the vertical plane with a cavity aspect ratio of 13.93. The aspect ratio referred here is $A_z = L/H$, where L is the

length of the cavity and H is its height. The aspect ratios in the respective fluid layers varied from 20.88 to 41.77 in view of change in their respective heights. The horizontal lower and upper surfaces are isothermal, while the vertical side walls are insulated. The temperature difference is applied parallel to the direction of the gravity field. The optical axis of the laser beam is oriented parallel to the longer side wall of the cavity, in order to capture the depth-averaged thermal fields in the fluid layers. Three layer heights for each combination of fluids have been selected for the experiments. The objectives for the rectangular cavity experiments are to examine:

- (a) the influence of Rayleigh number on the steady thermal field in the fluid layers;
- (b) unsteadiness in the thermal field with an increase in the Rayleigh number;
- (c) average interface temperature between the fluid layers and a comparison with the energy-balance calculation;
- (d) the heat transfer rates at the two walls in terms of the Nusselt number and comparison with single fluid correlations;
- (e) the nature of coupling mechanism established at the interface by interpreting the interferograms in terms of the orientation of the fringe patterns; and
- (e) the evaluation of shadowgraphs depicting the deformed interface and a correlation with the thermal field.

The second cavity is octagonal in plan with a radius-to-height ratio of 1.31¹⁹. The layer heights have been kept equal in the experiments for all combinations of fluids. The thermal boundary conditions are similar to the first test cell and are created in an identical manner. The test cell has been designed and fabricated to scan the thermal field for three-dimensionality. This was possible by turning the test cell to different view angles of 0, 45, 90 and 135° while maintaining the axis of the light source and the detector fixed. The objectives of this phase of research are summarized below:

- (a) Reconstruction of the three-dimensional features of the temperature field at different horizontal planes in the cavity using two-dimensional projection data obtained at each view angle;
- (b) Evaluation of the degree of axisymmetry of the thermal field; and
- (c) Study of the transient evolution of the fringe patterns in the fluid layers, once the two bounding surfaces have thermally stabilized.

A large range of Rayleigh numbers from as low as 25 to as high as 10E+06 in the respective fluid layers has been explored. The lower range was obtained in the rectangular test cell of cavity height of 32.1 mm. The higher range of Rayleigh numbers

¹⁹Since the thermal field was viewed with a parallel beam of light, a purley circular container could not be used in the experiments. The octagonal cross-section has occasionally been referred later as the axisymmetric test-cell.

was realized in the axisymmetric test cell with a cavity height of 50 mm. The overall aim of working with a wide range of Rayleigh numbers and two different geometries was to develop a deeper understanding of convection in superposed fluid layers.

Chapter 3

Apparatus and Instrumentation

Theoretical as well as experimental studies in two-layer convection encounter a severe problem of a high-dimensional parameter space. Thus the flow phenomena cannot be fully explored and portions of the parameter space remain unaccessed. Experimental difficulties are further compounded by two factors:

- (a) any given apparatus (in the laboratory experiments) will cover only a very small fraction of the space accessed; and
- (b) availability of truly immiscible liquids while working with liquid-liquid layers.

Nevertheless, many interesting features can be explored in the experiments. The data generated can be extrapolated to gain understanding of applications such as earth's mantle convection and liquid encapsulated crystal growth. At the same time, nonlinear effects (specifically at high Rayleigh numbers) which are not readily accessible to theoretical analysis can be recorded with careful measurements in the laboratory. With this viewpoint, experimental studies act as a benchmark for validating the theoretical observations in two-layer convection.

Rayleigh-Benard convection forms a subclass of applications involving buoyancy-driven flows and thermal convection. The experimental configuration for Rayleigh-Benard convection is quite simple in appearance. The complexities are seen in the flow patterns that form in the fluid medium. The experimental cavity is formed by two horizontal surfaces of high thermal conductivity that are maintained at different temperatures. The system is heated from below and cooled from the top. The vertical side walls are good insulators. The focus of the experiments is on the flow patterns that emerge in the fluids contained in the enclosed volume. A careful thought is sufficient to indicate a large number of difficulties experienced during experimentation. For example, uniformity and constancy of surface temperatures, parallelism of the walls defining the fluid layer, parallelism between optical windows placed at the entrance and exit to the laser beam

and properties of the insulating surfaces are factors that determine the quality of the experiment and its suitability for comparison with theory. Further, extraneous factors such as building vibrations, air currents and changes in the ambient temperature have a strong bearing on the quality of the recorded data. Thus Rayleigh-Benard experiments have to be conducted with due care and precaution.

3.1 Description of the experimental apparatus

Experiments with two different test cells have been conducted in the present work for studying convection patterns in differentially heated superposed fluid layers. The configuration of the cells are based on the Rayleigh-Benard system heated from below and cooled from the top with vertical side walls insulated. The two cavity geometries considered are (i) a cavity rectangular in plan and square in cross-section and (ii) a cavity octagonal in plan. The second test cell approximates an axisymmetric, i.e. a circular cavity. The construction of the two test cells are described in the following sections.

3.1.1 Rectangular cavity

The first test cell constructed to study convection in superposed fluid layers is shown in Figure 3.1. The test cell consists of three sections namely the top tank, the test section¹ and the bottom tank. The test section is rectangular in plan, with the cross-section being square of edge 32.1 mm and length equal to 447 mm. This leads to a cavity aspect ratio (A_z) of 13.93. This value can be classified as an intermediate aspect ratio. The aspect ratios of the individual layers based on the ratio of the length to the height of the two layers varies from the intermediate to a high value in the experiments. The fluid layers are confined above and below by two aluminium plates of 3 mm thickness. The vertical sides of the cavity are made of perspex-bakelite composite that serve as insulating walls (Figure 3.1). The combined thickness of the two sheets is 25.4 mm. The perspex sheet is in direct contact with the fluids in the cavity. The two ends of the cavity are covered by square optical windows ($50 \times 50 \times 10 \text{ mm}^3$) to permit the passage of the laser beam. The windows are made of commercially available laser-grade fused silica. The cold (top) and the hot (bottom) surfaces have been maintained at uniform temperatures by circulating water from constant temperature baths (Huber-variostat and Raagaa-cryostat). For the upper plate, a tank-like construction enabled extended contact between the flowing water and the aluminium surface. For the lower plate, special arrangement was required to

¹that acts as the main cavity.

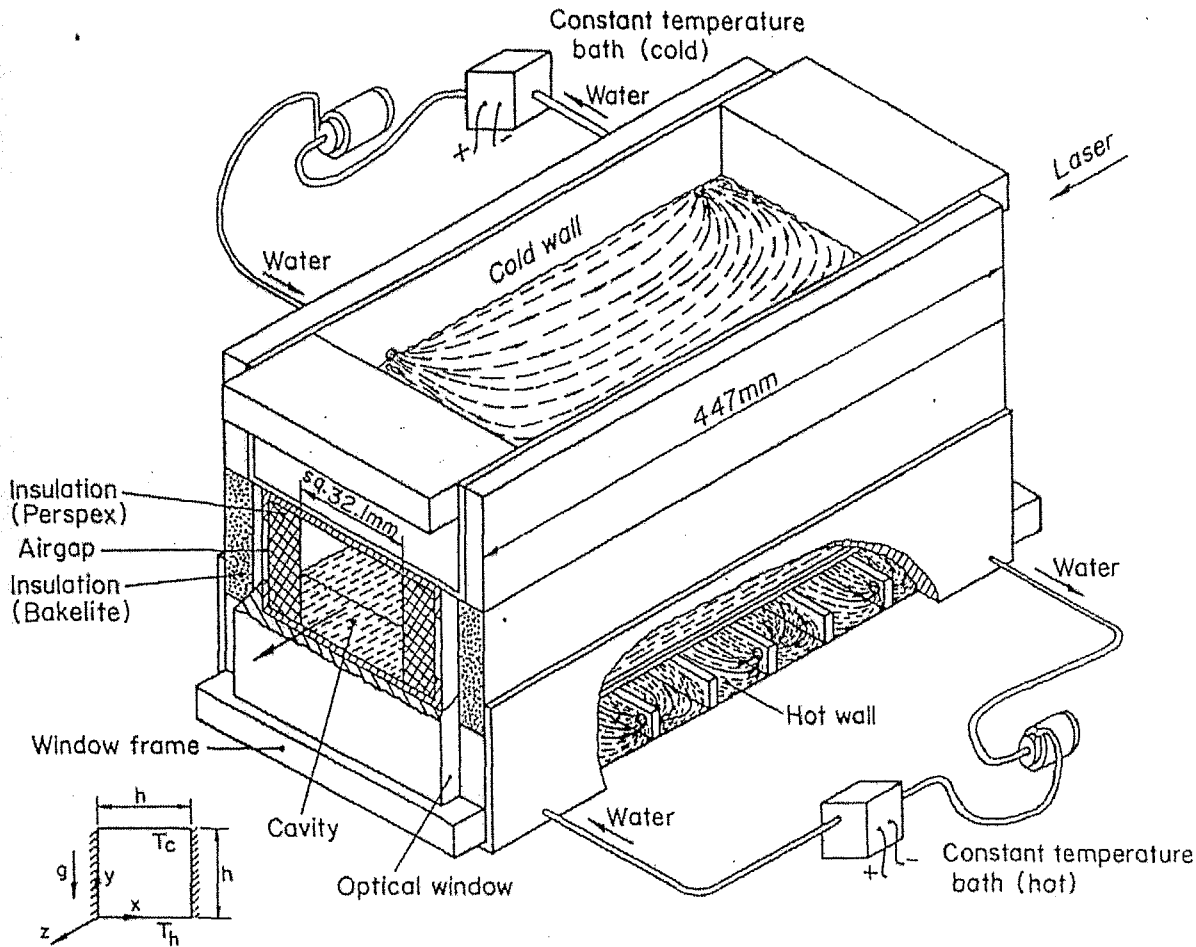


Figure 3.1: Schematic drawing of a rectangular test cell to study convection in superposed fluid layers.

maintain contact between water and aluminium. The flow of water below the lower surface was pressurized and the presence of 15 baffles acted as fins, thus increasing the effective interfacial contact area. Both walls have been maintained at their respective temperatures to within ± 0.1 K during the experiments. To reduce edge effects, the heat transfer areas of the two tanks were made quite large (≈ 2.2 times) compared to the cavity. Considerable attention was paid to the flatness of the aluminium sheets. The flatness of these plates was carefully established against a reference surface plate to be better than $10 \mu\text{m}$. After assembly the cavity height was uniform to within ± 1 mm over a length of 447 mm. This quality was adequate for resolving the near-wall fringes in air, but a few fringes were lost in the liquid phase owing to blockage.

In addition to the test cell, a reference cell has also been designed and fabricated

to compensate for initial differences in the geometrical and optical path lengths of the test and the reference beams. The reference cell is placed in the compensation chamber of the interferometer. Its cavity dimensions match those of the test cell quite closely². The reference chamber is also filled with the test fluids of appropriate thickness as in the test cell. The reference chamber is however thermally inactive.

3.1.2 Axisymmetric cavity

The second test cell used to study convection in superposed fluid layers is shown in Figure 3.2. The test cell consists of three sections namely the top tank, the test section and the bottom tank. The cavity is octagonal in plan and has a nominal diameter of 130.65 mm and height of 50 mm. The plan view closely approximates a circular geometry. The cavity and the individual layer aspect ratios defined here as diameter/height are 2.61 and 5.22 respectively for all the experiments. These values fall in the range of small aspect ratio container. In this part of the study, the layer aspect ratio has not been changed. The fluid layers, 25 mm thick are confined by two copper plates of thickness 1.6 mm above and below. The octagonal cavity is essentially made of square optical windows, 50 mm square and 3 mm thick, with 8 of them forming the octagon in plan. The windows are essential in the present work since they allow viewing the thermal fields at various angles. For the geometry adopted for the experimental apparatus, view angles of 0, 45, 90 and 135° are possible. The optical windows are made of commercially available laser-grade BK-7. The high quality windows permit the passage of the laser beam without refraction. The hot and the cold surfaces have been maintained at uniform temperatures by circulating water from constant temperature baths. As employed in the first test cell, a tortuous flow path has been created in the lower tank by installing 5 baffles. Due to an increased interfacial contact area, the heat transfer is enhanced and distributes the temperature uniformly over the plate. Both walls have been maintained at their respective temperatures to within ± 0.1 K during the experiments. The heat transfer areas of the two tanks have been made quite large (roughly 1.4 times the cavity surface area) to reduce edge effects.

To resolve near wall fringes, the two copper plates have been carefully checked for flatness and surface finish. The flatness of the plates registered against a reference face plate was around 50 μm . The surface finish measured through an instrument (Surfalyzer 5000) showed the RMS value to be close to 0.4 μm . During the experiments, the

²The degree of closeness was confirmed by the quality of the infinite fringe setting of the interferometer.

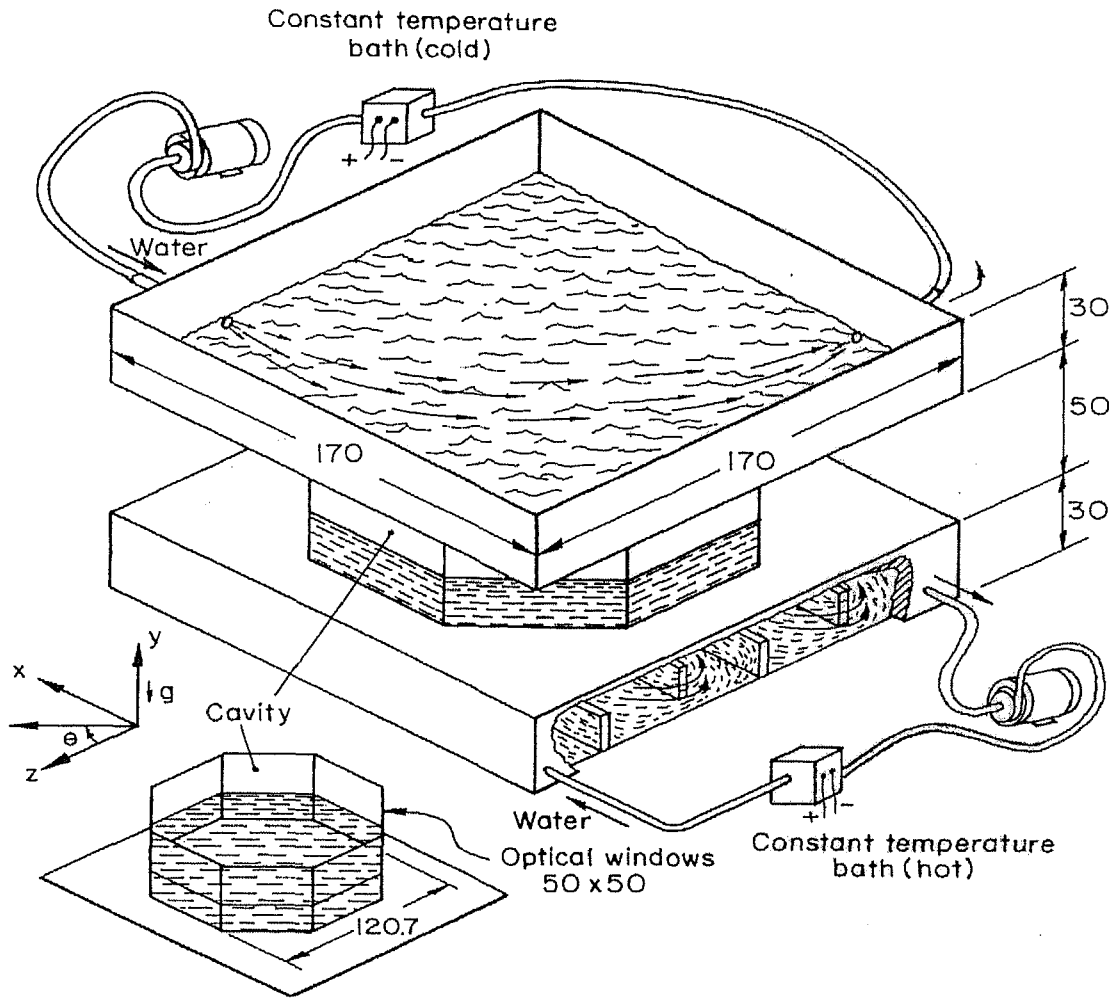


Figure 3.2: Schematic drawing of an axisymmetric test cell to study convection in superposed fluid layers (All dimensions are in mm).

optical windows are covered additionally by 12 mm thick perspex in order to insulate the test section with respect to the atmosphere. The perspex blocks of the opposite pair of optical windows are removed during data collection.

A reference cell is again required for balancing the geometrical and optical path lengths of the test and the reference beams. The reference cell utilized in the present experiments is rectangular in construction. It is placed in the compensation chamber of the interferometer. No thermal gradient is introduced in the reference cell during the course of experiments. By including the reference chamber, the interferograms exclusively reveal the variations in the thermal flow field in the test cell arising from the

imposition of a thermal gradient.

The complete view of the experimental setup with the accessories is shown in Figure 3.3.

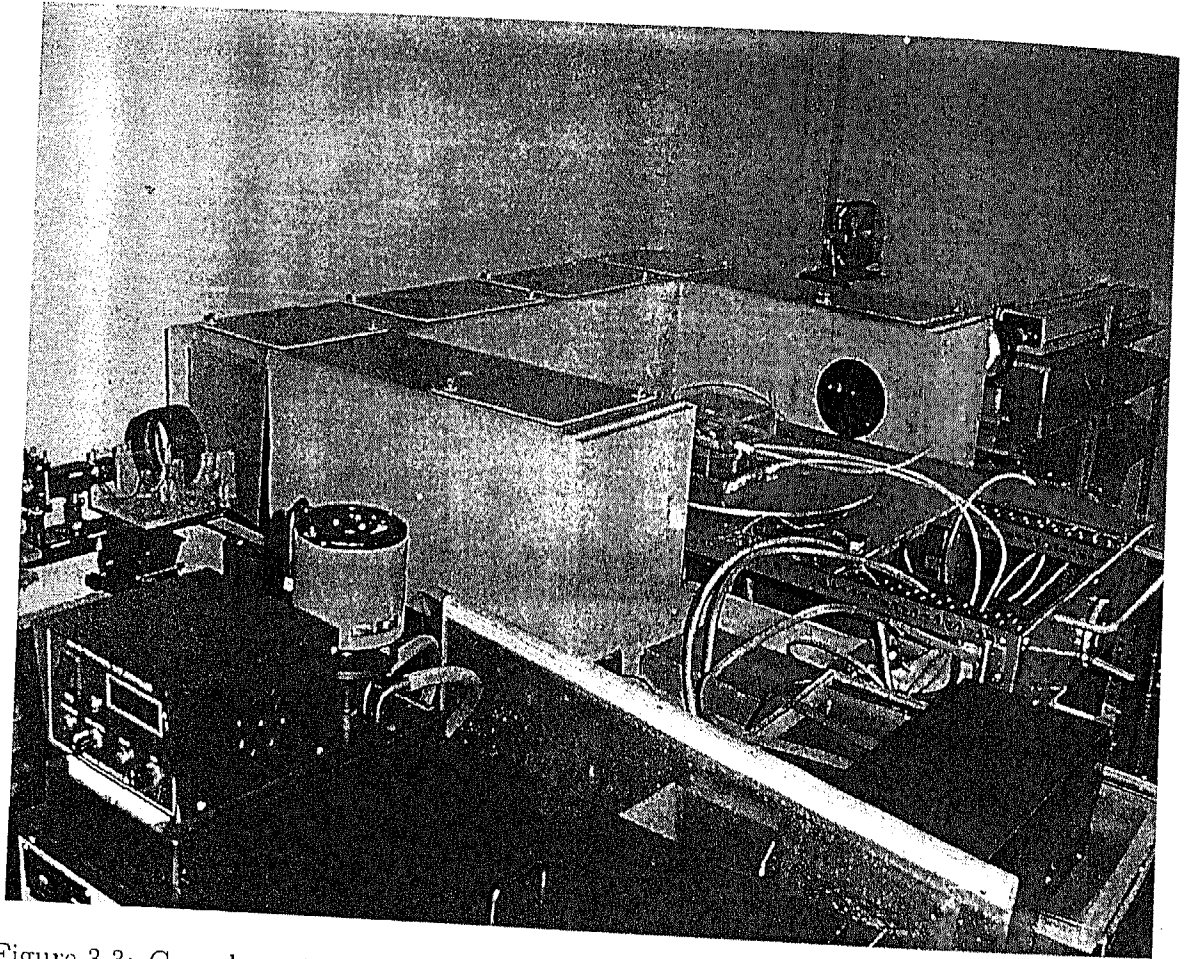


Figure 3.3: Complete view of the experimental setup to study convection in superposed fluid layers.

3.2 Design of the test cells

The design of the test cells for studying Rayleigh-Benard convection in superposed fluid layers involves the following steps:

Selection of Fluids: The selection was based on their transparency for studying convection using laser interferometry. The fluids employed in the present work are air, water and silicone oil (50 cSt). Combination of fluids such as air and water, air and silicone oil, and silicone oil and water have been selected for the experiments. The thermophysical properties of the fluids at 25 and 35°C are presented in Table 3.1. Properties

at intermediate temperatures were determined by second order quadratic interpolation.

Selection of the Cavity Dimensions: The principle of conservation of energy can be fruitfully employed at steady state to conduct a preliminary analysis. Thus heat transferred to the lower fluid (fluid 2) from the lower wall is equal to heat convected to the upper fluid (fluid 1). This in turn is conducted to the top wall. Using the single fluid correlations (for example, given by Gebhart *et al.* (1988)) for the average Nusselt number, one can estimate the average interface temperature. This procedure is described in Chapter 4. The interface temperature along with those of the walls can be used to

Table 3.1: Thermophysical properties of air, water and silicone oil (50 cSt) at 25°C.

Fluid	ρ (kg/m ³)	ν (m ² /s)	μ (kg/m/s)	K (W/m K)	α (m ² /s)	β (K ⁻¹)	Pr
Air	1.184	15.5E-06	18.4E-06	26.1E-03	2.19E-05	3.35E-03	0.71
Water	997.05	89.3E-08	89.04E-05	0.611	1.46E-07	20.57E-05	6.1
Silicone oil	960	5.00e-05	4.80e-02	0.151	1.05e-07	1.06e-03	476.2

Thermophysical properties at 35°C.

Fluid	ρ (kg/m ³)	ν (m ² /s)	μ (kg/m/s)	K (W/m K)	α (m ² /s)	β (K ⁻¹)	Pr
Air	1.146	16.4E-06	18.8E-06	26.9E-03	2.33E-05	3.24E-03	0.71
Water	994.03	72.3E-08	71.85E-05	0.625	1.51E-07	34.57E-05	4.8
Silicone oil	960	5.00e-05	4.80e-02	0.151	1.05e-07	1.06e-03	476.2

estimate the temperature difference driving convection in each fluid layer, and hence the individual Rayleigh numbers of the two fluid domains.

The cross-sectional dimensions of the first and second test cells have been estimated on the basis of the desired Rayleigh numbers of the individual layers. The length of the test cell was decided on the basis of aspect ratio A_z . The original objective was to work with a high aspect ratio cavity, quite long in the horizontal direction. Refraction errors in interferometry as well as the overall interferometer dimensions were limiting factors in the selection of the cavity length. The cavity cross-section was matched with that of commercially available optical windows. These factors led to a cavity of size $32.1 \times 32.1 \times 447$ mm³. The flow regime in each of the fluid layers could be predicted in advance using the flow regime diagram in Figure 2.1.

Material Selection: The choice of the material used for the two active surfaces was based on thermal conductivity. Aluminium and copper have respectively been selected for the

first and the second test cell owing to their high thermal conductivities. Thus perfectly conducting plates required for modeling Rayleigh-Benard convection could be achieved. The thickness of the plates were selected by considering the following factors: (a) small thickness for a negligible temperature drop, (b) small thickness to reduce weight, (c) sufficient thickness to permit adequate straightness of the surfaces, and (d) adequate thickness to control the thermal loading rate of the cavity. Factor (d) is discussed further in Section 3.4. Keeping these factors in view, sheets of 3 mm thick aluminium (rectangular) and 1.6 mm thick copper (axisymmetric) have been selected for the hot and the cold surfaces.

The vertical side walls of the rectangular cavity have been chosen on the basis of two factors: (a) permit accurate vertical spacing between two horizontal surfaces and (b) act as an insulating boundaries. A composite structure made of polyglas (perspex, 12.7 mm thick) and bakelite (12.7 mm thick) meets the above requirements. A thin air gap has been maintained between the two sheets. It is expected that after the passage of a sufficient amount of time, the thermal fronts in the side walls are frozen. This in effect would result in zero flux (namely, adiabatic) boundaries. The perspex surface formed the inner surface of the vertical side walls. This arrangement is advantageous because the smoothness of perspex surface delays condensation of moisture in the air-water experiments. In the axisymmetric test cell, the optical windows themselves act as perfect spacers between the two horizontal surfaces. In addition, perspex blocks have been placed adjacent to the optical windows, creating a small air gap. One pair of blocks had to be removed momentarily for recording the projection data for each view angle.

For visualization of flow, high grade optical windows³, 10 mm thick made of fused silica have been selected. Two such windows are required for rectangular cavity and the reference cell. Optical grade material BK-7 of 3 mm thickness has been chosen for constructing the axisymmetric test cell.

A traversing mechanism is needed to mount the apparatus in which the desired experiment is in progress. In practice, the optics and the light source cannot be moved to scan the flow field. The traversing mechanism enables translation and rotation of the test cell and thus plays a central role in alignment of the test cell with the optics employed (Figure 3.4). The base of the traversing mechanism is padded with a rubber sheet, 30 mm thickness. The sheet damps to an extent the external vibration from reaching the test cell. For a finer levelling adjustment of the test cell in the vertical plane, the base of the apparatus is rested on three bearing supports. In axial tomography, the projection

³The term *high grade* refers to the excellent surface quality, transparency and parallelism of the optical surfaces.

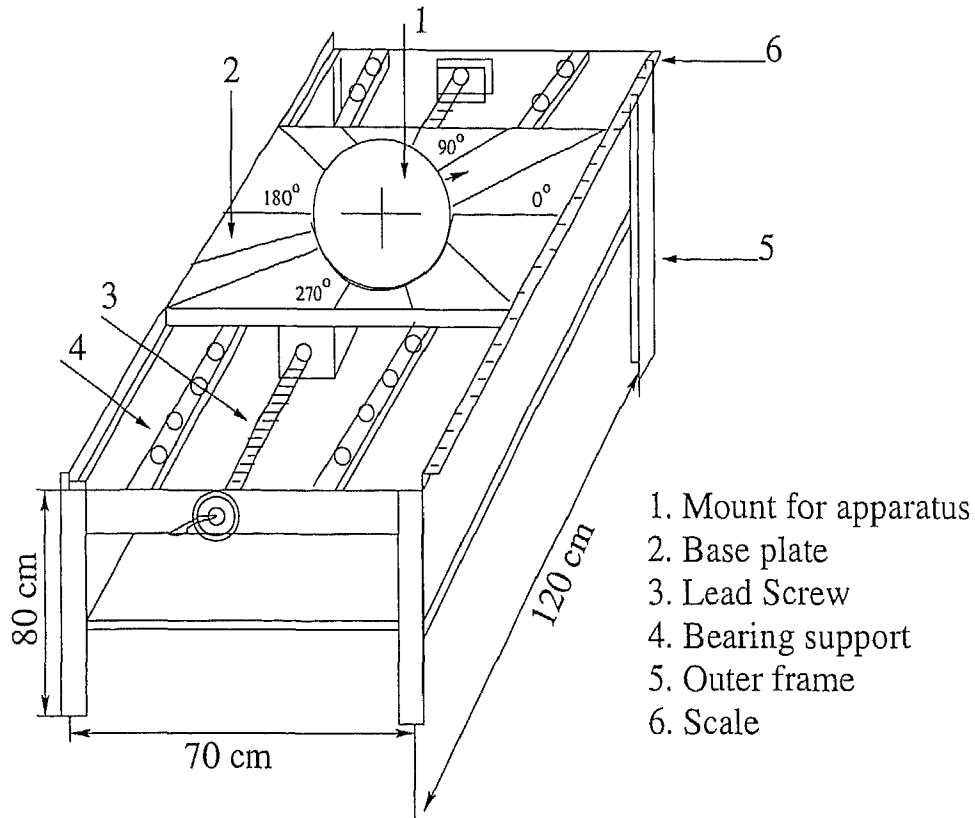


Figure 3.4: Schematic drawing of the traversing mechanism.

angle is very important. The angle is controlled by the rotation of the table-top of the traversing mechanism. It enables the center of the rotation of the test cell to be fixed and equal to the center of rotation of the table-top of the traversing mechanism.

3.3 Range of parameters

A wide range of Rayleigh numbers in the individual fluid layers have been explored in the rectangular cavity experiments. The fluid combinations considered in the present work are: air-water, air-silicone oil and silicone oil-water. Three layers heights namely $1/3$, $1/2$ and $2/3$ with respect to the cavity height have been studied. Since the cavity length is a constant, the cavity aspect ratio A_z is also fixed, the value being 13.93. The aspect ratio A_z with respect to the individual layer heights varies between 20.88 and 41.77 for each fluid. Temperature differences of 10, 15 and 18 K have been applied across the cavity, in a destabilizing configuration. A few selected experiments with an additional temperature difference of 0.3 K have also been conducted. The ambient temperature has been maintained at 23°C in all the experiments.

Table 3.2: Rayleigh number range for a rectangular cavity; Cavity filled with air (A) and water (W).

ΔT , K	Layer Heights	A_z (air)	A_z (water)	Ra (air)	Ra (water)
10	A-1/3, W-2/3	41.77	20.88	1242	35,727
	A-1/2, W-1/2	27.85	27.85	4185	16,413
	A-2/3, W-1/3	20.88	41.77	9939	4420
15	A-1/3, W-2/3			1794	64,404
	A-1/2, W-1/2			6044	30,772
	A-2/3, W-1/3			14,357	8023
18	A-1/3, W-2/3			2100	98,505
	A-1/2, W-1/2			7088	42,147
	A-2/3, W-1/3			16,844	10,666

The lowest temperature difference (0.3 K) was selected for the high Prandtl number fluid namely silicone oil because of refraction effects. High refraction errors were seen in the oil phase with increasing temperature difference above 0.3 K. The refraction errors are proportional to $(\text{length})^2$. Since the cavity length is quite large in the rectangular cavity the light beam lifted out of the field-of-view. Therefore no clear fringe patterns were noticed beyond 0.3 K in the oil phase.

The individual Rayleigh numbers explored in the experiments have been presented in Tables 3.2, 3.3 and 3.4 for three pairs of fluids. The respective Prandtl numbers for air, water and silicone oil are 0.71, 6.1 and 476.2.

The fringe patterns obtained in the experiments are to be interpreted as contours of the temperature field averaged in the direction of the light beam, namely along the length of the cavity in the horizontal plane. For Rayleigh numbers below a certain value, the thermal field in the individual fluid layers is two dimensional. The fringes would then coincide with the isotherms in the field. At higher Rayleigh numbers, the field is three dimensional, and the images donot carry strictly local information. The Rayleigh numbers in Tables 3.2-3.4 can be used as a guideline to anticipate the nature of the temperature field.

It has been observed that the interface in all the experiments was thermally active. This is confirmed by the appearance of dense fringes near it, being indicative of a high temperature gradient. It occurred despite the fact that the free surface is one of free-slip, without a prescribed constant temperature. Thus, in all the experiments, the superposed fluid layers behaved as two independent single phase systems connected at the interface. The nature of coupling as thermal or mechanical has been determined in the present

Table 3.3: Rayleigh number range for a rectangular cavity; Cavity filled with air (A) and silicone oil (O).

ΔT , K	Layer Heights	A_z (air)	A_z (oil)	Ra (air)	Ra (oil)
0.3	A-1/3, O-2/3	41.77	20.88	25	1611
	A-1/2, O-1/2	27.85	27.85	93	549
	A-2/3, O-1/3	20.88	41.77	226	140
10	A-1/3, O-2/3			1124	23,079
	A-1/2, O-1/2			3736	10,940
	A-2/3, O-1/3			8880	3183
15	A-1/3, O-2/3			1645	31,698
	A-1/2, O-1/2			5425	16,181
	A-2/3, O-1/3			12,900	4675
18	A-1/3, O-2/3			1920	40,452
	A-1/2, O-1/2			6383	19,301
	A-2/3, O-1/3			15,193	5541

work by examining the direction of the roll patterns and the joint unsteadiness in the respective fluid layers.

In the axisymmetric cavity, experiments have been carried out with equal layer heights for the three combinations of fluids. The cavity and the individual layer aspect ratios defined as the effective cavity diameter and the appropriate vertical dimension were 2.61 and 5.22 respectively. Experiments were conducted with the aim of reconstructing the three-dimensional thermal field inside the cavity, using principles of tomography. In the present experimental setup, four view angles namely 0, 45, 90 and 135° were possible for generating the two-dimensional projection data. Tables 3.5, 3.6 and 3.7 summarize the range of individual Rayleigh numbers explored in the present experiments.

The data recorded in all the experiments of the octagonal cavity is in the form of interferograms. These have been interpreted to understand the influence of increasing Rayleigh number on transition to three dimensionality and unsteadiness. The transient evolution patterns at 0 and 90° view angles have been presented for low Prandtl number fluids namely air and water. The evolution patterns of the thermal fields in the fluid layers were recorded at a regular interval of 30 minutes. The flow field in the cavity reached the stage of dynamic steady state after around 2.5 hours. The dominant state that prevailed for the longest duration was recorded. In silicone oil, a high Prandtl number fluid, even the Rayleigh number as high as 10^5 (based on the layer height) did not make the flow unsteady. However, distinct values of Rayleigh numbers were observed where two and three dimensional steady flow patterns were observed.

Table 3.4: Rayleigh number range for a rectangular cavity; Cavity filled with water (W) and silicone oil (O).

ΔT , K	Layer Heights	A_z (water)	A_z (oil)	Ra (water)	Ra (oil)
0.3	W-1/3, O-2/3	20.88	41.77	802	5163
	W-1/2, O-1/2	27.85	27.85	2710	2180
	W-2/3, O-1/3	41.77	20.88	6610	643
10	W-1/3, O-2/3			29,062	1.69E+05
	W-1/2, O-1/2			1.09E+05	69,849
	W-2/3, O-1/3			2.76E+05	20,564
15	W-1/3, O-2/3			55,700	2.54E+05
	W-1/2, O-1/2			2.07E+05	1.05E+05
	W-2/3, O-1/3			5.25E+05	30,924
18	W-1/3, O-2/3			73,482	3.10E+05
	W-1/2, O-1/2			2.83E+05	1.27E+05
	W-2/3, O-1/3			7.15E+05	37,184

Table 3.5: Rayleigh number range for an axisymmetric cavity; Cavity filled with air (A) and water (W).

ΔT , K	Layer Heights	A_z (air)	A_z (water)	Ra (air)	Ra (water)
6.5	A-1/2, W-1/2	5.22	5.22	9530	48,474
8.5	A-1/2, W-1/2	5.22	5.22	12,466	66,992
13	A-1/2, W-1/2	5.22	5.22	18,870	1.16E+05
18	A-1/2, W-1/2	5.22	5.22	27,068	1.72E+05

3.4 Experimental procedure

Tests were carried out under various conditions to ensure that the convection patterns in the fluid layers were insensitive to external disturbances such as floor vibration and water in circulation from the constant temperature baths. It was thus established that convection in fluid layers was driven by the temperature difference alone. For cavities filled with superposed liquids, the possibility of an air gap near the cold boundary at the top was carefully addressed. Silicone oil was introduced through a hole in the top tank by a hypodermic needle, while a second hole permitted the displacement of air. The process was continued till oil spilled over at both the hole locations.

In the present work, the experiments were started with the fluid layers and the bounding walls at the ambient temperature. All experiments continued for 4 hours to

Table 3.6: Rayleigh number range for an axisymmetric cavity; Cavity filled with air (A) and silicone oil (O).

ΔT , K	Layer Heights	A_z (air)	A_z (oil)	Ra (air)	Ra (oil)
0.4	A-1/2, O-1/2	5.22	5.22	470	2011
1.8	A-1/2, O-1/2	5.22	5.22	2237	6963
3.1	A-1/2, O-1/2	5.22	5.22	3861	12,781
4.0	A-1/2, O-1/2	5.22	5.22	5028	16,340
5.4	A-1/2, O-1/2	5.22	5.22	6881	21,880
8.5	A-1/2, O-1/2	5.22	5.22	11,153	33,980

Table 3.7: Rayleigh number range for an axisymmetric cavity; Cavity filled with water (W) and silicone oil (O).

ΔT , K	Layer Heights	A_z (water)	A_z (oil)	Ra (water)	Ra (oil)
0.4	W-1/2, O-1/2	5.22	5.22	17,266	10,955
1.8	W-1/2, O-1/2	5.22	5.22	88,157	48,402
3.1	W-1/2, O-1/2	5.22	5.22	1.58E+05	82,754
4.0	W-1/2, O-1/2	5.22	5.22	2.08E+05	1.06E+05
5.4	W-1/2, O-1/2	5.22	5.22	2.83E+05	1.43E+05
8.5	W-1/2, O-1/2	5.22	5.22	4.63E+05	2.23E+05
13.0	W-1/2, O-1/2	5.22	5.22	7.15E+05	3.38E+05
17.5	W-1/2, O-1/2	5.22	5.22	1.10E+06	4.57E+05

confirm that steady state was reached in terms of the fringe patterns. Although the flow field was usually fully evolved after 2 hours, the experiment was continued for an additional 2 hours for detecting small changes in the fringe field. The volume of the rectangular test cell being small, the thermal fields in the hot and the cold surfaces on one hand and the fluid layers on the other jointly approached steady state. In this respect, the thermal loading of the two-layer system may be categorized as continuous. This should be contrasted against a sudden loading, commonly employed in numerical calculations. The two types of loading are compared in Figure 3.5. The thermal loading curves were gradual and continuous in the rectangular and the axisymmetric test cell. The differences in the wall thickness and a smaller temperature difference in the latter resulted in a faster approach to steady state in the axisymmetric experiments. Thus the initial transients in the convective pattern⁴ could be recorded in these experiments, in particular for air and water. Transients appearing in the silicone oil experiments were

⁴distinct from temporal changes in the flow due to those in the driving potential, namely the cavity temperature difference across the fluid layer;

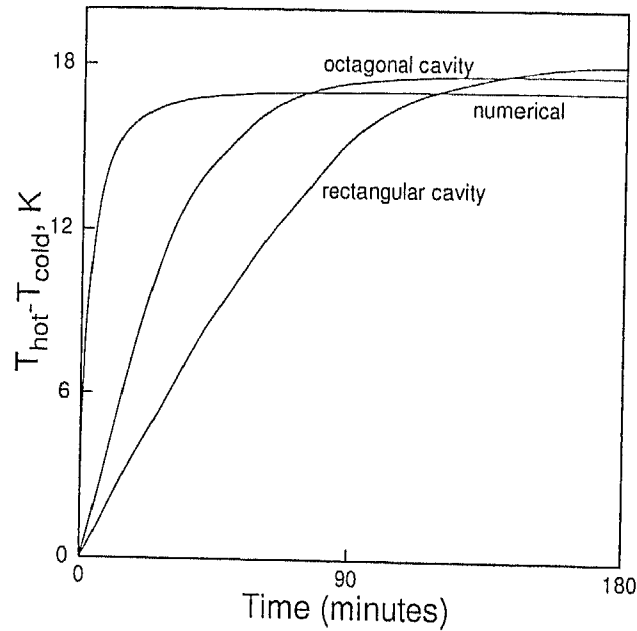


Figure 3.5: Schematic drawing of thermal loading patterns in a two-layer system seen in numerical calculations and experiments.

consistently short-lived.

3.5 Instrumentation

Optical visualization has been utilised in the present work to scan the thermal field in the superposed fluid layers. Other approaches to temperature measurement can also be discussed. For example, the temperature field can be obtained by scanning the fluid layer using a thermocouple. This approach has a serious drawback since the presence of the probe can distort the flow pattern, not just locally but over the entire cavity. The probe intrusion problem is particularly serious at high Rayleigh numbers. A flow visualization technique that has been widely employed for velocity measurement involves the use of tracer particles in the fluid. This method has been found to be successful mainly in liquids and less so in gases. In any case, the tracer route identifies the velocity field in the fluid but not the temperature field which is the focus of the present work. A subtle point to be noted in the context of flow visualization by tracers is the following: Since the particles respond to velocity, small time-dependent fluctuations are immediately noticed and portray an image of chaotic convection even at moderate Rayleigh numbers. Further, the tracer route has a fundamental drawback of not generating information regarding three dimensionality of the flow field.

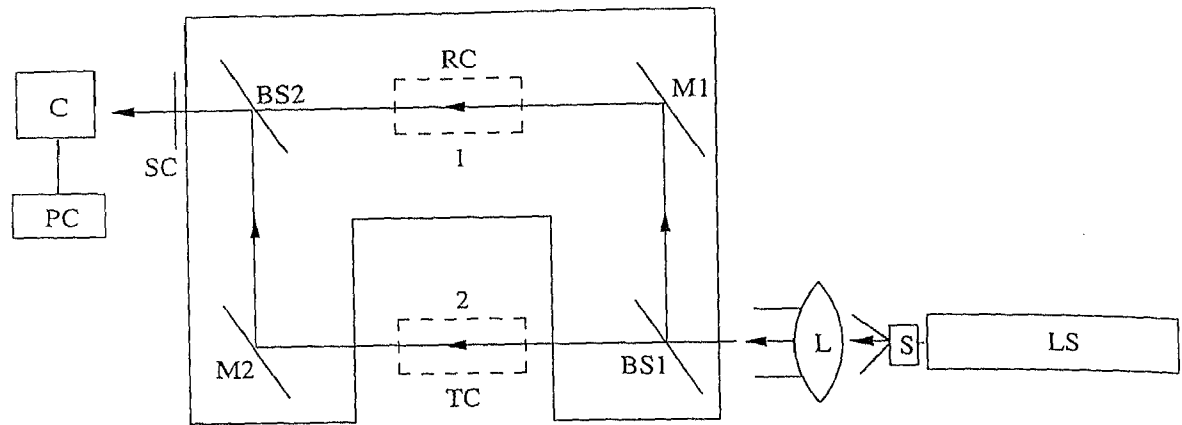
The limitations imposed by other approaches has paved way for adopting the optical method for determining the temperature field. Optical techniques have definite advantages with regard to the following issues:

- (a) Clearly identifiable fringe patterns are formed;
- (b) Three dimensional information about the temperature field can be extracted from the interferograms. Thus it is possible to deduce the shape of the structures in the fluid layers at various Rayleigh numbers;
- (c) Local as well as global heat transfer rates can be determined; and
- (d) Optical images remain well-defined over a meaningful range of Rayleigh numbers.

3.5.1 Mach-Zehnder interferometer

The Mach-Zehnder interferometer has been used as a primary instrument in the present work for temperature measurement in the fluid layers. Figure 3.6 is a schematic drawing of the interferometer. The optical components present in it namely the beam splitters BS1 and BS2 and mirrors M1 and M2, are inclined exactly at an angle of 45° with respect to the laser beam direction. The first beam splitter BS1 splits the incoming collimated beam into two equal parts, the transmitted and the reflected beams. The transmitted beam (2) is labelled as the test beam and the reflected beam (1) as the reference beam. The test beam passes through the test region where the convection process is in progress. It is reflected by the mirror M2 and recombines with the reference beam on the plane of the second beam splitter (BS2). The reference beam undergoes a reflection at mirror M1, passes through the reference-cell unaltered and is superimposed with the test beam at BS2. The two beams on superposition at the second beam splitter BS2, produce an interference pattern. This pattern contains the information of the variation of refractive index in the test region with respect to the reference. For measurements in liquids, a reference chamber is required to be included with the interferometer to compensate for refractive changes under isothermal conditions. Therefore, a reference cell (RC) has also been utilized in the present work. The mirrors and beam splitters employed in the present configuration are of 150 mm diameter. The beam splitter has 50% reflectivity and 50% transmittivity. The mirrors are coated with 99.9% pure silver and employ a silicon dioxide layer as a protective layer against oxidation.

The Mach-Zehnder interferometer can be operated in two modes, namely (a) Infinite fringe setting and (b) Wedge fringe setting. In (a) the test and reference beams are set to have identical geometrical path lengths and fringes form due to density and temperature changes alone. Since each fringe is a line of constant phase, it is also a line



M	Mirror	L	Plano-convex lens	1	Reference beam		
BS	Beam splitter	LS	Laser source	2	Test beam		
C	CCD camera	S	Spatial filter	TC	Test cell	RC	Reference cell
PC	Personal computer	SC	Screen				

Figure 3.6: Schematic drawing of the Mach-Zehnder interferometer.

of constant refractive index, a line of constant density and hence temperature and hence an isotherm⁵. It can also be shown that the fringe thickness is an inverse measure of the local temperature gradient (being small where gradients are high). The infinite fringe setting is employed for high-accuracy temperature measurements in the fluid. In (b), the mirrors and beam splitters are deliberately misaligned to produce an initial fringe pattern of straight lines. When a thermal disturbance is introduced in the path of the test beam, these lines deform and represent the temperature profiles in the fluid. The wedge fringe setting is commonly employed for heat flux measurements.

3.5.2 Shadowgraph

Shadowgraph is also an optical technique for measurement of rates of heat and mass transfer in the flow field. It is a single beam technique. Here, the reduction in light intensity with beam divergence is employed. Specifically, the shadowgraph measures the variation of the second order derivative of the index of refraction normal to the direction of propagation of the light beam. In the present work, the shadowgraph images of the deformed interfaces have been captured through the interferometer itself. The deformed interfaces of the fluid layers were imaged by blocking the reference beam. In effect the

⁵This statement is strictly true for two dimensional field. In three dimensional fields, fringes are lines of constant line-averaged temperature.

full image can be understood as shadowgraph of the convection pattern. Quantitatively, the intensity distribution is to be interpreted as the distribution of the Laplacian of the temperature field (Goldstein, 1996).

3.5.3 Laser source

A 35 mW, continuous wave (632.8 nm) He-Ne laser (Spectra Physics) is employed as the coherent light source for the interferometer. This laser is sturdy in construction, economical and stable in operation. The original laser beam is of 2 mm diameter. A spatial filter is required to expand the beam to any convenient size. In the present study, the expanded beam diameter is 72 mm. The spatial filter is a lens-pinhole arrangement with two adjustable screws. The distance between the pin hole and the lens is also adjustable. These screws determine the inplane location of the pin-hole and have to be adjusted so that the small laser beam is focussed on the pin-hole and the outgoing beam is expanded. A plano-convex lens has been used to produce a collimated beam for the experiments. The specifications of the laser used in the present study is given in Table 3.8.

Table 3.8: Specifications of the Helium-Neon laser.

Make	Spectra-physics
Model	Spectra-physics 127
Output power	60 mW (maximum), 35 mW average output
Wavelength	632.8 nm
Color	Orange red
Coherence length	20 cm - 30 cm
Power consumption	≈ 1.0 kW of electrical power
Efficiency	0.01 - 0.1 %
Beam diameter	1.25 ± 0.10 mm
Beam divergence	0.66 ± 0.06 mrad
Amplitude noise, 10 Hz -2 MHz	$< 1\%$ rms
Amplitude ripple, 45 Hz -1 kHz	$< 1\%$ rms
Life time	≈ 20000 hours of operation

3.5.4 CCD camera

A CCD (charged coupled device) camera (Pulnix, model: T5 565) of spatial resolution of 512×512 pixels has been used to capture the interferometric images. The interferogram formed at the second beam splitter of the Mach-Zehnder interferometer

is projected over a screen. The selection of the screen and collection of interferometric images from it form important steps since the clarity in the images will reduce the uncertainty in the subsequent calculations. For this purpose a tracing paper has been used to display the interferometric images. The attenuation of the laser beam through the thickness of the paper was found to be small. It was observed that two screens used together when physically disturbed led to distinctly clear images on the video monitor. This effect can be understood as a spatial averaging of the image over the two screens which makes the fringe pattern appear as smooth and clear. The CCD camera is connected to a PC-based image processing system through an 8 bit A/D card (PIP 1024 MATROX). The fringe pattern is stored in an integer matrix form with intensities varying between 0 to 255 (the gray scale), where 0 indicates black and 255 indicates white. With the present set up the image acquisition speed is at video rates, namely 50 frames per second. The output of the CCD camera is projected to a high resolution video monitor to visualize and focus the fringe patterns.

3.5.5 Pneumatic isolation mount

The optical components of the interferometer are extremely sensitive to vibrations. This was experienced during experiments from the fringes that formed on the screen. To avoid ground vibration from reaching the optics, the entire interferometer has been supported by four pneumatic isolation mounts (Newport Corporation). These mounts are connected to an air compressor for pressurization. Once the mounts are pressurized the entire interferometer floats over the mounts. This stabilizes the interferometric images and facilitates image acquisition. An air compressor of rated capacity 11 bar is used throughout the experiment to pressurize the mounts. The operating pressure for the mounts was rated at 3 bar. Hence a regulator valve was used to supply air to the mounts at the right pressure. The compressor was located sufficiently away from the interferometer to protect it from vibrational noise.

3.5.6 Constant temperature bath

The top wall of the cavity was cooled and the bottom wall heated by pumping water continuously from constant temperature baths. Special attention was given to ensure that isothermal conditions prevailed at the aluminium and copper plates respectively for the rectangular and the axisymmetric test cells. This was achieved by circulating a large volumetric flow rate of water. Specifically, the temperature drop between the incoming and outgoing fluid on both the hot and the cold side was found to be negligible. To lower the plate temperature below the ambient value a constant temperature bath (Huber,

model: variostat) was employed. The specification of the constant cold temperature bath is given in Table 3.9. For the hot surface, a constant temperature bath (Raagaa, model: cryostat) of the specifications mentioned in Table 3.10 was used.

Table 3.9: Specifications of the constant cold temperature bath (Huber model: variostat).

Operating temperature range	-30°C to 150°C
Temperature stability at -10°C	0.01 K
Temperature adjustment	Digital
Temperature indication	Digital
Temperature sensor	pt100
Force pump capacity	10 liters/min (max)
Suction pump capacity	7 liters/min (max)

Table 3.10: Specifications of the constant hot temperature bath (Raagaa model: cryostat) with proportional digital indicating controller.

Operating temperature range	ambient to 80°C
Capacity	50 litres
Resolution	± 0.01 K
Temperature adjustment	Digital
Temperature indication	Digital
Temperature sensor	pt100
Force pump capacity	5 liters/min (max)

3.5.7 Temperature recorder

The temperature of the aluminium and copper surfaces were monitored by K-type 18 gage thermocouples. The ambient temperature was measured independently by a thermocouple. The thermocouples were in turn connected to a 30 channel recorder (San-Ei) through out the experiment. The specifications of the temperature recorder used in the present study are listed in Table 3.11.

3.6 Alignment of the interferometer

Before the start of the experiment the interferometer has to be aligned. The alignment is carried out individually for the different fluids selected for the experiments. The initial

Table 3.11: Specifications of the multi-channel Temperature Recorder.

Make	NEC San-ei Instruments, Ltd.
Model	8H10
Display	Digital
No. of channels	30
Measuring range	-200°C to 1370°C
Resolution	0.1 K

alignment of the interferometer is not disturbed greatly from one experiment to the other for a particular combination of fluid layers. However, some fine tuning is essential to ensure that the interferometer operates at its highest sensitivity. The initial alignment of the interferometer is carried out as per the following steps.

1. The light output of the spatial filter is adjusted so that the diffraction rings which appear with the expanded beam vanish. In most experiments, the diffraction ring formed a complete circle and remained at the periphery of the expanded beam.
2. The laser power output is measured using a light meter. The change in the power output is not a transient phenomena but it decreases steadily with hours of operation. In the present work, the laser output was in the range 30-32 mW over a period of two years.
3. The location of the plano-convex lens is adjusted from the pinhole of the spatial filter so that the separation between the two is equal to the focal length of the lens. This produces a collimated laser beam needed for interferometric measurements.
4. The optical components of the interferometer are adjusted till their centers fall on a horizontal plane. Once this is accomplished, the first beam splitter (BS1) is adjusted till it is exactly at 45° to the incoming light rays. All the remaining optical components are then made parallel to each other by adjusting them one at a time. The mirrors and beam splitters are of 150 mm diameter, and the expanded beam of 72 mm diameter is made to pass through the central portion of the optical components. In the absence of the test and the reference cells, a clear infinite fringe field is obtained.
5. Adjustment for the infinite fringe setting is delicate when the test and the reference cells are in position. Imperfections in mounting the optical windows show up at this stage. In the absence of the fluids within the cavity, except for air, the windows

can be aligned to generate the infinite fringe setting once again. It is quite difficult to realize the infinite fringe setting in the liquid phase compared to a gas. The alignment calls for moving the optical elements of the interferometer so that the path lengths of the test and the reference light beams are balanced.

6. The interferometer is ready for use and temperature difference can now be applied across the cavity to start the convection process.

In the infinite fringe setting, the initial field of view is one of complete brightness since the interference between the test and reference beams is constructive. The geometrical and the optical path lengths of the test and reference beams are then equal in the absence of any thermal disturbances in the path of the test beam. Owing to imperfect adjustment of the mirrors and beam splitters by screws movement the exact infinite fringe setting in a theoretical sense may not be realized. As the interferometer approaches the infinite fringe setting, the distance between the fringes increases and the number of fringes decreases. In the present work, the quality of infinite fringe setting in all the experiments met the standards set by the cavity filled with air; this is shown in Figure 3.7. To illustrate fringe formation in the infinite fringe setting, a candle flame was put on the path of the test beam and the interferogram was recorded. The candle flame

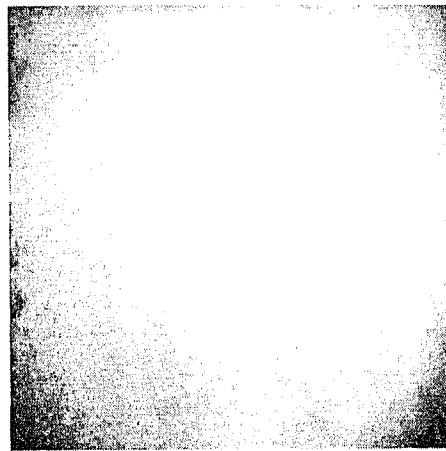


Figure 3.7: Infinite fringe setting of the Mach-Zehnder interferometer.

in the infinite fringe setting is shown in Figure 3.8. The fringes can be seen to correspond to isotherms around the candle flame. The wedge fringe setting is comparatively easier to set up. Here the initial fringes form due to deliberate misalignment between the optical components. The orientation of the fringes can be changed by adjusting the inclination of the optical components. Initially the fringes are adjusted so that they are almost straight. Figure 3.9 shows the initial wedge fringe setting of the interferometer

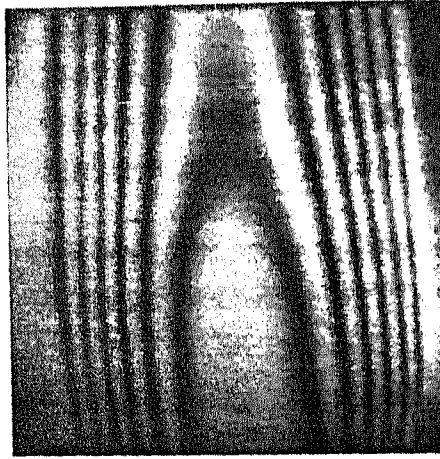


Figure 3.8: Candle flame seen in the infinite fringe setting of the interferometer.

in air. If a thermal disturbance is introduced in the path of the test beam, the fringes get displaced to an extent depending on the nature of the temperature profile. Hence the fringes in the wedge fringe setting of the interferometer are representative of the temperature profile in the medium under study. The candle flame experiment is shown in the wedge fringe setting mode in Figure 3.10. Here the fringes represent the temperature profile inside the flame. Note the symmetry in the temperature profile along the centerline of the flame. The infinite fringe setting in air-water, air-oil, and oil-water experiments are summarized in Figure 3.11 for the axisymmetric cavity.

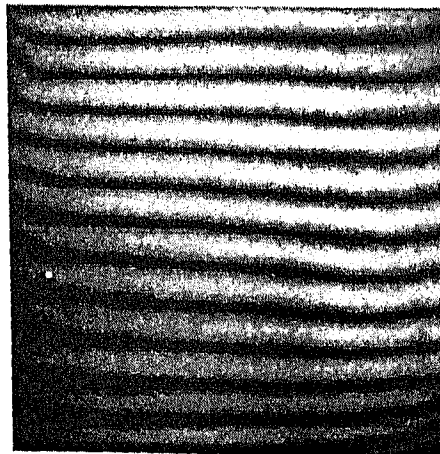


Figure 3.9: Wedge fringe setting of the interferometer.

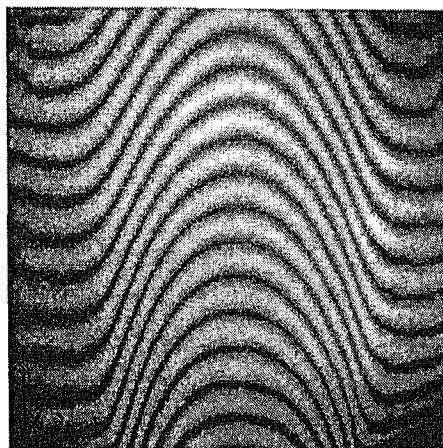


Figure 3.10: Candle flame seen in the wedge fringe setting of the interferometer.

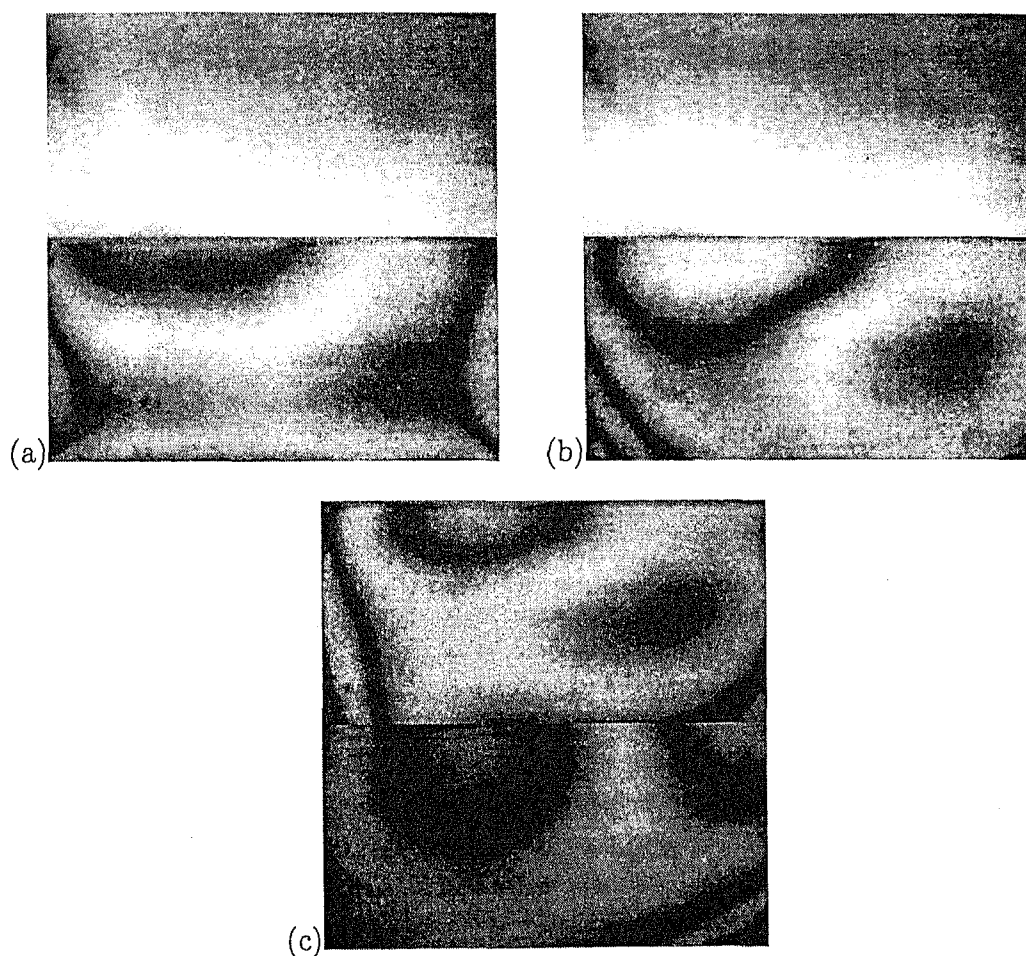


Figure 3.11: Infinite fringe setting in the axisymmetric cavity containing fluid layers of (a) air and water, (b) air and silicone oil, and (c) silicone oil floating over water.

3.7 Recording interferometric projections

In the rectangular cavity, projection data of the thermal field for only one view angle could be recorded in the form of an interferogram. The reconstruction of flow field from

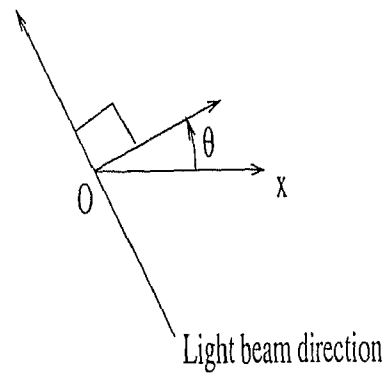


Figure 3.12: Definition of a view angle.

a single projection is not possible in the frame work of tomography. Axial tomography requires the projection data from various angles for the field to be reconstructed. The axisymmetric cavity of the present work is designed to record projection data from different view angles. The definition of the view angle θ is shown in Figure 3.12. The experiments were conducted by turning the axisymmetric test cell with reference to the light source. The position of the light source and the detector remained fixed in all the experiments. The experiments were conducted at view angles of 0, 45, 90 and 135°. For each angle, the size of the light beam covered 41% of the full width of the fluid layer (Figure 3.13).

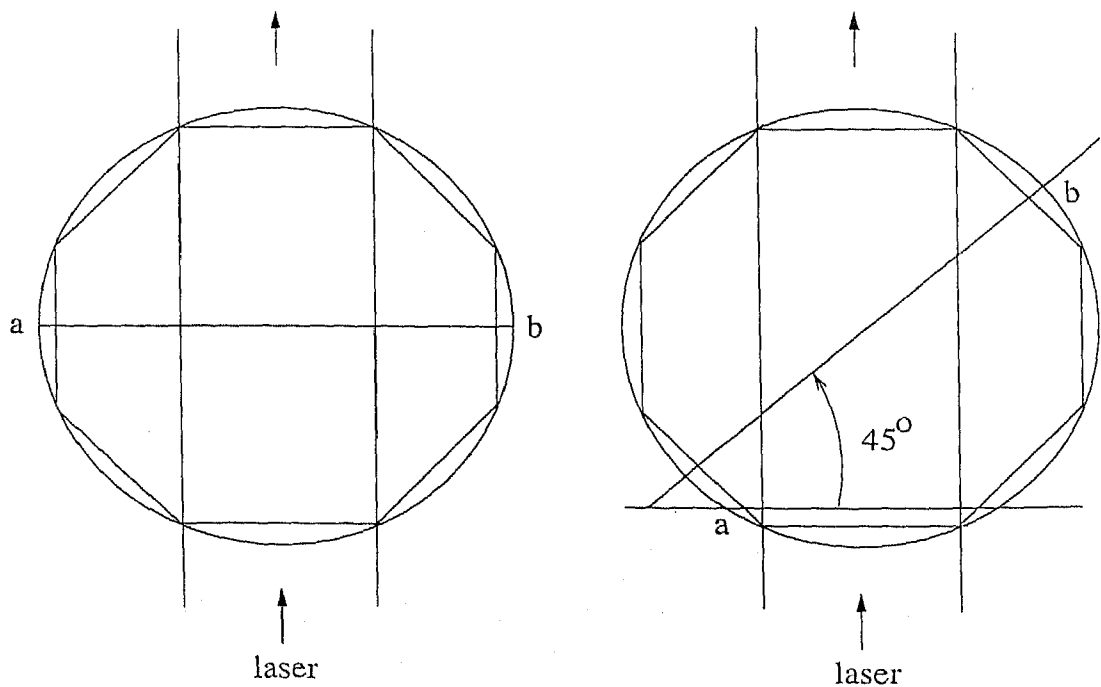


Figure 3.13: Schematic drawing to show projection angles of 0 (left) and 45° (right) for the nominally axisymmetric test cell.

Chapter 4

Data Reduction

The experimental data obtained in the form of interferograms show fringe patterns in the two fluid layers within the cavity. The image data has to be analyzed for the determination of parameters such as fringe temperatures, interface temperature distribution and the local and global heat transfer rates at the two walls. The evaluation of interferograms for the determination of the fringe temperature is discussed in the present chapter. The principles of interferometry with reference to the determination of the temperature field in the infinite fringe setting of a Mach-Zehnder interferometer have been presented. The fringes in the interferograms have been identified as isotherms, or isofunctions in the more general three dimensional context. To extract information from the recorded fringes, the interferograms have to be processed and interpreted in terms of temperature and the heat transfer rates. Image processing techniques become important in this context. The present chapter also addresses the issue of reconstruction of three-dimensional temperature field from its interferometric projections using principles of tomography. Lastly, the expected level of uncertainty in the experimental data has been discussed.

4.1 Interferometry

In the absence of any thermal disturbance, the optical path difference between the test and the reference beam is zero in the infinite fringe setting. Hence interference is constructive and a bright field-of-view is obtained. The image obtained is practically fringe-free (Figure 3.7) but may show imperfections associated with the spatial filter and the interferometer optics in the form of a single broad fringe¹. When nonisothermal conditions prevail in the path of the test beam (for example, a candle flame) each ray of light

¹The influence of a single fringe in the initial infinite fringe setting on the experimental record was found to be negligible.

undergoes a change of phase, depending on the extent of change of the refractive index of the medium. Hence an optical path difference is established between the test and the reference beams, resulting in a fringe pattern (Figure 3.8). In the wedge fringe setting, the optical components (primarily BS2, in Figure 3.6) are deliberately misaligned to produce a set of line fringes of any convenient spacing (Figure 3.9). In the presence of a thermal disturbance the fringes would be displaced towards regions of higher temperatures, thus producing a fringe pattern that resembles the temperature profile itself (Figure 3.10).

In the present chapter, attention is restricted to image patterns that form in the infinite fringe setting of the interferometer. Here, the test beam records information about the variation of the refractive index of the fluid with respect to a reference environment. To make temperature measurement possible, the refractive index variation must be related to that of temperature. The relationship between the refractive index n and temperature T is established as follows. For a homogeneous transparent medium such as water, the Lorenz-Lorenz relationship (Goldstein, 1996):

$$\frac{n^2 - 1}{\rho(n^2 + 2)} = \text{constant} (= C) \quad (4.1)$$

holds. This gives

$$\frac{dn}{d\rho} = \frac{C(n^2 + C)}{2n(1 - C\rho)} \quad (4.2)$$

Provided the change in the refractive index in a given experiment are small, the right hand side of Equation 4.2 is a constant for a particular liquid. The index of refraction of a liquid is thus primarily a function of density and hence temperature. In view of Equation 4.2, the relationship is practically linear.

For gases, $n \approx 1$ and Equation 4.1 simplifies to the relationship

$$\frac{n - 1}{\rho} = \text{constant} \quad (4.3)$$

Equation 4.3 is called the Gladstone-Dale relation. It follows that $dn/d\rho = \text{constant}$. For moderate changes in temperature, typically ≤ 20 K and nearly uniform bulk pressure, the gas density varies linearly with temperature as²

$$\rho = \rho_0(1 - \beta(T - T_0)) \quad (4.4)$$

It follows that dn/dT is also a constant, being purely a material property. In summary, changes in temperature simultaneously result in changes in refractive index of the fluid

²Here, the dependence of density on pressure has been taken to be of secondary importance.

medium. From principles of wave optics, it results in changes in the phase of the wave. This is the origin of fringe formation in the interferometric images. Direct measurements of the refractive index as a function of temperature show that the value of dn/dT in air and water at 20°C and 1 atm for a wavelength of 632.8 nm (as in the present work) are -0.927×10^{-6} and $-0.880 \times 10^{-4} \text{ K}^{-1}$ respectively (Goldstein, 1996).

If temperature differences within the physical region being studied are large, three factors arise which limit the usefulness of interferometry. These are: (1) the linearity of the relationship between density and temperature, (2) the linearity between density and refractive index, and (3) beam deflection due to a refractive index gradient. These factors complicate the data reduction process and make interferometry more of a qualitative tool. However, fringes continue to form and images can be used for flow visualization. In the present study, temperature differences between the test section and the ambient are small and the linear relation between refractive index, density and temperature has been taken to be valid.

Let $n(x, y)$ and $T(x, y)$ be the refractive index and temperature fields respectively in a two dimensional physical domain. With reference to the test cells in Figures 3.1 and 3.2, x and y form the vertical plane, while the z -axis is in the horizontal plane parallel to the direction of propagation of light. Let n_0 and T_0 be the reference values of n and T respectively as encountered by the reference beam. Let L be the total geometric path length covered by the test beam within the experimental chamber. The interferogram is a fringe pattern arising from the optical path difference (Hauf and Grigull, 1970):

$$\Delta PL(x, y) = \int_0^L (n(x, y) - n_0) ds \quad (4.5)$$

which in terms of temperature is

$$\Delta PL(x, y) = \frac{dn}{dT} \int_0^L (T(x, y) - T_0) ds \quad (4.6)$$

The integral is evaluated along the path of a light ray given by the coordinate s . Neglecting refraction effects, this path will be a straight line (coincident with the coordinate z) and the integral evaluation is greatly simplified. The fringes seen on the interferogram are locus of points that have equal optical path differences. Hence on any given fringe the optical path difference ΔPL is a constant and

$$\int_0^L (T(x, y) - T_0) ds = \frac{\Delta PL}{dn/dT} = \text{constant}$$

Hence

$$\int_0^L T(x, y) ds - T_0 L = \text{constant}$$

The integral $\int_0^L T(x, y) ds$ is defined as $\bar{T}L$, where \bar{T} is the average value of $T(x, y)$ over the distance L traversed by the laser beam through the test cell. In the absence of refraction, this is also the line integral of the function $T(x, y, z)$, in the z -direction. Hence, over a fringe

$$L(\bar{T} - T_0) = \text{constant} \quad (4.7)$$

In the infinite fringe setting Equation 4.7 holds good for all fringes. When refraction effects are small, the distance L is equal to the size of the test cell in the direction of propagation of light. Hence L is constant for all the rays, Equation 4.7 then implies that \bar{T} is a constant over the fringe and hence each fringe represents a locus of points over which the the average of the temperature field determined along the direction of the ray is a constant. For a two dimensional field $T(x, y)$, fringes would also be isotherms.

Consider a geometry where the length of the ray through the test cell changes for each ray. The line integral of the function $T(x, y)$ ($=\bar{T}_2$) at a location which corresponds to a length L_2 can be given in terms of the line integral of the function $T(x, y)$ ($=\bar{T}_1$) at some other location corresponding to a ray length of L_1 as

$$\bar{T}_2 = T_0 + \frac{L_1}{L_2}(\bar{T}_1 - T_0) \quad (4.8)$$

Since the change in the path length per fringe shift is a constant, the temperature drop per fringe shift is also a constant. Defining the function $L(\bar{T} - T_0)$ in Equation 4.7 as $f(\bar{T}, L)$, the fringe temperature on two successive fringes for a given value of L can be obtained as:

$$\begin{aligned} \text{fringe 1: } f_1(\bar{T}, L) &= \frac{\Delta PL}{dn/dT} \\ \text{fringe 2: } f_2(\bar{T}, L) &= \frac{(\lambda + \Delta PL)}{dn/dT} \end{aligned}$$

where λ is the wavelength of the laser used. Here, the approximation $L_1 = L_2 = L$ (no refraction) has been used. From these two equations, the temperature drop per fringe shift can be calculated as

$$\Delta T_e = \frac{1}{L} (f_2(\bar{T}, L) - f_1(\bar{T}, L)) = \frac{\lambda/L}{dn/dT} \quad (4.9)$$

Following Equation 4.5, the individual fringes reflect the equation

$$\Delta PL = \frac{dn}{dt} \int_0^L (T - T_0) ds$$

and hence the line integral of the temperature field. The set of all line integrals (an interferogram, in the present study) defines a projection of the temperature field. The

interferograms can be numerically evaluated so that the left side of the above equation is a known quantity for each fringe. The mathematical problem now is one of solving for the temperature field from its projections. If the original field is three dimensional, its projection is a field in a dimension reduced by unity, namely two. It is theoretically possible to record a large number of projections of the test field at various angles and reconstruct the original temperature function with accuracy. This process of three dimensional reconstruction from two dimensional projections is called *tomography*.

4.1.1 Refraction effects

The presence of a strongly refracting field can modify Equation 4.9 for the temperature difference between successive fringes. In the present context, a strongly refracting field will arise when a large transverse temperature gradient is encountered: Alternatively, a fluid such as silicone oil can also lead to a large refraction of the light beam. Under these circumstances, the light ray will not travel in a single horizontal plane. Specifically, depending on the magnitude of the temperature gradient, the ray will bend in the vertical plane. Refraction will thus introduce an additional path length to the test beam. Refraction effects can be precisely computed and accounted for. The extent of refraction determines the type of the three dimensional reconstruction algorithm that can be used in a particular experiment. In the present work, reconstruction has been applied under circumstances when refraction errors are negligible. With this approximation, a sequential plane-by-plane reconstruction approach was possible. Beyond a particular temperature gradient, whose magnitude depends on the choice of the fluid, the quality of interferograms was adversely affected and assigning temperatures to fringes was not possible.

An estimate of the increase in path length due to refraction is developed here. Consider the path of the light ray AB through a test cell (Figure 4.1) when it is affected by refraction effects. Let α be the bending angle at a location P of the test cell. The optical path length from A to B is given by (Jenkins and White, 1981):

$$\begin{aligned} AB &= \int_A^B n(x, y, z) ds \\ &= \int_0^L n(x, y, z) \frac{dz}{\cos \alpha} \end{aligned}$$

Here y is a coordinate parallel to the gravity vector and z is parallel to the direction of propagation of light. The length of the test section in the z -direction is indicated as L .

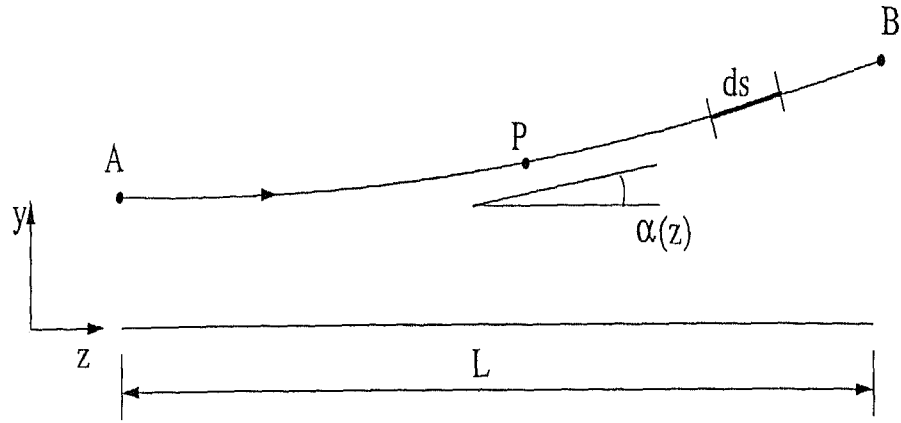


Figure 4.1: Calculation of the bending angle of a light ray due to refraction effects.

Assuming α to be small, $\cos \alpha$ can be expressed as

$$\cos \alpha = (1 - \alpha^2)^{1/2}$$

Using the first two terms of the binomial expansion, one can approximate

$$\cos \alpha \approx 1 - \frac{\alpha^2}{2}$$

Hence the optical path length is given by

$$AB = \int_0^L n(x, y, z) \left(1 - \frac{\alpha^2}{2}\right)^{-1} dz \quad (4.10)$$

$$= \int_0^L n(x, y, z) \left(1 + \frac{\alpha^2}{2}\right) dz \quad (4.11)$$

The angle $\alpha(z)$ at any location z can be calculated as described below.

Consider Figure 4.2 where two wave fronts are at times τ and $\tau + \Delta\tau$ as shown. At a time τ the ray is at a position z . After a time interval of $\Delta\tau$, the light has moved a distance of Δz . Hence

$$\Delta z = \Delta\tau \frac{c_0}{n}$$

where c_0 is the velocity of light in vacuum. There is a gradient in n along the y direction. The gradient in n results in a bending of the wave front. The distance $\Delta^2 z$ is given by

$$\begin{aligned} \Delta^2 z &= \Delta z_y - \Delta z_{y+\Delta y} \\ &\approx \Delta z_y - \Delta z_y + \frac{\Delta}{\Delta y} (\Delta z) \Delta y, \\ &= -c_0 \frac{\Delta 1/n(x, y, z)}{\Delta y} \Delta\tau \Delta y \end{aligned}$$

Let $\Delta\alpha$ represent the bending angle at a fixed location z . For a small increment in the angle, $\Delta\alpha$ can be expressed as

$$\begin{aligned}\Delta\alpha &= \tan(\Delta\alpha) = \frac{\Delta^2 z}{\Delta y} \\ &= -c_0 \frac{\Delta[1/n(x, y, z)]}{\Delta y} \Delta\tau \\ &= -n(x, y, z) \Delta z \frac{\Delta[1/n(x, y, z)]}{\Delta y}\end{aligned}\quad (4.12)$$

In the limiting case

$$d\alpha = \frac{1}{n(x, y, z)} \frac{\partial n(x, y, z)}{\partial y} dz \quad (4.13)$$

Hence the cumulative bending angle at any location along the z axis is

$$\begin{aligned}\alpha(z) &= \int_0^z \frac{1}{n(x, y, z)} \frac{\partial n(x, y, z)}{\partial y} dz \\ &= \frac{1}{\bar{n}(x, y)} \frac{\partial \bar{n}(x, y)}{\partial y} z\end{aligned}$$

where $1/\bar{n}(x, y)$ and $\partial \bar{n}(x, y)/\partial y$ are the average line integrals along the path of the ray over a distance 0 to z .

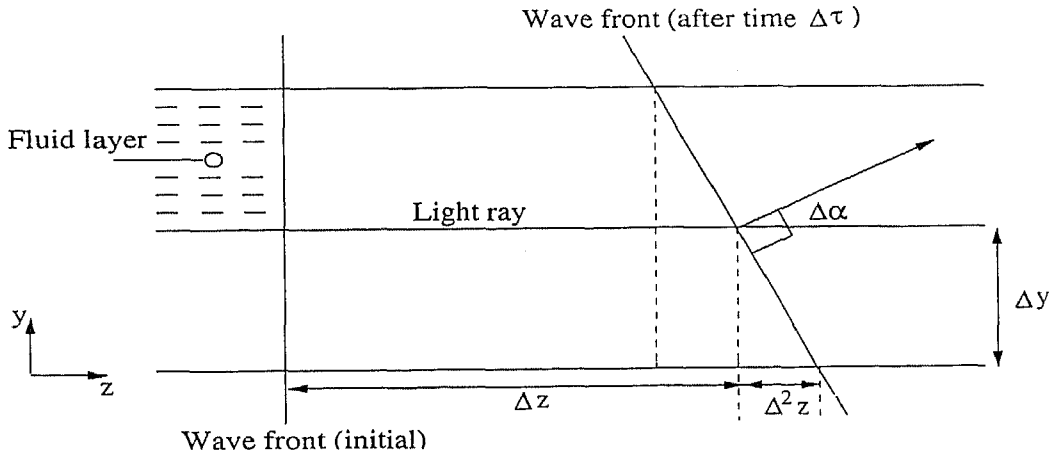


Figure 4.2: Bending of a light ray in the fluid medium due to refraction effects.

From Equation 4.11

$$AB = \int_0^L n(x, y, z) \left(1 + \frac{1}{2} \frac{1}{n^2} \left(\frac{\partial \bar{n}}{\partial y} \right)^2 z^2 \right) dz \quad (4.14)$$

$$= \bar{n}(x, y) L + \frac{1}{6 \bar{n}(x, y)} \left(\frac{\partial \bar{n}}{\partial y} \right)^2 L^3 \quad (4.15)$$

where $\bar{n}(x, y)$ is the average line integral of $n(x, y)$ over the complete length L . Similarly the expression $\partial\bar{n}/\partial y$ represent average line integral of the transverse derivative of \bar{n} over the length L .

The optical path of the reference beam is simply

$$\text{Reference path} = \int_0^L n_0 dz = n_0 L \quad (4.16)$$

Hence the difference in the optical path length in the presence of refraction effects is

$$\begin{aligned} \Delta PL &= \bar{n}(x, y)L + \frac{1}{\bar{n}(x, y)} \left(\frac{\partial \bar{n}}{\partial y} \right)^2 L^3 - n_0 L \\ &= (\bar{n}(x, y) - n_0)L + \frac{1}{\bar{n}(x, y)} \left(\frac{\partial \bar{n}}{\partial y} \right)^2 L^3 \\ &= (\bar{T}_1(x, y) - T_0)L \frac{dn}{dT} + \frac{1}{\bar{n}(x, y)} \left(\frac{\partial \bar{n}}{\partial y} \right)^2 L^3 \end{aligned}$$

where $\bar{T}_1(x, y)$ represents the average line integral of the temperature field along the direction of the ray at a given point on the fringe. The corresponding ray over the next fringe corresponds to an additional path of λ . Hence this can be written as

$$\Delta PL + \lambda = (\bar{T}_2(x, y) - T_0)L \frac{dn}{dT} + \frac{1}{\bar{n}(x, y)} \left(\frac{\partial \bar{n}}{\partial y} \right)^2 L^3$$

where $\bar{T}_2(x, y)$ represents the average line integral of the temperature field along the direction of the ray at a point on the next fringe. The successive temperature difference between two fringes is

$$\lambda = (\bar{T}_2(x, y) - \bar{T}_1(x, y))L \frac{dn}{dT} + \frac{1}{\bar{n}(x, y)} \left(\frac{dn}{dT} \right)^2 \left(\left(\frac{\partial T}{\partial y} \right)_2^2 - \left(\frac{\partial T}{\partial y} \right)_1^2 \right) L^3 \quad (4.17)$$

and the temperature drop per fringe shift is

$$\Delta T_e = \frac{\lambda - \frac{1}{\bar{n}(x, y)} \left(\frac{dn}{dT} \right)^2 \left(\left(\frac{\partial T}{\partial y} \right)_2^2 - \left(\frac{\partial T}{\partial y} \right)_1^2 \right) L^3}{L \frac{dn}{dT}} \quad (4.18)$$

Since the gradient in the temperature field is not known before the calculation of the fringe temperature the factor $\left(\frac{\partial T}{\partial y} \right)_2 - \left(\frac{\partial T}{\partial y} \right)_1$ must be calculated from a guessed temperature field. Thus, the final calculation of ΔT_e relies on a series of iterative steps with improved estimates of the temperature gradients. As an estimate, the temperature gradient can be replaced by its largest value, namely at the wall. A realistic estimate is

obtained by employing the average wall temperature gradient for location 1 and zero for location 2. The latter can be readily calculated using Nusselt number correlations.

The number of fringes expected in a projection can be estimated from the relation

$$\text{Number of fringes} = \frac{T_{hot} - T_{cold}}{\Delta T_e} \quad (4.19)$$

This equation is valid when (a) the refraction effects are negligible and (b) a single fluid is enclosed between hot and cold plates. In the present work, an interface is formed between the two fluid layers enclosed in the cavity. The interface acts as a free-slip boundary without a prescribed temperature. The average interface temperature at steady state can be obtained by applying the energy balance principle across the cavity. The value of ΔT_e is a constant for a particular fluid and is known for a given set of conditions such as the length of the cavity and the wavelength of the laser. Hence the temperature difference in Equation 4.19 can be based on the respective hot or cold plate temperature with respect to the average interface temperature.

The beam deflection δ over a length L in a single fluid medium can be seen from Equation 4.15 to be proportional to

$$\delta \sim \frac{1}{6n} \left(\frac{dn}{dT} \right)^2 \left(\frac{\partial T}{\partial y} \right)^2 L^3$$

In terms of the average Nusselt number, this expression can be written as

$$\delta = \frac{1}{6n} \left(\frac{dn}{dT} \right)^2 \text{Nu}^2 \left(\frac{\Delta T}{H} \right)^2 L^3 \quad (4.20)$$

where the Nusselt number is itself a function of Rayleigh number, and hence the cavity height H and temperature difference ΔT . Employing a correlation of the form (Gebhart *et al.*, 1988)

$$\text{Nu} = \text{Nu}(\text{Ra}, \text{Pr})$$

the beam deflection over a length L can be calculated from Equation 4.20. Estimates of δ as function of the cavity temperature difference are presented in Tables 4.1 and 4.2. A comparison of beam deflections in Tables 4.1 and 4.2 shows that refraction in silicone oil is significantly higher than in air and water³. Further, the refraction errors are more pronounced in the rectangular cavity than in the axisymmetric test-cell for all combinations of fluid layers. The reason for the difference is in the cavity length

³For a cavity temperature difference of 10 K, the temperature drop across the water layer was around 0.2 K. Hence refraction errors in water were much smaller than what is reported in Tables 4.1 and 4.2.

L , being 447 mm for the rectangular cavity and 120.7 mm for the axisymmetric test cell. Thus a higher temperature difference could be imposed in the experiments with the axisymmetric test cell for fluid combinations containing silicone oil, including air-oil and water-oil layers.

Table 4.1: Comparison of refraction errors in air, water and silicone oil as a function of the temperature difference in the rectangular cavity.

ΔT , K	n	dn/dT , K ⁻¹	δ , mm		
			air	water	silicone oil
10	1.000 (a)	-0.927E-06			
	1.333 (w)	-0.880E-04			
	1.402 (o)	-4.165E-04			
			768×10^{-6}	64.3	661
15			884×10^{-6}	67.8	866
18			946×10^{-6}	76.8	973

Table 4.2: Comparison of refraction errors in air, water and silicone oil as a function of the temperature difference in the axisymmetric cavity.

ΔT , K	n	dn/dT , K ⁻¹	δ , mm		
			air	water	silicone oil
10	1.000 (a)	-0.927E-06			
	1.333 (w)	-0.880E-04			
	1.402 (o)	-4.165E-04			
			6.19×10^{-6}	5.18×10^{-1}	5.33
15			7.12×10^{-6}	5.46×10^{-1}	6.98
18			7.63×10^{-6}	6.19×10^{-1}	7.84

4.2 Evaluation of interferograms

Thinned fringes rather than the fringe bands carry the essential information of the path integrated temperature field. Hence, to extract temperature profiles and heat transfer rates from the interferogram, the fringe skeleton rather than the original fringes is needed. For a three dimensional reconstruction of the temperature field, the line integral of the temperature field is required over a uniform grid so that tomographic algorithms can be applied. Consequently the calculation of temperature associated with the fringes is the most important step in interferometry. The methodology adopted for the calculation of

fringe temperature from a fringe skeleton is presented in this section. The technique has been discussed in the context of the Rayleigh-Benard experiment.

For definiteness, consider the fringe distribution as shown in Figure 4.3. The upper and lower walls in the figure have known temperatures, while the interface temperature is unknown. It is possible that high temperature gradients near the wall produce a large number of thin fringes. Hence during the recording and processing of the interferogram a few near wall fringes could be lost. The loss of near wall fringes could be due to the finite resolution of the CCD camera, and followed by a loss of information during filtering and other image processing operations. The first fringe seen in a thinned interferogram near the wall will thus be of arbitrary order. One cannot assign a temperature to the fringes directly from the wall temperature by using Equation 4.9 though the wall itself is an isotherm. Even when no near-wall fringe is lost, assigning a temperature to the first fringe is not straight-forward since the wall (though an isotherm) need not be a fringe, i.e. a site for destructive interference. The following procedure has been adopted in the present work to derive temperature values at the fringes.

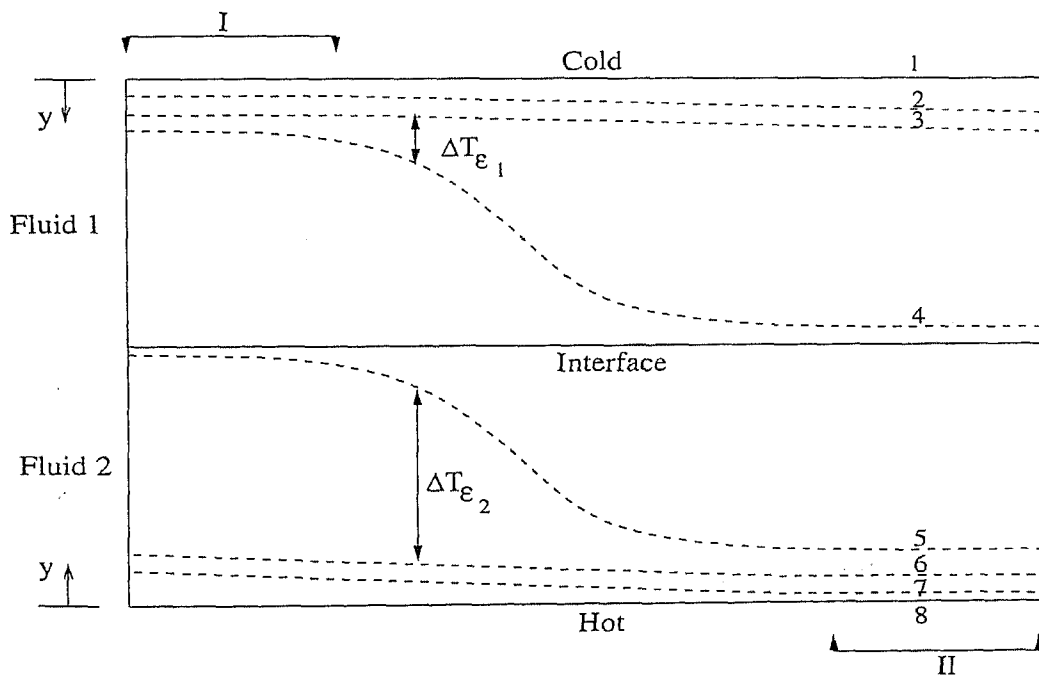


Figure 4.3: Calculation of the fringe temperature from an idealized fringe skeleton.

Two regions on the interferograms were selected, one where the fringes in the upper fluid 1 are close to the cold wall (marked I in Figure 4.3) and the other where the fringes in lower fluid 2 are close to the hot wall (marked II in Figure 4.3). Independent calculations were performed in both fluid layers to obtain the respective fringe temperatures in the

interferogram. The interface temperature was also estimated using this procedure. The final interface temperature then allotted was the average of the two estimates obtained independently from regions I and II⁴.

The procedure adopted for assigning temperature to fringes in fluid 1 is given below. Consider the fringes marked 2, 3, 4 (region I) in Figure 4.3. Fitting a function of the type

$$T(y) = a + by + cy^2 \quad (4.21)$$

where y is a vertical coordinate, one obtains

$$\Delta T_{e_1} = T_2 - T_3 = b(y_2 - y_3) + c(y_2^2 - y_3^2) \quad (4.22)$$

$$\Delta T_{e_1} = T_3 - T_4 = b(y_3 - y_4) + c(y_3^2 - y_4^2) \quad (4.23)$$

These two equations solve for the constants b and c . Here, ΔT_{e_1} is the temperature change per fringe shift in fluid 1 and y is a local coordinate measured from the upper wall.

The local wall temperature gradient is simply $(\partial T / \partial y)_{y=y_1}$. From Equation 4.21, this gradient can be expressed as $(b + 2cy_1)$. The gradient in the temperature field very near the wall is likely to be constant since conduction heat transfer is dominant. Hence the gradient in temperature field at the first fringe (fringe marked 2 in Figure 4.3) is expected to be close to the gradient at the wall in region I. The gradient in the temperature field at the first fringe is $(b + 2cy_2)$. The temperature gradient in the vicinity of the wall is allotted as an extrapolation step, the average of the two gradients. Once the gradient at the wall is known, the first fringe temperature near the cold wall can be calculated from Equation 4.21 as

$$T_2 = (y_2 - y_1) \frac{(b + 2cy_1) + (b + 2cy_2)}{2} + T_1 \quad (4.24)$$

Since ΔT_{e_1} , the temperature difference between successive fringes is known, the subsequent fringe temperatures are found out by simply adding the amount to the first fringe temperature where the sign of the temperature gradient is positive. Since the image is available in the form of an intensity matrix of integers, the above procedure for calculating the fringe temperature can be implemented at any column. The column where the near-wall fringes are dense (as in regions I and II) is preferred for this purpose. Column-to-column variation in the computed fringe temperatures was found to be generally small for the interferograms recorded in the experiments.

⁴Admittedly, temperature varies over the interface. Unless otherwise specified, the interface temperature in the discussion pertains to its average value.

The above procedure can also be applied for assigning fringe temperatures in fluid 2. Here, the first fringe closest to the hot wall is fringe number 7 (Figure 4.3). Thus T_7 can be calculated and subsequent fringe temperatures are found out by subtracting ΔT_{c_2} from the first fringe, since the temperature gradient in this zone is negative. The average interface temperature was determined from those of the fringes crossing the boundary.

4.3 Temperature data over a grid

Once the absolute fringe temperatures are obtained, this data must be transferred to a two-dimensional uniform grid over the fluid region. This is required to apply tomographic algorithms for the reconstruction of the three-dimensional temperature field. Two dimensional linear interpolation has been carried over the entire thinned image by superimposing a two-dimensional grid on it. The grid has 32 points along the horizontal and 21 points along the vertical direction. Once the interpolation was completed, isotherms were drawn to represent the fringes in the original image. This was done to cross-check the error involved in interpolation. It was found that the temperature data on the grid follows closely the pattern of the original thinned image and interpolation errors were negligible.

4.4 Image processing

The information generated by the Mach-Zehnder interferometer is available in the form of interference fringes. The interferograms contain information about the temperature itself in two-dimensional fields. In three-dimensional problems, interferometry must be recorded at various projection angles and must scan the complete fluid domain. Temperature distribution can subsequently be determined by interpreting the interferometric images as path integrals and applying principles of three-dimensional reconstruction. Tomographic algorithms are applicable in this context. Tomography falls in the class of inverse techniques and its performance is characterized by a definite dependence on noise levels in the prescribed data. Specifically, errors in data can be amplified during the reconstruction process. It is thus natural to examine the sensitivity of the reconstructed temperature field to uncertainties and errors that are intrinsic to image enhancement operations that are required while processing the interferograms⁵. For both two- and three-dimensional measurements, the fringe patterns thus have to be carefully analyzed.

⁵The work of Mishra *et al.* (Optics and lasers in engineering, 1999) shows that the data reduction procedure does play an important role in quantitatively determining the reconstructed field.

The recording of fringe patterns using a CCD camera results in storing the images as a string of numbers in the form of a 512×512 matrix. Each number corresponds to an intensity level. In the present study, an 8-bit analog-to-digital converter was employed. Hence the resulting images are discretized into 256 gray levels. An intensity level of 0 indicates black whereas 255 is white. Availability of the images on a gray scale is of help in data processing and the automation of the fringe extraction process.

The fringe patterns recorded using the interferometer need to be converted first into temperature records. Quantitative evaluation of the interferograms requires that the fringe skeleton be determined. From the thinned fringes, temperature information can be generated since a fringe is an isotherm and the same temperature prevails over its entire length. This step requires the following operations:

- (1) processing of the fringe images (**image processing**);
- (2) identifying intensity minima within fringes (**fringe thinning**);
- (3) measuring distances between fringes and determining the fringe order in terms of temperature units (**quantitative evaluation**); and
- (4) transferring the temperature information available at the fringes to a superimposed uniform grid (**interpolation**).

In most experiments, these four steps are difficult since operations such as locating fringe minima and edges result in ambiguity. One of the factors that cause difficulty in image analysis is *speckle*, a form of noise. Elaborate procedures must be employed to remove speckle from interferometric images. Examples of filtering strategies are Fourier-filtering using band-pass filters, histogram specification and Laplacian smoothing (Gonzalez and Woods, 1993). The strategies involved in processing the interferograms from the initial stage as a digitized image to finally a fringe skeleton are discussed in the present section.

Images of fringe patterns collected using the CCD camera and the A/D card tend to be noisy⁶. While a collection of fringes indicates a smooth wave-like variation of light intensity, experimental interferograms will have a superposition of higher harmonics of small amplitude. This is a source of ambiguity since it is now quite difficult to identify intensity maxima and minima. Noise is generated at different stages of the experiment: the imperfection of the optical components, noise in the CCD array, and digitization of the analog data. The flow and thermal fields under study also contribute to noise from edge effects due to refraction and nonuniform scattering and absorption. However, in the experience of most authors, speckle is the major source of noise in interferometry. It is a superposition of diffraction patterns over the basic interference image that constitutes

⁶Noise can be defined as extraneous and unwanted intensity variation which is superimposed over the useful portion of the data.

the signal in the present discussion. Speckle arises from imperfection of optical surfaces. The presence of microscopic unevenness on the surface of the optical elements leads to diffraction. The diffracted rays in turn interfere and generate local fringe patterns and corrupt the global intensity distribution. Thus speckle is characterized by high-wavenumber fluctuations in the intensity data. To recover the original intensity variation, there is a need to filter the image, remove noise and extract the signal.

Image processing applications are required to remove the noise present in the images on one hand and enhance the quality of the images on the other. Further, in experiments fringes are bands of finite thickness, and isotherms are associated with the minimum or maximum intensity level within a dark or a bright band. The process of replacing the fringe bands by curves passing through minimum or maximum intensity locations is called fringe thinning. Hence, the next objective of image processing is the generation of a thinned image. Image processing operations in interferometry can be broadly divided into three categories: (a) filtering, (b) image enhancement, and (c) thinning. These operations described in detail by Mishra *et al.* (1998) are briefly reviewed below.

4.4.1 Filtering of images

Once the image is stored in digital form, it is available as a matrix of integers. These fall in the range 0-255 and represent light intensity at spatial locations on the image. Speckle can be removed using Fourier filtering, median filtering and averaging. However Fourier filtering has been seen to be best suited for interferometric fringes. Median filtering has been applied locally to an image for better smoothing as an operation after Fourier filtering.

For the Fourier filtering operation, the image is first transformed to the wavenumber space with a two dimensional Fourier transform operation. Here the wavenumber is a spatial frequency, defined as the number of intensity cycles per pixel. Intuitively one can view the low wavenumber harmonics as information and those at a high wavenumber as noise. In the wavenumber space a two dimensional symmetric band-pass filter can be used to effectively set the high wavenumber components to zero. The size of the band-pass filter is decided by its ability to remove noise without appreciable loss of the signal, typically less than 5%. An inverse two dimensional Fourier transform restores the image in filtered form to the spatial domain. The symmetry of the filter referred above is related to the problem of aliasing with discrete Fourier transforms. The decision on the size of the band pass filter has to be found by trial-and-error. Since the light source and optics employed for all the experiment were identical, the noise pattern in the images

The recording of fringe patterns using a CCD camera results in storing the images as a string of numbers in the form of a 512×512 matrix. Each number corresponds to an intensity level. In the present study, an 8-bit analog-to-digital converter was employed. Hence the resulting images are discretized into 256 gray levels. An intensity level of 0 indicates black whereas 255 is white. Availability of the images on a gray scale is of help in data processing and the automation of the fringe extraction process.

The fringe patterns recorded using the interferometer need to be converted first into temperature records. Quantitative evaluation of the interferograms requires that the fringe skeleton be determined. From the thinned fringes, temperature information can be generated since a fringe is an isotherm and the same temperature prevails over its entire length. This step requires the following operations:

- (1) processing of the fringe images (**image processing**);
- (2) identifying intensity minima within fringes (**fringe thinning**);
- (3) measuring distances between fringes and determining the fringe order in terms of temperature units (**quantitative evaluation**); and
- (4) transferring the temperature information available at the fringes to a superimposed uniform grid (**interpolation**).

In most experiments, these four steps are difficult since operations such as locating fringe minima and edges result in ambiguity. One of the factors that cause difficulty in image analysis is *speckle*, a form of noise. Elaborate procedures must be employed to remove speckle from interferometric images. Examples of filtering strategies are Fourier-filtering using band-pass filters, histogram specification and Laplacian smoothing (Gonzalez and Woods, 1993). The strategies involved in processing the interferograms from the initial stage as a digitized image to finally a fringe skeleton are discussed in the present section.

Images of fringe patterns collected using the CCD camera and the A/D card tend to be noisy⁶. While a collection of fringes indicates a smooth wave-like variation of light intensity, experimental interferograms will have a superposition of higher harmonics of small amplitude. This is a source of ambiguity since it is now quite difficult to identify intensity maxima and minima. Noise is generated at different stages of the experiment: the imperfection of the optical components, noise in the CCD array, and digitization of the analog data. The flow and thermal fields under study also contribute to noise from edge effects due to refraction and nonuniform scattering and absorption. However, in the experience of most authors, speckle is the major source of noise in interferometry. It is a superposition of diffraction patterns over the basic interference image that constitutes

⁶Noise can be defined as extraneous and unwanted intensity variation which is superimposed over the useful portion of the data.

the signal in the present discussion. Speckle arises from imperfection of optical surfaces. The presence of microscopic unevenness on the surface of the optical elements leads to diffraction. The diffracted rays in turn interfere and generate local fringe patterns and corrupt the global intensity distribution. Thus speckle is characterized by high-wavenumber fluctuations in the intensity data. To recover the original intensity variation, there is a need to filter the image, remove noise and extract the signal.

Image processing applications are required to remove the noise present in the images on one hand and enhance the quality of the images on the other. Further, in experiments fringes are bands of finite thickness, and isotherms are associated with the minimum or maximum intensity level within a dark or a bright band. The process of replacing the fringe bands by curves passing through minimum or maximum intensity locations is called fringe thinning. Hence, the next objective of image processing is the generation of a thinned image. Image processing operations in interferometry can be broadly divided into three categories: (a) filtering, (b) image enhancement, and (c) thinning. These operations described in detail by Mishra *et al.* (1998) are briefly reviewed below.

4.4.1 Filtering of images

Once the image is stored in digital form, it is available as a matrix of integers. These fall in the range 0-255 and represent light intensity at spatial locations on the image. Speckle can be removed using Fourier filtering, median filtering and averaging. However Fourier filtering has been seen to be best suited for interferometric fringes. Median filtering has been applied locally to an image for better smoothing as an operation after Fourier filtering.

For the Fourier filtering operation, the image is first transformed to the wavenumber space with a two dimensional Fourier transform operation. Here the wavenumber is a spatial frequency, defined as the number of intensity cycles per pixel. Intuitively one can view the low wavenumber harmonics as information and those at a high wavenumber as noise. In the wavenumber space a two dimensional symmetric band-pass filter can be used to effectively set the high wavenumber components to zero. The size of the band-pass filter is decided by its ability to remove noise without appreciable loss of the signal, typically less than 5%. An inverse two dimensional Fourier transform restores the image in filtered form to the spatial domain. The symmetry of the filter referred above is related to the problem of aliasing with discrete Fourier transforms. The decision on the size of the band pass filter has to be found by trial-and-error. Since the light source and optics employed for all the experiment were identical, the noise pattern in the im

corresponds to high wavenumbers. Filtering may thus result in a loss of contrast. The visual appearance of a filtered image may not be good compared to the unfiltered image. But the filtered image is definitely an improvement over the unfiltered image in terms of the noise content. Image processing operations can be unambiguously applied to the filtered image.

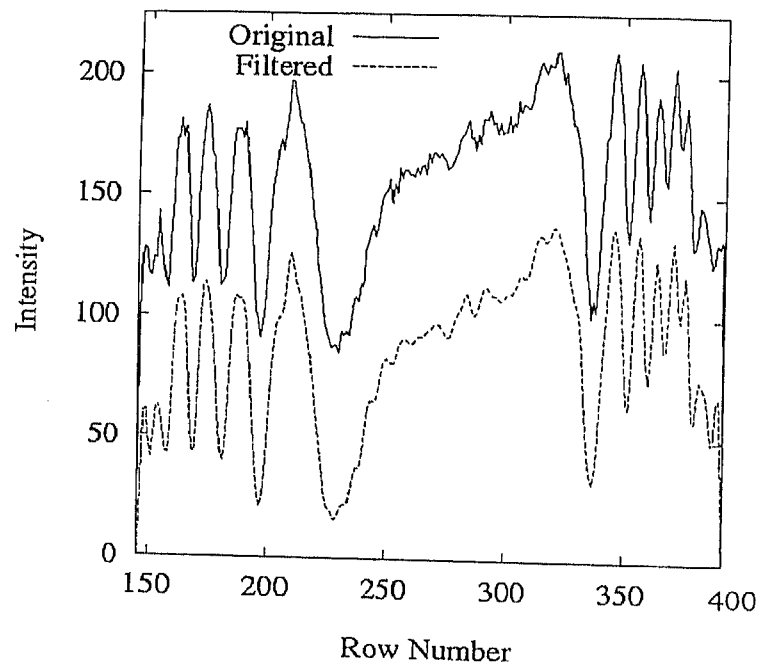


Figure 4.7: Original and Fourier-filtered intensity distributions.

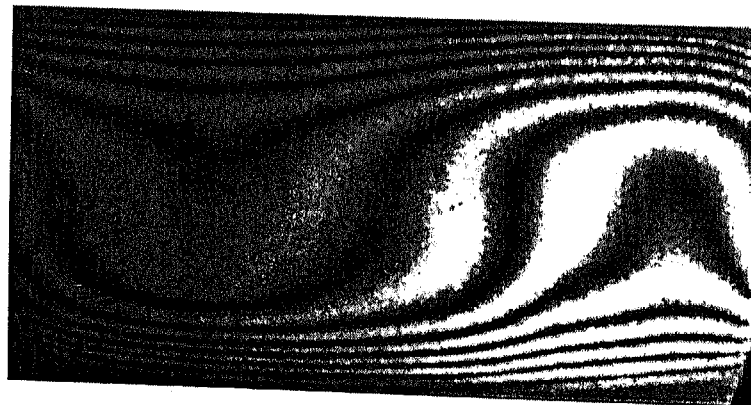


Figure 4.8: Filtered Interferogram

4.4.2 Image enhancement

The Fourier filtered images are generally blurred owing to loss of contrast. Hence, further operations are required to enhance the quality of the image. In particular, edge

enhancement and contrast improvement are essential for analyzing the interferograms. While various techniques are available in the literature for improving the images, the image enhancement techniques are problem-specific. The method of image enhancement for optical images generated from an interferometer may be completely different from the images obtained from a shadowgraph.

The techniques for image enhancement can be classified as spatial domain and wavenumber space methods. Spatial domain methods deal with the gray value at a pixel directly whereas the wavenumber space techniques manipulate the wavenumber spectra obtained from the Fourier transform of the image. The spatial domain enhancement techniques process the image over a point or a mask. Strategies that have proved to be useful for improving the appearance of the images are (Jain *et al.*, 1989): (a) specification of probability density function, (b) median filtering and (c) edge enhancement. Figure

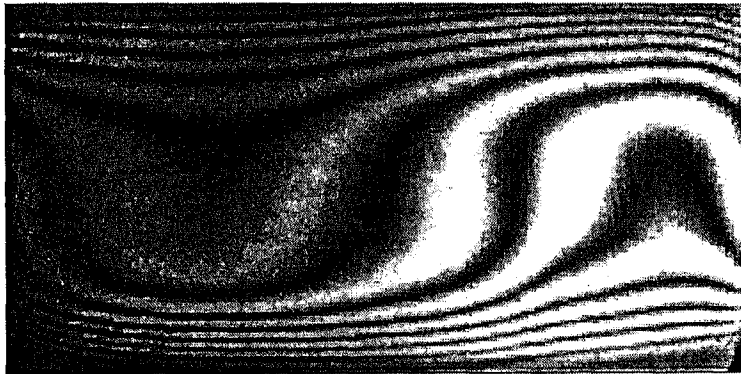


Figure 4.9: Contrast-improved Interferogram

4.9 shows a contrast improved image corresponding to the interferogram shown in Figures 4.4 and 4.8. It has been obtained by the histogram equalization method. The image processing software GIMP⁷ available in the linux platform has been employed in the present work.

Along with noise, the edges of fringes are also equivalent to the high wavenumber portion of the image spectrum because of the accompanying sharp change in the gray level. During Fourier-filtering, the high wavenumber part of the spectrum is set to zero and in this process some edge information is lost and the edges become blurred. Since the fringe thinning operations are carried out within the fringe band, a proper definition of fringe thickness is required. Hence the edges of the fringes need to be sharpened. An edge-enhanced image of Figure 4.9 obtained using GIMP is shown in Figure 4.10.

⁷Abbreviation for GNU image manipulation program.

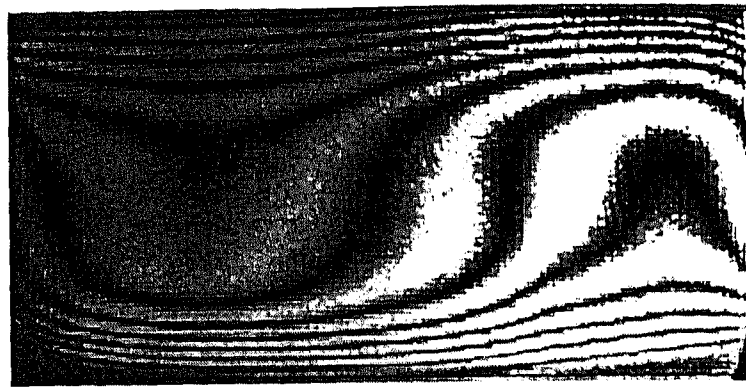


Figure 4.10: Interferogram with sharpened edges (edge enhancement).

4.4.3 Fringe thinning

Fringe thinning is one of the most important operations in the extraction of quantitative data from interferograms. Fringe thinning is a process of extraction of the set of points of minimum or maximum intensities in the dark and bright bands of the fringes. When the interferometer is operated in the infinite fringe setting, each fringe is a locus of points having an identical path difference. This can be interpreted as follows: For rays having a certain path difference, the corresponding pixels in the interferometric image will have identical light intensity. One of the direct ways to locate a typical locus of points is to connect all minimum intensity pixels within a dark band or the maximum intensity pixels within a bright band. The intensity will be a minimum at a point of complete destructive interference and hence will have a zero intensity. Similarly, a maximum in intensity will appear at a point where interference is constructive. In experiments, the original as well as partially processed images have superimposed noise. Hence the distribution of intensity across fringes will exhibit ambiguity. Specifically, the minimum intensity will not strictly be a zero and the maximum intensity in 8-bit digitization will not be 255. Hence the strategy that has been employed is to trace the intensity minima within dark bands and maxima within bright bands, rather than search for points of known intensity. This is the closest approximation that can be achieved to track a series of pixels that have low or high intensities. When a laser is used as a light source, one must also take into account the overall Gaussian profile of the light output. Hence, determination of extrema in intensity becomes a local operation in the image domain. Subsequently, the locus of minima or maxima need to be connected within a fringe band across the width of the image, to get a curve on which temperature itself or a temperature-dependent function is a constant. It is clear that under experimental conditions, only intensity minima can be traced since intensity itself is not precisely defined. In practice, one observes a greater noise level in the high intensity regions, possibly related to device

saturation in the recording camera. This makes locating intensity maxima a difficult task. Hence, fringe thinning operations referred in the present work are related to the location of intensity minima in the dark fringe bands.

Several fringe thinning methods are available in the literature. Most of the fringe tracing algorithms that have been suggested are problem-specific and cannot be accepted as being generally valid. A large number of published algorithms are based on edge detection by global thresholding but these are specific to a class of problems and appear to be inapplicable for interferometric images. In the presence of a non-uniform average level of illumination with superimposed noise, the task of automatic extraction of the fringe skeleton is difficult. This has been experienced even with the well-behaved fringe tracing algorithms given by Robinson (1983) and Krishnaswamy (1991) for interferometric fringes and by Ramesh and Singh (1995) for photoelastic fringe patterns. Funnell (1981) has suggested an easy-to-implement but not a fully automatic technique to trace the fringes. This method is likely to yield good results for low-quality images.

In the present study, an algorithm developed by Mishra *et al.* (1998) has been adopted for fringe thinning. This algorithm is automatic in the sense that no user input is required at any intermediate stage of the calculation. It is based on the actual two-dimensional gray level variations and the fringe skeleton is traced by searching along the minimum intensity direction while simultaneously maintaining connectivity of the points traced. In particular, the interferograms in air have been thinned using the algorithm. The fringe patterns obtained in water and oil phase tend to be quite dense due to their low values of ΔT_e , the temperature drop per fringe shift. The thinning algorithm could not be used in the regions of high fringe density. The paint-brush option available in GIMP has been used for fringe thinning in water and oil layers. In this approach, intensity minima are located by eye judgement. The implementation of the two fringe thinning algorithms suitable for interferograms recorded using the Mach-Zehnder interferometer are presented in the following section.

4.4.3.1 Automatic fringe thinning algorithm

The algorithm under discussion is similar to the one proposed by Funnell (1981), but in view of certain differences in the details, the full algorithm is presented below. However, it follows closely the proposal of Mishra *et al.* (1998). Once a single point is specified the present algorithm does not require user intervention while the tracing is in progress. It is in this respect the algorithm is fully automatic. It consists of tracing of the fringes in the direction of the minimum intensity. The direction is decided by using the intensity

information over a template of pixels. The computer code developed can run using different sizes of templates and handle complex fringe shapes. The input required for the code is the starting point for each of the fringes selected.

The algorithm uses the following ideas: The direction of the tracings are defined as (a) forward and (b) backward (Figure 4.11). The turning of fringes by more than $\pm 90^\circ$ results in a change of direction and is a special case. Such areas of the fringes where a turning is encountered have to be pre-defined in the form of a rectangle covering the area. These cases are classified into four categories depending on the angle of turning: (a) while in forward direction turning backward up, (b) while in forward direction turning backward down, (c) while in backward direction turning forward up and (d) while in backward direction turning forward down (Figure 4.12). To locate the point of minimum intensity, eight directions of movement (1-8) are defined (Figure 4.13). The direction in which the minima should be searched is located by placing a template whose size is user-specified at the concerned pixel. The choice of size of the template is related to the fringe thickness. The near wall fringes in the present study were very thin owing to a large heat flux. Hence the choice of template size was limited to the minimum possible, namely a 3×3 square. A larger template is likely to interfere with neighbouring fringes and is hence undesirable. However a larger template can be used when the fringe bands spread over several pixels. Use of 7×7 and 9×9 templates results in an average direction of minimum intensity and tends to produce a smooth tracing. Local unphysical variations in the traced fringe can be bypassed by using a template larger than 3×3 . A 5×5 template appears to be an optimal choice for interferometric fringes away from the heated and cooled surfaces.

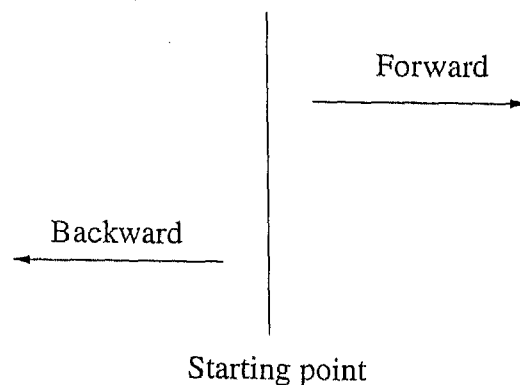


Figure 4.11: Two major directions for tracing of fringes.

The direction in which the fringe is to be traced is determined as follows. The sum of the intensities in all the eight directions are computed and the two sequences of numbers along which the minima occur are searched. The directions producing the

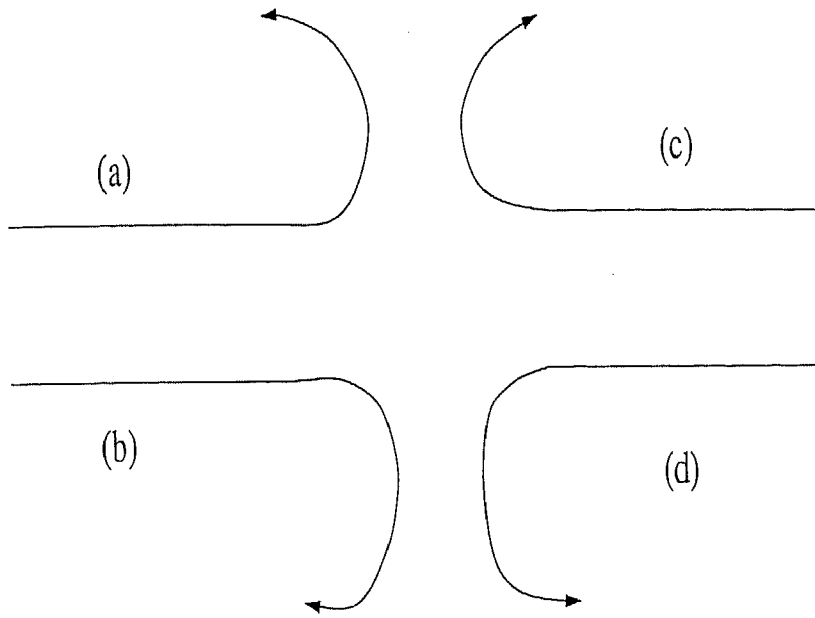


Figure 4.12: Four possible turning options for fringes.

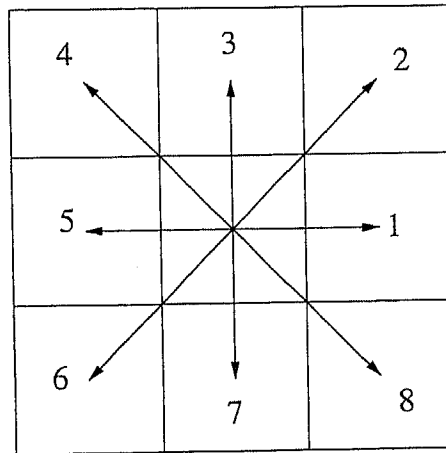


Figure 4.13: Eight possible directions for movement.

minimum intensity sums are accepted as the minimum intensity directions within a fringe band. One of these is the previous direction already identified. Hence the new direction is the one along which the fringe curve has to be extended. In practice the two intensity sums may not be identical since the average intensity level of the image is not constant. Any given pixel will be connected to two neighbouring pixels in a thinned image. Hence the past direction of movement has to be preserved to decide the future connecting points. Because of residual noise present in the image, it is likely that a pixel may show two new directions in addition to its last movement. In such a case the sum of intensities that is closer to the previous direction is ignored and the second direction is accepted as the direction for the next movement.

The above algorithm can produce loops if precautions are not taken. If a fringe is in the forward tracing mode and the special turning condition is not supplied, the fringe is forced to move in the specified direction of (1, 2, 3, 7 and 8) and not (4, 5 and 6), the backward direction (Figure 4.13). Similarly during backward tracing, the direction (1, 2 and 8) is not allowed. If one of the directions that is not permissible during forward tracing is encountered as the final direction of movement, a loop-like structure is formed. Tracing may not be completed in some cases. To avoid the formation of loops the nearest forward direction needs to be found iteratively, till one advances to the next pixel. This is accomplished as follows. Once a reverse direction of movement is encountered, the nearest possible direction is adopted in its place. For example, if the direction of movement is 4 while the tracing is in the forward direction, the direction nearest to 4 is 3. Similarly 7 can be replaced by 6. If the direction found is 5, then both 3 and 7 are equally likely. In such a case, the most unbiased estimate to 5 is direction 1.

Reallotment of a direction as described above may result in a wrong movement. For example, the direction of movement identified may be one of the previously detected points on the thinned image. In such a case the above steps are repeated and the next closest direction is searched. If the new pixel located falls in one of the four special cases for turning, the image is rotated by 90° in the clockwise direction. Depending on one of the four cases, one may then have to move temporarily in forward or backward directions. During implementation, the code is prepared in a modular fashion to trace forward and backward fringes. Rotation of the image enables one of the modules to be used without any change in the marked areas of the fringes. The boundaries of the image, i.e. the window size are to be prescribed as an input to the computer code. On reaching the boundary, control in the computer code is transferred to the starting point so that the rest of the fringe in the opposite direction can be traced.

The algorithm used for fringe tracing is summarized below:

1. Initialize the thinned image as white (intensity 255).
2. Read the image containing the interferogram including the boundaries.
3. Read the starting point data for all the fringes to be traced in the image.
4. Specify the desired template size at the starting point.
5. Specify the initial direction of movement to the right or left.
6. Obtain the intensity sums in the eight directions and identify the two directions for which the sums are the least.
7. Start tracing in the direction of the minimum intensity. If it coincides with the previous direction, proceed along the next direction for which intensity sum is a minimum.

8. At the boundary, transfer control to starting point.
9. Start tracing in the opposite direction till the boundary is reached.
10. Assign a gray level of 0 to the traced pixels.
11. Repeat the process for all the fringes.

In the present work, the interferogram obtained in the air phase of air-water experiments in the rectangular cavity have been chosen to demonstrate the application of the fringe thinning algorithms. Figure 4.14 (a) shows the filtered and contrast improved image, while Figure 4.14 (b) shows the thinned image developed using the procedure given above.

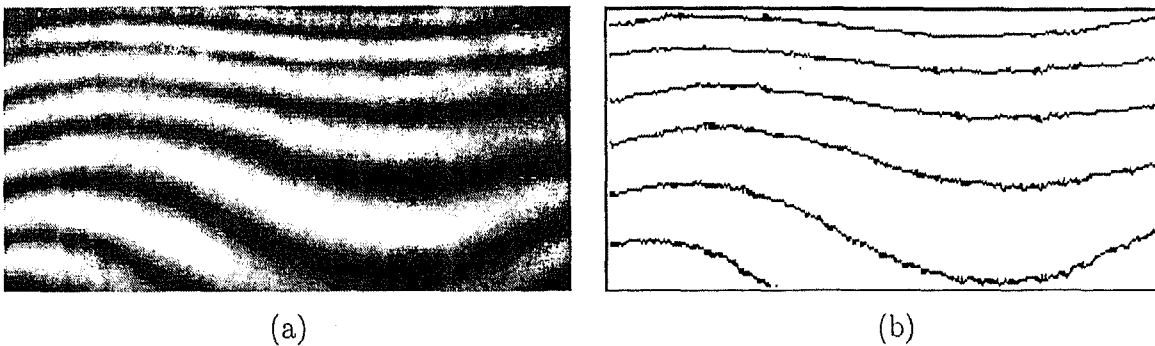


Figure 4.14: (a) Filtered and contrast improved interferogram. (b) Thinned image obtained using the automatic fringe thinning algorithm.

4.4.3.2 Paint-brush drawing

This is a free-hand drawing technique where the midpoints within a dark band of the interferogram are approximately located and joined by a smooth curve. It relies entirely on eye judgement. The paint-brush utility available in the image processing software GIMP in the linux operating system has been employed in this study. The image containing the fringe curves and the original image are subtracted to get the fringe skeleton. Interferogram of Figure 4.4 obtained in the oil phase of air-oil experiments in the axisymmetric cavity have been chosen to demonstrate the paint-brush option. Figure 4.15(a) shows the thinned image after subtracting the original image from the fringe skeleton. The superposition of the original interferogram and the fringe skeleton is shown in Figure 4.15(b). The paint-brush approach has the disadvantage of not locating the minimum intensity location. It can be advantageous under certain conditions since it does not require code development and is hence reasonably fast.

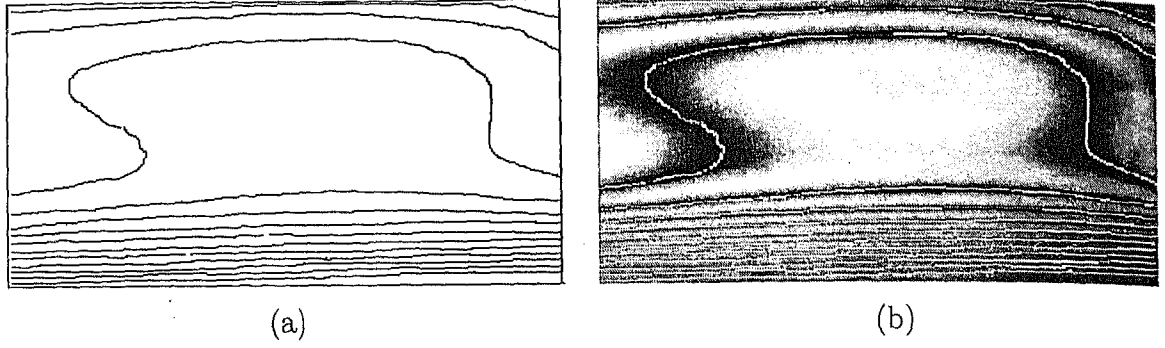


Figure 4.15: (a) Thinned image obtained by the paint-brush method. (b) Superimposed thinned image with original image.

4.5 Local and global heat transfer rates

Heat transfer rates at the top and bottom walls of the cavity have been reported in the present study in terms of the Nusselt number. It is defined as

$$\text{Nu} = \frac{-\tilde{H}}{T_{hot} - T_{cold}} \frac{\partial T}{\partial y} \bigg|_{y=0, \tilde{H}} \quad (4.25)$$

Here, \tilde{H} represents the layer height of the individual fluid layers. The derivative has been calculated by a one-sided, second order finite difference formula using the thinned fringes of the interferogram. This procedure is discussed in Section 4.2 of the present chapter. For calculating the Nusselt number at the cold top wall (fluid 1), T_{hot} is replaced by T_I , the interface temperature in Equation 4.25. Similarly, for the hot wall (fluid 2), T_{cold} is the interface temperature T_I for the estimation of Nusselt number. Thus the distribution of the local Nusselt number at the hot and cold walls can be calculated using Equation 4.25 in the superposed fluid layers. This distribution is along the width of the cavity i.e. the x -direction of the co-ordinate system. The average Nusselt number for the entire surface of the hot and the cold plates can be computed from the local Nusselt number by numerical integration. The average Nusselt number can also be obtained from the width-averaged temperature profile of the projection data. Here the slope of the temperature profile at bounding planes corresponds to the average Nusselt number. In the present work, the average Nusselt number at the two surfaces have been reported in the cavities of rectangular and axisymmetric test-cell. The projection data obtained in the rectangular cavity includes the entire width of the cavity since the beam diameter (72 mm) is larger than the cavity width (32.1 mm). In the axisymmetric test-cell, the angular projections at each view angle donot contain the entire width of the cavity. It

is however expected that the average Nusselt number over the partial length will be representative of the entire width of the cavity.

In the present work on superposed fluid layers, the average Nusselt number for each of the plates has been compared with the experimental correlation reported by Gebhart *et al.* (1988). The correlation is based on independently conducted experiments on a single fluid in a horizontal differentially heated cavity. It has a large uncertainty band of around $\pm 20\%$. Differences are to be expected with reference to the present study since the correlations are based on a single fluid layer, where the top and bottom boundaries are rigid no-slip walls, while in the two-fluid configuration, one of the boundaries is a fluid interface. The single fluid correlations of Gebhart *et al.* (1988) for average Nusselt number employed in the present work are summarized below.

For air, the correlation is given by:

$$\text{Nu (air)} = 1 + 1.44 \left[1 - \frac{1708}{\text{Ra}} \right] + \left[\left(\frac{\text{Ra}}{5830} \right)^{1/3} - 1 \right], \text{Ra} < 10^6 \quad (4.26)$$

where the square bracketed terms are set to zero if they are negative.

For water, the correlation is given by:

$$\begin{aligned} \text{Nu (water)} = 1 + 1.44 \left[1 - \frac{1708}{\text{Ra}} \right] + \left[\left(\frac{\text{Ra}}{5830} \right)^{1/3} - 1 \right] \\ + 2 \frac{\text{Ra}^{1/3}}{140} \left[1 - \ln \frac{\text{Ra}^{1/3}}{140} \right], \text{Ra} < 10^6 \end{aligned} \quad (4.27)$$

For silicone oil, the correlation of large Prandtl number fluids namely

$$\text{Nu (silicone oil)} = 0.089 \text{Ra}^{1/3} \quad (\text{Pr} \gg 1, \text{Ra} < 10^9) \quad (4.28)$$

has been selected. Once again, the square bracketed terms of Equation 4.27 are taken to be zero if they have negative values. The additional term for water suggested by Gebhart *et al.* (1988) is due to the appearance of thermals⁸. For $\text{Ra} \leq 1708$, the heat transfer across the fluid layers occurs by conduction and $\text{Nu}=1$. When applied to superimposed fluid layers, Rayleigh numbers in Equations 4.26-4.28 have been based on the temperature difference between the interface and the nearest solid boundary. Though the interface is not an isotherm, the temperature variation over most part of it was found to be smaller than 0.02 K, and hence negligible. Larger variation in the interface temperature was noticed adjacent to the side walls.

⁸Intermittent plumes rising from a heated surface are called *thermals*.

4.6 Interface temperature from correlations

The principle of conservation of energy can be applied for estimating the average interface temperature at steady state. With reference to Figure 4.3, we have

$$\begin{aligned} \text{heat conducted from bottom plate} &= \text{heat transfer by convection in fluid 2} \\ &= \text{heat transfer by convection in fluid 1} \\ &= \text{heat conducted to top plate} \end{aligned}$$

The thicknesses of the top and bottom surfaces are small and the material conductivities are quite high. Hence significant temperature gradients occur only in the fluid media. Using the simplified result we get:

$$\text{heat transfer by convection in fluid 2} = \text{heat transfer by convection in fluid 1}$$

$$h_2(T_h - T_I)A = h_1(T_I - T_c)A \quad (4.29)$$

where

$$h_1 = \frac{\text{Nu}_1 k_1}{d_1} \quad (4.30)$$

and

$$h_2 = \frac{\text{Nu}_2 k_2}{d_2} \quad (4.31)$$

Here d_1 and d_2 are the characteristic dimensions of the fluid layers, namely their heights in the present calculation. In the case of cavity filled with fluid of equal layer heights, their characteristic dimensions are equal ($d_1 = d_2$). In general, the energy balance equation can be expressed as:

$$\frac{\text{Nu}_2 k_2 (T_h - T_I)}{fH} = \frac{\text{Nu}_1 k_1 (T_I - T_c)}{(1-f)H} \quad (4.32)$$

Here, H is the total cavity height and f is the fraction of the layer height of fluid 2 with respect to total cavity height. The average Nusselt number in the Equation 4.32 can be substituted by the correlations given by Gebhart *et al.* (1988), Equations 4.26-4.28. For combinations of fluid such as air (fluid 1) and water (fluid 2), Equations 4.26 and 4.27 can respectively be applied on left and right hand sides of Equation 4.32. The properties of fluids 1 and 2 have been evaluated at the average fluid temperature in the Nusselt number correlations. For a given cavity height and wall temperatures, one can calculate all the properties of the fluids, using a quadratic expression of the form

$$y = a_0 + a_1 T + a_2 T^2 \quad (4.33)$$

at the average fluid temperature⁹. The interface temperature can be computed from Equation 4.32 using the following algorithm:

⁹Values of the coefficients a_0 , a_1 and a_2 for water and air are summarized in Table 4.3. For oil, the properties are assumed to be constant for the temperature range selected in the experiments.

1. Assume the interface temperature to be a value between T_c and T_h .
2. Compute the respective fluid properties, layer Rayleigh number and the layer Nusselt number.
3. Estimate the interface temperature from Equation 4.32.
4. Repeat steps 2 and 3 till convergence is attained in the interface temperature.

Table 4.3: Values of constants for fluid properties of water and air.

Fluid Properties	Water			Air		
	a_0	a_1	a_2	a_0	a_1	a_2
ρ	994.02	-3.3630e-01	-0.3954e-02	1.167	-0.3901e-02	1.2943e-05
c_p	4.177	-0.1588e-03	1.7957E-05	1.006	3.8435e-05	1.6452e-06
μ	7.1e-04	-1.5678e-05	2.2898e-07	18.575	0.4721e-01	-2.7708e-05
K	0.625	0.1348e-02	-9.8594e-06	26.43	0.7746e-01	-5.2806e-05
β	3.4e-04	8.7521e-06	-4.8548e-08	3.4e-03	-5.52e-06	2.31e-08

4.7 Calculation of interface shape

The geometrical shape of a fluid-fluid interface, its movement, and the static or dynamic state of the contiguous bulk phases bounding it are each strongly dependent upon steep, fine-scale inhomogeneties in volumetric physical properties prevailing across the transition zone between the bulk phases (Edwards *et al.*, 1991). The volumetric inhomogeneties include for example, nonuniformities in the overall mass density of the fluid, species mass density, and shear viscosity fields, each rapidly varying in a direction normal to the macroscopic interface. The consequences of large physical property gradients are dramatically illustrated by the example of a rapidly varying pressure field across a strongly curved interface. This microscopic pressure differences relate to the short-range, attractive forces within the interfacial zone. These are finally responsible at the coarser, scale, for the existence of a tensional force at the interface. Contrasting deformation of the interface by surface tension and buoyancy are depicted in Figures 4.16-4.19.

Consider a horizontal liquid layer resting upon a solid surface that is heated relative to the film temperature. After a sufficient time, a steady-state is achieved wherein a temperature gradient is established across the thickness of the liquid film (Figure 4.16). A mechanical disturbance or thermal fluctuations results in a small disturbance in velocity and temperature fields in the vicinity of the interface. Inhomogeneties in surface

temperature cause a variation of interfacial tension. The resulting interfacial tension gradients cause fluid flow at the interface and the adjacent liquid layer. Consequently,

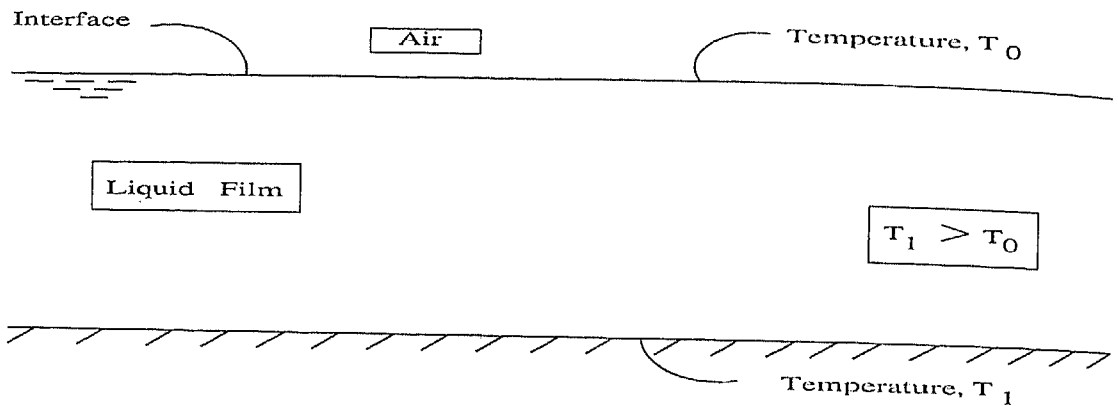


Figure 4.16: A thin liquid film rests upon a heated solid surface.

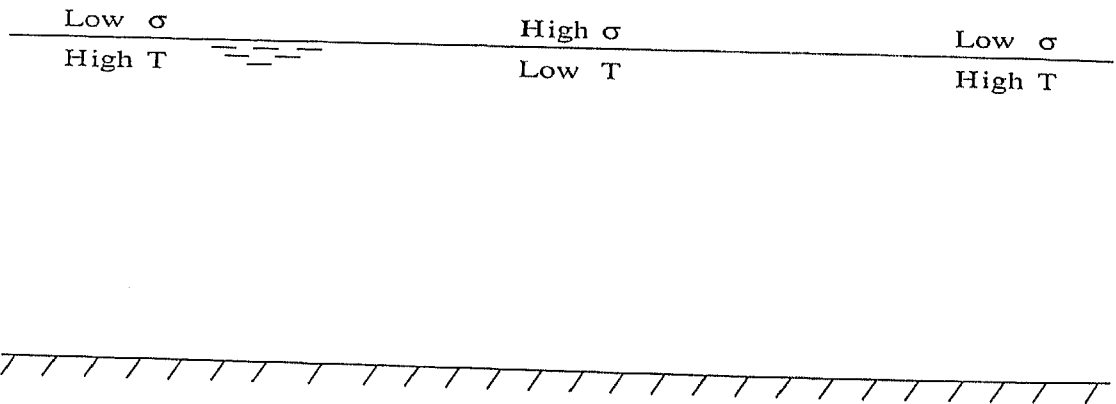


Figure 4.17: Thermal fluctuations occur within the film, resulting in temperature inhomogeneities along the interface.

the liquid from areas of low interfacial tension are carried to those of high tension (Figure 4.17). Circulatory convection patterns are thereby created within the film, with liquid rising towards depressed areas of low tension and away from the raised areas of high tension (Figure 4.18). This is an example of Marangoni-driven instability (Edwards *et al.*, 1991). Cellular convection patterns can also be created in the bulk fluid, where the liquid rises towards centers of high elevation and descends away from the centers of depressed regions (Figure 4.19). This pattern is characteristic of buoyancy-driven instability in the fluid layer (Edwards *et al.*, 1991).

In the present work, an order-of-magnitude analysis revealed Marangoni effects to be only of secondary importance in comparison to buoyancy for the dimensions employed in the apparatus (Johnson *et al.*, 1999). Marangoni number can be calculated at the free

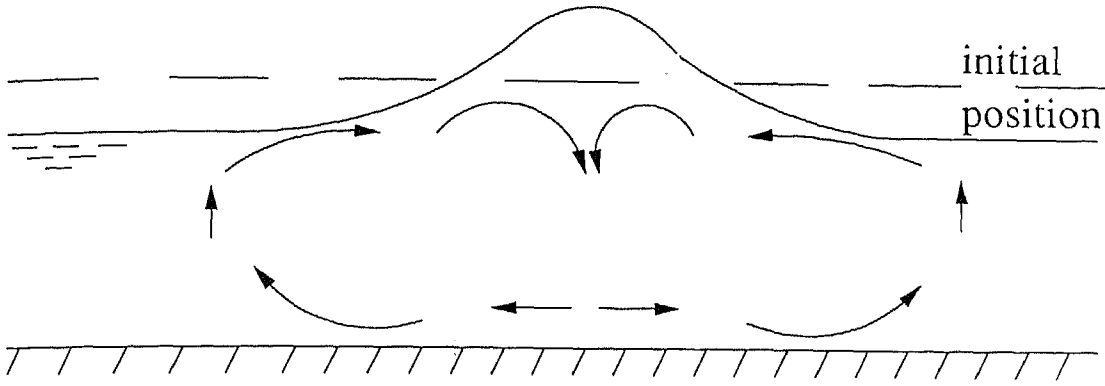


Figure 4.18: The interfacial tension gradients drive flow in the bulk liquid phase, creating cellular convection patterns.

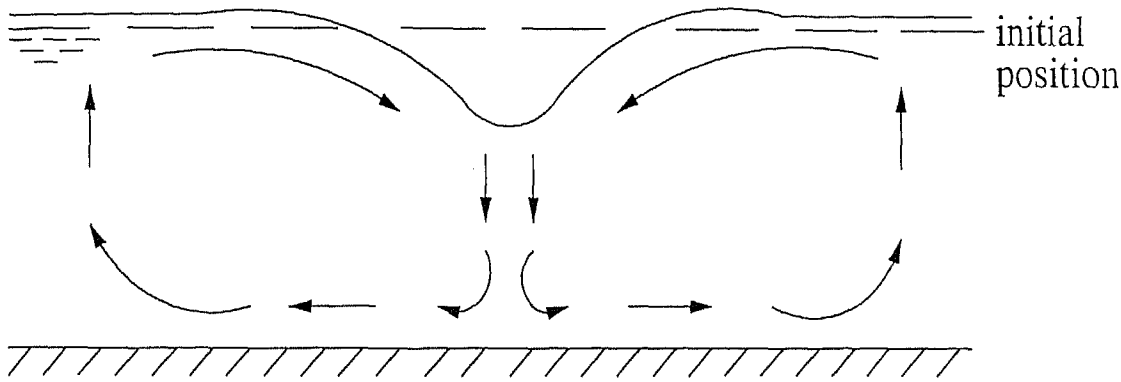


Figure 4.19: The buoyancy driven instabilities generates flow in the bulk liquid phase, creating cellular convection patterns.

surface of air-water as:

$$\text{Ma} = \frac{\sigma_T \Delta T d}{\mu \alpha} \quad (4.34)$$

Here, ΔT is the temperature scale considered at the interface of the fluid layers. The temperature scale used to calculate the Marangoni number is given by Shyy *et al.* (1996) as:

$$\Delta T = 0.1 \times \frac{q_{max}}{k} d \quad (4.35)$$

where q_{max} is the maximum value of the heat flux specified on the boundary, k is the thermal conductivity of water and d is the characteristic length scale representative of the meniscus. In the air-water experiments at $\Delta T = 18$ K, the values obtained for q_{max} , k and d were 63 W/m^2 , 0.6251 W/m-K and $6.14 \times 10^{-5} \text{ m}$ respectively¹⁰. These yield a value of $\Delta T = 0.036 \text{ K}$ from Equation 4.35. Based on the properties of water, the Marangoni number can thus be calculated from Equation 4.34 to be 3.6. This is quite a

¹⁰The calculation of the shape of the meniscus is discussed in Appendix B.

small value when compared to the critical Marangoni number of 79.60 needed to initiate convection (Dauby and Lebon, 1996).

Small values of the Marangoni number were seen for other combinations of fluid layers as well. Marangoni convection can thus be neglected because of a negligible temperature gradient established at the interface for the fluids selected, the large fluid layer heights, that make buoyancy a dominant mechanism and large cavity widths, that diminish the surface curvature. It was observed in the present work that the depressed region of interface was correlated with a positive downward velocity and the elevated regions with a positive upward velocity. The dominance of buoyancy-driven convection was confirmed by correlating the orientation of the roll patterns in the interferogram with the deformed interface shape.

4.8 Benchmarking

The proposed experiments on superposed fluid layers such as air and water can be benchmarked by individually examining convection in the cavity filled with air and water. The present section discusses the experiments performed with a single fluid confined in a rectangular cavity of square cross-section. The results obtained in the form of an interferogram have been processed to quantitatively evaluate the temperature distribution in the flow field and the heat transfer rates at the two walls in terms of the Nusselt number. The experimental values have been compared with the correlations of Gebhart *et al.* (1988) applicable for a single fluid confined in a cavity. Temperature contours at three different planes along the width of the cavity have been reported. The experimentally obtained interferograms have been compared Qualitatively with the numerically generated thermal field in Appendix B of the present thesis.

4.8.1 Convection in a cavity filled with air

The convection patterns in the square cavity of Figure 3.1 with air are shown in Figure 4.20(a). In this experiment, the top surface temperature is kept at 16°C and the lower surface temperature is 26°C. Thus the temperature difference of 10 K is maintained across the cavity. This leads to a Rayleigh number of 34,200 in air. In a two dimensional field, the fringes are isotherms; even otherwise they represent the nature of thermal field in the cavity. The spacing among the fringes near the wall are seen to be small compared to the mid-plane of the cavity. The spacing gradually increases towards the fringe edges.

Since each fringe is an isotherm, a small fringe spacing gives rise to a large local heat flux. The largest local heat flux at the cavity walls at steady state occurs around the mid-plane of the cavity. From Figure 4.20(a) it is clear that the isotherm spacings near the top and bottom walls of the cavity are less than the spacing in the central region of the test section. This is related to the fact that near the boundaries, diffusive heat transfer rates and hence the temperature gradients are higher. In the central region of the test section, conduction heat transfer is practically absent and the dominant mode of transport is advection.

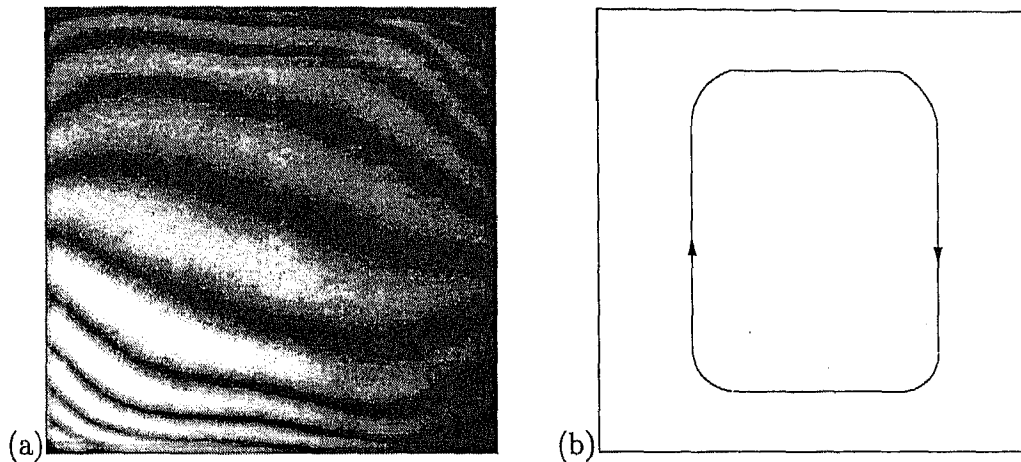


Figure 4.20: Long-time isotherms (a) and the corresponding roll patterns (b) in a cavity filled with air; cavity temperature difference is 10 K.

Flow develops in air in the form of a unicellular roll as shown in Figure 4.20(b). The fluid accelerates on one side of the mid-plane, reaches a maximum at this point and decelerates to small values on the other side of the cavity, as it approaches the side walls. The overall flow pattern in the cavity is hence unicellular with sense of rotation in the clockwise direction. The roll pattern in Figure 4.20(b) represents a velocity field that has resulted from the density gradient established in the fluid layer.

Figure 4.21 shows the transient evolution of the thermal field in the cavity till steady state is reached. The interferograms were collected at regular intervals of 30 minutes till steady state was reached. Since the cavity is small, the times required for the temperature of the walls to become constant and the flow to reach steady state are small. For early time (of less than an hour) the wall temperatures had not stabilized and the corresponding fringe patterns have not been shown. With the passage of time, the number of fringes increases till steady state is reached. Once the flow field is fully evolved, the fringe patterns were observed to be quite steady without any sideways

movements of the fringes. The movement of fringes was observed for higher Rayleigh numbers. Figures 4.21(d-f) show the truly steady state nature of the flow field. The number of fringes in the present experiment ($= 8$) are close to that estimated by the formula $N = (T_h - T_c)/\Delta T_c$.

The steady state variation of temperature is plotted as a function of the vertical distance in Figure 4.22(a) for three equally spaced columns along the width of the cavity. The columns chosen are $x/W = 0.33, 0.50$ and 0.67 respectively measured from the left side of an interferogram. Figure 4.22(a) actually shows the variation of the line integrals of the temperature field averaged over a horizontal plane as a function of the vertical coordinate. The line integrals are simply the temperatures as computed from the interferograms. Here, the abscissa is the non-dimensional temperature $\theta = (T - T_c)/(T_h - T_c)$, while the ordinate is the dimensionless distance y/H . Here $y/H=0$ represents the hot bottom wall and $y/H=1$ is the cold top wall. The slopes of the curves at the top and the bottom walls are practically equal. It shows the formation of a thermal boundary-layer of constant thickness in the mid-region of the cavity.

Based on the temperature profiles of Figure 4.22(a), the local heat transfer rates can be calculated at the hot and the cold walls. Heat transfer rates as represented by local Nusselt number can be obtained using Equation 4.25. Figure 4.22(b) shows the variation of local Nusselt number at the top and the bottom walls of the cavity. Here the x -coordinate is non-dimensionalised in terms of the width of the cavity as x/W . An important conclusion to emerge from Figure 4.22(b) is that the energy balance check is closely realized at the hot and the cold walls. The width-averaged Nusselt number at the respective walls can be obtained through numerical integration of the local values. The individual plate-averaged Nusselt numbers in air are 3.18 and 3.12 at the cold and the hot surfaces respectively of the cavity. This gives an experimental cavity averaged Nusselt number to be 3.15 in air. The cavity averaged Nusselt number has also been compared with the correlation given by Gebhart *et al.* (1988), Equation 4.26. The value of average Nusselt number as calculated from Equation 4.26 is 3.17 for this case. The comparison between the present experiments and the published correlation is thus seen to be quite good.

Convection in air as a function of Rayleigh numbers have been shown in Figures 4.23(a-c). Temperature differences imposed across the cavity are 2, 4 and 7 K respectively. The corresponding Rayleigh numbers were 6380, 12,900 and 23,300. The images obtained were quite steady.

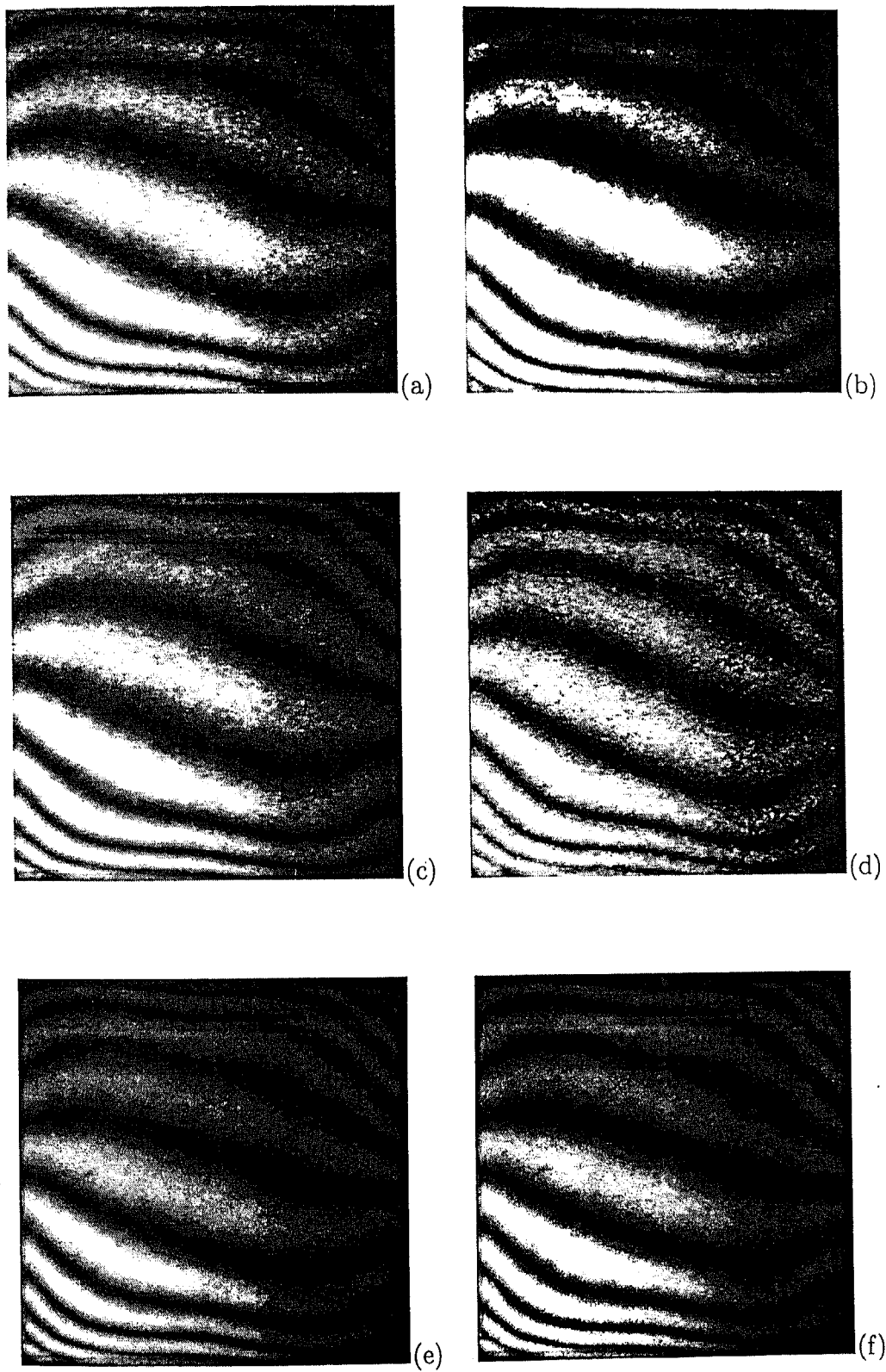


Figure 4.21: Transient evolution patterns in air for a cavity temperature difference of 10 K; time interval between two successive interferograms is 30 minutes.

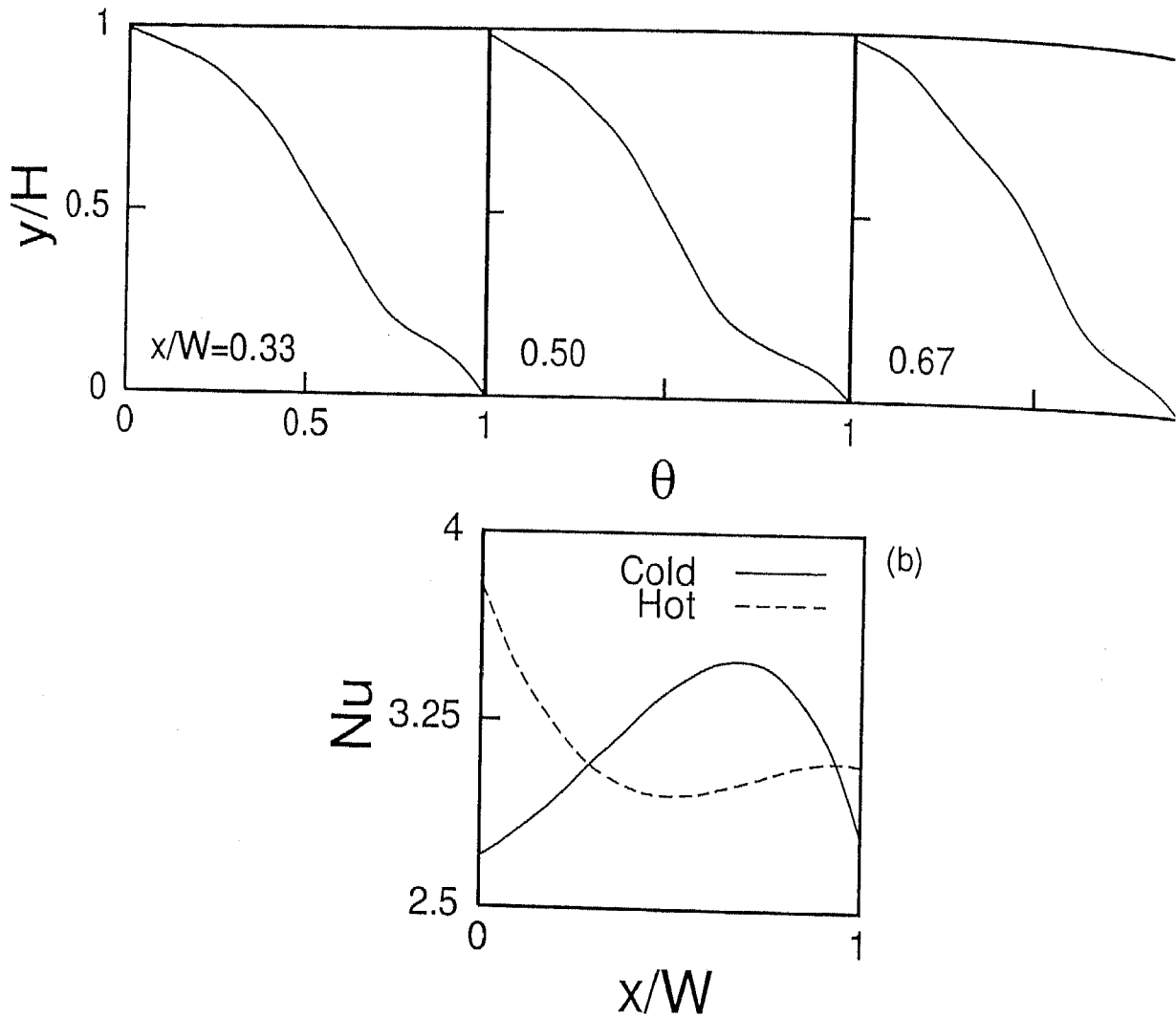


Figure 4.22: (a) Temperature profiles at three columns along the width of the cavity and (b) local Nusselt number variation at the two walls for a cavity filled with air; Cavity temperature difference is 10 K.

4.8.2 Convection in a cavity filled with water

Experiments in the cavity filled with water are reported in the present section. The hot and the cold walls of the cavity were maintained at 16 and 26°C respectively, the effective temperature difference is 10 K. To get meaningful fringe patterns, it was found necessary to fill the reference chamber also with water. The Rayleigh number for the present experiment was calculated to be $1.7E+06$. Interferograms were recorded at various time instants, but no clear steady state was to be seen. This is understandable because the Rayleigh number for the present experiment stretches well into the turbulent regime. Keeping in mind the low sensitivity of refractive index of water to temperature,

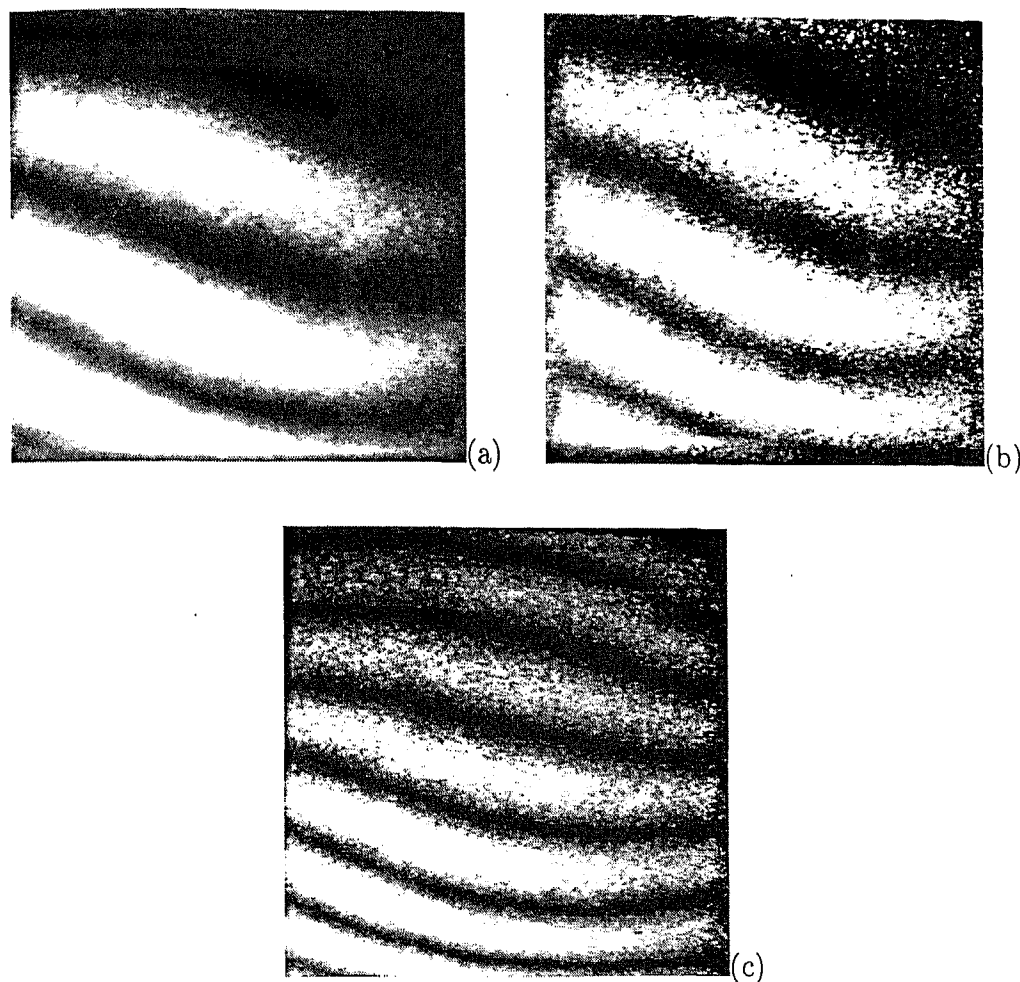


Figure 4.23: Steady state interferograms in a cavity filled with air; cavity based temperature differences are (a) 2 K, (b) 4 K, and (c) 7 K.

one can anticipate a large number of fringes in water. Since the Rayleigh number is extremely high, the fringe patterns were seen to change rapidly. The long-time images of Figure 4.24 show that the flow is in the three-dimensional turbulence zone. In the present experiment, it was not possible to clearly identify the near wall fringes. Therefore, the local and hence the average wall heat transfer rates could not be calculated. Continuous fringes however could be seen in the middle of the test cell. A comparison in terms of the heat transfer rates is not possible between experiments and the correlations due to the absence of steady state in the water-filled cavity.

The transient evolution of the fringe patterns depicting high turbulence in water was captured in a time interval of 5 seconds. These are shown in Figures 4.25(a-d). The recording of interferograms was started once the two walls of the cavity were thermally stabilized in around two hours. The experiments continued for another 4 hours to explore the possibility of a stable structure, but no such result was obtained.

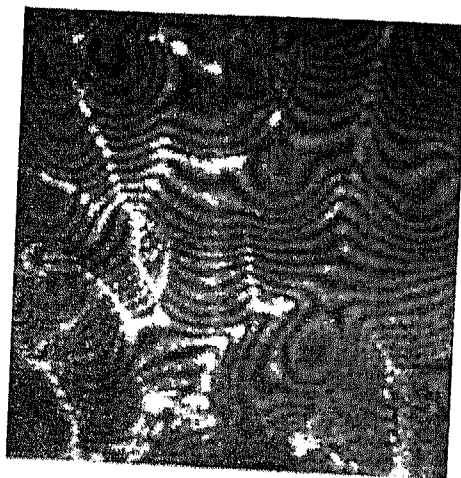


Figure 4.24: Long-time interferogram obtained for a cavity filled with water; cavity temperature difference is 10 K.

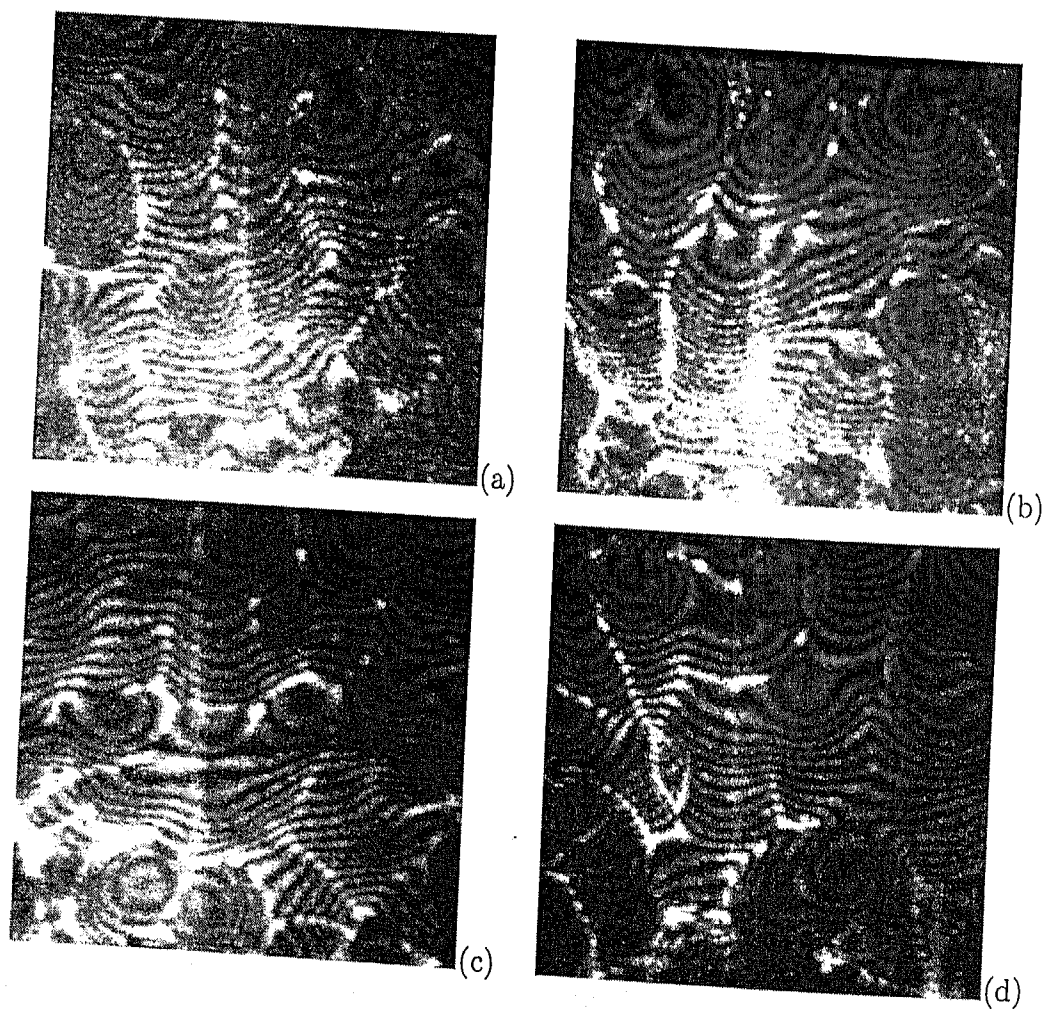


Figure 4.25: Transient evolution of fringe patterns in water for a cavity temperature difference of 10 K; time interval between two successive interferograms is 5 seconds.

The long-lived interferograms in water for two cavity based temperature differences of 1.4 and 5.3 K are shown in Figures 4.26(a-b) respectively. The corresponding Rayleigh numbers obtained were 2.67×10^5 and 9.24×10^5 . An increase in the Rayleigh number led the flow to become highly unsteady.

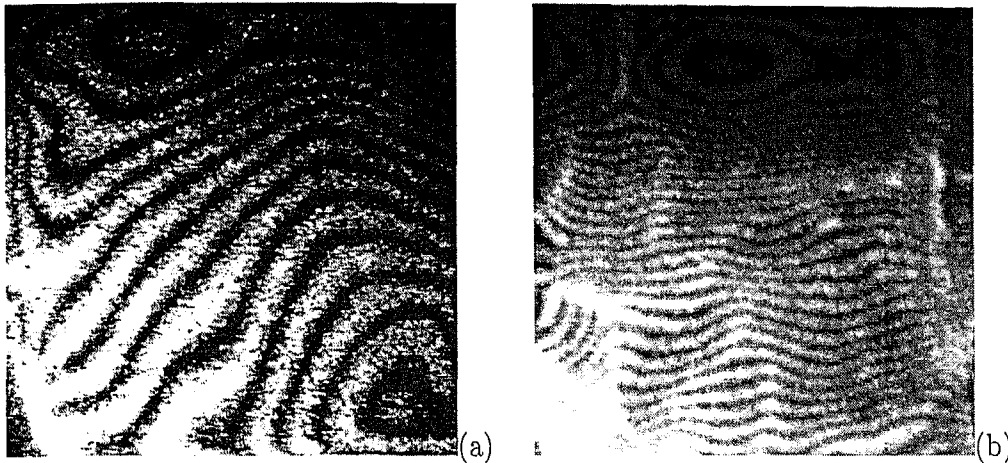


Figure 4.26: Long-time interferograms in a cavity filled with water; cavity based temperature differences are (a) 1.4 K and (b) 5.3 K.

4.9 Tomography

The three dimensional temperature field can be reconstructed from its interferometric projections using principles of tomography. Tomography is the process of recovery of a function from a set of its line integrals evaluated along some well-defined directions. In interferometry, the source of light (the laser) and the detector (CCD camera) lie on a straight line with a test-cell in between. Further a parallel beam of light is used. This configuration is called *transmission* tomography in a *parallel beam* geometry (Herman, 1980). Tomographic algorithms used in interferometry reconstruct two dimensional fields from their one dimensional projections. Reconstruction is then applied sequentially from one plane to the next till the third dimension is filled.

Tomography can be classified into: (a) transform (b) series expansion and (c) optimization methods. Transform methods generally require a large number of projections for a meaningful answer (Lewitt, 1983). In practice, projections can be recorded either by turning the experimental set up or the source-detector combination. In interferometry, the latter is particularly difficult and more so with the Mach-Zehnder configuration. With the first option, it is not possible to record a large number of projections, partly owing to inconvenience and partly due to time and cost. The limited projection data

available from interferometry can however be suitably increased for implementing the transform method for reconstruction. Limited-view tomography is best accomplished using the series expansion method (Censor, 1983). With limited data, the reconstruction will not yield a unique solution, and the algorithms are expected to be sensitive to the initial guess of the field that starts the iterations. Optimization-based algorithms are known to be independent of initial guess, but the choice of the optimization functional plays an important role in the result obtained. Depending on the mathematical definition used, the entropy extremization route may yield good results, while the energy minimization principle may be suitable in other applications.

In measurements involving commercial grade optical components and recording and digitizing elements, the projection data is invariably superimposed with noise. Software operations such as interpolation and image processing can also contribute to errors in the projection data. Experience of Mishra *et al.* (1998) with interferometric experiments shows that the RMS noise level of greater than 5% can result in unphysical artifacts in the solution, if iterative methods are used.

In the present work, the transform method is adopted for reconstruction of three-dimensional temperature field in an axisymmetric cavity. Convolution back projection (CBP) has been chosen as the tomographic algorithm in view of its established convergence properties. In situations when measurements for numerous projections over the total viewing angle of 180° are possible, the backprojection method is recommended. These methods are usually faster to compute and require less computer memory than the those using series expansion (Mayinger, 1994).

With the present experimental setup, only four views were possible for generating the projection data. These are namely 0° , 45° , 90° and 135° . The projection data obtained at a view angle of 180° (fifth view) is identical to that of the 0° view angle. For each view angle, the size of the light beam covered 41% of the full width of the fluid layer in the cavity. This corresponds to a partial projection data that is captured in the central portion of the cavity.

In tomography, the projection data required for reconstruction should be available for the full width of the flow field from each view angle rather than the partial width. This means that the light beam should scan the thermal field covering the entire width of the cavity for all view angles. In the present experimental configuration, it was not possible to scan the full width owing to the laser beam diameter (72 mm) being less than the total nominal diameter (130.65 mm) of the cavity. To overcome this limitation, the projection data was increased by applying a suitable interpolation and extrapolation

schemes. In these schemes, the number of view angles was increased from 5 to 81 by linearly interpolating the experimental data available for the central portion¹¹ of the cavity. The obtained interpolated data still covers the partial width of the fluid layer. In order to scan the full width of the thermal field, a suitable extrapolation procedure was adopted. This extrapolation scheme was implemented with reference to a circle that closely approximates the shape of the axisymmetric test cell. For a circular geometry, the chord length of integration diminishes from the diameter of the circle at the center to zero at its edges. Thus, the sensitivity of the interferometric measurement is at its highest closer to the center, as compared to the sides. The drop in sensitivity is seen in the form of a drastic reduction in the number of fringes. Inverting this data to recover temperature is mathematically inappropriate. Tomographic algorithms such as CBP require projection data for the complete width of the fluid layer. The extrapolation procedure adopted in the present work comprises of assuming the temperature field to be spatially uniform outside the central core of 41%. Allowances for the change in the chord length are however included. This procedure is not expected to affect the quality of the original partial projection data obtained directly from the experiments.

The projection data for each view angle should be consistent in terms of the average fluid temperature over a given plane of the fluid layer. In other words, the average temperature is constant for a given plane irrespective of the view angles. This check was enforced in the line integral data before reconstruction.

The salient features of the CBP algorithm for reconstruction, as discussed by Herman (1980) and Muralidhar (2002) in a review article has been presented in the following section.

4.9.1 Convolution backprojection

The convolution backprojection (CBP) algorithm for three-dimensional reconstruction classifies as a transform technique. It has been used for medical imaging of the human brain over the past few decades. Significant advantages of this method include (a) its noniterative character, (b) availability of analytical results on convergence of the solution with respect to the projection data, and (c) established error estimates. A disadvantage to be noted is the large number of projections normally required for good accuracy¹². In engineering applications, this translates to costly experimentation, and nonviability of

¹¹This step does not increase the information content of the projections.

¹²It is clear that CBP is not the most suitable algorithm for data inversion of the present work. Iterative techniques such as ART will be explored in the future.

recording data in unsteady experiments. The use of CBP continues to be seen in steady flow experiments, particularly when the region to mapped is physically small in size. The statement of the CBP algorithm is presented below.

Following Munshi (1997), let the path integral equation be written as

$$p(s, \theta) = \int_C f(r, \phi) dz \quad (4.36)$$

where p is the projection data recorded in the experiments and f is the unknown function to be determined by inverting the above equation. In practice, the function f is a field variable such as density, void fraction, attenuation coefficient, refractive index, or temperature. The symbols s , θ , r , and ϕ stand for the ray position, view angle, position within the object to be reconstructed, and the polar angle, respectively (Figure 4.27). The integration is performed with respect to the independent variable z along the chord C of the ray defined by s and θ . Following Herman (1980), the *projection slice theorem* can be employed in the form

$$\bar{p}(R, \theta) = \bar{f}(R \cos(\theta), R \sin(\theta)) \quad (4.37)$$

where the overbar indicates the Fourier transform and R is the spatial frequency. The frequency R is the Fourier counterpart of the distance s . The use of the symbol R follows from the literature on medical imaging. In words, the projection slice theorem states the equivalence of the one-dimensional Fourier transform of $p(s, \theta)$ with respect to s and the two-dimensional Fourier transform of $f(r, \phi)$ with respect to r and ϕ . A two-dimensional Fourier transform of this theorem leads to the well known Radon transform

$$f(r, \phi) = \int_0^\pi \int_{-\infty}^{\infty} \bar{p}(R, \theta) \exp(i2\pi R r \cos(\theta - \phi)) |R| dR d\theta \quad (4.38)$$

where

$$\bar{p}(R, \theta) = \int_{-\infty}^{\infty} p(s, \theta) \exp(-i2\pi R s) ds \quad (4.39)$$

The first integral in the form given is divergent with respect to the spatial frequency R . Practical implementation of the formula replaces $|R|$ by $W(R)|R|$, where W is a window function that vanishes outside the interval $[-R_c, R_c]$. The cut-off frequency R_c can be shown to be inversely related to the ray-spacing for a consistent numerical calculation of

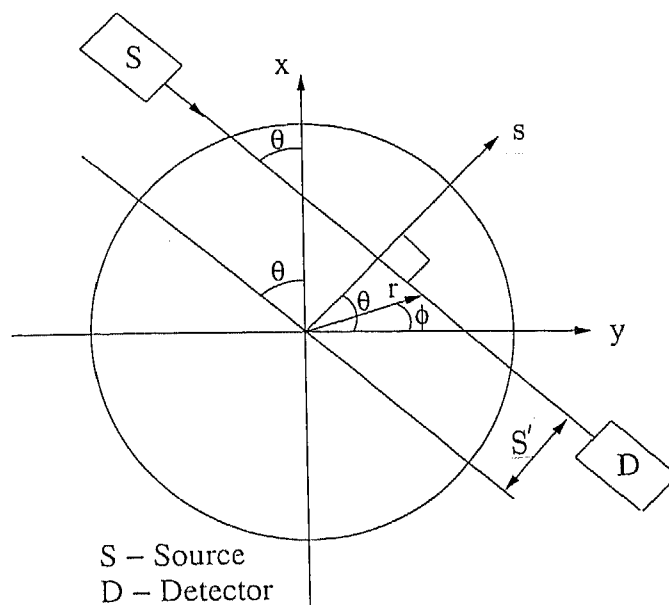


Figure 4.27: Nomenclature for the convolution backprojection algorithm.

the integral. When the filter is purely of the band-pass type, the Radon formula can be cast as a convolution integral (Ramachandran *et al* (1970)):

$$f(r, \phi) = \int_0^\pi \int_{-\infty}^{\infty} p(s, \theta) q(s' - s) ds d\theta \quad (4.40)$$

where

$$q(s) = \int_{-\infty}^{\infty} |R| W(R) \exp(i2\pi Rs) dR \quad (4.41)$$

and

$$s' = r \cos(\theta - \phi) \quad (4.42)$$

The inner integral over s is a one-dimensional convolution and the outer integral, an averaging operation over θ is called *back projection*. CBP method is also known as the filtered back projection algorithm because of the filtering of the Fourier transform of the projection data, \bar{p} by the window (or filter) $W(R)$, Equation 4.41. The function $q(s)$, known as the convolving function, is evaluated once and stored for repeated use for different views (or different angles). This implementation of the convolution backprojection algorithm is commonly used in medical imaging.

In a practical implementation of the CBP algorithm, the function $q(s)$ is determined in advance by numerical integration. Equation 4.40 is subsequently evaluated (once again by numerical integration) with $p(s, \theta)$ replaced by \bar{T}_{ij} , the depth-averaged temperature as a function of the ray number i and view angle j . In the present study, both i and j vary from 1 to 81. The reconstruction T_{kl} is then available for the local temperature on a $k \times l$ grid spread over a square enclosing the circular cavity (Singh *et al.*, 2002).

4.10 Uncertainty and measurement errors

Errors in the experimental data are associated with misalignment of the apparatus with respect to the light beam, image processing operations including filtering, thinning and assigning temperature of fringes. All experiments were conducted several times to establish the repeatability of the fringe patterns. In the event of mild unsteadiness, the dominant pattern that prevailed for the longest duration was recorded. Errors related to refraction effects in case of water and specifically in silicone oil was found to be high and affected the interface location.

Careful measures have been adopted to reduce the uncertainty involved in the experiments. Parallelism of the two opposite pairs of the optical windows for flow visualization was the issue related to the quality of the infinite fringe setting of the interferometer. To achieve high parallelism, the horizontal and the vertical side walls that form the cavity were fabricated with a flatness of around $50 \mu\text{m}$. A reference template of the required cross-section was fabricated to check the constancy of the dimensions achieved throughout the length of the test cell. After assembly the rectangular cavity height was uniform to within $\pm 1 \text{ mm}$ over a length of 447 mm . The similar procedure was adopted in forming the reference cell placed in the compensation chamber of the interferometer. The overall configuration was quite parallel and was confirmed by the quality of infinite fringe setting during the experiments.

Constancy of temperature on the two horizontal walls is a source of error in the experiments. Measures have been taken to maintain the two walls at their respective temperatures to within $\pm 0.1^\circ\text{C}$ during the experiments. The hot and the cold surfaces have been maintained at uniform temperatures by circulating a large volume of water from constant temperature baths. For the lower tank, tortuous path was created by installing baffles in the path of water. Due to increased interfacial contact area, the heat transfer was enhanced. Thus the distribution of temperature over the plate was uniform.

Uncertainty in recording fringe patterns in air in the air-water experiments was high

due to the mist formation in the test cell. As the cavity was air-tight, evaporation from the water surface led to the formation of mist in the test cell. The mist was deposited over the optical window surfaces and obstructed the flow visualization of the thermal field inside the cavity. In particular, for temperature differences larger than 18 K, the mist formation was severe and the fringes could not be recorded. To reduce the mist formation at lower temperature differences, two holes of 3 mm diameter was drilled in the upper tank close to the optical windows. The holes were extended to the top wall of the cavity and were sealed during the experiments. Once the flow field stabilized after 4 hours of experimentation, the seal was removed for a short period of time (5 min) till the mist gets disbursed in the environment prevailing outside the cavity. The holes were sealed again and the stable fringes were recorded.

For single fluid experiments, the plate-averaged Nusselt number was found to be in good agreement with published correlations (Gebhart *et al.*, 1988). Here the correlations were coupled to an energy balance calculation that required the energy transferred across any horizontal plane to be a constant at steady state. Differences are to be expected with reference to the present study on superposed fluid layers. In a single fluid layer the top and bottom boundaries are rigid no-slip walls, while in the two-fluid configuration, one of the boundaries is a fluid interface. Uncertainties noticed in the experiments in rectangular and axisymmetric (nominally circular) test cells have been presented in this section.

In the rectangular cavity filled with air and water, the Nusselt number in air matched the correlation to within $\pm 5\%$ and in water it was within $\pm 17\%$. The differences are higher in water as compared to air due to refraction errors and mild unsteadiness in the flow patterns. For the cavity 2/3rd filled with water at a Rayleigh number of 98,505, the variation in Nusselt number was the highest. Interface temperatures determined in the experiments were within $\pm 4\%$ for all layer heights reported in the air-water experiments. In air-oil experiments, high refraction errors were noticed in the oil layer beyond a temperature difference of 0.3 K imposed across the cavity. Nusselt number obtained in the oil at 0.3 K matched the correlation within $\pm 8\%$. Interferograms in air for the air-oil experiments were recorded for higher temperature differences of 10, 15 and 18 K. The results show the Nusselt number to be within $\pm 13\%$ for all temperature differences and layer heights, except for the case of the cavity 1/3rd filled with oil ($Ra(\text{air})=15,193$), where the uncertainty increased to 19% due to time-dependent movement of fringe patterns in air. The interface temperature matched the correlations within $\pm 5\%$ for all Rayleigh numbers. In oil-water experiments, the Nusselt number in oil and water were within $\pm 10\%$ at low Rayleigh numbers. The interface temperatures were within $\pm 3.5\%$

for all Rayleigh numbers reported. Results obtained in the present work can thus be taken to be quantitatively meaningful and are summarized in Chapter 5.

In an axisymmetric test-cell, uncertainty due to refraction errors was smaller as compared to the rectangular cavity owing to smaller geometrical path length. In air-water experiments, fringe patterns obtained in water alone could be processed for generating quantitative data. In air, the number of fringes formed were inadequate due to very high ΔT_e value of 5.65 K. Interface Nusselt number compared with the correlations based on single fluid experiments matched on the water side within $\pm 7\%$ and $\pm 12\%$ respectively at lower and higher Rayleigh numbers. The interface temperature matched the correlations within $\pm 1.5\%$ for all the Rayleigh numbers considered in the experiments. Nusselt number obtained at the hot wall for all projection angles and Rayleigh numbers were within an uncertainty band of $\pm 2\%$. In air-oil experiments, Nusselt number at the hot wall in oil and interface temperatures matched the correlations to within $\pm 5\%$ and $\pm 0.5\%$ respectively for lower Rayleigh numbers obtained in the experiments. When Rayleigh numbers are increased further, the uncertainty in measurements became quite high due to (a) unresolved high density fringe patterns by the CCD camera ($\Delta T_e = 0.012$ K) in oil and (b) high refraction errors near the hot wall. In oil-water experiments, the quantitative evaluation of fringe patterns was possible for the Rayleigh numbers of 10,955 and 48,402 in oil. At higher Rayleigh numbers, only qualitative measurements were possible due to reasons (a) and (b) cited above. In the water layer, the fringe patterns showed mild unsteadiness at a Rayleigh number of 17,266. Thus only an instantaneous measurement of Nusselt number at the hot wall was possible. The Nusselt number matched the correlations within $\pm 18\%$. Nusselt number in the oil phase at the interface region matched the correlations within $\pm 4\%$, while the interface temperatures were within $\pm 0.5\%$ at a Rayleigh number of 10,955. With an increase in Rayleigh number to 48,402, the uncertainty in measurements of Nusselt number increased to 16.5% possibly due to a few unresolved fringes near the wall. On the whole, the results obtained in an axisymmetric cavity for all view angles can be taken to be quantitatively as well as qualitatively meaningful and are presented in Chapter 6 of the present thesis.

Uncertainty can also arise due to the following edge effects:

1. While scanning the temperature field using a laser, the test beam encounters a sudden change in temperature as it enters the fluid layer. This introduces a bending in the laser due to a large temperature gradient. The same effect is expected when the beam comes out of the test cell into the ambient. The bending of laser beam due to these changes in temperature gradients at the two ends will be equal and opposite under ideal conditions.

Hence theoretically the effect is nullified. In practice this may lead to a small error in the projection data.

2. All the projections were recorded after the passage of sufficient time to avoid the thermal transients in the heated and cooled surfaces. However the time required for reaching the thermal equilibrium in the vertical insulated side walls is expected to be much larger, perhaps 10-12 hours. It is expected that the side wall heat fluxes decay rapidly within one hour. Hence, transients in the side walls do not interfere significantly with fluid motion in the cavity.

Chapter 5

Two-layer Convection in a Rectangular Cavity

Experimental data on two-layer convection in a rectangular cavity are reported in the present chapter. The cavity has a square cross-section in the vertical plane and the cavity aspect ratio is 13.93 as shown in Figure 3.1. Fluid combinations considered are air-water, air-silicone oil and silicone oil-water. Layer heights of $1/3$, $1/2$ and $2/3$ with respect to the cavity height have been studied. Temperature differences of 10, 15 and 18 K were applied across the cavity, in a destabilizing configuration. A few selected experiments with an additional temperature difference of 0.3 K were also conducted. Thus a wide range of Rayleigh numbers in the individual fluid layers have been explored. The range of Rayleigh and Prandtl numbers studied are summarized in Tables 3.1-3.4 of Section 3.3.

Results have been presented with respect to the individual Rayleigh numbers of the fluid layers. The Rayleigh numbers have been calculated on the basis of the temperature difference between the nearest wall and the average interface temperature, along with the height of the fluid layer. The interface temperature can be determined from the interferograms. Alternatively, it can be estimated by applying the energy balance equation (Equation 4.32) for the individual fluid layers by calculating the average heat transfer coefficient for each of the heated surfaces. In this approach, the correlations given by Equations 4.26, 4.27 and 4.28 can be made use of. These equations are applicable only at steady state, and for cavities bounded by solid surfaces. They do not include an explicit dependence on the aspect ratio. Despite these limitations, the interface temperatures determined by the two approaches were found to be quite close and within $\pm 2\%$ of the cavity temperature difference. The Rayleigh numbers referred in the present chapter are based on the interface temperature obtained from the energy balance approach.

The experimental data obtained in the form of interferograms have been interpreted in the present chapter to understand the influence of Rayleigh number on the steady thermal field, heat transfer rates at the walls and the nature of flow coupling between the fluid layers. Results are also presented for the interface deformation with increasing temperature difference across the cavity, and the nature of unsteadiness at large cavity temperature differences.

5.1 Air-water experiments

Interferograms recorded in the cavity containing superposed air-water layers are discussed in the present section. The fringes are to be interpreted as contours of the temperature field averaged in the direction of the light beam, namely along the length of the cavity. For Rayleigh numbers below a certain value, the thermal fields in the individual fluid layers are two dimensional. The fringes would then coincide with the isotherms in the field. At higher Rayleigh numbers, the field is three dimensional, and the images do not carry strictly local information. The early experiments of Krishnamurti (1970, 1973), summarized in Figure 2.1, reveal the regimes of Rayleigh and Prandtl numbers in which convection in a horizontal fluid layer is two dimensional, followed by three dimensionality and unsteadiness. For a cavity rectangular in plan, stability analysis shows that the rolls would be aligned with their axis parallel to the shorter side. Rolls oriented with axis parallel to the longer side are also possible under conditions discussed by various authors (Chapter 2). It is broadly to be expected that the interferograms of the present chapter represent the side view of the principal roll patterns in the cavity. To a first approximation, the flow patterns in the respective fluid layers can be assumed to follow the regime map of a single fluid corresponding to the Rayleigh numbers based on the layer height and the temperature difference with respect to the interface.

In view of the higher thermal conductivity of water compared to air, the largest temperature drop in the cavity occurs in the air layer, and the interface temperature is quite close to that of the lower heated surface. The two fluid layers have their individual Rayleigh numbers, and the corresponding flow regimes can be expected to be distinct. It is thus possible for convection in one of the layers to be unsteady, while steady two/three dimensional flow prevails in the other.

5.1.1 Cavity filled 2/3rd with water

In this section, the convection patterns obtained in the rectangular cavity filled with water upto 2/3rd the cavity height have been presented. Fringe patterns for cavity tem-

perature differences of 10, 15 and 18 K are respectively shown in Figures 5.1(a,b,c). The corresponding roll patterns for the fringe patterns of Figures 5.1(a,b,c) have been shown respectively in Figures 5.1(a1,b1,c1). In Figure 5.1(a), a temperature difference of 10 K is imposed across the cavity, the surface temperatures being 16 and 26°C respectively at the cold and the hot walls. Based on the correlations of Equations 4.26 and 4.27, the interface temperature was calculated using the energy balance criterion to be 25.80°C, while the experimentally determined interface temperature was 25.72°C. The Rayleigh numbers calculated on the basis of the former interface temperature are 1242 and 35,727 respectively in the air and water layers. This indicates a higher driving buoyancy potential in water compared to air. The relative strength of the driving forces can be explored in terms of the ratio Ra_2/Ra_1 where, 2 represents the lower layer, and 1 is the upper layer. In Figure 5.1(a), the Rayleigh number ratio is 29.

Even though the overall temperature difference taking place here is quite small, the fringes in the water phase can be seen to be quite dense. This is because the temperature drop per fringe shift (ΔT_e) is much smaller for water as compared to air, the values being 0.016 and 1.527 K respectively. The higher Rayleigh number in water also indicates a more vigorous buoyant motion. This is confirmed by the greater displacement of the fringes, while those in air are almost straight¹. The interferogram of Figure 5.1a was captured after an experimental run time of 4 hours, when the flow field was fully evolved and the fringe patterns were quite steady. Since each fringe is closely associated with an isotherm, regions of a small fringe spacing can be associated with a large local diffusive heat flux. In the wall region, the high fringe density represents a large local Nusselt number.

In Figure 5.1(b), the temperature difference of 15 K was imposed between the two bounding surfaces. The cavity average temperature for this experiment was 23.5°C. The interface temperature was calculated to be 30.70°C, the experimental value after a considerable passage of time being 29.41°C. Accordingly, the Rayleigh numbers calculated in the air and the water layers were 1794 and 65,404 respectively. Mild unsteadiness was noticed in the water layer near the central region due to an increased buoyancy potential. In air, the flow was completely steady. Owing to fluid motion, the fringes were seen to develop a certain degree of curvature. The roll patterns in the water layer were seen to change between 2-6 rolls in time, revealing a degree of unsteadiness as well as three dimensionality. The long-lived fringe patterns that emerged as the dominant mode have been shown in Figure 5.1(b).

¹For a confined fluid layer, a Rayleigh number of less than 1708 indicates a no-flow, conduction state.

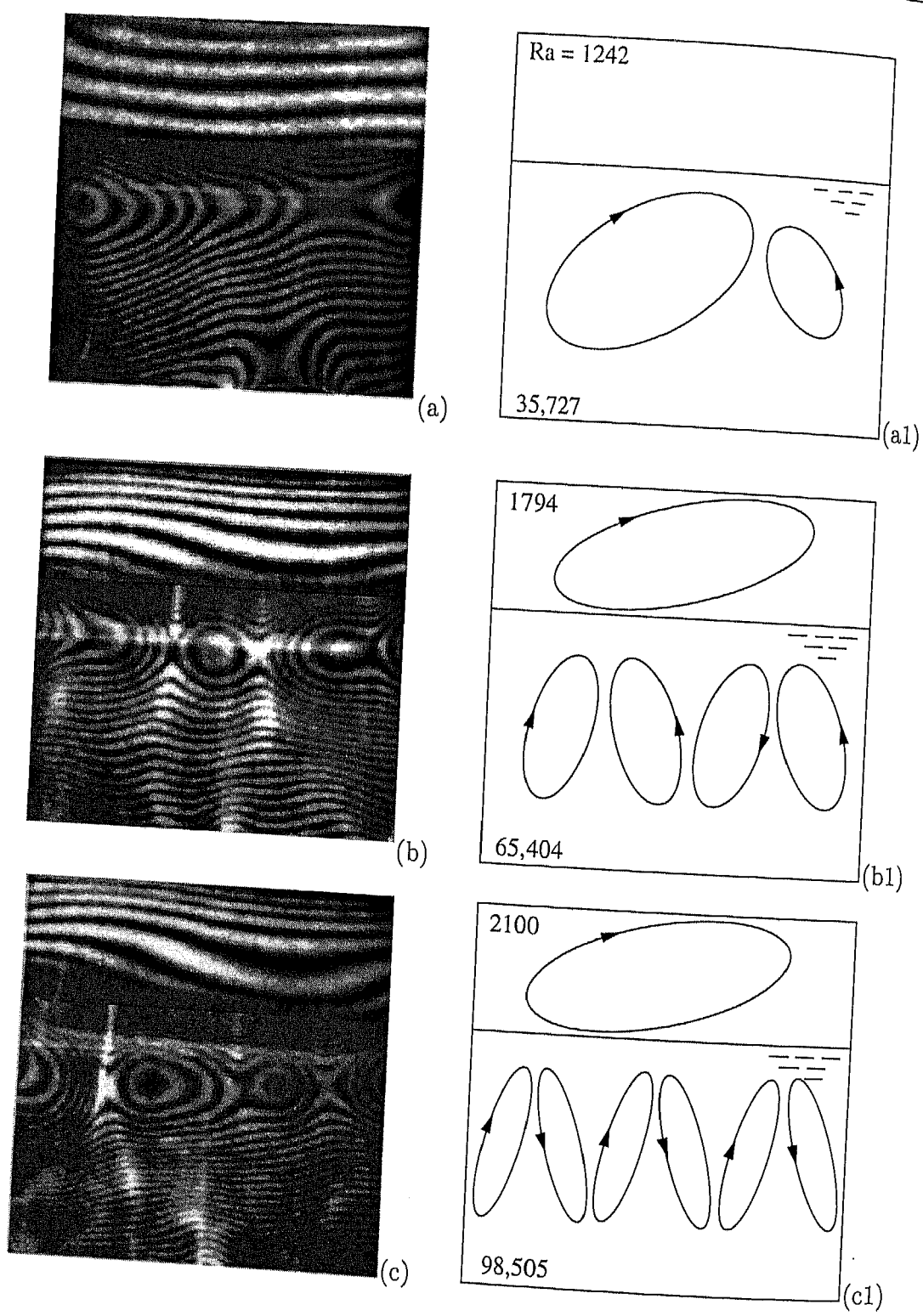


Figure 5.1: Long-time interferograms (a,b,c) and the corresponding roll patterns in the side view (a1,b1,c1) for air-water system. Cavity 2/3rd filled with water. Temperature differences are (a) 10 K, (b) 15 K and (c) 18 K. Layer Rayleigh numbers are marked on the right column.

In Figure 5.1(c), the temperature difference imposed between the two surfaces was 18 K. The estimated and the experimental values of the interface temperature for the experiment were 33.65 and 32.30°C respectively. The Rayleigh numbers in the air and the water layers were calculated to be 2100 and 98,505 respectively. These numbers show an extremely high driving buoyancy potential in water as compared to air. In the experiments, convection in water showed significant unsteadiness, while that in air was quite steady. The number of rolls in the water layer was seen to change from 4 to 8; quite possibly the flow was three dimensional as well.

In the portion of the cavity filled with air, the no-flow condition exists in Figure 5.1(a), as the Rayleigh number falls below the critical Rayleigh number value of 1708. The isotherms are equally spaced with negligible curvature due to the complete dominance of diffusive over convective heat transfer. As the Rayleigh number exceeds the critical value, Figures 5.1(b-c), the flow develops in the form of a single cell. The fluid rises along the left wall and descends along the right wall. This gives a unicellular pattern in the cavity with a clockwise sense of rotation in the side view. In the water layer, the flow develops in the form of two and six counter-rotating rolls (Figure 5.1(a1), (c1)) respectively with flow descending and four counter-rotating rolls (Figure 5.1(b1)) with ascending flow along the vertical axis close to the cavity center. The roll formed on the left side near the interface is quite strong as compared to that on the right side (Figure 5.1(a1)). The recirculating flow in water exhibits stronger convection compared to air. This is seen in the greater curvature of the individual fringes. The largest local heat flux at the lower cavity wall at steady state occurs near the inter-cell boundaries. The fringes are denser near the lower hot wall and the interface in comparison to the central region². Dense fringes near the interface indicates the free surface to be a thermally active boundary.

The presence of a convective field in the individual fluid layers leads to a coupling between them. Convective flow is absent in the air phase at the lowest temperature difference (Figure 5.1(a1)), indicating a case of pure thermal coupling at the interface. An increase in the cavity temperature difference and hence the layer Rayleigh numbers results in flow to occur in air (Figures 5.1(b1), (c1)). The water layer exhibits buoyant motion for all the three temperature differences imposed across the walls. The appearance of a single roll in the air layer is quite similar to the pattern seen in an air-filled cavity (Figure 4.20). Convection in air is thus a result of a temperature difference between the cold upper wall and the interface. The considerable difference in the velocity

²Dense fringes near the lower solid wall shows the heat flux to be dominated by the diffusive component. In the central core, convective velocities reduce temperature gradients and the fringes have a greater separation.

fields in the two fluids shows that the layers are thermally coupled, mechanical coupling being of secondary importance.

Using the fringe patterns of Figures 5.1(a-c), the line-of-sight averaged temperature profiles in the air and water layers of the cavity have been determined. These temperature profiles have been plotted as a function of the non-dimensionalised vertical

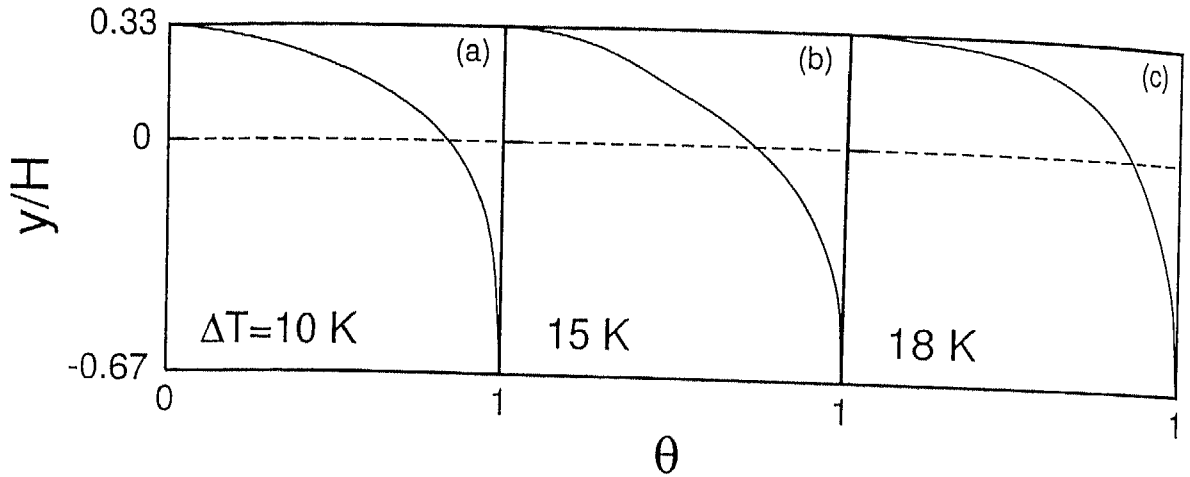


Figure 5.2: Depth-averaged temperature profiles in a cavity 2/3rd filled with water in air-water experiments; Cavity temperature differences are (a) 10 K, (b) 15 K and (c) 18 K.

distance (y/H) in Figures 5.2(a-c). Here, the y -coordinate is measured from the air-water interface. The dimensionless temperature is defined as $\theta = \frac{T-T_c}{T_h-T_c}$. The principal observation to emerge from the Figures 5.2(a-c) is that the largest portion of the temperature drop occurs in air, in comparison to water. This is clearly due to the higher thermal conductivity of water compared to air. The temperature profiles in each layer also exhibit continuity at the interface indicating that the layers are thermally coupled. The slopes of the temperature profiles at the hot and the cold walls show a monotonic increase with the cavity temperature difference. Thus the energy transferred across the cavity increases as the temperature difference is raised. The interface temperature did not show a gradually increasing trend, particularly between Figures 5.2(b-c). It could be due to a higher degree of unsteadiness in water, when compared to air at a cavity temperature difference of 18 K.

The temperature gradients were computed at 11 x -locations along each of the walls. Using the temperature profiles in the fluid layers (Figures 5.2(a-c)), the local heat transfer rates were determined at the hot and the cold walls of the cavity using Equation 4.25. The heat transfer rates at the walls have been represented in terms of the Nusselt

number³. The variation of the local Nusselt number at the respective walls with respect to the coordinate parallel to the width of the cavity is shown in Figures 5.3(a-c). Strictly speaking, the slope of the Nusselt number distribution should be zero at the side walls ($x = 0$, and W), since they are insulating surfaces. Since the analysis was carried out for the cavity interior, the zero slope condition has not been consistently reproduced. The local Nusselt numbers in air are close to unity, since a strong convective field was not set up in the experiments. In water, the Nusselt numbers are significantly higher. The variation of Nusselt number with the x -coordinate does not correlate directly with the appearance of rolls. Since a number of rolls that form in water is large, the Nusselt number profile doesnot display any characteristic trend.

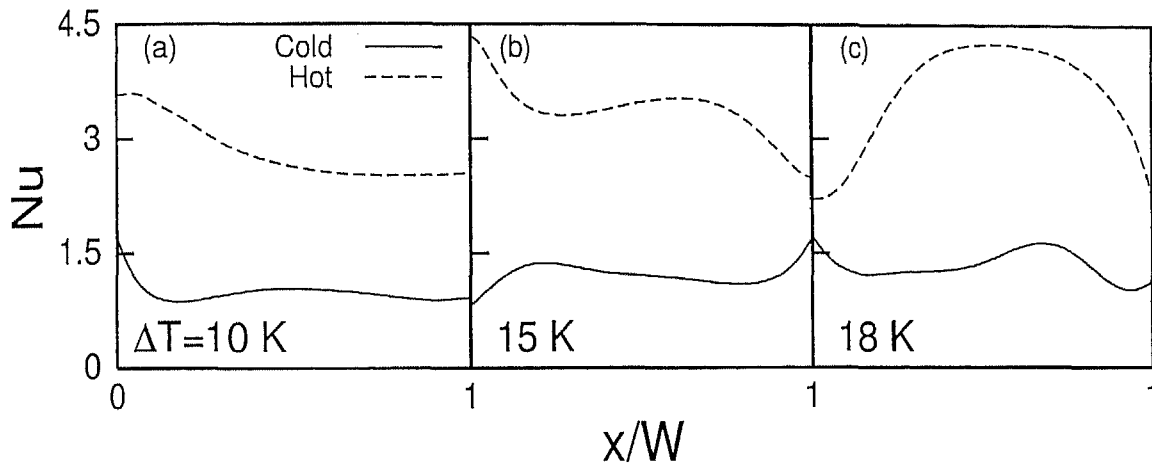


Figure 5.3: Local Nusselt number variation at the hot and the cold walls of the cavity 2/3rd filled with water in air-water experiments; Cavity temperature differences are (a) 10 K, (b) 15 K and (c) 18 K.

Based on the respective local Nusselt number variation at the hot and the cold walls, the width-averaged (global) Nusselt number for the two walls can be calculated. A summary of the width-averaged Nusselt number for the three experiments of Figures 5.1(a-c) are summarized in Table 5.1. They have been compared with the correlations for air and water respectively given by Equations 4.26 and 4.27. The correlations are applicable for a cavity with no-slip walls. Factors that result in a discrepancy between the measured Nusselt numbers and the correlations are: (a) the presence of a free-slip boundary and (b) three dimensionality and unsteadiness in the fringe patterns at elevated Rayleigh numbers. Experimental interface temperatures are also compared with the values derived from energy balance in Table 5.1. In Table 5.1 the discrepancy between the experimental and correlation Nusselt numbers is higher ($\approx 26\%$) for the water side

³For water, the characteristic temperature difference is $(T_h - T_l)$, while for air it is $(T_l - T_c)$.

in comparison to the air side ($\approx 2\%$). This may be attributed to larger unsteadiness and three dimensionality for water than in air.

Table 5.1: Comparison of the experimentally determined width-averaged Nusselt number and interface temperatures with the correlations (marked 'Ref') in a cavity 2/3rd filled with water in air-water experiments.

ΔT , K	T_I (Exp), °C	T_I (Ref), °C	Nu (air)	Nu (Ref)	Nu (water)	Nu (Ref)
10	25.72	25.80	0.98	1.0	3.21	4.35
15	29.41	30.7	1.21	1.1	3.40	4.93
18	32.30	33.65	1.34	1.27	3.60	5.37

5.1.2 Cavity filled with equal layer heights of air and water

The interferograms obtained in the rectangular cavity half-filled with water and the rest being air are presented in this section. Figures 5.4(a,b,c) show the fringe patterns obtained respectively for the temperature differences of 10, 15 and 18 K across the bounding surfaces of the cavity⁴. The respective roll patterns of Figures 5.4(a,b,c) have been shown in Figures 5.4(a1,b1,c1). In Figure 5.4(a), the interface temperature calculated on the basis of Equations 4.26-4.27 was 25.79°C, while it was determined to be 25.82°C from the experiments. The Rayleigh numbers in air and water layers are 4185 and 16,413 respectively. The higher Rayleigh number in water indicates once again a more vigorous buoyant motion, in comparison to air. This is confirmed by the greater displacement of the fringes in water, while those in air are straighter. The Rayleigh number ratio is smaller, when compared to the experiments of Section 5.1.1. The fringes in the water phase can be seen to be dense, even though the overall temperature drop here is quite small.

In Figure 5.4(b), the temperature difference of 15 K was imposed between the two bounding surfaces, the average of the surface temperatures being 23.5°C. The interface temperature in the present experiment was found to be 30.8°C. Based on correlations (Equations 4.26-4.27), the interface temperature was calculated to be 30.7°C. Accordingly the Rayleigh numbers calculated in the air and the water layers were 6044 and 30,772 respectively. The higher buoyancy potential in water was seen to impart some unsteadiness to the fringes. This influenced the fringe patterns on the air side as well, which reflected slight unsteadiness. The interferogram in Figure 5.4(b) is a representative

⁴The slight interface deformation has not been shown; instead it has been replaced by a solid line.

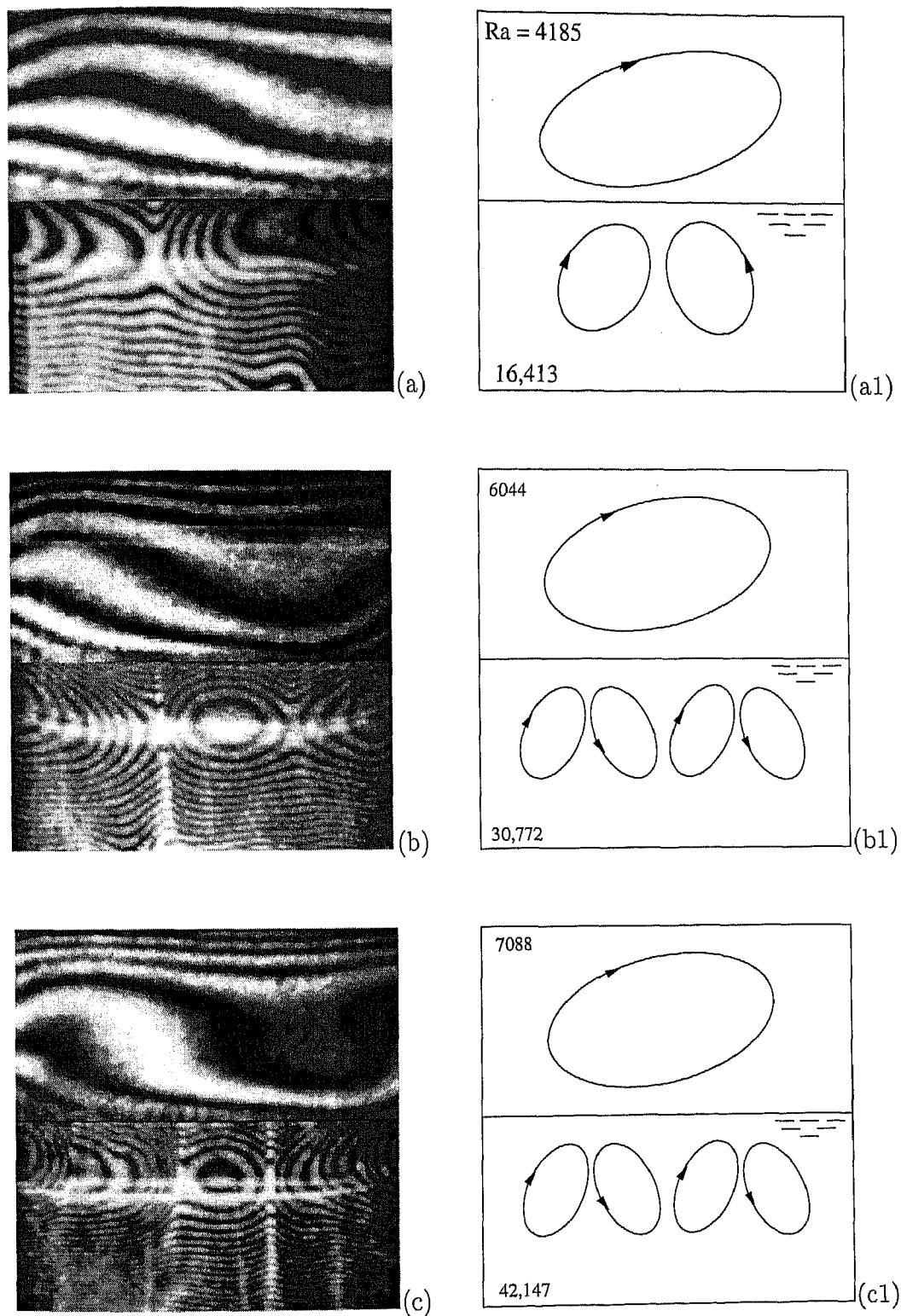


Figure 5.4: Long-time interferograms (a,b,c) and the corresponding roll patterns in the side view (a1,b1,c1) for a cavity half-filled with water, the rest being air; Cavity temperature differences are (a) 10 K, (b) 15 K and (c) 18 K. Layer Rayleigh numbers are marked on the right column.

field in the two-layers after 4 hours of experimentation.

In Figure 5.4(c), the temperature difference imposed between the two surfaces was 18 K. The interface temperature was calculated to be 33.64°C , the experimental value being 33.72°C . The Rayleigh numbers were determined in the air and the water layers to be 7088 and 42,147 respectively. A high Rayleigh number in water was seen to lead to unsteadiness in the fringe patterns, particularly in the central region of the cavity. It was observed that the air layer also registered unsteady flow patterns, a stronger convection current leading to increased fringe curvature. The interferogram depicted in Figure 5.4(c) is a representative field predominantly seen at the end of 4 hours.

Figures 5.4(a-c) show the fringes in water intersecting the interface at several points. In this respect the interface is not a constant temperature boundary. Since the temperature drop per fringe shift is quite small in water, the extent of temperature variation over the interface is also small. For Figures 5.4(a-c) it was estimated to less than 0.1 K.

In air, the interferograms reveal that the flow develops in the form of a single cell for all the three temperature differences referred above. This can be inferred from the expectation that the fringe displacement will occur in the direction of the local fluid velocity. In Figures 5.4(a-c), the fluid rises along the left side wall and descends along the right wall. This gives a unicellular pattern in the cavity with a clockwise sense of rotation in the side view (Figures 5.4(a1-c1)). In the water phase, the flow develops in the form of two (Figure 5.4a1) and four (Figure 5.4b1, 5.4c1) counter-rotating rolls. For the smaller temperature difference, the descent of the colder fluid is closer to the cavity center. As the temperature difference increases, additional rolls form in water, but they are of unequal size. Those near the vertical mid-plane of the cavity are smaller and indicate flow to be in the vertically upward direction. The fluid movement in water is confined to a region close to the interface. Hence the cell sizes in water are smaller than those in air, that in turn scale with the layer height.

In the portion of the cavity filled with air, the largest local wall heat flux at steady state occurs at around the mid-plane of the cavity where the fringe spacing is a minimum. The strength of convection in air increases with the cavity temperature difference. The isotherms are closely spaced near the top wall as well as the interface in comparison to the central core region. The reason for this behaviour is the dominance of diffusive heat transfer near the walls as against convection in the central region. Near the interface the dense fringes indicate that the zone is thermally active, despite the fact that the water surface is one of free-slip, without a prescribed thermal boundary condition. In the water phase, the largest local steady state heat flux at the lower wall occurs near

the inter-cell boundaries.

The appearance of a single roll in the air layer is quite similar to the pattern seen in an air-filled cavity (Figure 4.20). Convection in air is thus a result of a temperature difference between the cold upper wall and the heated interface. To this extent, the interface is a prescribed temperature boundary. It indicates that the air and water layers are thermally coupled. The interface is not strictly an isotherm, as can be seen from the fringes in the water layer intersecting with it. The temperature variation over the interface is however marginal, the temperature drop across the water phase itself being quite small. The rolls in the two phases are not correlated, indicating that the layers are not mechanically coupled, in a time-averaged sense.

For the three temperature differences employed in the experiments, results have been presented on the basis of individual Rayleigh numbers of the fluid layers. With respect to the stability map of Krishnamurti (1970, 1973) for single fluid layers, these values are such as to make the convection pattern steady and two dimensional for $\Delta T = 10$ K in both air and water. For 15 K, it is three dimensional in water, two dimensional in air but steady. At a temperature difference of 18 K, it is unsteady and three dimensional (pattern forming) in both fluid layers. However, in air the unsteadiness is expected to be marginal since the Rayleigh number just crosses the stability boundary. The stronger unsteadiness seen in air in the present experiments can be attributed to that in water. It is transmitted to air across the interface, resulting in fringe displacement with time. In this respect the layers are mechanically coupled in the time domain.

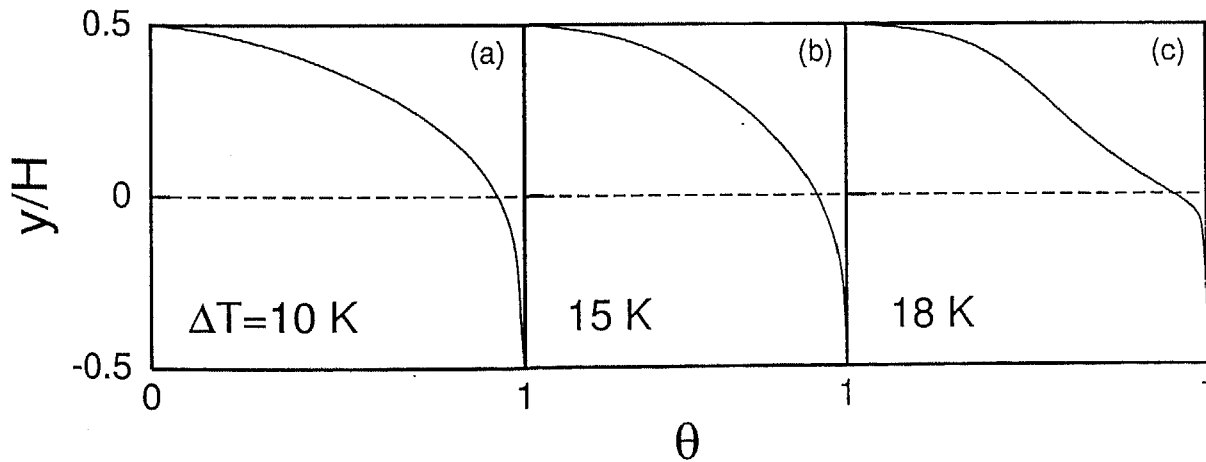


Figure 5.5: Depth-averaged temperature profiles in a cavity half filled with water in air-water experiments; Cavity temperature differences are (a) 10 K, (b) 15 K and (c) 18 K.

Using the fringe patterns of Figures 5.4(a-c), the temperature profiles in the air and

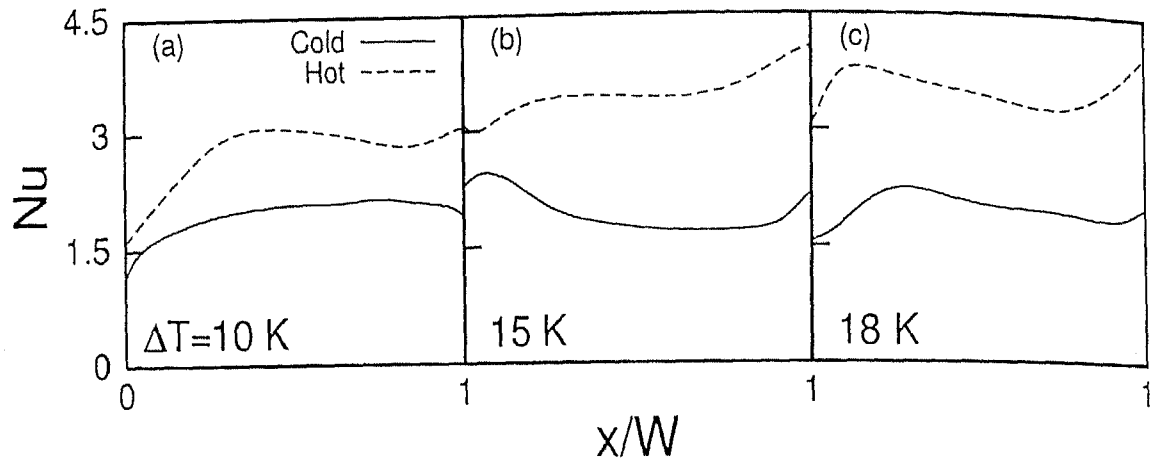


Figure 5.6: Local Nusselt number variation at hot and cold walls in a cavity half filled with water in air-water experiments; Cavity temperature differences are (a) 10 K, (b) 15 K and (c) 18 K.

Table 5.2: Comparison of the experimentally determined averaged Nusselt number and interface temperature with correlations (marked 'Ref') in a cavity half-filled with water.

ΔT , K	T_I (Exp), °C	T_I (Ref), °C	Nu (air)	Nu (Ref)	Nu (water)	Nu (Ref)
10	25.82	25.79	1.96	1.85	2.97	3.68
15	30.80	30.70	1.94	2.04	3.40	4.21
18	33.72	33.64	1.99	2.16	3.70	4.50

water layers of the cavity have been determined. The line-of-sight averaged temperature profiles are shown in Figures 5.5(a-c). The figures clearly bring out the large temperature drop in air as compared to water. In Figures 5.5(a-b) the continuity of the temperature profiles suggest the flow to be strictly thermally coupled. Figure 5.5(c) showed slight discontinuity in temperature near the interface which may be linked to the appearance of mechanical coupling⁵. A steady increase in the wall temperature gradient in both layers with the cavity temperature difference is also visible.

Using the temperature profiles in the fluid layers (Figures 5.5(a-c)), the local Nusselt number distribution was calculated at selected columns of the hot and the cold walls of the cavity. The variation of the local Nusselt number at the respective walls with respect to the coordinate parallel to the width of the cavity is shown in Figures 5.6(a-c). Heat transfer rates were higher on the right as compared to that on the left side for

⁵Strictly speaking, temperature around the interface is continuous. In mechanical coupling, the continuity has only a local influence. On the scale of fringe spacing, an apparent discontinuity shows up.

both hot and the cold walls indicating roll skewness. This was noticed for all the three temperature differences imposed across the cavity (Figures 5.6(a-c)). Width-averaged Nusselt number have been calculated at the hot and cold walls using the local distribution of Nusselt number. They have been compared with the correlations of Equations 4.26 and 4.27 in Table 5.2. The average interface temperatures for the three experiments of Figures 5.4(a-c) have also been summarized in Table 5.2. The agreement between the experiments and the energy balance calculation is seen to be good. Differences in Nusselt number are higher in the water compared to air, owing to unresolved fringes near the lower hot wall as well as unsteadiness.

5.1.3 Cavity filled 1/3rd with water

The present section discusses the convective field in a cavity 1/3rd filled with water, the rest being air. Interferometric patterns in the cavity are shown in Figures 5.7(a-c) for temperature differences of 10, 15 and 18 K respectively across the cavity. The corresponding roll patterns of Figures 5.7(a-c) have been shown respectively in Figures 5.7(a1-c1). In Figure 5.7(a), for a temperature difference of 10 K, the average interface temperatures based on correlations and experiments were found to be 25.81 and 24.62°C respectively. The corresponding Rayleigh numbers have been calculated to be 9939 and 4420 respectively in air and water layers. These values indicate a vigorous convective motion in air compared to water. In the experiments, the thermal field in air showed high unsteadiness, unlike water where the flow was quite steady. The interferogram seen in Figure 5.7(a) corresponds to the dominant pattern that appeared for the largest fraction of time. Though the fringe patterns showed unicellular motion in the air layer, a weak secondary roll was also noticed in the experiments. Here, the primary roll (in air) rises along the left side wall and descends near the right side wall.

In Figure 5.7(b), the temperature difference of 15 K was applied across the two walls. The interface temperature based on correlations was calculated to be 30.73°C, while the experimentally obtained interface temperature was 30.0°C. Accordingly, the Rayleigh numbers in air and water layers were 14,357 and 8023 respectively. In the experiments, a high degree of unsteadiness was noticed in air compared to water due to a higher driving buoyancy potential. Fringe patterns in the water layer showed some movement, driven by the unsteadiness in air. A comparison of Figures 5.7(a) and 5.7(b) shows a fundamental change in the fringe patterns in air as well as in water, going from unicellular at the lower Rayleigh number to a bicellular state at the higher Rayleigh number. In air, the flow descends near the center of the cavity and rises near the two

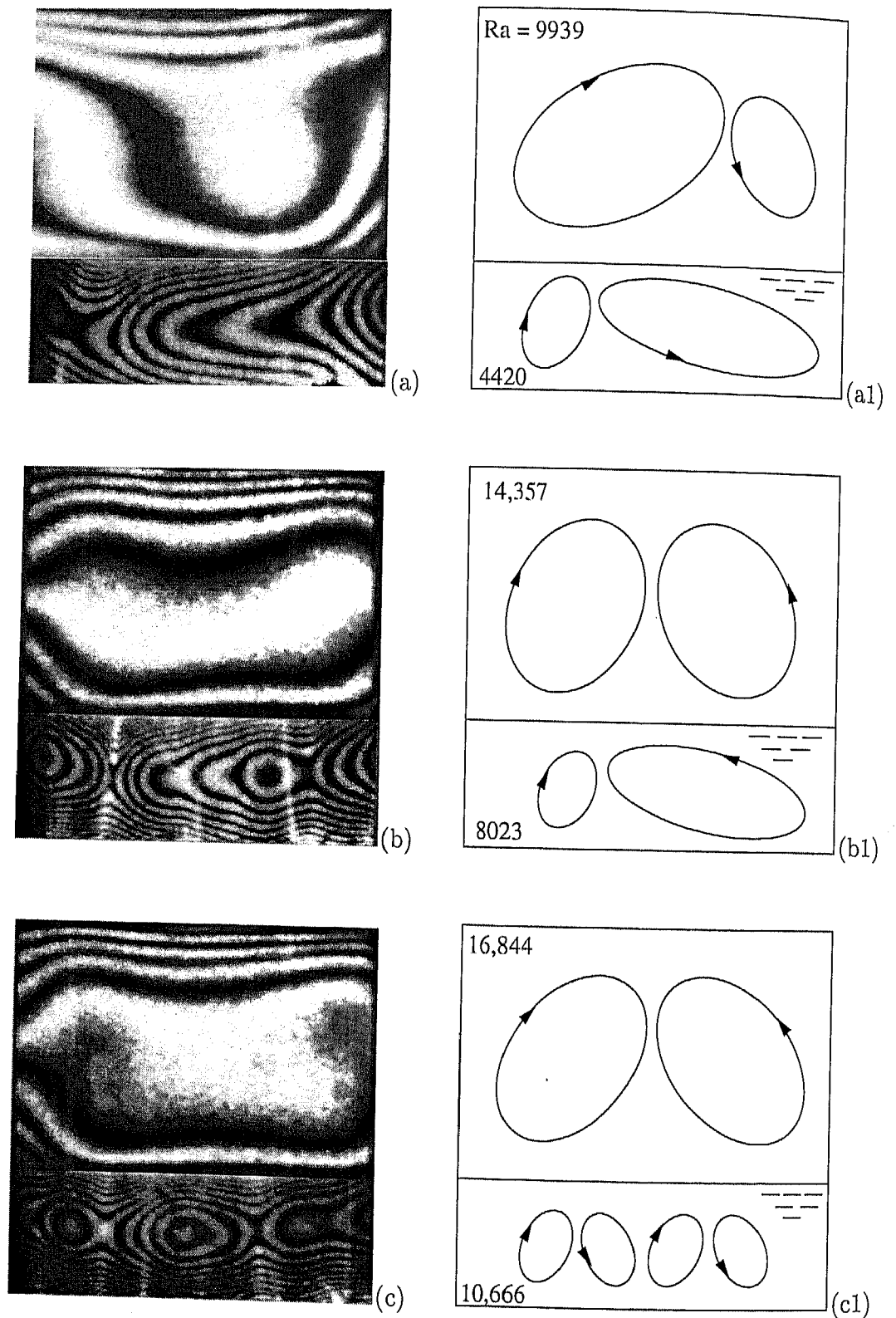


Figure 5.7: Long-time interferograms (a,b,c) and the corresponding roll patterns in the side view (a1,b1,c1) for air-water system in a cavity 1/3rd filled with water; Cavity temperature differences employed are (a) 10 K, (b) 15 K and (c) 18 K. Layer Rayleigh numbers are marked on the right column.

side walls.

In Figure 5.7(c), the imposed temperature difference was 18 K. The correlated and experimental interface temperatures were 33.69 and 31.21°C respectively. The Rayleigh numbers for this experiment were calculated in air and water to be 16,844 and 10,666 respectively. The fringes in air displayed considerable unsteadiness in the central portion of the cavity, in turn imparting slight unsteadiness to water, which was otherwise steady. The interferogram in Figure 5.7(c) is representative of a fully evolved flow field. Here, a bicellular flow in the air and four counter-rotating rolls in the water phase can be noticed.

The rolls in Figure 5.7(a1) are oppositely oriented, being clockwise in air and counter-clockwise in water. Thus the water particles can be visualized as being dragged by the motion of air above, and the layers are now mechanically coupled. At higher Rayleigh numbers (Figure 5.7(c1)), the above trend continues in the sense that the descending flow close to the cavity center in air meets the ascending flow in water. The unsteadiness noticed in the water phase at higher Rayleigh numbers can also be linked to the fluids being mechanically coupled at the interface in the time domain.

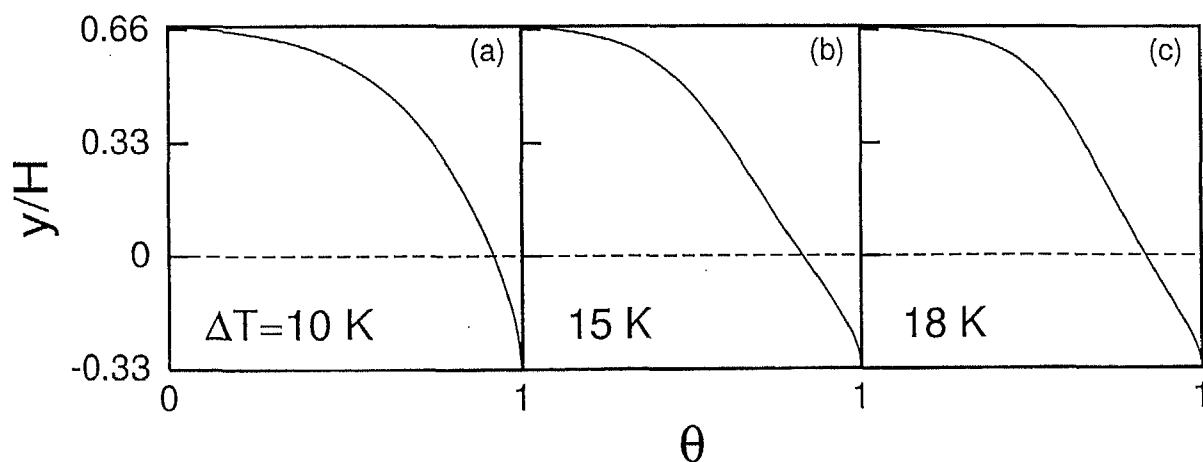


Figure 5.8: Depth-averaged temperature profiles in a cavity 1/3rd filled with water in air-water experiments; Cavity temperature differences employed are (a) 10 K, (b) 15 K and (c) 18 K.

Using the interferograms of Figures 5.7(a-c), the line-of-sight averaged temperature profiles have been plotted in Figures 5.8(a-c). The principal observation to emerge here is that the largest portion of the temperature drop occurs in air, in comparison to water. There is a noticeable but gradual change in the shape of the temperature profile at higher Rayleigh numbers. This is significant in experiments where the layers are mechanically coupled. As a consequence of mechanical coupling, convection in the water

layer is controlled by the strength of convection in air, and leads to a reduction in the temperature gradient at the lower wall. The gradient on the air-side is barely affected⁶. As the Rayleigh number increases, the rolls no longer span the full height of the water phase, leading to a nearly linear variation of temperature adjacent to the heated wall.

Local and average heat transfer rates in terms of the Nusselt number has been calculated from the temperature profiles. The local Nusselt number variation at the hot and the cold walls for the three experiments of Figures 5.7(a-c) are presented in Figures 5.9(a-c). A summary of dimensionless wall heat transfer rates and interface temperatures for the experiments are summarized in Table 5.3. The local Nusselt number variation in air broadly reflects the roll movement. This correlation can be seen in water at the lowest cavity temperature difference of 10 K. At 15 and 18 K, the rolls are closer to the interface. Hence the Nusselt number variation in water does not reflect the formation of a multiplicity of rolls. For the three temperature differences, it can be inferred from Table 5.3 that the energy balance equation has been partially approximated in the experiments. The differences are higher at a cavity temperature difference of 18 K where the fluid layers are mechanically coupled. The errors are however within the limits of uncertainty in the experiments since the flow fields are also time-dependent.

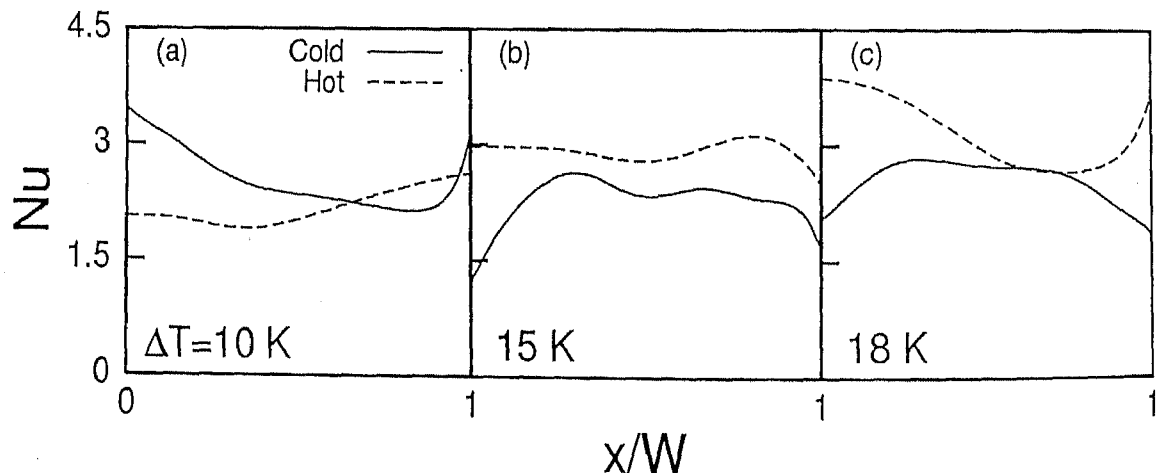


Figure 5.9: Local Nusselt number variation at the hot and cold walls of the cavity 1/3rd filled with water; Cavity temperature differences employed are (a) 10 K, (b) 15 K and (c) 18 K.

⁶though slightly enhanced.

Table 5.3: Comparison of the experimentally determined averaged Nusselt number and interface temperature with correlations (marked 'Ref') in a cavity 1/3rd filled with water.

ΔT , K	T_I (Exp), °C	T_I (Ref), °C	Nu (air)	Nu (Ref)	Nu (water)	Nu (Ref)
10	24.62	25.81	2.60	2.38	2.09	2.62
15	30.00	30.73	2.40	2.61	2.99	3.08
18	31.21	33.69	2.53	2.71	3.03	3.32

5.1.4 Temporal evolution

The following section presents interferograms captured during the time-wise evolution of the flow field inside the cavity. The evolution of flow field refers to the time sequence of fringe patterns recorded after the two bounding surfaces are thermally stabilized. As stated in Section 3.4, the temperatures of the two walls approached steady state jointly with the flow field within the cavity. The fringe patterns exhibiting quasi-steady state after 4 hours of experimentation have been presented in Sections 5.1.1-5.1.3. The subsequent temporal evolution of the fringe patterns for cavity temperature differences of 15 and 18 K is depicted in Figures 5.10-5.13. The unsteadiness was more pronounced in water as compared to air and forms the basis of the present discussion. For a cavity 1/3rd filled with water, the fringes in water were quite steady, though the fringes in air displayed movement. This experiment has not been discussed below.

For a cavity 2/3rd filled with water (Figures 5.10-5.11), dense fringes form near the lower hot wall as well as the interface with air. The unsteadiness in flow is seen in the central portion alone, the wall and the interface regions being relatively steady. With an increase in the cavity temperature difference, the affected region increases in size. The dominant effect is however a lowering of the time scale of unsteadiness from 20 to 10 seconds. For a cavity half-filled with water, the wall region is relatively steady, though the unsteadiness now has spread upto the interface. The increased size of the unsteady zone is accompanied by an increase in time scale to 1 minute⁷. The time scale reduces from 1 minute to 30 seconds for an increase in the cavity temperature difference from 15 to 18 K. The unsteadiness at the interface is the origin of mechanical coupling between air and water for a cavity with equal layer heights. For a cavity 1/3rd filled with water, unsteadiness is first set up in air, and is subsequently transmitted to water.

The reciprocal of the Fourier numbers ($Fo = \frac{\alpha_w \tau}{H_w^2}$) based on the time scale τ referred

⁷The time scale was visually established during the experiment as the time required for a significant change in the thermal field.

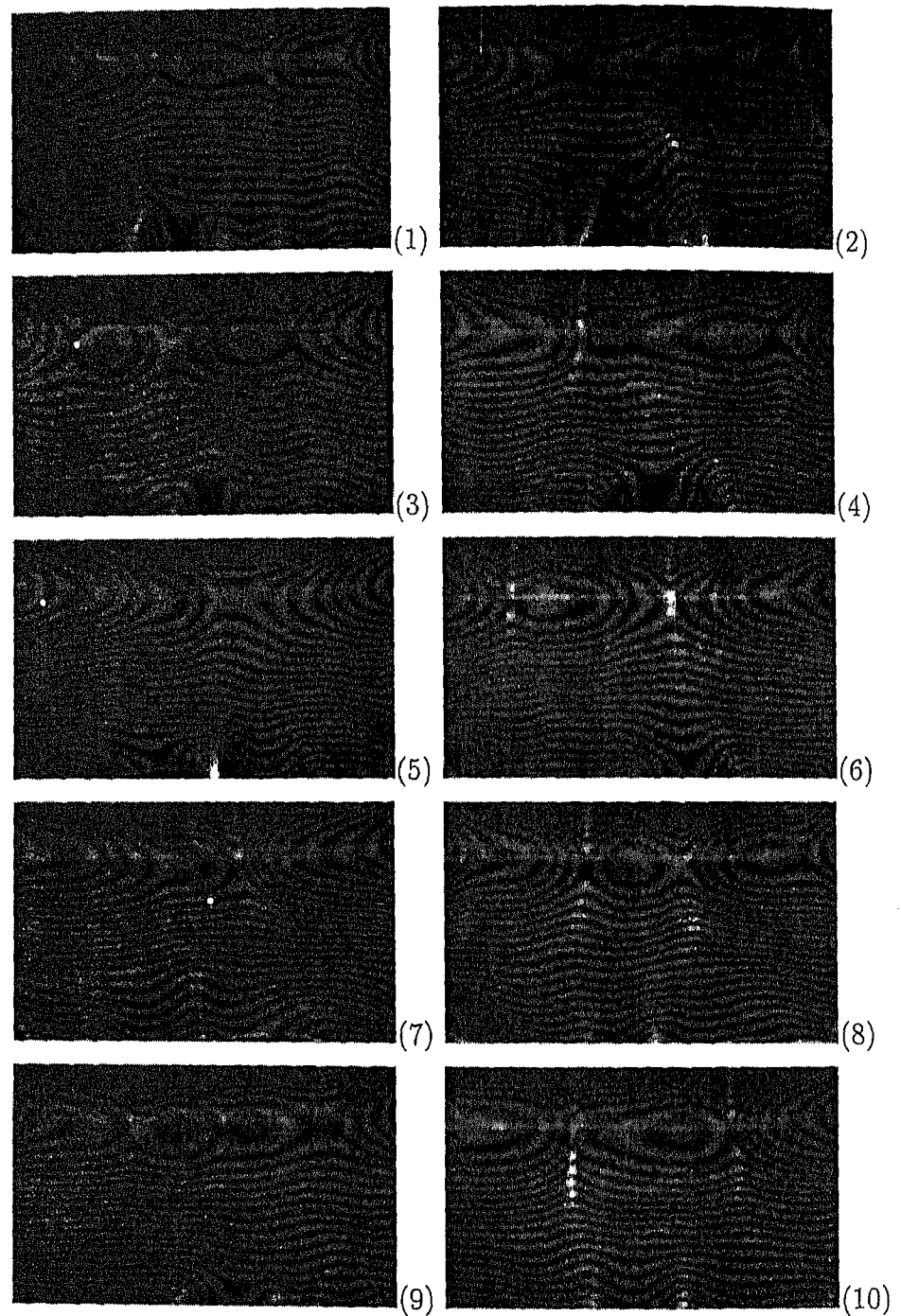


Figure 5.10: Time sequence of interferograms in a cavity 2/3rd filled with water for a cavity temperature difference of 15 K; air-water experiments. Time interval = 20 seconds between successive images.

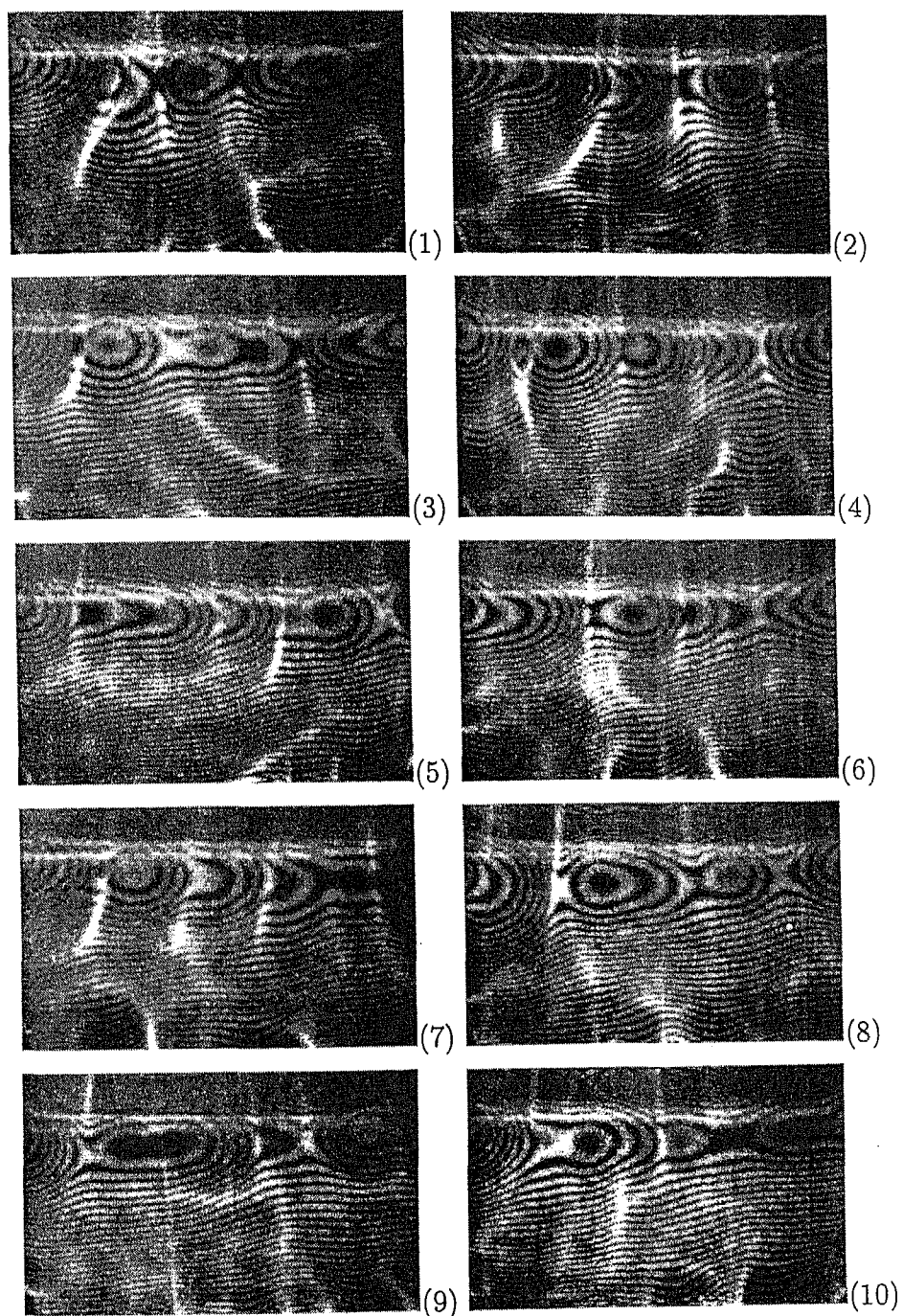


Figure 5.11: Time sequence of interferograms in a cavity 2/3rd filled with water for a cavity temperature difference of 18 K; air-water experiments. Time interval = 10 seconds between successive images.

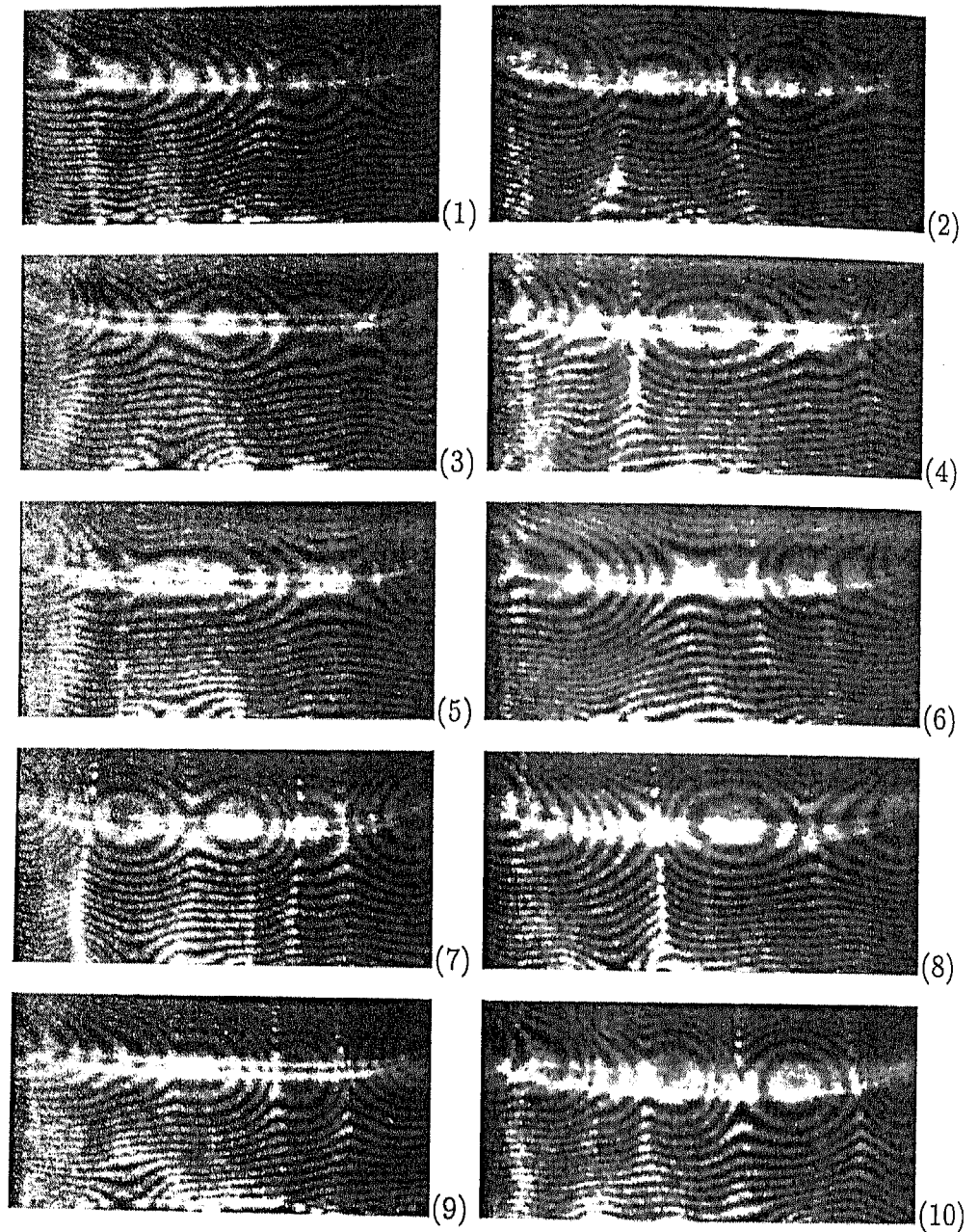


Figure 5.12: Time sequence of interferograms in a cavity half filled with water for a cavity temperature difference of 15 K; air-water experiments. Time interval = 1 minute between successive images.

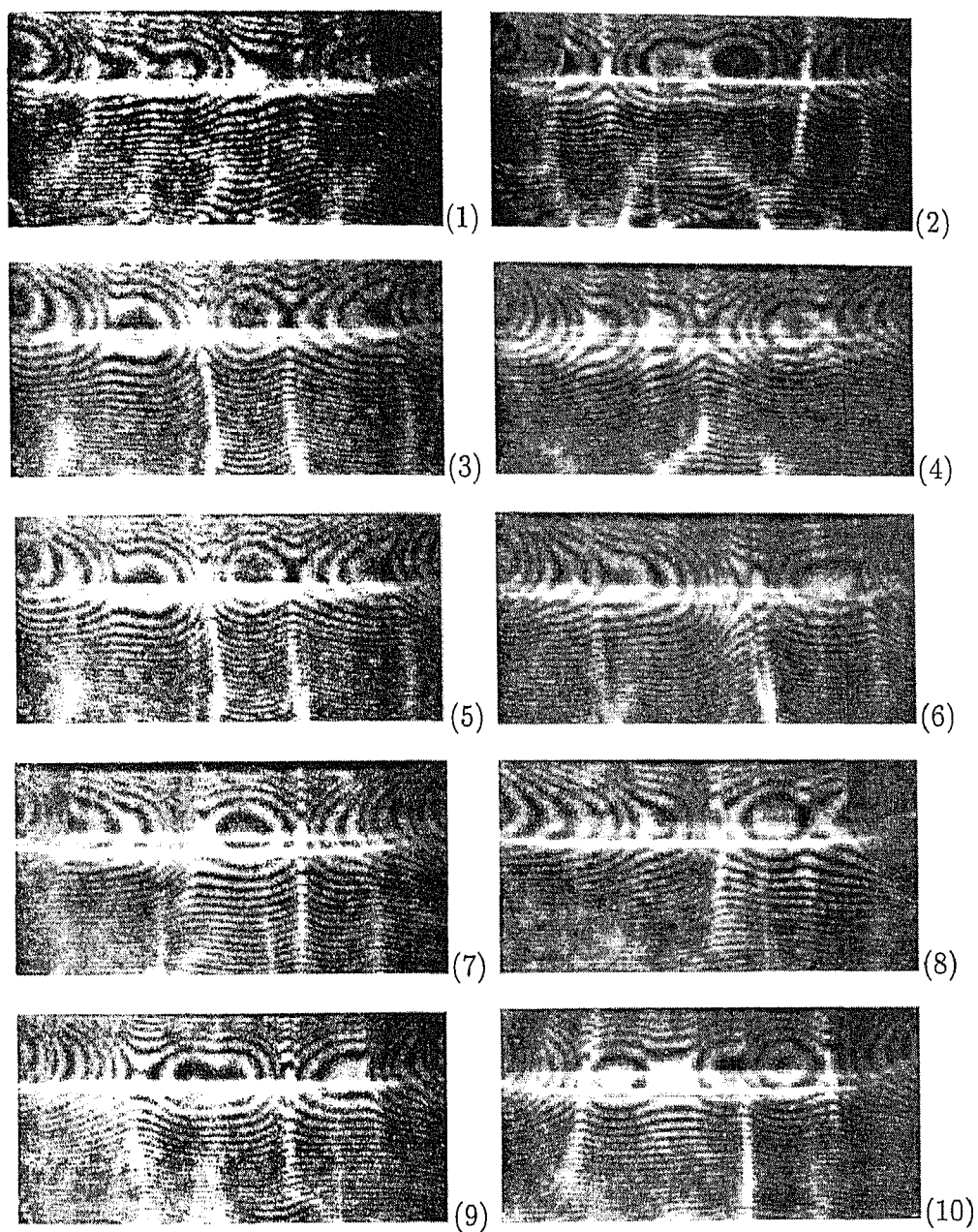


Figure 5.13: Time sequence of interferograms in a cavity half filled with water for a cavity temperature difference of 18 K; air-water experiments. Time interval = 30 seconds between successive images.

above and the layer height H_w of water are summarized in Table 5.4. A clear increase in the reciprocal of the Fourier number with an increase in the height of the water layer as well as the overall temperature difference is to be seen. This is indicative of an increase in the frequency of oscillations in water and a greater possibility of the unsteadiness being transmitted to air.

Table 5.4: Fourier number as a function of Rayleigh number in an air-water cavity.

air	water	ΔT , K	Ra (air)	Ra (water)	1/Fo (water)
1/3	2/3	15	1794	64,404	154
1/3	2/3	18	2100	98,505	303
1/2	1/2	15	6044	30,772	29
1/2	1/2	18	7088	42,147	59

5.2 Air-silicone oil experiments

Experiments in a rectangular cavity containing superposed layers of air and silicone oil are discussed in the present section. In view of the optical properties of silicone oil, refraction effects were found to be quite severe (Section 4.1.1). Refraction in silicone oil was seen to be significantly higher than in air and water. During experiments, the light beam passing through the oil medium got sufficiently displaced to contaminate the intensity of the light beam passing through air. Hence, fringes in silicone oil could be recorded only for a small overall temperature difference of 0.3 K. At higher temperature differences of 10, 15 and 18 K, the light passing through oil was blocked, and the air layer alone was imaged. Layer heights of 1/3, 1/2 and 2/3 with respect to the cavity height have been studied for the three temperature differences imposed across the cavity.

5.2.1 Cavity 2/3rd filled with silicone oil

The following section presents the convection patterns recorded in a cavity filled with 2/3rd oil, the rest being air. The interferogram of the entire cavity at an imposed temperature difference of 0.3 K is shown in Figure 5.14(a). The respective roll patterns of Figure 5.14(a) have been shown in Figure 5.14(al). The cold and the hot surfaces were maintained at 25.7 and 26°C respectively. The experimental interface temperature obtained was 25.90°C. Using the energy balance principle (Equations 4.26 and 4.28), the interface temperature was calculated to be 25.91°C. Accordingly, the Rayleigh numbers

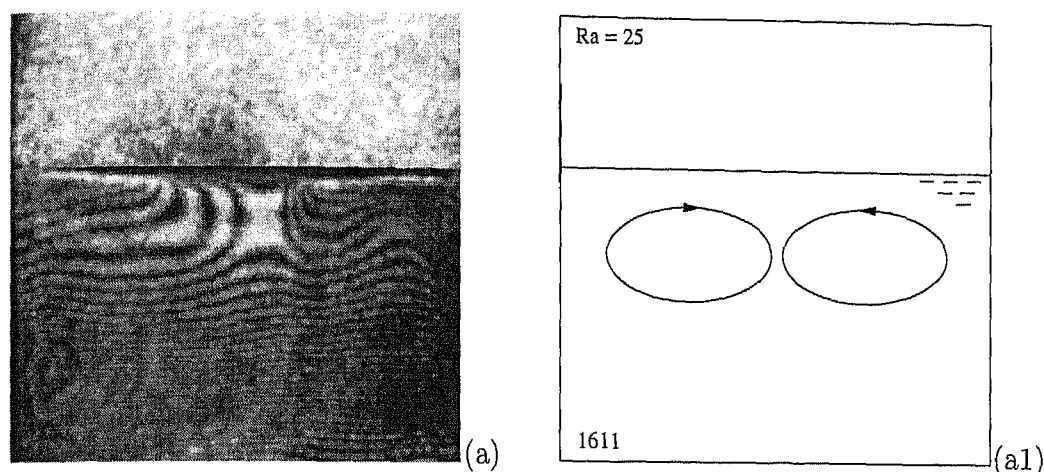


Figure 5.14: Steady state interferograms (a) and the corresponding roll patterns in the side view (a1) in a cavity 2/3rd filled with silicone oil. Cavity temperature difference is 0.3 K. Layer Rayleigh numbers are marked on the right column.

were 25 and 1611 in air and oil respectively. These are smaller than the critical Rayleigh number of 1708 for an infinite fluid layer to initiate convection. In the oil phase, the Rayleigh number is close to the critical value, and convection was initiated near the interface region. This resulted in a convective flow near the interface and was quite steady after 4 hours of experimentation. The interface region was thus seen to be thermally active since it was a site for the initiation of flow. The fringes elsewhere in silicone oil were seen to be practically straight. No fringes were recorded in air since the temperature drop per fringe shift is 1.527 K for air, while it is 0.0034 K in silicone oil.

With reference to Figure 5.14(a1), it can be seen that flow develops in the form of two counter-rotating rolls that form near the interface in the oil medium. The fluid moves with a negative velocity near the center of the cavity along the vertical axis, while the velocity is positive along the side walls. The rolls do not scale the full height of the oil layer and are confined near the interface region. The fringes near the lower wall are straight, indicating the near-absence of fluid motion.

Using the fringe patterns of Figure 5.14(a), the temperature profiles and the local Nusselt number distribution have been determined. The line-of-sight temperature profile in the oil phase is shown in Figure 5.15(a). The temperature profile distribution could only be determined in the oil portion since no fringes appeared in the field-of-view of the air phase. Here, the y -coordinate is measured from the interface represented by $y/H=0$ with air above and oil below it. The main conclusion to emerge from Figure 5.15(a) is that a larger portion of the temperature drop occurs in air, in comparison to oil. The temperature profile in the air portion (shown as dashed line in Figure 5.15(a))

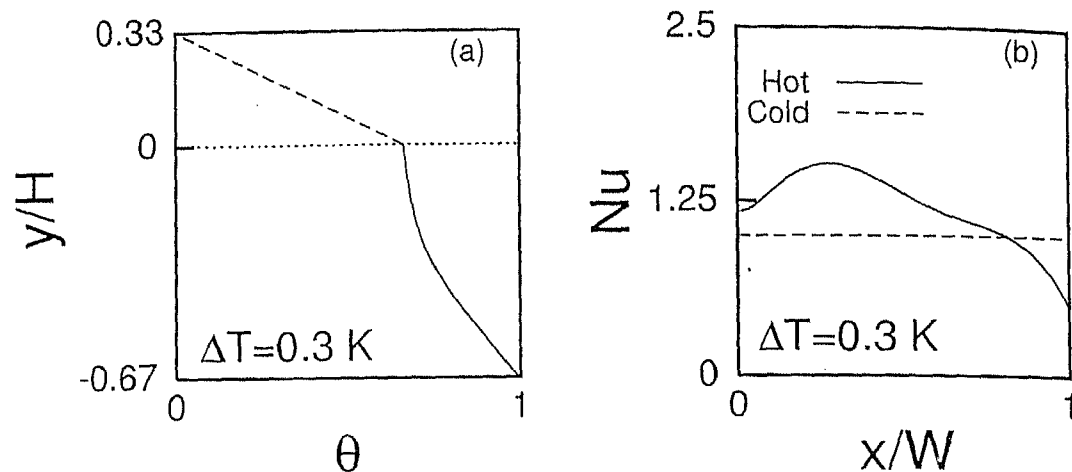


Figure 5.15: (a) Depth-averaged temperature profile and (b) local Nusselt number variation in a cavity 2/3rd filled with oil in air-oil experiments; Cavity temperature difference is 0.3 K.

is expected to have linear variation due to the dominance of conduction at the extremely low Rayleigh number of 25. The variation of the local Nusselt number at the hot wall with respect to the coordinate parallel to the width of the cavity is shown in Figure 5.15(b). While the average Nusselt number is close to unity, the local Nusselt number shows a small variation with the x -coordinate. The slight deformation of the wall fringes is related to the rolls formed near the air-oil interface. Based on the local Nusselt number variation at the hot wall, the width-averaged Nusselt number has been calculated. The dimensionless heat transfer rates in terms of averaged Nusselt number and the interface temperature have been compared with the published correlations in Table 5.5.

Fringes in silicone oil for higher cavity temperature differences could not be recorded owing to excessive refraction errors. Interferograms obtained at higher temperature differences of 10, 15 and 18 K in the air phase are shown in Figures 5.16(a,b,c). The roll patterns of Figures 5.16(a,b,c) have been shown respectively in Figures 5.16(a1,b1,c1). In view of the lower thermal conductivity of oil when compared to water, the temperature drop in oil was higher. This resulted in a reduction of the temperature difference driving convection in air, and hence the Rayleigh number, in relation to the available driving potential in the air-water experiments. In Figure 5.16(a), a temperature difference of 10 K was imposed across the cavity. The interface temperatures obtained from experiments and correlation were 25.17 and 24.81°C respectively. The Rayleigh numbers calculated in the air and oil side were 1124 and 23,079 respectively. Despite the Rayleigh number in air being less than the critical value, the air layer revealed convective flow. This is possible if the larger buoyancy potential available in oil, drives the motion of the air.

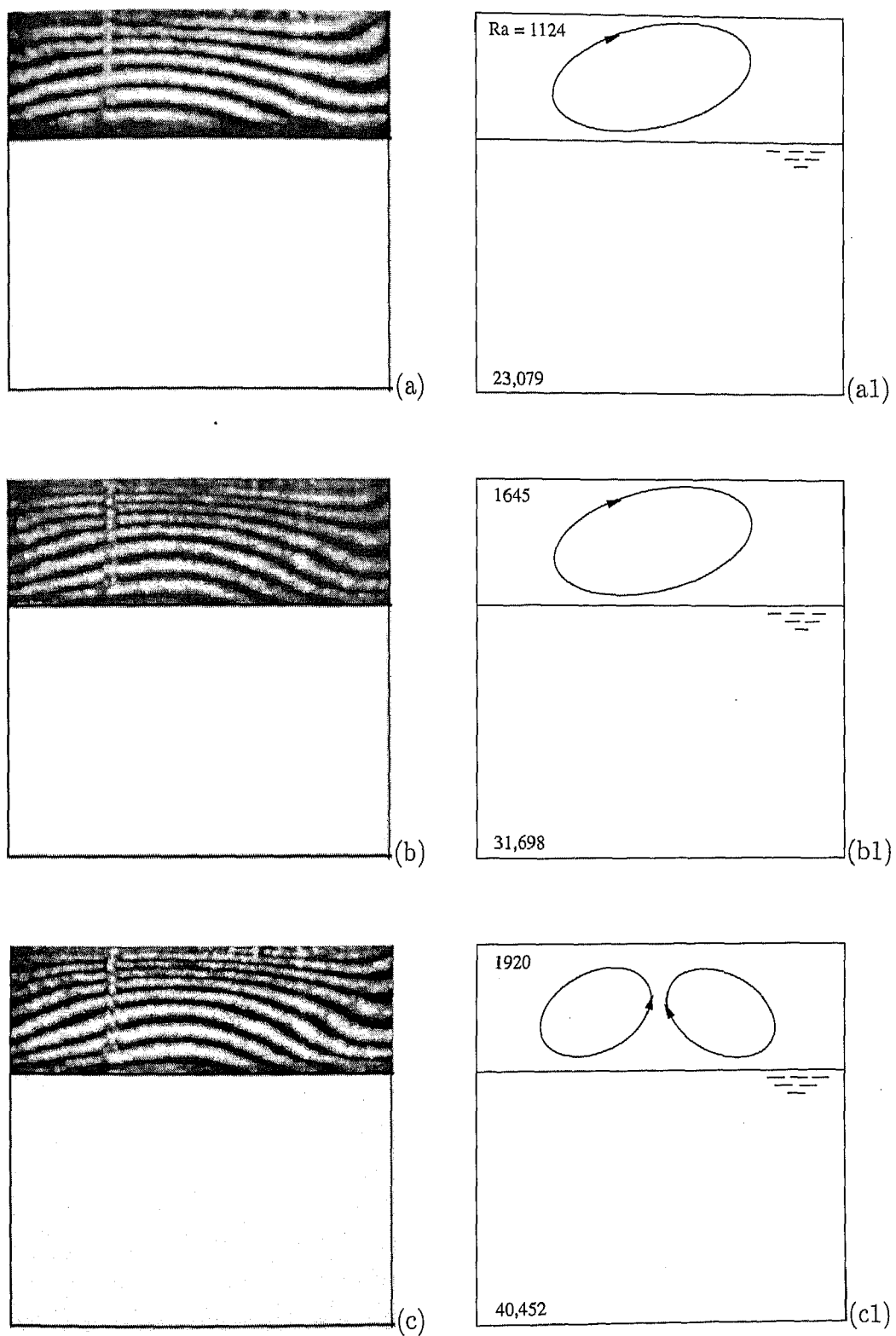


Figure 5.16: Steady state interferograms (a,b,c) and the corresponding roll patterns in the side view (a1,b1,c1) in air for a cavity 2/3rd filled with silicone oil. Cavity temperature differences are (a) 10 K, (b) 15 K and (c) 18 K. Layer Rayleigh numbers are marked on the right column.

Thus the fluid layers are seen to be mechanically coupled, air layers being entrained by the buoyant motion in oil. Although, the convective flow in the oil region in the form of an interferogram could not be recorded, its influence is to increase the fringe curvature in air. The fringe curvature is higher near the interface region as compared to the cold wall. The flow in the air layer develops in the form of an unicellular pattern with sense of rotation in the clockwise direction. The fluid rises along the left side and descends along the right side wall (Figure 5.16(a1)). The flow pattern was seen to be quite steady once the thermal field stabilized.

In Figure 5.16(b), the temperature difference of 15 K was imposed across the cavity. The experimental and estimated interface temperatures are presented in Table 5.5. The Rayleigh numbers calculated in the air and oil were 1645 and 31,698 respectively. The influence of oil movement in the air phase can be noted by the increased fringe curvature in air. This is again an evidence of mechanical coupling. The flow in air develops once again in the form a single cell with sense of rotation in the clockwise direction.

In Figure 5.16(c), the temperature difference imposed between the two surfaces was 18 K. The experimental and estimated interface temperatures are presented in Table 5.5. The Rayleigh numbers were determined in the air and the oil layers to be 1920 and 40,452 respectively. The Rayleigh number in the air phase is higher than the critical value of 1708 to initiate convection. But the convective flow in air is influenced by mechanical coupling between the fluid layers at the interface. Thus the higher Rayleigh number in air supplements the mechanically-driven flow and imparts additional curvature to the fringes. The flow field changes to a bicellular form, instead of unicellular as in the experiments at lower temperature differences (Figures 5.16(a1-c1)). The flow develops in the form of two counter-rotating rolls with flow ascending close to the cavity center along the vertical axis and descending along the vertical side walls. This pattern is symbolic of thermally driven convection. Under the present circumstances, the fluid layers are thermally as well as mechanically coupled.

Using the fringe patterns of the three experiments of Figure 5.16(a-c), the depth-averaged temperature profiles have been determined. The temperature profiles could only be plotted for air and are shown in Figures 5.17(a-c), while the expected variation in oil is shown by dashed lines. Here, $y/H=0$ and 0.33 represents the interface and the cold wall respectively, and $y/H=-0.67$ represents the hot wall. The main observation to emerge from Figures 5.17(a-c) is the large temperature drop in air when compared to oil. As the Rayleigh number increases, the temperature drop decreases from 92 to 81% in the air layer. Hence the temperature drop in oil increases with an increase in the cavity temperature difference. This is understandable because a higher cavity

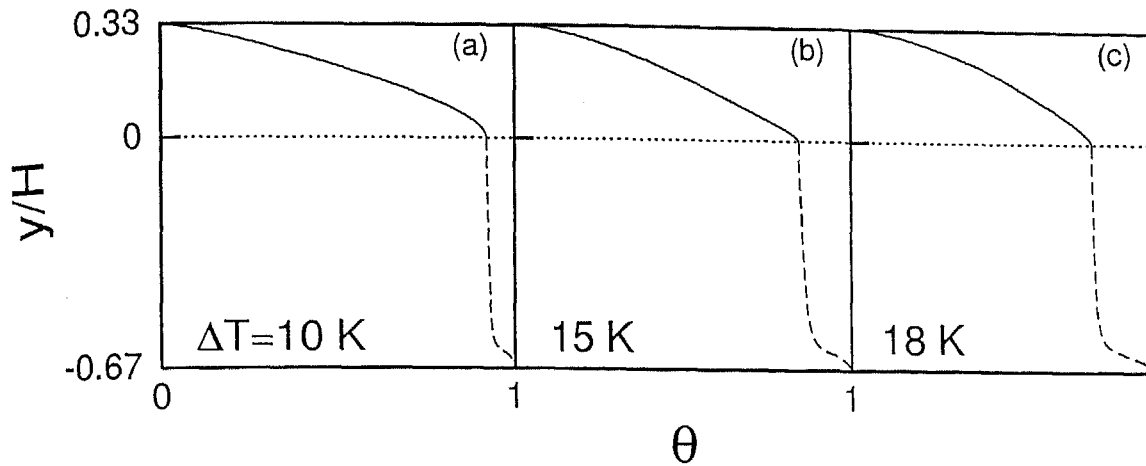


Figure 5.17: Depth-averaged temperature profile in the air layer of a cavity 2/3rd filled with oil; Cavity temperature differences are (a) 10 K, (b) 15 K and (c) 18 K.

temperature difference leads to a vigorous air movement and an increase in the effective conductivity of air. The convective motion in oil is not large enough to sufficiently augment its conductivity. As a result, the dimensionless temperature drop in air is smaller compared to that in oil, when the cavity temperature difference is increased. The present discussion also indicates that the fluid layers are initially mechanically coupled. As the cavity temperature difference is raised, thermal coupling become significant as well.

Based on the temperature profiles of Figures 5.17(a-c), the local Nusselt number variation at the cold wall have been plotted in Figures 5.18(a-c). The width-averaged Nusselt number has been calculated on the basis of Figures 5.18(a-c) and compared with the published correlations in Table 5.5. The bicellular motion in air at a higher cavity temperature difference of 18 K is seen to produce greater variation in the local Nusselt number at the cold wall, and a larger deviation from the single layer convection.

Table 5.5: Comparison of the experimentally determined width-averaged Nusselt number and interface temperatures with the correlations (marked 'Ref') in a cavity 2/3rd filled with oil in air-silicone oil experiments.

ΔT , K	T_I (Exp), °C	T_I (Ref), °C	Nu (air)	Nu (Ref)	Nu (oil)	Nu (Ref)
0.3	25.90	25.91	-	1.0	1.20	1.04
10	25.17	24.81	1.10	1.0	-	2.53
15	28.68	29.37	1.12	1.0	-	2.81
18	30.22	31.91	1.41	1.16	-	3.05

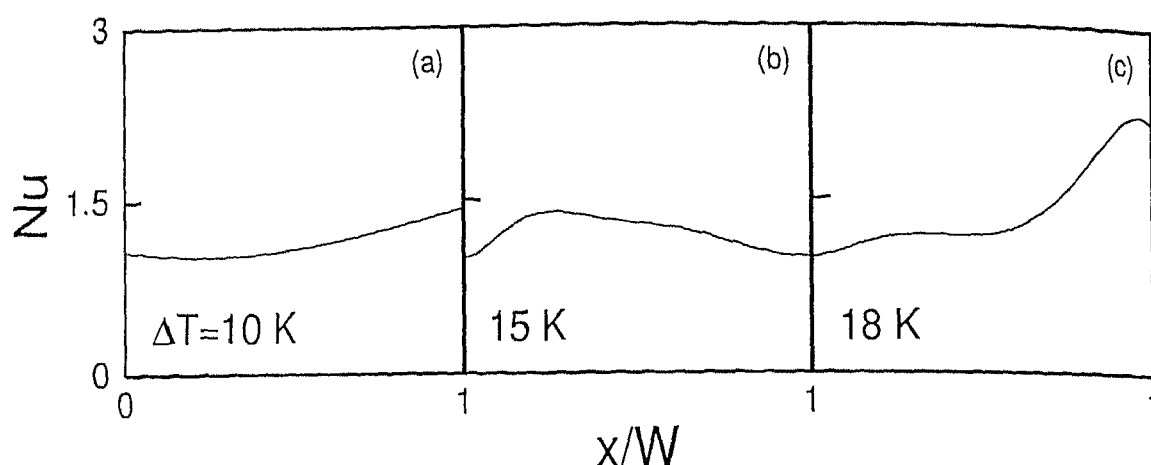


Figure 5.18: Local Nusselt number variation at the cold wall in air. Cavity 2/3rd filled with oil; Cavity temperature differences are (a) 10 K, (b) 15 K and (c) 18 K.

5.2.2 Cavity filled with equal layers of air and silicone oil

The following section presents the results for a cavity filled with equal layer heights of air and silicone oil. The interferogram of Figure 5.19 is obtained at temperature difference of 0.3 K applied across the horizontal walls. Based on the estimated interface temperature, the Rayleigh numbers were calculated to be 93 and 549 respectively in the air and the oil phases. The no-flow condition is realized in the fluids due to an extremely low Rayleigh number with respect to the critical value of 1708. The fringes in silicone oil are practically straight, while the air phase did not register any fringe at all. The fringes are denser near the wall compared to the interface where the oil medium is exposed to air. Thus a higher temperature gradient is obtained at the wall as compared to the interface. This is shown in Figure 5.20(a), where depth-averaged non-dimensional temperature is plotted with respect to the non-dimensional vertical coordinate (y/H).

From Figure 5.20(a), it can be concluded that largest portion of the temperature drop ($\approx 64\%$) occurs in air compared to oil. Using Figure 5.20(a), the local Nusselt number distribution at the hot wall has been determined. This is shown in Figure 5.20(b) with respect to the non-dimensional coordinate (x/W) along the width of the cavity. The heat transfer rates are higher near the vertical side walls as compared to the center of the cavity because of the corners of the cavity cross-section⁸. Based on Figure 5.20(b), the width-averaged Nusselt number have been calculated and compared with correlations (Equation 4.28) in Table 5.6. The experimentally determined average interface temperature is seen

⁸The long-lived transients in a purely conduction dominated experiment also play a role in the local Nusselt number profile.

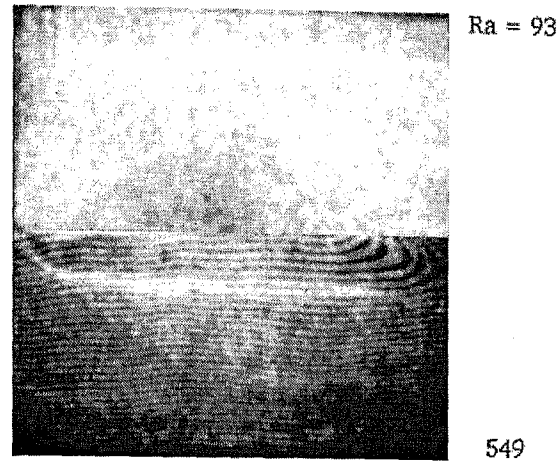


Figure 5.19: Steady state interferograms in a cavity filled with equal layer heights of air and silicone oil. Cavity temperature difference is 0.3 K. Layer Rayleigh numbers are marked on the right side.

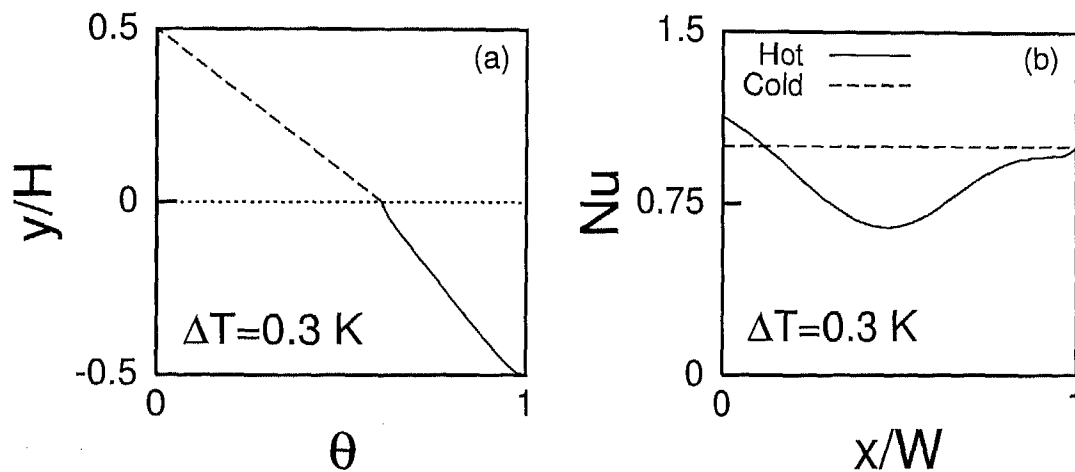


Figure 5.20: (a) Depth-averaged temperature profile and (b) local Nusselt number variation at the hot wall in a cavity filled with equal fluid heights in air-oil experiments; Cavity temperature difference is 0.3 K.

to match the value derived from correlations.

At higher cavity temperature differences, the fringes could not be recorded in silicone oil. The fringes have been recorded at higher temperature differences in the air phase and are presented in Figures 5.21(a,b,c). The corresponding roll patterns of Figures 5.21(a,b,c) have been presented respectively in Figures 5.21(a1,b1,c1). In Figures 5.21(a-c), the temperature differences applied across the cavity were 10, 15 and 18 K respectively. Accordingly, the Rayleigh numbers were calculated in air to be 3736, 5425 and 6383. The corresponding values in oil were 10,940, 16,181 and 19,301. The experimental and the estimated interface temperatures for the three experiments have been

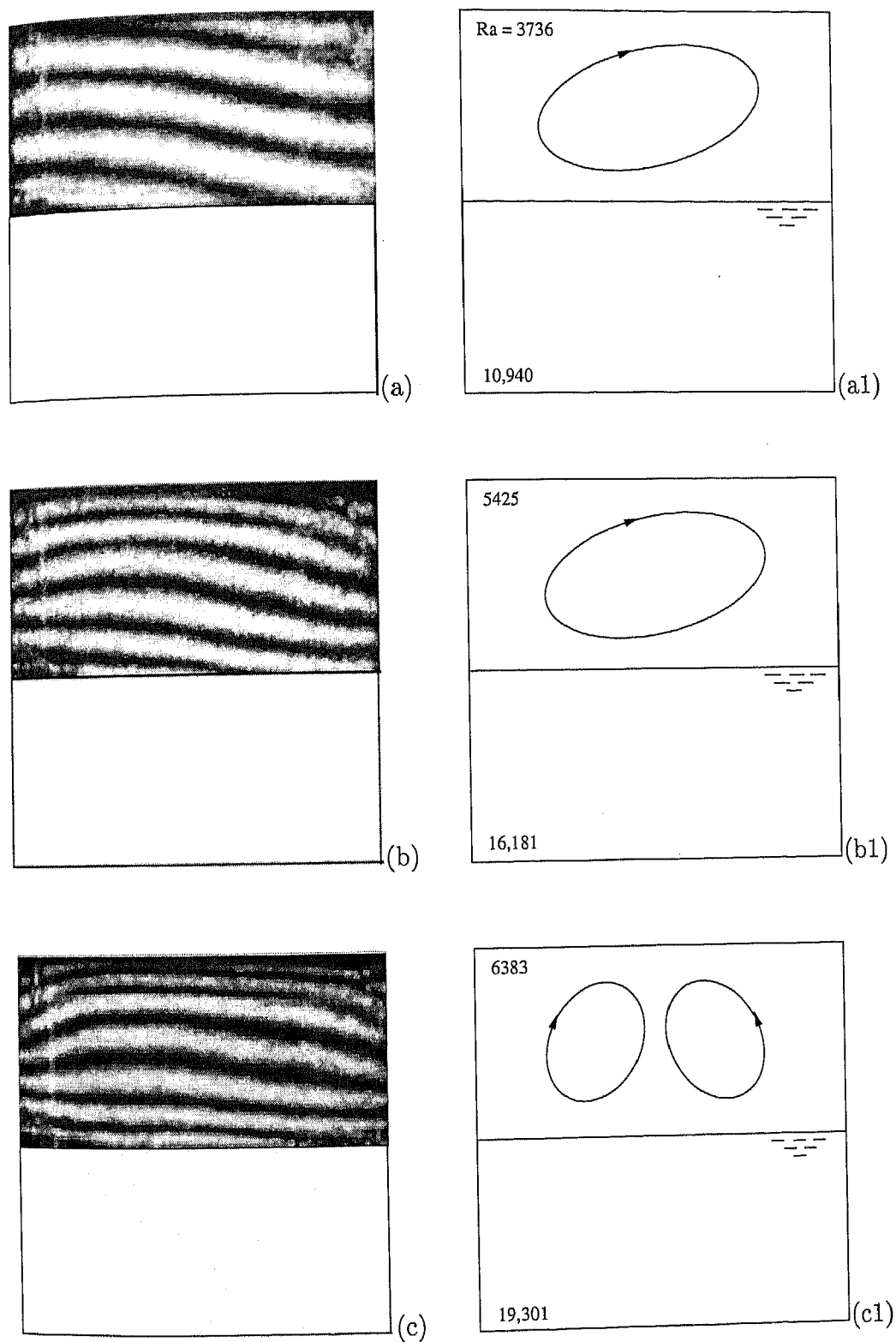


Figure 5.21: Steady state interferograms (a,b,c) and the corresponding roll patterns in the side view (a1,b1,c1) in air for a cavity filled with equal layer heights of silicone oil and air. Cavity temperature differences are (a) 10 K, (b) 15 K and (c) 18 K. Layer Rayleigh numbers are marked on the right column.

summarized in Table 5.6. The interferograms recorded in air were quite similar to those seen in the air-water experiments, in particular Figures 5.4(a-b). In view of the reduced Rayleigh numbers, the fringe displacements were marginally smaller in the air-oil experiments. The Rayleigh numbers in oil being smaller with respect to water (owing to a higher viscosity), the flow patterns in oil were quite stable in time. Hence the coupling between the layers was thermal in origin, as in the water experiments. The possibility of mechanical coupling in the time domain was eliminated since the flow fields in oil were steady at the Rayleigh numbers encountered. The steadiness of the flow field was confirmed against the stability diagram of Krishnamurti (1970, 1973). This result is quite understandable because mechanical coupling is expected to become weaker (and thermal coupling stronger) with an increase in the liquid-to-gas viscosity ratio and smaller buoyancy potential ratio.

Using the fringe patterns of the three experiments of Figures 5.21(a-c), the depth-averaged temperature profiles have been generated. These are shown in Figures 5.22(a-c). It is clear from the figures that the largest temperature drop occurs in air ($\approx 83\%$) as compared to oil. Further, with an increase in the Rayleigh number, the temperature gradient increases at the cold wall ($y/H=0.5$), indicating stronger convection in air.

Local Nusselt number distribution at the cold wall based on the temperature profiles in air are shown in Figures 5.23(a-c). The local Nusselt number variation can be understood in terms of the cellular flow fields prevailing in air. Figure 5.21 shows the field to be unicellular in (a1) and (b1), while it is bicellular in (c1). Width-averaged Nusselt number have been compared with the correlations in Table 5.6. The experimental values are seen to match the correlations quite well.

Table 5.6: Comparison of the experimentally determined width-averaged Nusselt number and interface temperature with the correlations (marked 'Ref') in a cavity filled with equal layer heights of air and oil.

ΔT , K	T_I (Exp), °C	T_I (Ref), °C	Nu (air)	Nu (Ref)	Nu (oil)	Nu (Ref)
0.3	25.88	25.70	-	1.0	0.842	0.728
10	24.33	24.66	1.85	1.78	-	1.97
15	28.28	29.02	1.90	1.98	-	2.25
18	31.28	31.64	2.00	2.08	-	2.39

The interface temperatures in the 2/3rd filled and 1/2 filled cavities can be compared. In the former (Figure 5.17), the interface temperature increases rapidly owing to an intense convective field in air, starting from nearly a conductive state. In Figure

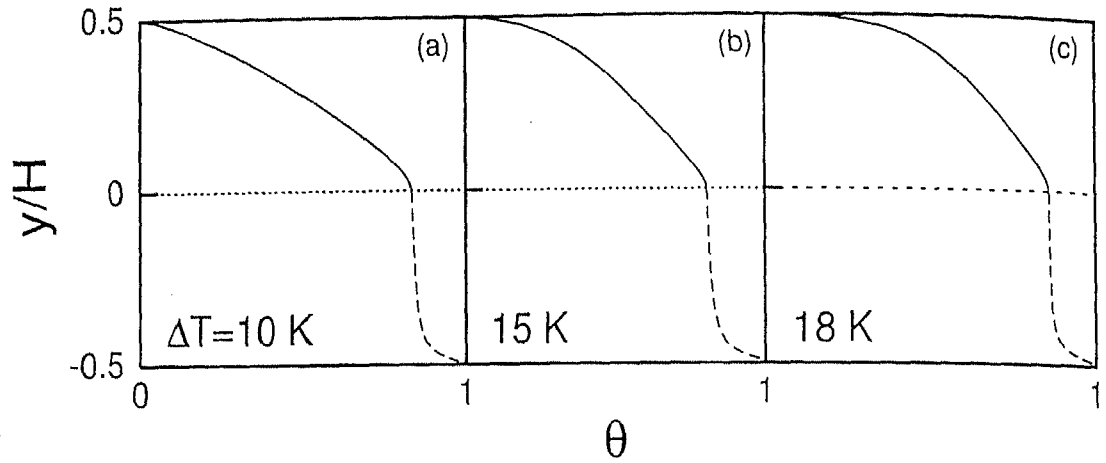


Figure 5.22: Depth-averaged temperature profile in air for a cavity filled with equal layer heights of air and oil; Cavity temperature differences are (a) 10 K, (b) 15 K and (c) 18 K.

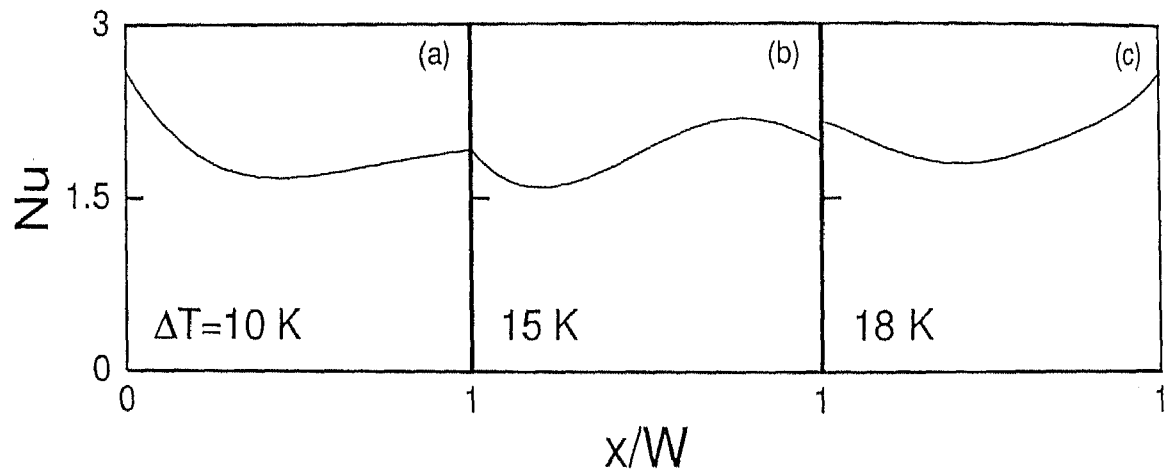


Figure 5.23: Local Nusselt number variation at the cold wall in air for a cavity filled with equal layer heights of air and oil; Cavity temperature differences are (a) 10 K, (b) 15 K and (c) 18 K.

5.22, the buoyant motion in air changes more gradually, making the corresponding effective conductivity nearly a constant. Thus the fractional temperature drops in air and oil are practically unchanged with an increase in the cavity temperature difference. A reasonably good match of the interface temperature and Nusselt number with correlation confirms that the fluid layers are thermally coupled for the three Rayleigh numbers encountered in the experiments.

5.2.3 Cavity 1/3rd filled with silicone oil

The following section presents convection patterns in a rectangular cavity 1/3rd filled with oil, the rest being air. For a temperature difference of 0.3 K applied across the hot and the cold walls, the interferogram is shown in Figure 5.24. The experimentally calculated interface temperature was 25.95°C , while the value from energy balance was 25.94°C . The Rayleigh numbers obtained were 226 and 140 in the air and oil side respectively. As expected at low Rayleigh numbers, almost straight fringes in the oil layer were noticed. Due to large value of ΔT_e for air, no fringe was obtained in air and the field-of-view was bright.

Using the fringe patterns of Figure 5.24 in oil, the depth-averaged temperature profile has been plotted. This is shown in Figure 5.25(a). Due to higher thermal conductivity of oil compared to air, a large temperature drop ($\approx 82\%$) is established across the air layer. Near the hot wall ($y/H = -0.33$), the temperature gradient is lower than at the interface. This is seen in the variation of fringe density within the oil layer. The local Nusselt number distribution based on the temperature profile of Figure 5.25(a) has been

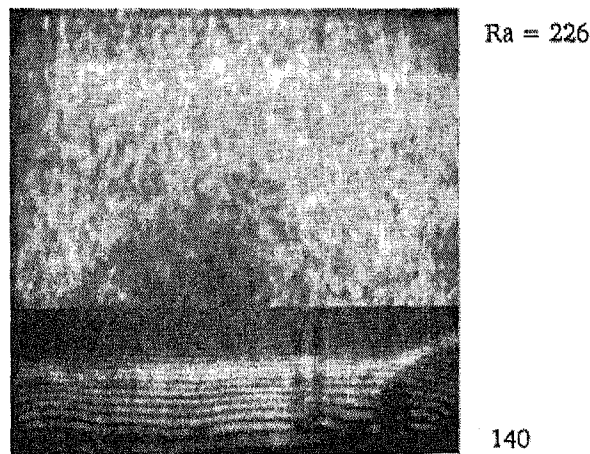


Figure 5.24: Steady state interferograms in a cavity 1/3rd filled with silicone oil. Cavity temperature difference is 0.3 K. Layer Rayleigh numbers are marked on the right side.

presented in Figure 5.25(b). The width-averaged Nusselt number has been calculated on the basis of Figure 5.25(b) and is compared with the single fluid correlations in Table 5.7⁹.

At temperature differences higher than 0.3 K air alone could be imaged and are

⁹The Nusselt number correlation for high Prandtl number fluids permits Nu to fall below unity for low Rayleigh numbers, but is clearly incorrect. In experiments, erroneous Nusselt numbers can emerge at low Rayleigh numbers owing to high fringe density and long-time thermal transients.

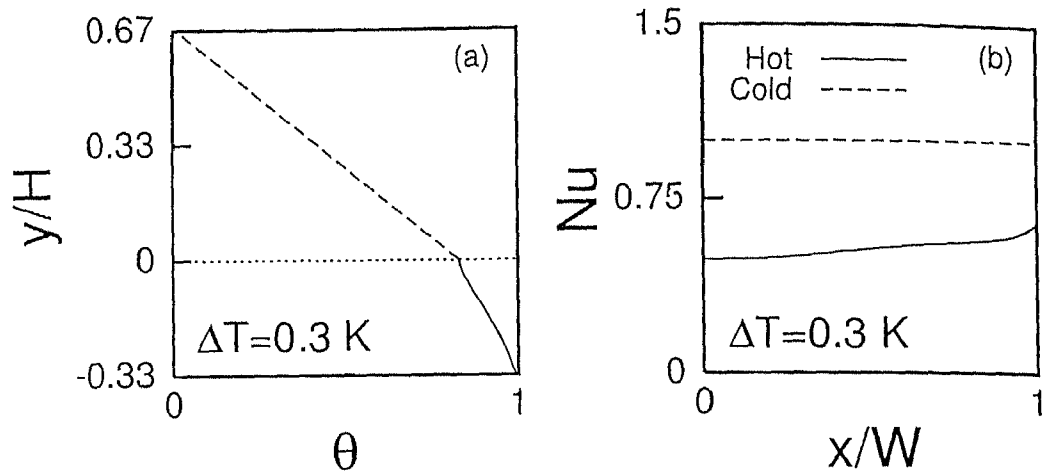


Figure 5.25: (a) Depth-averaged temperature profile in oil and (b) local Nusselt number variation at the hot wall in a cavity 1/3rd filled with oil; Cavity temperature difference is 0.3 K.

shown in Figures 5.26(a,b,c) for 10, 15 and 18 K respectively. The corresponding roll patterns of Figures 5.26(a,b,c) have been respectively shown in Figures 5.26(a1,b1,c1). The Rayleigh numbers calculated in air were 3880, 12,900 and 15,193 respectively and 3183, 4675 and 5541 in silicone oil¹⁰. At the lowest Rayleigh number (Figure 5.26(a)), the pattern was quite steady after the passage of initial transients. For higher Rayleigh numbers (Figure 5.26(b-c)), unsteadiness was noticed in the fringe patterns. Specifically, time-dependent movement between two mode shapes was observed (Figure 5.27). Since a large fraction of the cavity temperature difference occurred in air, the convective motion here was seen to be quite vigorous. As a result, the fringe density near the wall and the interface was extremely high. These images could not be analyzed satisfactorily for local temperature information and Nusselt number. The switching phenomenon, namely the formation of two modes of convection in the fluid layer is characteristic of high Rayleigh numbers. It is itself a topic of interest and has been discussed by Mishra *et al.* (1999). It is indicative of an intermediate step in transition towards chaos.

In the present study, it was possible to capture the momentary appearance of the second mode. The estimated time scale between successive occurrence of the second mode was in the range of 20 seconds, corresponding to a frequency of 0.05 Hz.

Since convection in air is driven by the temperature difference between the interface and cold wall, the nature of coupling in the present experiment between the fluid layers is to be classified as thermal. In the absence of a comparison in terms of the interface

¹⁰The interface temperature for the three experiments were calculated from correlations to be 24.68, 29.07 and 31.71°C, for a hot wall temperatures of 26, 31 and 34°C.

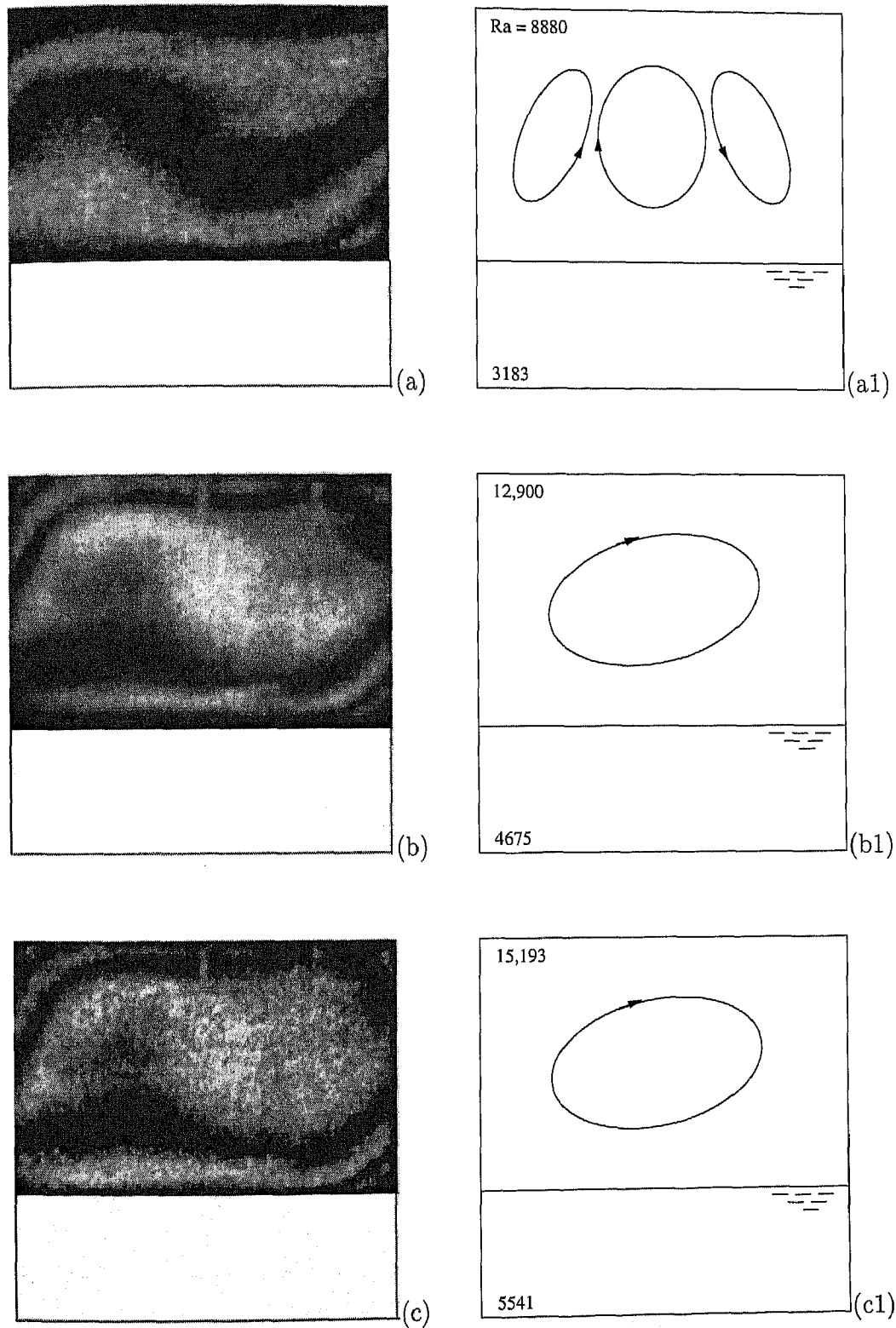


Figure 5.26: Steady state interferograms (a,b,c) and the corresponding roll patterns in the side view (a1,b1,c1) in air for a cavity 1/3rd filled with oil, the rest being air. Cavity temperature differences are (a) 10 K, (b) 15 K, and (c) 18 K. Layer Rayleigh numbers are marked on the right column.

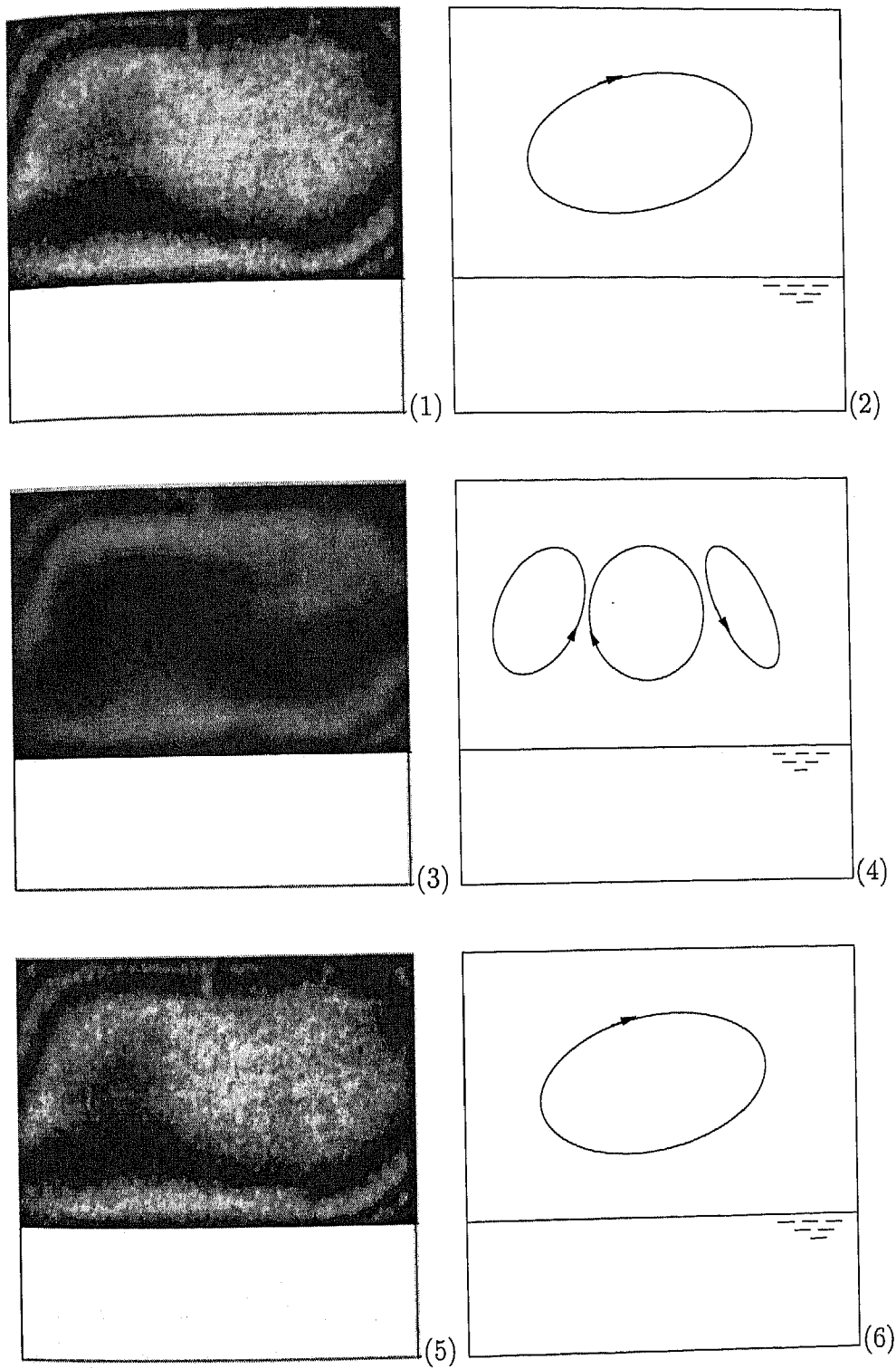


Figure 5.27: Air-silicone oil experiments with $Ra(\text{air}) = 15,193$. The sequence of fringe patterns (1,3,5) and the corresponding roll patterns (2,4,6) formed during the switching phenomenon: Unicellular pattern (1,2) tricellular pattern (3,4) and a return to unicellular rolls (5,6) are to be seen.

temperature and Nusselt number, the extent of mechanical coupling cannot be commented upon.

Table 5.7: Comparison of the experimentally determined width-averaged Nusselt number and interface temperature with the correlations (marked 'Ref') in a cavity 1/3rd filled with oil.

ΔT , K	T_I (Exp), °C	T_I (Ref), °C	Nu (air)	Nu (Ref)	Nu (oil)	Nu (Ref)
0.3	25.95	25.94	-	1.00	0.53	0.46

5.3 Silicone oil-water experiments

Two-layer experiments with silicone oil floating over water within the cavity are reported in the present section. The oil layer thicknesses have been taken to be 1/3, 1/2 and 2/3 with respect to the cavity height. As discussed in the context of air-oil experiments, it was not possible to record the interferograms of convection in oil for temperature differences above $\Delta T=0.3$ K, owing to high refraction errors. These errors were large enough to broaden the dark band at the interface. The band was removed by image processing operations and has not been shown in the present section. Fringe patterns have been recorded at higher temperature differences of 10, 15 and 18 K in the water layer of the cavity. Owing to refraction errors on one hand and a high fringe density on the other, the overall uncertainty in the numerical values of temperature and Nusselt number is expected to be higher in the oil-water experiments.

5.3.1 Cavity 2/3rd filled with silicone oil

The convective patterns obtained in the rectangular cavity filled with 2/3rd oil floating over 1/3rd water are presented in this section. Figure 5.28(a) shows the interferograms seen in the oil-water experiment for an overall temperature difference of 0.3 K. The corresponding roll patterns of Figure 5.28(a) expected on the basis of fringe displacement is shown in Figure 5.28(a1). The cold and the hot surfaces were maintained at 25.7 and 26°C respectively. Using the correlations (Equations 4.27 and 4.28), the interface temperature was calculated to be 25.96°C, while the interferograms gave an average temperature of 25.81°C. Using the correlation-determined interface temperature, the Rayleigh numbers in oil and water were found to be 5163 and 802 respectively. The displacement of the fringes in oil show that convection is in progress. In water, the hot

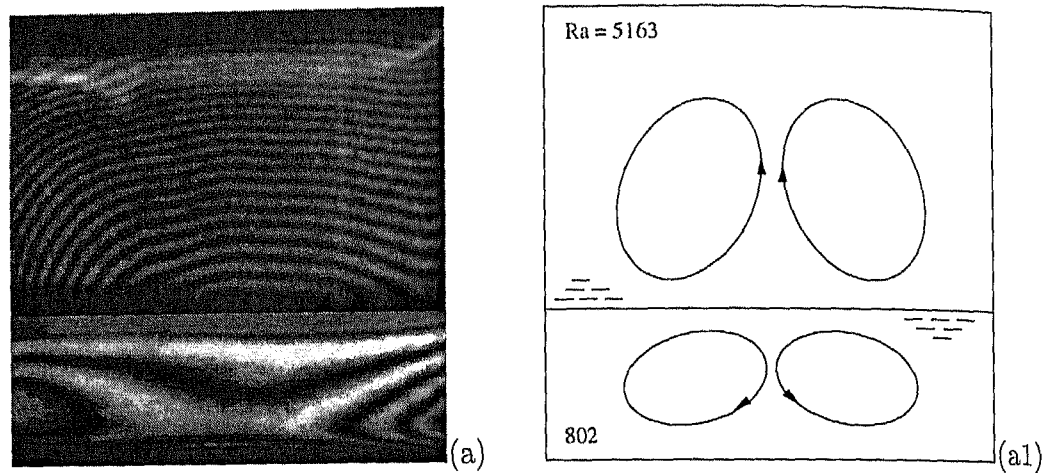


Figure 5.28: Steady state interferograms (a) and the corresponding roll patterns in the side view (a1) in a cavity 2/3rd filled with silicone oil in oil-water experiments; Cavity temperature difference is 0.3 K. Layer Rayleigh numbers are marked on the right column.

wall and the interface region depicts almost straight fringes indicating conduction heat transfer. The central region of the water layer shows initiation of convective motion despite the Rayleigh number being less than the first critical value of 1708. The patterns in both phases were found to be exceptionally steady after the passage of the initial transients. This is in agreement with the stability diagram of Krishnamurti (1970, 1973) at the Rayleigh and Prandtl numbers considered. The number of fringes in silicone oil is greater than in water owing to the smaller temperature drop per fringe shift in oil, being 0.0034 and 0.016 K respectively. The roll orientation in the water layer (however marginal the motion is) can be seen in Figure 5.28 to be quite dependent on the motion in the oil phase. It can be conceived that oil drives convective motion in water via mechanical coupling established at the interface. Based on the fringe displacement, the circulation in silicone oil and water can be established to be bi-cellular (Figure 5.28(a1)). Here, the ascending flow in oil at the cavity center along the vertical axis drives the descending flow of water, suggesting the rotation of the rolls on either side to be in the opposite directions. Thus the coupling between the layers is mechanical in nature.

Using the fringe patterns of Figure 5.28(a), the depth-averaged temperature profiles in the two layers have been determined. This is shown in Figure 5.29(a). Here, the y -coordinate is measured from the interface represented as $y/H=0$ in the plot with oil above and water below it. Figure 5.29(a) shows that the temperature drops in oil ($\approx 64\%$) is higher as compared to water. Due to high density fringes, temperature gradient near the hot wall ($y/H = -0.33$) is marginally higher than the cold wall ($y/H = 0.67$). At the interface, discontinuity in the slope of the temperature profile is to be noticed.

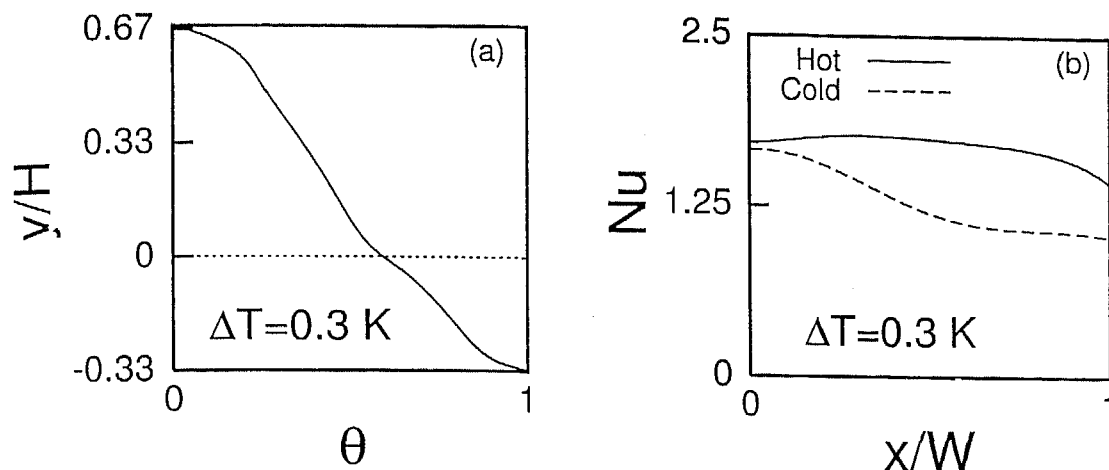


Figure 5.29: (a) Depth-averaged temperature profile and (b) local Nusselt number variation at the two walls in a cavity filled with 2/3rd oil and 1/3rd water; Cavity temperature difference is 0.3 K.

The slope discontinuity is a consequence of the mismatch in thermal conductivities of the two fluids. It is clearly brought out in experiments whenever the number of fringes in the interface region is large. Based on the temperature profiles of Figure 5.29(a), the distribution of local Nusselt number at the hot and cold walls was calculated, and is shown in Figure 5.29(b). The width-averaged Nusselt number obtained from Figure 5.29(b) has been compared with the published correlations in Table 5.8. An examination of the local Nusselt number variation shows it to be flat, independent of the roll structure. This is because the rolls are closer to the interface and do not fill the height available within the cavity. This feature is characteristic of layers that are mechanically coupled. For thermally coupled systems, the presence of the rolls can be felt in the local Nusselt number profiles since the rolls span the distance between the differentially heated surfaces (Section 5.1).

Interferograms in water at higher temperature differences of 10, 15 and 18 K are shown in Figures 5.30(a,b,c). The respective roll pattern of Figures 5.30(a,b,c) have been shown in Figures 5.30(a1,b1,c1). The interface temperatures for the three experiments along with the estimated values have been presented in Table 5.8. The Rayleigh numbers calculated in water for the three temperature differences were 29,062, 55,700 and 73,482 respectively. In oil, the respective Rayleigh numbers were $1.69\text{E}+05$, $2.54\text{E}+05$ and $3.10\text{E}+05$. At the lowest Rayleigh number, the flow pattern was quite stable with time. With an increase in the Rayleigh number, a slight unsteadiness was noticed near the interface. The dominant pattern that was realized in the experiment was captured through the camera and is shown in Figures 5.30(b-c). With an increase in the Rayleigh

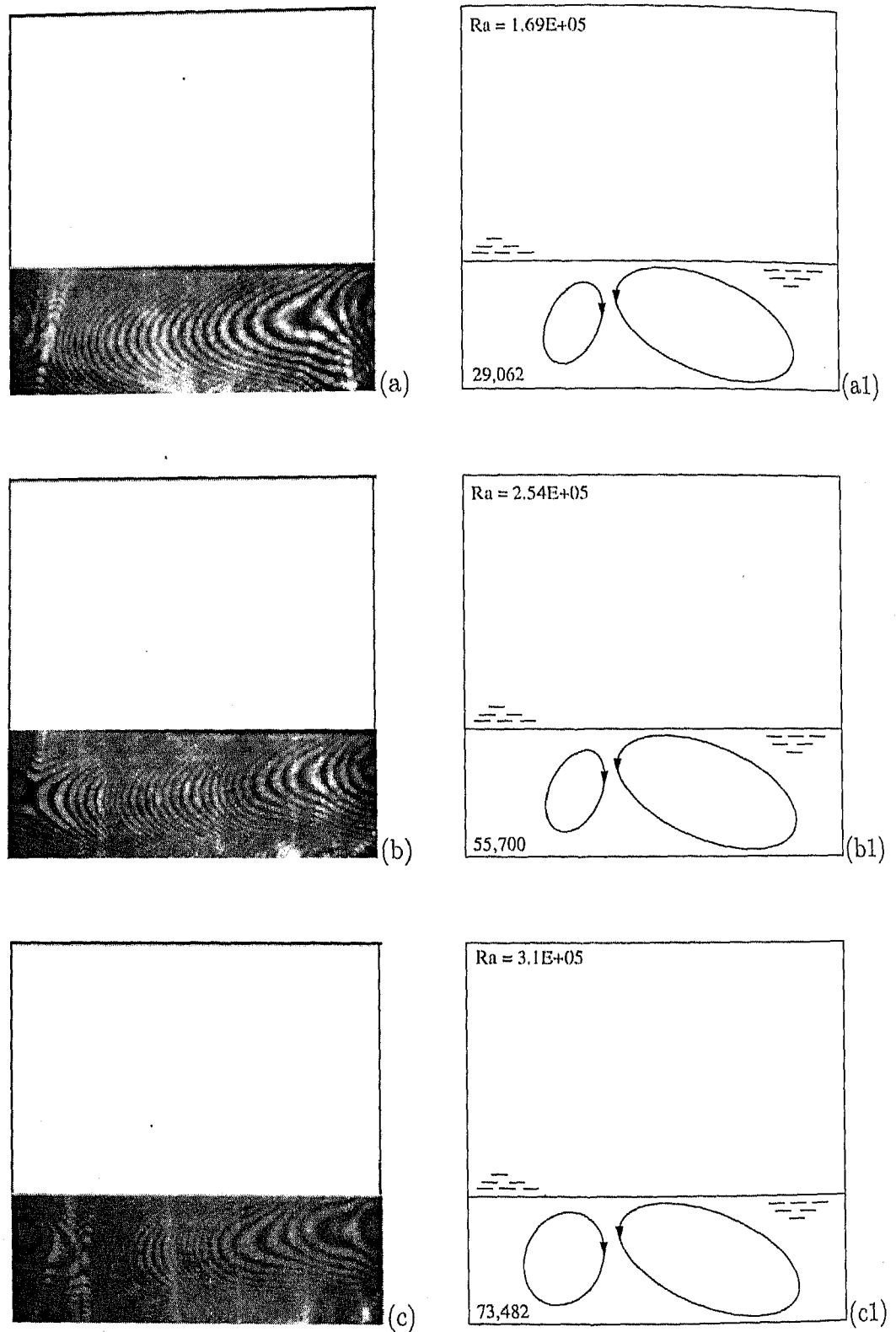


Figure 5.30: Steady state interferograms (a,b,c) and the corresponding roll patterns in the side view (a1,b1,c1) in water for a cavity filled with 2/3rd silicone oil and 1/3rd water. Cavity temperature differences are (a) 10 K, (b) 15 K and (c) 18 K. Layer Rayleigh numbers are marked on the right column.

number, the density of fringes increased to such an extent that the camera could not satisfactorily resolve them, Figure 5.30(c) in particular. In all the three experiments, the flow develops in the form of two counter-rotating rolls with right side roll being quite strong as compared to the left (Figures 5.30(a1-c1)). The left roll can be treated as a weak secondary flow which gains strength as the Rayleigh number increases. It was also noticed that the rolls filled the layer height, extending from the interface to the hot wall.

Using the fringe patterns of Figures 5.30(a-c), the depth-averaged temperature profiles have been plotted in Figures 5.31(a-c). The main conclusion to emerge is that the largest temperature drop takes place in the oil portion (shown by dashed lines in Figures 5.31(a-c))¹¹. With an increase in the Rayleigh number, the temperature drop in oil increases. Using the temperature profiles of Figures 5.31(a-c), the local Nusselt number distribution at the hot wall have been determined. This is shown in Figures 5.32(a-c). The width-averaged Nusselt number based on the local distribution have been calculated and compared with the correlations in Table 5.8. In view of the diminished quality of the interferograms, the uncertainty in temperature and Nusselt number values is expected to be high. The deformation of fringes over the entire cavity height however suggests that the convective field fills the water layer and the fluids are thermally coupled. A continuous increase in the interface temperature with the cavity temperature difference is also a confirmation of this result. There is a consistent reduction in Nusselt number at the hot wall with respect to the single layer correlation, and a corresponding increase in the interface temperature. The origin of this result could be the retardation of the flow in water by the silicone oil layer above. To this extent, the layers are mechanically coupled as well.

Table 5.8: Comparison of the experimentally determined width-averaged Nusselt number and interface temperature with the correlations (marked 'Ref') in a cavity filled with 2/3rd oil and 1/3rd water.

ΔT , K	T_I (Exp), °C	T_I (Ref), °C	Nu (water)	Nu (Ref)	Nu (oil)	Nu (Ref)
0.3	25.81	25.96	1.71	1.49	1.31	1.53
10	25.75	24.77	3.90	4.16	-	4.92
15	30.72	29.16	4.04	4.77	-	5.64
18	33.70	31.76	4.21	5.05	-	6.02

¹¹The dashed lines have been shown by requiring that $\frac{(\partial T/\partial y)|_o}{(\partial T/\partial y)|_w} = k_w/k_o$ at the interface.

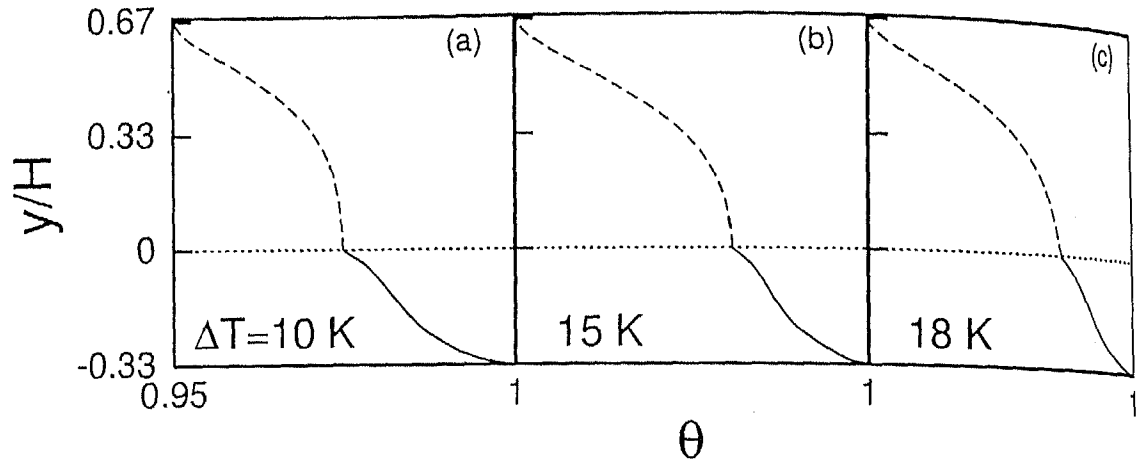


Figure 5.31: Depth-averaged temperature profile in water in a cavity filled with 2/3rd oil and 1/3rd water; Cavity temperature differences are (a) 10 K, (b) 15 K and (c) 18 K.

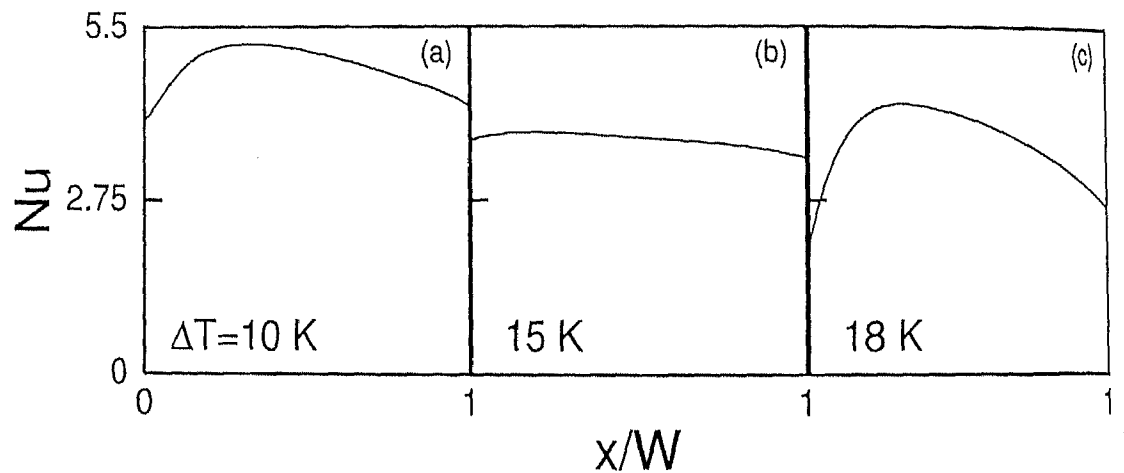


Figure 5.32: Local Nusselt number variation at the hot wall in a cavity filled with 2/3rd oil and 1/3rd water; Cavity temperature differences are (a) 10 K, (b) 15 K and (c) 18 K.

5.3.2 Cavity filled with equal layers of silicone oil and water

The following section discusses convection in the cavity containing equal layer thicknesses of silicone oil and water. The interferogram obtained at a temperature difference of 0.3 K across the cavity is shown in Figure 5.33(a). The respective roll patterns of Figure 5.33(a) have been shown in Figure 5.33(a1). The experimental and the estimated interface temperatures for the present experiment are 25.82 and 25.96°C respectively. Accordingly, the Rayleigh numbers in oil and water were found to be 2178 and 2710, both of which are greater than the critical value of 1708 for the initiation of convection. The displacement of the fringes in both oil and water show that the convection is in

progress in both fluid layers. The patterns were found to be exceptionally steady after the passage of the initial transients. The thermal fields in the two layers can be seen in Figure 5.33 to be partly correlated. Based on the fringe displacement, the circulation in silicone oil can be deduced to be close to bi-cellular, while that in water is practically unicellular (Figure 5.33(a1)). The coupling between the layers is thermal in nature as far as the second (clockwise) roll in silicone oil is concerned. However the primary rolls are mechanically coupled. The fringe patterns of Figure 5.33(a) has been utilised to

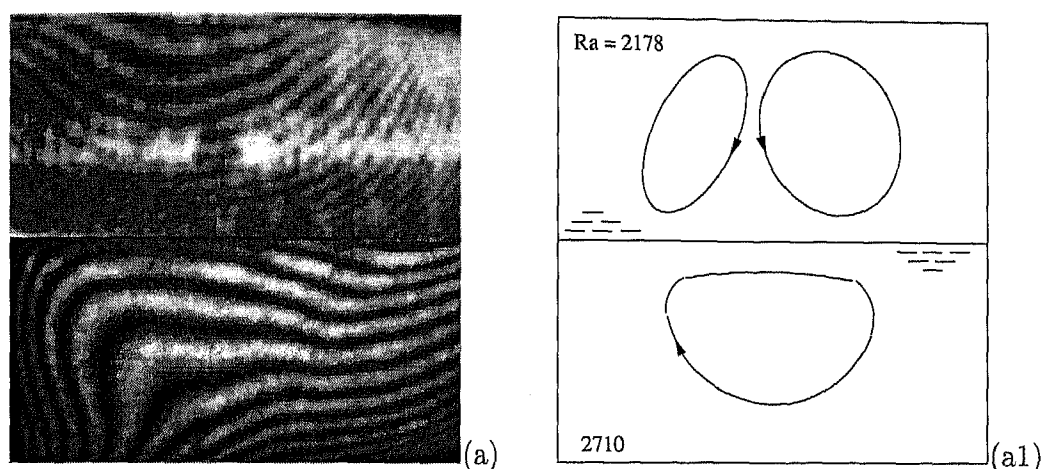


Figure 5.33: (a) Steady state interferograms and (a1) the corresponding roll patterns in a cavity filled with equal layer heights of silicone oil and water; Cavity temperature difference is 0.3 K. Layer Rayleigh numbers are marked on the right column.

determine the depth-averaged temperature profile in the fluid layers. The temperature profile is plotted with respect to non-dimensional vertical coordinate y/H and is shown in Figure 5.34(a). The profile is closer to being linear, since the Rayleigh numbers are only marginally greater than critical. The slope of the temperature profile appears to be continuous at the interface. This suggests the fluids to be thermally coupled at the interface. Using the depth-averaged temperature profile (Figure 5.34(a)) in the fluids, the local Nusselt number variation over hot and cold walls can be determined. This distribution of Nusselt number with respect to non-dimensional horizontal coordinate x/W is shown in Figure 5.34(b). Based on local variation at the two walls, the width-averaged Nusselt number has been calculated and compared with the correlations in Table 5.9.

The portion of the interferogram depicting convection in silicone oil has been omitted while that in water is shown in Figures 5.35(a,b,c) for temperature differences of 10, 15 and 18 K respectively. The corresponding roll patterns of Figures 5.35(a,b,c) have been shown respectively in Figures 5.35(a1,b1,c1). The interface temperatures for

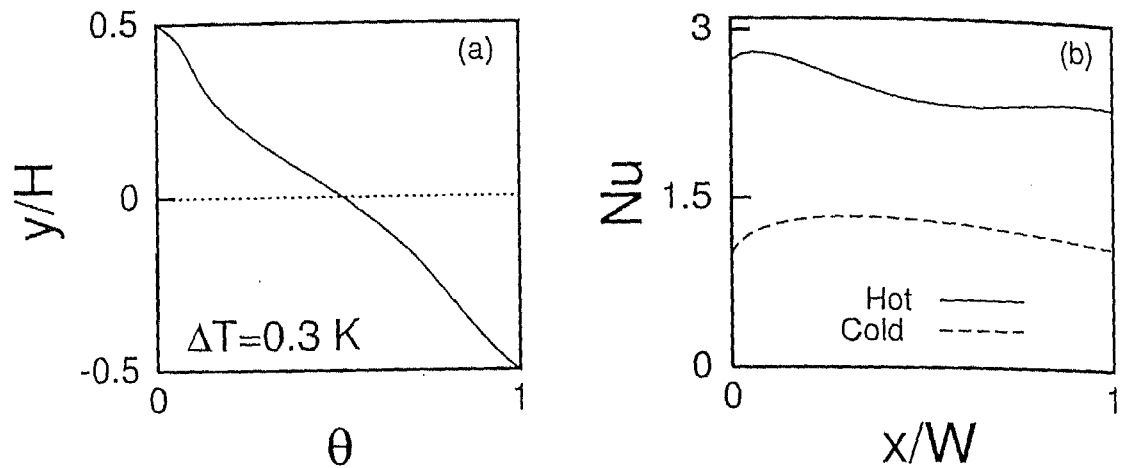


Figure 5.34: (a) Depth-averaged temperature profile and (b) local Nusselt number variation at the two walls in a cavity filled with equal layer heights of oil and water; Cavity temperature difference is 0.3 K.

the three experiments are summarized in Table 5.9. The Rayleigh numbers obtained in water are 1.09×10^5 , 2.07×10^5 and 2.83×10^5 respectively for the three temperature differences. The corresponding values for silicone oil are 69,849, 1.05×10^5 and 1.27×10^5 . The driving buoyancy potential in water indicates more vigorous buoyant motion in the fluid. At the lowest Rayleigh number (Figure 5.35(a)), the fringes displayed an almost steady pattern in time. This was confirmed by continuing the experiment for six to eight hours. Steady flow patterns obtained in water at a Rayleigh number of 1.09×10^5 is a result contrary to the flow regime diagram of Krishnamurti (1970, 1973). The steadiness can only be attributed to the presence of silicone oil above water, and the resulting stabilizing influence. The wide disparity in the average interface temperatures calculated by the correlation as well as the experiment can be traced to this factor. It is also to be expected that the thermal fields in the experiment are fully three dimensional. The interferograms obtained at the higher Rayleigh numbers (Figures 5.35(b-c)) showed some unsteadiness, the fringe patterns switching among 3-4 and 5-6 states respectively in the central portion of the cavity. The most long-lived pattern recorded during four hours of experimentation has been shown in Figures 5.35(b-c). Using the fringe patterns of Figures 5.35(a-c), the temperature profiles in the water portion of the cavity have been drawn in Figures 5.36(a-c). The figure indicates a larger temperature drop in oil as compared to water. The temperature drop first decreases and then increases in the oil portion with increase in the Rayleigh number. Correspondingly, the changes in the interface temperature are not monotonic. This situation is encountered when the effective conductivity (molecular + convective) of one layer does not change systematically with respect to the other. The molecular conductivity can be augmented by fluid motion via

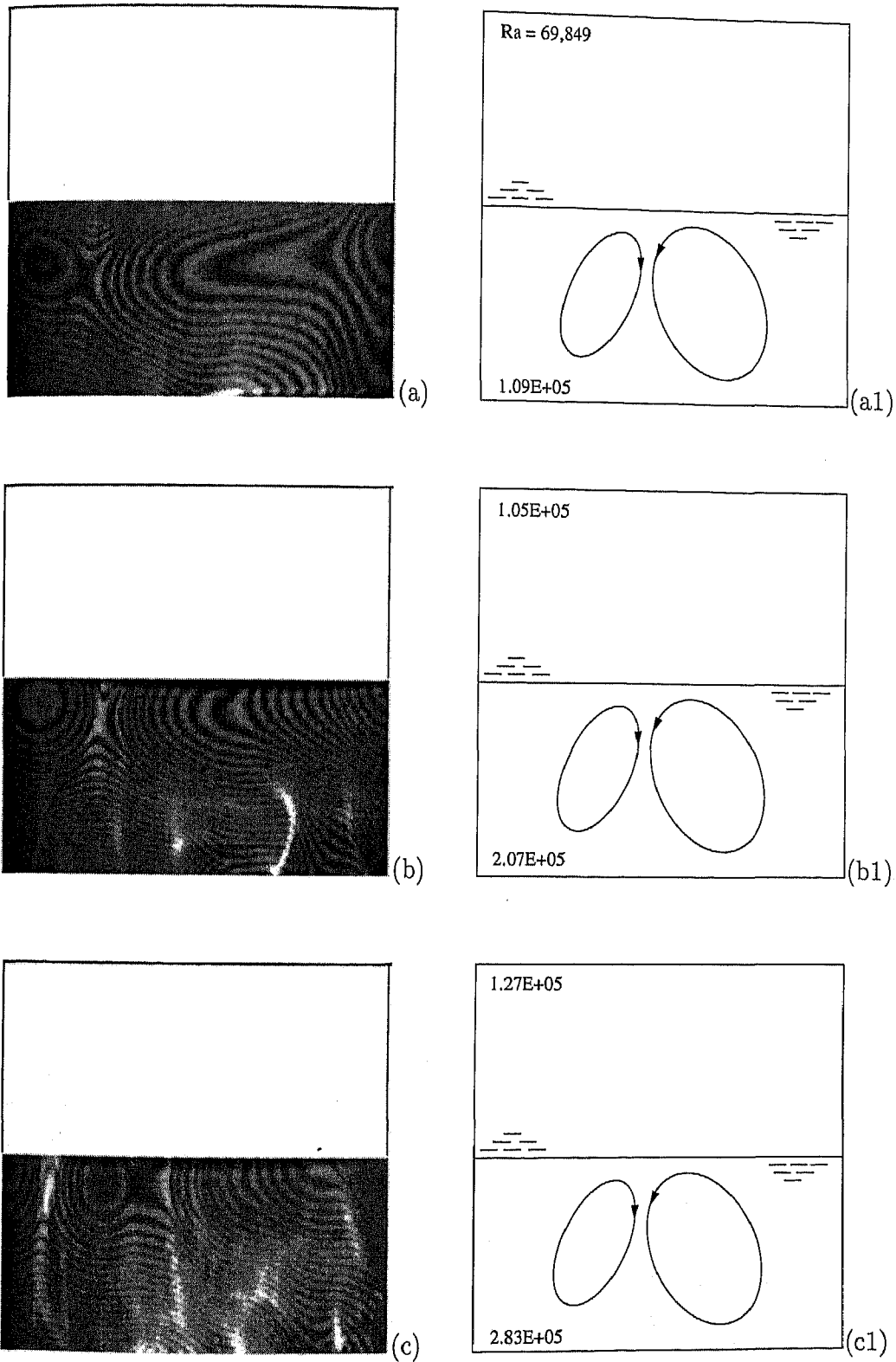


Figure 5.35: Steady state interferograms (a,b,c) and the corresponding roll patterns in the side view (a1,b1,c1) in water for a cavity filled with equal layer heights of silicone oil and water. Cavity temperature differences are (a) 10 K, (b) 15 K and (c) 18 K. Layer Rayleigh numbers are marked on the right column.

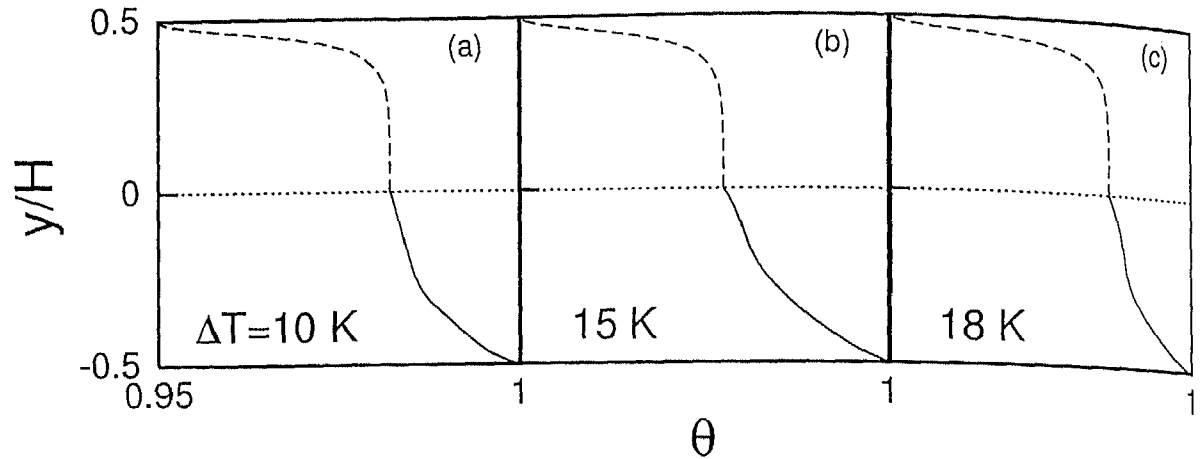


Figure 5.36: Depth-averaged temperature profile in the water portion in a cavity filled with equal layer heights of oil and water; Cavity temperature differences are (a) 10 K, (b) 15 K and (c) 18 K.

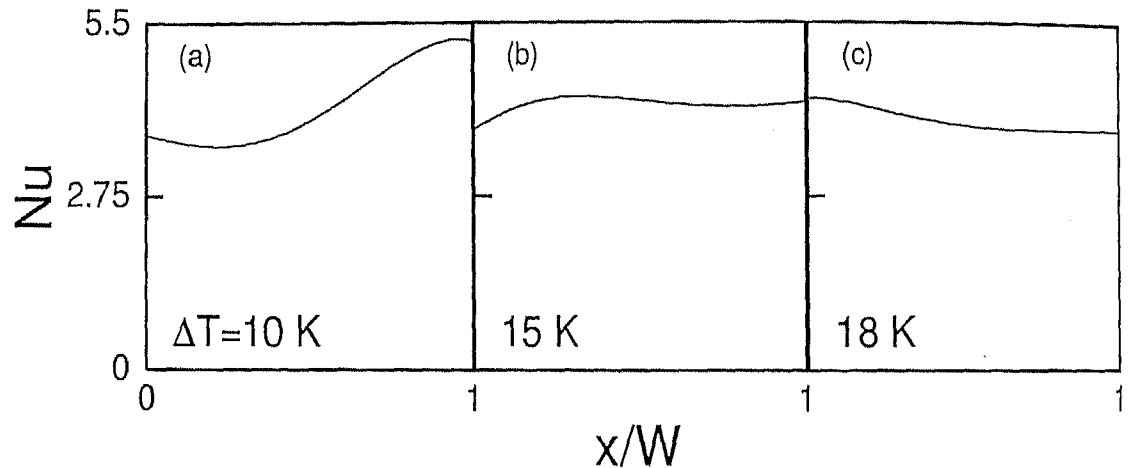


Figure 5.37: Local Nusselt number variation at the hot wall in a cavity filled with equal layer heights of oil and water; Cavity temperature differences are (a) 10 K, (b) 15 K and (c) 18 K.

the Nusselt number and hence the Rayleigh number. The augmentation is more pronounced (a) at lower Rayleigh numbers, and (b) at points of transition in the flow pattern. The augmentation is seen in gas-liquid as well as liquid-liquid combinations, though it is more prominent in the later since the molecular conductivity contrast is smaller. Equivalently, The Rayleigh number ratio is closer to unity unless the layer heights are equal. In gas-liquid layers, the basic temperature profile (and the overall Rayleigh number ratio) is determined by the conductivity ratio, but smaller fluctuations in the interface temperature occur with a change in the cavity temperature difference.

The local Nusselt number distribution at the hot wall is shown in Figures 5.37(a-c).

Table 5.9: Comparison of the experimentally determined width-averaged Nusselt number and interface temperature with correlations (marked 'Ref') in a cavity filled with equal layer heights of oil and water.

ΔT , K	T_I (Exp), °C	T_I (Ref), °C	Nu (water)	Nu (Ref)	Nu (oil)	Nu (Ref)
0.3	25.82	25.96	2.49	2.20	0.93	1.15
10	25.86	24.60	4.20	5.49	-	3.67
15	30.66	28.90	4.21	6.29	-	4.21
18	33.68	31.50	3.95	6.72	-	4.47

Based on Figures 5.37(a-c), the heat transfer rates at the walls have been presented in terms of width-averaged Nusselt number and compared with the correlations in Table 5.9. The discrepancy in the comparison can be traced to mechanical coupling between the fluid layers at lower temperature differences and unsteadiness in water at higher temperature differences. The first factor namely the retardation of the convection cells, is dominant over the entire temperature range studied. This is to be seen by the consistent reduction in the Nusselt number in water, with respect to the correlations.

5.3.3 Cavity 2/3rd filled with water and 1/3rd oil

In the present section, convection patterns based on the water layer filling 2/3rd of the cavity are discussed. Figure 5.38(a) and 5.38(a1) respectively shows the interferogram and the corresponding roll patterns for the oil-water experiment with a temperature difference of 0.3 K across the cavity. The experimental and estimated interface temperatures were 25.85 and 25.96°C respectively. Accordingly, the Rayleigh numbers calculated on the water and oil sides temperature were 6610 and 643 respectively. In the oil phase, no-flow condition exists as the Rayleigh number is less than the critical value and the fringes appeared straight. The water phase being subjected to a higher Rayleigh number showed convective flow that was quite steady in time. The fringe displacement in Figure 5.38(a) suggests the circulation to be close to unicellular in the clockwise direction (Figure 5.38(a1)). Here, the interface acts as a cold and hot boundary respectively for the water and the oil layers. Since the motion in water is barely communicated to oil, it may be predicted that the two-layers are thermally coupled at the interface. Based on the fringe patterns of Figure 5.38(a), the depth-averaged temperature profile has been plotted in Figure 5.39(a). The profile looks close to linear with comparable temperature drops in oil and water. The slope discontinuity is partially revealed at the interface. Based on the depth-averaged temperature profiles, the local Nusselt number distribution

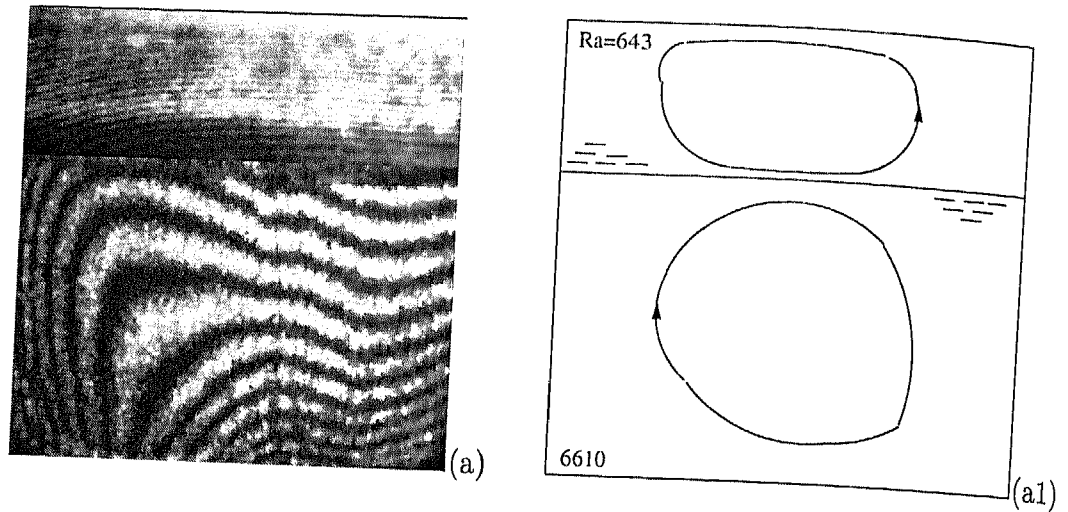


Figure 5.38: (a) Steady state interferograms and (b) corresponding roll patterns in a cavity filled with 1/3rd silicone oil and 2/3rd water; Cavity temperature difference is 0.3 K. Layer Rayleigh numbers are marked on the right column.

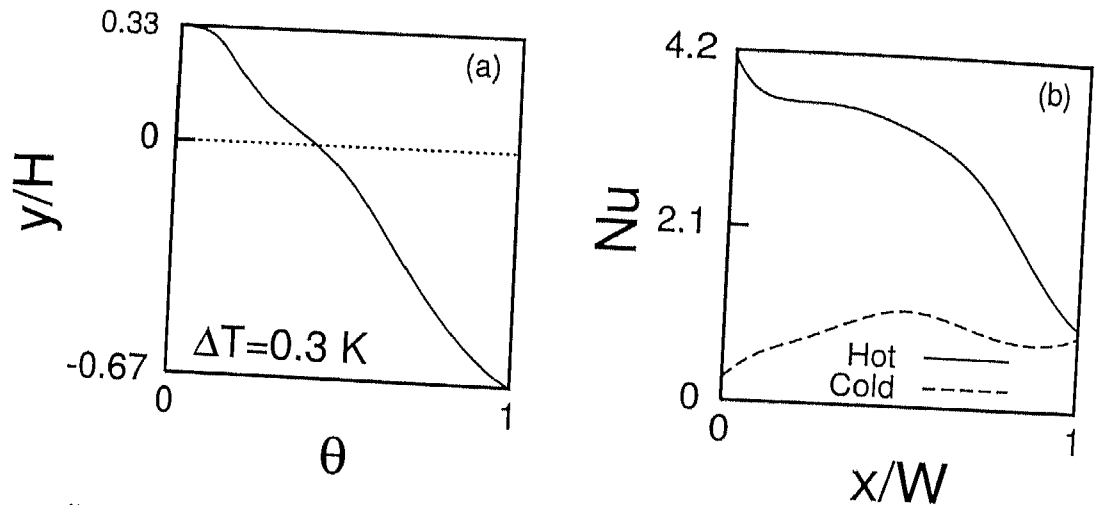


Figure 5.39: (a) Depth-averaged temperature profile and (b) local Nusselt number variation at the two walls in a cavity filled with 1/3rd oil and 2/3rd water; Cavity temperature difference is 0.3 K.

at the two walls have been depicted in Figure 5.39(b). The local Nusselt number in water shows considerable variation with distance. It is however close to unity in oil, indicating a conduction regime. The width-averaged Nusselt number at hot and cold walls based on Figure 5.39(b) have been compared with the correlations in Table 5.10. In view of thermal coupling between the layers, the experimental average Nusselt number in water is in good agreement with the correlations.

For the higher cavity-based temperature differences of 10, 15 and 18 K, the interferograms in water have been shown in Figures 5.40(a,b,c). The respective roll patterns of Figures 5.40(a,b,c) have been shown in Figures 5.40(a1,b1,c1). The interface temper-

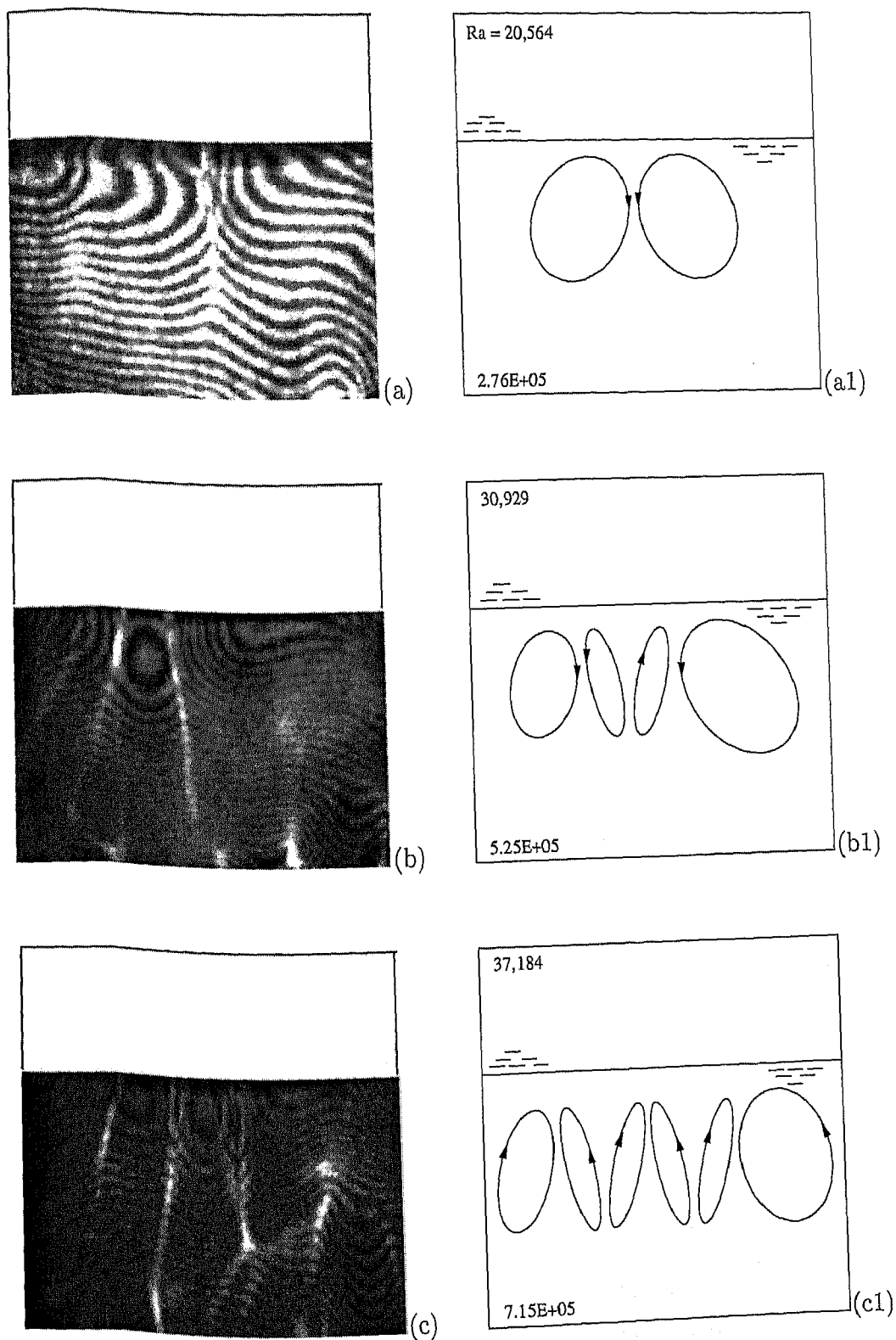


Figure 5.40: Steady state interferograms (a,b,c) and the corresponding roll patterns (a1,b1,c1) in water for a cavity filled with layer heights of 1/3rd silicone oil and 2/3rd water. Cavity temperature differences are (a) 10 K, (b) 15 K, and (c) 18 K. Light streaks are possibly inter-roll boundaries.

atures obtained have been summarized in Table 5.10. The Rayleigh numbers calculated in the water phase were 2.76×10^5 , 5.25×10^5 and 7.15×10^5 respectively for the three temperature differences. The corresponding values for oil were 20,564, 30,924 and 37,184. The flow patterns obtained in Figure 5.40(a) were quite steady with time even though the driving buoyancy potential was very high. This is once again due to the stabilizing effect of oil which retards the flow in water. It is clear evidence of mechanical coupling between the fluid layers. With an increase in the Rayleigh number (Figures 5.40(b-c)), the flow in water showed some unsteadiness near the interface. The flow were seen to switch among 4-6 states with time. The dominant pattern has been captured and are presented in Figures 5.40(b-c). Using the fringe patterns of the three experiments of Figures 5.40(a-c), the depth-averaged temperature profiles in the water phase have been determined. This are shown in Figures 5.41(a-c). The main conclusion to emerge from the figure is that a considerably larger temperature drop occurs in oil as compared to water. The interface temperature shows a greater variability with respect to the cavity temperature difference. The local Nusselt number distribution based on the temperature profiles have been estimated at the hot wall and is shown in Figures 5.42(a-c). The width-averaged Nusselt number at the hot wall was calculated and compared with the correlations, Table 5.10. A high discrepancy is to be noticed between the two sets of interface temperatures and Nusselt numbers. As in Section 5.3.2, the source of the discrepancy is mechanical coupling at $\Delta T = 10$ K, and additionally, fringe unsteadiness at higher temperature differences.

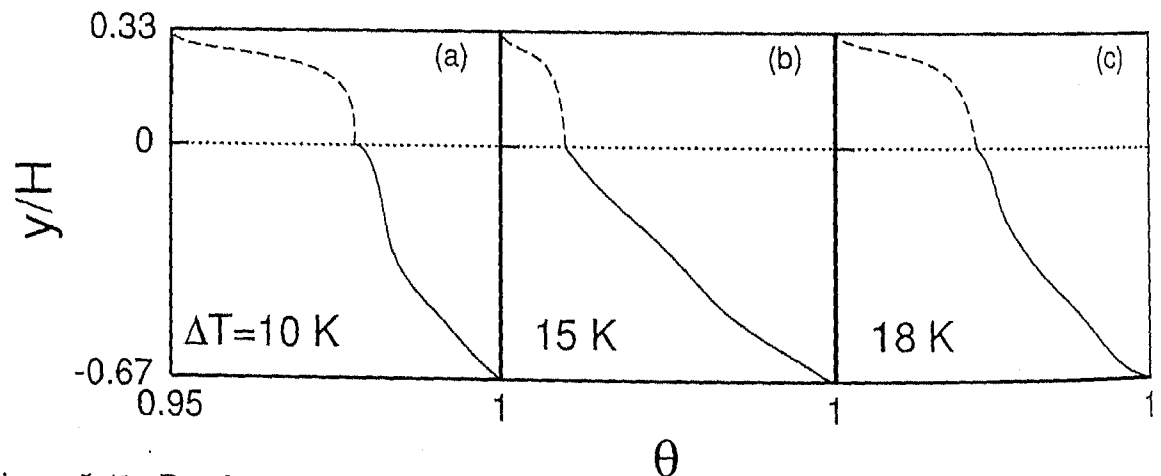


Figure 5.41: Depth-averaged temperature profile in water for a cavity filled with layer heights of 1/3rd oil and 2/3rd water; Cavity temperature differences are (a) 10 K, (b) 15 K and (c) 18 K.

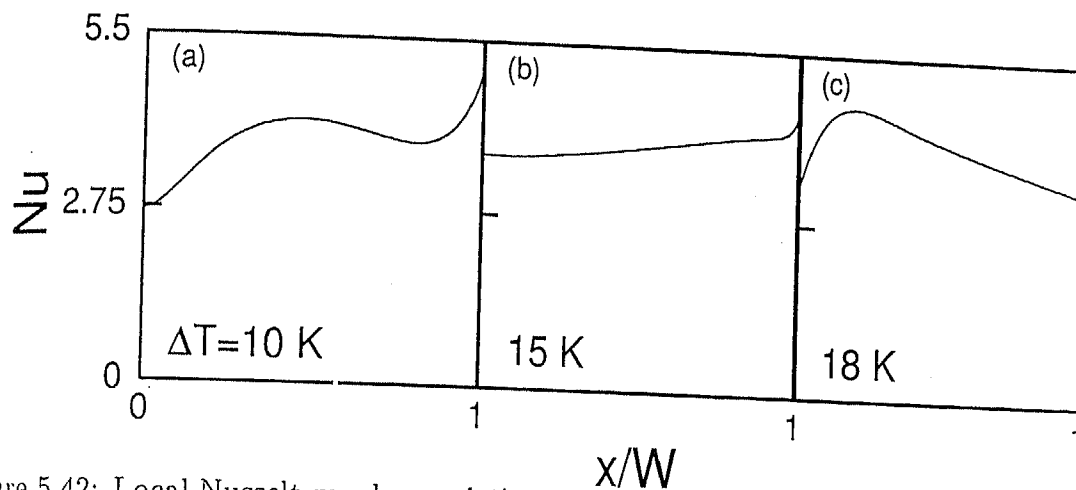


Figure 5.42: Local Nusselt number variation at the hot wall in a cavity filled with 1/3rd oil and 2/3rd water; Cavity temperature differences are (a) 10 K, (b) 15 K and (c) 18 K.

Table 5.10: Comparison of the experimentally determined width-averaged Nusselt number and interface temperature with correlations (marked 'Ref') in a cavity filled with layer heights of 1/3rd oil and 2/3rd water.

ΔT , K	T_f (Exp), °C	T_i (Ref), °C	Nu (water)	Nu (Ref)	Nu (oil)	Nu (Ref)
0.3	25.85	25.96	3.03	2.91	0.87	0.76
10	25.86	24.48	4.80	6.69	-	2.43
15	30.67	28.74	3.71	7.70	-	2.79
18	33.49	31.32	3.74	8.25	-	2.97

5.3.4 Temporal evolution

A time sequence of interferograms in an unsteady field in silicone oil-water experiments is presented below. The fringe patterns shown are for water. Layer heights of 1/2 and 2/3 with respect to the cavity height and a temperature difference of 18 K have been considered.

The fringe patterns of Figure 5.35(c) (1/2 oil-1/2 water, 18 K) was the dominant pattern recorded for data analysis. The unsteadiness noticed in that experiment has been shown in Figures 5.43(a-f). The time interval between two successive image captured was around 15 seconds. The fringe patterns in the region near the hot wall were almost steady indicating dominance of diffusive heat transfer. Higher unsteadiness was observed near the interface region. The unsteady fringe patterns for the experiments of Figures 5.40(b-c) (1/3 oil-2/3 water, 18 K) have been presented in Figures 5.44(a-f). Unsteadiness was noticed both at the hot wall and the interface region. The time interval between two successive images was around 5 seconds, indicating a stronger convective motion. Both

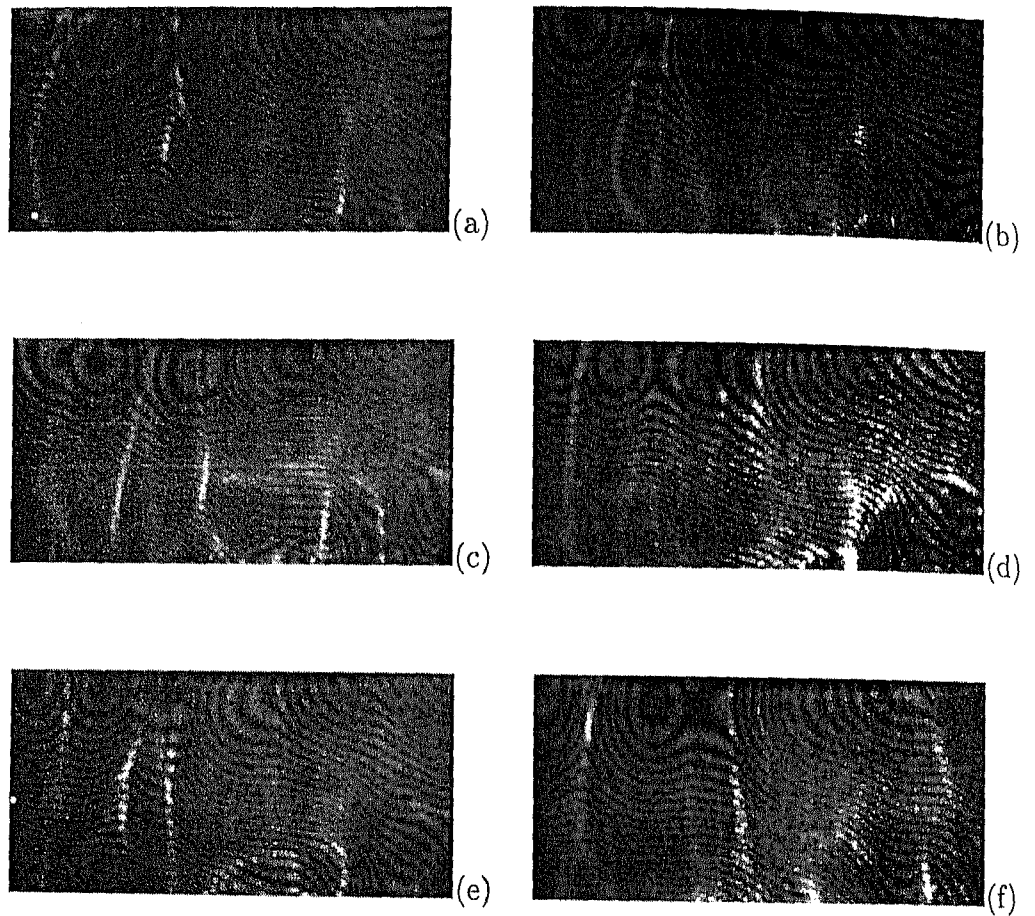


Figure 5.43: Time sequence of interferograms in water for a cavity temperature difference of 18 K; silicone oil-water experiments with equal layer thicknesses. Time interval between two successive images is 15 seconds.

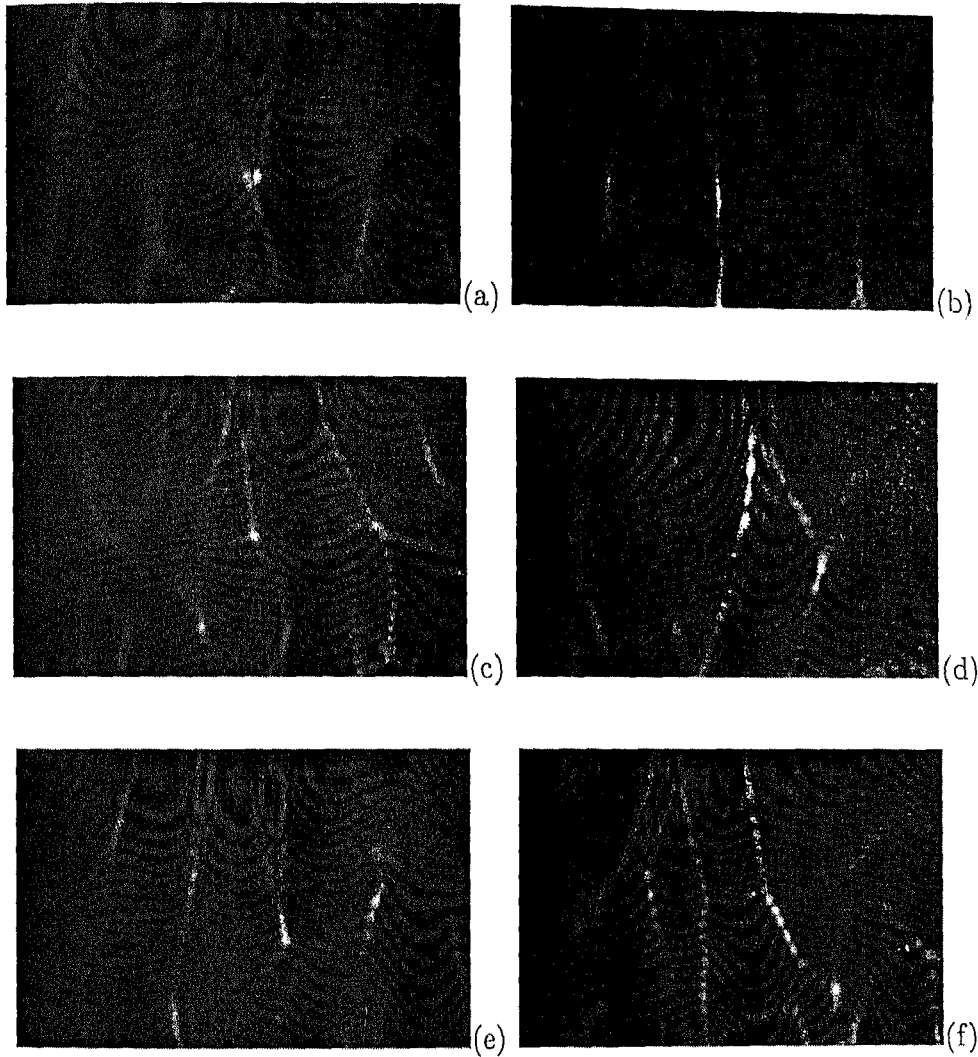


Figure 5.44: Time sequence of interferograms in water for a cavity temperature difference of 18 K; silicone oil-water experiments with 2/3rd water and 1/3rd oil in the cavity. Time interval between two successive images is 5 seconds.

sets of images show light streaks coinciding with local fringe extrema. They can be associated with large thermal gradients and hence strong refraction.

5.4 Nature of coupling

The two modes of coupling namely thermal and mechanical, obtained in the experiments for all fluid combinations and layer heights have been summarized in Table 5.11. In any given experiment, both modes are present. Differences are seen only with respect to their relative importance. The following observations are to be recorded with reference to the coupling mechanism established at the interface.

Table 5.11: Summary of Mechanical (M) and Thermal (T) coupling modes obtained in air-water, air-oil and oil-water experiments for all layer heights. A dominant thermal coupling in which mechanical coupling is present but secondary is indicated as T_M . When both modes are important, the notation T-M is employed.

Fluid combinations	ΔT , K				Remarks
	0.3	10	15	18	
1/3 air 2/3 water	-	T	T	T	1, 4, 5, 6, 7 and 8
1/2 air 1/2 water	-	T	T	T_M	1, 4, 5, 6, 7 and 8
2/3 air 1/3 water	-	M_T	M_T	M_T	5, 6
1/3 air 2/3 oil	T	M_T	M_T	T-M	4, 5 and 6
1/2 air 1/2 oil	T	T	T	T	4, 6 and 7
2/3 air 1/3 oil	T	T	T	T	2, 4 and 6
1/3 water 2/3 oil	M_T	M_T	M_T	M_T	3, 5 and 7
1/2 water 1/2 oil	M_T	M_T	M_T	M_T	3, 4, 5, 6 and 8
2/3 water 1/3 oil	T_M	M_T	M_T	M_T	3, 4, 5, 6 and 8

1. In the experiments involving air, the layers were found to be thermally coupled. The unsteadiness in water could however be transmitted to air in the mechanical coupling mode.
2. The switching phenomena, a step towards chaos via time-dependent flow, was noticed in the air portion of air-oil experiments at Rayleigh numbers higher than 12,900.
3. The presence of silicone oil over water led to mechanical coupling in the sense that the convective field in water was visibly retarded.
4. The interface temperature determined from the experiments matched those from correlations for a single fluid whenever the coupling was thermal in origin. The differences were higher during mechanical coupling and in cases where the time-dependent switching phenomena occurred. The temperature drop developed in the upper fluid layer based on the interface temperature obtained is shown with respect to the cavity based temperature difference in Figure 5.45.
5. Heat transfer rates in terms of the non-dimensional width-averaged Nusselt number matched well with the correlations at lower Rayleigh numbers. Deviation tends to increase with increase in the Rayleigh numbers, in particular with the experiments involving water.
6. During thermal coupling, the flow regimes in the individual layers matched those

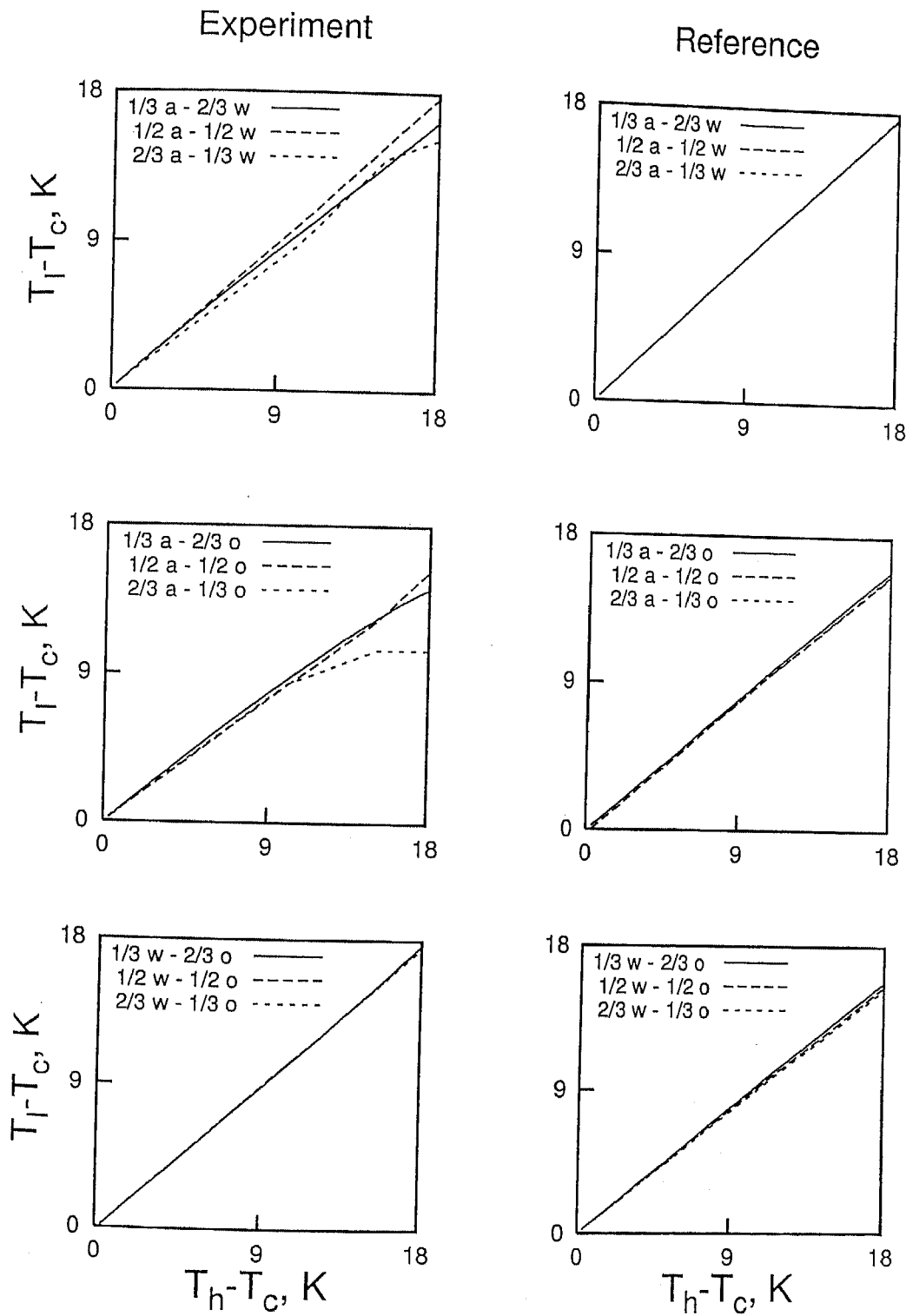


Figure 5.45: Comparison between experiment (left column) and reference (right column) for the cavity temperature difference as a function of the temperature drop across the upper fluid layer for all fluid combinations and layer heights.

specified for single fluid layers at the Rayleigh number based on the layer height and the temperature difference with respect to the interface.

7. The interface deformation was uniformly small in all the experiments, indicating that mechanical coupling though present, had not become a primary mechanism linking the fluid layers. Surface tension as well as its gradients were also uniformly small in the experiments. The interface deformation correlated with the roll movement visible in the fringes.
8. Based on interface deformation, three-dimensional effects were noticed in the experiments involving water that led to movement of interface and oscillation of light streaks with their origin at the lower heated surface of the cavity.

5.5 Flow characteristics at comparable Rayleigh numbers

Convection patterns in the individual fluid layers in different experiments for Rayleigh numbers that are within $\pm 10\%$ of each other are compared in the present section. In single-fluid convection, the thermal field is uniquely determined by the Rayleigh and Prandtl numbers. In superposed fluid layers, a variety of other parameters are significant. However, in the present study the additional factor that was seen to control convection was the nature of coupling between the fluid phases, and the thermal conductivity and viscosity ratios.

Interferograms in air from air-water and air-oil experiments are compared in Figure 5.46. The Rayleigh number here is close to the critical value of 1708. In the air-water experiment, a weak convective roll is to be seen. In the air-oil experiment, the fluid movement closer to the cavity center is indicative of two rolls, despite a subcritical Rayleigh number. The appearance of one as opposed to two rolls is related to the uncertainties of the Rayleigh-Benard experiment itself. The single roll, however is characteristic of convection in an air-filled cavity and thus may be expected under conditions of thermal coupling. The twin rolls in the air-oil experiment at subcritical Rayleigh numbers can be linked to mechanical coupling of the fluid layers¹².

The fringe patterns in air at higher Rayleigh numbers are compared in Figures 5.47(a-b) for air-water and air-oil combinations and equal fluid layer heights. The thermal fields in air look similar in terms of the displacement and fringe spacing. The convective

¹²Mechanical coupling initiates fluid motion in this experiment.

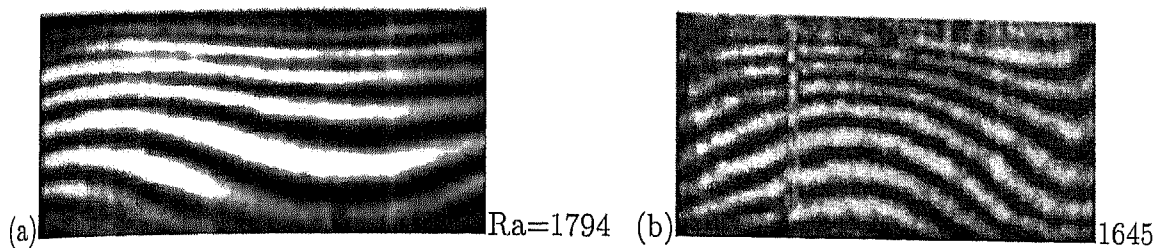


Figure 5.46: Interferograms obtained in air in a cavity containing layers of (a) 1/3 air and 2/3 water, $\Delta T = 15$ K and (b) 1/3 air and 2/3 oil, $\Delta T = 15$ K.

field is more vigorous in (a) compared to (b). The thermal fields in both experiments

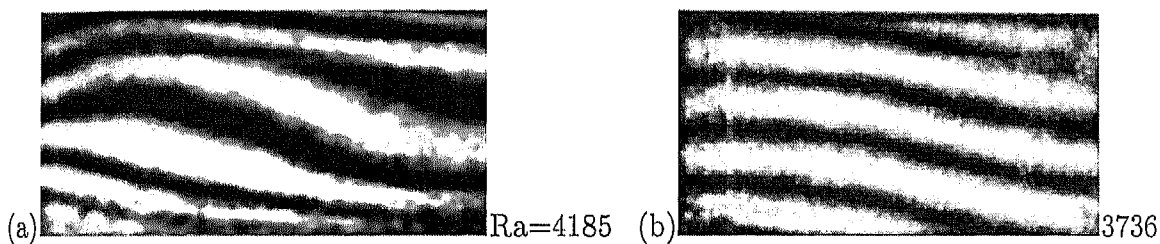


Figure 5.47: Interferograms obtained in air in a cavity containing layers of (a) 1/2 air and 1/2 water, $\Delta T = 10$ K and (b) 1/2 air and 1/2 oil, $\Delta T = 10$ K.

were quite steady, while flow pattern was unicellular in the clockwise direction. The nature of coupling can be inferred to be thermal for this set of experiments.

The fringe patterns obtained in water for different fluid combinations are compared in Figures 5.48(a-b). Four and two counter-rotating rolls are seen in (a) and (b) respec-

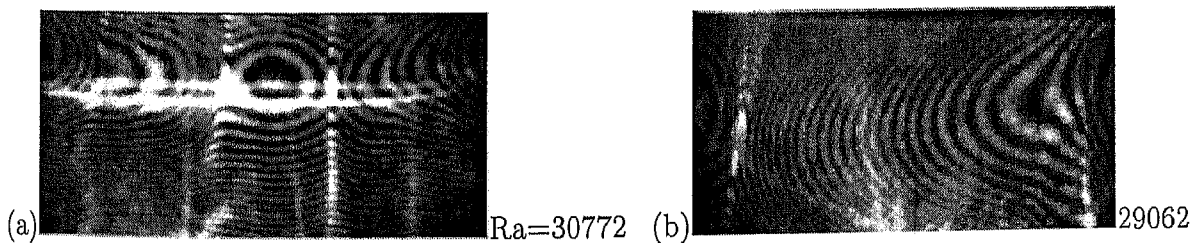


Figure 5.48: Interferograms obtained in water in a cavity containing layers of (a) 1/2 air and 1/2 water, $\Delta T = 15$ K and (b) 1/3 water and 2/3 oil, $\Delta T = 10$ K.

tively. The rolls in the air-water experiment are closer to the interface region while those in air-oil scale the full cavity height. The flow in (a) exhibited mild unsteadiness while in (b) it was quite steady. The flow field in (b) is thus stabilized by the presence of oil above indicating the oil and water layers to be mechanically coupled. In water, the flow field is practically three dimensional and unsteady, as expected in a water-filled cavity at this Rayleigh number. Hence it can be concluded that water is thermally coupled with air above.

Interferograms in water at vary high Rayleigh numbers are compared in Figures 5.49(a-b). High unsteadiness in (a) and quite steady fringe patterns in (b) were obtained. In (a), the number of rolls changed from 6-8 with time near the interface, on the other

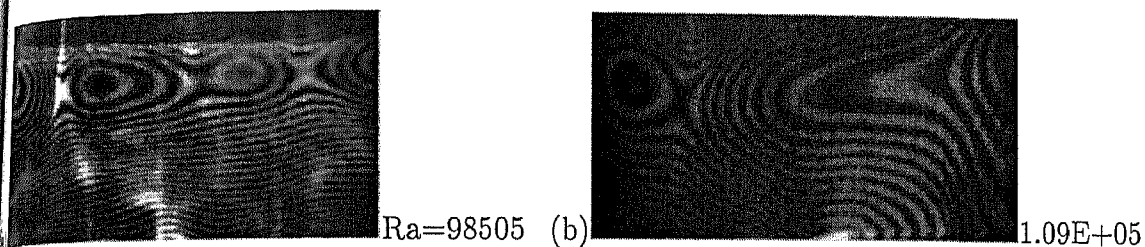


Figure 5.49: Interferograms obtained in water in a cavity containing layers of (a) 1/3 air and 2/3 water, $\Delta T = 18$ K and (b) 1/2 water and 1/2 oil, $\Delta T = 10$ K.

hand, 2 counter-rotating rolls were seen in the full cavity in (b) and the pattern was practically steady. In air, the nature of coupling changed from mechanical to thermal in the air-oil experiment at higher Rayleigh numbers. In contrast, the type of coupling in water is seen to be invariant with respect to Rayleigh number, being thermal in air-water experiments and mechanical in oil-water experiments. In the latter, mechanical coupling retards vigorous convection taking place in water.

Figures 5.50(a-b) show interferograms in the oil phase at subcritical Rayleigh numbers. Owing to the complete dominance of conduction over convection heat transfer, straight fringes appear in the field-of-view in particular in (a). However, the fringe pat-

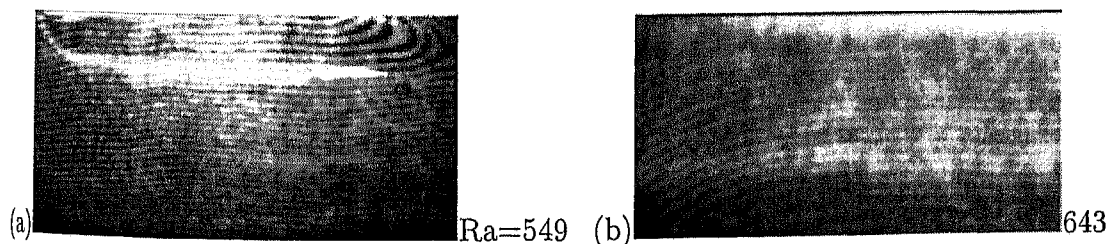


Figure 5.50: Interferograms obtained in oil in a cavity containing layers of (a) 1/2 air and 1/2 oil, $\Delta T = 0.3$ K and (b) 2/3 water and 1/3 oil, $\Delta T = 0.3$ K.

terns of (b) show some curvature with the possibility of the formation of a unicellular roll in the counter-clockwise direction. Fringe curvature can also be related to two dimensionality of the thermal field in the conduction regime. At the limit of zero flow, the fluid layers can only be thermally coupled.

The results obtained at near critical Rayleigh numbers in the oil phase are compared in Figures 5.51(a-b). The flow is seen to be initiated near the interface in (a) in the form of two counter-rotating rolls. The two counter-rotating rolls scale the full cavity

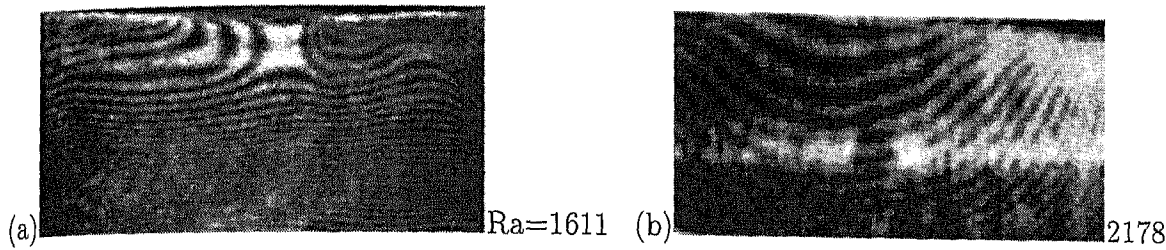


Figure 5.51: Interferograms obtained in oil in a cavity containing layers of (a) 1/3 air and 2/3 oil, $\Delta T = 0.3$ K and (b) 1/2 water and 1/2 oil, $\Delta T = 0.3$ K.

height in (b), a strong descending flow being closer to the cavity center. As discussed in Section 5.3.2, the flow orientation in (b) is opposite to that in water and the two layers are mechanically coupled, thermal coupling being of secondary importance. In (a), the interface region is active and the layers are thermally coupled¹³ (Section 5.2.1).

5.6 Interface deformation

The deformation of the fluid-fluid interface in the present experiments was not observed to be significant. Hence, in the above discussion on the convective fields in the individual fluid layers, the influence of a deformed interface was not highlighted. It was however possible to detect small changes in the interface shape with temperature difference, by configuring the interferometer to record shadowgraph images. The major conclusion to emerge from the images is that the interface deformation follows the cellular convective field in the fluids, and is associated with the mechanical coupling of the fluid layers.

Figure 5.52 shows the deformed interfaces for air-water, air-silicone oil and silicone oil-water layers. The layer thicknesses in each pairs of the fluids are maintained equal (1/2-1/2). Two cases wherein the fluids are stationary ($\Delta T = 0$ K) and in motion with the highest temperature difference across the walls ($\Delta T = 18$ K) have been presented. The images have been magnified in the vertical direction, while the horizontal dimension represents the width of the cavity. An examination of the shadowgraphs at zero temperature difference shows that the base interface shape is quite flat. Thus surface tension does not play a significant role in the present experiments.

For the air-water experiments (Figures 5.52(a-b)) at $\Delta T = 18$ K, the overall temperature drop across the water layer in the horizontal direction was only 0.36 K. Thus the temperature variation established over the interface was negligible. As a result,

¹³Thermal coupling was favoured in all air-oil experiments and Rayleigh numbers; mechanical coupling was seen to the extent that air was set into motion at Rayleigh numbers below 1708.

Marangoni convection can be expected to be of secondary importance. In contrast, an upward displacement of the interface occurs at regions where the fluid has a positive vertical velocity. Thus the orientation of the roll patterns (Figure 5.4(c1)) in the interferograms of the water layer correlate well with the deformed interface shape¹⁴. This result is also in agreement with the observations of Edwards *et al.* (1991) for buoyancy-driven convection, where the rise of fluid occurs towards centers of high elevation and falls in the depressed region.

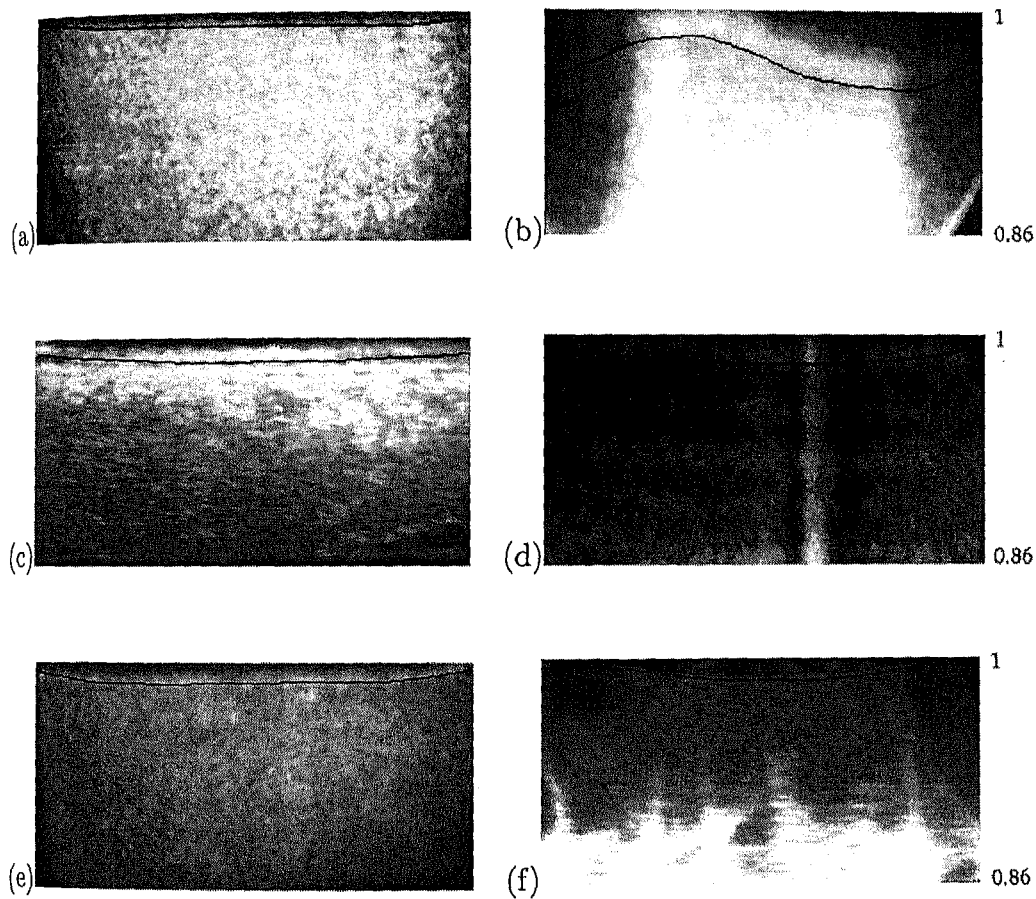


Figure 5.52: Interface deformation in a cavity for equal layer heights consisting of air-water (a-b), air-oil (c-d), and oil-water (e-f) respectively; Cavity temperature difference of 0 (a,c,e) and 18 K (b,d,f) imposed across the cold (top) and hot (bottom) walls. Deformed interfaces are emphasized in black. The vertical scale is for y/h .

In the experiments carrying water, the region below the interface (and near the wall) shows a higher light intensity (Figures 5.52(b) and 5.52(f)) with an increase in the temperature difference. The bright regions represent refraction of the laser beam from the lower wall into the bulk of the water layer, in the direction of decreasing

¹⁴The interface displacement correlates best with the strongest roll; in other words, not every roll will produce a change in elevation.

temperature. This effect is not pronounced at lower temperature differences. It is seen to be more prevalent in the oil-water experiment (Figure 5.52(f)) as compared to the air-water experiment (Figure 5.52(b)). In the former, the light intensity patterns show individual streaks that are characteristic of a three dimensional thermal field. These observations are quite consistent with the temperature drops and the individual Rayleigh numbers referred in Sections 5.1-5.3. In the experiment with air and silicone oil (Figures 5.52(c-d)), the entire light beam was lifted off the region being imaged, leading to the field appearing darker at $\Delta T=18$ K, when compared to the image for zero temperature difference.

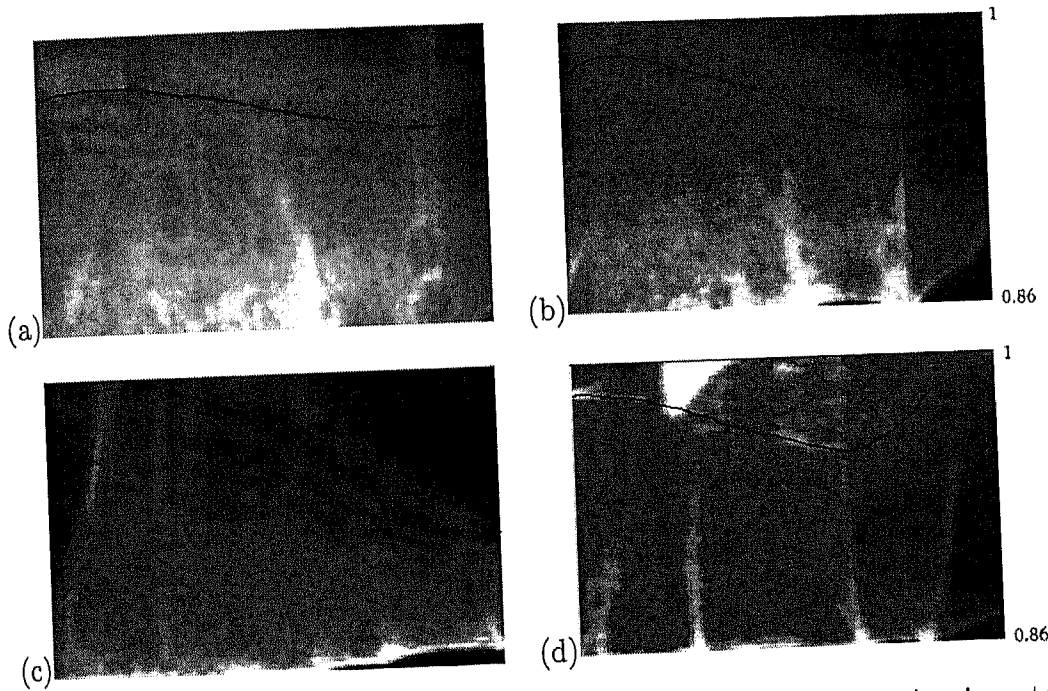


Figure 5.53: Interface deformation in a cavity 2/3rd filled with water in air-water experiments; Cavity temperature differences are (a) 5 K, (b) 10 K, (c) 15 K and (d) 22 K. Deformed interfaces are emphasized in black.

Unequal layer heights of fluids in air-water and oil-water combinations have also been selected for imaging the interface shape. In air-water experiments, two layer heights (2/3rd and 1/2 water) and four temperature differences (5, 10, 15 and 22 K) have been considered for the interface experiments. The results for 2/3rd and 1/2 water filled cavity are respectively shown in Figures 5.53(a-d) and 5.54(a-d). Deformations at the interface were seen to be higher in the 2/3rd-filled cavity as compared to 1/2-filled. This is because of the vigorous buoyant motion in water that led to a higher degree of unsteadiness in the 2/3rd-filled cavity.

In the present experiments on oil-water layers, the time-dependent movement of

the interface was clearly visible. The movement of the interface has been shown in the form of shadowgraph images of the water layer, at a regular time interval. Figures 5.55(a-h) and 5.56(a-h) show the interface displacement in a cavity filled respectively with 1/2 and 2/3rd water (the rest being oil) in an oil-water experiment at an imposed temperature difference of 18 K across the cavity surfaces. Three-dimensional effects are more pronounced in Figure 5.56 as compared to Figure 5.55. This is brought out by the large individual streaks of light emanating from the lower hot wall. It was also noticed that the streaks of light oscillate with the moving interface. It is expected that the buoyant motion that drives the fluid flow also regulates the interface shape even while switching between different states. In principle, the shadowgraph images can be processed to extract information about temperature gradients and velocity. It is proposed to take up this study in the future.

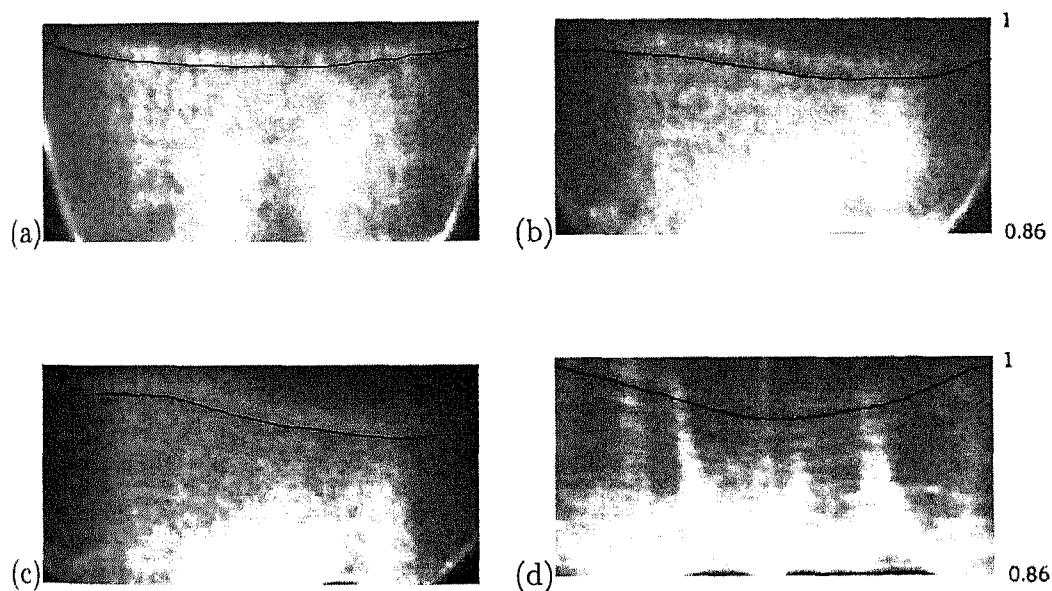


Figure 5.54: Interface deformation in a half-filled cavity in air-water experiments; Cavity temperature differences are (a) 5 K, (b) 10 K, (c) 15 K and (d) 22 K. Deformed interfaces are emphasized in black.

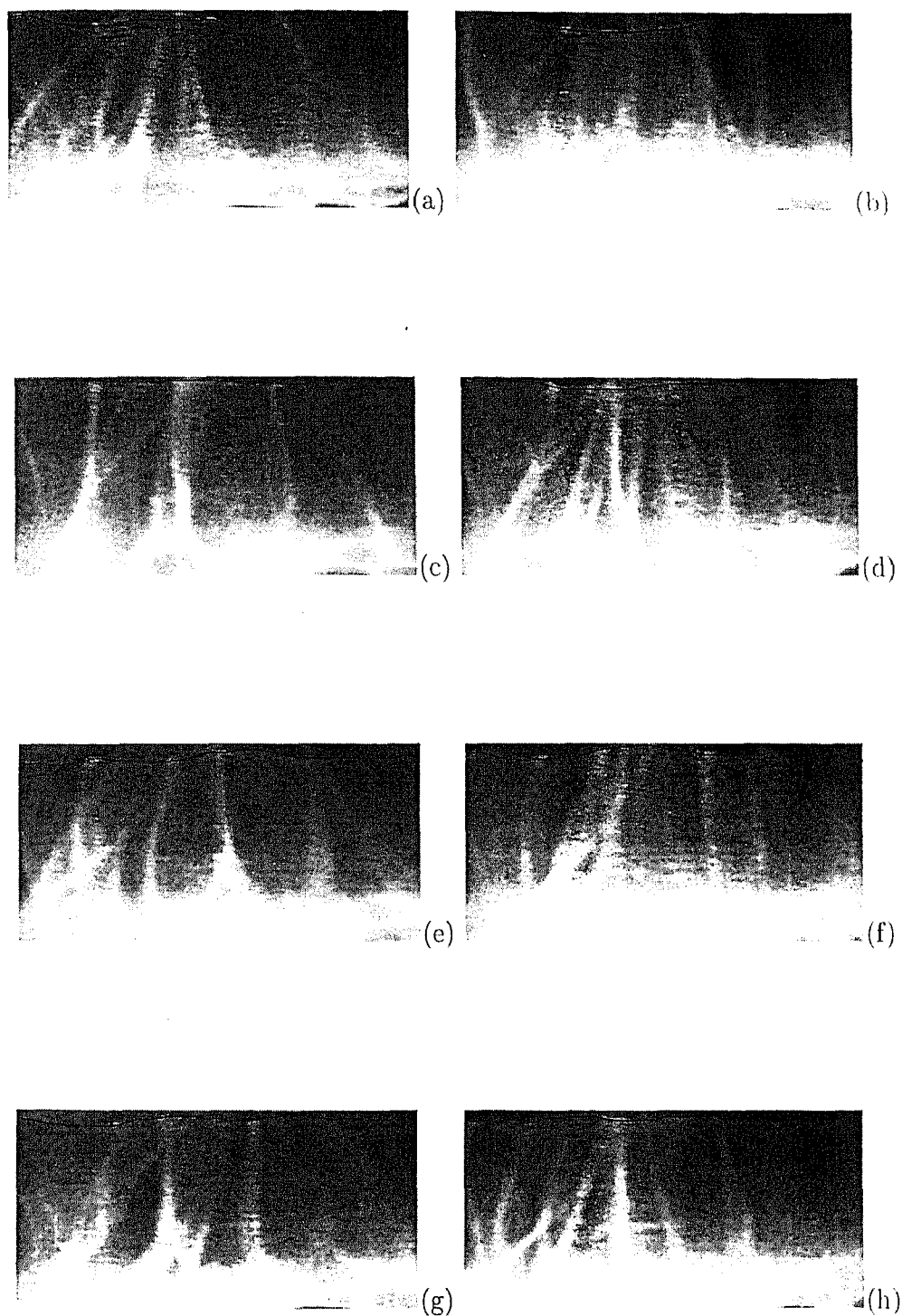


Figure 5.55: Moving interface in water for a cavity temperature difference of 18 K; silicone oil-water experiments with equal layer thicknesses. Time interval between two successive images is 15 seconds. Moving interfaces are emphasized in black.

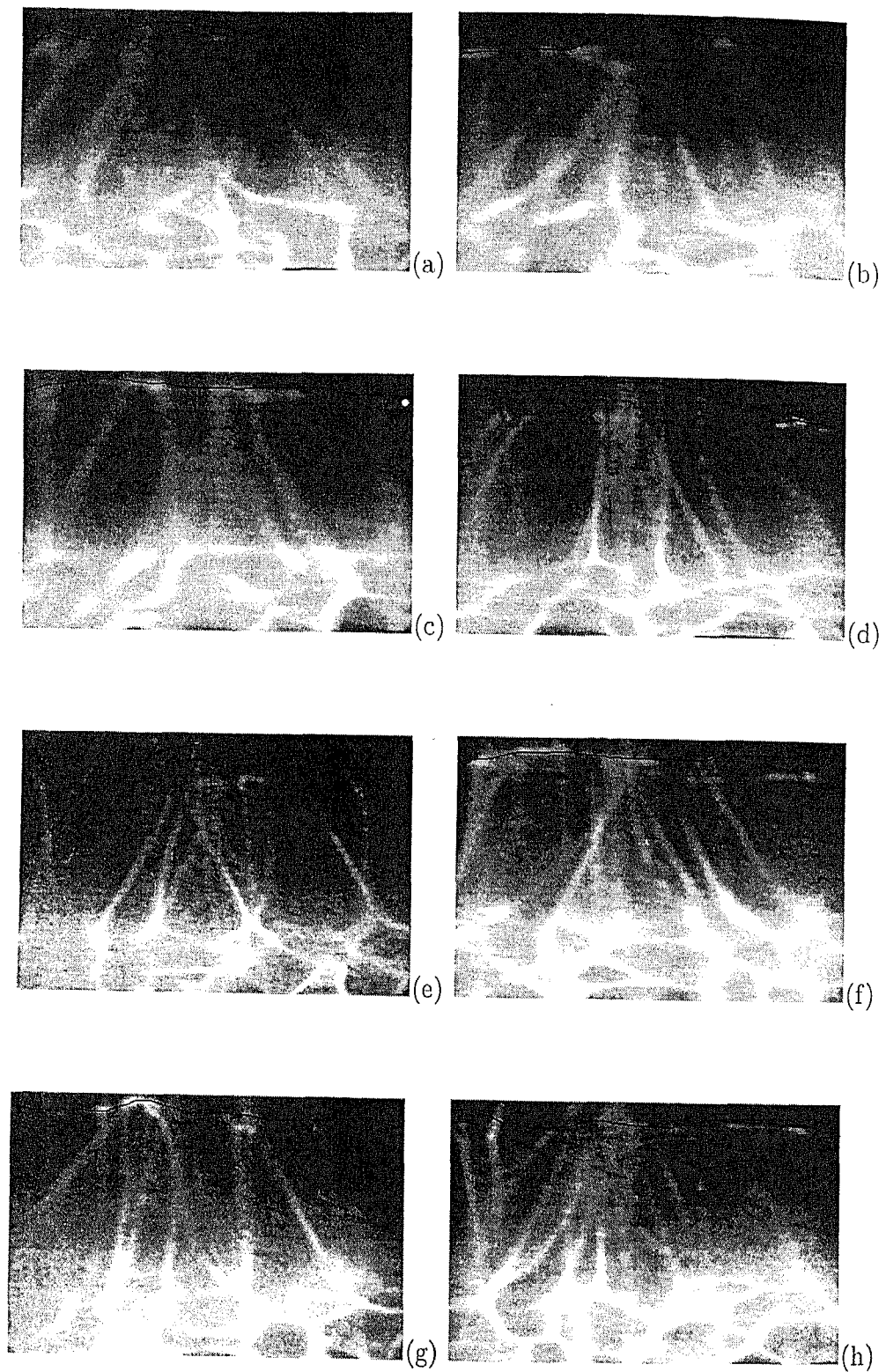


Figure 5.56: Moving interface in water for a cavity temperature difference of 18 K; silicone oil-water experiments with layer thicknesses of $2/3$ rd water and $1/3$ rd oil. Time interval between two successive images is 5 seconds. Moving interfaces are emphasized in black.

5.7 Closure

In air-water experiments, the convective motion in each layer was driven by the individual temperature difference across the respective fluid layer, indicating thermal coupling at the interface. However, the convection cells in water destabilized the circulation in air, by introducing unsteadiness through the mechanical coupling mode. In air-silicone oil experiments, the field-of-view in air was completely bright, while straight fringes occurred in oil at very low Rayleigh number. A time-dependent flow in air was realized at a Rayleigh number higher than 12,900. Convection in oil led to incipient convection in air at subcritical Rayleigh numbers. The fluid layers were found to be thermally coupled for small layer heights of silicone oil. In other experiments, oil had a tendency to retard convection in air. In silicone oil-water experiments, the conductivity ratio determined the Rayleigh number ratio in the cavity. Generally, the convective flow in water was retarded owing to the stabilizing influence of silicone oil floating over water. This suggested the flow to be mechanically coupled at the interface.

When the layers were thermally coupled, the experimental interface temperature and Nusselt numbers matched the single layer correlations. Larger discrepancies were seen when the layers were mechanically coupled and beyond the onset of unsteadiness. For time dependent flow, the layers were thermally as well as mechanically coupled.

High unsteadiness in the fringe patterns was noticed in the experiments involving water. The time sequence of the interferograms indicated a change in the number of rolls formed as a function of time. The unsteadiness in the rolls was noticed more in the central as compared to the interface region. The unsteadiness at the interface could be linked in many cases to the start of mechanical coupling.

The interface deformation was uniformly small in all the experiments. The correlation of the roll movement (for example, Figure 5.1(a1)) with the deformed interfaces (Figure 5.53(b)) suggested the flow to be buoyancy-driven, while surface tension-driven convection was of secondary importance. Movement of interfaces and oscillation of light streaks indicated the presence of three-dimensional effects in the experiments involving water.

Chapter 6

Two-layer Convection in a Circular Cavity

Experiments on two-layer convection in a circular cavity are reported in the present chapter. The apparatus is octagonal in plan that closely approximates a circular cavity. It has a nominal diameter of 130.65 mm and a height of 50 mm. The layer heights have been kept equal to 25 mm for all fluid combinations. This yields the cavity and the individual layer aspect ratios ($= \text{diameter/layer height}$) of 2.61 and 5.22 respectively for all experiments. The schematic drawing of the test cell is shown in Figure 3.2 and is not repeated here. The fluid combinations of air and water, air and silicone oil, and silicone oil floating over water have been selected for the experiments. The grade of the silicone oil employed in the experiments is 50 cSt. Temperature differences as low as 0.4 K to 18 K were applied across the cavity in a destabilizing configuration. This resulted in a wide range of individual Rayleigh numbers to be explored in the fluid layers. The range of Rayleigh and Prandtl numbers studied are summarized in Table 3.1 and in Tables 3.5-3.7 of Section 3.3 (Chapter 3).

Reconstruction of the thermal field in the fluid layers using principles of tomography could not be accomplished in the rectangular cavity owing to projection data being obtained from a single view angle (Chapter 5). This limitation was overcome in the circular cavity. The apparatus was fabricated to scan the thermal field from four different view angles namely 0, 45, 90 and 135°. The fifth view angle of 180° is identical to 0°. The projection data was collected with square optical windows arranged vertically between two horizontal copper plates. Since a parallel beam of light is used in the experiments, a purely circular cavity could not be used. Since the aspect ratio of an individual layer is greater than 5, it is expected that the convection patterns of a circular cavity will be broadly reproduced in the octagonal.

The experiments have been performed in the infinite fringe setting of the interferometer. When a thermal disturbance is introduced in the path of the test beam, fringes appear in the field-of-view. The fringes represents contours on which the path integral of the temperature field along the direction of the light beam is a constant. The alignment of the interferometer in the infinite fringe setting was individually carried out for the fluid phases to capture the interferograms. For this purpose, the reference chamber whose length closely matched the distance between the optical windows, was filled with fluid layers of equal thickness as in the test cell. The reference chamber was required to be thermally inactive. A reduced geometric path length in the present circular cavity made the interferometer sensitive to temperature changes in water and silicone oil, but not air. The situation is in contrast to the observations in the rectangular cavity of Chapter 5, where clear fringes were recorded in air.

The planform of the cellular pattern is determined largely by the shape of the apparatus. Thus the roll structures obtained in the rectangular and the circular cavity are expected to be quite different. In a rectangular cavity, the cells tend to be aligned parallel to the shorter side; alternatively a collection of longitudinal rolls is obtained. In the circular cavity, the rolls are expected to form concentric rings. The possible roll formation in the two geometries of the test cell are compared in Figures 6.1(a) and 6.1(b) respectively¹.

When a laser beam is used to image the thermal field, the interferometric fringes align with roll pattern for a rectangular cavity. Conversely, the roll pattern can be identified from the fringe displacement. For a circular cavity, the fringe field forms as a superposition of several rolls. It can be shown that for the roll pattern of Figure 6.2(b), the fringes (namely, the contours of constant depth-averaged temperature) arrange themselves to form a symmetric Ω (omega) pattern. The full thermal field of the fluid layer is a collection of omegas (Ω) and inverse omegas (\mathcal{O}) inter-linked with one another (Figure 6.2). Such patterns have also been noticed in experiments and calculations for buoyancy-driven convection in a large aspect ratio circular cavity by Srivastava and Panigrahi (2002).

In the present chapter, the experimental data obtained in the form of interferograms have been interpreted to understand the influence of increasing Rayleigh number on transition to three dimensionality and unsteadiness. Results have also been presented to examine the axisymmetry of the thermal field and the reconstructed isotherms by applying a tomographic algorithm for selected planes in the cavity.

¹These patterns represent streamlines and break down with increasing Rayleigh number.

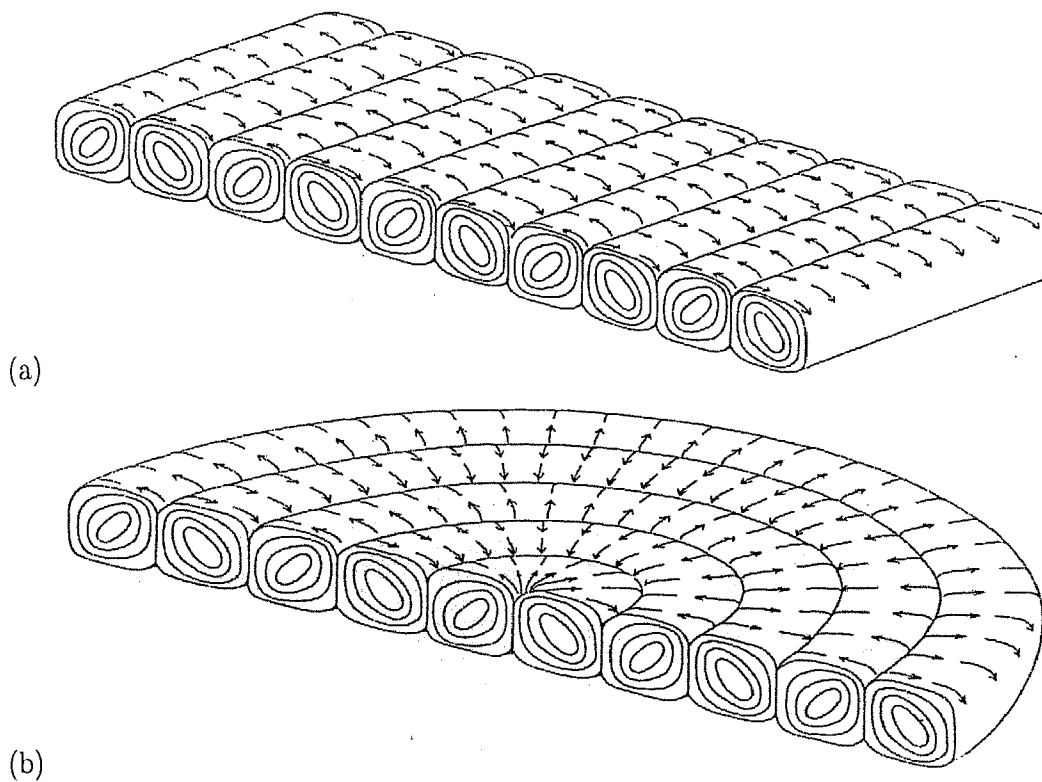


Figure 6.1: Roll formation in (a) rectangular and (b) circular cavities, after Velarde and Normand (1980), at moderate Rayleigh numbers.

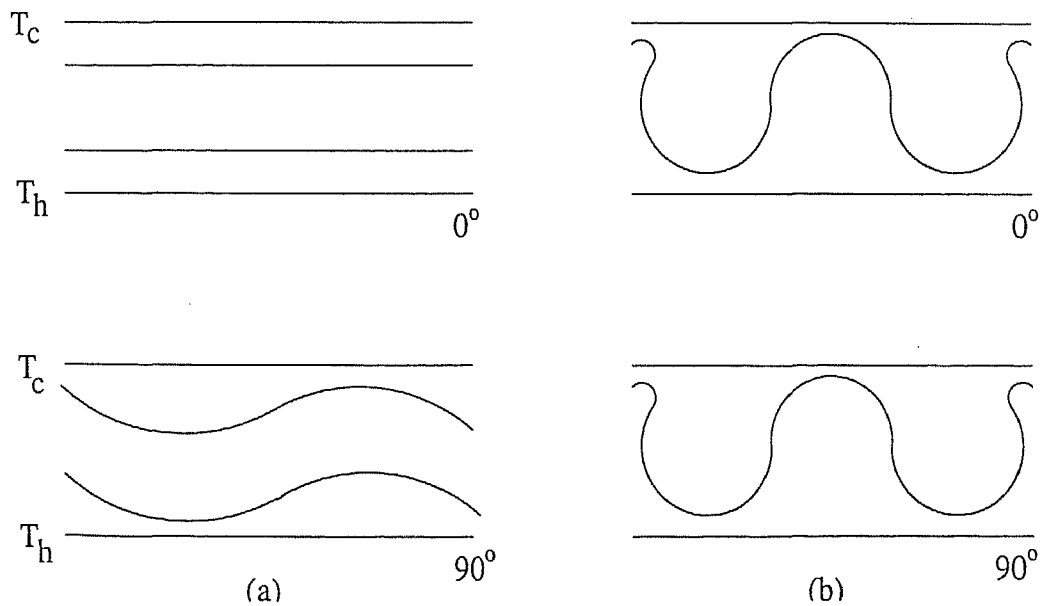


Figure 6.2: Idealized isotherms in orthogonal viewing of (a) rectangular and (b) circular cavities, corresponding to the rolls in Figure 6.1.

6.1 Air-water experiments

Results on two-layer convection in a cavity containing air-water layers are presented in the following section. The heights of fluid layers in the experiments were maintained

equal at 25 mm. Experiments were conducted with four temperature differences namely 6.5, 8.5, 13 and 18 K in a thermally destabilizing configuration. Interferograms for the view angles of 0, 45, 90 and 135° in terms of the projection data of the thermal field in the fluid layers were recorded. Based on the projection data, the temperature field on selected planes of the fluid layer has been reconstructed using the convolution back projection algorithm.

6.1.1 Steady state thermal field

Fringe patterns in a cavity half-filled with water and the rest being air are presented in Figures 6.3(a-b) respectively for the view angles of 0 and 90°. The interferogram has been captured after an experimental run time of 4 hours, when the flow field was fully evolved and the fringe patterns were quite steady. The top and bottom surfaces have been maintained at the temperatures of 22.5 and 29°C respectively by circulating water from constant temperature baths. Thus a temperature difference of 6.5 K is imposed across the cavity. Based on correlations for single fluid (Gebhart *et al.*, 1988, Equations 4.26 and 4.27) along with an energy balance calculation, it is possible to determine the interface temperatures and the layer Rayleigh numbers. The experimental and the estimated interface temperatures from the correlations have been obtained as 28.0 and 28.86°C respectively². The Rayleigh numbers can thus be calculated to be 9,530 and 48,474 in air and water respectively. Figures 6.3(a-b) show that the flow patterns at different view angles looks similar in terms of orientation of fringe patterns, number of fringes and the fringe spacing. Owing to similarity of fringe patterns obtained with respect to the view angle, the thermal field may be expected to be axisymmetric. The fringes in the water phase are denser than in air, because the temperature drop per fringe shift are quite different, being 0.059 and 5.655 K respectively for water and air.

The characteristic inverse- Ω pattern of fringes can be seen on the left side of the cavity, while they are incomplete elsewhere. The S-shaped fringes in air can also be interpreted as portions of Ω , that would have been fully visible if the entire cavity had been fully imaged. This is a hypothetical point since a parallel beam of light would refract at inclined surfaces. It can now be concluded that convection in the two fluid layers is broadly axisymmetric. The concentric rolls formed in air and water are seen to be broadly similar. The flow field in each layer is driven by the respective temperature difference between the nearest wall and the interface. Therefore, it can be concluded

²The average interface temperature was determined from the interferograms by starting the calculations of Chapter 4 from the heated wall.

that the two layers are thermally coupled. High density fringes were noticed near the interface region suggesting the interface to be thermally active, despite being a free-slip boundary. The regions of a small fringe spacing can be associated with a large local diffusive heat flux in the liquid phase.

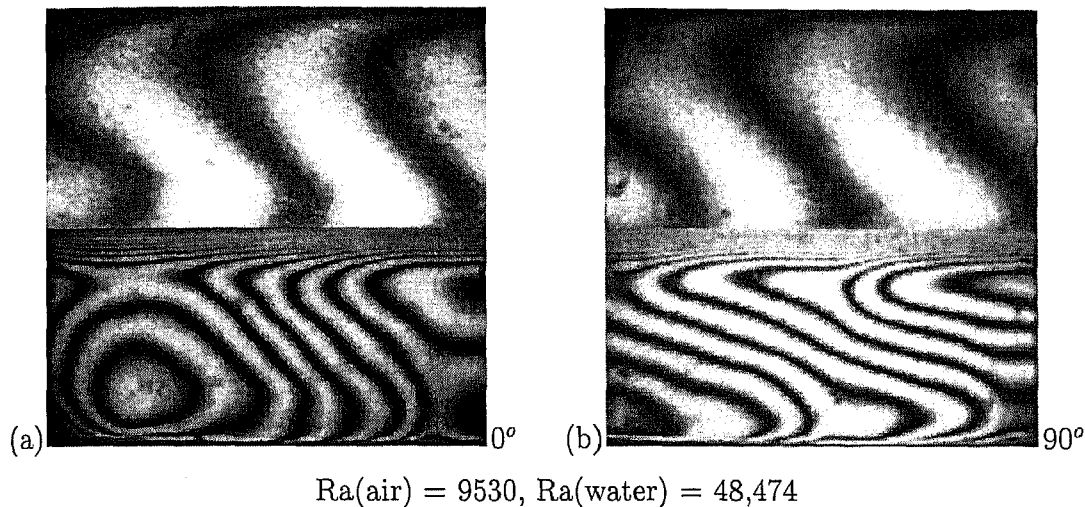


Figure 6.3: Interferograms obtained at steady state in the cavity containing air and water for a temperature difference of 6.5 K. View angles considered: (a) 0° and (b) 90°.

In Figures 6.3(a-b), closed fringes are to be noticed in the water layer. These fringes have not been included in the temperature calculation. It is expected that valid isotherms would intersect the insulating side walls as well, since temperature here would monotonically decrease from the highest value at the lower boundary to the lowest at the top. The closed fringes can be thought of as higher order fringes³ that are formed by an additional path difference between the test and the reference beam by refraction. This has been verified by an additional experiment in the water phase performed with the wedge fringe setting of the interferometer, the view angle being 0°. The initial wedge fringe setting of the interferometer before the start of the experiment is shown in Figure 6.4(a). Away from the lower wall, the fringes are practically straight and can be used to map the temperature profiles in water. For a temperature difference of 6.5 K, the interferogram was recorded after the flow field was fully evolved and is shown in Figure 6.4(b). In the wedge fringe setting, the fringe patterns show the temperature profiles in the fluid medium. In the core of the fluid layer, the temperature variation is monotonic, confirming that closed isotherms cannot form in the experiment being performed. Therefore the higher order fringes have been neglected in the quantitative measurements of the thermal field in the fluid layers.

³for which the phase difference is not zero but $2n\pi$, $n = 1, 2, \dots$

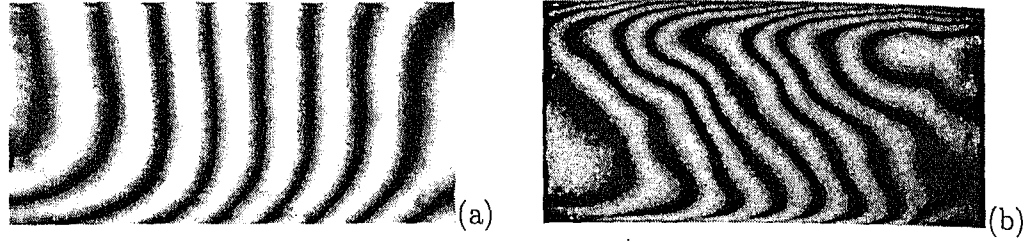


Figure 6.4: Initial (a) wedge fringe setting and (b) wedge fringes during convection obtained in the water layer at a temperature difference of 6.5 K; View angle considered is 0° .

The fringe patterns of Figures 6.3(a-b) can be utilised to evaluate the temperature field and Nusselt number variation in the cavity. Based on Figures 6.3(a-b), the line-of-sight averaged temperature profiles in the water layer of the cavity have been determined. Quantitative measurement of temperature field in the air layer is restricted by the small number of fringes formed. This difficulty arises due to high temperature drop per fringe shift ($\Delta T_c = 5.655$ K) in air. The expected temperature profile based on the fringe patterns in air is plotted by a dashed line. The line-of-sight averaged temperature profiles in the fluid layers are shown in Figure 6.5(a). These temperature profiles have been plotted as a function of the non-dimensionalised vertical distance (y/H), where the y -coordinate is measured from the air-water interface⁴. The principal observation to emerge from the Figure 6.5(a) is that the largest portion of the temperature drop occurs in air, in comparison to water. This is clearly due to the higher thermal conductivity of water compared to air. In water, the slope near the hot wall and the interface indicates the existence of large temperature gradient as compared to the central region.

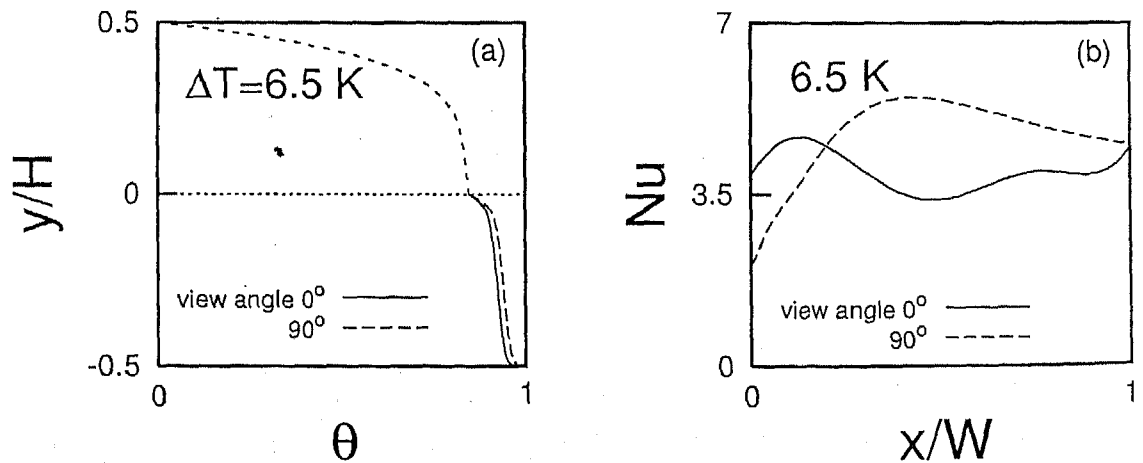


Figure 6.5: (a) Depth-averaged temperature profiles and (b) local Nusselt number variation at the interface in a cavity half filled with water, the rest being air; Cavity temperature difference is 6.5 K.

⁴The dimensionless temperature is defined as $\theta = (T - T_c)/(T_h - T_c)$.

Using the temperature profiles in water (Figure 6.5(a)), the local heat transfer rates in terms of Nusselt number were determined at the interface using Equation 4.25. The interface was chosen for temperature gradient calculation instead of hot wall since clear fringes that covered the whole width of the cavity were obtained in this region. The variation of the local Nusselt number at the interface with respect to the coordinate parallel to the width of the cavity is shown in Figure 6.5(b). Based on the respective local Nusselt number variation for two view angles, the width-averaged Nusselt number at the interface has been calculated. The width-averaged Nusselt number for 0 and 90° were found to be 3.95 and 3.96 respectively in the experiments. The two values obtained are quite close to each other and confirms the steady axisymmetric regime in the cavity. The interface temperature and the Nusselt number are compared with the correlations in Table 6.1. Based on the correlations, the global Nusselt number was estimated to be 3.50. The correlations are applicable for a cavity with no-slip walls. A factor that can cause discrepancy between the measured Nusselt numbers and the correlations is the presence of a free-slip boundary.

In Figures 6.6(a-b), a temperature difference of 8.5 K was imposed between the two horizontal surfaces. The cold and the hot surfaces were maintained at 21.5 and 30°C respectively. The experimental and the estimated interface temperature were calculated to be 28.66 and 29.72 respectively. Based on the estimated interface temperature, the Rayleigh numbers calculated in the air and water layers were 12,466 and 66,992 respectively. Due to an increased Rayleigh number in both the layers, slight unsteadiness in the fringe patterns was observed. The long-lived patterns have been captured and is shown in Figure 6.6. Here the fringe patterns of Figure 6.6 show a representative field obtained after four hours of experimentation. Interferograms obtained in water at 2 different view angles show dissimilarity in terms of fringe orientation, number of fringes, and fringe spacing. The air phase exhibits some degree of similarity in terms of roll orientation and number of fringes. Thus, it may be concluded that the thermal field in the cavity is two dimensional in air and three dimensional in water. An increased number of higher order fringes in the water layer during the course of experiments can be associated with higher temperature gradients and hence greater refraction within the fluid layer.

Using the fringe patterns of Figure 6.6, the line-of-sight temperature profiles in the water layer were determined. In the air phase, the expected nature of the temperature profile alone could be plotted. The temperature profiles in the fluid layers are shown in Figure 6.7(a). Once again it can be seen from Figure 6.7(a) that the temperature drops are higher in air as compared to water. A comparison of Figures 6.5 and 6.7 shows that a small increase in the cavity temperature difference has sharply decreased

the temperature drop in water, Correspondingly, that in air has increased. The result is to be understood against the background that the flow field in water is unsteady for the higher temperature difference. The increase in the interface temperature and a drop in the effective conductivity of water, thus represents a significant transition in the flow regime.

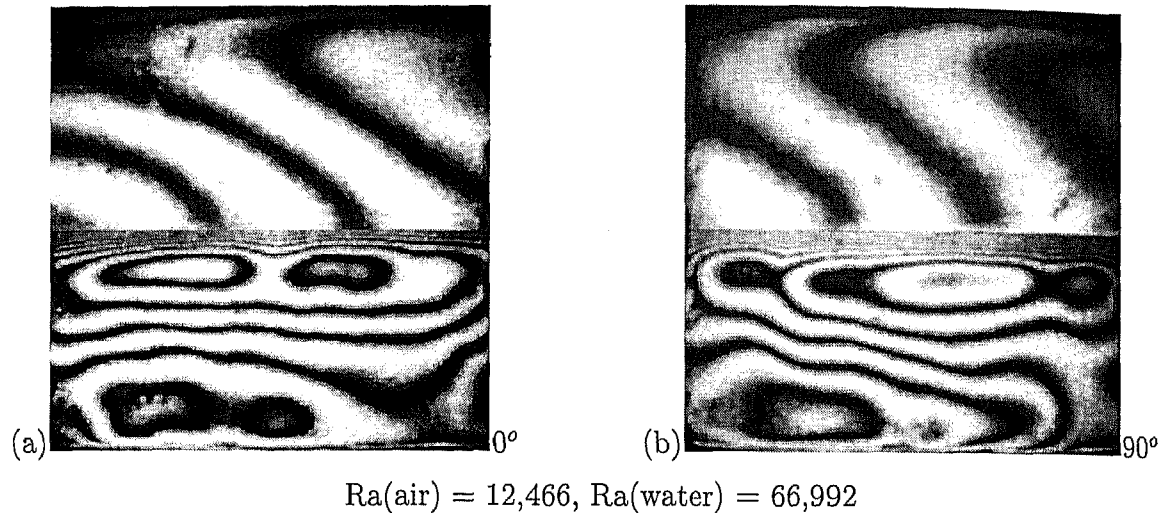


Figure 6.6: Long-time interferograms obtained in the axisymmetric cavity containing air and water for a temperature difference of 8.5 K. View angles considered are (a) 0° and (b) 90° .

Based on the temperature profiles of Figure 6.7(a) in water, the local Nusselt number variation at the interface has been calculated. The variation of Nusselt number for the two view angles is shown in Figure 6.7(b). Applying numerical integration, the width-averaged Nusselt number can be calculated. The respective width-averaged Nusselt number for 0° and 90° view angle are 4.55 and 4.65 (Table 6.1). The estimated width-averaged Nusselt number from correlations was 3.74. A higher discrepancy can be linked to unsteadiness as well as three dimensionality in the flow established in water.

Table 6.1: Comparison of the interface temperature and Nusselt number with Gebhart *et al.* (1988) (marked 'Ref') in a cavity containing layers of air and water of equal thickness.

ΔT , K	T_I (Exp), $^\circ\text{C}$	T_I (Ref), $^\circ\text{C}$	Nu (interface)		
			view angle 0°	view angle 90°	Ref
6.5	28.00	28.86	3.95	3.96	3.50
8.5	28.66	29.72	4.55	4.65	3.74

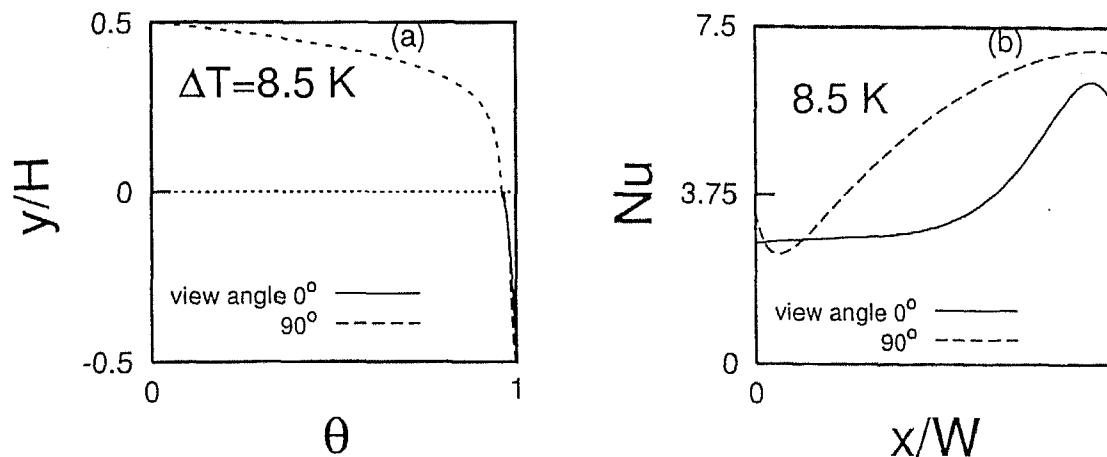


Figure 6.7: (a) Depth-averaged temperature profiles and (b) local Nusselt number variation at the interface in a cavity half filled with water, the rest being air; Cavity temperature difference is 8.5 K.

6.1.2 Transient evolution of thermal field

The transient evolution of the flow fields in the fluid layers are presented below. The view angles considered are 0 and 90° . The evolution of flow field refers to the time sequence of fringe patterns recorded after the two bounding surfaces are thermally stabilized⁵. In the rectangular cavity, the transient evolution patterns could not be recorded as the thermal field at the bounding surfaces and the flow field in the fluid layers jointly reached steady state.

The cavity temperature difference considered here is 13 K. The corresponding Rayleigh numbers are 18,870 and $1.16\text{E}+05$ in air and water layers respectively. The evolution patterns of the thermal fields in the fluid layers were recorded at a regular interval of 30 minutes. These patterns are respectively shown in Figures 6.8(a-f) and 6.9(a-f) for the view angles of 0° and 90° . The flow field in the cavity reached a dynamic steady state after around 2.5 hours. In this state a temporally periodic spatial movement of fringe patterns was noticed. The dominant state that prevailed for the longest duration are shown in Figures 6.8(f) and 6.9(f) respectively for the view angles of 0° and 90° . The fringe patterns obtained in the fluid layers at two view angles show dissimilarity in terms of the orientation of the fringe patterns and the spacing between fringes. Thus it may be concluded that the fluid layers are unsteady as well as three dimensional. The observation is in agreement with the flow regime diagram for single fluids, (Figure 2.1).

⁵This happened quite early, in less than 50 minutes.

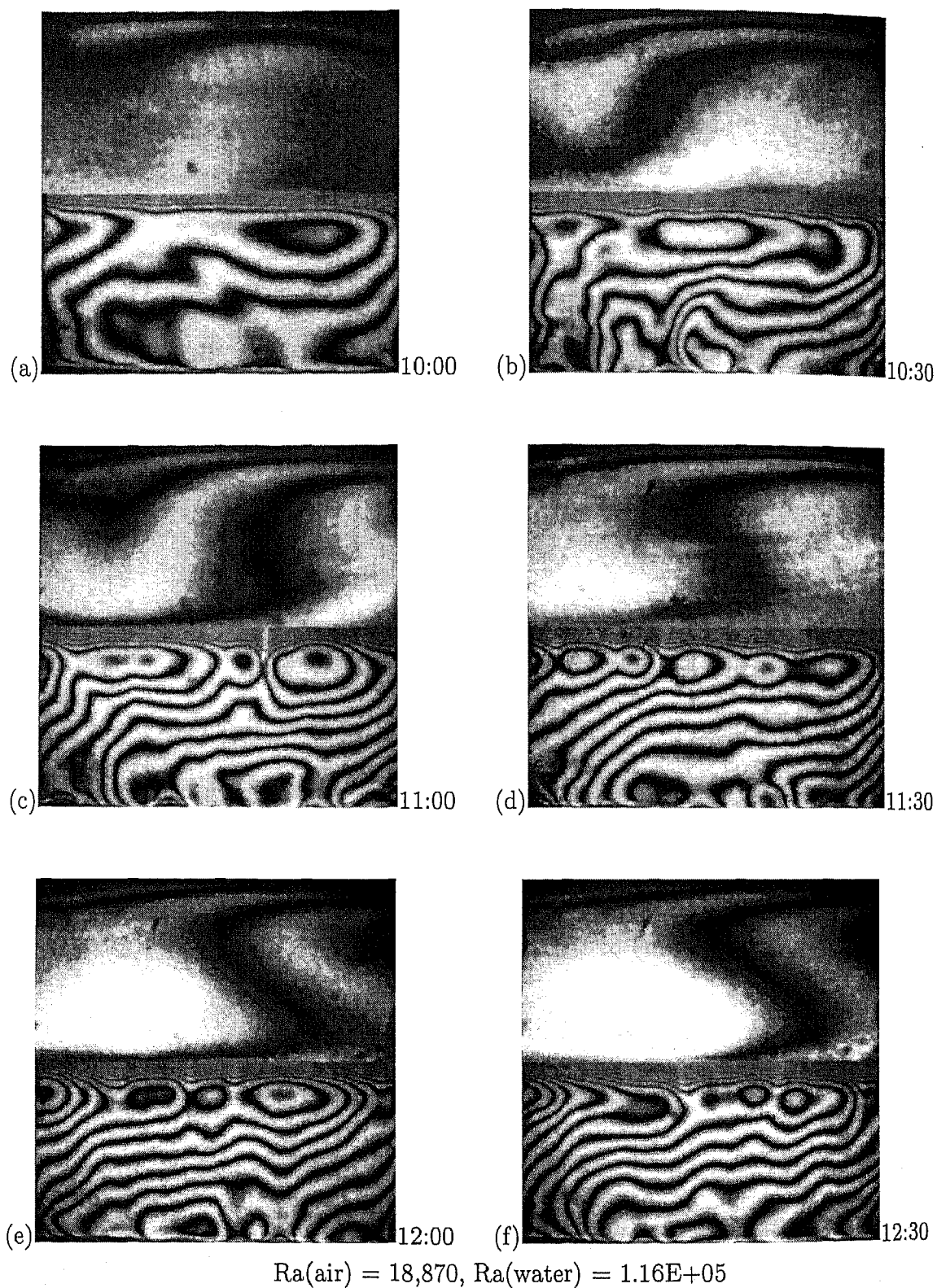


Figure 6.8: Transient evolution of fringe patterns in the cavity containing air and water. View angle considered is 0° , and the cavity temperature difference is 13 K. Time in hr:min.

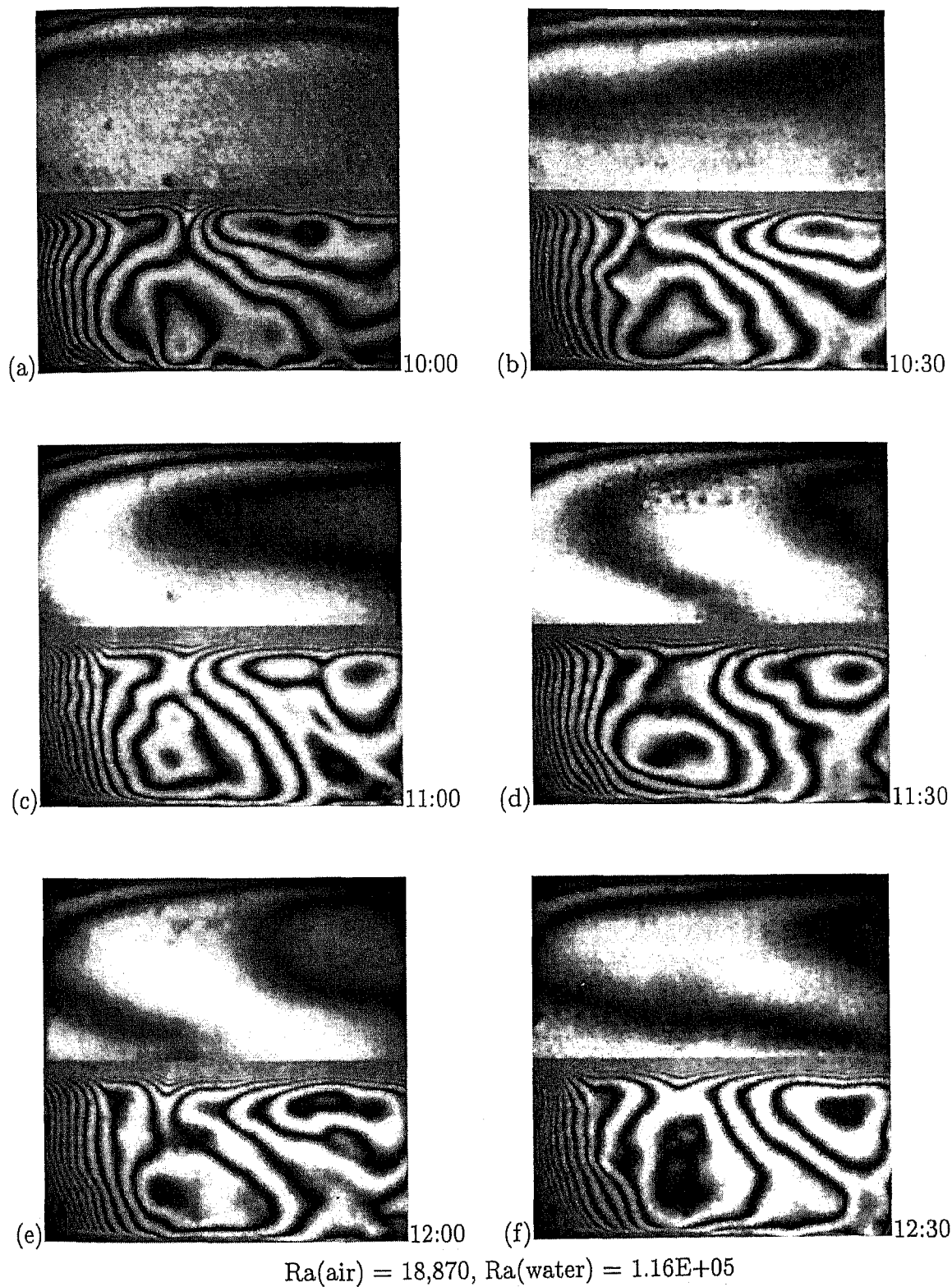


Figure 6.9: Transient evolution of fringe patterns in the cavity containing air and water. View angle considered is 90° , and the cavity temperature difference is 13 K. Time in hr:min.

6.1.3 Three dimensional structures

Temperature fields on selected planes of the fluid layers have been reconstructed from its interferometric projections obtained at view angles of 0, 45, 90 and 135°. The projection data obtained at a view angle of 180° (fifth view) is identical to that of the 0° view angle and has also been used. Convolution back projection (CBP) has been chosen as the tomographic algorithm in the present work and is discussed in Section 4.9.1 (Chapter 4).

A large number of projections is required to apply effectively the reconstruction algorithm. In the present experimental setup, 5 view angles alone could be recorded in the form of interferometric projection data. Further, projection data obtained from a view angle covered 41% of the full width of the fluid layer in the cavity. The partial data has been obtained in the central portion of the cavity in the experiments. As required in tomography, the laser beam should scan the full width of the thermal field in each view. To achieve the requirement, the projection data was suitably extrapolated by a numerical scheme, (Section 4.9). The data size thus generated was a square matrix of size 81(rays)×81(view angles). The extrapolated data covered the full width of the cavity⁶. As discussed in Chapter 4, the extrapolation errors are not expected to be serious since the interferometric measurement is less sensitive towards the edges of the test cell where the geometric path length is small. Information that is de-emphasized in one projection is however captured in the next. In this respect, the thermal field is fully represented by the partial data itself. The process of extrapolation casts it in a form that is suitable for the numerical implementation of CBP.

The original projection data is available at five view angles, resulting in an angular increment of 45°. It is known that a coarse increment, common to *limited-data* tomography reconstructs the major features of the thermal field, while the minor features (in terms of physical size) are lost (Natterer, 1986). For this reason, tomography has been used in the present study to examine axisymmetry of temperature distribution, but not the small scale features such as knots and spokes.

In Section 6.1.1, the interferograms obtained at the view angles of 0° and 90° were discussed. For applying tomographic algorithm, the interferograms for all view angles namely 0, 45, 90 and 135° have been evaluated quantitatively through image analysis techniques to determine the temperature field in the fluid layers. Steady state interferograms for all view angles are shown in Figures 6.10(a-d) and 6.11(a-d) respectively for

⁶Mishra *et al.*, 1999 have shown this size to be a reasonably large data set in terms of discretization.

temperature differences of 6.5 K and 8.5 K across the cavity.

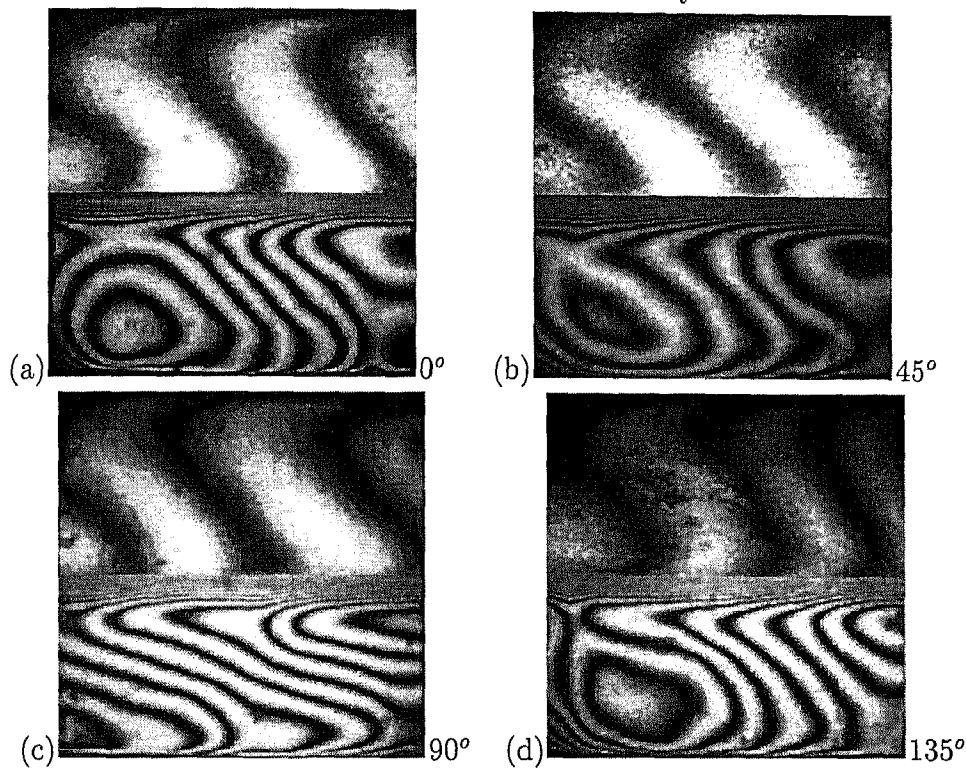


Figure 6.10: Long-time interferograms obtained in a cavity filled with air and water for a temperature difference of 6.5 K. View angles are (a) 0° , (b) 45° , (c) 90° and (d) 135° .

Three horizontal planes, namely $y/h = 0.15$, 0.5 and 0.85 have been considered for reconstruction. Here, y is the vertical co-ordinate and h is the water layer height. The projection temperatures obtained at the three planes have been plotted with respect to the transverse coordinate for all view angles in Figures 6.12(a-c) for a temperature difference of 6.5 K.⁷ Here, the transverse coordinate is parallel to the width of the cavity, and $y/h = 0$ represents the hot wall of the cavity. For the cavity based temperature difference of 8.5 K, the projection data in water for the three planes are respectively shown in Figures 6.13(a-c). In Figures 6.12(a-b), the view angles of 45° and 135° show a degree of axisymmetry in the data as compared to the other view angles. This trend is noticed for the lower ($y/h = 0.15$) as well as the mid-plane ($y/h = 0.5$) in water. As the selected plane approaches the interface ($y/h = 0.85$), there is a loss of axisymmetry for all the view angles (Figure 6.12c). In Figures 6.13(a-c), a temperature difference of 8.5 K was imposed across the cavity. A total loss of axisymmetry is noticed in the projection data for all the view angles and planes considered. This was also observed in the interferograms (Figures 6.11(a-d)), where the flow field had attained three dimensionality.

⁷Temperatures within a single optical windows (rather than the full cavity) have been shown.

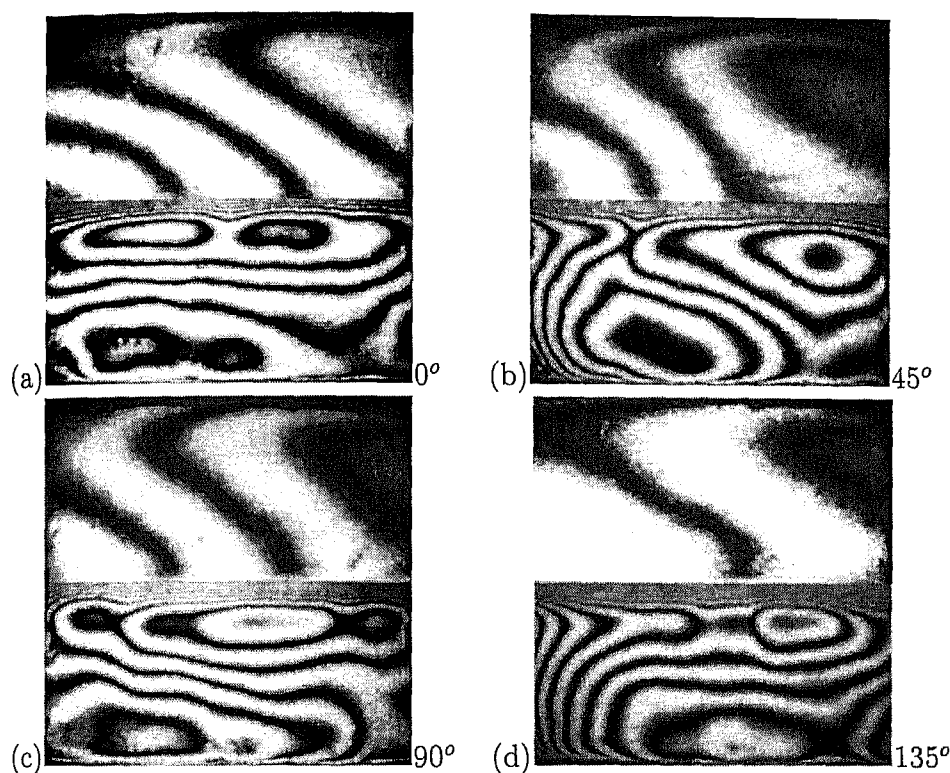


Figure 6.11: Long-time interferograms obtained in a cavity filled with air and water for a temperature difference of 8.5 K. View angles are (a) 0° , (b) 45° , (c) 90° and (d) 135° .

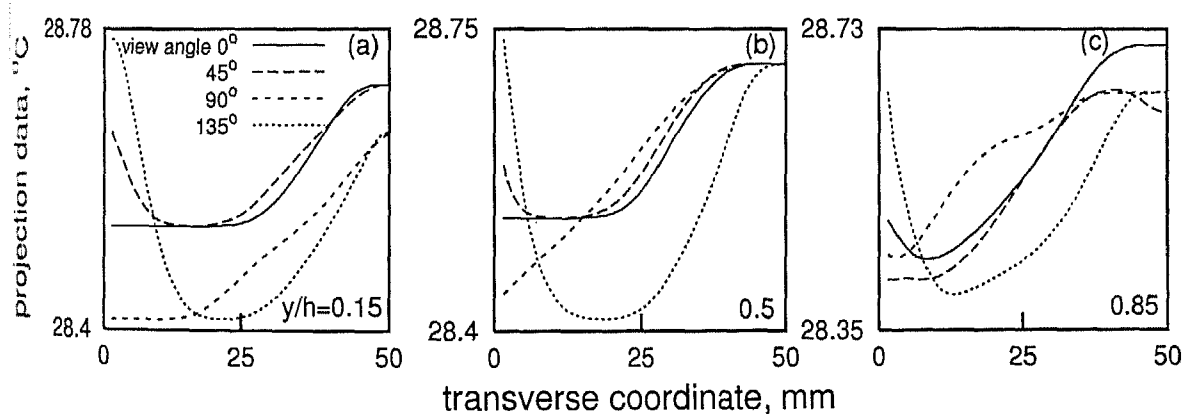


Figure 6.12: Projection data in water at three horizontal planes along the width of the cavity. Cavity half-filled with water, the rest being air for a temperature difference of 6.5 K.

At steady state, the average temperature over a given plane should be a constant for all the view angles. The projection data of Figures 6.12 and 6.13 show inconsistency in this respect though the differences are within the limits of experimental errors. The constancy of the average temperature has been strictly enforced by linear scaling of the projection data before applying the tomographic algorithm. For the correction, the grand average of all the projection data over a given plane was calculated. The average

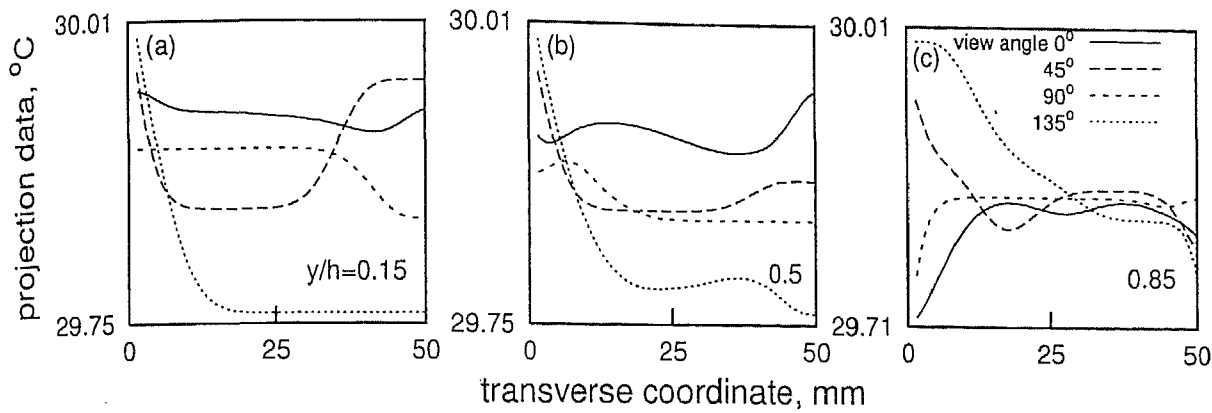


Figure 6.13: Projection data in water at three horizontal planes along the width of the cavity. Cavity half-filled with water, the rest being air for a temperature difference of 8.5 K.

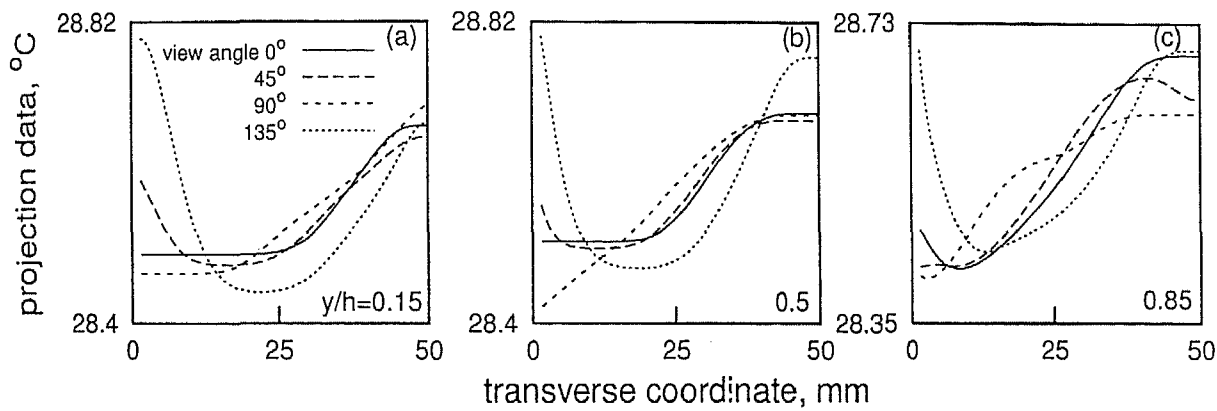


Figure 6.14: Consistent projection data in water at three horizontal planes along the width of the cavity. Cavity half-filled with water, the rest being air for a applied temperature difference of 6.5 K.

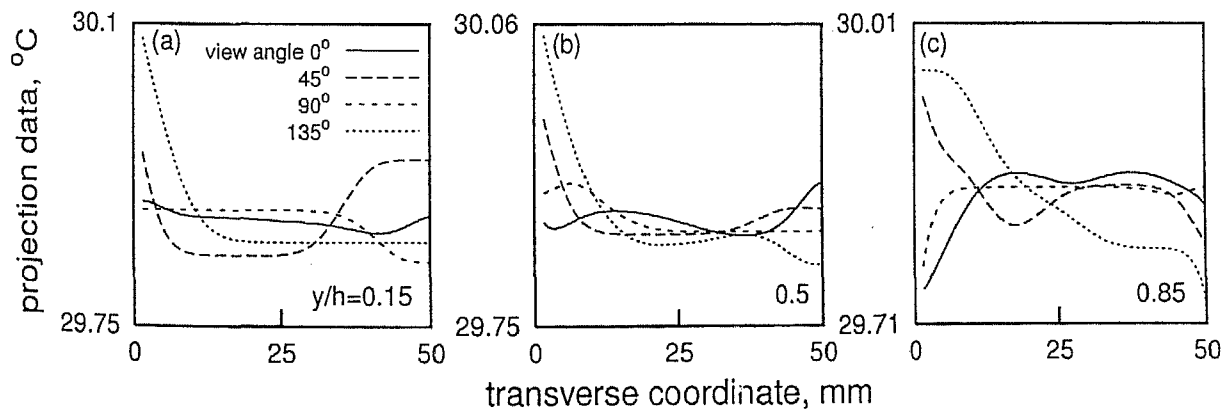


Figure 6.15: Consistent projection data in water at three horizontal planes along the width of the cavity. Cavity half-filled with water, the rest being air for a applied temperature difference of 8.5 K.

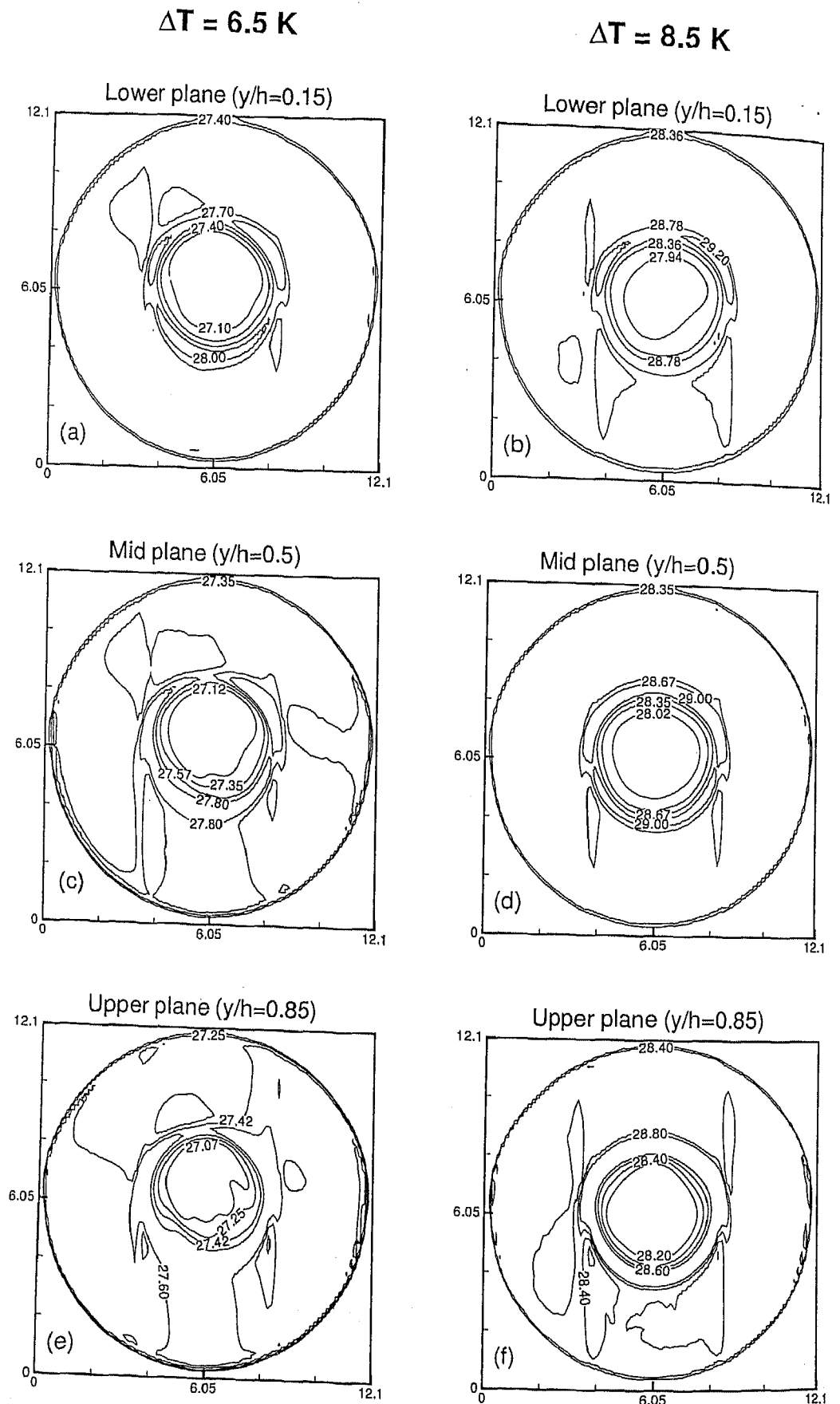


Figure 6.16: Reconstructed temperature contours in the water layer. Cavity is half-filled with water, the rest being air. Temperature differences are 6.5 K (a,c,e) and 8.5 K (b,d,f) respectively at lower, mid- and upper planes of the cavity.

of projection data for each view angle was then forced to be equal to the grand average. With this approach, the individual trends for each view angle were retained and at the same time, the average temperature was a constant for a given plane, with respect to the individual projections. Figures 6.14(a-c) and 6.15(a-c) show the projection data respectively for 6.5 and 8.5 K after the consistency checks have been enforced for the three horizontal planes. The improved consistency of the data is now quite evident.

The consistent data set can now be supplied as an input for the reconstruction of the three-dimensional thermal field. The reconstruction of the temperature field in water over three horizontal planes from its interferometric projection are shown in Figures 6.16(a-f). The cavity temperature differences are 6.5 K in Figures 6.16(a,c,e) and 8.5 K in Figures 6.16(b,d,f). For the lower Rayleigh number in Figures 6.16(a,c,e), a degree of axisymmetry is to be noticed in the form of concentric rings in the central portion of the cavity. The concentricity of the thermal field in the central region is seen to decrease from the near wall ($y/h = 0.15$) to the interface region ($y/h = 0.85$). The temperature contours show the center to be at a lower temperature as compared to its surrounding region. There is also a progressive reduction in the size of the isotherm of $T = 27.4^\circ\text{C}$. This indicates that the cooler fluid descends at the center while the warmer fluid ascends at a neighbouring location to form a full roll. This scenario is schematically shown in Figure 6.17. At a higher Rayleigh number (Figures 6.16b,d,f) the extent of

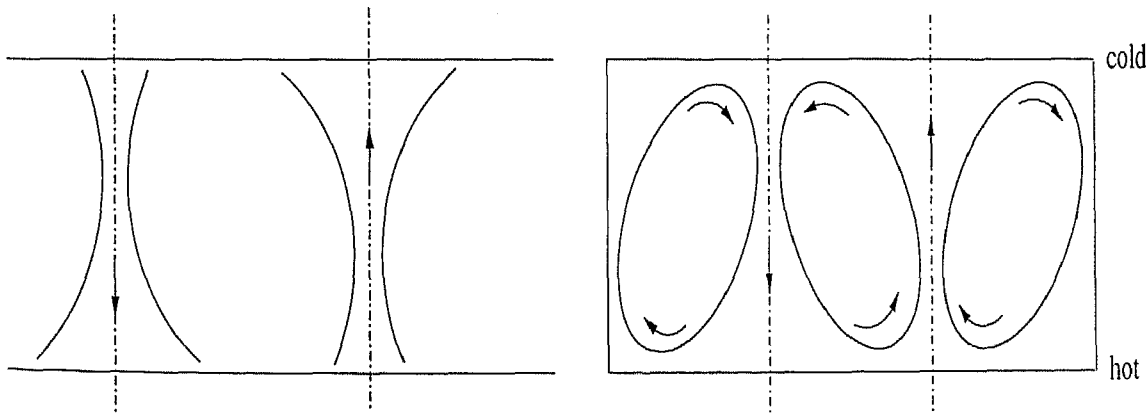


Figure 6.17: Possible roll formation in a circular cavity.

axisymmetry is uniform. This is surprising because convection at $\Delta T = 8.5$ K was found to be strongly time-dependent. The similarity of the reconstructed temperatures shows that the dominant interferograms recorded for each view angle correspond to a particular roll-structure, that in turn is close to axisymmetric. The sign of circulation within the roll is indeterminate because no broadening of the isotherm (for example, $T = 28.4^\circ\text{C}$) is to be seen, going from one plane to the next.

6.1.4 Interface deformation

In the present section, the unsteadiness in the fringe patterns recorded in water and the deformation of the air-water interface have been discussed. The cavity based temperature difference considered is 18 K. The corresponding Rayleigh numbers in air and water were 27,068 and $1.72\text{E}+05$ respectively. High unsteadiness in the water layer was captured with respect to time and are shown in Figures 6.18(a-j), for a view angle of 0° . The recording of interferograms started only after 4 hours of experimentation when the flow field was fully evolved. The time interval between successive images in Figure 6.18 is 1 minute. Dense fringes indicating an active thermal region can be noticed near the interface.

At the lower Rayleigh numbers, the deformation of the interface was not significant and therefore has not been discussed. However with increase in the Rayleigh number to $1.72\text{E}+05$ in water, the deformation in the interface was noticeable. The interface location changed with respect to time. The interface was captured in the form of a shadowgraph. Moving interfaces are shown in Figures 6.19(a-j). The time interval between successive images is 1 minute once again. The top portion near the interface is seen to be dark while the remaining portion looks bright. The bright region arises from the refraction of light from the high near-wall temperature gradients. Similar gradients are present at the interface as well. Refraction in this zone takes light out of the water layer, into air, thus rendering the region dark. Light streaks similar to the rectangular cavity experiments are to be observed in the present test cell. They can be related to the three dimensional unsteady field being established in water. The light streaks also bear a correlation to the change in curvature of the interface and point towards buoyant (rather than Marangoni) convection in the cavity⁸.

6.2 Air-silicone oil experiments

Experiments in a circular cavity containing superposed layers of air and silicone oil are discussed in the present section. The heights of fluid layers in the experiments were maintained equal at 25 mm. For high temperature differences in the rectangular cavity, refraction errors in the oil layer restricted the interferograms to be recorded in air alone. This difficulty was not encountered since the cavity length was smaller by a factor of 3.7. Thus the overall range of Rayleigh numbers that could be imaged increased in the air-oil experiments. For measurements, temperature differences of 0.4, 1.8, 3.1 and 4.0

⁸The correlation was seen to be realized spatially as well as in time.

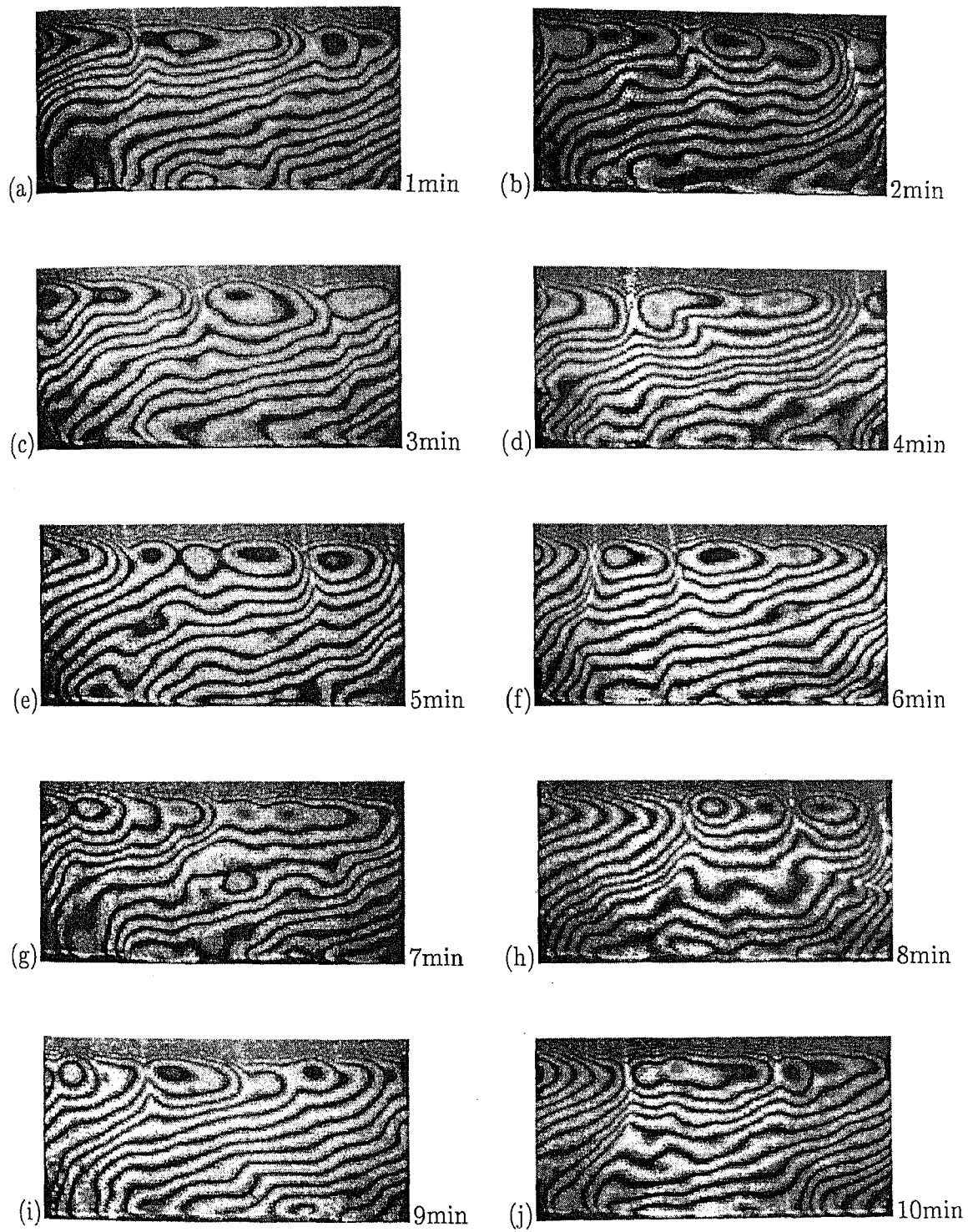


Figure 6.18: Interferograms obtained in water in the cavity containing half filled water, the rest being air at $\Delta T = 18$ K; Time interval between two consecutive images is 1 minute.

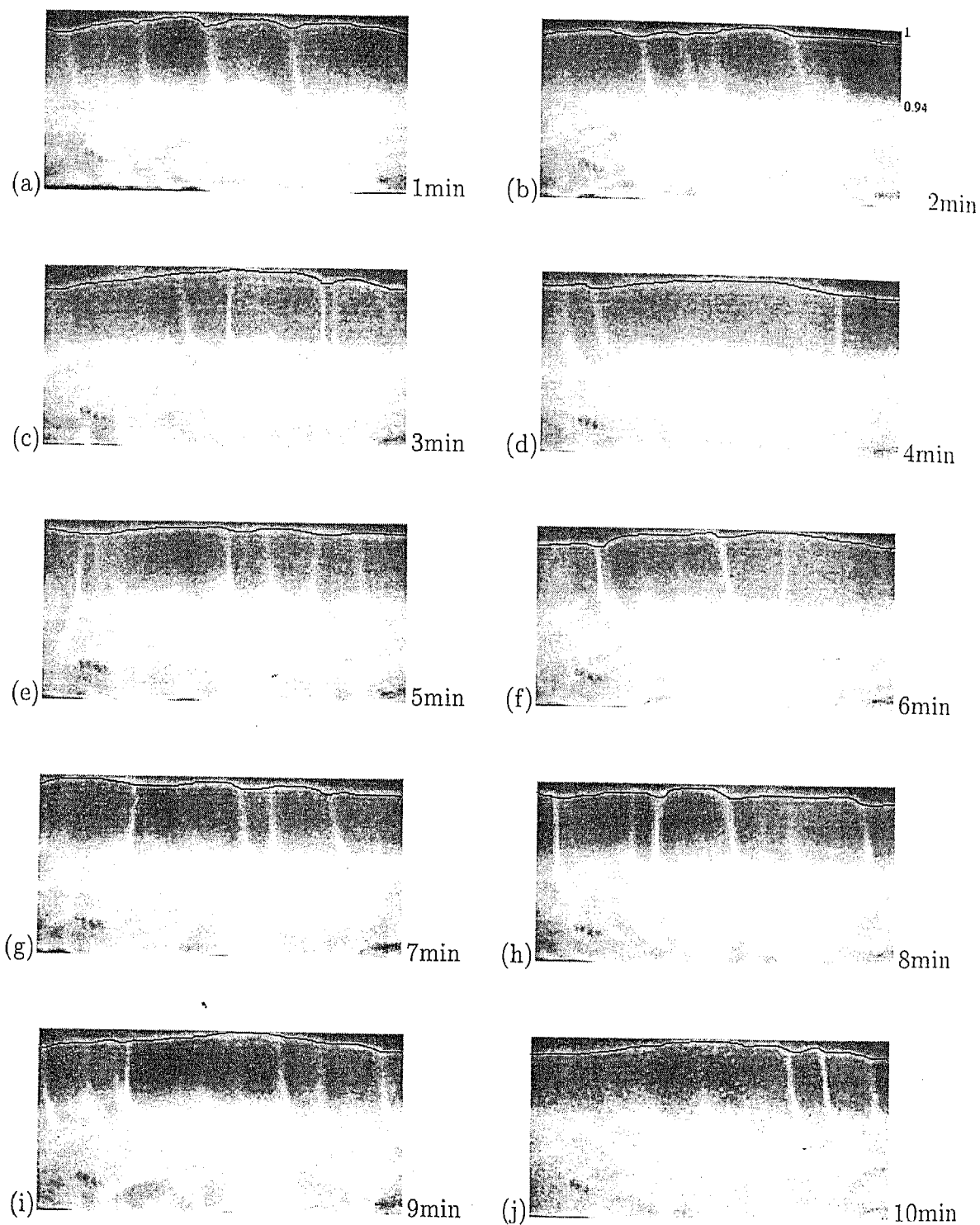


Figure 6.19: Deformed interfaces in the cavity half-filled with water, the rest being air; $\Delta T = 18$ K; Time interval between two consecutive images is 1 minute. Interfaces are emphasized in black.

K were applied across the cavity. At higher temperature differences of 5.4 and 8.5 K, the unresolved high density fringes and the refraction in the oil layer restricted the analysis of interferograms. Fringes for view angles of 0, 45, 90 and 135° were recorded in the experiments for reconstructing the three dimensional thermal field in the oil layer.

6.2.1 Steady state thermal field

In the present section, steady state fringe patterns obtained at two view angles namely 0 and 90° have been presented. Figures 6.20(a-b) show the interferograms recorded for a temperature difference of 0.4 K across the cavity. The two bounding cold and hot surfaces were maintained at temperatures of 29.7 and 30.1°C respectively. The experimental interface temperature obtained was 29.93°C, while the estimated interface temperature was 30.03°C. Based on the estimated value, the corresponding Rayleigh numbers in air and oil were 470 and 2011 respectively. Though the largest temperature drop occurs in air rather than in oil, no fringes in air were seen. On the other hand, dense fringes in the oil layer were obtained, the temperature drop per fringe shift (ΔT_c) in air and oil being 5.65 and 0.012 K respectively. Fringe patterns were captured when the flow field in the cavity was quite steady, after 4 hours of experimentation.

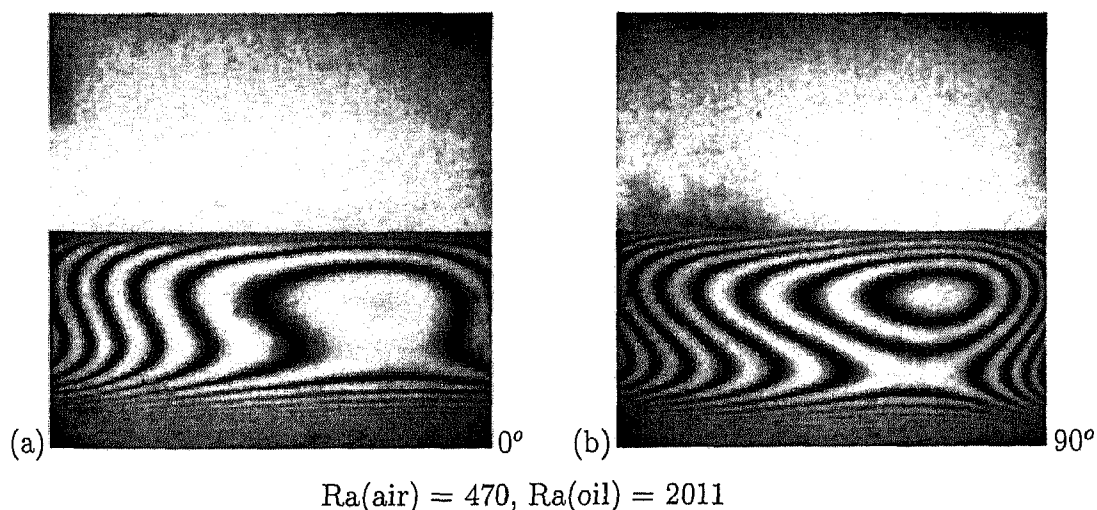


Figure 6.20: Interferograms obtained at steady state in the cavity containing air and silicone oil for a temperature difference of 0.4 K. View angles considered: (a) 0° and (b) 90°.

Fringe patterns in the oil phase, Figures 6.20(a,b), show an Ω -pattern. This indicates the thermal field to be axisymmetric about the vertical axis passing through the center of cavity. Thus the flow developed in the oil layer classifies as steady 2-dimensional

in the regime map of Figure 2.1. The fringe density is quite high near the lower wall, indicating that the rolls are closer to the interface. In air, no fringes were obtained, though a conduction state is to be expected owing to the Rayleigh number being less than the critical value of 1708.

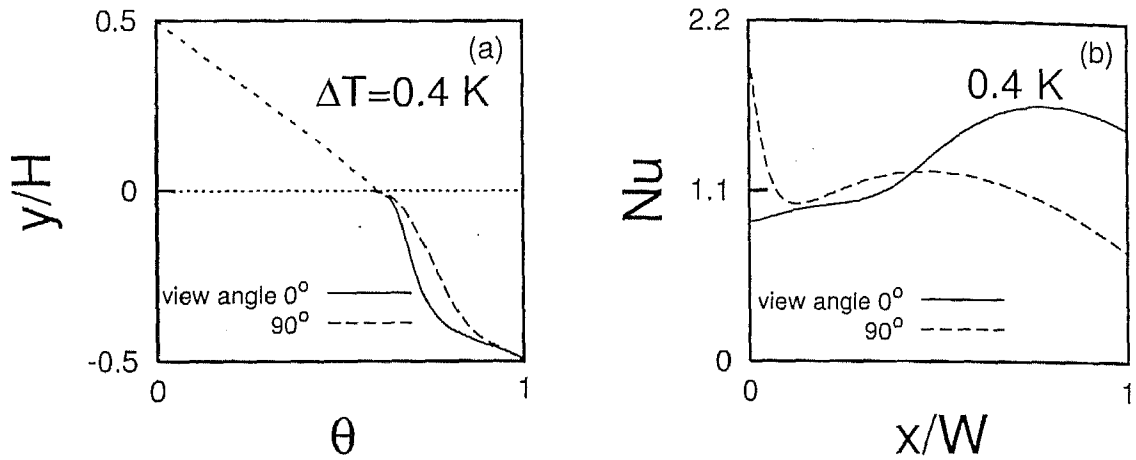


Figure 6.21: (a) Depth-averaged temperature profiles and (b) local Nusselt number variation at the hot wall in a cavity half-filled with silicone oil, the rest being air; Cavity temperature difference is 0.4 K.

Using the fringe patterns of Figures 6.20(a,b), the line-of-sight averaged temperature profiles can be plotted in the oil layer. Figure 6.21(a) shows the temperature profiles obtained in the oil layer for two view angles namely 0 and 90° . Though the air phase does not show any fringe, the expected nature of the temperature profile has been shown by dashed lines in Figure 6.21(a). A larger temperature drop takes place in air as compared to the oil owing to great difference in their thermal conductivities. A higher temperature gradients near the lower wall correlates well with the higher fringe density of the corresponding interferograms.

Based on the temperature profiles of Figure 6.21(a), the local Nusselt number variation over the hot wall of the cavity has been determined. This is shown in Figure 6.21(b) for the two view angles of 0 and 90° . Width-averaged Nusselt number at the hot wall in the oil layer has been calculated using the local variation. This is found to be 1.17 and 1.18 respectively for the view angles of 0 and 90° . The averaged Nusselt number based on the single fluid correlations (Equations 4.26 and 4.28) coupled with the energy balance principle was 1.12. The experimental value thus matched quite well with the correlation and is summarized in Table 6.2.

In Figures 6.22(a,b), the temperature difference of 1.8 K was imposed across the cavity containing equal layer heights of air and oil respectively for the view angles of 0 and

90°. The experimental and the estimated interface temperatures calculated were 29.80 and 29.87°C respectively. Accordingly, the Rayleigh numbers were determined to be 2237 and 6963 respectively in the air and the oil layers. An increase in the Rayleigh numbers led to vigorous convection in the cavity. The thermal boundary layer formed near the lower wall was of lower thickness, indicating an increase in the roll size. The number of fringes in oil was higher due to an overall increase in the temperature drop between the lower wall and the interface. Once again, fringes were not seen in air. Steady Ω -shaped isotherms, though with a distortion were obtained in the oil layer (Figures 6.22(a,b)).

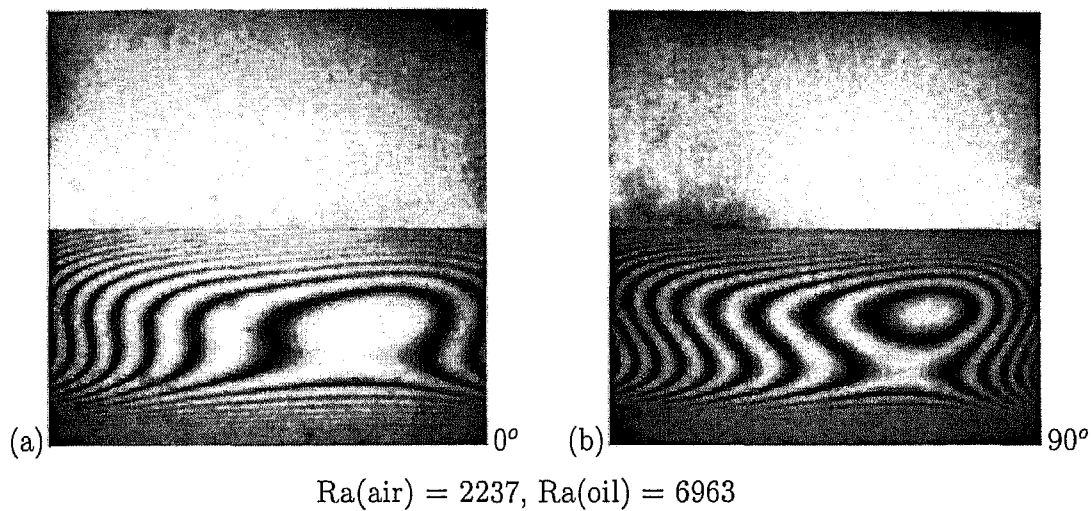


Figure 6.22: Interferograms obtained at steady state in the cavity containing air and silicone oil for a temperature difference of 1.8 K. View angles considered: (a) 0° and (b) 90°.

Based on the fringe patterns of Figures 6.22(a,b), the line-of-sight averaged temperature profiles have been determined in the oil layer and shown in Figure 6.23(a) for the view angles of 0 and 90°. The two view angles show practically identical temperatures, and thus a degree of axisymmetry in the thermal field. It is clear that the larger temperature drop in air with respect to the oil is due to the wide difference in their thermal conductivities. With an increase in the Rayleigh number, the convective rolls increase in size and tend to fill the oil layer. Accordingly, the temperature profile tends to become straighter, except for large gradients near the boundaries. Using the temperature profiles of Figure 6.23(a), the local Nusselt number variation at the hot wall in the oil layer can be calculated. This is shown in Figure 6.23(b) for the two view angles of 0 and 90°. Based on the local variation, the width-averaged Nusselt number obtained at the hot wall were 1.83 and 1.88 respectively for the view angles of 0 and 90°. The estimated averaged Nusselt number based on the correlations was found to be 1.70, and is reported in Table 6.2.

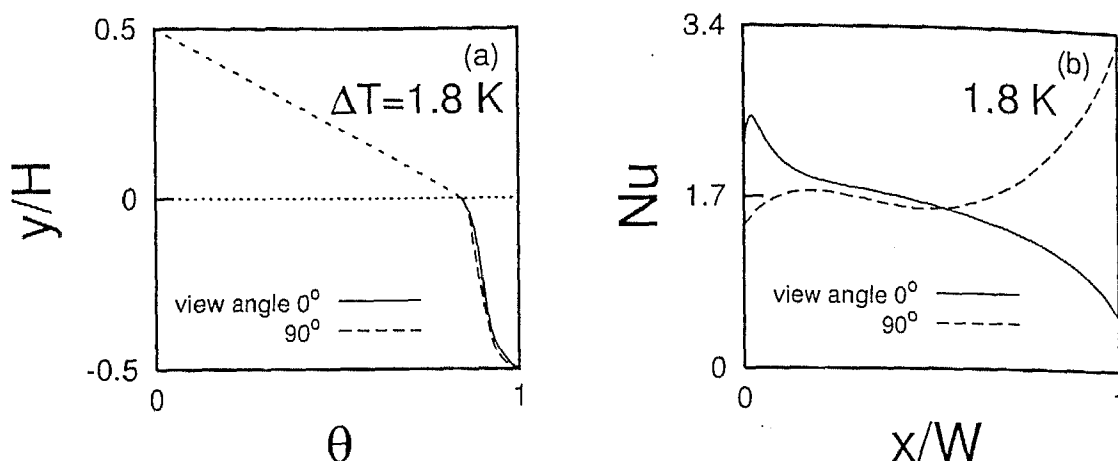


Figure 6.23: (a) Depth-averaged temperature profiles and (b) local Nusselt number variation at the hot wall in a cavity half-filled with silicone oil, the rest being air; Cavity temperature difference is 1.8 K.

For a imposed temperature difference of 3.1 K across the cavity, the fringe patterns obtained for the view angles of 0 and 90° are shown respectively in Figures 6.24(a,b). The cold and the hot bounding surfaces were maintained respectively at 27 and 30.1°C . The experimental interface temperatures were 29.70 and 29.76°C for 0 and 90° view angles respectively. While, the estimated interface temperature was found to be 29.68°C . The Rayleigh numbers thus calculated were 3861 and 12,781 respectively in air and oil. Interferograms were captured after 4 hours of experimentation, when the flow field inside the cavity becomes quite steady with time. A single fringe appeared in the field-of-view of the air phase near the cold (top) wall owing to an increase in the temperature drop across it. Line-of-sight averaged temperature profiles in the oil layer have been determined from the fringe patterns and are shown in Figure 6.25(a). Based on the temperature profiles, the local Nusselt number variation at the hot wall has been plotted in Figure 6.25(b). The width-averaged Nusselt number from the local variations were 2.16 and 2.18 respectively for the 0 and 90° view angles. The estimated Nusselt number from the correlations was 2.08, Table 6.2.

Figures 6.26(a,b) show the interferograms obtained at an applied temperature difference of 4.0 K across the cavity for the view angles of 0 and 90° respectively. The interface temperatures calculated from the experiments at 0 and 90° view angles were 29.62 and 29.84°C respectively, while the estimated temperature was 29.57°C . The individual Rayleigh numbers calculated in air and oil layers were 5028 and 16,340 respectively. Long-time interferograms show the thermal field to be quite steady with time after 4 hours of experimentation.

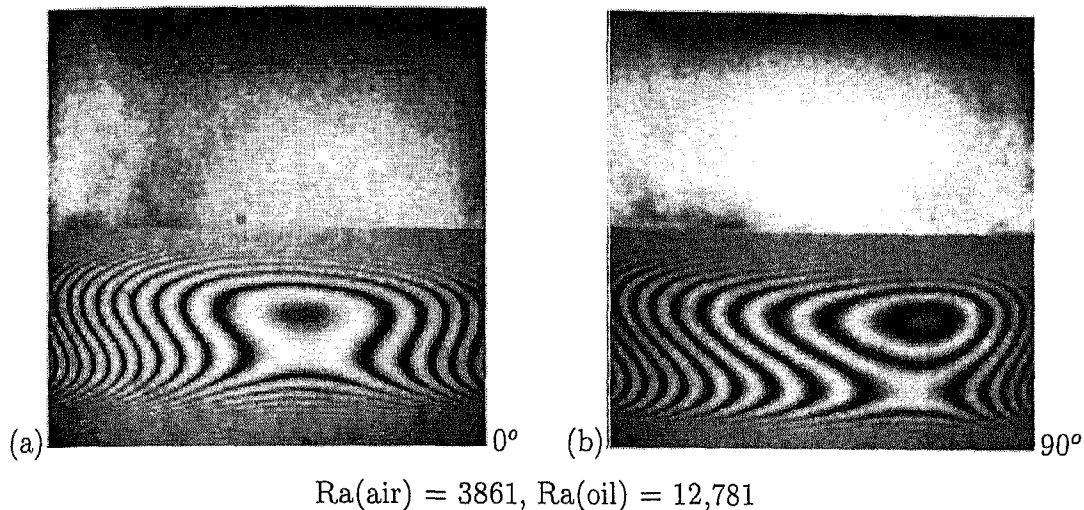


Figure 6.24: Interferograms obtained at steady state in the containing air and silicone oil for a applied temperature difference of 3.1 K. View angles considered: (a) 0° and (b) 90°.

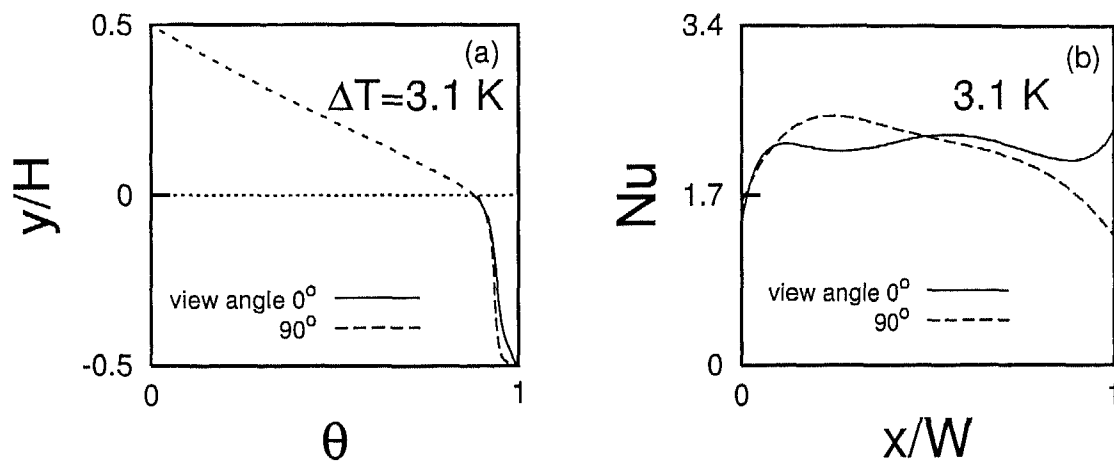


Figure 6.25: (a) Depth-averaged temperature profiles and (b) local Nusselt number variation at the hot wall in a cavity half-filled with silicone oil, the rest being air; Cavity temperature difference is 3.1 K.

Based on the fringe patterns, the line-of-sight averaged temperature profiles have been presented in Figure 6.27(a). Local Nusselt number variations at the hot wall have been calculated on the basis of the temperature profiles, Figure 6.27(b) for the two view angles (0 and 90°). The width-averaged Nusselt number were 2.37 and 2.35 respectively for 0 and 90°, the estimated value being 2.26 from the correlations, Table 6.2.

In air-silicone oil experiments, the transient evolution of the fringe patterns could not be recorded for temperature differences of 0.4, 1.8, 3.1 and 4.0 K. Unsteadiness was not induced even at as high a cavity temperature difference as 8 K. The spatial

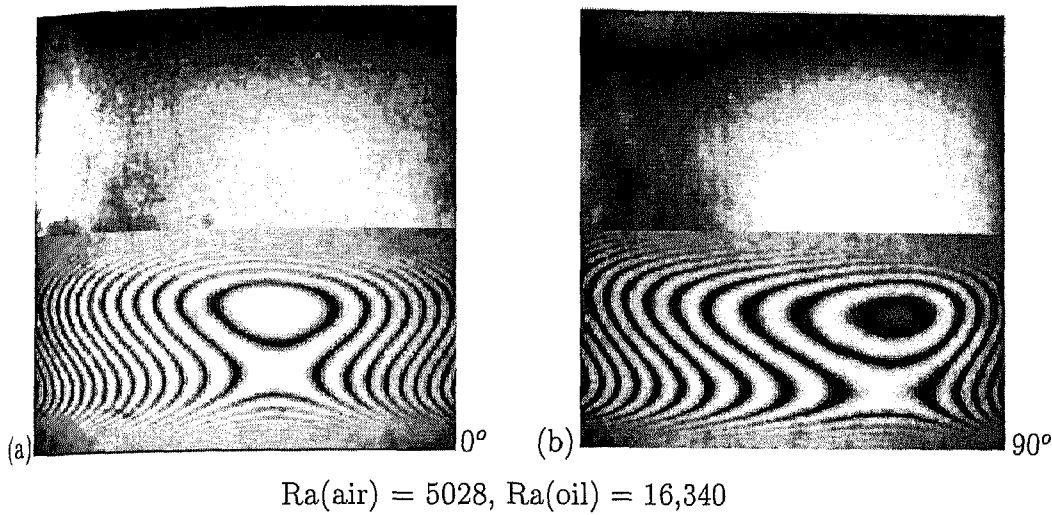


Figure 6.26: Interferograms obtained at steady state in the cavity containing air and silicone oil for a temperature difference of 4.0 K. View angles considered: (a) 0° and (b) 90° .

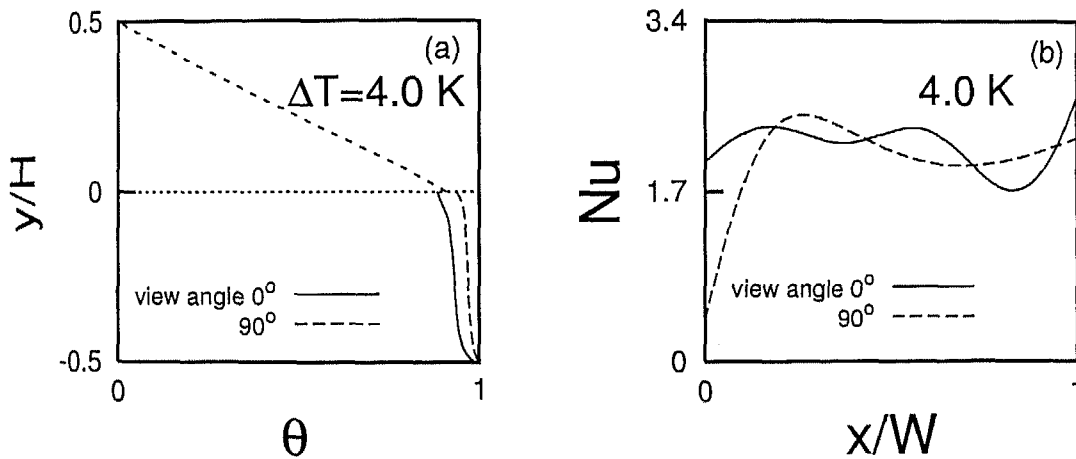


Figure 6.27: (a) Depth-averaged temperature profiles and (b) local Nusselt number variation at the hot wall in a cavity half-filled with silicone oil, the rest being air; Cavity temperature difference is 4.0 K.

structure of the flow field was one of concentric rolls in all the experiments, though strict axisymmetry was not observed.

The interferograms in silicone oil show that:

1. the overall temperature drop depends on the air-oil thermal conductivity ratio;
2. diffusion boundary-layers form near the hot wall and the interface;
3. unless close to the criticality condition ($\Delta T = 0.4$ K), the convective roll fills the oil layer with the Ω -roll centrally placed;

Table 6.2: Comparison of the interface temperatures and Nusselt numbers with Gebhart *et al.* (1988) (marked 'Ref') in a cavity containing layers of air and silicone oil of equal thickness. View angle is marked as 'V'.

ΔT , K	T_I (Exp) V - 0°	V - 90°	T_I (Ref), °C	Nu (Oil)		
				V - 0°	V - 90°	Ref
0.4	29.93	29.93	30.03	1.17	1.18	1.12
1.8	29.80	29.80	29.87	1.83	1.88	1.70
3.1	29.70	29.86	29.68	2.16	2.18	2.08
4.0	29.62	29.84	29.57	2.37	2.35	2.26

4. axisymmetry is better noticed at higher Rayleigh numbers, presumably because hexagonal rolls are initially preferred;
5. a close match in Nusselt number and the interface temperature for the two view angles between correlations and experiments indicates thermal coupling between air and oil.

6.2.2 Three dimensional structures

The three dimensional thermal fields reconstructed in the fluid layers are presented in this section. The reconstruction was possible only in the oil layer where sufficiently large number of fringes were obtained. In Section 6.2.1, the data analysis was presented for the view angles of 0 and 90°. For tomographic reconstruction, the interferograms obtained for all the view angles namely 0, 45, 90 and 135° have been similarly analyzed by applying image processing techniques.

Steady state interferograms for all the view angles have been shown in Figures 6.28(a-d) to 6.31(a-d) for temperature differences of 0.4, 1.8, 3.1 and 4.0 K respectively. Interferograms for temperature differences of 5.4 K and 8.5 K have also been presented. Application of image analysis techniques was not possible for higher temperature differences, owing to large unresolved fringes and high refraction errors near the hot wall of the cavity. However, the fringe patterns of Figures 6.32(a-d)-6.33(a-d) obtained respectively for 5.4 and 8.5 K can be qualitatively evaluated. Based on the estimated interface temperature, the Rayleigh numbers have been calculated to be 6881 and 21,880 in air and the oil layers respectively, Figure 6.32. Fringe patterns obtained from different view angles in the oil layer show dissimilarity in terms of the fringe spacing and its orientation. In air the interferograms show similar fringe patterns in all the views. The trend continues for the temperature difference of 8.5 K (Figure 6.33(a-d)). The individual

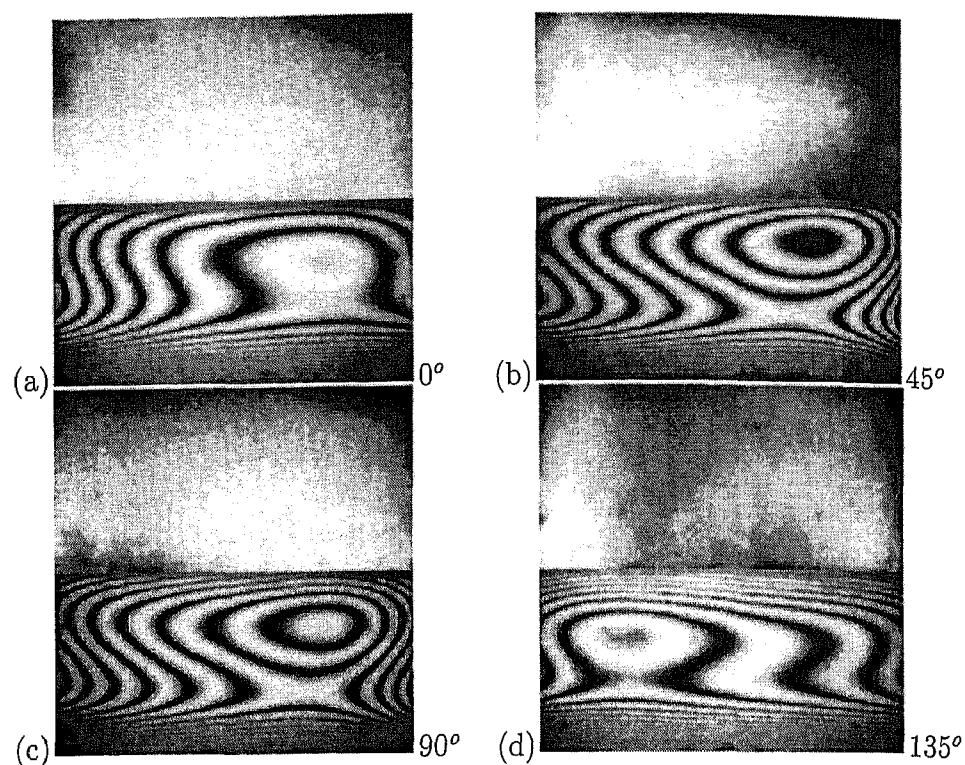


Figure 6.28: Interferograms in a cavity filled with air and silicone oil; Cavity temperature difference is 0.4 K. View angles are (a) 0°, (b) 45°, (c) 90° and (d) 135°.

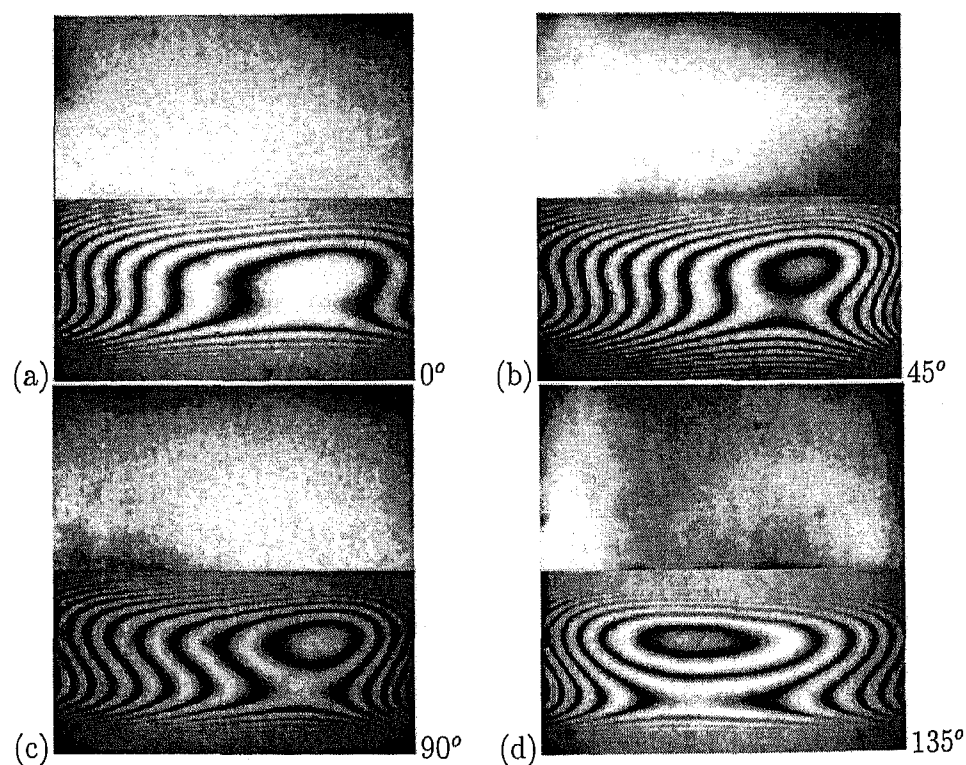


Figure 6.29: Interferograms in a cavity filled with air and silicone oil; Cavity temperature difference is 1.8 K. View angles are (a) 0°, (b) 45°, (c) 90° and (d) 135°.

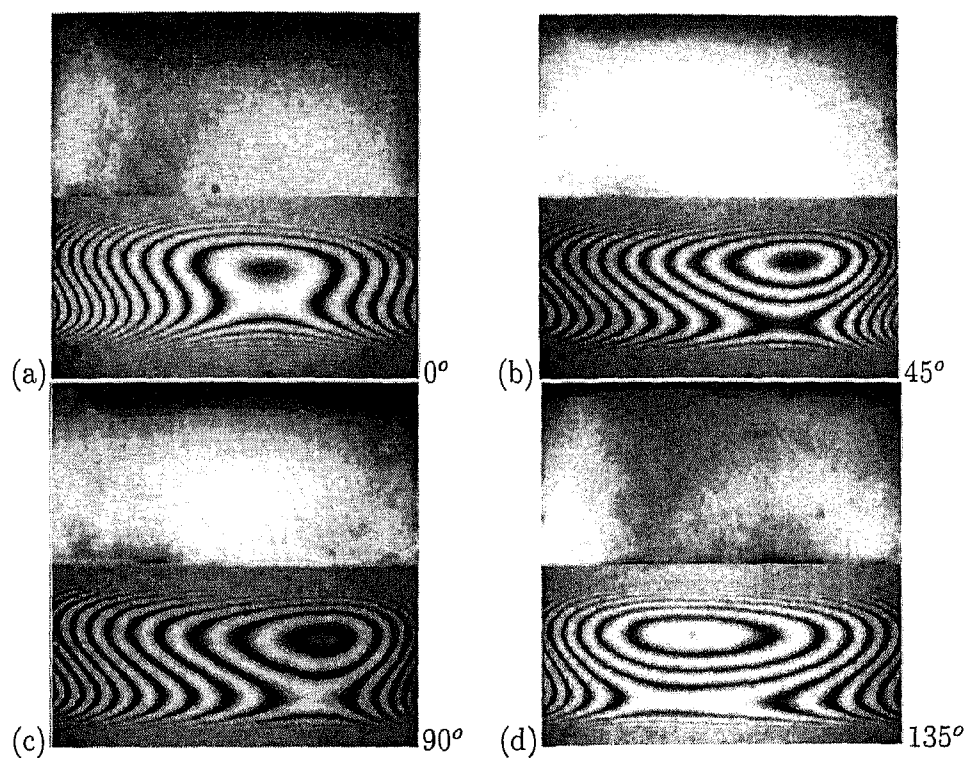


Figure 6.30: Interferograms in a cavity filled with air and silicone oil; Cavity temperature difference is 3.1 K. View angles are (a) 0°, (b) 45°, (c) 90° and (d) 135°.

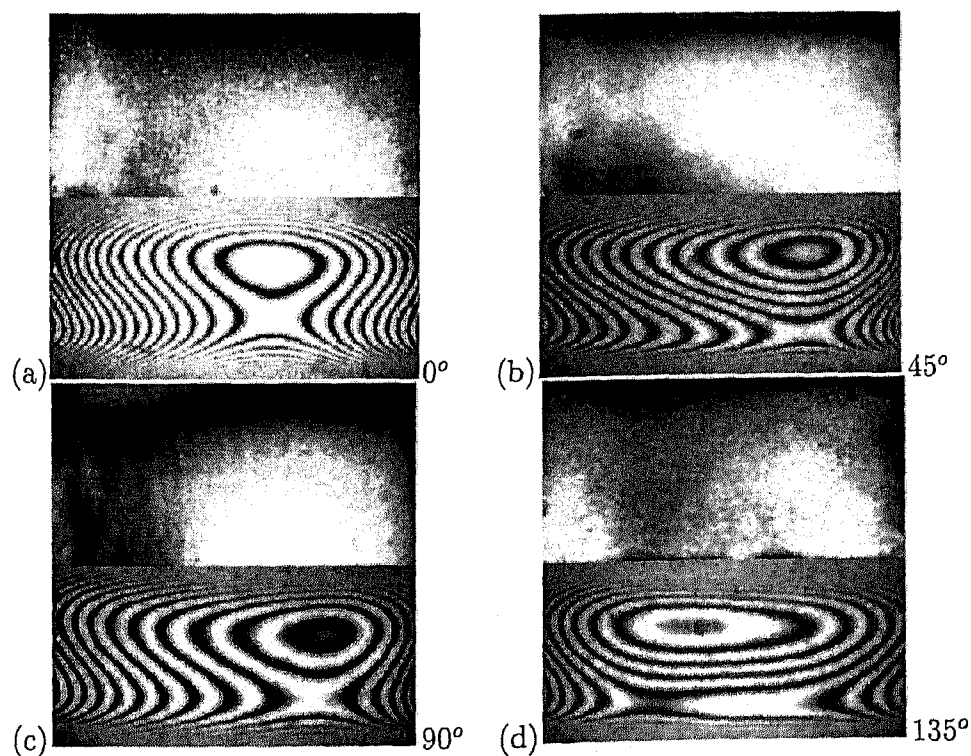


Figure 6.31: Interferograms in a cavity filled with air and silicone oil; Cavity temperature difference is 4.0 K. View angles are (a) 0°, (b) 45°, (c) 90° and (d) 135°.

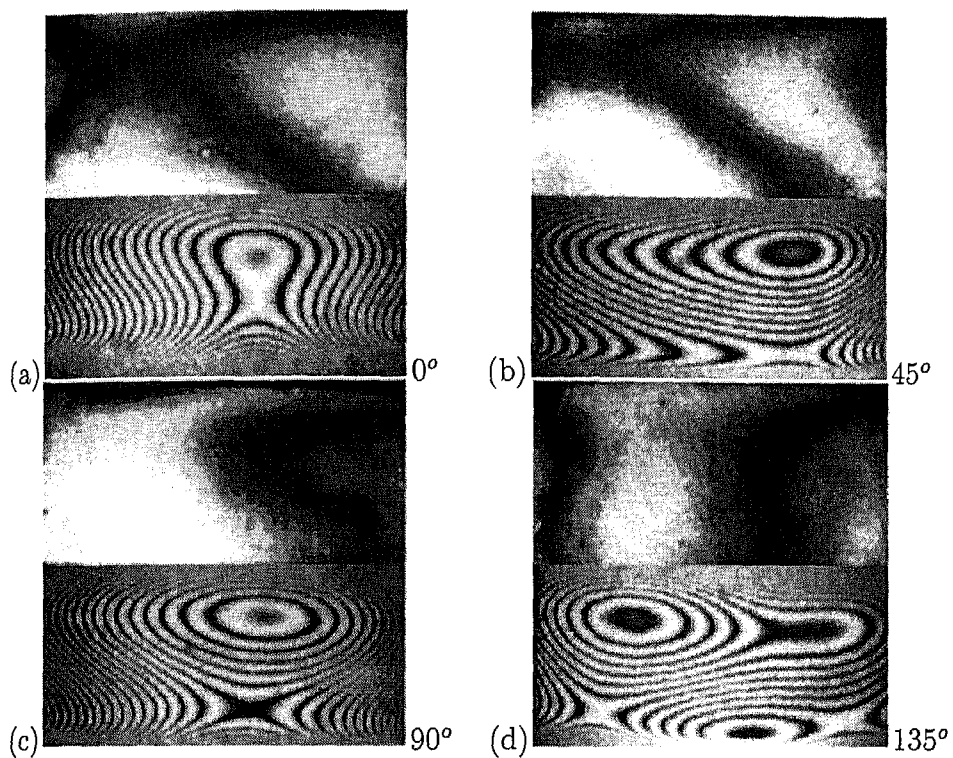


Figure 6.32: Interferograms in a cavity filled with air and silicone oil; Cavity temperature difference is 5.4 K. View angles are (a) 0° , (b) 45° , (c) 90° and (d) 135° .

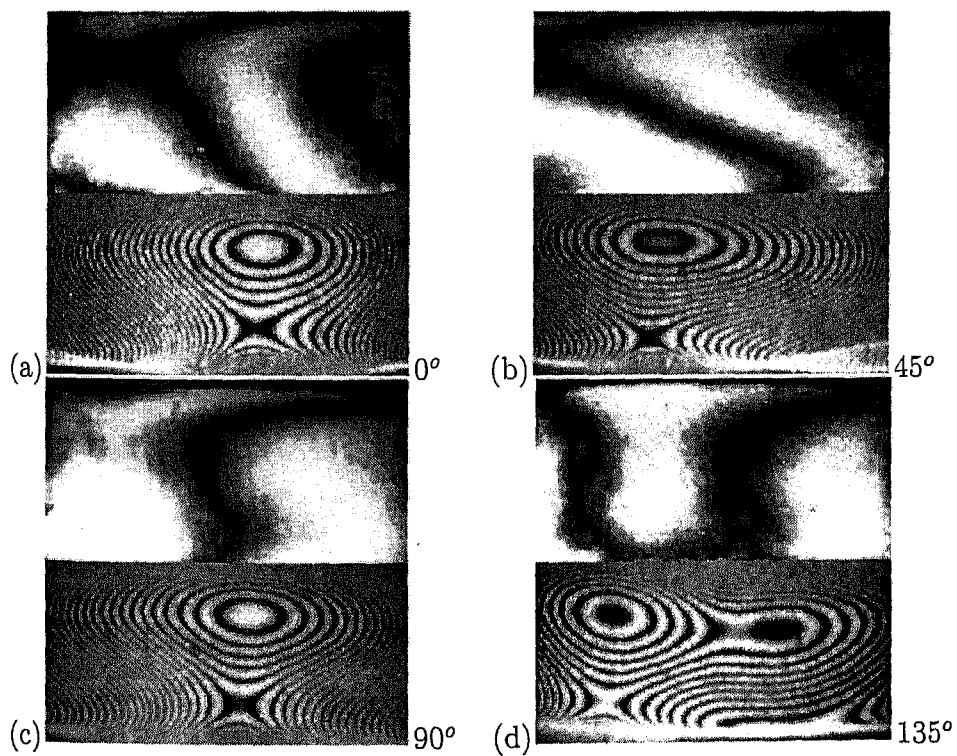


Figure 6.33: Interferograms in a cavity filled with air and silicone oil; Cavity temperature difference is 8.5 K. View angles are (a) 0° , (b) 45° , (c) 90° and (d) 135° .

Rayleigh numbers have been calculated as 11,153 and 33,980 respectively in the air and oil. The fringe patterns in oil were quite steady with time. Thus it can be concluded that the flow pattern in oil layer changed from axisymmetric (2-D) to steady 3-dimensional flow with an increase in the Rayleigh number. The unsteadiness in air was seen in the experiments to be less pronounced, despite a high Rayleigh number⁹. In the absence of an adequate number of fringes, the axisymmetry of the thermal field in air could not conclusively established.

The interferometric data for lower temperature differences has been tomographically inverted for three different horizontal planes of the cavity. Planes at $y/h = 0.15$, 0.50 and 0.85 have been considered, where the vertical coordinate $y/h = 0$ indicates the lower (hot) wall and h is the height of the oil layer. The projection data for cavity temperature differences of 0.4, 1.8, 3.1 and 4.0 K for the three horizontal planes are shown respectively in Figures 6.34(a-c) to 6.37(a-c). Figures 6.34(a-c) show that the symmetry in the projection data has increased from the lower ($y/h = 0.15$) to the mid plane ($y/h = 0.5$), while departing from symmetry at the plane $y/h = 0.85$ closer to the interface region. With increase in the Rayleigh number, Figures 6.35(a-c), greater symmetry in the projection data is noticed for all the planes. With further increase in the Rayleigh number (Figures 6.36(a-c)), the symmetry in the projection data has further improved. The convection dominated mid-plane shows the highest axisymmetry for all Rayleigh numbers. Figures 6.37(a-c) show a loss of axisymmetry in the projection data with the next increase in the Rayleigh number, indicating the onset of three dimensionality in the oil layer.

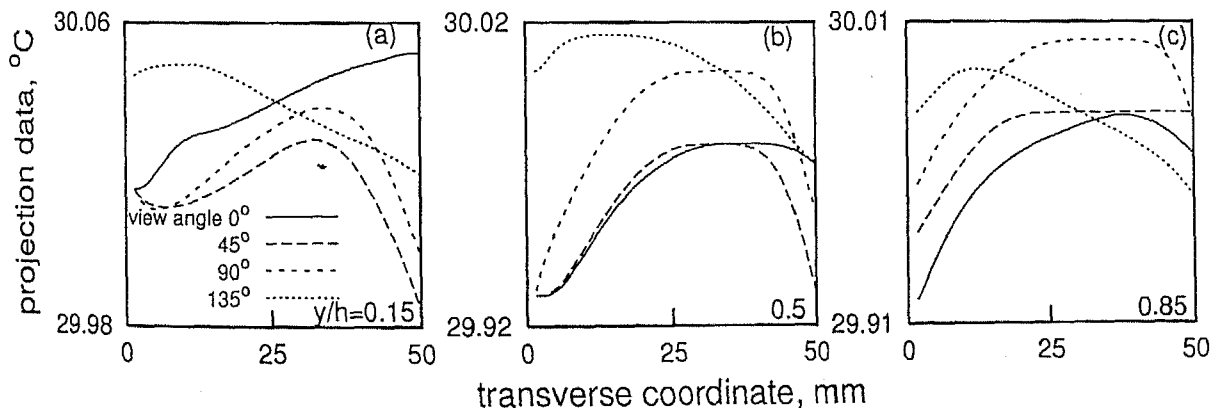


Figure 6.34: Projection data in oil at three horizontal planes along the width of the cavity. Cavity half-filled with silicone oil, the rest being air for a temperature difference of 0.4 K.

⁹To this extent, the fluid layers are mechanically coupled; with oil damping temporal fluctuations in air.

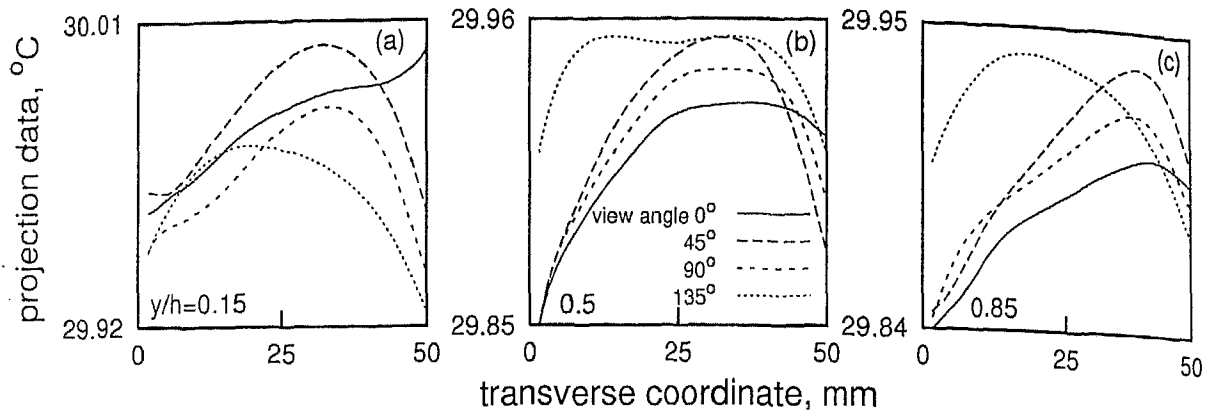


Figure 6.35: Projection data in oil at three horizontal planes along the width of the cavity. Cavity half-filled with silicone oil, the rest being air for a temperature difference of 1.8 K.

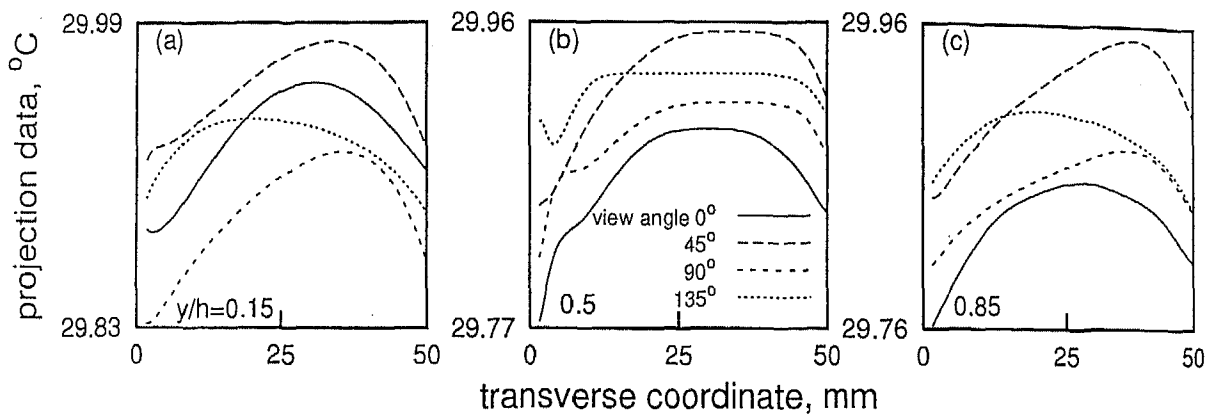


Figure 6.36: Projection data in oil at three horizontal planes along the width of the cavity. Cavity half-filled with silicone oil, the rest being air for a temperature difference of 3.1 K.

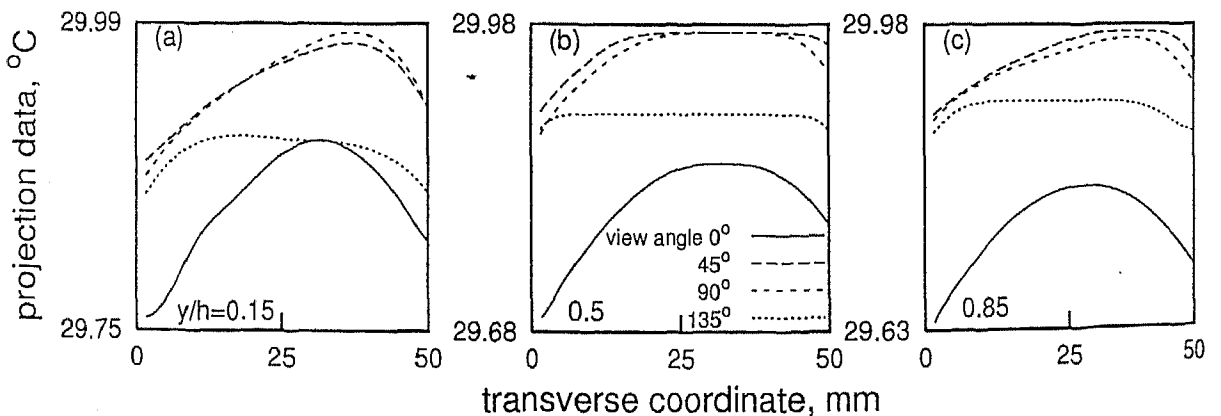


Figure 6.37: Projection data in oil at three horizontal planes along the width of the cavity. Cavity half-filled with silicone oil, the rest being air for a applied temperature difference of 4.0 K.

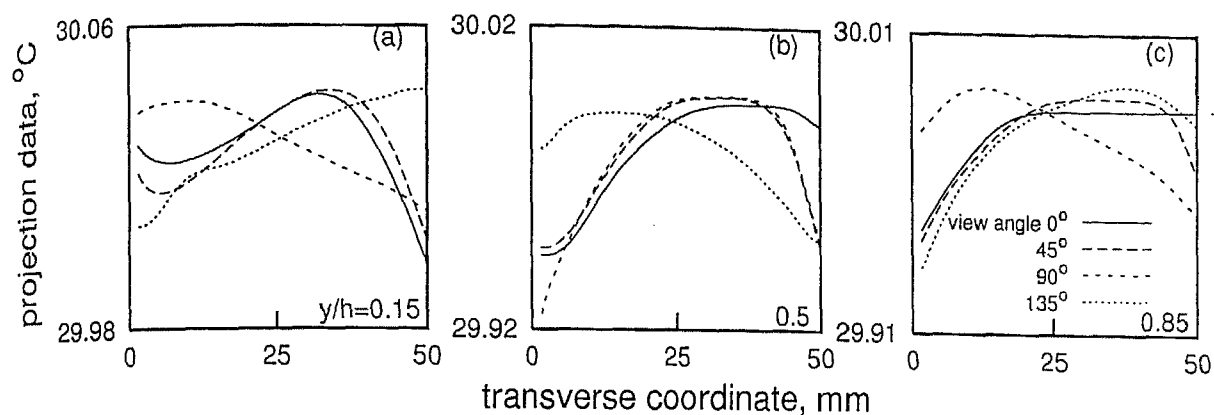


Figure 6.38: Consistent projection data in oil at three horizontal planes along the width of the cavity. Cavity half-filled with silicone oil, the rest being air for a temperature difference of 0.4 K.

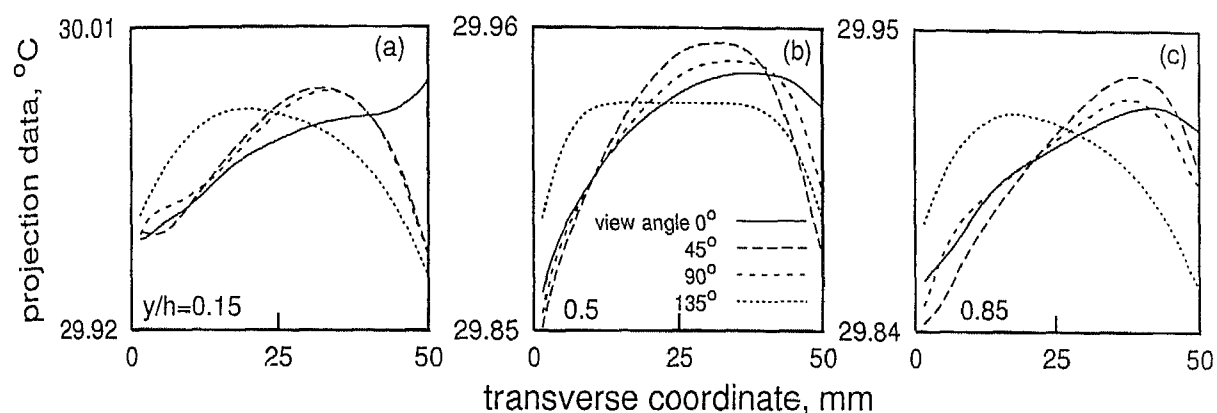


Figure 6.39: Consistent projection data in oil at three horizontal planes along the width of the cavity. Cavity half-filled with silicone oil, the rest being air for a temperature difference of 1.8 K.

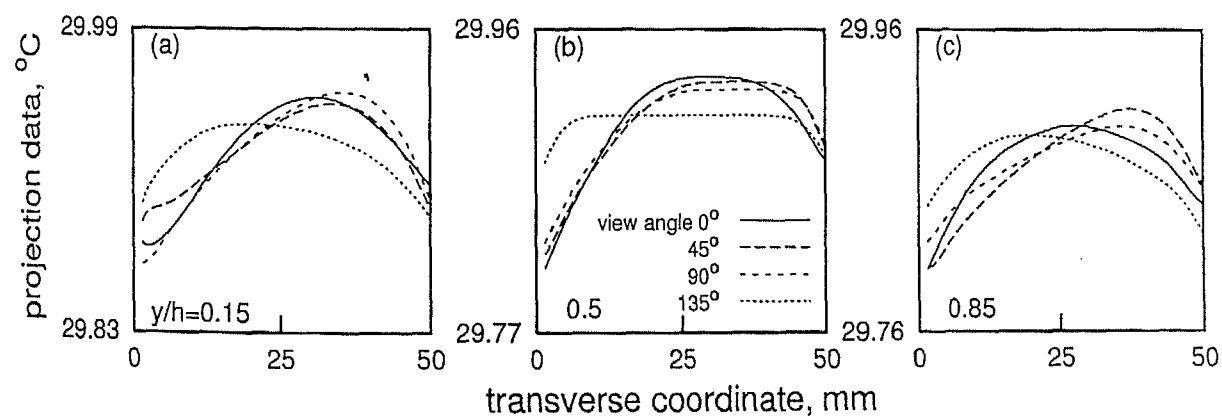


Figure 6.40: Consistent projection data in oil at three horizontal planes along the width of the cavity. Cavity half-filled with silicone oil, the rest being air for a temperature difference of 3.1 K.

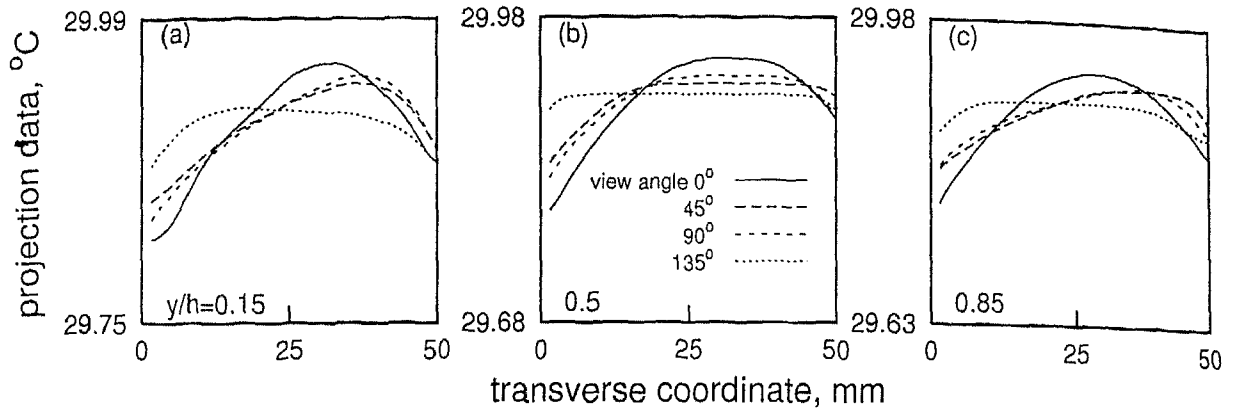


Figure 6.41: Consistent projection data in oil at three horizontal planes along the width of the cavity. Cavity half-filled with silicone oil, the rest being air for a temperature difference of 4.0 K.

The data obtained in Figures 6.34(a-c) to 6.37(a-c) show inconsistency in terms of the average fluid temperature over a given plane. Thus consistency checks have to be applied in the projection data as discussed in Section 6.1.3. The corrected projection data is shown in Figures 6.38(a-c) to 6.41(a-c) for the temperature differences of 0.4, 1.8, 3.1 and 4.0 K respectively. This data set is used as an input to the CBP algorithm for reconstructing the three dimensional thermal field.

Reconstructed temperature contours from its interferometric projection in oil are shown in Figures 6.42(a-f) and Figures 6.43(a-f) respectively for the temperature differences of 0.4, 1.8, 3.1 and 4.0 K for the three horizontal planes selected. In Figure 6.42, the reconstructed field for the temperature differences of 0.4 K (a,c,e) and 1.8 K (b,d,f) have been shown for the lower ($y/h = 0.15$), mid ($y/h = 0.5$) and the upper ($y/h = 0.85$) planes. Near-concentric rings are obtained in the central portion of the cavity for all the planes. This is a confirmation of axisymmetry in the projection data obtained from the experiments. Concentricity is higher at the mid and the upper plane as compared to the lower plane. This is owing to the presence of rolls in those planes, while a thermal boundary layer is formed near the lower plane. The temperature contour closer to the center is seen to be at a lower temperature compared to its immediate neighbour. For cavity temperature differences of 0.4 and 1.8 K, the central isotherm obtained at the respective planes is seen to decrease in size from the lower to upper plane. The isotherms at the lower and the mid planes are almost equal in size. The plume model of Figure 6.17 proposed for water is applicable in the present context as well.

Figures 6.43(a-f) show the reconstructed temperature contours for the temperature differences of 3.1 K (a,c,e) and 4.0 K (b,d,f) respectively for the three horizontal planes.

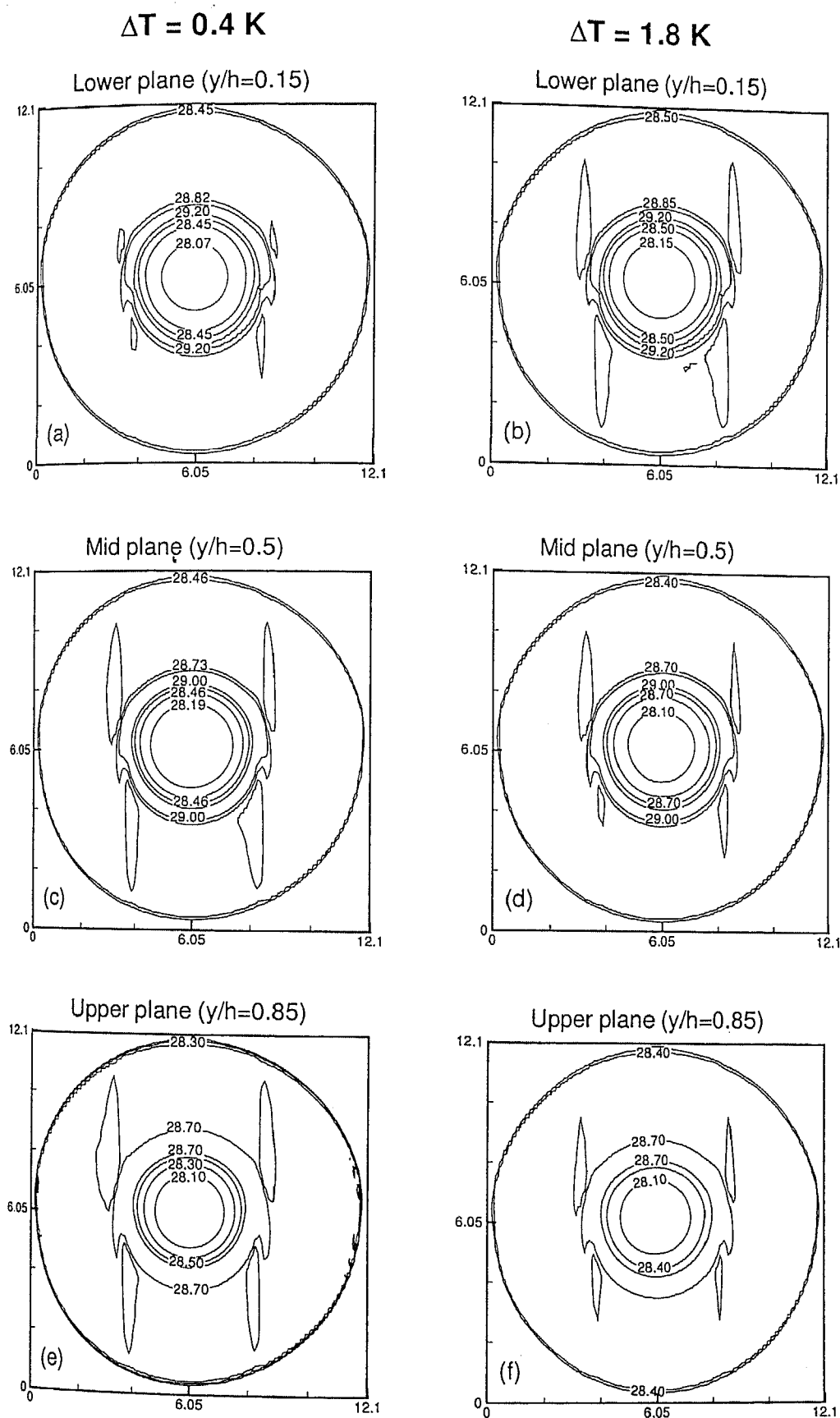


Figure 6.42: Reconstructed temperature contours in the oil layer in the cavity half-filled with silicone oil, the rest being air at temperature differences of 0.4 K (a,c,e) and 1.8 K (b,d,f) respectively at lower, mid- and upper planes of the cavity.

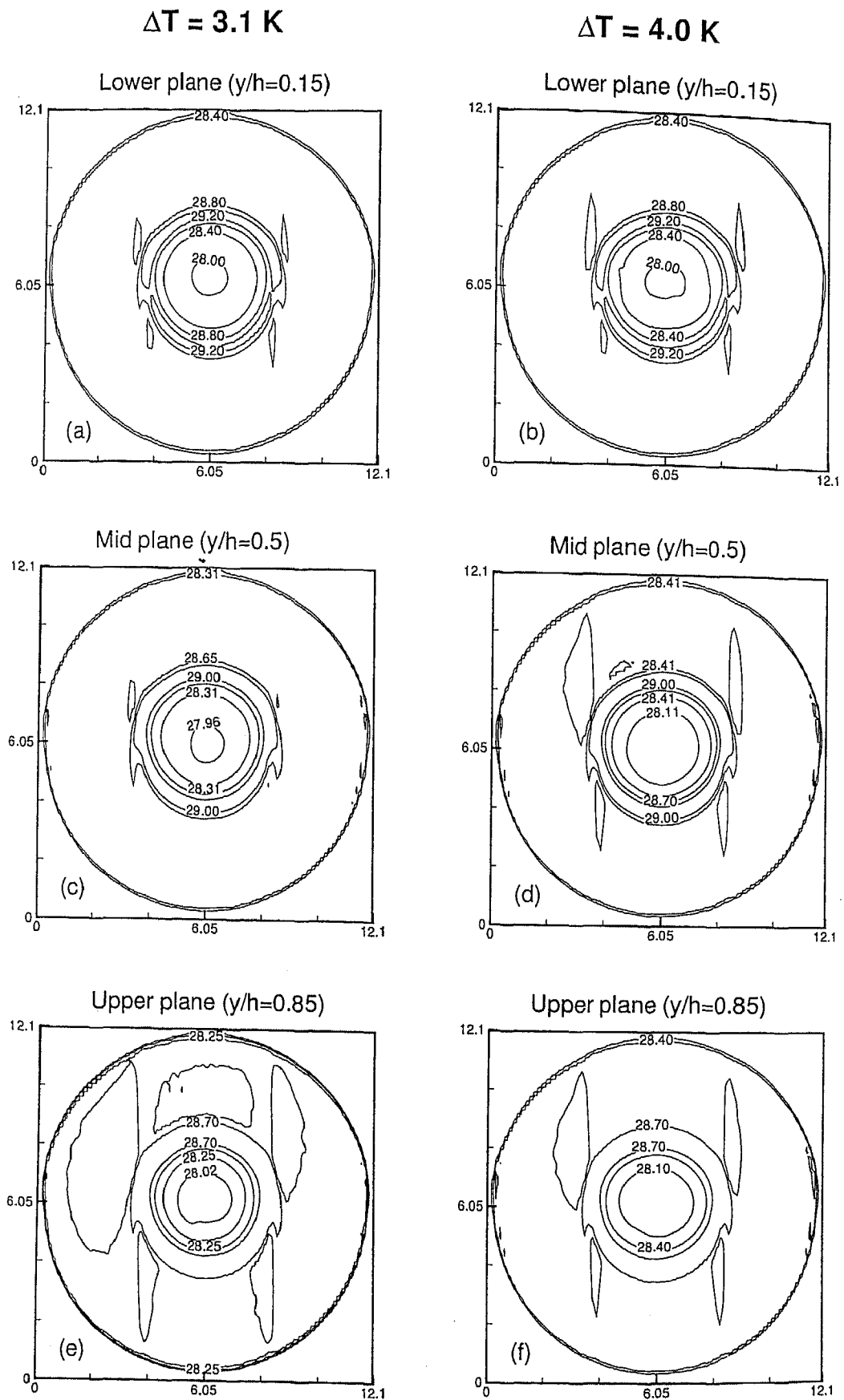


Figure 6.43: Reconstructed temperature contours in the oil layer in the cavity half-filled with silicone oil, the rest being air at temperature differences of 3.1 K (a,c,e) and 4.0 K (b,d,f) respectively at lower, mid- and upper planes of the cavity.

Near-concentric rings are obtained once again for all the planes considered. Deviation from concentricity is greater at a higher temperature difference of 4.0 K. This temperature difference also signals the onset of three dimensional flow in oil. Temperature contours again show a lower value at the center compared to its vicinity. The gradual decrease in the size of the central isotherm from the lower to the upper planes indicates a broader hot plume rising near the lower wall and a narrower cold plume descending close to the interface.

6.3 Silicone oil-water experiments

In the present section, the results obtained in the axisymmetric cavity containing fluid layers of silicone oil floating over water have been presented. Equal fluid layer thicknesses of 25 mm have been maintained in the cavity for all the experiments. Temperature differences of 0.4 and 1.8 K have been imposed across the cavity in a destabilizing configuration. The interferograms at temperature differences of 3.1 and 4.0 K have been presented for comparison. At temperature differences higher than 1.8 K, the interferograms could not be processed owing to refraction errors in oil and high unsteadiness in the water layer. Reconstruction of the three dimensional thermal field in the fluid layers of oil and water are discussed at lower Rayleigh numbers.

6.3.1 Long-time thermal field

In this section, the results obtained in the form of interferograms are presented for the cavity based temperature differences of 0.4 K and 1.8 K. Figures 6.44(a,b) show the long-time (not strictly steady) interferograms for view angles of 0 and 90° at an imposed temperature difference of 0.4 K across the cavity. The cold and the hot bounding surfaces were maintained at the temperatures of 29.7 and 30.1°C respectively. Based on the averages of the two estimates from oil and water side, the interface temperatures have been calculated to be 29.93 and 29.90°C respectively for 0 and 90°. The estimated interface temperature based on correlations was found to be 30.05°C. Subsequently, the Rayleigh numbers have been calculated as 10,955 and 17,266 in oil and water respectively. Though the temperature drop in oil is slightly larger than that in water, a larger number of fringes appeared in the field-of-view of the oil phase owing to its smaller ΔT_e value of 0.012 K as compared to 0.059 K for water. The flow field in oil was quite steady, while in water some unsteadiness was noticed with time. The dominant patterns were captured when the flow field was fully evolved in the fluid layers in the cavity. Figures 6.44(a,b)

show the long-time fringe patterns obtained after 4 hours of experimentation.

In the oil layer, the flow develops close to the cold wall in the form of an inverted omega (Ω). Thus the fringe patterns represent a concentric roll. In water, the isotherms prominent in the projection data do not form a specific pattern, Figures 6.44(a,b). A high fringe density is to be noticed near the interface of the oil layer. Thus the interface between the fluid layers act as a thermally active region. Interferograms obtained at the two view angles of 0 and 90° in the oil layer are quite similar in terms of the fringe orientation, number of fringes, and fringe spacing. A greater degree of dissimilarity is realized in the water layer. Thus, it may be concluded that the thermal field in the cavity is axisymmetric in oil and non-axisymmetric (specifically, three dimensional) in water. Since the three dimensionality in water has not predominantly influenced the thermal field in oil, one can conclude that mechanical coupling between the layers is of secondary importance.

Based on the fringe patterns of Figures 6.44(a,b), the line-of-sight averaged temperature profiles have been determined. Temperature profiles of fluid layers is shown in Figure 6.45(a). The main conclusion to emerge from Figure 6.45(a) is that almost equal temperature drops occur in oil and water as expected from the fluid conductivity ratio. The temperature gradient is higher near the hot wall as compared to the cold wall. The high fringe density near the interface in oil can be attributed to the Rayleigh number mismatch for the fluid layers. The axisymmetric rolls cannot sustain the high heat transfer rates and are consequently pushed towards the colder wall. The appearance of dense fringes in silicone oil deserve comment. Since the temperature drop per fringe shift in silicone oil is the smallest as compared to air and water, the fringe density in oil is naturally quite high. In addition, the thermal conductivity of oil is smaller than for water by a factor of four, though larger than air by a factor of 6. Hence, in the oil-water experiment, a greater fraction of temperature drop occurs in oil. When combined with a lower value of ΔT_e , a large number of fringes are preferentially observed in oil, while the number in water is smaller. In oil-air experiments, a small temperature drop is sufficient to generate fringes in the oil layer, while at best, only a few are seen in air.

In the conduction regime, the fringes in oil are practically straight. When the convective rolls set in, the fringe density near the wall and the interface increase since the heat transfer rate across the cavity is now increased above the conduction value. Fringe deformation is seen in the central portion of the oil layer where transport is advection-dominated. The dense fringes near the wall and the interface represent large temperature gradients and can be identified qualitatively as a diffusion boundary layer. With increasing cavity temperature difference, the layer Rayleigh number increases and

the boundary-layer thickness decreases. Similar changes occur in air and water as well (in the axisymmetric regime), except that adequate number of fringes are not available for demonstrating the phenomena.

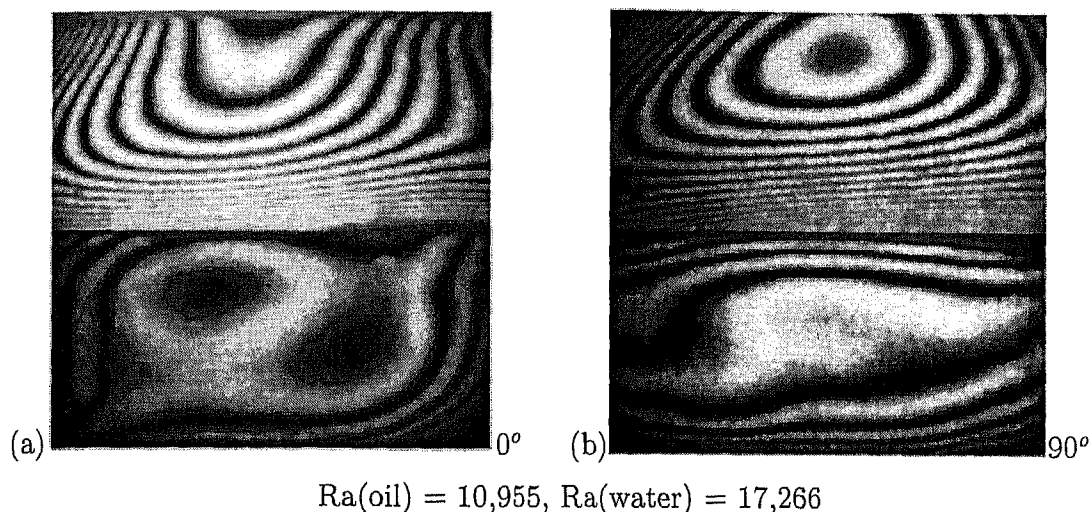


Figure 6.44: Long-time interferograms obtained in the cavity containing silicone oil floating over water for a applied cavity temperature difference of 0.4 K. View angles considered: (a) 0° and (b) 90° .

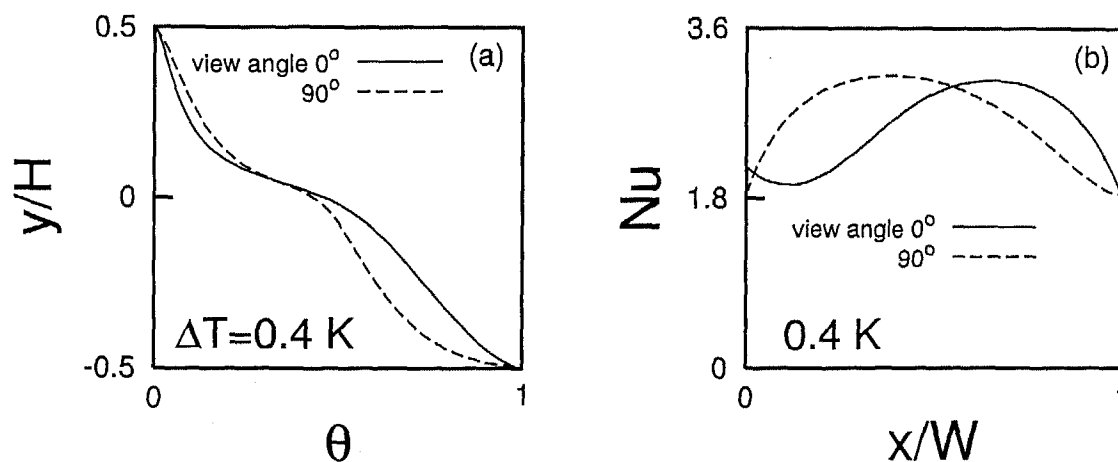


Figure 6.45: (a) Depth-averaged temperature profiles and (b) local Nusselt number variation at the interface in a cavity filled with equal layer thicknesses of silicone oil and water; Cavity temperature difference is 0.4 K.

Using the temperature profiles of Figure 6.45(a), the local Nusselt number variation can be determined for the two view angles of 0 and 90° . Fringes near the interface region covers the whole width of the fluid layer in the oil phase. Therefore, the local Nusselt number variation at the interface has been calculated using the fringes of the oil layer. Local Nusselt number variation at the interface of the fluid layers is shown in Figure

6.45(b). The local variation for the two views show a shift, while the averages are close to each other. The width-averaged Nusselt number based on the local variations of Figure 6.45(b) were 2.60 and 2.64 respectively for the view angles of 0 and 90°. The estimated width-averaged Nusselt number based on the correlations was 2.84, Table 6.3.

Figures 6.46(a,b) show the long-time fringe patterns formed in oil and water at a temperature difference of 1.8 K across the cavity. The two view angles considered are namely 0 and 90° respectively. The cold and the hot plates are maintained at the temperatures of 28.3 and 30.1°C. The experimental interface temperatures were calculated to be 29.27 and 29.23 respectively for 0 and 90°. The estimated interface temperature from correlations was 29.86°C. Accordingly, the individual Rayleigh numbers calculated were 48,402 and 88,157 in the oil and the water layer respectively. A vigorous convective motion was observed in the water layer due to a high Rayleigh number. Steady state was not obtained even after 7 hours of experimentation. The long-lived dominant patterns have been captured and are shown in Figures 6.46(a,b). However the fringe patterns in the oil layer quickly reached steady state with respect to time. The inverted omega (Ω) isotherms have been obtained in the oil layer. This indicates the rolls to be in the form of concentric rings, though not axisymmetric.

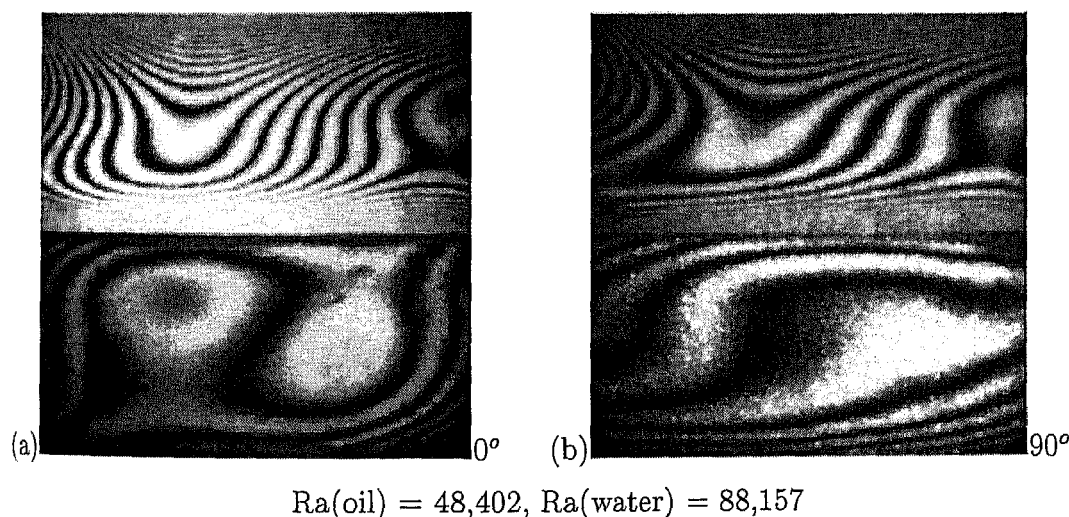


Figure 6.46: Long-time interferograms obtained in the cavity containing silicone oil floating over water for a cavity temperature difference of 1.8 K. View angles considered: (a) 0° and (b) 90°.

The fringe patterns in the oil layer are similar in the two views. In the water layer, the fringe patterns as well as their orientation are quite different. Specifically, rolls similar those in air for a rectangular cavity can be seen in water. This is indicative of a pattern that is not dependent on the shape of the confining boundaries. The thermal

field developed in the fluid layers are steady and three dimensional in oil, and unsteady but three dimensional in water.

The flow in the individual fluid layer is driven by the respective temperature difference between the nearest wall and the interface. The unsteadiness in the fringe patterns of water at the Rayleigh number obtained is unaffected by the stabilizing influence of silicone oil, a result opposite to that of the rectangular test cell. This suggests the flow to be thermally rather than mechanically coupled at the interface.

Using the fringe patterns of Figures 6.46(a,b), the depth-averaged temperature profiles in the fluid layers have been determined. This is shown in Figure 6.47(a). Nearly equal temperature drop is to be noticed in oil and water. Near the interface region on both sides, high temperature gradient are established. The gradient decreases drastically in the central portion of the fluid layers, in particular in the oil phase, again increasing near the two walls. This is because of the dominance of convective transport in the

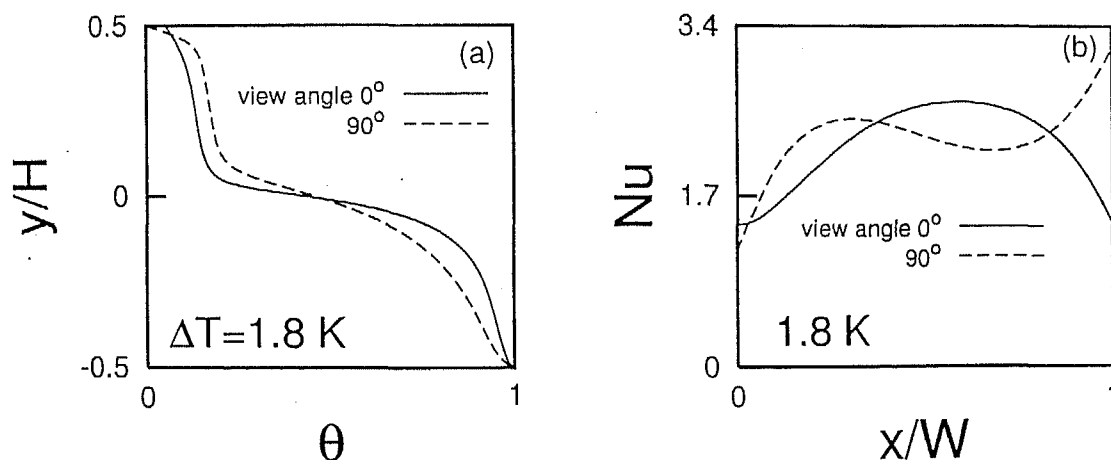


Figure 6.47: (a) Depth-averaged temperature profiles and (b) local Nusselt number variation at the cold wall in a cavity filled with equal layer thicknesses of silicone oil and water; Cavity temperature difference is 1.8 K.

central regions of the respective fluid layers.

Based on the temperature profiles of Figure 6.47(a) in oil, the local Nusselt number variation at the cold (upper) wall can be calculated. Local Nusselt number distribution at the cold wall for the two view angles of 0 and 90° is shown in Figure 6.47(b). Though two Nusselt number profiles are displaced, their average value for each plate are similar. The width-averaged Nusselt number obtained at the cold wall are 2.22 and 2.23 respectively for the view angles of 0 and 90° . The estimated averaged Nusselt number based on the single fluid correlations can be calculated as 3.24 (Table 6.3). A high discrepancy in

the results can be due to a few unresolved fringes near the cold wall, the presence of an interface, and interferogram representing only 41% of the cavity diameter.

Nusselt number calculations are based on Equation 4.25 and require flow to be steady¹⁰. This equation can however be applied to estimating the instantaneous Nusselt number in the fluid layer exhibiting unsteadiness. In the water layer of the oil-water experiments, the instantaneous local Nusselt number variation at the hot wall has been determined from the interferograms. This is shown in Figures 6.48(a,b) for the temperature differences of 0.4 K and 1.8 K respectively. The instantaneous variations show a lower Nusselt number in the projection data, of 0° as compared to 90° for both temperature differences. The instantaneous width-averaged Nusselt numbers were obtained as 3.03 and 4.99 for the view angles of 0 and 90° respectively. In Figure 6.48(b), the values are 3.34 and 4.67 respectively. The estimated Nusselt number based on the single fluid correlations are 3.72 and 5.25 for temperature differences of 0.4 K and 1.8 K. It is surprising that the discrepancy in average Nusselt number due to unsteadiness is not as high as that arising from a change in the spatial pattern, for example in the oil layer.

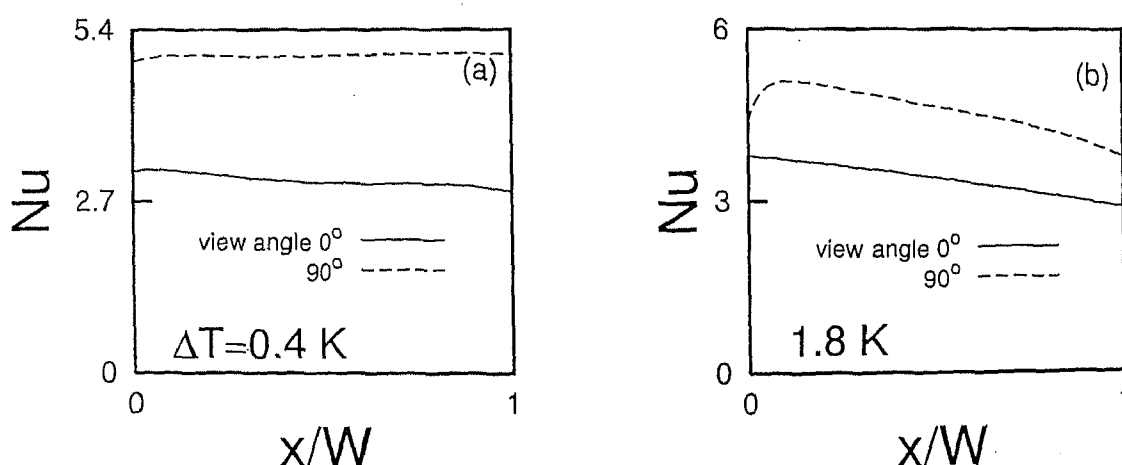


Figure 6.48: Local Nusselt number variations at the hot wall in a cavity filled with equal layer thicknesses of silicone oil and water; Cavity temperature differences are (a) 0.4 K and (b) 1.8 K.

6.3.2 Three dimensional structures

The present section discusses the reconstruction of the thermal field in the oil layer floating over water in the circular cavity. In Section 6.3.1, the temperature calculations were shown for the projection data at view angles of 0 and 90°. To reconstruct the thermal

¹⁰For unsteady convection, the correlations give a time-average value.

Table 6.3: Comparison of the interface temperatures and Nusselt numbers with Gebhart *et al.* (1988) (marked 'Ref') in a cavity containing layers of silicone oil and water of equal thickness. View angle is marked as 'V'.

ΔT , K	T_I (Exp) V - 0°	V - 90°	T_I (Ref), °C	Nu		
				V - 0°	V - 90°	Ref
0.4	29.93	29.90	30.05	2.60	2.64	2.84
1.8	29.27	29.23	29.86	2.22	2.23	3.24

field over the cross-section, identical analysis has been carried out for the projection data of 45 and 135° as well.

Long-time interferograms for temperature differences of 0.4 K and 1.8 K for all the view angles have been shown in Figures 6.49 to 6.50. Fringe patterns for higher temperature differences of 3.1 K and 4.0 K could be only qualitatively analyzed owing to large number of unresolved fringes and refraction errors. These are shown respectively in Figures 6.51 and 6.52 for the four view angles considered in the experiments. Based on the estimated interface temperature, the Rayleigh numbers were calculated to be 82,754 and 1.58E+05 in oil and water layer respectively for $\Delta T = 3.1$ K, Figure 6.51. In the experiments, the fringe patterns were steady in oil but highly unsteady in water. Three dimensionality was however observed in the oil layer. The time-dependent regime in water displayed periodicity, the time period being approximately 60 seconds. The interferograms that persisted for a longer duration have been shown in Figures 6.51(a-d). In Figure 6.52 ($\Delta T = 4$ K), the Rayleigh numbers obtained were 1.06E+05 and 2.08E+05 in oil and water. Once again, steady three dimensional flow in oil and time-dependent flow in water have been observed. The frequency of fluctuations in the fringe patterns in water increased, the time period being around 50 seconds.

The projection data obtained from the experiments at $\Delta T = 0.4$ K and 1.8 K and all the view angles is now considered. The temperature field in the fluid layers have been plotted at three horizontal planes namely $y/h = 0.15$, 0.5 and 0.85 with respect to the coordinate parallel to the width of the cavity. Here, in the oil layer $y/h = 0$ indicates the top (cold) wall, while in the water layer, it is the bottom (hot) wall. The value of $y/h = 0.85$ represents the region near the interface for both the fluid layers. The experimental projection data for the central part of the cavity are shown in Figures 6.53 to 6.56 for temperature differences of 0.4 K and 1.8 K. Figures 6.53(a-c) and 6.54(a-c) show respectively the projection data in oil and water layers for the three horizontal planes and a temperature difference of 0.4 K across the cavity. Axisymmetry in the

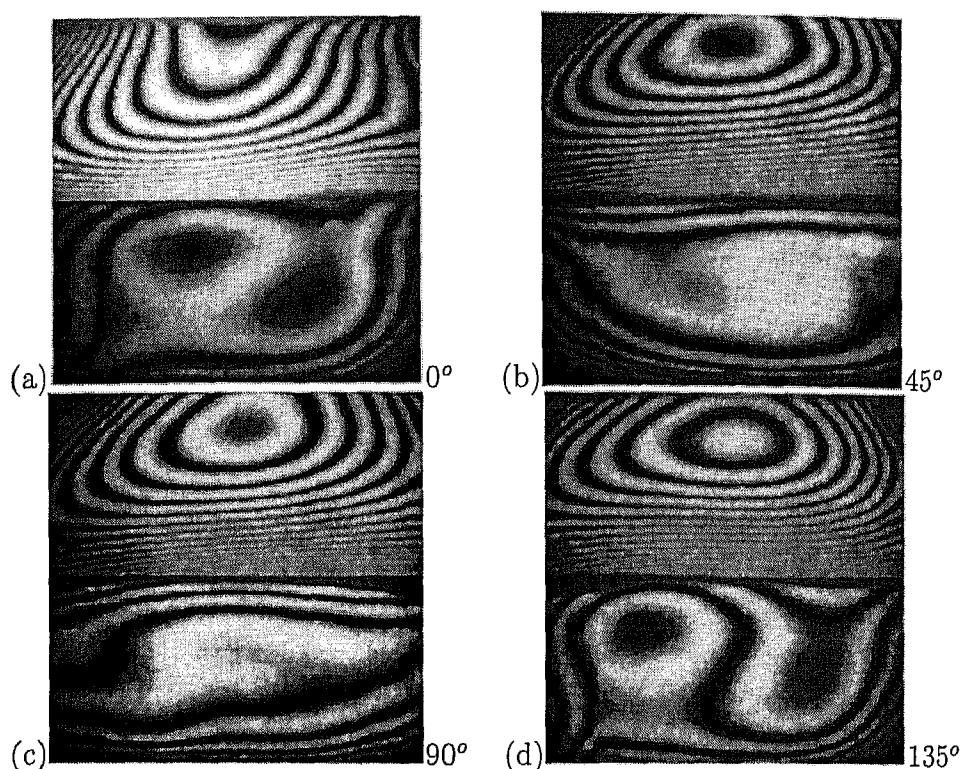


Figure 6.49: Long-time interferograms in a cavity filled with silicone oil and water; Cavity temperature difference is 0.4 K. View angles are (a) 0° , (b) 45° , (c) 90° and (d) 135° .

thermal field is realized near the top wall, Figure 6.53(a). The projection data obtained for view angles of 45° and 90° are quite close to each other near the cold wall. At the mid-plane of the oil layer, the axisymmetry diminishes, while at the lower plane adjacent to the interface, the loss of axisymmetry is complete, Figures 6.53(b-c). In Figures 6.54(a-c), the thermal field in the water layer is non-axisymmetric for all the view angles and planes considered in the experiments. With an increase in the Rayleigh number, Figures 6.55(a-c), axisymmetry is partially restored in the thermal field in the oil layer. Here, the projection data for the view angles of 0° and 45° on one hand and 90° and 135° on the other are close to each other. Loss of axisymmetry is more pronounced with an increase in Rayleigh number in the water layer, Figures 6.56(a-c).

The consistent data set that satisfies the requirement that the average fluid temperature over a plane is a constant for all view angles is shown in Figures 6.57-6.60. The CBP algorithm can now be applied for the reconstruction of the thermal field in each of the planes of the fluid layers.

Figures 6.61-6.62 show the reconstructed temperature contours in the fluid layers of oil and water for temperature differences of 0.4 K and 1.8 K respectively. Three planes have been considered in both the fluid layers. The temperature contours in oil

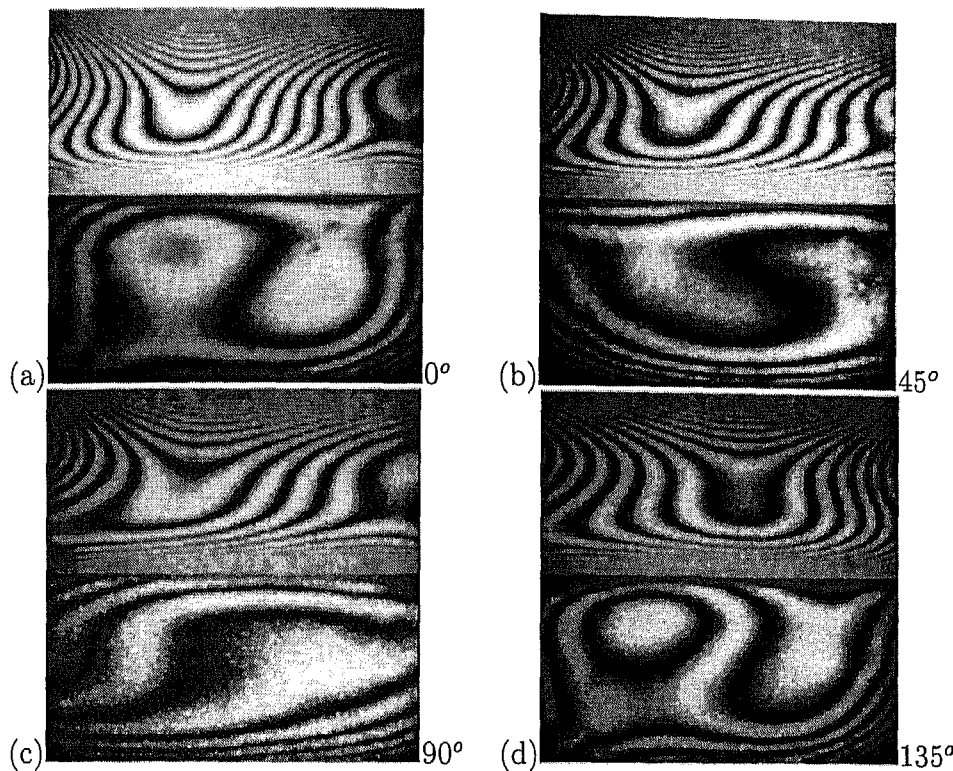


Figure 6.50: Long-time interferograms in a cavity filled with silicone oil and water; Cavity temperature difference applied 1.8 K. View angles are (a) 0° , (b) 45° , (c) 90° and (d) 135° .

for the planes of Figures 6.61(a,c) show near-concentric rings in the central portion of the cavity, while the concentricity is smaller near the interface (Figure 6.61(e)). This indicates that the flow is axisymmetric near the cold wall ($y/h = 0.15$) and the mid-plane region ($y/h = 0.5$). There is a gradual increase in the size of the isotherm of $T = 28.57^\circ\text{C}$ from the upper to the mid-plane in oil. This can be understood in terms of flow descending from the center of the upper plane to form a roll as in Figure 6.17. Temperature contours in water (Figures 6.61(b,d,f)) show closed but distorted isotherms for all the planes considered. This is understandable because the thermal field in water is three dimensional. The temperature contours near $T = 28.48^\circ\text{C}$ show no measurable change in the size while moving from one to the other plane.

Figures 6.62(a,c,e) show the reconstructed temperature contours obtained in oil at a cavity-based temperature difference of 1.8 K. With an increased Rayleigh number, the overall axisymmetry in the thermal field is better, particularly near the midplane (Figure 6.62c), while it is lowered at the plane near the interface (Figure 6.62e). The size of the isotherms barely change from one plane to the other. This shows an indeterminate behaviour in terms of the roll direction of the fluid flow in the central portion of the cavity. With an increase in Rayleigh number, the temperature contours in water (Figures

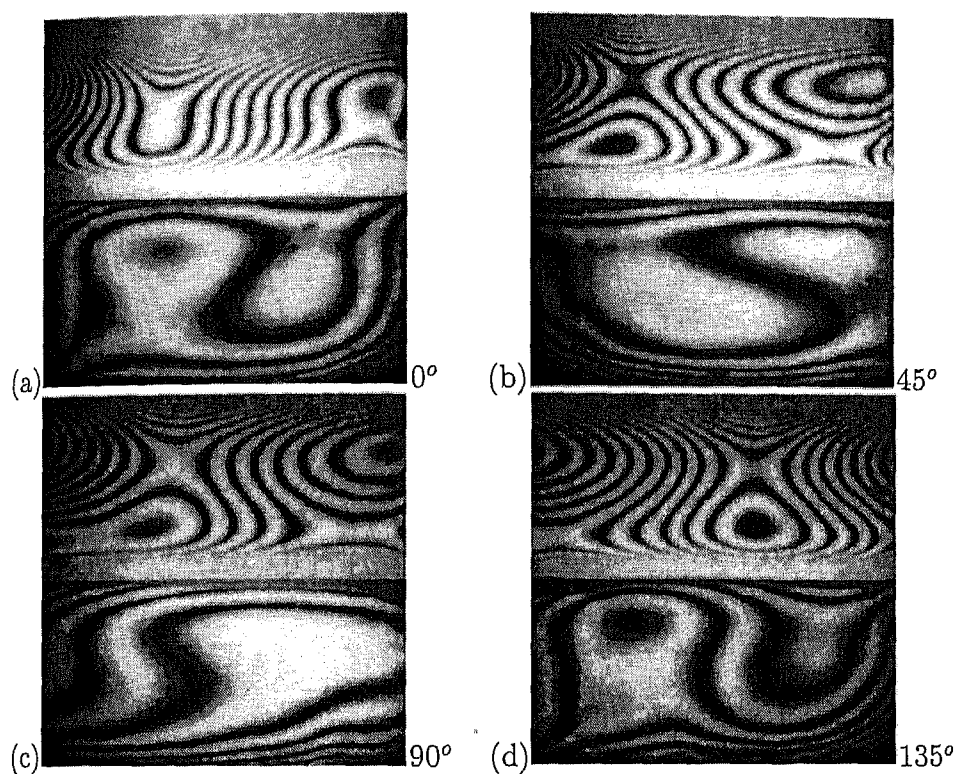


Figure 6.51: Long-time interferograms in a cavity filled with silicone oil and water; Cavity temperature difference is 3.1 K. View angles are (a) 0°, (b) 45°, (c) 90° and (d) 135°.

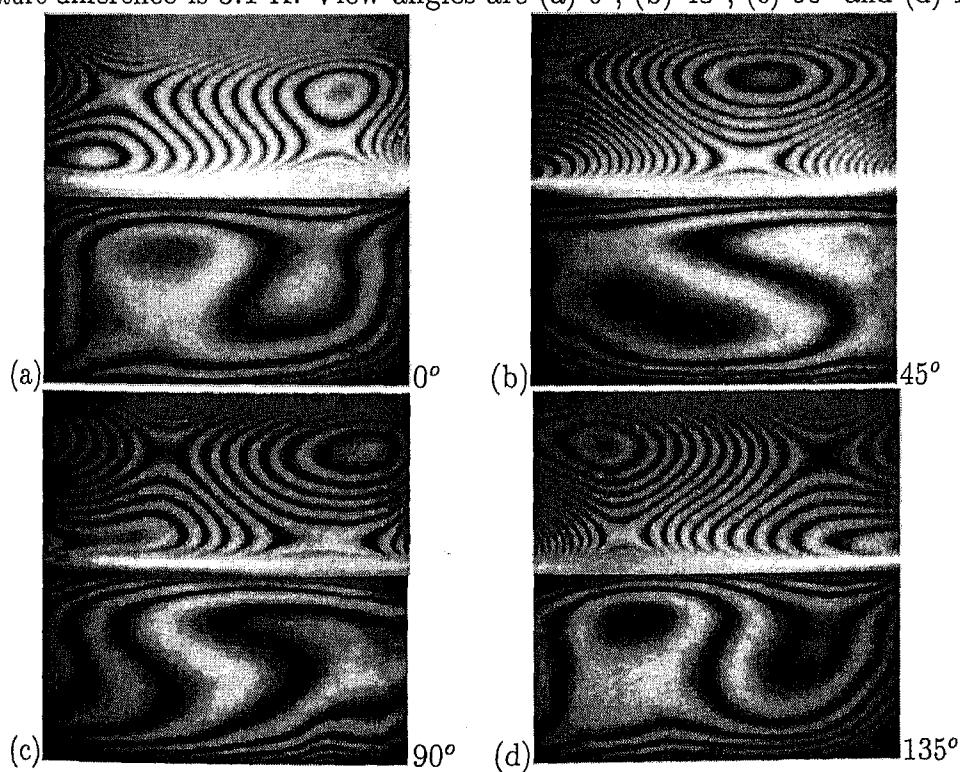


Figure 6.52: Long-time interferograms in a cavity filled with silicone oil and water; Cavity temperature difference is 4.0 K. View angles are (a) 0°, (b) 45°, (c) 90° and (d) 135°.

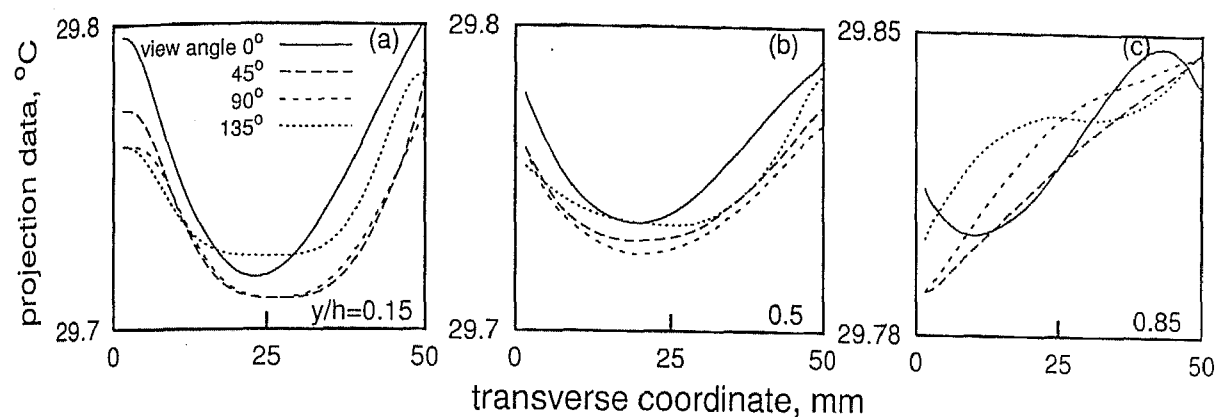


Figure 6.53: Projection data in oil at three horizontal planes along the width of the cavity. Cavity filled with silicone oil and water at a temperature difference of 0.4 K.

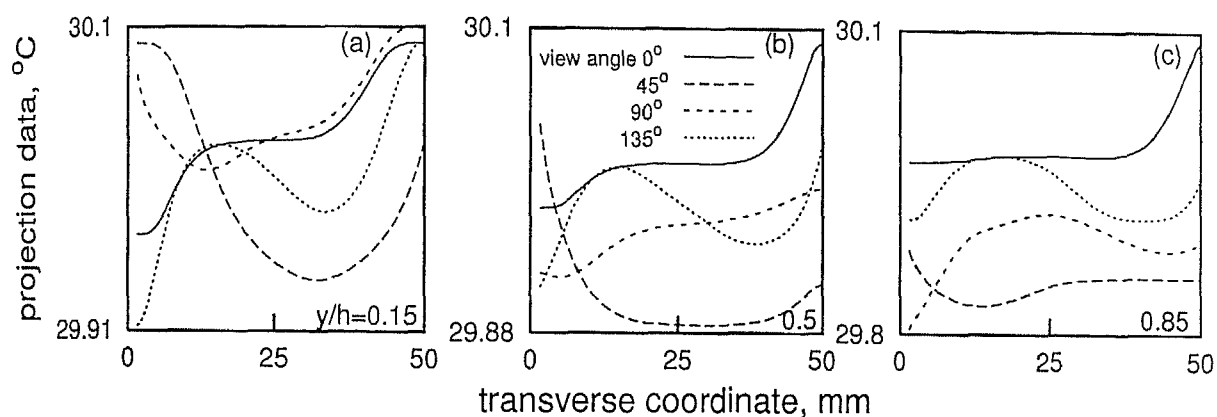


Figure 6.54: Projection data in water at three horizontal planes along the width of the cavity. Cavity filled with silicone oil and water at a temperature difference of 0.4 K.

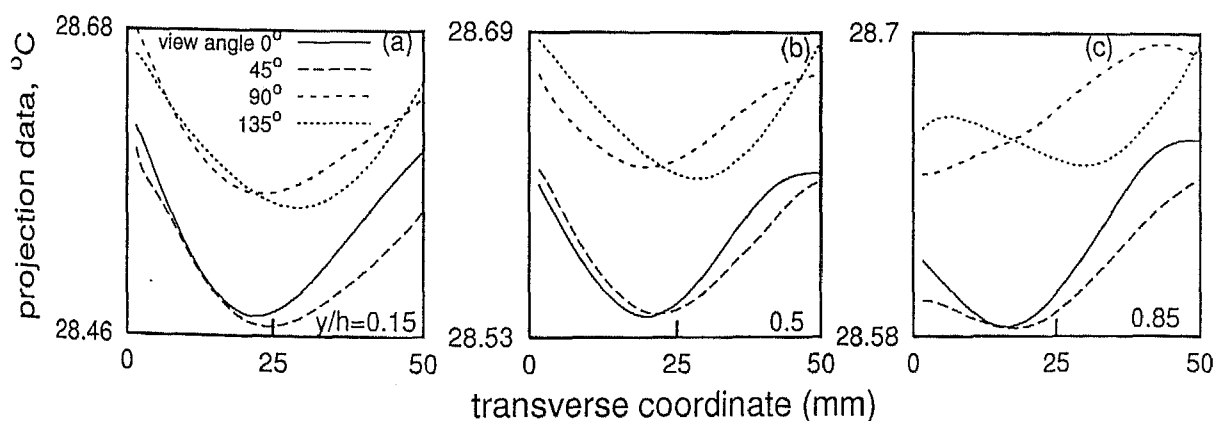


Figure 6.55: Projection data in oil at three horizontal planes along the width of the cavity. Cavity filled with silicone oil and water at a temperature difference of 1.8 K.

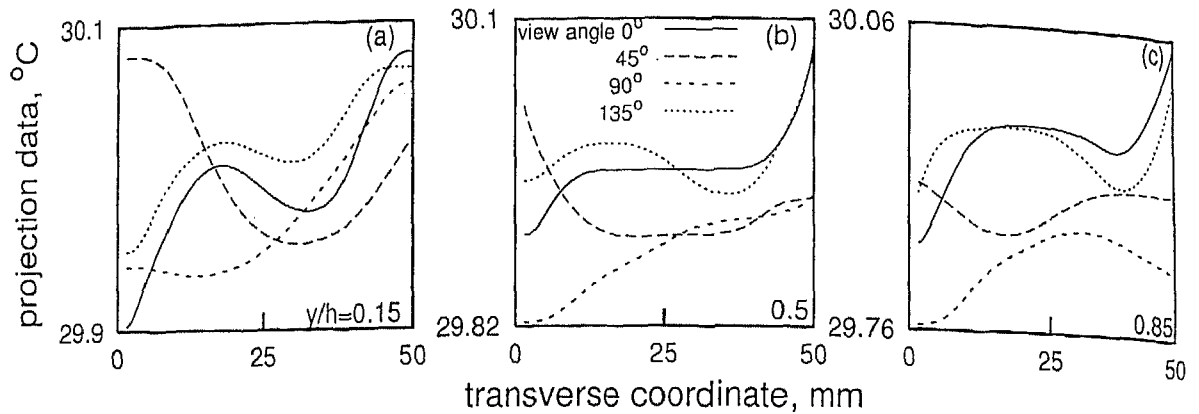


Figure 6.56: Projection data in water at three horizontal planes along the width of the cavity. Cavity filled with silicone oil and water at a temperature difference of 1.8 K.

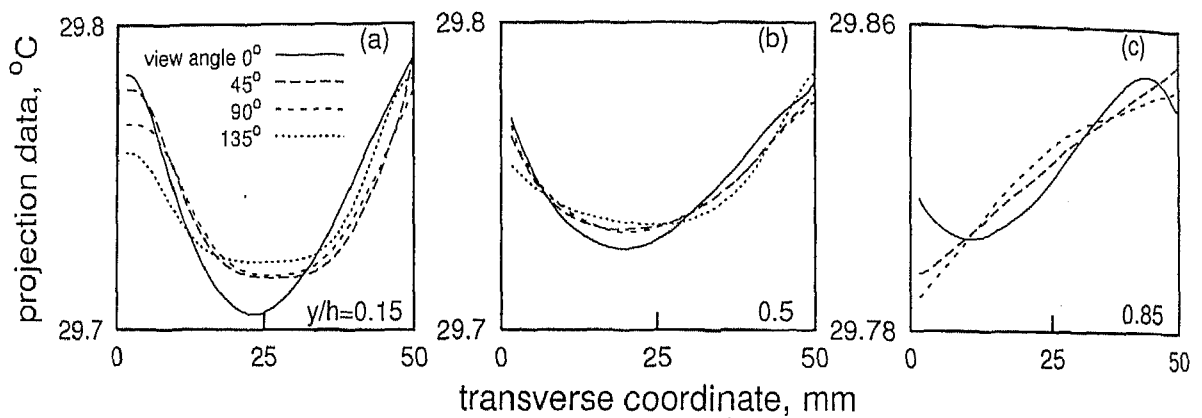


Figure 6.57: Consistent projection data in oil at three horizontal planes along the width of the cavity. Cavity filled with silicone oil and water for a temperature difference of 0.4 K.

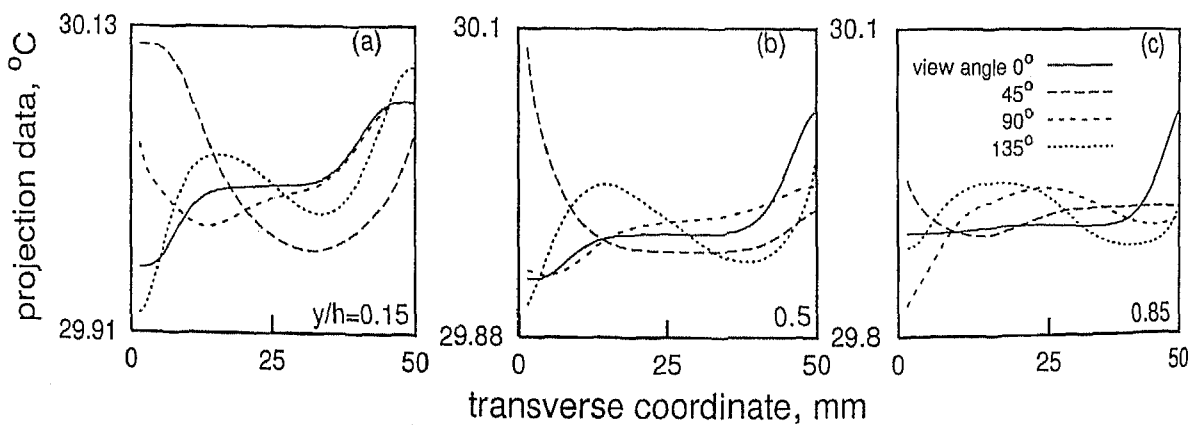


Figure 6.58: Consistent projection data in water at three horizontal planes along the width of the cavity. Cavity filled with silicone oil and water for a temperature difference of 0.4 K.

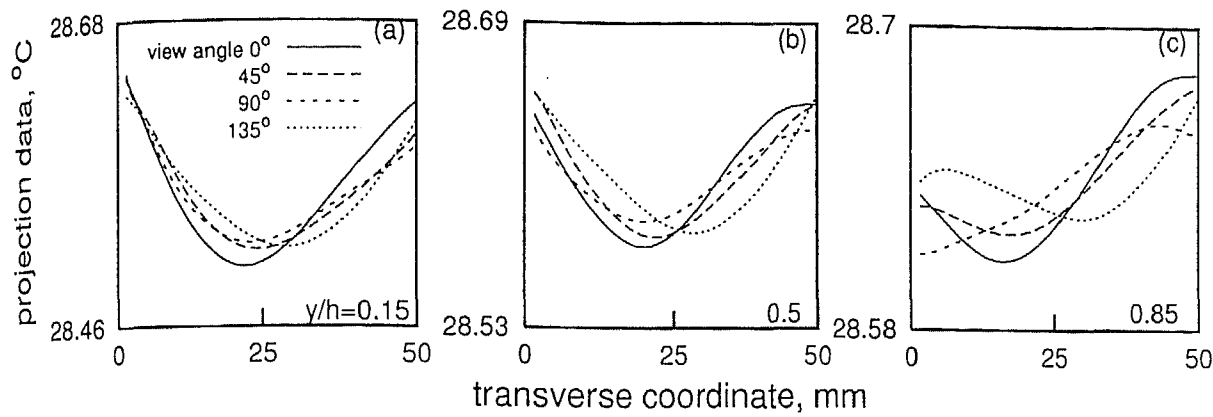


Figure 6.59: Consistent projection data in oil at three horizontal planes along the width of the cavity. Cavity filled with silicone oil and water for a temperature difference of 1.8 K.

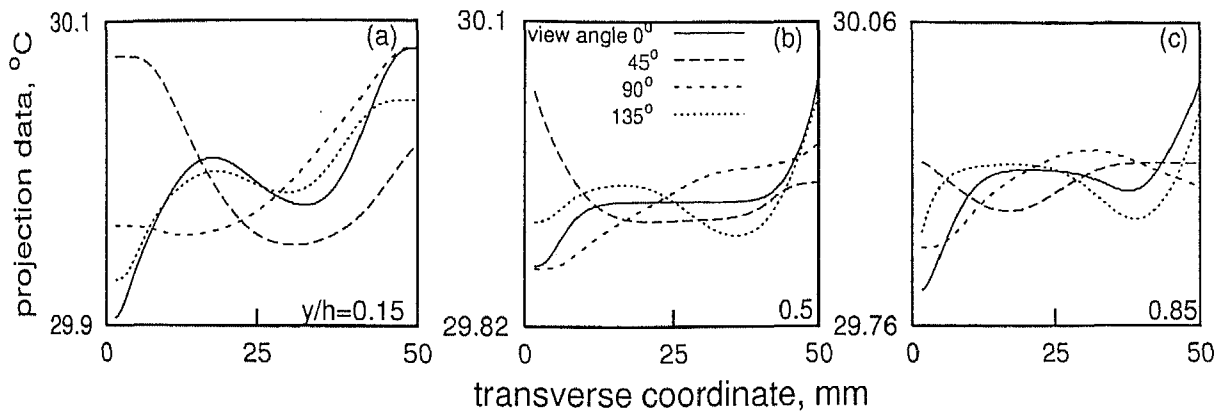


Figure 6.60: Consistent projection data in water at three horizontal planes along the width of the cavity. Cavity filled with silicone oil and water for a temperature difference of 1.8 K.

6.62(b,d,f)) considerable distortion in the axisymmetry of the thermal field. Since the projection data has been recorded in the central 41% of the cavity width, it is not appropriate to comment on the isotherms obtained beyond this region.

6.3.3 Unsteady thermal field

The present section discusses the result obtained in the oil-water experiments at high Rayleigh numbers. As stated earlier, high refraction errors in the oil layer restrict the study to be purely qualitative in nature. Further, the interferograms could be obtained only in the water portion of the cavity. This is owing to the limitations imposed by severe refraction in the oil layer. Temperature differences of 8.5 K, 13 K and 17.5 K across the cavity in a destabilizing configuration have been considered. The interferograms

$\Delta T = 0.4 \text{ K}$

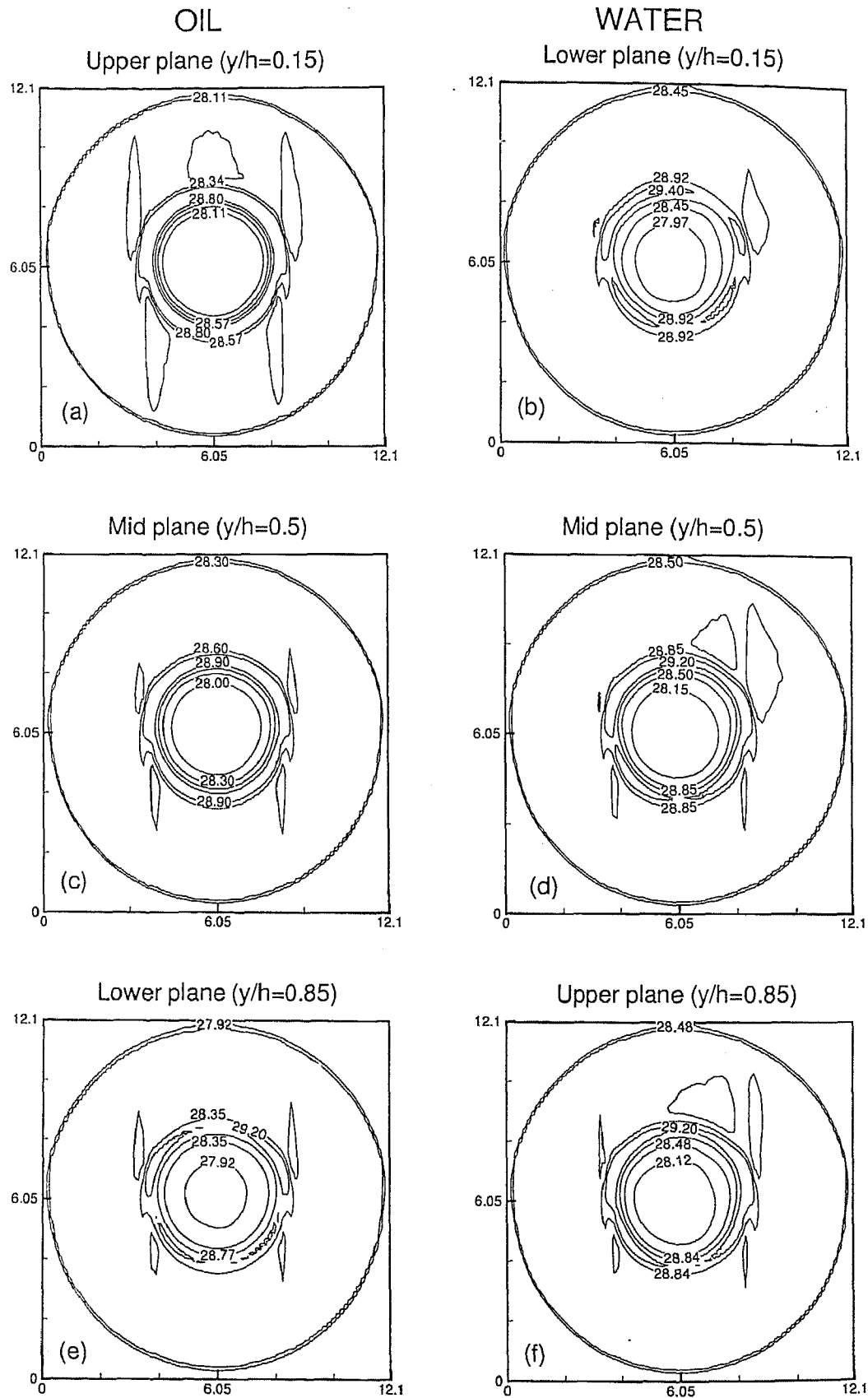


Figure 6.61: Reconstructed temperature contours in the oil (a,c,e) and the water layer (b,d,f) respectively at the three planes; Cavity temperature difference is 0.4 K.

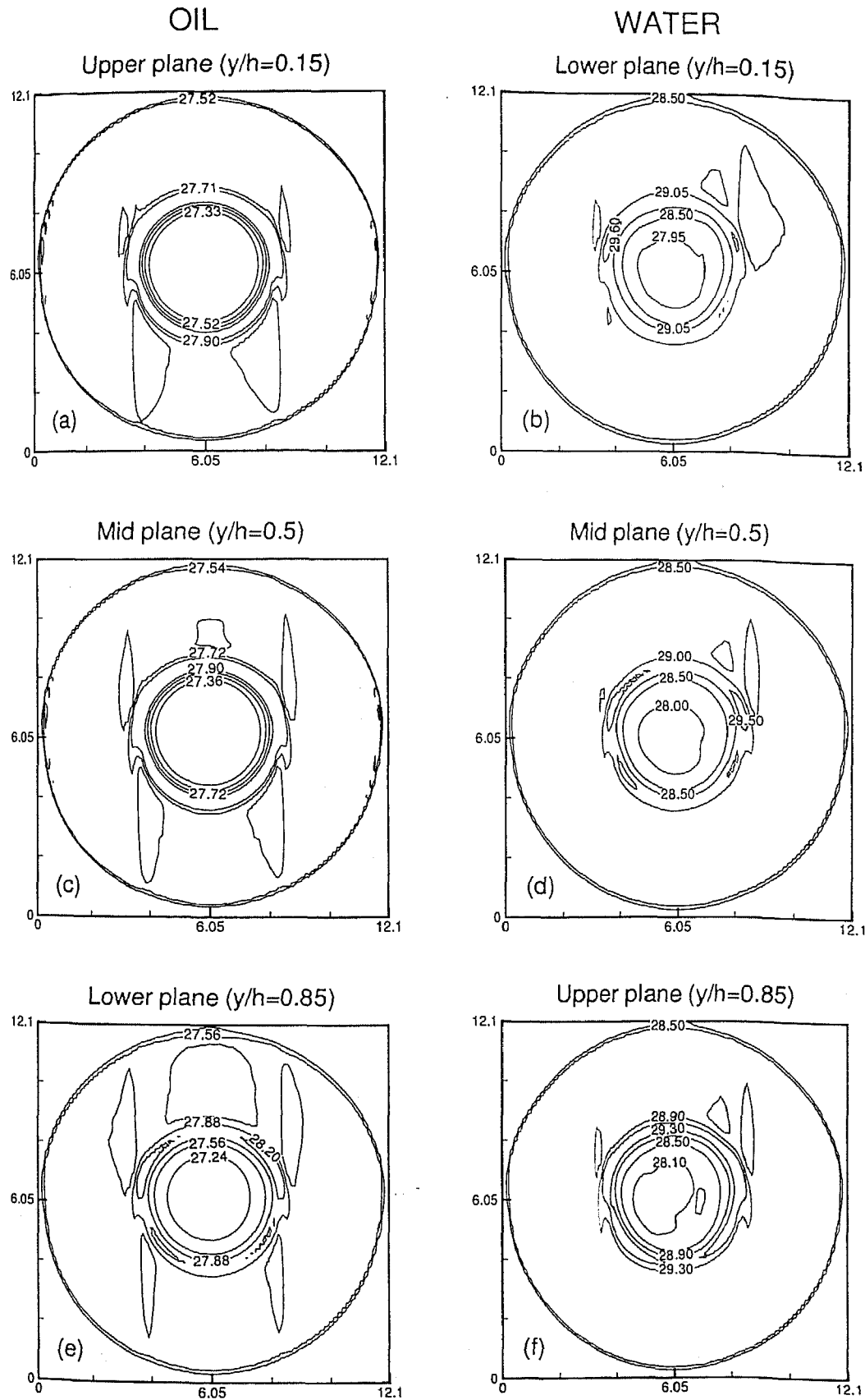
$\Delta T = 1.8 \text{ K}$ 

Figure 6.62: Reconstructed temperature contours in the oil (a,c,e) and the water layer (b,d,f) respectively at the three planes; Cavity temperature difference is 1.8 K.

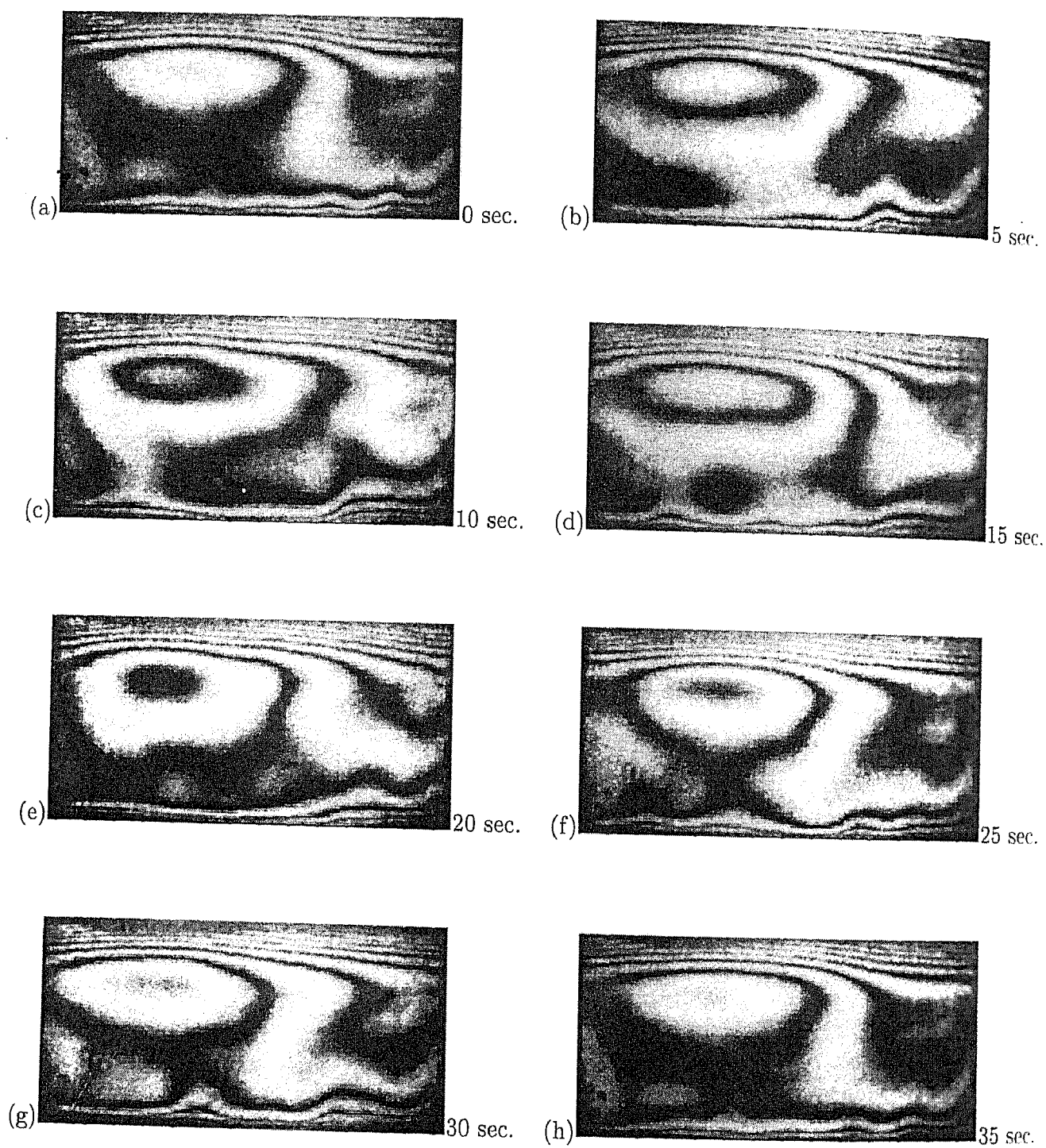


Figure 6.63: Unsteady patterns in water in the oil-water experiments for a temperature difference of 8.5 K. View angle considered is 0° . Time interval between two successive interferograms is 5 seconds.

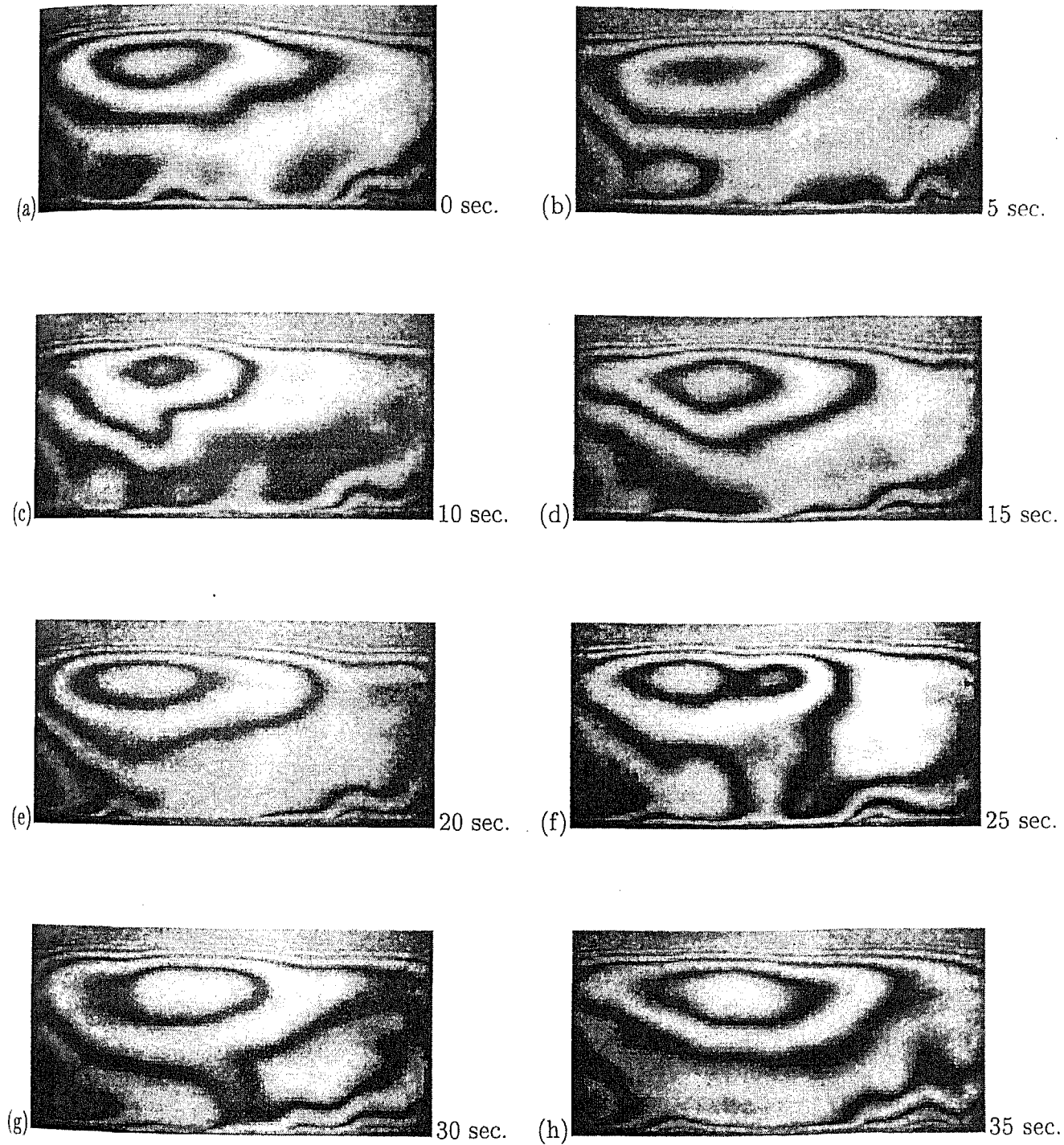


Figure 6.64: Unsteady patterns in water in the oil-water experiments for a temperature difference of 13 K. View angle considered is 0° . Time interval between two successive interferograms is 5 seconds.

have been recorded in a time sequence. The recording was initiated in the experiments after the hot and the cold walls were thermally stabilized. Specifically, the images were recorded only when the flow field was fully evolved and a time scale of unsteadiness could be identified. The time scale for the present experiment was 5 seconds. This is also the timegap between successive interferograms.

Figure 6.63 show the unsteady patterns in water for temperature difference of 8.5 K for the view angle of 0° . The estimated Rayleigh numbers based on the correlations are $2.23\text{E}+05$ and $4.63\text{E}+05$ in oil and water respectively. The flow field established in the cavity is seen to be highly unsteady. A longer time scale for the re-appearance of a fringe pattern was identified in the experiments to be 35 seconds.

In Figure 6.64, the overall temperature difference is 13 K. The estimated Rayleigh numbers calculated are $3.38\text{E}+05$ and $7.15\text{E}+05$ in oil and water layers respectively. Interferograms have been presented at a time interval of 5 seconds, while the longer time scale was again found to be 35 seconds. The corresponding Fourier number in water is $4.2\text{E}-02$. It is to be compared with the values of $3.3\text{E}-03$ and $6.5\text{E}-03$ for a rectangular cavity at Rayleigh numbers of 98,505 and 64,404 in water. This indicates that the geometry of the confining boundaries plays an important role in the characteristics of large-scale, long time unsteadiness in high Rayleigh number convection. A secondary role of geometry is to be expected for the small-scale, small time fluctuations¹¹.

6.3.4 Interface deformation

Figures 6.64(a-g) and 6.64(a1-g1) show respectively the interferograms and their corresponding deformed interfaces in the water layer of oil-water experiments. A temperature difference of 17.5 K was imposed across the cavity. The interface deformation was not detectable at lower temperature differences. The individual Rayleigh numbers for the experiment are $4.57\text{E}+05$ and $1.10\text{E}+06$ in oil and water respectively. Interfaces were recorded using a single (test) beam of the interferometer. The flow field developed in the water layer showed extremely high unsteadiness with absolutely no periodicity in time. The fringe patterns were visible in the turbulent regime. The corresponding interfaces showed a degree of movement with time, (Figures 6.64(a1-g1)). Unexpectedly, the shadowgraphs didnot reveal streaks of light, suggesting the break down of all large scale structures such as rolls to smaller scales.

¹¹This point needs to be studied separately in detail.

6.4 Nature of coupling

The flow regimes obtained in water did not experience a stabilizing influence of oil floating above. Thus, in contrast to the rectangular cavity, the fluid layers in the circular cavity are thermally coupled for all fluid combinations and temperature differences. This result has been summarized in Table 6.4. The absence of mechanical coupling can be partially associated with a higher width-to-height aspect ratio of the fluid layers, but more fundamentally with the change in the geometry of the confining walls.

Table 6.4: Summary of Mechanical (M) and Thermal (T) coupling modes obtained in air-water, air-oil, and oil-water experiments for equal layer heights.

Fluid combinations	ΔT , K					
	0.4	1.8	3.1	4.0	6.5	8.5
air and water	-	-	-	-	T	T
air and oil	T	T	T	T	-	-
water and oil	T	T	T	T	-	-

6.5 Closure

In the cavity containing air and water, the fluid layers show a degree of axisymmetry in the thermal field at a lower Rayleigh number. With an increase in Rayleigh number, three dimensionality is seen to be dominant in water while axisymmetry still persists in air. With further increase in the Rayleigh number, a dynamic steady-state in air is observed which leads to spatial movement of the fringe patterns with time. In the air-oil experiments, omega-shaped (Ω) fringe pattern indicating steady two dimensional thermal field is obtained in the oil layer. High fringe density at the interface and the hot wall indicate diffusion boundary layers in those regions. Axisymmetry in the thermal field in oil is seen to increase with increase in the Rayleigh number with the Ω -roll shifting towards the center. In the oil-water experiments, \mathcal{U} -shaped isotherms in oil and a distorted thermal field in water is to be noticed. At very high Rayleigh numbers, steady three dimensional flow in oil and time-dependent flow in water have been observed. The convective motion in each layer in all fluid combinations was driven by the individual temperature difference across the respective fluid layer, indicating thermal coupling at the interface.

The experimental interface temperature match the estimated temperature from

single fluid correlations fairly well for all fluid combinations. Discrepancy in the Nusselt number is seen at higher Rayleigh numbers in fluid layers that involve water.

Three dimensional reconstruction at three selected planes in the fluid layers confirms the thermal field to be axisymmetric for a limited range of parameters. Under favourable conditions, a plume structure is discernable in the flow field.

The interface deformation is uniformly small in all the experiments. The movement of the interface and the oscillation of light streaks correlate well, indicating the three dimensionality of convection as the source of interface deformation.

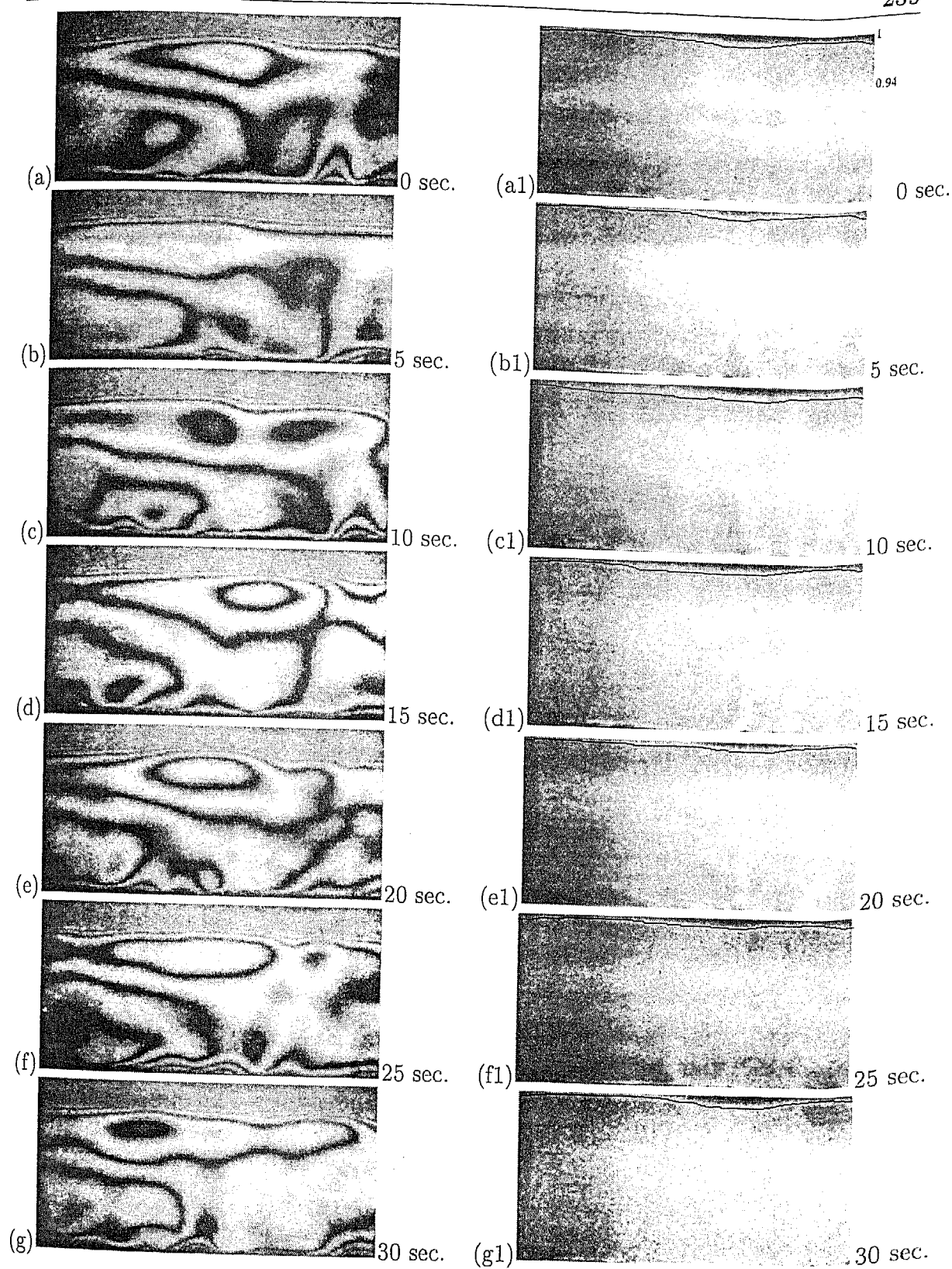


Figure 6.65: Interferograms (a-g) and their corresponding interfaces (a1-g1) in water in the oil-water experiments for a temperature difference of 17.5 K. View angle considered is 90° . Time interval between two successive interferograms and shadowgraphs is 5 seconds. Interfaces are emphasized in black.

Chapter 7

Conclusions and Scope for Future Work

7.1 Conclusions

Buoyancy-driven convection in differentially heated superposed horizontal fluid layers was studied experimentally using laser-interferometry. The thermal fields in the individual fluid layers were mapped using a Mach-Zehnder interferometer. Fluid combinations comprising of air and water, air and silicone oil, and silicone oil floating over water were selected for the experiments. The grade of silicone oil employed in the experiments was 50 cSt. Fluid layers were confined between two horizontal, isothermal plates heated from below and cooled from above. The overall thermal configuration is a modified form of the Rayleigh-Benard problem.

Two cavities of different overall geometry were designed and fabricated for performing the experiments. These are: (i) a cavity rectangular in plan and square in cross-section and (ii) a cavity octagonal in plan. The latter approximates a circular cavity. The cavity sizes are such as to classify them as intermediate aspect ratio enclosures. A majority of Rayleigh numbers considered are well beyond the first critical point of instability. The resulting convection patterns are dependent on the geometry of the confining boundaries.

The predominant observation that emerges from the experiments of both cavities is the following. The cavity temperature difference splits between the two fluid layers inversely in proportion their thermal conductivities. These local temperature differences drive convection in the respective layers. Hence, in a majority of experiments, two-layer convection is a collection of two single-layer convection experiments. The latter is

dependent on the cavity geometry. Departure from this base line trend is seen in the form of augmentation of thermal conductivity by fluid motion, flow retardation at large viscosity ratios, and transmission of unsteadiness. The specific results arrived at in the present work are summarized below.

7.1.1 Rectangular cavity

In the rectangular cavity, the layer thicknesses were taken to be $1/3$, $1/2$ and $2/3$ with respect to the cavity height for each combination of fluids. Experiments were primarily conducted with three cavity temperature differences of 10, 15 and 18 K. An additional temperature difference of 0.3 K was selected to capture the fringe patterns in the silicone oil phase. The following observations have been recorded in the study:

1. In the experiments involving air, the layers were found to be thermally coupled. The unsteadiness in water could however be transmitted to air in the mechanical coupling mode.
2. The switching phenomena, a step towards chaos via time-dependent flow, was noticed in the air portion of air-oil experiments at Rayleigh numbers higher than 12,900.
3. The presence of silicone oil over water led to mechanical coupling in the sense that the convective field in water was visibly retarded.
4. The interface temperature determined from the experiments matched those from correlations for a single fluid whenever the coupling was thermal in origin. The differences were higher during mechanical coupling and in cases where the time-dependent switching phenomena occurred.
5. Heat transfer rates in terms of the non-dimensional width-averaged Nusselt number matched well with the correlations at lower Rayleigh numbers. Deviation was higher at higher Rayleigh numbers, in particular with the experiments involving water.
6. Three-dimensional effects were noticed in the experiments involving water. The interface deformation was uniformly small, but correlated well with the roll movement visible in the fringes. Here, the movement of the interface and the oscillation of light streaks in the shadowgraph were seen to be aligned.

7.1.2 Circular cavity

In the circular cavity, the layer heights in each fluid combination were maintained equal to $1/2$ with respect to the total cavity height. The flow field was mapped from four different view angles namely 0 , 45 , 90 and 135° using a Mach-Zehnder interferometer for each fluid combination and cavity based temperature difference. The projection data obtained from different view angles was utilised in reconstructing the three dimensional temperature field using a tomographic algorithm. A range of temperature differences from as low as 0.4 K to as high as 18 K were imposed across the cavity in a destabilizing configuration. The following observations have been recorded in the experiments:

1. In the cavity containing air and water, the fluid layers showed a degree of axisymmetry in the thermal field at lower Rayleigh number. Three dimensionality was seen to be dominant in water while axisymmetry still prevailed in air with an increase in the Rayleigh number. With further increase in the Rayleigh number, a dynamic steady-state in air was observed which led to spatial movement of the fringe patterns with time.
2. In the air-oil experiments, Ω -shaped fringe patterns indicating a steady two dimensional thermal field was obtained in the oil layer.
3. In the oil-water experiments, \mathcal{O} -shaped isotherms in oil and a distorted thermal field in water was noticed. At very high Rayleigh numbers, steady three dimensional flow in oil and time-dependent flow in water was recorded.
4. The experimental interface temperature matched the estimated temperature from single fluid correlations fairly well for all fluid combinations. Discrepancy in the results of Nusselt number was noticed at higher Rayleigh numbers particularly in the fluid layers containing water.
5. Three dimensional reconstruction at three selected planes in the fluid layers confirmed the thermal field to be axisymmetric, silicone oil in particular. A plume structure was identified in the flow field on the basis of reconstruction.
6. Except at $Ra > 1.72E+05$, the interface deformation was uniformly small in all the experiments. Here the movement of interfaces and the oscillation of light streaks in the shadowgraph image confirmed three dimensionality in water.

7.2 Scope for future work

A large number of issues on buoyancy-driven convection in the superposed fluid layers are yet to be resolved. In the rectangular cavity, the fringe patterns parallel to the short side wall could be recorded to correlate long and short rolls. Three dimensional reconstruction at the interface could be useful for understanding flow coupling mechanism between the fluid layers. The complexities in interface deformation as seen by the light streaks and its oscillation and moving interfaces can be correlated with the unsteady temperature fields. The computation of the velocity field from the temperature data could well lead to establishing the relative influence of the respective rolls of the fluid layers coupled at the interface. There is a need to compare the experimental data with three dimensional numerical simulation, so that the latter can be used to identify the transition points in two-layer convection.

References

- [1] Ahlers, G. and Behringer, R. P., 1978, Evolution of Turbulence from Rayleigh-Benard Instability, *Physical Review Letters* Vol. 40, pp 712-716.
- [2] Andereck, D. C., Colovas, M. M., and Peter, W. D., 1996, Observation of time-dependent behaviour in the two-layer Rayleigh-Benard system, *Proceedings of the third Microgravity Fluid Physics Conference*, pp. 313-318.
- [3] Bau, H. H., 1999, Control of Marangoni-Benard convection, *IJHMT*, Vol. 42, pp. 1327-1341.
- [4] Bejan, Adrian, 1984, *Convection Heat Transfer*, A Wiley-Interscience Publication, New York.
- [5] Biswal, P. C. and Ramachandra Rao, A., 1999, Onset of oscillatory Marangoni convection in a two-layer system of conducting fluid in the presence of a uniform magnetic field, *Microgravity Science and Technology*, Vol. 12, No. 1, pp. 9-15.
- [6] Biswal, P. C. and Ramachandra Rao, A., 2001, Thermal instability in a three-dimensional rigid container with prescribed heat flux at lower boundary, *International Journal of Engineering Science*, Vol. 39, No. 12, pp. 1315-1325.
- [7] Boeck, T. and Thess, A., 1999, Benard-Marangoni convection at low Prandtl number, *J. Fluid Mecahanics*, Vol. 399, pp. 251-275.
- [8] Burkersroda, C. V., Prakash, A., and Koster, J. N., 1994d, Interfacial tension between fluorinert liquids and silicone oils, *Microgravity Q*, Vol. 4, No. 2, pp. 93-99.
- [9] Busse, F. H., 1978, Non-Linear Properties of Thermal Convection, *Rep. Progr. Phys.*, Vol. 41, pp. 1929-1976.
- [10] Busse, F. H., 1980, Transition to Turbulence in Rayleigh-Benard Convection in *Topics in Applied Physics, Hydrodynamic Instabilities and the Transition to Turbulence*, Edited by Swinney H.L. and Gollub J.P., Vol. 45, pp. 97-137, Springer-Verlag, Berlin.

- [11] Busse, F. H., 1981, *Physc. Earth Planet. Int.*, Vol. 24, p. 320.
- [12] Busse, F. H. and Sommermann, G., 1996, Double-layer convection: a brief review and some recent experimental results, in *Advances in Multi-fluid flows*, Editors: Y.Y. Renardy, A.V. Coward, D.T. Papageorgiou, and S.-M. Sun, SIAM publication, pp. 33-41.
- [13] Chandrasekhar, S., 1961, *Hydrodynamic and Hydromagnetic stability*, Oxford University Press, London.
- [14] Chavanne, X., Chilla, F., Castaing, B., and Hebral, B., 2001, Turbulent Rayleigh-Benard convection in gaseous and liquid Helium, *Physics of Fluids*, Vol. 13, No. 5, pp. 1300-1320.
- [15] Dauby, P. C. and Lebon, G., 1996, Benard-Marangoni instability in rigid rectangular containers, *J. Fluid Mechanics*, Vol. 329, pp. 25-64.
- [16] Dauby, P. C., Lebon, G., and Bouhy, E., 1997, Linear Benard-Marangoni instability in rigid circular containers, *Physical Review E*, Vol. 56, No. 1, pp. 520-529.
- [17] Degen, M. M., Colovas, P. W., and Andereck, C. D., Time-dependent patterns in the two-layer Rayleigh-Benard system, *Physical Review E*, Vol. 57, 6647.
- [18] Dijkstra, H. A., 1992, On the structure of cellular solutions in Rayleigh-Benard-Marangoni flows in small-aspect-ratio containers, *J. Fluid Mechanics*, Vol. 243, pp. 73-102.
- [19] Doi, T. and Koster, J. N., 1993, Thermocapillary convection in two immiscible liquid layers with free surface, *Physics of Fluids A: Fluid Dynamics*, Vol. 5, No. 8, pp. 1914-1927.
- [20] Drazin, P. G. and Reid, W. H., 1981, *Hydrodynamic stability*, Cambridge University Press, Australia.
- [21] Edwards, D.A., Brenner, H., and Wasan, D.T., 1991, *Interfacial Transport Processes and Rheology*, Butterworth-Heinemann Publication, USA.
- [22] Engel, A. and Swift, J. B., 2000, Planform selection in a two-layer Benard-Marangoni convection, *Physical Review E*, Vol. 62, 6540.
- [23] Gebhart, B., Jaluria, Y., Mahajan, R.L., and Sammakia, B., 1988, *Buoyancy-Induced Flows and Transport*, Hemisphere Publishing Corporation, New York.

- [24] Georis, By. Ph., Hennenberg, M., Lebon, G., and Legros. J. C., 1999, Investigation of thermocapillary convection in a three-liquid system, *J. Fluid Mechanics*. Vol. 389. pp. 209-228.
- [25] Goldstein R.J., 1983 (2nd ed. 1996) (Editor), *Fluid Mechanics Measurements*. Hemisphere Publishing Corporation, New York.
- [26] Gollub J. P. and Benson S. V., 1980, Many routes to tubulent convection. *J. Fluid Mechanics*, Vol. 100, Part 3, pp. 449-470.
- [27] Golovin, A. A., Nepomnyashchy, A. A., and Pismen, L. M., 1997, Nonlinear evolution and secondary instabilities of Marangoni convection in a liquid-gas system with deformable interface, *J. Fluid Mechanics*, Vol. 341, pp. 317-341.
- [28] Gonzalez, R. C. and Woods, R. E., 1993, *Digital Image Processing*, Addison-Wesley Publishing Company, USA.
- [29] Hauf, W., and Grigull, U., 1970, Optical Methods in Heat Transfer, *Advances in Heat Transfer*, Vol. 6, Edited by J.P.Hartnett and T.F.Irvine Jr., pp. 134-362.
- [30] Herman, G. T., 1980, *Image reconstruction from projections*, Academic Press, New York.
- [31] Jain A.K., 1989, *Fundamentals of Digital Image Processing*, Prentice-Hall International Editions, USA.
- [32] Jenkins, F. A. and White, H. E., 1981, *Fundamentals of Optics*, McGraw-Hill, Singapore.
- [33] Johnson, D. and Narayanan, R., 1996, Experimental observation of dynamic mode switching in interfacial-tension-driven convection near a codimension-two point, *Physical Review E*, Vol. 54, No. 4, pp. 3102-3104.
- [34] Johnson, D. and Narayanan, R., 1997, Geometric effects on convective coupling and interfacial structures in bilayer convection, *Physical Review E*, Vol. 56, No. 5, pp. 5462-5472.
- [35] Johnson, D., Narayanan, R., and Dauby, P. C., 1999, The effect of air height on the pattern formation in liquid-air bilayer convection, *Fluid Dynamics at Interfaces*, Cambridge University Press, Cambridge, pp. 15-30.

- [36] Juel, A., Burgess, J. M., McCormick, W.D., Swift, J. B., and Swinney, H. L., 2000, Surface tension-driven convection patterns in two liquid layers, *Physica D: Nonlinear Phenomena*, Vol. 143, No. 1, pp. 169-186.
- [37] Kim, D. M. and Viskanta, R., 1984, Study of the effects of wall conductance on natural convection in differently oriented square cavities, *J. Fluid Mechanics*, Vol. 144, pp 153-176.
- [38] Kirchartz, K. R. and Oertel, H. (Jr), 1988, Three-dimensional thermal cellular convection in rectangular boxes, *J. Fluid Mechanics*, Vol. 192, pp. 249-286.
- [39] Koizumi, H. and Hosokawa, I., 1996, Controlling the flow pattern of Rayleigh-Benard cells in an enclosure, *Ninth international symposium on transport phenomena in thermal-fluids engineering, Singapore*, pp. 975-980.
- [40] Kolodner P, Walden R. W., Passner A., and Surko C. M., 1986, Rayleigh-Benard convection in an intermediate-aspect-ratio rectangular Container, *J. Fluid Mechanics*, Vol. 163, pp 195-226.
- [41] Koschmieder, E. L. and Prahl, S. A., 1990, Surface-tension-driven Benard convection in small containers, *J. Fluid Mechanics*, Vol. 215, pp. 571-583.
- [42] Koster, J. N. and Nguyen, K. Y., 1996, Steady natural convection in a double layer of immiscible liquids with density inversion, *IJHMT*, Vol. 39, No. 3, pp. 467-478.
- [43] Krishnamurti R., 1970a, On the transition to turbulent convection. Part 1: The transition from two- to three-dimensional flow, *J. Fluid mechanics*, Vol. 42, Part 2, pp 295-307.
- [44] Krishnamurti R., 1970b, On the transition to turbulent convection. Part 2: The transition to time-dependent flow, *J. Fluid mechanics*, Vol. 42, Part 2, pp. 309-320.
- [45] Krishnamurti, R., 1973, Some further studies on the transition to turbulent convection, *J. Fluid Mechanics*, Vol. 60, part 2, pp. 285-303.
- [46] Krishnamurti, R., 1998, Low frequency oscillations in turbulent Rayleigh-Benard convection, *Sadhana - Academy Proceedings in Engineering Sciences*, Vol. 23, No. 5, pp. 605-613.
- [47] Manga, M. and Weeraratne, D., 1999, Experimental study of non-Boussinesq Rayleigh-Benard convection at high Rayleigh and Prandtl numbers, *Physics of Fluids*, Vol. 11, No. 10, pp. 2969-2976.

- [48] Mayinger, F., 1994, (Editor), *Optical Measurements: Techniques and Applications*, Springer-Verlag, Berlin.
- [49] Michael Y. C. and Yang K. T., 1992, Three-dimensional Mach-Zehnder interferometric tomography of the Rayleigh-Benard problem, *ASME J. Heat Transfer*, Vol. 114, pp. 622-629.
- [50] Mishra, D., 1998, Experimental study of Rayleigh-Benard convection using interferometric tomography, Ph.D thesis, I.I.T Kanpur, India.
- [51] Mishra, D., Muralidhar, K., and Munshi, P., 1999, Performance evaluation of fringe thinning algorithms for interferometric tomography, *Optics and Lasers in Engineering*, Vol. 30, pp. 229-249.
- [52] Mishra, D., Muralidhar, K., and Munshi, P., 1999, Interferometric study of Rayleigh-Benard convection using tomography with limited projection data, *Experimental Heat Transfer*, Vol. 12, No. 2, pp. 117-136.
- [53] Mishra, D., Muralidhar, K., and Munshi, P., 1999, Isotherms in a horizontal differentially heated cavity at intermediate Rayleigh numbers, *International Communications in Heat and Mass Transfer*, Vol. 26, No. 5, pp. 729-738.
- [54] Mishra, D., Muralidhar, K., and Munshi, P., 1999, A robust MART algorithm for tomographic applications, *Numerical Heat Transfer B (Fundamentals)*, Vol. 35, No. 4, pp. 485-506.
- [55] Mishra, D., Muralidhar, K., and Munshi, P., 1999, Interferometric study of Rayleigh-Benard convection at intermediate Rayleigh numbers, *Fluid Dynamics Research*, Vol. 25, No. 5, pp. 231-255.
- [56] Mukutmoni, D. and Yang, K. T., 1991, Flow transitions in a three-dimensional rectangular enclosure heated from below, *ASME/JSME Thermal Engg Proc.*, Vol. 1, pp. 77-82.
- [57] Mukutmoni, D. and Yang, K. T., 1992, Wavenumber selection for Rayleigh-Benard convection in a small aspect ratio box, *International Journal of Heat and Mass Transfer*, Vol. 35, No. 9, pp. 2145-2159.
- [58] Munshi, P., 1997, Application of Computerized Tomography for Measurements in Heat and Mass Transfer, *Proceedings of the 3rd ISHMT-ASME Heat and Mass Transfer Conference Held at IIT Kanpur (India) during 29-31 December 1997*, Naraosa Publishers, N.Delhi.

- [59] Muralidhar, K., 2002, Temperature field measurement in buoyancy-driven flows using interferometric tomography, *Annual Review of Heat Transfer*, Vol. 12, Edited by Chang-Lin Tien, Vishwanath Prasad and Frank Incropera, pp. 265-375.
- [60] Muralidhar, K., Patil, V. B., and Kashyap, R., 1996, Interferometric study of transient convection in a square cavity, *J. of Flow Visualization and Image Processing*, Vol. 2, No. 4, pp. 321-333.
- [61] Natterer, F., 1986, *The Mathematics of Computerized Tomography*, John Wiley and Sons, New York.
- [62] Ondarcuhu, T., Mindlin, G. B., Mancini, H. L., and Garcia, C. P., 1993, Dynamical patterns in Benard-Marangoni convection in a square container, *Physical Review Letters*, Vol. 70, No. 25, pp. 3892-3895.
- [63] Prakash, A. and Koster, J. N., 1993a, Natural and thermocapillary convection in three layers, *European J. of Mechanics B/Fluids*, Vol. 12, No. 5, pp. 635-655.
- [64] Prakash, A., Fujita, D., and Koster, J. N., 1993b, Surface tension and buoyancy effects on a free-free layer, *European J. of Mechanics B/Fluids*, Vol. 12, No. 1, pp. 15-29.
- [65] Prakash, A. and Koster, J. N., 1994a, Convection in multiple layers of immiscible liquids in a shallow cavity - I: Steady natural convection, *Int. J. Multiphase Flow*, Vol. 20, No. 2, pp. 383-396.
- [66] Prakash, A. and Koster, J. N., 1994b, Convection in multiple layers of immiscible liquids in a shallow cavity - II: Steady thermocapillary convection, *Int. J. Multiphase Flow*, Vol. 20, No. 2, pp. 397-414.
- [67] Prakash, A. and Koster, J. N., 1994c, Thermocapillary convection in three immiscible liquid layers, *Microgravity Q*, Vol. 4, No. 1, pp. 47-54.
- [68] Prakash, A. and Koster, J. N., 1996a, Steady thermocapillary convection in a GaAs melt encapsulated by molten B_2O_3 , *J. Materials Synthesis and Processing*, Vol. 4, No. 1, pp. 43-50.
- [69] Prakash, A. and Koster, J. N., 1996b, Steady Rayleigh-Benard convection in a two-layer system of immiscible liquids, *Transactions of the ASME, J. Heat Transfer*, Vol. 118, pp. 366-373.
- [70] Prakash, A. and Koster, J. N., 1997, Steady natural convection in a two-layer system of immiscible liquids, *Int. J. Heat and Mass Transfer*, Vol. 40, No. 12, pp. 2799-2812.

- [71] Prakash, A., Yasuda, K., Otsubo, F., Kuwahara, K., and Doi, T., 1997, Flow coupling mechanism in two-layer Rayleigh-Benard convection, *Experiments in Fluids*, Vol. 23, pp. 252-261.
- [72] Ramachandran, G. N. and Laxminarayanan, A. V., 1970, Three-Dimensional Reconstruction from Radiographs and Electron Micrographs: Application of Convolution instead of Fourier Transforms, *Proc. Nat., Acad. USA*, Vol. 68, pp. 2236-2240.
- [73] Rasenat, S., Busse, F. H., and Rehberg, I., 1989, A theoretical and experimental study of double-layer convection, *J. Fluid Mechanics*, Vol. 199, pp. 519-540.
- [74] Rednikov, A. YE., Colinet, P., Velarde, M. G., and Legros, J. C., 2000, Rayleigh-Marangoni oscillatory instability in a horizontal liquid layer heated from above: coupling and mode mixing of internal and surface dilational waves, *J. Fluid Mechanics*, Vol. 405, pp. 57-77.
- [75] Renardy, Y. and Joseph, D. D., 1985, Oscillatory instability in a Benard problem of two fluids, *Physics of Fluids*, Vol. 23, No. 3, pp. 788-793.
- [76] Ruediger, S. and Feudel, F., 2000, Pattern formation in Rayleigh-Benard convection in a cylindrical container, *Physical Review E*, Vol. 62, No. 4, pp. 4927-4931.
- [77] Schatz, M. F., VanHook, S. J., McCormick, W. D., Swift, J. B., and Swinney, H. L., 1999, Time-independent square patterns in surface-tension-driven Benard convection, *Physics of Fluids*, Vol. 11, No. 9, pp. 2577-2582.
- [78] Settles, G.S., 2001, *Schlieren and Shadowgraph Techniques*, Springer, New York.
- [79] Shyy, W., Udaykumar, H. S., Rao, M. M., and Smith, R. W., 1996, *Computational Fluid Dynamics with Moving Boundaries*, Taylor and Francis, USA.
- [80] Srivastava, A. and Panigrahi, P. K., 2002, A combined numerical-experimental study of convection in an axisymmetric differentially heated fluid layer, *Indian Journal of Engineering and Materials Sciences* (to appear).
- [81] Theerthan, S. A. and Arakeri, J. H., 2000, Planform structure and heat transfer in turbulent free convection over horizontal surfaces, *Physics of Fluids*, Vol. 12, No. 4, pp. 884-894.
- [82] Tokaruk, W. A., Molteno, T. C. A., and Morris, S. W., 2000, Benard-Marangoni convection in two layered liquids, *Phys Rev Lett*, Vol. 84, 3590.

-
- [83] Velarde, M. G. and Normand, C., 1980, Convection, Scientific American, Vol. 243, No. 1, pp. 79-94.
- [84] Vrentas, J. S., Narayanan, R., and Agarwal, S. S., 1981, Free surface convection in a bounded cylindrical geometry, IJHMT, Vol. 26, No. 9, pp. 1513-1529.
- [85] Zaman, A. A. and Narayanan, R., 1996, Interfacial and buoyancy-driven convection - The effect of geometry and comparison with experiments, J. Colloid and Interface Science, Vol. 179, pp. 151-162.
- [86] Zeren, R. W. and Reynolds, W. C., 1972, Thermal instabilities in two-fluid horizontal layers, J. Fluid Mechanics, Vol. 53, No. 2, pp. 305-327.
- [87] Singh, S., Muralidhar, K., and Munshi, P., 2002, Image Reconstruction from Incomplete Projection data using Combined ART-CBP Algorithm, Defence Science Journal, Vol. 52, No. 3, pp. 303-316.
-

Appendix A

Fast Fourier Transform Algorithm

The one dimensional version of the FFT algorithm is briefly presented here. Any waveform with a zero mean can be looked upon as a combination of a number of sinusoids. Hence the wavenumber of each of these sinusoids with their corresponding amplitude are representative of the signal in the wavenumber space. The Fourier transform of a function transforms the information about the signal in the space or time domain to the wavenumber domain. Let $f(x)$ be a continuous function of a real variable x . The Fourier transform of $f(x)$ is defined as

$$F(\omega) = \int_{-\infty}^{+\infty} f(x) \exp(-j2\pi\omega x) dx \quad (\text{A.1})$$

In a spatial domain calculation, ω represents the wavenumber, defined here as the reciprocal of wavelength. In a time domain calculation, ω is a frequency variable. The symbol j represents the imaginary number, defined as $j = \sqrt{-1}$. The function $f(x)$ can be recovered by an inverse Fourier transform as:

$$f(x) = \int_{-\infty}^{+\infty} F(\omega) \exp(j2\pi\omega x) d\omega \quad (\text{A.2})$$

In a discrete calculation, the function $f(x)$ is available at N points as f_0, f_1, \dots, f_{N-1} with a spacing $\Delta x = L/(N-1)$ where L is the length of the signal. The reciprocal of L can be viewed as the wavenumber of the fundamental harmonic in the wavenumber space. The above definition of Fourier transform can be modified for discrete analysis as:

$$F(\omega) = \frac{1}{N} \sum_{i=0}^{N-1} f_i \exp\left(\frac{-j2\pi\omega i\Delta x}{N}\right) \quad (\text{A.3})$$

where ω is also a discrete variable, in the range $1/L$ to N/L . The spacing $\Delta\omega$ is the minimum wavenumber that can be measured, that is $1/L$. Hence the wavenumbers are discretized into $N - 1$ intervals. Similarly the inverse discrete Fourier transform can be defined as

$$f(i\Delta x) = \sum_{\omega=0}^{N-1} F(\omega) \exp\left(\frac{j2\pi\omega i\Delta x}{N}\right) \quad (\text{A.4})$$

The use of the fast Fourier transform algorithm requires that the sampling of the continuous function be made over 2^m divisions, where m is an integer. Hence 2^m is an even number and can be expressed as

$$N = 2^m = 2M \quad (\text{A.5})$$

where M is an integer. Equation A.3 can now be written in the form

$$F(\omega) = \frac{1}{2M} \sum_{i=0}^{2M-1} f_i \exp\left(\frac{-j2\pi\omega i\Delta x}{2M}\right) \quad (\text{A.6})$$

The right hand side of this equation can be split as

$$\frac{1}{2} \left[\frac{1}{M} \sum_{i=0}^{M-1} f_{2i} \exp\left(\frac{-j2\pi\omega 2i\Delta x}{2M}\right) + \frac{1}{M} \sum_{i=0}^{M-1} f_{(2i+1)} \exp\left(\frac{-j2\pi\omega (2i+1)\Delta x}{2M}\right) \right]$$

Hence

$$F(\omega) = \frac{1}{2} \left[\frac{1}{M} \sum_{i=0}^{M-1} f_{2i} \exp\left(\frac{-j2\pi\omega 2i\Delta x}{M}\right) + \frac{1}{M} \sum_{i=0}^{M-1} f_{(2i+1)} \exp\left(\frac{-j2\pi\omega (2i+1)\Delta x}{M}\right) \exp\left(\frac{-j2\pi\omega}{2M}\right) \right] \quad (\text{A.8})$$

Breaking the discrete values of the function into even and odd terms one gets

$$F_{\text{even}}(\omega) = \frac{1}{M} \sum_{i=0}^{M-1} f_{2i} \exp\left(\frac{-j2\pi\omega 2i\Delta x}{M}\right) \quad (\text{A.9})$$

$$F_{odd}(\omega) = \frac{1}{M} \sum_{i=0}^{M-1} f_{2i+1} \exp\left(\frac{-j2\pi\omega(2i+1)\Delta x}{M}\right) \quad (\text{A.10})$$

Equation A.8, can now be put in the form

$$F(\omega) = \frac{1}{2} \left[F_{even}(\omega) + F_{odd}(\omega) \exp\left(\frac{-j2\pi\omega}{2M}\right) \right] \quad (\text{A.11})$$

Noting that

$$\begin{aligned} \exp\left(\frac{-j2\pi(\omega + M)}{M}\right) &= \exp\left(\frac{-j2\pi\omega}{M}\right) \\ \text{and } \exp\left(\frac{-j2\pi(\omega + M)}{2M}\right) &= -\exp\left(\frac{-j2\pi\omega}{2M}\right) \end{aligned}$$

one can derive

$$F(\omega + M) = \frac{1}{2} \left[F_{even}(\omega) - F_{odd}(\omega) \exp\left(\frac{-j2\pi\omega}{2M}\right) \right] \quad (\text{A.12})$$

Equations A.11 and A.12 are central to the success of the FFT algorithm. They show that the actual Fourier transform can be computed for two halves of the series (odd and even) and that of the original series can be determined by recombination. Each half of the full series can be further divided into even and odd parts. This breaking up into even and odd parts can be repeated till we reach a stage where only one term remains in each of the series. Equation A.6 can be used to show that the Fourier transform of only one term is the term itself. Hence Equations A.11 and A.12 can be used to compute the Fourier transform of the original series.

The FFT algorithm for calculation of the Fourier transform of a discrete set of data requires only $N \log_2 N$ number of calculations (multiplications and additions). The discrete Fourier transform using direct Fourier transform formula requires N^2 number of calculations, where N represents the number of discrete data points. The FFT algorithm has a requirement of 2^m number of data points, m being an integer. If the number of points is not equal to an integer power of 2, FFT can still be used to compute the Fourier transform of the series of data. This is achieved by adding 0's to the data on both sides of the series so that the nearest integer power of 2 can be obtained. This method of adding zeroes to a series of data points, so that FFT can be applied on it is known as zero padding. In the present work, the images obtained are of the size of 512×512 pixels. Hence for FFT applications no zero padding was required.

The computer implementation of the FFT algorithm is briefly discussed here. The major point to be taken care of during the implementation of the FFT algorithm is to arrange the discrete data in order for successive applications of Equations A.11 and A.12. The ordering procedure is also referred as the *butterfly* algorithm. The butterfly algorithm for ordering of the discrete data for implementation of the FFT algorithm is shown schematically in Figure A.1. The figure shows an example of the 8-point Fourier transform. The input data, to the algorithm are $\{f_0, f_1, \dots, f_7\}$. This set of data can be divided into two series of data as the odd and even series. The odd series is $\{f_1, f_3, f_5$ and $f_7\}$ and the even series is $\{f_0, f_2, f_4$ and $f_6\}$. Each of these 4-points series can be split further as odd and even series with 2-point data. These are $\{f_0, f_4\}$, $\{f_1, f_5\}$ as the even series and $\{f_2, f_6\}$, $\{f_3, f_7\}$ as the odd series. No further splitting is required, since in a 2-point series one even and one odd term are present. Hence the input series to the algorithm requires the ordering as:

$$\{f_0, f_4, f_2, f_6, f_1, f_5, f_3 \text{ and } f_7\}$$

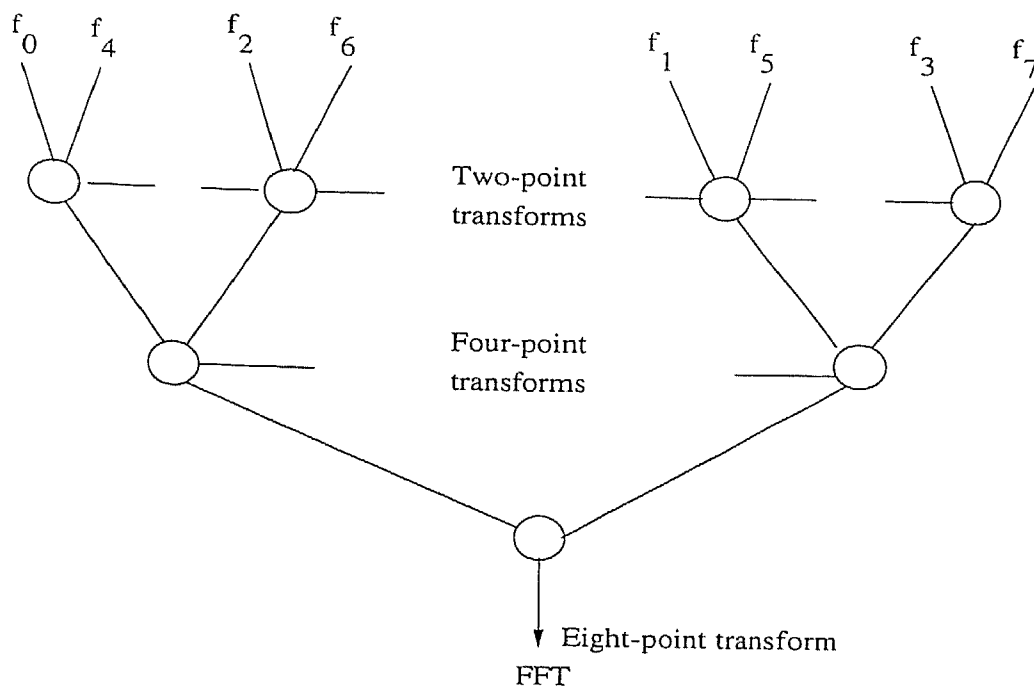


Figure A.1: Schematic of Butterfly Algorithm, for Implementation of FFT

The butterfly algorithm for ordering operates as shown in Figure A.1. The first step is calculation of the four 2-point transforms. The next step uses these results to obtain two 4-point transforms. The third step uses these results to produce the final 8-point transform. The reordering of data follows a simple rule of the corresponding binary number. This is known as bit-reversal. If n represents the argument value in the actual

series of input data, the corresponding argument of the data in the reordered series can be directly obtained by expressing the number n in its binary form, reversing the bits from left-to-right and then obtaining the corresponding number. For example the 4th element of the 8-points series considered above in the input data is f_3 . The number 3 (argument of the 4th element) can be expressed as 011 in binary form. Applying the bit-reversal rule the modified binary number is 110 which corresponds to an argument of 6. Hence the data f_3 will occupy the position of argument 6 in the reordered data, that is the 7th element from the beginning.

The one dimensional FFT algorithm discussed above can be extended to a two dimensional FFT algorithm. To this end the one dimensional FFT was implemented successively (row-by-row) in the two directions to obtain the two dimensional Fourier transform. The inverse Fourier transform was obtained in the similar way by adopting successively the one dimensional inverse FFT. The number of arithmetic operations in one dimensional FFT being $N \log_2 N$, that for two dimensional FFT is clearly $N^2 \log_2 N$.

Appendix B

Numerical study of buoyancy-driven convection in air-water layers

Buoyancy-driven convection in superposed air-water layers within a cavity has been numerically computed. The convection patterns obtained numerically have been compared with experiments. The numerical solution has been derived by solving the coupled flow and heat transfer equations by a finite volume method. A commercial package was employed in this respect. The cavity in which the fluid layers are contained has overall dimensions of $32.1 \times 32.1 \text{ mm}^2$ in cross-section, and 447 mm in length. The layer heights are taken to be equal. The numerical simulation has been carried out for a two as well as three dimensional cavity geometries. For the two-dimensional geometry, three temperature differences of 10, 15 and 18 K were imposed across the cavity walls, the sides being insulated. Three-dimensional cavity filled individually with air and water have also been considered for numerical simulation. A temperature difference of 10 K was imposed across the hot and the cold walls in the three dimensional simulation. The convection fields have been analyzed in terms of (a) the steady state behaviour, (b) flow coupling mechanisms between the fluid layers, (c) temperature profiles and wall heat transfer, and (d) the interface shape deformation with increasing temperature difference.

Simulation of natural convection in enclosures is a problem of considerable complexity. Convective transport at fluid-fluid interfaces poses additional difficulties in modeling, and has not been adequately understood. The present appendix reports a preliminary approach towards characterizing convective phenomena in the presence of interfaces with a numerical model.

B.1 Numerical solution

Numerical solution of the fluid flow equations and heat transfer was carried out using the commercially available FLUENT package (version 5)¹. The flow was taken to be two dimensional, laminar and incompressible, and steady state was obtained by marching in time. The boundary conditions corresponding to specified temperatures at the lower and the upper surfaces were applied, the side walls being treated as insulating boundaries. The grid was generated over the cross-section of the cavity. In two dimensions, 61×61 grid was found to be adequate to capture the major features of the flow patterns. The FLUENT software employs the finite volume formulation for discretization of the partial differential equations. It has been validated against a wide range of benchmark problems. The code is quite versatile with respect to geometry and boundary conditions. However, treatment of two fluids with an interface was difficult to model with the tools available in FLUENT. To circumvent this problem, the air and the water portions of the cavity were individually treated, with the coupling at the interface being enforced by the following approach:

1. Specify the water surface to be stress-free with a convective boundary-condition for heat transfer. The heat transfer coefficient is determined on the basis of the Rayleigh number for air.
2. Solve for velocity and temperature distribution in water.
3. Determine the average velocity and temperature of the air-water surface.
4. Solve for velocity and temperature distributions in air.
5. Determine the average heat transfer coefficient at the interface and repeat calculations from step 2 onwards.

This led to an iterative procedure, with air and water phases being alternately solved till convergence. The air-water interface was assumed to be flat in the flow and temperature calculations. The CPU time per run was of the order of 4 hours on a SUN-sparc workstation.

Three dimensional simulation was also carried out using FLUENT in a box-shaped cavity that was identical to that used in experiments (Chapter 5). The top and the bottom faces were isothermally cooled and heated respectively, while all other faces

¹available from FLUENT India Pvt Ltd, Pune.

were kept insulated. The CPU time for a three dimensional calculation was of the order of several days. Hence, the three dimensional calculation was restricted to cavities filled with either air or water. In a cavity filled with water, the flow was simulated as three-dimensional and turbulent owing to very high Rayleigh number encountered for an imposed temperature difference of 10 K. The k - ϵ model of turbulence has been utilised in the simulation. A $31 \times 31 \times 418$ grid could be used in the present work. It is expected that a few of the major features of three dimensional convection are brought out with this grid on the transverse and longitudinal planes of the box. The CPU time per run for water was of the order of 220 hours. In water, even after 220 hours of simulation, the flow was not truly steady and visible unsteadiness persisted in the flow structures.

B.1.1 Effect of surface-tension on the shape of the free surface

Deformation of the air-water interface due to surface tension has also been computed numerically by the following approach. The shape of the free surface is described in parametric form $y=f(x)$, and is governed by the second-order nonlinear ordinary differential equation (Shyy *et al.*, 1996):

$$f'' = \left(\frac{f}{l^2} + D\right)(1 + f'^2)^{3/2} \quad (\text{B.1})$$

where $l = (\sigma/\Delta\rho g)^{1/2}$ is the capillary length, $\Delta\rho = \rho_2 - \rho_1$, and D is a constant with dimensions of inverse length. Suffixes 1 and 2 refer to air and water respectively. The primes on the function f denote differentiation with respect to the x -coordinate that is oriented along the width of the cavity. The surface tension coefficient between air and water has been taken to $\sigma = 0.073$ N/m. Variation of σ with temperature can be accounted for by using the value of $d\sigma/dT = -1.7\text{E-}04$ N/m-K, with no further changes in the formulation. The quantity D in Equation B.1 is a free parameter that represents the excess pressure in water with respect to air. It can be determined by reference to the constraint of the constancy of the fluid volume under deformed conditions. The total volume of water contained under the free surface² is given as

$$V = h \times W + 2 \int_0^{W/2} f(x) dx \quad (\text{B.2})$$

and is a known quantity. Here, h is the mean height of water level from the base of the cavity and W is the cavity width. Equation B.1 is solved subject to the boundary conditions:

²per unit length of the cavity in the z -direction

$$\begin{array}{ll} x = 0 & f' = (\tan\phi)^{-1} \\ x = W/2 & f = 0; \quad f' = 0 \end{array}$$

where ϕ is the contact angle of water at the solid surface. The contact angle has been taken to be 45 degrees in the present study. Equation B.1 along with the volume constraint and the boundary conditions has been solved by a 4th order Runge-Kutta method and the Newton-Raphson scheme.

B.2 Comparison of results

The objective of the present work is to examine the extent to which a commercially available computational software is capable of reproducing the flow and thermal fields arising in a complex experiment. To test the software, the comparison has been carried out with a simpler configuration in which the cavity contains air and water alone. Subsequently, the numerical predictions have been compared against experiments with a cavity half-filled with air and water respectively. The issues addressed for comparison between the two sets of results are the steady thermal field, flow coupling mechanism between fluid layers, temperature profiles and the width-averaged Nusselt number. Interface temperatures and the width-averaged Nusselt number at the two walls have also been compared with the correlations proposed by Gebhart *et al.* (1988), Equations 4.26-4.27.

B.2.1 Convection in an air-filled cavity

The convection patterns in the square cavity of Figure 3.1 when filled with air are shown in Figure B.1. The cavity temperature difference is 10 K in the Figure. The numerical results have been shown in the form of isotherms (Figure B.1(a)), while the interferometric fringes are shown in Figure B.1(b). In a two dimensional field, the fringes are isotherms; even otherwise they represent the thermal field in the cavity. A direct comparison of the numerical and the experimental temperature profiles at selected locations in the cavity is presented in Figure B.2. The dominant picture to emerge from Figure B.1 is the formation of a roll pattern that transports from the fluid from the hot surface to the cold, followed by the descent of the cold fluid.

The Rayleigh number in the experiments as well as the simulation for the conditions of Figure B.1 was $34,200^3$. Using the correlation of Equation 4.26, the average cavity

³At this Rayleigh number, the regime diagram of Figure 2.1 shows the flow to be unsteady. During

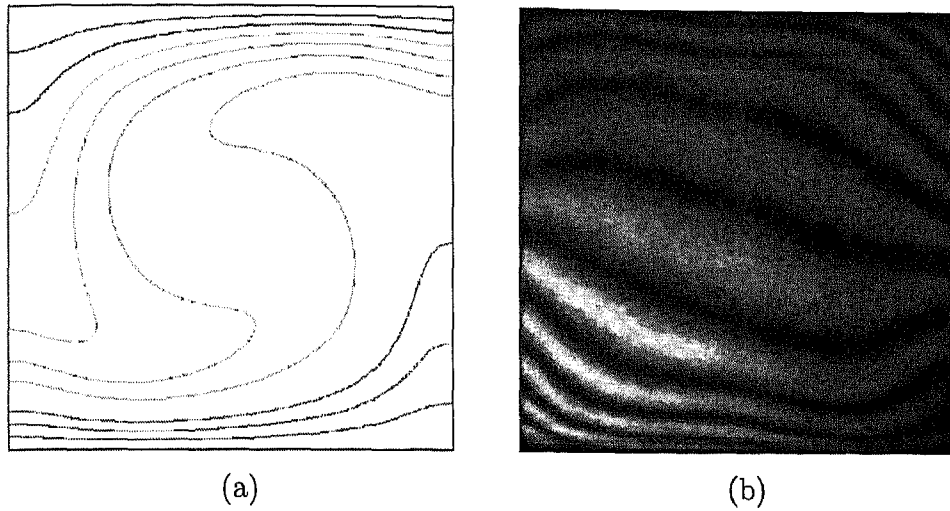


Figure B.1: Comparison of the numerical isotherms (a) with experimental fringe patterns (b) for a cavity filled with air; Cavity temperature difference $\Delta T = 10$ K.

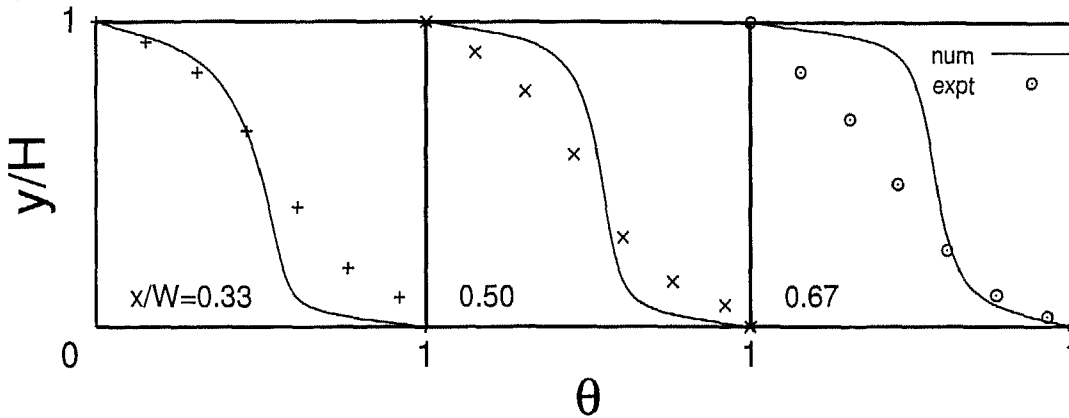


Figure B.2: Comparison of the numerically calculated temperature profiles with experiments at selected planes for a cavity filled with air; Cavity temperature difference $\Delta T = 10$ K.

Nusselt number was calculated to be 3.17. The corresponding value from the FLUENT package was 3.21, while the fringe patterns yielded 3.12 at the hot wall and 3.18 at the cold wall. The agreement among the three methods can thus be considered to be satisfactory.

The direction of movement of the roll in the numerical prediction is counter-clockwise (Figure B.1(a)). This can be derived by recognizing that the isotherms are displaced in the direction of the local fluid velocity. The roll movement in the experiment is clockwise (Figure B.1(b)). This difference is however not significant. It is now recog-

numerical simulation, a definite steady state was obtained. Mild unsteadiness was however seen in the experiments as discussed in Chapter 4. The side walls of the box play a stabilizing role on convection, an issue not considered in Figure 2.1.

nized that the sense of movement in the cavity is indeterminate in principle. It is fixed by the propagation of errors in the numerical simulation, and on the other hand, the imperfections in the experimental apparatus. The experimentally observed roll pattern is however similar to the one reported by Kim and Viskanta (1984). Despite an overall similarity in the thermal fields between the simulation and the experiment, there is a degree of mismatch in the temperature contours as well as the point-wise temperature profiles (Figure B.2). Possible reasons can be traced to the fact that the boundary conditions in the experiment cannot match closely the simulation. Examples are non-uniformity of the surface temperatures, partially conducting side walls and three dimensionality of the convection pattern itself.

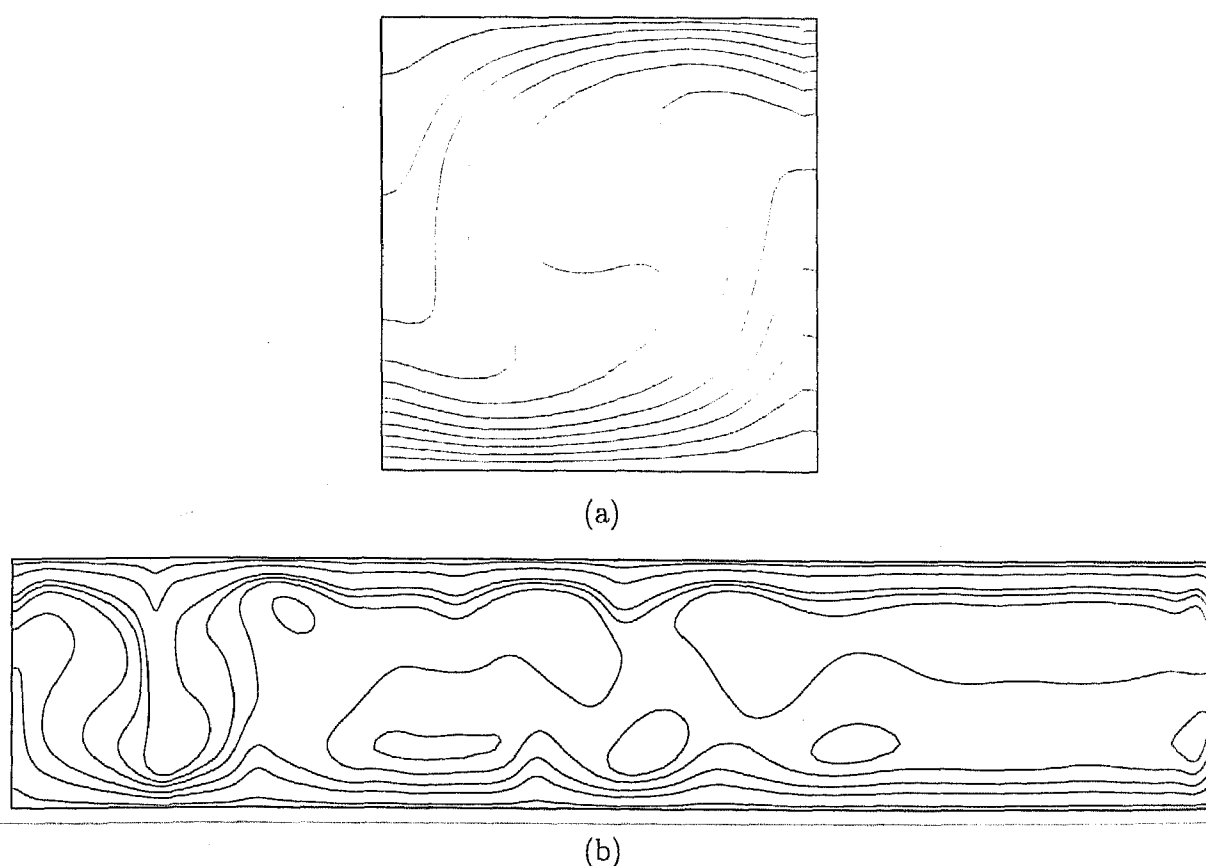
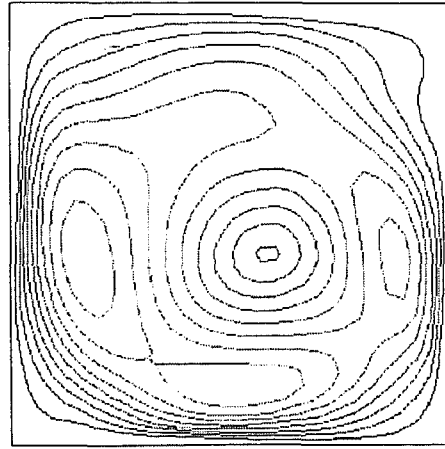


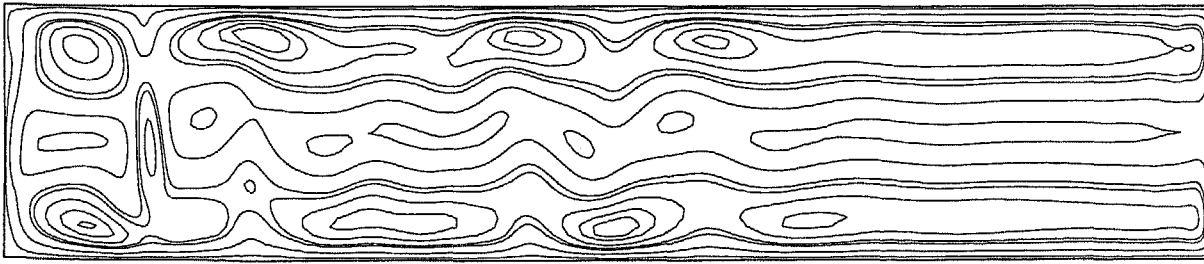
Figure B.3: Isotherms for depth-averaged temperature obtained in a three-dimensional simulation of convection in a cavity filled with air at (a) transverse and (b) longitudinal planes; Cavity temperature difference is 10 K.

The full three dimensional simulation of convection in a cavity filled with air was carried out in the rectangular box whose geometry was identical to that used in the experiment. Results have been presented on two sections that are symmetrically placed

perpendicular and parallel to the longer side wall of the cavity. It is worth recalling that in the experiments, the projection of the thermal field along the length of the box alone is recorded. The results of numerical simulation are presented in Figures B.3(a-b). On comparison, the results of two and three-dimensional simulation in terms of fringe patterns are seen to be similar on the transverse plane. A unicellular roll with its axis aligned parallel to the longer side of the cavity is obtained. No additional rolls were obtained on the longitudinal plane (Figure B.3(b)). The isotherms show the effect of three-dimensionality through periodically spaced closed loops along the length of the cavity. The corresponding velocity vectors shown in Figures B.4(a-b) confirm the absence of rolls in the longitudinal plane of the cavity.



(a)



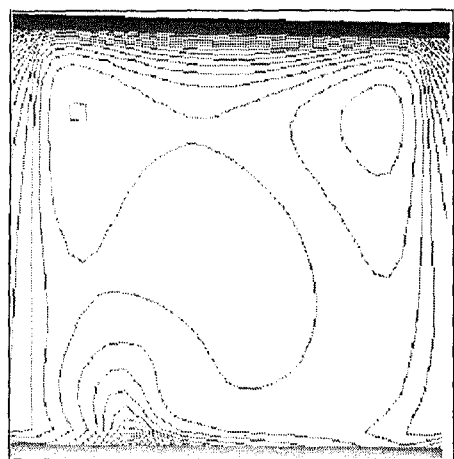
(b)

Figure B.4: Depth-averaged velocity field obtained in a three-dimensional simulation in a cavity full of air at (a) transverse and (b) longitudinal sections; Cavity temperature difference is 10 K.

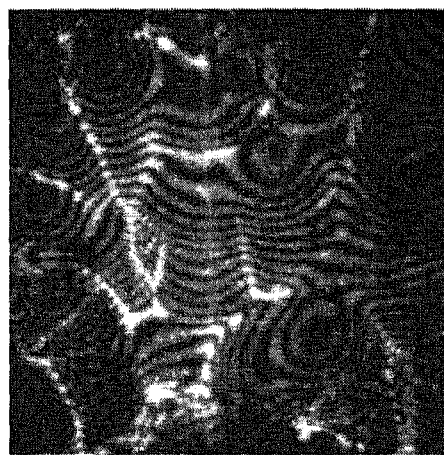
B.2.2 Convection in a water-filled cavity

Three-dimensional simulation of convection was carried out in a cavity filled with water for a temperature difference of 10 K. The isotherms have been presented in Figures B.5(a-c). The Rayleigh number for the present calculation was $1.7\text{E}+06$. Comparing

the simulated results of Figure B.5(a) on the transverse mid-plane with the experiments (Figure B.5(b)), it is observed that the isotherms are considerably deformed. Thus a vigorous state of convection is established in the cavity. The isotherms in Figure B.5 are to be interpreted as instantaneous snapshots. Dense fringes are obtained near the two walls indicating that the wall heat transfer has been significantly enhanced. The isotherms derived from simulation clearly show a three-dimensional convection pattern in the thermal field. This is confirmed by the presence of secondary closed rolls. No primary roll is to be seen in the cross-sectional plane of the cavity with a specific sense of rotation. On the longitudinal midplane (Figure B.5(c)), clear primary rolls are obtained with their axis aligned parallel to the short side walls of the cavity. These results can be confirmed from the velocity vector plots of Figure B.6.



(a)



(b)



(c)

Figure B.5: Comparison of isotherms obtained in simulation (a and c) and (b) experimental projection data; Cavity filled with water for an imposed temperature difference of 10 K. Temperature values for isotherms are equally spaced.

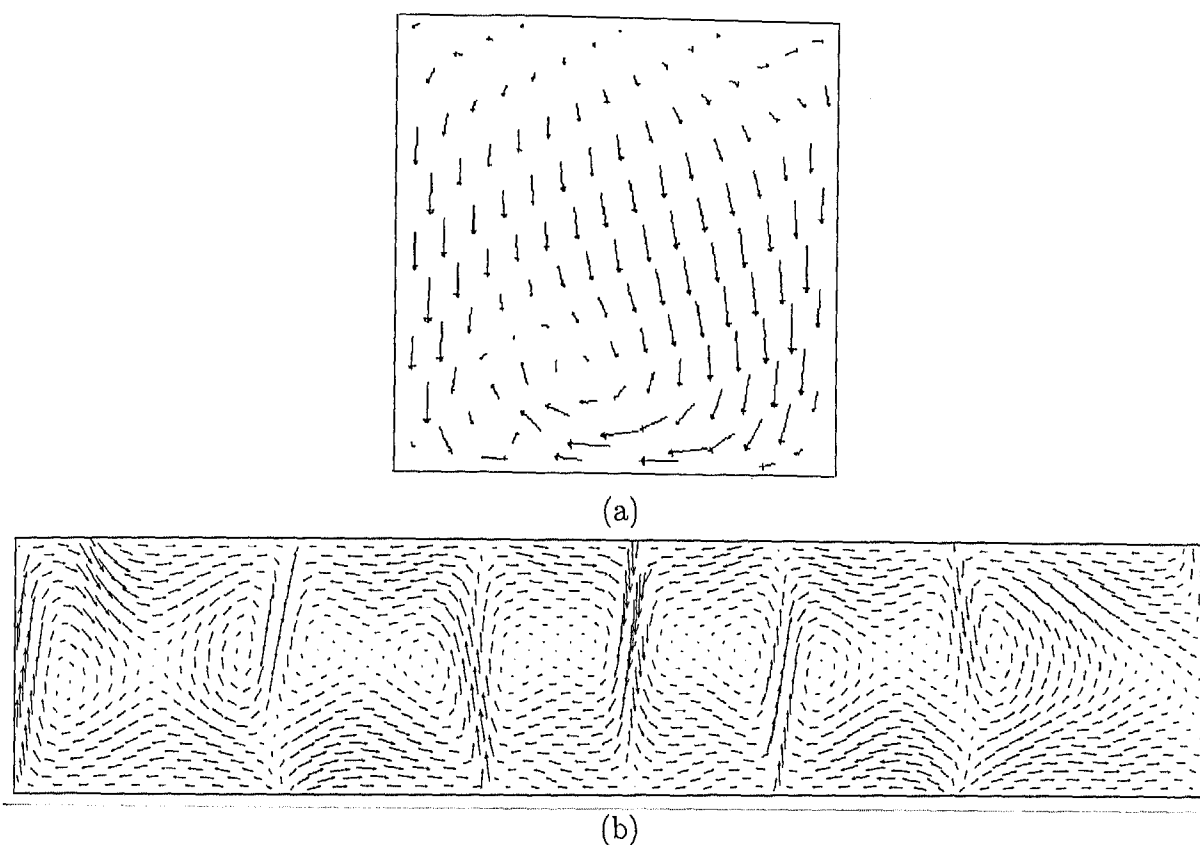


Figure B.6: Velocity vectors obtained in a three-dimensional simulation at (a) transverse and (b) longitudinal sections; Cavity filled with water for an imposed temperature difference of 10 K.

B.2.3 Convection in superposed air-water layers

Experiments as well as two dimensional simulation were carried out for convection in the cavity containing air and water layers of equal thickness⁴. Experiments have been performed in a rectangular box with a square cross-section as reported in Chapter 5. The simulation was carried out on a square cross-section with identical geometry and thermal boundary condition as in the experiments. Data for cavity temperature differences of 10, 15 and 18 K have been reported. In the experiments, the temperatures of the lower and the upper walls have been monitored by thermocouples, but other temperatures have to be determined from the interferograms. An important quantity that determines the nature of the flow field in the fluid layers is the interface temperature. For the three values of the cavity temperature difference, the interface temperature determined from the experiments, simulation and the correlation of Gebhart *et al.* (1988) are summarized in Table B.1. The overall agreement is quite satisfactory. The Rayleigh numbers in the individual phases range from 4000-7000 in air and 16000-42000 in water. The

⁴Owing to the large CPU time requirement, three dimensional calculations could not be performed.

corresponding average Nusselt numbers at the walls adjoining the horizontal walls of the cavity are summarized in Tables B.2 and B.3. The overall agreement in air is seen to be satisfactory. Larger discrepancies are seen in water, the correlation of Equation 4.27 over-predicting significantly the Nusselt number. The numerical prediction is however closer to the present experiments.

A direct comparison of the numerically computed isotherms with the experimental fringe patterns for the three cavity temperature differences is presented in Figures B.8(a-f). The temperature profiles obtained by the two approaches at selected columns of the cavity are shown in Figures B.9(a-c). While the two fields show similarity in certain respects, the overall conclusion to emerge from this comparison is that the predicted point-wise fields are quite different. The temperature drop in the water layer is small when compared to air, in view of their differing thermal conductivities. This result is seen in the computation as well as the experiment. The convective field predicted by the simulation is quite organized in the form of counter-rotating rolls in each layer. The number of rolls and their size are seen to change significantly in the experiments with the cavity temperature difference. Flow characteristics obtained in the experiments at the three temperature differences have been discussed in Chapter 5 (Section 5.1).

A direct comparison of numerically recorded isotherms with experimental interferograms has also been reported by Prakash and Koster (1996) and is reproduced in Figure B.7. The numerical calculations reported here are purely two dimensional. Experiments were conducted in a vertical cavity that was very thin in the viewing direction, corresponding to an Aspect ratio $A_z = 0.14$. The fluids considered were 100 cSt silicone oil ($Pr = 917$) floating over ethylene glycol ($Pr = 159$). The Rayleigh number range considered was such as to generate a steady flow field in the cavity. The numerical predictions were seen to match the experiments quite closely. For a lower range of Rayleigh numbers (Figure B.7(a)), the ascending plume in the lower fluid layer was accompanied by an ascending plume in the upper layer, indicating thermal coupling between them. These trends were seen in the numerical simulation at higher Rayleigh numbers as well. The interferograms of Figure B.7(b) at a higher Rayleigh number reveal oppositely oriented (multiple) rolls in the fluid layers, a sign of mechanical coupling. In this respect the comparison between the numerical calculations and experiments is inadequate.

In contrast to the work of Prakash and Koster (1996), the results presented in Figures B.8-B.10 are applicable for:

1. superposed fluid layers of air ($Pr = 0.71$) and water ($Pr = 6.1$),

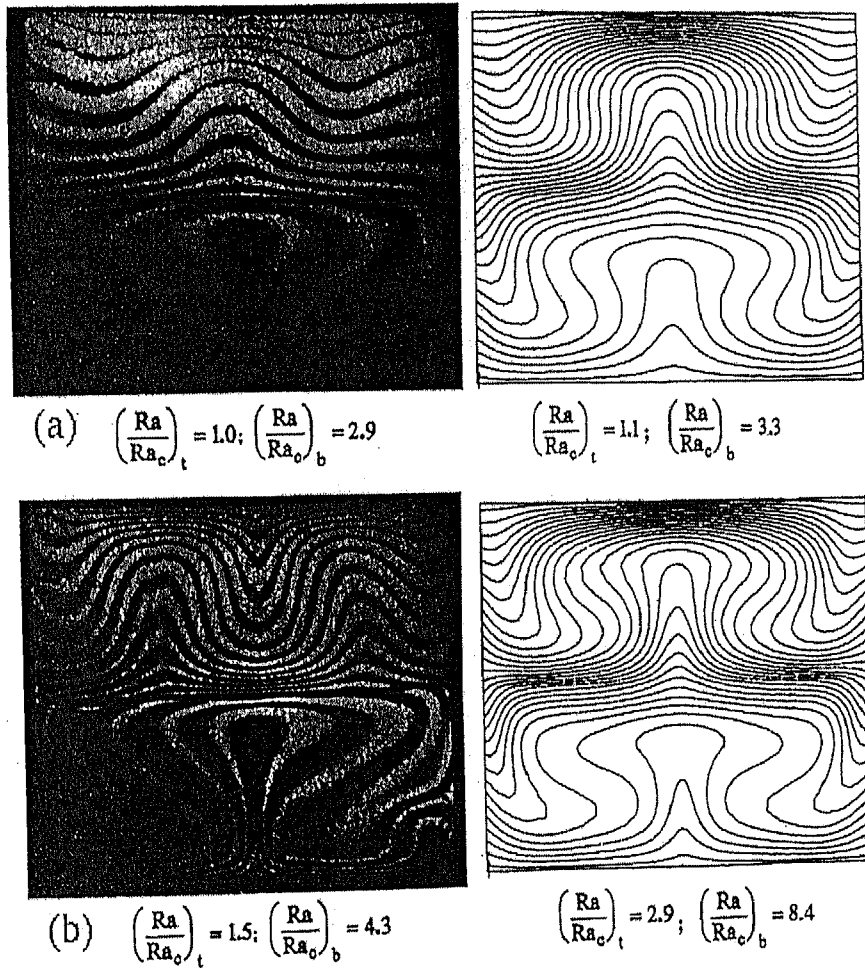


Figure B.7: Silicone oil 100 cSt over ethylene glycol; equal layer height: interferograms (left column) and numerical simulation (right column), after Prakash and Koster, 1996.

2. a higher range of Rayleigh numbers ($Ra/Ra_c|_{air} = 4.15$, $Ra/Ra_c|_{water} = 24.7$).
3. a cavity with a higher aspect ratio.

The numerical results consistently reveal mechanical coupling between the fluid layers. Experimentally, the nature of coupling is thermal since the roll pattern in air is seen to be unicellular, that in water being multi-cellular and three dimensional. To this extent, a two dimensional model has been invalidated in the present work.

Numerically generated velocity vectors and roll patterns for the three cavity temperature differences are presented below. The results have respectively been shown for three temperature differences in Figures B.10(a-b), B.10(c-d), and B.10(e-f). Velocity vectors and roll patterns in all three cases clearly indicate the two counter-rotating rolls in air as well as in water. They also depict that the ascending flow in air meets the

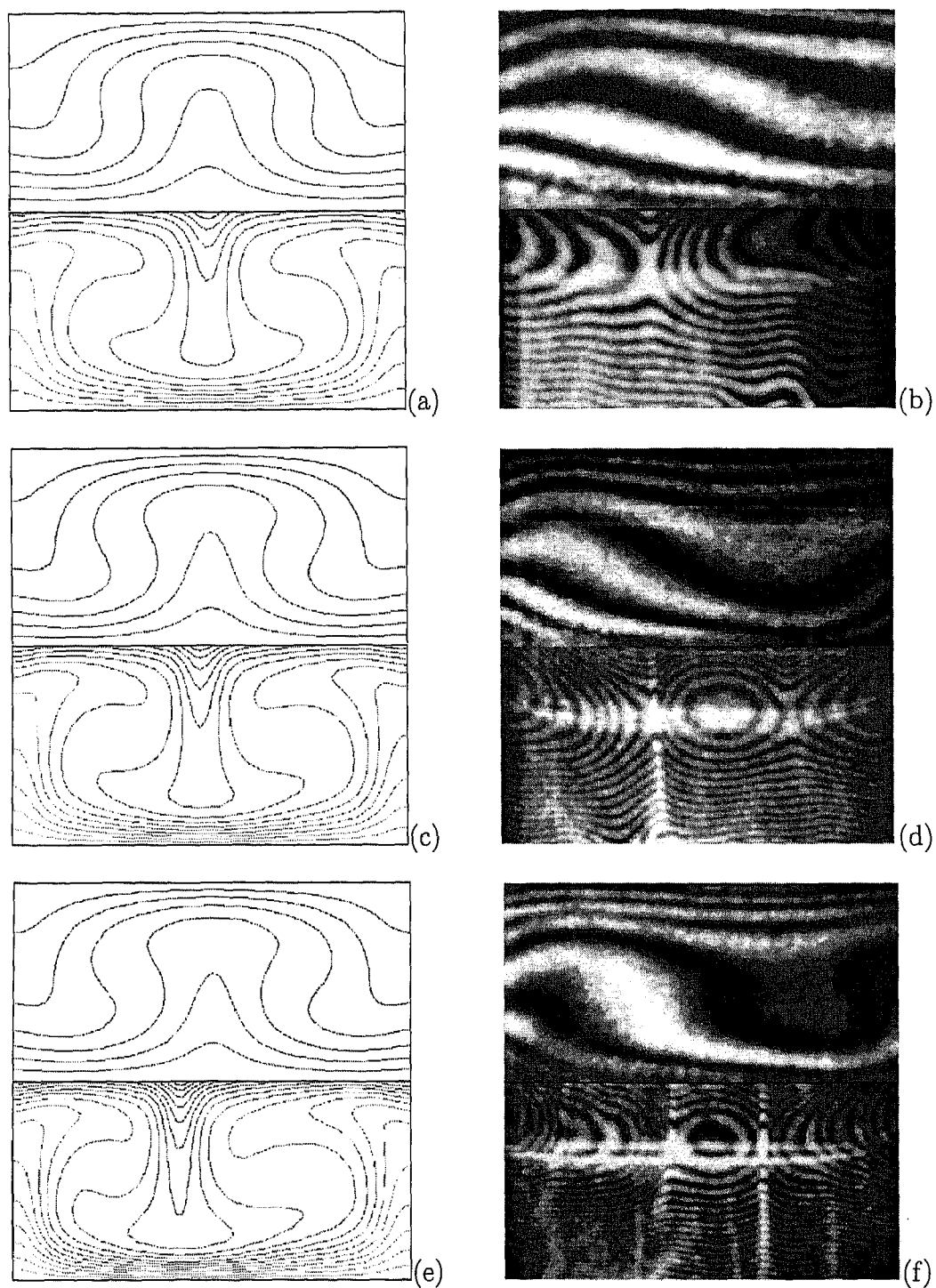


Figure B.8: Isotherms generated numerically (left column) and experimentally (right column) for cavity temperature differences of 10 K (a,b), 15 K (c,d), and 18 K (e,f). In numerical calculation, isotherms in air and water were generated step-by-step with a temperature increment of 1 K.

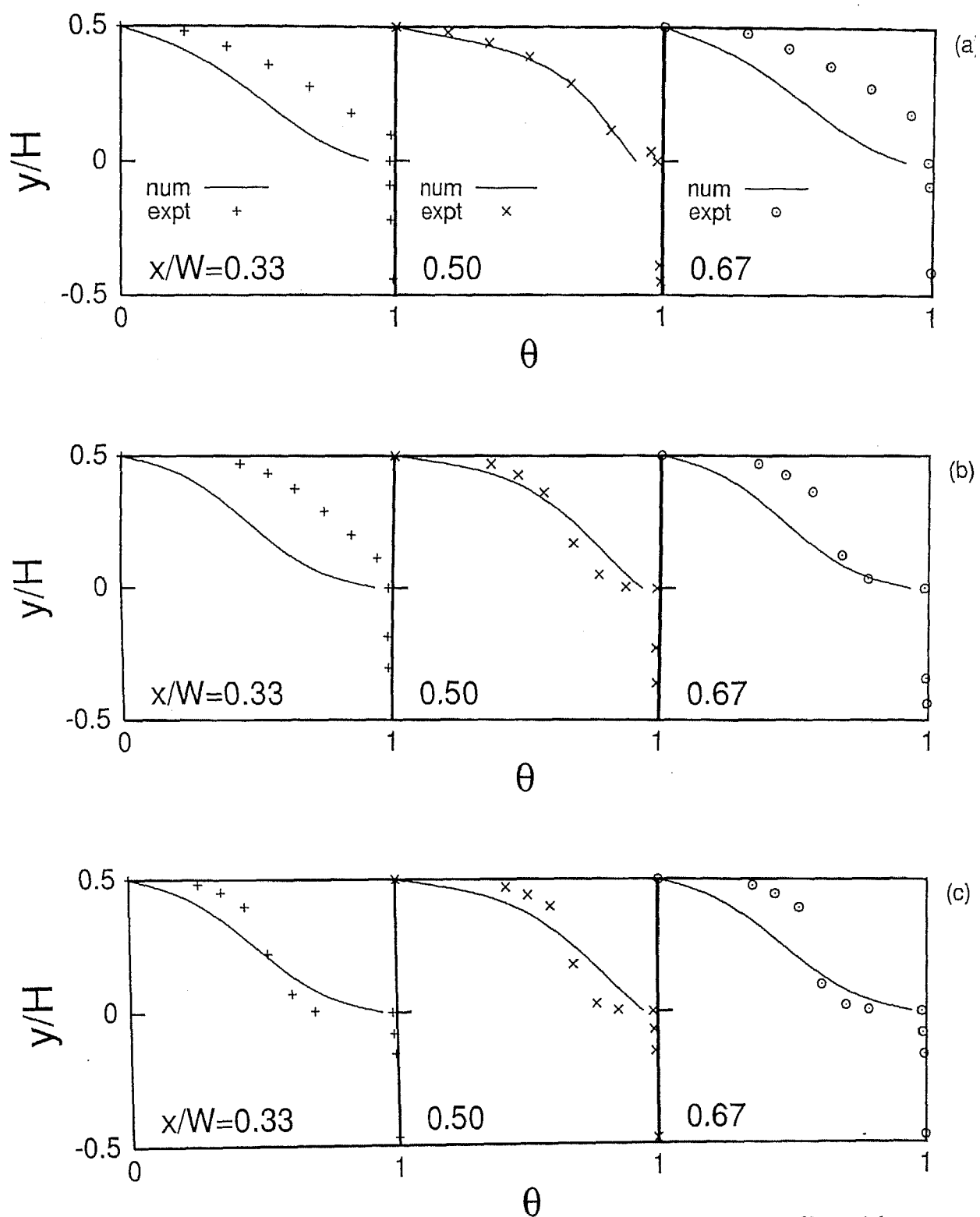


Figure B.9: Comparison of the experimentally obtained temperature profiles with numerical calculations at selected columns for a cavity half filled with water in air-water experiments; Cavity temperature differences are (a) 10 K, (b) 15 K, and (c) 18 K.

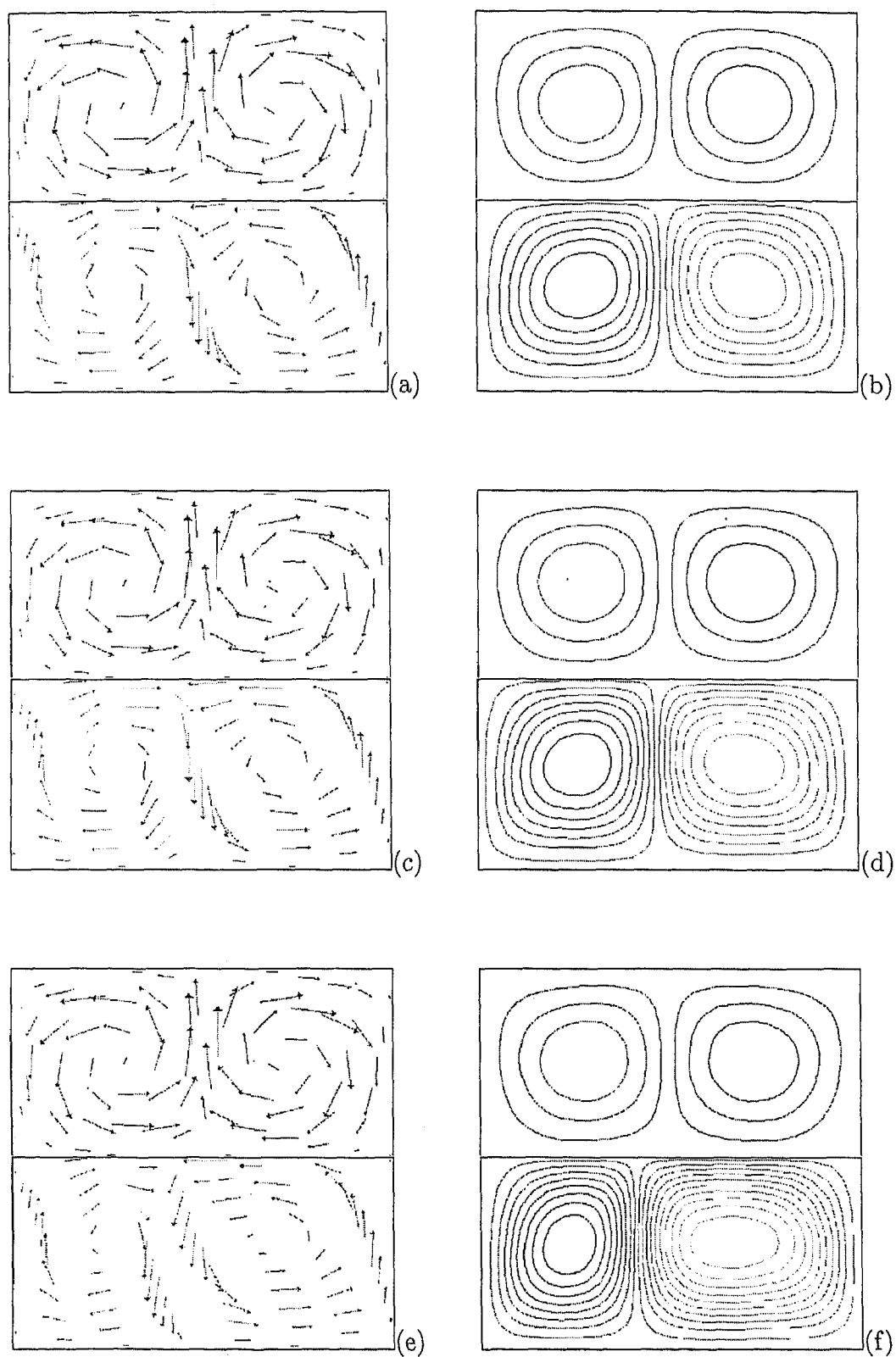


Figure B.10: Numerically generated velocity vectors (left column) and roll patterns (right column) for cavity temperature differences of 10 K (a,b), 15 K (c,d), and 18 K (e,f).

Table B.1: Comparison of the numerical and the experimental interface temperatures with Gebhart *et al.* (1988) (marked 'Reference') in a cavity containing layers of air and water of equal thickness.

ΔT , K	T_i , °C		
	Numerical	Experimental	Reference
10	25.68	25.82	25.79
15	30.49	30.80	30.70
18	33.38	33.72	33.64

Table B.2: Comparison of the Numerical and the Experimental average Nusselt numbers on the air-side with Gebhart *et al.* (1988) (marked 'Reference').

ΔT , K	Ra	Numerical	Experimental	Reference
10	4185	1.86	1.97	1.85
15	6044	2.15	1.94	2.04
18	7088	2.15	1.99	2.16

Table B.3: Comparison of the Numerical and the Experimental average Nusselt numbers on the water-side with Gebhart *et al.* (1988) (marked 'Reference').

ΔT , K	Ra	Numerical	Experimental	Reference
10	16,413	2.72	2.97	3.68
15	30,772	2.84	3.40	4.21
18	42,147	3.15	3.70	4.50

descending flow in water along the vertical axis at the center of the cavity near the interface. This indicates that the sense of rolls to be oppositely oriented and thus the two-layers are mechanically coupled at the interface. In this respect, the numerical and the experimental data are at variance with each other. From Figure B.10, it is also clear that the velocity vectors are continuous at the interface. This can be interpreted as follows: The layer just below the interface drags the layer above through the mechanism of viscosity, and thus a mechanical coupling at the interface is established. Numerical results showed that the maximum velocities increased from 2.1 cm/s to 3.5 cm/s in air, and from 0.058 cm/s to 0.08 cm/s in water, for an increase in ΔT from 10 K to 18 K. This indicates that the increase in kinetic energy due to buoyancy forces is higher in air as compared to water. It is consistent with a higher temperature drop in air when compared to water. An interesting feature was noticed in the simulated roll pattern developed in the water phase. As the temperature increased from 10 K to 18 K

strength of convection increased on the right side, while it has decreased on the left side. Thus the pattern developed asymmetry with respect to the central vertical axis of the cavity for higher temperature differences.

B.2.4 Deformation of the air-water interface

The change in the shape of the interface with increasing temperature differences across the two walls has been presented in this section. The numerical plots are based on the surface tension formulation of Section B.1.1, also discussed by Edwards *et al.* (1991). They have been compared with the experimentally recorded interface shapes. The comparison is shown in Figure B.11. Experimental results are depicted in the form of a shadowgraph, in which only one light beam of the interferometer was used. The experimental images in Figure B.11 show only the water layer where its free surface gets deformed continuously with an increasing temperature difference.

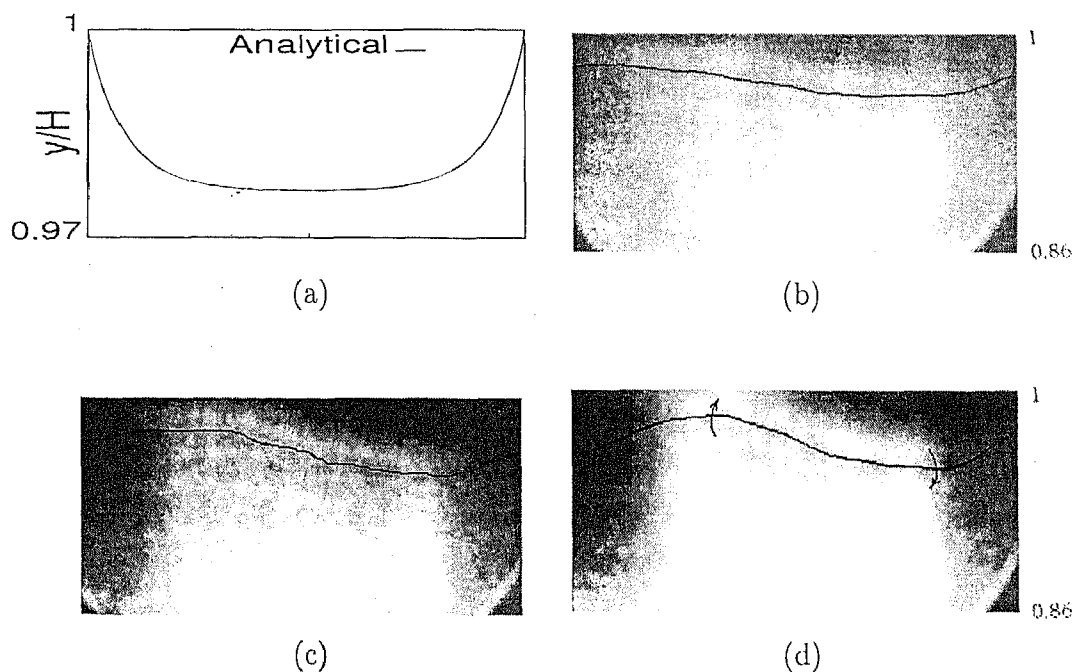


Figure B.11: Experimentally recorded air-water interface shapes at cavity temperature differences of $\Delta T = 10$ K (b), 15 K (c) and 18 K (d) and comparison with the analytic model (a).